

Wayan Suparta
Mardina Abdullah
Mahamod Ismail *Editors*

Space Science and Communication for Sustainability

 Springer

Space Science and Communication for Sustainability

Wayan Suparta · Mardina Abdullah
Mahamod Ismail
Editors

Space Science and Communication for Sustainability

 Springer

Editors

Wayan Suparta
Department of Electrical Engineering
Sanata Dharma University
Yogyakarta
Indonesia

Mardina Abdullah
Institute of Climate Change, Space Science
Centre
Universiti Kebangsaan Malaysia
Bangi
Malaysia

Mahamod Ismail
Department of Electrical, Electronic and
Systems Engineering, Faculty of
Engineering and Built Environment
Universiti Kebangsaan Malaysia
Bangi
Malaysia

ISBN 978-981-10-6573-6 ISBN 978-981-10-6574-3 (eBook)
<https://doi.org/10.1007/978-981-10-6574-3>

Library of Congress Control Number: 2017952532

© Springer Nature Singapore Pte Ltd. 2018

This work is subject to copyright. All rights are reserved by the Publisher, whether the whole or part of the material is concerned, specifically the rights of translation, reprinting, reuse of illustrations, recitation, broadcasting, reproduction on microfilms or in any other physical way, and transmission or information storage and retrieval, electronic adaptation, computer software, or by similar or dissimilar methodology now known or hereafter developed.

The use of general descriptive names, registered names, trademarks, service marks, etc. in this publication does not imply, even in the absence of a specific statement, that such names are exempt from the relevant protective laws and regulations and therefore free for general use.

The publisher, the authors and the editors are safe to assume that the advice and information in this book are believed to be true and accurate at the date of publication. Neither the publisher nor the authors or the editors give a warranty, express or implied, with respect to the material contained herein or for any errors or omissions that may have been made. The publisher remains neutral with regard to jurisdictional claims in published maps and institutional affiliations.

Printed on acid-free paper

This Springer imprint is published by Springer Nature
The registered company is Springer Nature Singapore Pte Ltd.
The registered company address is: 152 Beach Road, #21-01/04 Gateway East, Singapore 189721, Singapore

Preface

This book highlights the field of space science and communications. This field is one of the pillars of sustainable development from the study of Earth Sciences to the form of space science. Research and development (R & D) in this field plays a crucial role in sustainability development. The space issue is always relevant. Obtaining essential data from the physical world to interpret the universe and to predict what will happen in the future is very challenging. Valid information to understand trends, evaluate needs, and create sustainable development policies and programs in the best interest of all people is indispensable.

This book discusses in detail the latest application of space science and space technology as summarized in the working group of space science and communication. In this working group, some modern systems with high accuracy have been explored to enhance their capability to work in the vast atmosphere from the Earth's surface to the development of antennas for the study of space science.

This contributed volume presents 28 selected papers from the 2017 International Conference on Space Science and Communication (*IconSpace2017*). The book is divided into three scientific sections: (i) Atmospheric Physics, (ii) Environmental Sciences and Remote Sensing, and (iii) Communication Systems and Space Technology. It is addressed to professors, postgraduate students, scientists and engineers who are taking part in R & D in areas such as meteorological applications, environmental monitoring, space weather, and materials for antenna systems based on wide applications in various fields of science and technology.

Yogyakarta, Indonesia

Wayan Suparta

Contents

Characterization of Lightning Energy During Summer and Winter of 2014–2015 Over the Antarctic Peninsula	1
Wayan Suparta and Siti Khalijah Zainudin	
Parametric Studies of ANFIS Family Capability for Thunderstorm Prediction	11
Wayan Suparta and Wahyu Sasongko Putro	
Performance and Evaluation of Eight Cloud Models on Earth—Space Path for a Tropical Station	23
Temidayo Victor Omotosho, Oladimeji Mustapha Adewusi, Marvel Lola Akinyemi, Sayo Akinloye Akinwunmi, Oluwafumilayo Oluwayemisi Ometan and Williams A. Ayara	
Comparison of In situ Observation, NOAA-AIRS Satellite and MACC Model on Surface Ozone Over the Ushuaia, Southern Ocean and Antarctic Peninsula Region	37
M.S.M. Nadzir, M.F. Khan, W. Suparta and S.K. Zainudin	
A Brief Review: Response of the Ionosphere to Solar Activity Over Malaysia	47
Siti Aminah Bahari and Mardina Abdullah	
The Time Derivative of the Horizontal Geomagnetic Field for the Low Latitude MAGDAS Langkawi Station for the Estimation of Geomagnetically Induced Current	57
Farah Adilah Mohd Kasran, Mohamad Huzaimy Jusoh, Akimasa Yoshikawa, Zahira Mohd. Radzi and MAGDAS/CPMN Group	
Comparison of Measured and Predicted HF Operating Frequencies During Low Solar Activity	73
Rafidah Abd Malik, Mardina Abdullah, Sabirin Abdullah and Mariyam Jamilah Homam	

Ionospheric TEC Response to the Partial Solar Eclipse Over the Malaysian Region	87
Rohaida Mat Akir, Mardina Abdullah, Kalaivani Chellappan and Siti Aminah Bahari	
Effect of Geomagnetic Storms on Fluctuations of Total Electron Content at an Equatorial Station	97
Siti Zainab Hamzah and Mariyam Jamilah Homam	
Analysis of Critical Frequency Measured from Ionosonde System During Low Solar Activity in Malaysia Region	109
Sabirin Abdullah and Ahmad Faizal Mohd Zain	
Comparison Between UKMtrapcast and SPENVIS in Forecasting Distribution of High Energy Protons in the SAA Region	121
Gusrizal, Wayan Suparta and Karel Kudela	
Space Weather Monitoring System Competition for Secondary School Students in Malaysia	135
Mardina Abdullah, Rosadah Abd Majid, Badariah Bais, Nor Syaidah Bahri and Mohd Hezri Mokhtar	
Current Status of Radio Astronomy in University of Malaya	147
Zamri Zainal Abidin and Zainol Abidin Ibrahim	
GPS PWV and Its Response to ENSO Activities in the Western Pacific Region During 2009–2011	157
Wayan Suparta, Ahmad Iskandar and Ford Lumban Gaol	
Impact of Sea Level Rise on the Coastal Ecosystem	173
Khairul Nizam Abdul Maulud, Fazly Amri Mohd, Wan Hanna Melini Wan Mohtar, Othman Jaafar and Yannie Anak Benson	
Manifestation of SVM-Based Rectified Linear Unit (ReLU) Kernel Function in Landslide Modelling	185
Biswajeet Pradhan and Maher Ibrahim Sameen	
Subsurface Structural Pattern Distributions of the Magnetic Anomalies in Part of the Nigerian South-Western Precambrian Basement Complex for Sustainability	197
John Stephen Kayode, Mohd Nawawi Mohd Nordin and Khiruddin Abdullah	
The Measurement of Solar Ultraviolet Ambient Dose Using EBT3 Film	213
Intan Nadia Mohammad Saleh, Ummi Shuhada Osman and Ahmad Fairuz Omar	

Open Platform Orbit Determination Systems Using a Mixture of Orbit Estimator and Orbit Propagator 223
 Hilmi Sanusi and Wayan Suparta

Deployment Challenges and Co-tier Interference Management Techniques for Ultra-dense Femtocell Networks 239
 Ibrahim Shgluof, Mahamod Ismail, Rosdiadee Nordin,
 Nor Fadzilah Abdullah and Azizul Azizan

Design and Analysis of an Optimized S-shaped Resonator Based Triple Band Microstrip Antenna for Satellite Applications 253
 Md. Naimur Rahman, Gan Kok Beng, Md. Samsuzzaman, Touhidul Alam
 and Mohammad Tariqul Islam

Negative- μ Metamaterial-Based Stacked Antenna for 1U CubeSat Communication 265
 Farhad Bin Ashraf, Touhidul Alam, Mengu Cho, Norbahiah Misran
 and Mohammad Tariqul Islam

Performance Analysis of an X-Band Circular Polarized Antenna for Nanosatellite Communication 275
 Touhidul Alam, Mandeep Singh Jit Singh, Mengu Cho
 and Mohammad Tariqul Islam

A Reflector Type 3D Triband Directional Antenna for CubeSat Applications 285
 Md. Amanath Ullah, Farhad Bin Ashraf, Touhidul Alam,
 Mohd Tarmizi Ali and Mohammad Tariqul Islam

An Effective Medium Ratio Obeying Wideband Left-Handed Meta-Atom for Multiband Applications 295
 Mohammad Jakir Hossain, Mohammad Rashed Iqbal Faruque
 and Mohammad Tariqul Islam

A Terahertz Meta-Surface with Left-Handed Characteristics for Absorbing Applications 305
 Md. Mehedi Hasan, Mohammad Rashed Iqbal Faruque
 and Mohammad Tariqul Islam

Microstrip Feed Slotted Ground Antenna with Parasitic Element for UWB Applications 317
 Girish Awadhwal and Ali Bostani

Bee-Comb-Shape Left-Handed Metamaterial for Terahertz Application 339
 Md. Mehedi Hasan, Mohammad Rashed Iqbal Faruque,
 Mohammad Tariqul Islam and Sikder Sunbeam Islam

Characterization of Lightning Energy During Summer and Winter of 2014–2015 Over the Antarctic Peninsula

Wayan Suparta and Siti Khalijah Zainudin

Abstract The aim of this paper is to characterize the lightning energy over the Antarctic Peninsula through the distribution of PWV, precipitation rate and the events that occur. Calculation of PWV is made by using a two-year-period of surface meteorological data (pressure, temperature, and relative humidity) and data during summer and winter are analyzed. To strengthen the analysis, data for the precipitation rate and events with the most lightning strike occurrence in the summer and winter during the daytime were compared. Analysis showed that lightning strikes mostly occur during the winter morning with an average energy of 8,120.46 J. PWV distribution on the map showed that the value of PWV is high at locations where there is a higher concentration of lightning strikes. There are also increases of precipitation rate a few hours before and after the events along with the occurrence of snow, rain, and fog.

1 Introduction

Antarctica is located at the South Pole, at latitudes between 60°S to 90°S and longitudes of 180°W to 180°E which contribute to its extreme conditions of low temperature and precipitation. The presence of precipitation events is accompanied by the discharge of electricity when the thundercloud releases its excess electrical

W. Suparta (✉) · S.K. Zainudin
Space Science Centre (ANGKASA), Institute of Climate Change, Universiti Kebangsaan Malaysia, 43600 Bangi, Selangor Darul Ehsan, Malaysia
e-mail: wayan@ukm.edu.my; drwaynesparta@gmail.com

W. Suparta
National Antarctic Research Center (NARC), University of Malaya, 50603 Kuala Lumpur, Malaysia

W. Suparta
Dept of Electrical Engineering, Sanata Dharma University, Yogyakarta 55282, Indonesia

charge. Most lightning strikes occur in tropical areas and formations of thunderstorms are very few in Antarctica to the point that almost nothing happens. However, a lightning strike was recorded on a Sunday morning at Casey station. Before the strike, there was a period of intense low pressure with gale-force winds and blizzards, followed by a thunderstorm half an hour later [1].

At the South Pole, summer begins in December and ends in February and fall comes in between March and May. Winter occurs from June until August while spring occurs from September to November. The highest temperature was 17.5 °C which was recorded at Hope Bay, Antarctic Peninsula while the lowest temperature of -89.2 °C was recorded at Vostok station in 1983 [2]. More recently, Vizcarra [3] reported a lowest temperature of -92 °C to -94 °C as obtained from the National Snow and Ice Data Center (NSIDC). However, the specific process and measurements of the drastic changes in temperature are still unknown.

The aim of this paper is to study the meteorological characteristics during the event of a lightning strike in summer and winter over the Antarctic Peninsula from 2014 to 2015. This will highlight whether lightning occurs due to extreme temperatures or as a result of another meteorological parameter. The results obtained will be beneficial in improving weather forecasting.

2 Methodology

2.1 Data and Location

The meteorological data (pressure, temperature and relative humidity) were obtained from the British Antarctic Survey (BAS) at <https://legacy.bas.ac.uk/cgi-bin/metdb-form-1.pl>, while the lightning data were obtained from the World Wide Lightning Location Network (WWLLN). The precipitation rate was taken from two sources, which were Global Precipitation Measurement (GPM) and NASA Tropical Rainfall Measurement Mission (TRMM). These can be found at the Goddard Earth Sciences Data and Information Services Center. The main source of data was GPM, however, data for 2014 were lacking. Hence, data from TRMM was used to complete the missing data. On the other hand, the precipitation events were obtained from Weather Underground at <https://www.wunderground.com/>.

The meteorological data used for this study were collected from Base San Martin, Base Marambio, Bernardo O'Higgins, Butler Island, Carlini Base (formerly known as Base Jubany), Fossil Bluff, Palmer and Rothera stations. These stations are located in the Antarctic Peninsula. Figure 1 shows the locations of the meteorological stations (red circle) and lightning sensors (blue triangle) while the geographical coordinates of the meteorological stations are listed in Table 1. The lightning and precipitation rate data were collected from an area at latitudes of 59°E to 80°E and longitudes of 53°S to 86°S. Weather Underground provided the precipitation events at Marambio, O'Higgins, Carlini, Fossil Bluff, Palmer, and

Fig. 1 Location of meteorological stations and WWLN lightning sensors on the Antarctic Peninsula

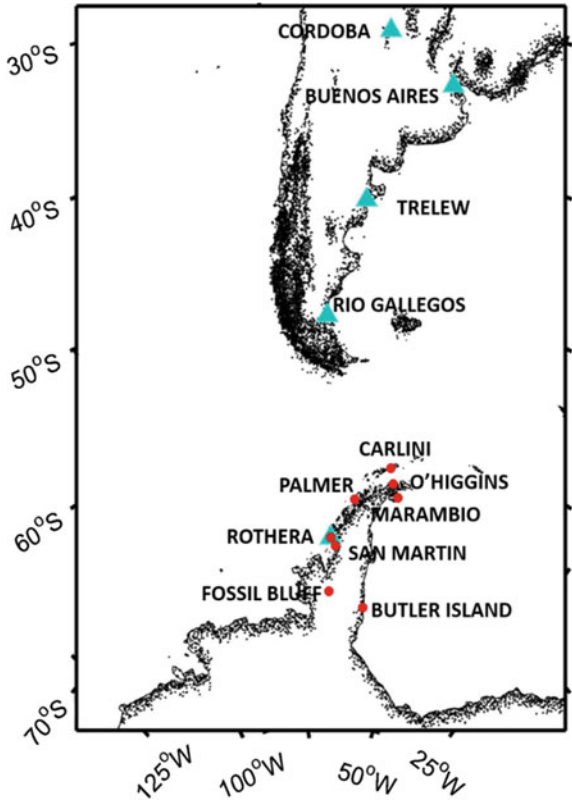


Table 1 Locations of selected meteorology stations on the Antarctic Peninsula

Station name	Latitude (°S)	Longitude (°W)	Elevation (m)
Base San Martin	68.12	67.13	4
Base Marambio	64.23	56.72	198
Bernardo O'Higgins	63.32	57.90	10
Butler Island	72.21	60.17	205
Carlini	62.23	58.63	4
Fossil Bluff	71.32	68.28	55
Palmer	64.77	64.08	8

Rothera. The Rothera station (67.57°S, 68.13°W), which is the only sensor located on the Antarctic Peninsula and four other sensors located in Argentina provided the data from lightning sensors. All data were collected over two years and were then categorized into summer or winter seasons.

2.2 Data Processing

The Adaptive Neuro-Fuzzy Inference System (ANFIS) developed by Suparta and Kemal [4] was employed to calculate Zenith Path Delay (ZTD). The surface meteorological data (pressure, temperature, and relative humidity) collected were used as an input to the system. The meteorological data were also used to calculate PWV by using a modified calculation of PWV from GPS developed by Suparta et al. [5]. The PWV were then plotted on a map using an R program [6]. The R program was used to describe the distribution of PWV during lightning events. WWLLN used very low-frequency receivers around the globe in order to observe lightning. Hence, the selected lightning data from WWLLN were plotted on the map using Matlab in order to observe the densest area of lightning strikes on the Antarctic Peninsula during summer and winter. The year with the most lightning strikes in summer and winter is characterized by its meteorological conditions.

3 Result and Discussion

3.1 Lightning Strike

The energy that the lightning produced varied in summer and winter with an average difference of 5,829.68 J. There were 73 lightning strikes recorded in 2014 while a total of 103 lightning strikes was recorded in 2015. In summer and winter alone, a total of 32 and 53 strikes were recorded in 2014 and 2015 respectively. A comparison of lightning energy between summer and winter is shown in Table 2.

A single lightning strike can produce energy from below 10 J to above 400,000,000 J. The highest energy produced by a lightning strike occurred in winter with an energy of 97,457.11 J or ten times more than the highest strike in summer. Based on Table 2, it can be seen that lightning strikes in the Antarctic Peninsula area occurred more often during the winter than the summer. In 2014, the number of lightning strikes during summer and winter differed by 25% while there was a difference of 54.72% in lightning strikes between the two seasons in 2015. Figure 2 shows the lightning strikes in summer and winter.

As shown in Fig. 2, during summer, lightning strikes (green square) can be seen at and near the coastal area, while during winter the strikes (blue star) are concentrated in the ocean area. 52.94% of the total lightning strikes during the summer

Table 2 The means of lightning energy and strike counts in summer and winter

Year	Mean energy (J)		Lightning count	
	Summer	Winter	Summer	Winter
2014	809.05	7,650.65	12	20
2015	3,772.51	8,590.27	12	41
Total	4,581.56	16,240.92	24	61

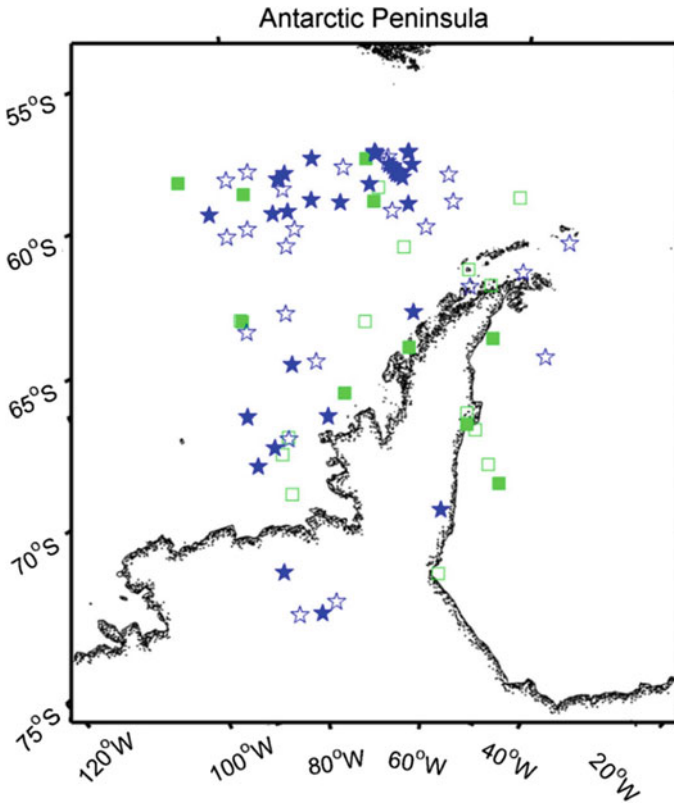


Fig. 2 Scattering of lightning strikes in summer and winter represented by a green square (□) and blue star (☆), respectively

and winter of 2014–2015 had more than 1,000 J of energy, as represented by the shaded/colored squares and stars in Fig. 2. The majority of high energy lightning strikes occurs over the sea rather than on the land.

3.2 Lightning Strike and PWV

Figures 3 and 4 show the mapped comparison of PWV and lightning strikes over the Antarctic Peninsula during summer and winter of 2014 and 2015.

Figures 3a and 4a, show the distribution of PWV across the Antarctic Peninsula in summer and winter while Figs. 3b and 4b show the spread of lightning strike locations with a blue circle for the energy of lightning strike produced below 1,000 J and a red circle for the energy of the lightning strike produced being equal to or above 1,000 J during summer and winter of 2014–2015. In Fig. 3a,

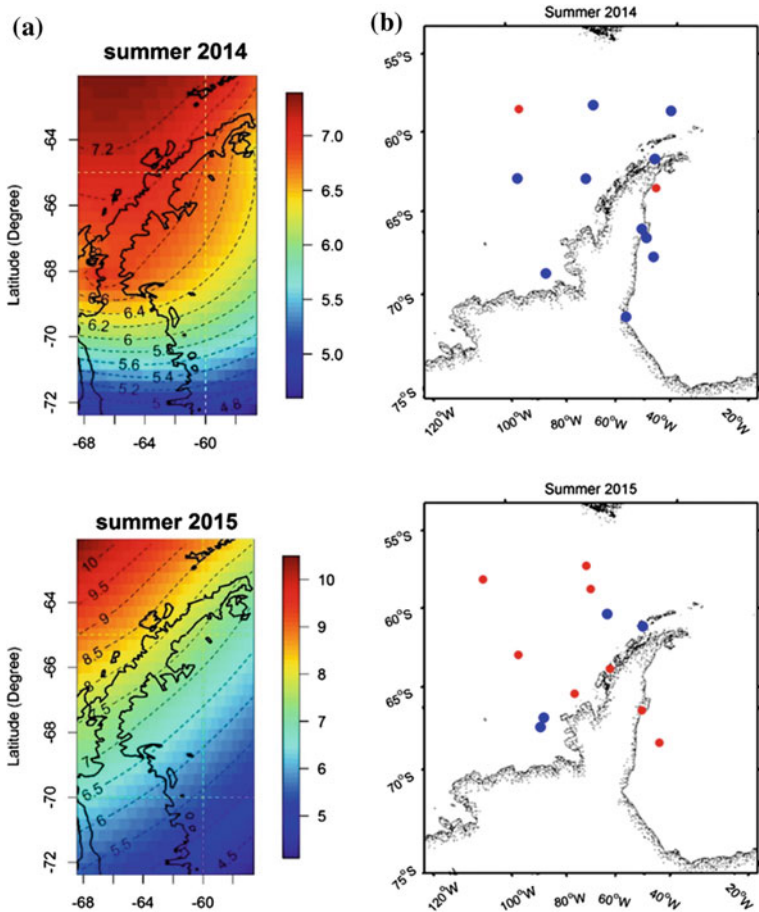


Fig. 3 The mapping shows the **a** distribution of PWV in summer, **b** location of lightning strikes in summer

the distribution of PWV across the Antarctic Peninsula had a maximum value of about 7.2 mm in 2014, while in 2015 the PWV value reached 9.0 mm. Figure 3b shows that in 2014, the energy of the lightning strikes that were equal to or above 1,000 J was lower compared to during 2015 where there was a wider spread of strikes at the coast and at sea.

Figure 4a shows the winter distribution of PWV across the Antarctic Peninsula while Fig. 4b shows the scattering of strikes which mainly occurred at the sea. Compared to the Fig. 3b, the spread of the strikes is a lot larger. However, the mapping of PWV distribution is lower only reaching 6.5 mm in 2014 and 4.2 mm in 2015.

When Figs. 3a and 4a (PWV map) are compared with Figs. 3b and 4b (scatter of strikes), it can be seen that as more energy was produced by the strike (red circle),

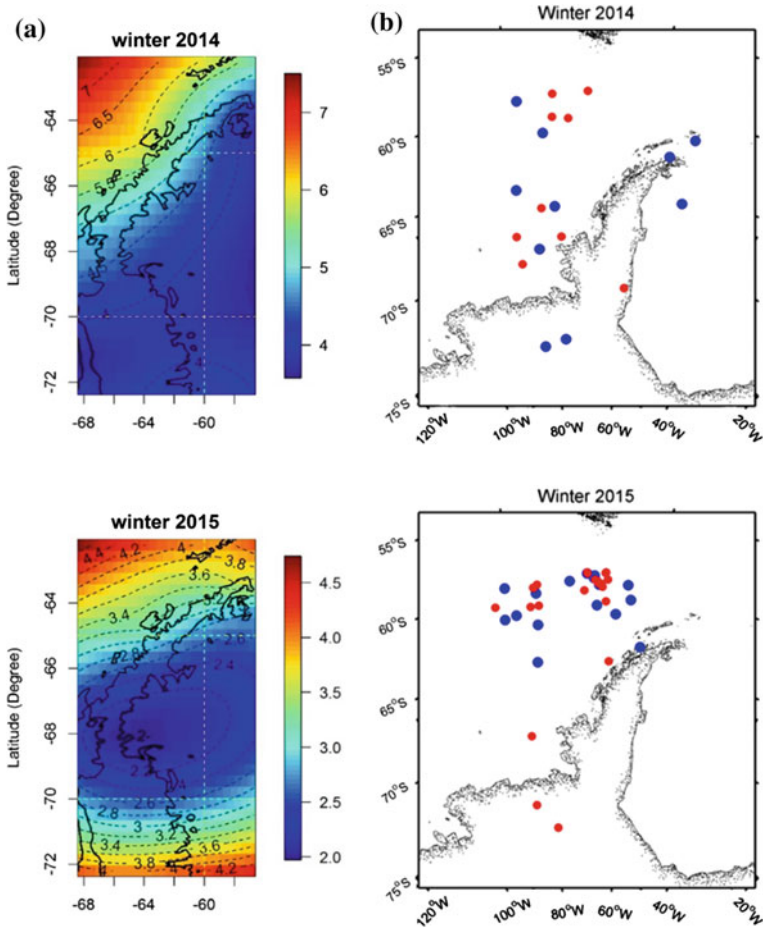


Fig. 4 The mapping shows **a** the distribution of PWV in winter and **b** location of lightning strikes in winter

the distribution of PWV also increased. From Fig. 3 (summer season), it can be seen that as the count of the lightning strikes and the energy produced by the strikes increased, the PWV value also increased. However, in the case of Fig. 4 case (winter season), although there is a higher count of lightning strikes and energy produced compared to summer, the PWV value decreased as can be seen in Fig. 4 Winter 2014 and Fig. 4 Winter 2015.

The highest count of lightning strikes in a single day during winter was on 6th August 2015. On the 3rd and 4th February 2015 (summer), lightning strikes were recorded two days in a row and fewer than 11 h apart. The precipitation rate and lightning events on 3rd and 4th February 2015 are depicted in Fig. 5. The figure compares the hourly precipitation rate recorded on 3rd and 4th February 2015 (Fig. 5a) with that on 6th August 2015 (Fig. 5b). Here, it can be seen that at each

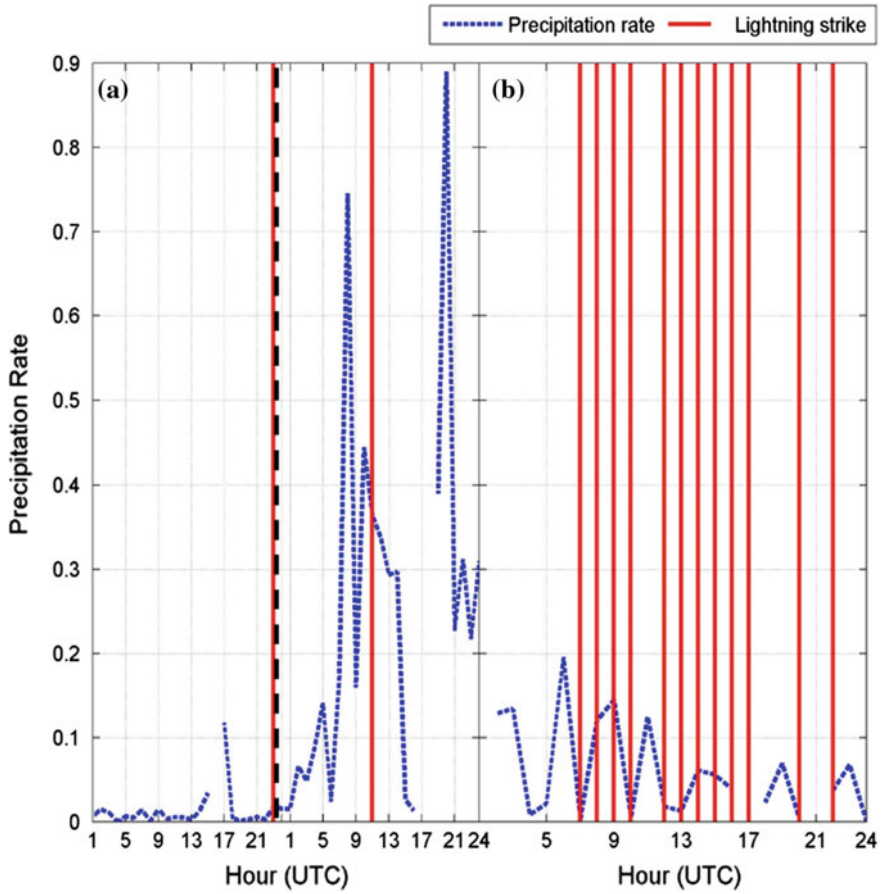


Fig. 5 **a** Hourly precipitation rate and lightning strikes in summer and **b** Hourly precipitation rate and lightning strikes in winter

Table 3 A 3-hour event during summer (3rd–4th February 2015) and winter (6th August 2015)

Season	Time date		12	3	6	9
Summer	3–Feb–2015	AM	Snow	Snow	Snow	Snow
		PM	Rain	Fog	Fog	Rain
	4–Feb–2015	AM	–	Snow	Fog	–
		PM	–	Fog	–	–
Winter	6–Aug–2015	AM	Snow	Fog-Rain	Snow-Rain	Snow
		PM	Snow	Snow	Snow-Rain	Snow

lightning strike, there were changes in precipitation rate before and after the strike. The average daily precipitation rate was 0.01 mm/day, 0.24 mm/day and 0.04 mm/day for 3rd and 4th February 2015 and 6th August 2015 respectively.

Although there was only one lightning strike recorded on 4th February, the precipitation rate on that day was high, reaching a total of 9.22 mm.

3.3 *Precipitation Rate and Event*

Table 3 shows the events that occurred on the days in summer and winter with the most lightning strikes. The events are characterized every 3 h. On 3rd February the events that occurred were mostly snow followed by rain and fog while the events that occurred on 4th February were mostly snow followed by fog, with the absence of rain. Conditions were clear with a light haze on that day. On the other hand, the events on 6th August were mostly snow with a bit of rain and fog that occurred in the morning and evening.

4 Conclusion

Lightning occurred on the Antarctic Peninsula at a 43.53% higher rate during the winter than the summer. Most lightning strikes occurrences were concentrated above the Antarctic Peninsula around South America. The PWV distribution showed similar results. Most lightning strikes occurred in the morning during summer and winter, particularly between 05:00–07:00 in the morning during the winter season. The findings of this study highlight the fact that the Antarctic Peninsula is also affected by lightning activities and the coverage of the affected area of the lightning strikes during summer and winter was the same in 2014 as that in 2015. Further studies on lightning in Antarctic Peninsula still need to be undertaken, mainly regarding the distribution of other meteorological factors such as pressure, cloud, and the wind with the distribution of lightning strike to justify the finding in this study.

Acknowledgements This work is supported by MOSTI Flagship Program, under the ZF-2014-016 grant. The meteorological data were provided by BAS. The meteorological data were provided by BAS. We would also like to thank the NASA Tropical Rainfall Measurement Mission (TRMM) for the data and acknowledge the Giovanni online data system. Analyses used in this paper were produced with the Giovanni online data system, developed and maintained by the NASA GES DISC.

References

1. Australian Antarctic Division (2011) A day for the records web, 4 Mar 2016. <http://www.antarctica.gov.au/living-and-working/stations/casey/this-week-at-casey/2011/this-week-at-casey-23-December-2011/1>

2. Petit JR, Jouzel J, Raynaud D, Barkov NI, Barnola JM, Basile I, Bender M, Chappellaz J, Davis M, Delaygue G, Delmotte M, Kotlyakov VM, Legrand M, Lipenkov VY, Lorius C, Pepin L, Ritz C, Saltzman E, Stievenard M (1999) Climate and atmospheric history of the past 420,000 years from the Vostok ice core, Antarctica. *Nature* 399:429–436
3. Vizcarra N (2013) Landsat 8 helps unveil the coldest place on Earth, National Snow and Ice Data Center. Accessed 27 Dec 2016
4. Suparta W, Alhasa KM (2015) Modeling of zenith path delay over Antarctica using an adaptive neuro fuzzy inference system technique. *Expert Syst Appl* 42:1050–1064
5. Suparta W, Abdul Rashid ZA, Mohd Ali MA, Yatim B, Fraser GJ (2008) Observations of Antarctic precipitable water vapor and its response to the solar activity based on GPS sensing. *J. Atmos. Sol. Terr. Phys.* 70:1419–1447
6. Zuur A, Ieno EN, Meesters E (2009) A beginner's guide to R. Springer Science & Business Media. Springer, New York, pp 127–168

Parametric Studies of ANFIS Family Capability for Thunderstorm Prediction

Wayan Suparta and Wahyu Sasongko Putro

Abstract Thunderstorms are an unpredictable natural hazard. They affect daily human life especially for space launcher development program in the near future. The variations in meteorological parameters were used to capture thunderstorm activity. In this study, six parameters, namely pressure, temperature, relative humidity, cloud, rainfall and precipitable water vapor were analyzed in order to develop a thunderstorm prediction system. To realize the development of this thunderstorm prediction system, we developed a thunderstorm prediction model based on the Adaptive Neuro-fuzzy Inference System (ANFIS) family (ANFIS FCM, ANFIS FSC, and ANFIS Human Expert). Three models from the ANFIS family were assessed to ascertain their capability for thunderstorm prediction. Input and output variables were taken from the Tawau meteorology station. The results showed that the thunderstorm prediction model based on ANFIS Human Expert showed a good efficiency with an estimated error prediction of <2% with root mean square error (RMSE) and percentage error (PE) values of 3.028% and 23.545% respectively compared to RMSE and PE of ANFIS FCM and ANFIS FSC.

1 Introduction

Unpredicted natural hazards pose a risk to human life. High thunderstorms activity is composed of pressure, temperature, relative humidity, and cloud (oktas) parameters, etc. Fluctuations in atmospheric variability will particularly affect the environmental thunderstorm level in region such as in Tawau, Sabah. The thunderstorm level in this area increases during the intermonsoon period (from summer

W. Suparta (✉)

Dept of Electrical Engineering, Sanata Dharma University, 55282 Yogyakarta, Indonesia

e-mail: drwaynesparta@gmail.com; wayan@ukm.edu.my

W. Suparta · W.S. Putro

Space Science Centre (ANGKASA), Institute of Climate Change,

Universiti Kebangsaan Malaysia, 43600 Bangi, Selangor Darul Ehsan, Malaysia

© Springer Nature Singapore Pte Ltd. 2018

W. Suparta et al. (eds.), *Space Science and Communication for Sustainability*,

https://doi.org/10.1007/978-981-10-6574-3_2

to winter) [1]. The frequency of rainfall has increased since September 2014) [2] and this has resulted in flash flood events. To anticipate the thunderstorm damage in this area, many researchers have studied the atmospheric conditions in order to characterize and develop a thunderstorm prediction model.

A preliminary study of atmospheric characterization over the Tawau area was successfully conducted by Suparta and Putro [1] to classify thunderstorm activity. The thunderstorm activity increased during the intermonsoon periods (from winter to summer and summer to winter). However, in winter and summer the thunderstorm activity decreased by 10~20% due to climate change effects on the seasonal monsoon in Asia [3]. Loo et al. [4] studied the seasonal monsoon in Asia throughout the twentieth century and discovered a connection between monsoon rainfall and global warming. The increasing rainfall frequencies were caused by Typhoon Saola and then Typhoon Haikui [5]. Due to dangerous effect of thunderstorms, Albar et al. [6] successfully estimated thunderstorm activities by using rainfall radar data from Jeddah, Saudi Arabia. Empirical relationship methods (reflectivity and rainfall rate) were used to assess the rainfall depth and thunderstorm status. However, the empirical relationship methods have a disadvantage due to the lack of area coverage and a low level of detectable signal. In order to improve this shortcoming, Velden et al. [7] used measurements from satellite images (the Dvorak technique) to find thunderstorm status based on cloud evolution. Spiridonov and Čurić also successfully developed a thunderstorm forecasting model to evaluate the status of thunderstorm using a numerical method [8]. However, the numerical method has a disadvantage when large amounts of data are used. Litta et al. [9] successfully developed a thunderstorm forecasting model using Artificial Neural Network (ANN) with Levenberg Marquardt and Delta-Bar-Delta logarithms to improve the training process using the numerical model. Suykens et al. [10] obtains the limitations of the ANN method when it reached a state of convergence (steady).

The capability of ANN decreased at a relatively slow pace before they reached a steady position. However, Rajasekaran and Pai [11] successfully improved the capability of ANN with an added Fuzzy algorithm, namely the Adaptive Neuro-Fuzzy Inference System (ANFIS). Suparta and Alhasa [12] studied two types of ANFIS, namely ANFIS Fuzzy C-Means (FCM) and ANFIS Fuzzy Subtractive clustering (FSC) in atmospheric applications by using surface meteorological data. The estimation result showed that ANFIS FCM is comparable to ANFIS FSC. The disadvantage of ANFIS FCM depends on the situation in question and the application. Cao et al. [13] successfully designed the ANFIS New Fuzzy Reasoning Model (NFRM), called the ANFIS Human Expert (HE), and this has greater capability than ANFIS FCM and FSC. As a result of this problem, ANFIS HE was proposed to estimate and measure the thunderstorm model. In this study, we compare the capability of ANFIS HE with ANFIS FCM and FSC to predict thunderstorm events in Tawau, Sabah, Malaysia.

2 Methodology

2.1 Data and Location

As thunderstorm activity increases over Tawau area during the intermonsoon periods, this region was selected to be an area of study. Stohlgren [14] obtained four meteorological parameters (temperature, wind flow, precipitation and relative humidity) as the source of thunderstorm activity in the Rocky Mountains area (USA) during spring and summer. Based on the different geographical conditions between Tawau and the Rocky Mountains, six meteorological parameters, namely pressure (P), temperature (T), relative humidity (H), cloud intensity (C), precipitation (Pr), and precipitable water vapor from radiosonde (RSPWV) were analyzed to reveal thunderstorm activity. Data from 1 January 2013 to 31 December 2013 taken from the Malaysian Meteorological Department (MetMalaysia), weather underground, NASA, and Wyoming University over Tawau ground-based station (located at 4.32°N, 118.12°E and at an elevation of 17 m) were used to develop a thunderstorm prediction model. The data were processed using Matlab and an error measurement was filtered from the ground-based sensor by replacing it with Not a Number (NaN) data.

2.2 Adaptive Neuro-Fuzzy Inference System (ANFIS)

Based on the conceptual study to improve training process using ANN, the Fuzzy Inference System (FIS) was constructed to develop a degree of membership functions (MFs) of both input and output data. Here, input and output data were clustered to create fuzzification process over FIS. The two types of FIS, Sugeno and Mamdani were applied with a linear technique. In this study, Sugeno FIS were applied to create an ANFIS family model (ANFIS FCM, ANFIS FSC, and ANFIS Human Expert). The main concept of membership function Sugeno FIS has two input rules (A and B) and two consequent parts (f_1 and f_2) of the output rule, where f_1 (p_1, q_1, r_1) and f_2 (p_2, q_2, r_2) are a premise part of the linear parameter for the Takagi-Sugeno fuzzy model. The sum product of f_1 and f_2 for the final weight is expressed as

$$f = \overline{w_1}f_1 + \overline{w_2}f_2 \quad (1)$$

where f , $\overline{w_1}$ and $\overline{w_2}$ are linear parameter average for the output target, and weight average rule one and two respectively. Furthermore, the premise and consequent parameter of the Takagi-Sugeno concept of the FIS and fuzzy reasoning mechanism is described in Fig. 1. Here, the premise and consequent parameter of the Takagi-Sugeno concept had two input rules and output rules [12].

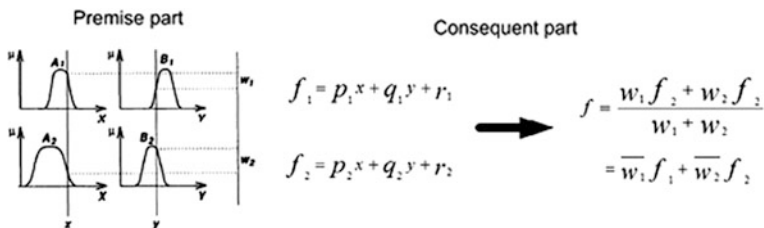


Fig. 1 Fuzzy reasoning mechanism and Takagi-Sugeno FIS

Thus, according to Eq. (1), the Takagi-sugeno ANFIS model as described in Fig. 2 used two rules x and y which is A_1 and A_2 , B_1 and B_2 as MFs of input parameter, respectively [12].

Rule 1 : if x is A_1 and y is B_1 then $f_1 = p_1x + q_1y + r_1$

Rule 2 : if x is A_2 and y is B_2 then $f_2 = p_2x + q_2y + r_2$

Furthermore, the architecture of the ANFIS model consists of five layers. Each layer has its own function to process input data. In the first layer, we generated the MFs for every node with an output parameter and generalized using a Gaussian function. In layer two, we found the output result using an AND operator (T-Norm operator) for each node. In layer three, we calculated the ratio of firing strength to find the best output result. In layer four, we calculate the total output based on the parameter input of all firing strength nodes. In the last layer, the calculation of average signal input from the input parameter was performed. In this study, we used a Gaussian function and three MFs from the selected parameters. The selected parameters were analyzed using Minitab software in order to find the best configuration parameter of input and output.

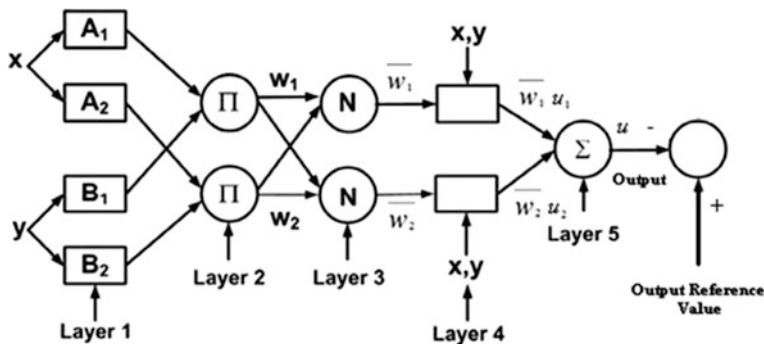


Fig. 2 Adaptive Neuro-Fuzzy Inference System structure

2.3 Capability of ANFIS Family to Predict Thunderstorm Events

As thunderstorms are categorized as a deadly natural hazard, the capabilities of the ANFIS family—FCM, FSC and Human Expert (HE)—were compared. The different concepts of three types of ANFIS are located in the MFs design over FIS. Figure 3 shows the comparison of MFs designed over FIS for input and output parameters. The MFs of (3a) the ANFIS FCM and (3b) FSC models were designed using a cluster generated by a Matlab program. However, the MFs of (3c) the ANFIS HE model were designed using an author expert and a Gaussian function to improve training, testing, and validation results.

The results from training data using ANFIS designed with MFs over FIS were processed to obtain an estimation model. The best estimation model was chosen on the basis of iteration limit and training time. However, in other cases iteration and training will not guarantee a good estimation result. Thus, the RMSE and Percent True were calculated in order to obtain the best estimation result for the testing and

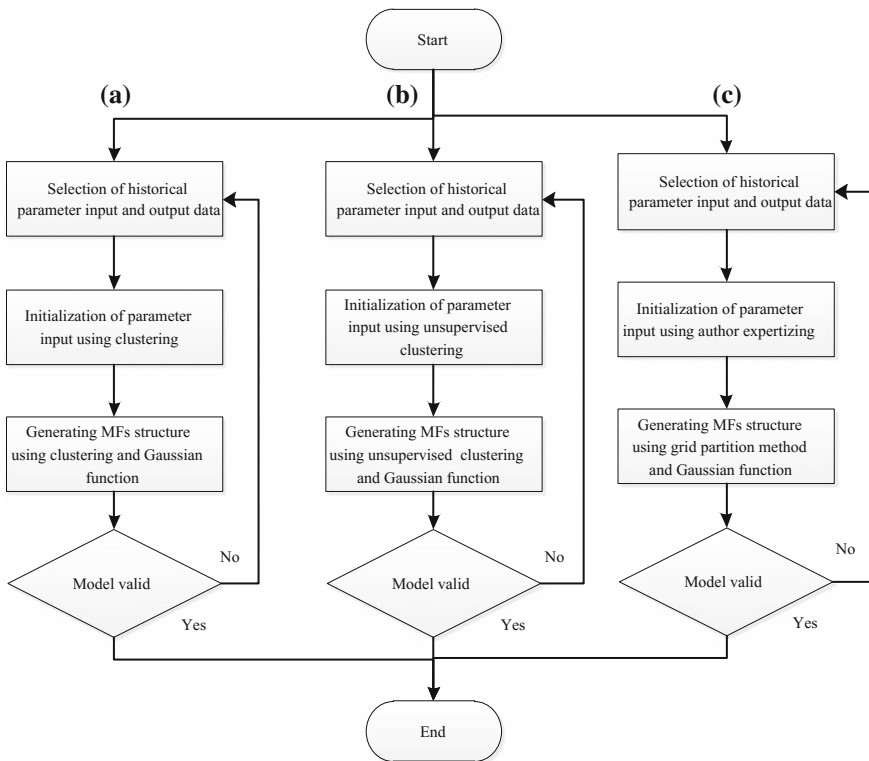


Fig. 3 Flowchart of MFs design of ANFIS families for a FCM, b FSC, and c HE

validation process. In this study, the prediction of thunderstorm events was calculated using an exponent Lyapunov chaotic time series [15] as expressed in Eq. 2

$$\vec{X}(t) = [(x(t), x(t - \tau), \dots, x(t - (m - 1)\tau)] \quad (2)$$

where $\vec{X}(t)$ is the prediction result, t is the scalar index of the estimation result (from the ANFIS model), τ is the time delay and m is the collapse dimension.

3 Results and Discussion

Figure 4 shows the variation of six meteorological parameters over Tawau station used as input parameters to find thunderstorm events. Data from six input parameters due to a lack of measurement data were processed using a Matlab software. Here, blank data is Not a Number (NaN) captured from lack of measurement after processing using Matlab software. In addition, hourly measurement data from the meteorological sensor were averaged on a daily basis and with a target to estimate thunderstorm data using a Matlab software.

During intermonsoon season I (winter to summer) in March, April, and May the RSPWV decreased when the temperature (T) was normal and relative humidity (H) increased by less than 90% respectively during mid-April 2013. However, during intermonsoon season II (summer to winter) in September, October, and

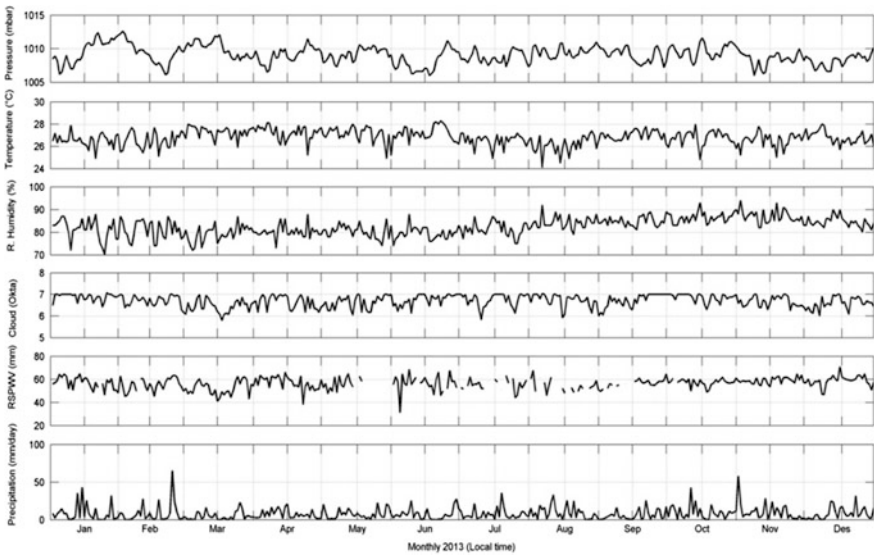


Fig. 4 The variation of meteorological parameters used to find thunderstorm events over Tawau station

November, the T parameter increased when the H parameter decreased and RSPWV data was normal respectively during mid-October 2013. The different situation between intermonsoon seasons I and II was due to a tropical storm event in the south Philippines [1]. Thus, to capture the tropical storm event the configuration method was proposed to calculate the standard error (S-value). Furthermore, six parameter inputs and one output parameter (thunderstorm) were paired into 148 configuration inputs and outputs to calculate the S-value using Minitab software. The best result of configuration parameter input and output are provided in Table 1. Here, the best configuration meteorological parameters are H and RSPWV.

The best configuration parameters (H and RSPWV) were selected to predict thunderstorm activity. During the development of the new model, the six configuration parameters were used to design the MFs using a Gaussian function. Figure 5 presents the degree of MFs surface meteorological data for the ANFIS model. As shown in the figure, the three Gaussian MFs were chosen to design the FIS model on the basis of accuracy, training time, and case study. The FIS was added to layer one of the ANFIS model for the thunderstorm estimation model. During training, testing, and validating of the observation parameters in the ANFIS model, we selected the data into 70%, 10%, and 20%, respectively for input parameter and with the target of thunderstorm activity. Furthermore, the comparison of results between ANFIS FCM, FSC, and HE used to capture thunderstorm activity over 2013 are described in Fig. 6. Here, the ANFIS family models were successful in predicting thunderstorm activity using six configuration input parameters.

Figure 6 shows the results for estimation of thunderstorm activity using ANFIS HE, FCM, and FSC. Generally, all the ANFIS models follow the observation pattern except for May 2013 due to there being no data of RSPWV. A statistical method was applied to obtain the capability of ANFIS HE, FCM, and FSC models (see Table 2).

Table 1 The best configuration parameter for predicting thunderstorm events

Configuration input parameter	Output parameter	Standard error (S-value)
$P, T, \text{ and } H$	Thunderstorm	0.431
...
...
$P, T, H, \text{ and } C$	Thunderstorm	0.438
$P, T, H, C, \text{ and } \text{RSPWV}$	Thunderstorm	0.439
$P, T, H, C, \text{ RSPWV, and } Pr$	Thunderstorm	0.429
$H \text{ and } \text{RSPWV}$	Thunderstorm	0.427
$T, H, \text{ and } \text{RSPWV}$	Thunderstorm	0.432
$T \text{ and } H$	Thunderstorm	0.431
...
$T, H, \text{ and } C$	Thunderstorm	0.431

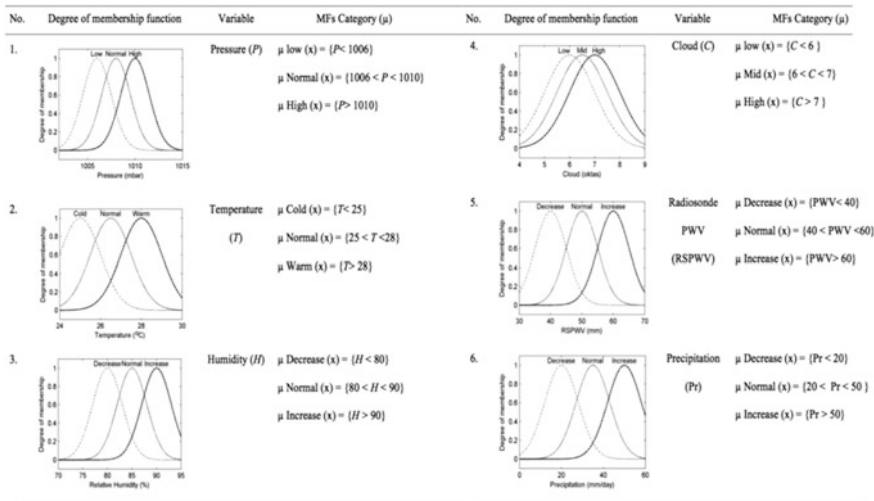


Fig. 5 The degree of MFs meteorological data for the ANFIS model

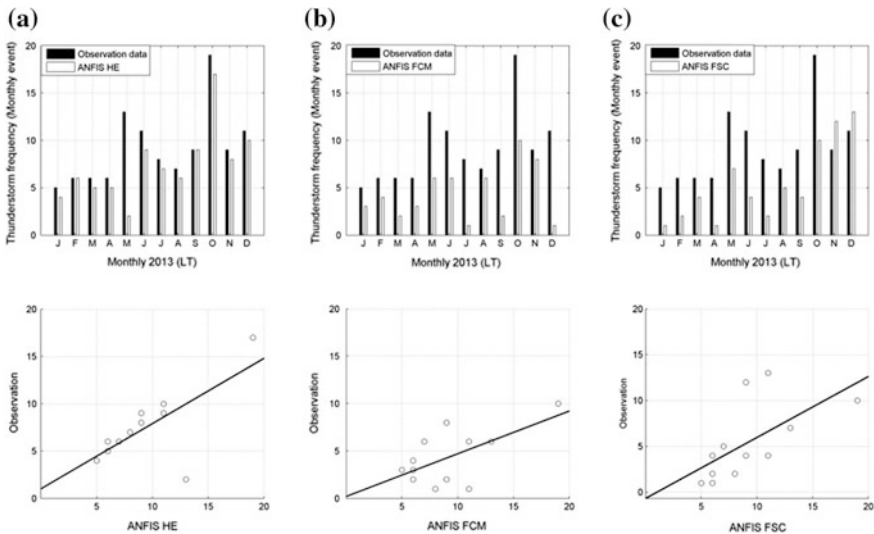


Fig. 6 Comparison of observation data and their relationship in terms of thunderstorm frequency with a ANFIS HE, b ANFIS FCM, and c ANFIS FSC

In order to reach a thunderstorm prediction model, the chaotic time series were applied in the ANFIS model by using five reference data. The comparison of estimation error from the thunderstorm prediction models is compiled in Fig. 7. The figure shows that the thunderstorm value increased every day/event. The trends of estimation error for each step in thunderstorm prediction increased up to eight steps

Table 2 Statistical comparison of each ANFIS family model’s ability to estimation thunderstorm events

ANFIS Model	Correlation (R^2)	RMSE (%)	MAE (%)	PE (%)
HE	0.868	3.028	2.333	23.545
FCM	0.739	4.173	3.250	36.471
FSC	0.582	5.091	4.417	49.276

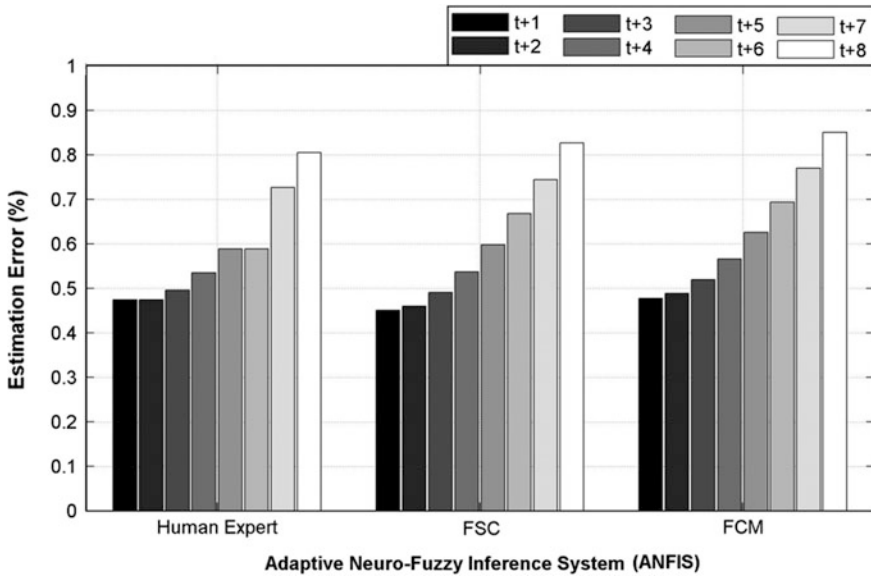


Fig. 7 The comparison of estimation error in thunderstorm prediction using three models from one step to eight steps ahead

ahead (max). The increase in the estimation error was caused by data resolution on a daily basis. Finally, ANFIS HE was used to establish a prediction model with the greatest capability compared with ANFIS FCM and FSC.

4 Conclusion

A comparison of the ANFIS families conducted using meteorological data as the input has the capability to predict thunderstorm activity. The input used was six configurations of meteorological parameters and one output of thunderstorm frequency, and were applied to design MFs over FIS. The estimation result showed that ANFIS HE had a favorable result compared to ANFIS FCM and FSC. Furthermore, the estimation error of the thunderstorm prediction results indicates

that ANFIS HE also shows a good capability to detect thunderstorm events over the Tawau area. However, the ANFIS model looks roughly to follow the trend of observation data in May 2013 due to a lack of RSPWV data. To improve the RSPWV data, it is suggested that it must be constructed using PWV data from GPS data in the near future.

Acknowledgements This research is supported by Ministry of Science, Technology and Innovation Malaysia (MOSTI) under Science Fund 01-01-02-SF1100 grant and partly funded by Flagship Program: ZF-2014-016 grant. The authors would like thank MetMalaysia, weather underground, NASA and Wyoming University for providing the meteorological data used in this study.

References

1. Suparta W, Putro WS, Singh MSJ, Asillam MF (2015) Characterization of GPS and meteorological parameters for mesoscale convective systems model over Tawau, Malaysia. *Adv Sci Lett* 21:203–206
2. Suparta W, Putro WS, Singh MSJ, Asillam MF (2015) The estimation of rainfall and precipitation variation during 2011 convective system using an artificial neural network over Tawau, Sabah. Paper presented at the 2015 IEEE international conference on space science and communication, space science centre (ANGKASA), Universiti Kebangsaan Malaysia, Langkawi, 10–12 August 2015
3. Chen TC, Wang SY, Yen MC (2007) Enhancement of afternoon thunderstorm activity by urbanization in a valley: Taipei. *J Appl Meteorol Climatol* 46:1324–1340
4. Loo YY, Billa L, Singh A (2015) Effect of climate change on seasonal monsoon in Asia and its impact on the variability of monsoon rainfall in Southeast Asia. *Geosci Front* 6:817–823
5. Heistermann M, Crisologo I, Abon CC, Racoma BA, Jacobi S, Servando NT, David CPC, Bronstert A (2013) Using the new Philippine radar network to reconstruct the Habagat of August 2012 monsoon event around Metropolitan Manila. *Nat Hazards Earth Syst Sci* 13:653–657
6. Albar AMH, AL-Khalaf AK, Mohamed HAB (2015) Radar rainfall estimation of a severe thunderstorm over Jeddah. *Atmos Clim Sci* 5:302
7. Velden C, Harper B, Wells F, Beven JL II (2006) The Dvorak tropical cyclone intensity estimation technique. *Bull Am Meteorol Soc* 87:1195
8. Spiridonov V, Curic M (2015) A storm modeling system as an advanced tool in prediction of well organized slowly moving convective cloud system and early warning of severe weather risk. *Asia Pac J Atmos Sci* 51:61–75
9. Litta AJ, Mary Idicula S, Mohanty UC (2013) Artificial neural network model in prediction of meteorological parameters during premonsoon thunderstorms. *Int J Atmos Sci* 1:1–14
10. Suykens JAK (2001) Nonlinear modeling and support vector machine. Paper presented at the 2001 IEEE instrumentation and measurement technology conference, Budapest convention centre, Budapest, Hungary, 21–23 May 2001
11. Rajasekaran S, Pai GV (2004) Neural networks. *Fuzzy Logic and Genetic Algorithms*. PEU Learning Pvt. Ltd, New Delhi, pp 17–456
12. Suparta W, Alhasa KM (2015) Modeling of zenith path delay over Antarctica using an adaptive neuro fuzzy inference system technique. *Expert Syst Appl* 42:1050–1064
13. Cao Z, Kandel A, Li L (1990) A new model of fuzzy reasoning. *Fuzzy Sets Syst* 36:311–325

14. Stohlgren TJ, Chase TN, Pielke RA, Kittel TG, Baron J (1998) Evidence that local land use practices influence regional climate, vegetation, and stream flow patterns in adjacent natural areas. *Glob Change Biol* 4:495–504
15. Xu X, Tang Q, Xia H, Zhang Y, Li W, Huo X (2016) Chaotic time series prediction for prenatal exposure to polychlorinated biphenyls in umbilical cord blood using the least squares SEATR model. *Sci Rep* 6:25005

Performance and Evaluation of Eight Cloud Models on Earth—Space Path for a Tropical Station

Temidayo Victor Omotosho, Oladimeji Mustapha Adewusi,
Marvel Lola Akinyemi, Sayo Akinloye Akinwunmi,
Oluwafumilayo Oluwayemisi Ometan and Williams A. Ayara

Abstract This is a review of eight cloud models and a statistical analysis of radiosonde data and cloud cover data in order to obtain attenuation distributions and cloud cover statistics for a tropical location, Ota (6.7°N, 3.23°E) at a computed elevation angle of 56.18° to an Astra 2B satellite located at 31.5°E. Cloud models are mathematical algorithms scientifically designed to predict cloud attenuation impact on propagating electromagnetic signals in the troposphere, using data on each model's required parameters such as temperature, pressure, cloud height, cloud occurrence and liquid water content of clouds. The station's cloud cover statistics, namely average amount of cloud, cloud base height, and frequency of occurrence were computed from extracted cloud data to obtain their monthly and seasonal variations. The results show that minimum attenuation values were predicted by both the Gun and East and the ITU-R models, while the Liebe and Slobin models predicted consistently maximum values of attenuation for all the cloud models tested. Cloud attenuation statistics computed for each of the models show that at 0.01% exceedance probability, the averages of the predicted cloud attenuation for uplink and downlink at Ota, ranges between 0.45 dB and 0.44 dB for Ku, 1.85 dB and 0.75 dB for Ka, and 3.50 dB and 2.50 dB for V bands. At 0.1% the averages are between 0.30 dB and 0.27 dB, 0.95 dB and 0.47 dB, 2.45 dB and 1.51 dB at Ku, ka and V bands for both uplink and downlink respectively.

1 Introduction

The effects of suspended water droplets (SWD) and suspended ice crystals (SIC) which constitute clouds are a major concern in the design and successful operation of satellite communication systems at frequencies above 10 GHz. This is

T.V. Omotosho (✉) · M.L. Akinyemi · S.A. Akinwunmi · W.A. Ayara
Department of Physics, Covenant University, P.M.B 1023, Ota, Ogun State, Nigeria
e-mail: omotosho@covenantuniversity.edu.ng

O.M. Adewusi · O.O. Ometan
Department of Physics, Lagos State University, Ojo, Lagos, Nigeria

because the hydrometeor reduces the system's availability substantially as frequency increases, particularly in tropical locations. Signal transmission loss occurs when the propagating signal's energy is absorbed at high frequencies due to rotational and vibrational transitions in atmospheric polar molecules induced by tiny water droplets in clouds [1]. While the SWD is majorly responsible for cloud attenuation, the SIC contribution is negligible in the microwave frequency range though it is noted to cause signal depolarization. It has been observed that the tropical lower atmosphere is more often cloudier than that of temperate regions. Thus, for low-availability satellite services such as VSAT and USAT, at high frequencies, deep fades may occur due to the higher probability of occurrence of cloud cover in the tropics [2, 3].

Limited experimental facilities for the measurement and estimation of cloud attenuation delayed studies on the subject and also the development of useful a theoretical platform relative to rain attenuation. However, a good number of theoretical and experimental developments have led to the design and production of research equipment for the study of clouds, including cloud radar (surface), radiosondes, radiometers and satellite observation radar for use in the measurement of cloud liquid water and the realization of 3D cloud structures. Cloud measurement methods include using radiances measured by satellites on the one hand, and using visual observations of cloud from the earth's surface stations on land and on ships in the ocean, on the other. For example, in the satellite approach the Cloud-Aerosol Lidar with Orthogonal Polarization (CALIOP) provides reliable heights of thin high altitude cirrus clouds containing small ice particles, but the 94 GHz Cloud Profiling Radar (CPR) has a low sensitivity to them, hence a ground observation approach may be used to provide a good validation for satellite data and vice versa [4]. The chaotic atmosphere has the following model types: Cloud-Resolving Models (CRMs), Mesoscale Models, Numerical Weather Prediction (NWP) Models, Regional Climate Models (RCMs) and Global Circulation Models (GCM) [5]. Their modeling framework includes acquiring system equations and their numerical representations and solutions through parameterizing state variables, and initial and boundary conditions, as well as time integration schemes. To model a real object such as a cloud, a spatial or matrix model may be most appropriate, as in the three-dimensional cloud profiling by recent satellite missions, [5]. The general objective of cloud models is to accurately estimate the amount of cloud liquid water to determine the amount of cloud attenuation along a satellite earth-space transmission path. Numerous cloud models have been independently developed using empirical data over the last eight decades based on Rayleigh scattering and Mie absorption theories, [4]. They assumed uniform cloud cover horizontally and vertically, and that non-precipitating clouds are composed of spherical droplets having radii $\ll 50 \mu\text{m}$, small enough to keep them suspended in the atmosphere. These cloud models include the Gun and East Model (1954), Staelin Model (1966), Slobin Model (1982), Liebe et al. Model (1989), Altshuler and Marr Model (1989), Salonen Model (1990), Salonen and Uppala Model (1991), and the ITU-R Model (2009). The models' general parameters include particle size distribution function, cloud density, temperature, permittivity and angle of elevation [4, 6–11].

2 The Cloud Models

Gun and East (1954) based on Rayleigh approximation of Mie's theory, accounts for the energy scattering and absorption by the particles in a non-absorbing medium and explains the converted propagating signal's energy as scattering and absorbed energy by the lossy dielectric water particles, when the water particle diameters are significantly less than λ/π , where λ is the wavelength of the incident signal wavelength. Their cloud attenuation co-efficient (α) algorithm in dB/km (given in Table 1) includes an implicit temperature dependent, imaginary component $\text{Im}[-k]$. Gerace and Smith (1990) published the graphical relationship between the $\text{Im}[-k]$ and frequency. Also based on the Rayleigh theoretical work, Staelin (1966) produced an algorithm (listed in Table 1) which includes explicit temperature dependence, for the computation of a cloud attenuation coefficient (α) per cm [4, 12]. Slobin's (1982) detailed study of radio wave propagation effects of clouds in locations in the United States resulted in another cloud model. He used extensive data on cloud characteristics gathered from twice-daily radiosonde measurements and determined regions of statistically consistent clouds from which he defined fifteen cloud regions. He modified the Staelin model's algorithm and obtained a cloud attenuation coefficient model (listed in Table 1) in dB/Km.

Liebe et al. (1989) derived an attenuation model for haze, fog and cloud which predicts a cloud attenuation coefficient in dB/Km, through defined loss spectrum equivalent to $N''(f)$, such that the loss spectrum is basically the imaginary part of the complex refractivity N . Liebe declared the model to be more reliable for predicting radio propagation effects in the frequency range of 100 GHz and above [13].

Altshuler and Marr (1989) studied atmospheric attenuation through extinction measurements with respect to the sun in the Boston area at frequencies of 15 and 35 GHz under conditions of partial and complete cloud cover at 29 elevation angles, ranging between 0° and 20° . Their studies include attenuation dependence on signal slant path, absolute humidity, frequency and elevation angle, [4]. Measurement periods for each data set were during minimum solar activity and of short duration (about 2 h), hence an insignificant solar instability error. Errors were estimated to be about 0.1 dB for low attenuation and 2 dB for attenuation above 20 dB. The error introduced by using CSC (θ) dependence has been investigated, hence the elevation angle limits [14].

Salonen et al. (1990) defined a critical humidity function $U_c(P)$ for cloud detection and evolved a computational algorithm for cloud liquid water content, listed in Table 1. The algorithm is further scrutinized to accommodate relevant water phases $P_w(t)$, resulting in $W_L(t, h)$ and $W_i(t, h)$ which are the liquid water density and solid water density respectively, [8]. Salonen and Uppala (1991) developed a cloud attenuation (A_L) algorithm (listed in Table 1) due to cloud liquid water content effect on a propagating signal of frequency (f) at an elevation angle θ .

Table 1 Comparative list of the cloud models

Model name	Model algorithm and parameters	Limitations
Gun and East (1954)	$\alpha = 0.4343 [6\pi/(\lambda\rho_a)]\text{Im} [- (\epsilon - 1)/(\epsilon + 2)]\rho_1$ α = Attenuation coefficient (dB/Km), ρ_a = density of water (g/cm^{-3}) ρ_1 = liquid water content of the cloud, λ = wavelength (cm) of incident signal Im = “imaginary part of”, ϵ = complex relative dielectric constant of water	
Staelin (1966)	$\alpha = \rho_1 [10^{(0.0122(291 - T) - 6)}] / \lambda^2$ α = Attenuation coefficient (cm^{-1}), ρ_1 = liquid water content of the cloud (g/m^3) T = temperature (K), λ = wavelength (cm) of incident signal.	Valid for 10 to 37.5 GHz
Slobin (1982)	$\alpha = 4.343 \rho_1 [10^{(0.0122(291 - T) - 1)}] 1.16 / \lambda^2$ α = Attenuation coefficient (dB/km), ρ_1 = liquid water content of the cloud T = temperature (K), λ = wavelength of incident signal	Valid for 10 to 50 GHz
Altshuler and Marr (1989)	$A = \left(-0.0242 + 0.00075\lambda + \frac{0.403}{\lambda^{1.15}} \right) (11.3 + \rho) \text{csc}(\theta)$, for $\theta > 80^\circ$ $= \{ [(a_e + h_e)^2 - a_e^2 \text{Cos}^2(\theta)]^{1/2} - a_e \text{Sin}(\theta) \}$, for $\theta \leq 80^\circ$ A = Attenuation (dB), λ = wavelength of incident signal, ρ = surface absolute humidity, θ = elevation angle, $a_e = 8,497$ km and $h_e = (6.35 - 0.302\rho)$ Km	Valid between 15 to 100 GHz. Assume 10°C as nominal cloud temperature
Liebe et al. (1989)	$\alpha = \rho_1 a \theta^b$ θ = relative inverse temperature = $300/[T (^\circ\text{C}) + 273.15]$ α = Attenuation coefficient (dB/Km), ρ_1 = liquid water content of the cloud (g/m^3), a and b are variable constants for different frequency ranges.	Temperature limit: $10 \pm 10^\circ\text{C}$ and frequency range 100 GHz and above.
Salonen (1990)	$\mathbf{w}(t, \mathbf{h}) = \mathbf{w}_o \exp(\mathbf{c}t)[(\mathbf{h} - \mathbf{h}_b)/\mathbf{h}_r]$ $\mathbf{W}_L(t, \mathbf{h}) = \mathbf{W}(t, \mathbf{h})P_w(t)$; $\mathbf{W}_j(t, \mathbf{h}) = \mathbf{W}(t, \mathbf{h})[1 - P_w(t)]$ where: 1 , if $0 < t$ $P_w(t) = 1 + t/20$, if $-20^\circ\text{C} < t < 0^\circ\text{C}$ 0 , if $t < -20^\circ\text{C}$ $w_o = 0.17 \text{ g}/\text{m}^{-3}$ and $c = 0.04^\circ\text{C}^{-1}$	
Salonen and Uppala (1991)	$A_L(P) = \frac{0.819f}{\epsilon''(1+\eta^2)} W_{red}(\mathbf{h}) \frac{1}{\text{Sin}\theta}$ $A_L(P)$ = Slant Path Attenuation, P = Probability (%), $\eta = (2 + \epsilon')\epsilon''$ ϵ' and ϵ'' are the real and imaginary parts of liquid water permittivity ϵ at 0°C .	
ITU-RP (2013)	$Y_c = K_I M$ (dB/km) and $K_I = \frac{0.819f}{\epsilon''(1+\eta^2)} \text{ dB}/\text{km} (\text{g}/\text{m}^3)^{-1}$ $A = (LK_I/\text{Sin}\theta) \text{dB}$, $90^\circ \geq \theta \geq 5^\circ$ L = total columnar content of cloud liquid water θ = Elevation angle; K_I = specific attenuation coefficient.	

W_{red} is a height (h) function temperature dependence called reduced liquid water content along the signal slant path. In the frequency range 10 to 60 GHz, when the temperature dependence is almost a constant, ITU-R stated $W_{\text{red}} = 0.5 \text{ Kgm}^{-2}$, where no meteorological information is available [10, 15].

The International Telecommunication Union (ITU) recommendation (P.840-4, 2009) states that for clouds or fog consisting entirely of small water droplets generally less than 0.01 cm, the Rayleigh approximation of Mie theory is valid for frequencies below 200 GHz and that it is possible to express attenuation in terms of the total cloud water content per unit volume. The specific attention (γ_c)—an equivalent of the attenuation coefficient (α) in the earlier cloud models, and K_L —a specific attenuation coefficient (dB/Km) for a cloud or fog are defined. For frequencies up to 1000 GHz, the stated ITU-R mathematical model (listed in Table 1) based on Rayleigh scattering, uses the double-Debye formula for the dielectric permittivity $\epsilon(f)$ of water in calculating the value of the specific attenuation coefficient (K_L) in $(\text{dBKm}^{-1})/(\text{gm}^{-3})$. It also recommends consideration be given to using 0 °C as the temperature in this model for cloud attenuation (A) in dB for a given exceedance probability. The statistics of the total columnar content of liquid water may be obtained from radiometric measurements or from radiosonde launches [10].

2.1 The Cloud Cover

The extracted cloud cover statistics include average cloud amount, average base height and frequency of occurrence for each of the low clouds—Stratus (St), Cumulus (C) Stratocumulus (Sc), Cumulonimbus (Cb), and Nimbostratus (Ns) derived from ground and satellite observations (1971–1996) [16]. The station's seasonal variations with the clouds' average base heights and the frequency of occurrence charts were obtained.

2.2 Data Processing and Analysis

The attenuation distributions for each of the eight models were computed using radiosonde data observations for periods between 1953 and 2011. Using the data analysis and solver application, the attenuation statistics for each model were computed, from which their respective attenuation cumulative probability distributions for the fifty-eight years were obtained. The required parameters for evaluation of the attenuation distribution for each of the cloud models vary as indicated in Table 1.

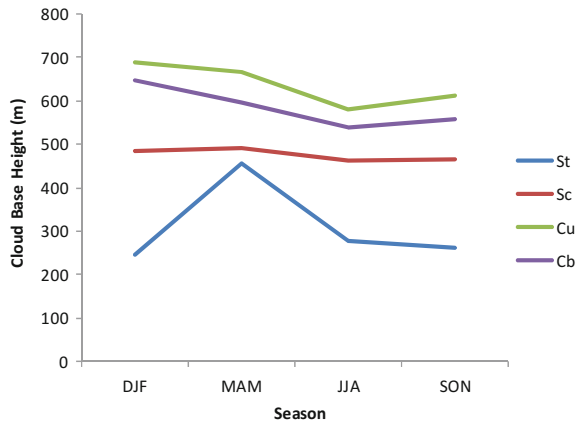
The Gun and East, Staelin, Slobin, Altshuler and Marr, Liebe et al., Salonen-Uppala and the ITU-R models generally require the liquid water content of the cloud and the propagating signal’s frequency, and most of them also require the signal path length (L_{sp}) through each cloud layers’ series (CLS). While the Staelin, Slobin and Liebe et al. models explicitly require the temperature of the cloud layers at their respective heights, others have implicit or fixed temperatures for evaluation of their cloud attenuation distribution. The consolidated radiosonde data was filtered and extracted to obtained each cloud layers’ values for the required primary parameters—pressure (hP_a), temperature (K) and calculated geopotential height (m). The attenuation distribution for each model is used to compute their sets of percentage exceedances for the frequency range 10 to 50 GHz.

3 Results and Discussion

The computed cloud cover statistics such as average cloud amount, average cloud base height, and frequency of occurrence were used to obtain their monthly and seasonal variations as shown in Figs. 1 and 2.

The output chart for the cloud attenuation (dB) relationship with frequency for the models is shown in Fig. 3, and their output charts for the relationship between cloud attenuation and the corresponding percentage exceedances for Ku, Ka and V bands are shown in Figs. 4, 5, 6, 7, 8 and 9. Cloud attenuation statistics computed for each of the models show that at 0.01% exceedance probability, the averages of

Fig. 1 Ota seasonal average cloud base heights



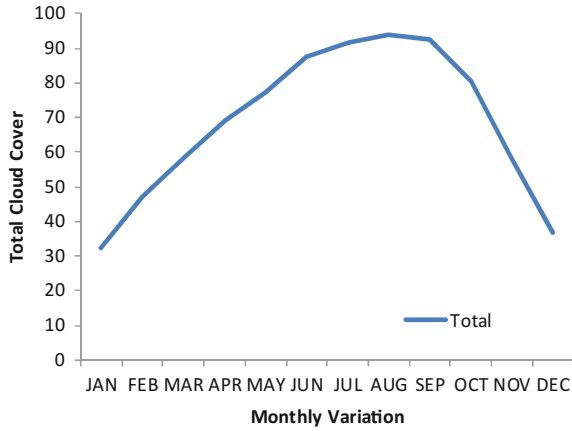


Fig. 2 Ota total cloud cover

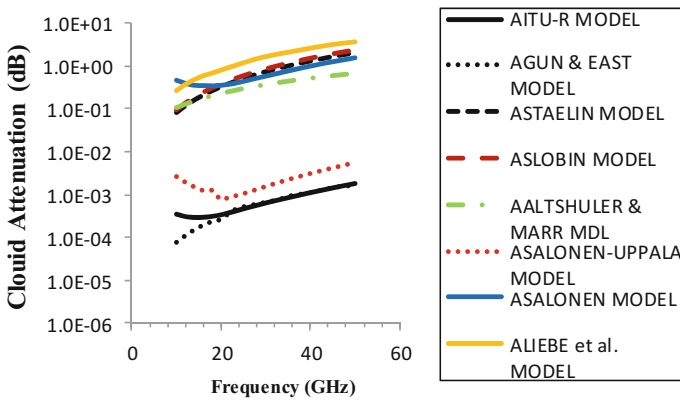


Fig. 3 Cloud attenuation versus frequency (GHz)

their predicted cloud attenuation for Ota uplink and downlink ranges between 0.45 dB and 0.44 dB, 1.85 dB and 0.75 dB, 3.50 dB and 2.50 dB for the Ku, Ka and V bands At 0.1% the averages are between 0.30 dB and 0.27 dB, 0.95 dB and 0.47 dB, 2.45 dB and 1.51 dB respectively for the bands, as shown in Table 2.

Fig. 4 Cloud attenuation (A^{12}) versus % Exceedances for 12 GHz

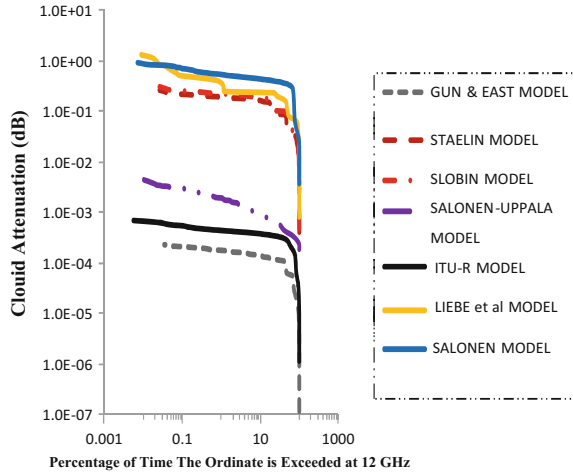


Fig. 5 Cloud attenuation (A^{14}) versus % exceedances for 14 GHz

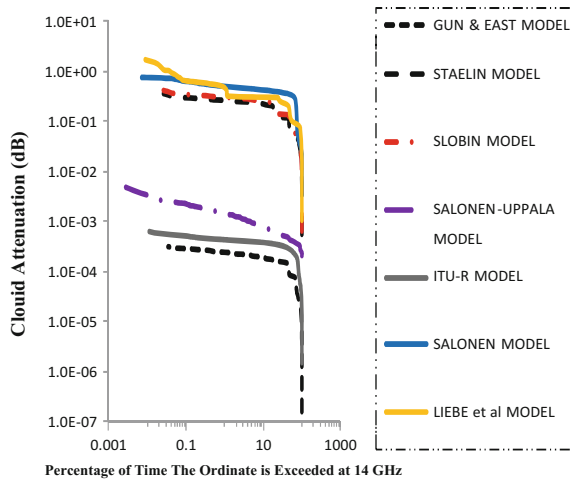


Table 2 shows that the Gun and East model is the minimum attenuating model at the Ku, Ka, and V-bands, except at 30 GHz in the Ka band where the ITU-R model is the minimum attenuating model. Table 2 also shows that the Liebe et al. model to be the maximum attenuating model in the Ku, Ka, and V-bands except at 50 GHz in the V-band where the Slobin model is the maximum attenuating model.

Fig. 6 Cloud attenuation versus % exceedances for 20 GHz

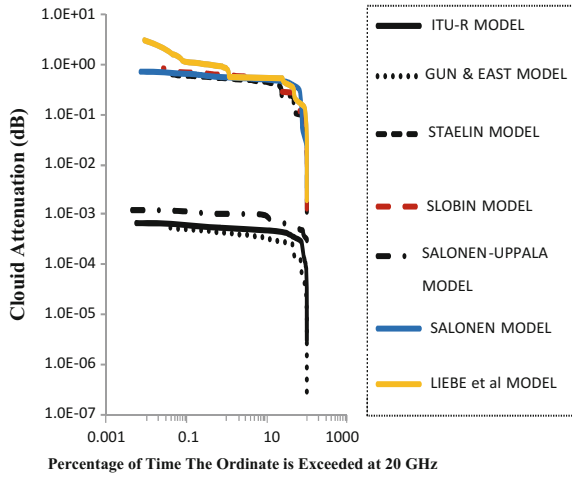


Fig. 7 Cloud attenuation versus % exceedances for 30 GHz

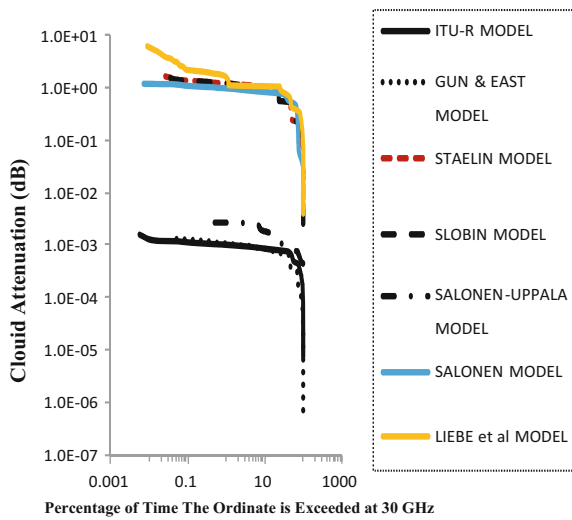


Fig. 8 Cloud attenuation versus % exceedances for 40 GHz

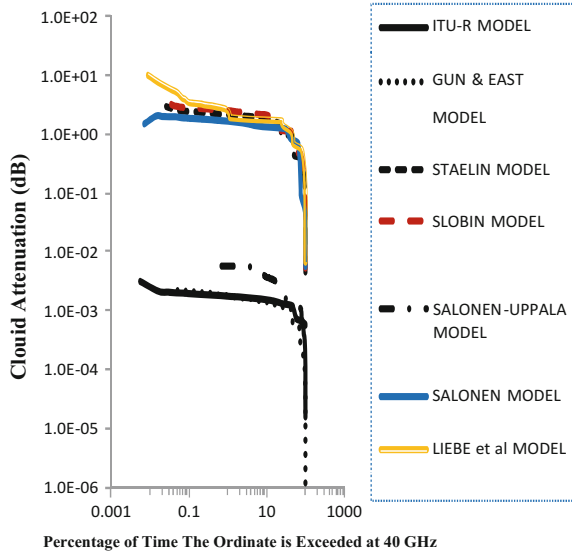


Fig. 9 Cloud attenuation versus % exceedances for 50 GHz

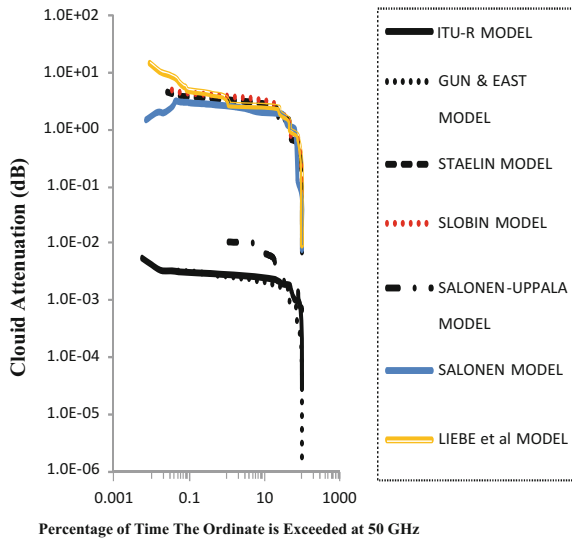


Table 2 Predicted uplink and downlink margins for Ota at Ku, Ka and V bands

S/N	Cloud model	Ku band				Ka band				V band				
		0.01%		0.01%		0.1%		0.01%		0.1%		0.01%		
		A ₁₄ (dB)	A ₁₂ (dB)	A ₁₄ (dB)	A ₁₂ (dB)	A ₃₀ (dB)	A ₂₀ (dB)	A ₃₀ (dB)	A ₂₀ (dB)	A ₅₀ (dB)	A ₄₀ (dB)	A ₅₀ (dB)	A ₄₀ (dB)	
1	a	1.5 × 10 ⁻⁴	1.3 × 10 ⁻⁴	1.35 × 10 ⁻⁴	1.2 × 10 ⁻⁴	1.17 × 10 ⁻⁴	1.7 × 10 ⁻⁴	1.5 × 10 ⁻⁴	1.0 × 10 ⁻⁴	1.5 × 10 ⁻⁴	1.55 × 10 ⁻³	1.7 × 10 ⁻⁴	1.35 × 10 ⁻³	1.5 × 10 ⁻⁴
2	b	0.56	0.50	0.49	0.35	3.5	0.95	0.85	2.0	0.85	7.5	5.0	5.5	3.1
3	c	0.57	0.51	0.5	0.4	3.5	0.97	0.97	2.0	0.87	7.6	5.1	5.6	3.2
4	d	1.5 × 10 ⁻³	1.6 × 10 ⁻²	1.3 × 10 ⁻³	1.4 × 10 ⁻³	1.5 × 10 ⁻³	1.2 × 10 ⁻³	1.2 × 10 ⁻³	1.4 × 10 ⁻³	1.9 × 10 ⁻⁴	1.1 × 10 ⁻²	1.8 × 10 ⁻³	1.0 × 10 ⁻²	1.8 × 10 ⁻³
5	e	0.15	0.13	0.15	0.13	0.37	0.23	0.23	0.37	0.23	0.68	0.52	0.68	0.52
6	f	0.92	0.76	0.63	0.74	1.19	0.73	0.73	1.1	0.67	2.02	2.03	2.97	1.8
7	g	1.32	1.7	0.63	0.53	6.2	3.11	3.11	2.16	1.14	10.2	7.37	4.8	3.47
8	h	1.8 × 10 ⁻⁴	1.8 × 10 ⁻⁴	1.65 × 10 ⁻⁴	1.65 × 0 ⁻⁴	1.1 × 10 ⁻³	1.8 × 10 ⁻⁴	1.7 × 10 ⁻⁴	1.0 × 10 ⁻³	1.7 × 10 ⁻⁴	1.6 × 10 ⁻³	1.4 × 10 ⁻³	1.4 × 10 ⁻³	0.3 × 10 ⁻³
	α	g	g	g	g	g	g	g	g	g	g	g	c	g
	β	a	a	a	a	h	a	a	a&h	a	a	a	a	a
Average		0.44	0.45	0.30	0.27	1.85	0.75	0.47	0.95	0.47	3.50	2.50	2.45	1.51

a = Gun and East, **b** = Saelim, **c** = Slobin, **d** = Salonen and Uppala, **e** = Altshuler and Marr, **f** = Salonen, **g** = Liebe et al., **h** = ITUR

α = Maximum Attenuating Model

β = Minimum Attenuating Model

4 Conclusion

The results show that relationships exist between each model's predicted cloud attenuations and signal propagation frequencies between 10 and 50 GHz for all the cloud models tested, and between the cloud attenuations and their corresponding percentage exceedances for Ku, Ka and V bands. Table 2 shows the minimum values that were predicted by the Gun and East and the ITU-R models, while the Liebe and Slobin models predicted consistently maximum values. It displays the predicted uplink and downlink margins for the station at Ka, Ku and V bands. On-going radiometric measurement, cloud visual data and meteorological acquisition at Covenant University, Ota, will be processed and analysed, and its cloud attenuation statistics will be compared with the above results to determine the best performing cloud attenuation model with the measured cloud attenuation at Ota.

Acknowledgements We hereby express our sincere appreciation to Physics Department and Covenant University Center for Research and Innovation Development (CUCRID) for sponsoring this research work.

References

1. Das S, Chakraborty S, Maitra A (2013) Radiometric measurements of cloud attenuation at a tropical location in India. *J Atmos Sol Terr Phys* 105–106:97–100
2. Eva RI, Gustavo AS, Jose MR et al (2015) Atmospheric attenuation in wireless communication systems at millimeter and THz frequencies. *IEE Antenna Propag Mag* 57(1):48–61
3. Omotosho TV, Mandeep JS, Mardina A (2013) Cloud attenuation studies of the six major climatic zones of Africa for Ka and V satellite system design. *Ann Geophys* 56(6):1–2
4. Gerace GC, Smith EK (1990) A comparison of cloud models. *IEEE Antennas Propag Mag*
5. Kit KS (2002) An overview of atmospheric models. In: MAGS model cross-training workshop. York University 5–9:9
6. Gun KL, East TW (1954) The Microwave properties of precipitation particles. *Quart J R Meteor Soc* 80:522–545
7. Slobin S (1982) Microwave noise temperature and attenuation of clouds: statistics of these effects at various sites in United States, Alaska and Hawaii. *Radio Sci* 17(6):1443–1454
8. Salonen E, Karhu S, Jokela P et al (1990) Study of propagation phenomena, for low availabilities. ESA/ESTEE/Final Report
9. International Telecommunication Union-Radio Propagation Recommendation, (ITU-RP 2009) Attenuation due to Clouds and Fog, p 840–844
10. Salonen E, Uppala S (1991) New prediction method of cloud attenuation. *Electron Lett* 27:1106–1108
11. Mattioli V, Basili P, Bonafoni S et al (2009) Analysis and improvements of cloud models for propagation studies. *Radio Sci* 44, RS2005
12. Staelin DH (1966) Measurements and interpretation of the microwave spectrum of the terrestrial atmosphere near 1-centimeter wavelength. *J Geophys Res* 71(12):2875–2881
13. Liebe HJ, Manabe T, Hufford GA (1989) Millimetre wave attenuation and delay rates due to Fog/Cloud conditions. *IEEE Trans Ant Prop* 37(12):1617–1623

14. Altshuler EE, Marr AR (1986) Slant path absorption correction for low elevation angles. *IEEE Trans Antennas Propag* AP-34(5):717–718
15. Antonio M, Marina B, Ermanno F et al (2002) Propagation effects due to atmospheric gases and clouds. COST 255, ESA, Netherlands
16. Hahn CJ, Warren SG (1999) Extended edited cloud reports from ships and land stations over the globe, 1952–1996, Carbon Dioxide Information Analysis Center (CDIAC), Department of Energy, Oak Ridge, TN, Numerical Data Package NDP-026C

Comparison of In situ Observation, NOAA-AIRS Satellite and MACC Model on Surface Ozone Over the Ushuaia, Southern Ocean and Antarctic Peninsula Region

M.S.M. Nadzir, M.F. Khan, W. Suparta and S.K. Zainudin

Abstract This study aims to determine surface ozone (O_3) mixing ratios from in situ observations during the Malaysian Antarctic Scientific Expedition Cruise 2016 (MASEC'16), by using The Monitoring Atmospheric Composition and Climate (MACC) global model assimilation system developed by the European Centre for Medium-Range Weather Forecasts (ECMWF) and satellite products from the National Oceanic and Atmospheric Administration-Atmospheric Infrared Sounder (NOAA-AIRS) over the Antarctic Peninsula region. We also compared all three types of observation of surface O_3 during the period of MASEC'16. The results showed that surface O_3 levels from MACC reanalysis and NOAA-AIRS were twice higher than those from in situ observations over Ushuaia, the Drake Passage (Southern Ocean) and the Antarctic Peninsula respectively. Nevertheless, the surface O_3 mixing ratios pattern from MACC and NOAA-AIRS were similar to the in situ measurements where mixing ratios of the surface O_3 were in the order of Ushuaia < Southern Ocean < Antarctic Peninsula meaning that the NOAA-AIRS satellite and MACC model products are likely to be effective proxies for atmospheric composition over a given region.

M.S.M. Nadzir (✉)

School of Environmental and Natural Resource Sciences, Faculty of Science and Technology, Universiti Kebangsaan Malaysia, 43600 Bangi, Selangor, Malaysia
e-mail: shahrulnadzir@ukm.edu.my

M.S.M. Nadzir · M.F. Khan

Centre for Tropical Climate Change System, Institute of Climate Change, Universiti Kebangsaan Malaysia, 43600 Bangi, Selangor, Malaysia

S.K. Zainudin

Space Science Centre (ANGKASA), Institute of Climate Change, Level 5, Research Complex Building, Universiti Kebangsaan Malaysia, 43600 Bangi, Selangor Darul Ehsan, Malaysia

W. Suparta

Department of Electrical Engineering, Sanata Dharma University, Yogyakarta 55282, Indonesia
e-mail: drwaynesparta@gmail.com

© Springer Nature Singapore Pte Ltd. 2018

W. Suparta et al. (eds.), *Space Science and Communication for Sustainability*, https://doi.org/10.1007/978-981-10-6574-3_4

1 Introduction

Surface ozone, O_3 is hazardous greenhouse gas which can cause problems for humans and vegetation in earth's ecosystem. In the Antarctic, surface O_3 can act as a uv radiation absorber and cause surface warming phenomena. Surface O_3 can be produced in the atmosphere by anthropogenic and biogenic O_3 precursors in the presence of uv radiation and nitric oxide, NO_x . The Antarctic region is surrounded by the Southern Ocean and is the fifth largest continent and even though it is far from any other continent, trans-boundary O_3 precursors can travel from both other continents and local sources. Different locations over Antarctica may experience different mixing ratios of surface O_3 due to topographical and meteorological factors. For example, measured surface O_3 mixing ratios in the range of 21.6 to 29.4 ppbv over six different stations in Antarctica were measured from previous study [1].

Research activities in Antarctic were believed to be difficult to conduct for long-term study purposes due to the financial and logistical limitations of the harsh environment and climate. Therefore, satellite and data assimilation-based products are useful tools to support in situ ground observation in the future. Satellite and data assimilation is now increasingly being used in the atmospheric research field [2, 3]. Previous study by [4], conducted data assimilation on surface O_3 .

This data assimilation provides state-of-the art atmospheric modelling with earth observation data (in situ observation). Thus, in this study, we will approach data assimilation of in situ observation, available free satellite and global model products for comparison purpose. The Monitoring Atmospheric Composition and Climate (MACC) global model assimilation system was developed by the European Centre for Medium-Range Weather Forecasts (ECMWF), a European and international agency based in the UK. MACC is a research project with the aim of establishing core global and regional atmospheric environmental services for the European GMES (Global Monitoring for Environment and Security) initiative [4]. The data from MACC were used in a previous study on the analysis of long-term atmospheric composition data by [4] to give an indication of its quality compared to in situ observations. Their results showed the mean relative MACC reanalysis and ozonesonde tropospheric O_3 measurements were within ± 5 to 10% in the NH and over the Antarctic.

We present here measurements of surface O_3 mixing ratios in the marine boundary layer over Ushuaia, the southern part of the SO (the Drake Passage) and the Antarctic Peninsula. The measurements were taken from an oceanographic research vessel during MASEC 2016 as part of the Sultan Mizan Antarctic Research Foundation Grant (YPASM) program and as part of the Malaysia Antarctic Research Program (MARP). This study describes the Atmospheric Infrared Sounder (AIRS) of an NOAA satellite and MACC reanalysis of O_3 at 1000 hPa during the period of MASEC'16. The purpose of this is to validate data agreement between the NOAA satellite, MACC reanalysis and onboard O_3 measurements with sufficient density and continuity to deliver strongly consistent

analyses between freely available satellite and global model products. This chapter is part of the manuscript and described detail in Mohd Nadzir et al., (2017) (manuscript submitted and under final revision in Environmental Science and Pollution Research Journal).

2 Methodology

2.1 Measurement and Sampling

MASEC'16 started between January 16th and February 8th 2016, travelling from Ushuaia, Argentina to Darboux Island and back to Ushuaia (Graham Coast, the Antarctic Peninsula) as shown in Fig. 1. On each cruise an EcoTech (Australia) model Serinus 10 O₃ analyzer was used onboard the *RV Australis* to measure the surface O₃. The EcoTech was calibrated prior to the measurement. The calibration was based on a 7-point standard from low to high concentration, with a range of interest of 0 to 200 ppb (parts per billion by volume) and detection limits of 0.05 ppb. The O₃ analyzer was deployed at the back of the vessel and a 10 m long 1/4" ID Teflon sample line was used to draw air samples from the outside of the vessel.

The vessel sailed across sub-Antarctic and Antarctic regions in various conditions. The *RV Australis*' route started from the town of Ushuaia, Argentina (55°S, 68°W) with a population of 42,000. The analyzer was deployed from the 16th to the

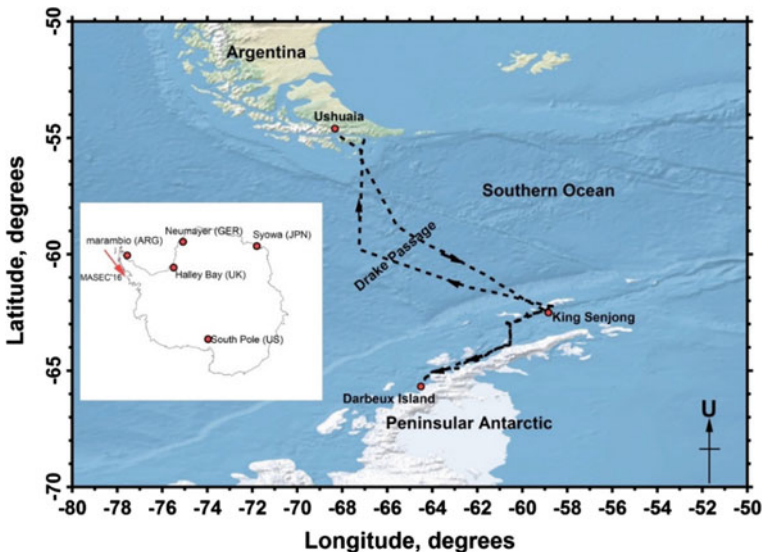


Fig. 1 Cruise route during MASEC'16 (note: the small Antarctic map inside shows research stations which measured surface O₃ concentration)

18th January at Ushuaia and throughout the Drake Passage, and surface O_3 was measured for 24 h. The vessel arrived at the South Korean King Sejong station on the 24th January and anchored for a day. The cruise then continued to the Antarctic Peninsula and ended at Graham Land (Darbeux Island) on the coast of the Antarctic Peninsula.

2.2 *Satellite-Derived and MACC Reanalysis*

The surface O_3 data recorded during by the EcoTech ozone analyzer onboard the *R/V Australis* were validated using the corresponding monthly averages of the long term (multi-year) data, which is freely available online satellite and model data. The AIRS satellite-derived surface O_3 (1000 hPa) mixing ratios were derived from the NASA “Giovanni” online database (<http://giovanni.nasa.gov/>) and were used to determine apparent surface O_3 values in the $1 \times 1^\circ$ grid square nearest to each sampling point. In this study, the MACC reanalysis of surface O_3 (1000 hPa) values in the $0.125^\circ \times 0.125^\circ$ grid square nearest to each sampling point were derived from <http://apps.ecmwf.int/datasets/data/>. The period data from the MACC reanalysis were retrieved for Jan/Feb 2016 in the area where the MASEC’16 was present. For further investigation, MASEC’16 data for Ushuaia, the Drake Passage and the Antarctic Peninsula region were validated with AIRS satellite and MACC reanalysis data which will be discussed in the next section.

3 **Result and Discussion**

3.1 *Surface O_3 During MASEC’16*

Hourly surface O_3 mixing ratios were measured from the 16th to the 19th January 2016 prior to departure. Figure 2 shows the mixing ratio of surface O_3 over Ushuaia, the Drake Passage and the Antarctic Peninsula. The production and loss chemical reactions were believed to be related to the diurnal pattern of surface O_3 in the atmosphere. In this study, we measured surface O_3 in the range of ~ 4 to ~ 11 ppb over the Ushuaia region. These values were slightly lower than the previous measurements observed by [5] over Ushuaia in 2008 with values of 12 to 27 ppb (during January). Surface O_3 precursors such as carbon monoxide (CO) emissions from Ushuaia city and wind speed may influence the mixing ratio drop (due to NO_x titration). This region is known for high winds and turbulent seas, which keep the atmosphere well mixed and the day-to-day variations in O_3 to a minimum [5].

The Beagle Channel in situ observation showed that surface O_3 mixing ratios decreased to ~ 4.2 ppb and increased over the open ocean up to ~ 12.3 ppb as

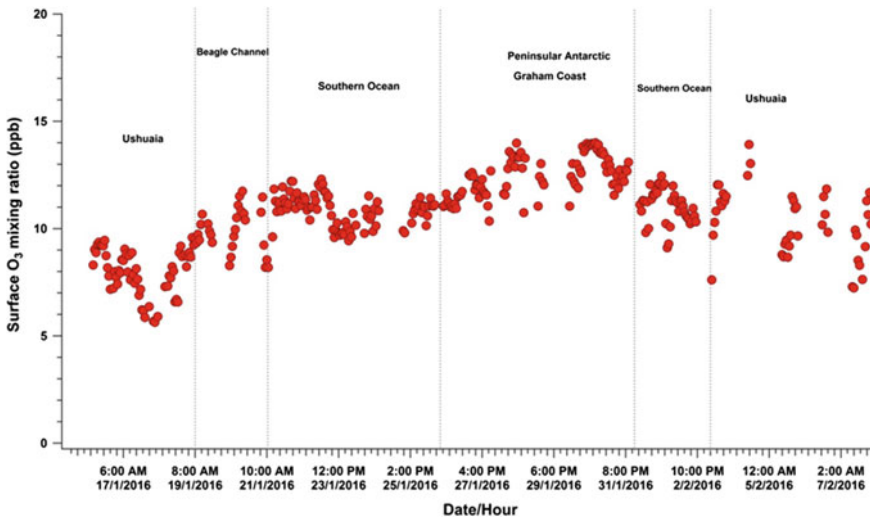


Fig. 2 Hourly Surface O_3 mixing ratio data from the onboard O_3 analyzer during MASEC'16

shown in Fig. 2. Previous study over the SO by [5] observed that surface O_3 mixing ratios increased up to 25 ppb travelling 2000 km from Ushuaia into the SO. A previous study by [6] found that the surface O_3 mixing ratios were in the range of 5 to 30 ppb and 10 to 30 ppb over the Pacific Ocean and the Indian Ocean respectively. Certain marine environments can experience high surface O_3 levels originating from the outflow of high O_3 and its formation from surface O_3 precursors such as nitrogen oxide (NO_x) and carbon monoxide (CO) during atmospheric transport from coastal regions [5]. Changes in surface O_3 mixing ratios in the marine boundary layer (MBL) from the Beagle Channel to the open ocean are believed to be influenced by natural chemical processes (sea-spray) and air transport from land. Sea-spray aerosol may produce O_3 precursors such as nitryl chloride ($ClNO_2$) [6]. In addition, OH and Cl radicals in the MBL can also increase surface O_3 formation with Cl [7–10]. The observations over the Drake Passage in this study are likely to be influenced by the sea-spray process and anthropogenic activities from South America such as in the Ushuaia region. For example, Johnson et al. [6] reported that surface O_3 levels over the Indian Ocean during the SAGA cruise 87 at $50^\circ N$ to $40^\circ N$, were extremely high at up to 60 ppb due to forest fire emissions from Northeastern China.

3.2 Satellite and MACC Reanalysis

The surface O_3 mixing ratios data from the NOAA AIRS satellite products and MACC reanalysis were retrieved for Jan and Feb 2016, when MASEC'16 took

place. Only daily averages of surface O₃ mixing ratios can be retrieved from NASA's "Giovanni" online database (<http://giovanni.nasa.gov/>).

Satellite: The Satellite AIRS surface O₃ data at 1000 hPa during the period of MASEC'16 was extracted from the NASA Goddard "Giovanni" online database (<http://oceancolor.gsfc.nasa.gov/SeaWiFS/>). The daily averages for Ushuaia and the Antarctic Peninsula were compared with MASEC'16 and are shown in Fig. 3. The average daily mixing ratios of surface O₃ patterns were similar but the values were almost twice as high in the case of satellite data (1000 hPa) with values in the range ~14 to 23 ppb compared to the cruise data with daily average values of ~7 to 12 ppb. Nevertheless, both the datasets showed a similar surface O₃ pattern over the three different regions with high mixing ratios over the Antarctic Peninsula compared to Ushuaia. The average daily levels over Ushuaia and the Antarctic Peninsula between the AIRS satellite and the cruise data were correlated with $r^2 = 0.48$ and $p < 0.01$. The statistical values for the AIRS, the MACC reanalysis and MASEC'16 are summarized in Table 1.

MACC reanalysis: Figure 4 shows the hourly surface O₃ mixing ratios from the MACC reanalysis during MASEC'16 at 1000 hPa. The values were slightly higher compared to the in situ onboard values of *RV Australis*, with daily values of ~9 to 22 ppb and 7 to 12 ppb for the MACC reanalysis and MASEC'16 respectively. The reanalysis shows predictions approximately twice as high as in situ observation over Ushuaia, the Drake Passage and the Antarctic Peninsula respectively. Inness et al. [4], showed that validation of MACC O₃ against ozonesondes of surface O₃ has a small positive bias of ±5–10% over the Northern Hemisphere and Antarctic region between 200 to 1000 hPa. The large level surface O₃ with MACC reanalysis is not understood at present. Other authors (e.g., [4, 11]) assessed the impact of assimilating O₃ data on surface O₃ mixing ratios and recommended that further

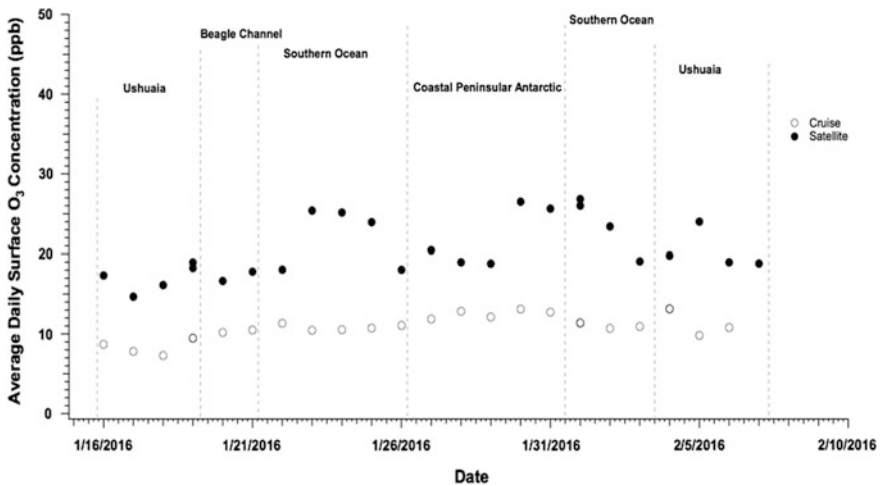


Fig. 3 Average daily surface O₃ mixing ratio from the AIRS satellite and in situ MASEC'16 measurements

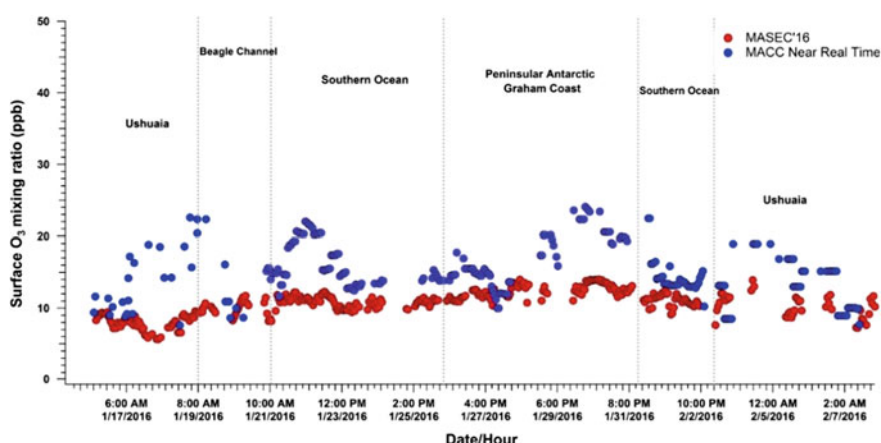
Table 1 Statistical data of surface O₃ from MACC reanalysis and MASEC'16

	This study (Hourly)	MACC reanalysis (Hourly)	AIRS satellite (Daily)
The Antarctic Peninsula	10.31 ^a	20.17 ^a	19.59 ^a
	10.58 ^b	20.25 ^b	19.64 ^b
	±1.81 ^c	±1.10 ^c	±0.64 ^c
The Drake Passage	8.67 ^a	22.60 ^a	14.28 ^a
	9.50 ^b	17.91 ^b	14.81 ^b
	±2.96 ^c	±1.82 ^c	±1.02 ^c
Ushuaia	6.85 ^a	19.04 ^a	13.54 ^a
	7.45 ^b	16.59 ^b	14.12 ^b
	±2.18 ^c	±2.07 ^c	±0.84 ^c

Note ^aAverage

^bMedian

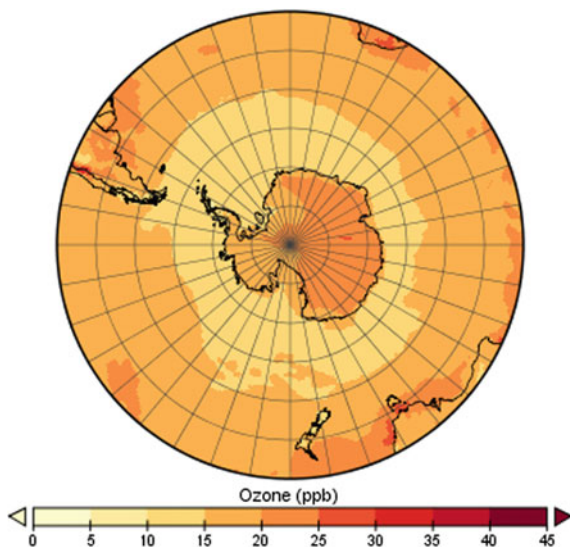
^cStandard Deviation (±)

**Fig. 4** Hourly surface O₃ mixing ratios from the MACC reanalysis and in situ MASEC'16 measurements

studies are needed for assimilating the surface O₃ into the MACC system, The correlation between the MACC reanalysis and MASEC'16 was positive with $r^2 = 0.5$, $p < 0.01$.

In Fig. 5, the MACC reanalysis shows that monthly mixing ratios of surface O₃ increased when approaching the Antarctic region. This monthly reanalysis supported the hourly and daily average observed in situ and by satellite, where high mixing ratios of surface O₃ were observed over the Antarctic region compared to the Ushuaia and SO regions. This event may be linked to the O₃ precursors which are emitted naturally such as from marine and ice surfaces. Both satellite and MACC reanalysis products showed twice higher than in situ observation during the period of MASEC'16. However, the higher observations from satellite and MACC products are still unknown. Therefore, in the future, the surface O₃ precursor data

Fig. 5 MACC reanalysis of surface O_3 monthly mixing ratio during MASEC'16



over the region are needed either from in situ or satellite-based products in order to understand the uncertainties between these two different approaches.

4 Conclusion

Surface O_3 levels are believed to be a result of a combination of complex conditions and chemical processes in the Antarctic boundary layer dependent on the location and the proximity to the coast, the stratospheric O_3 sink, O_3 precursor distribution and human influences. The in situ observation of surface O_3 onboard of *RV Australis* during MASEC'16, NOAA-AIRS satellite and MACC model were successfully compared. All observations showed that surface O_3 measured over the Antarctic Peninsula was the highest, approaching ~ 14 , ~ 25 , and 22 ppb by in situ, NOAA-AIRS and MACC reanalysis respectively. The satellite and MACC reanalysis data showed a consistent trend pattern with the in situ observations where mixing ratios were in the order of Ushuaia < the Drake Passage (CO) < the Drake Passage (SO) < Antarctic Peninsula. Both the satellite and MACC mixing ratio patterns are generally in very good agreement with in situ observations. However, the values were slightly higher at $\sim 80\%$ than MASEC'16 over the three locations. From this study, both free online satellite and MACC reanalysis data can be used as a qualitative tool for the determination of hotspot regions for surface O_3 at any given location. However, to quantify the surface O_3 via satellite and MACC reanalysis approaches, we suggest long-term cruise measurements of surface O_3 and its precursors such as CO and NO_x are needed in order to understand the surface O_3 distributions over the SO and Antarctic Peninsula. In addition, long term satellite

and MACC reanalysis approaches to observations of the O₃ precursors are important for validation purposes of in situ observations.

Acknowledgements We would like to thank the Sultan Mizan Antarctic Research Foundation Grant (YPASM) program registered as ZF-2015-001 as part of the Malaysia Antarctic Research Programme (MARP) under the Malaysian Ministry of Science, Technology and Innovation (MOSTI) and Universiti Kebangsaan Malaysia (UKM) GUP-2014-041 for giving opportunities and financial support to the Research Centre for Tropical Climate Change System (IKLIM) of the Institute of Climate change (ICC), UKM to participate in this scientific cruise. Secondly, we would like to thank Professor Dr. Sharifah Mastura Syed Abdullah, director of ICC-UKM. We also like to thank Captain Benjamin Wallis and his *R/V Australis* crew members and MASEC'16 scientists on board *R/V Australis* and Envirotech Sdn. Bhd who helped a lot with the exploration activities and Dr. Rose Norman (UK) for her assistance in proofreading this article. This study relies on archived surface O₃ data sets that were retrieved from the WMO World Data Centre for Greenhouse Gases (<http://gaw.kishou.go.jp/wdceg.html>). We would also like to thank the international research stations that provided all the data to the website.

References

1. Helmig D, Oltmans SJ, Carlson D et al (2007) A review of surface ozone in the polar regions. *Atmos Environ* 41:5138–5161. doi:[10.1016/j.atmosenv.2006.09.053](https://doi.org/10.1016/j.atmosenv.2006.09.053)
2. Hólm EV, Untch A, Simmons A, Saunders R, Bouët F, Andersson E (1999) Multivariate ozone assimilation in four dimensional data assimilation. In: Proceedings of the soda workshop on chemical data assimilation, KNMI, De Bilt, the Netherlands, 9–10 Dec1998
3. Dragani R (2011) On the quality of the ERA-Interim ozone reanalyses: comparisons with satellite data. *Q. J. Roy Meteorol Soc* 137:1312–1326. doi:[10.1002/qj.821](https://doi.org/10.1002/qj.821)
4. Inness A, Baier F, Benedetti A et al (2013) The MACC reanalysis: an 8 yr data set of atmospheric composition. *Atmos Chem Phys* 13:4073–4109. doi:[10.5194/acp-13-4073-2013](https://doi.org/10.5194/acp-13-4073-2013)
5. Boylan P, Helmig D, Oltmans S (2015) Ozone in the Atlantic Ocean marine boundary layer. *Elem Sci Anth* 3:000045. doi:[10.12952/journal.elementa.000045](https://doi.org/10.12952/journal.elementa.000045)
6. Johnson JE, Gammon RH, Larsen J, Bates TS, Oltmans SJ (1990) Ozone in the marine boundary layer over the Pacific and Indian Oceans: Latitudinal gradients and diurnal cycles. *J Geophys Res* 95(D8):11847–11856
7. Monks PS, Carpenter LJ, Penkett SA et al (1998) Fundamental ozone photochemistry in the remote marine boundary layer: the SOAPEX experiment, measurement, and theory. *Atmos Environ* 32(21):3647–3664
8. Monks PS, Salisbury G, Holland G et al (2000) A seasonal comparison of ozone photochemistry in the remote marine boundary layer. *Atmos Environ* 34(16):2547–2561
9. Monks PS (2005) Gas-phase radical chemistry in the troposphere. *Chem Soc Rev* 34:376–395
10. Conley SA, Faloon IC, Lenschow DH et al (2011) A complete dynamical ozone budget measured in the tropical marine boundary layer during PASE. *J Atmos Chem* 68(1):55–70
11. Foret G, Hamaoui L, Schmechtig C et al (2009) Evaluating the potential of IASI ozone observations to constrain simulated surface ozone concentrations. *Atmos Chem Phys* 9:8479–8491

A Brief Review: Response of the Ionosphere to Solar Activity Over Malaysia

Siti Aminah Bahari and Mardina Abdullah

Abstract The variability of solar activity plays an important role in controlling the chemical reactions and physical processes in the ionosphere. To improve our understanding of the characteristics of the ionosphere over Malaysia, a study of the effects of solar activity on the ionosphere is required. This paper focuses on the variations in the ionosphere as a result of solar activity. Variations in the ionosphere are divided into (1) critical frequency profile, (2) maximum usable frequency and minimum frequency, (3) variations of TEC to solar activity, (4) ionospheric delay, (5) scintillation and (6) the equatorial plasma bubble. The paper also provide new information towards a comprehensive explanation of the basis processes involved in improving the prediction capability of the ionospheric model and its related applications.

1 Introduction

The relationship between the ionosphere and solar activity has received the attention of numerous researchers, both past and present [1]. The plasma in the Earth's upper atmosphere is produced by the solar extreme ultraviolet variability (EUV) and X-ray radiations [2]. Solar activity varies with time and is defined by an 11-year-cycle. The solar EUV and X-ray radiation are known to be the primary energy sources for producing plasma in the Earth's upper atmosphere [1]. Thus, it is believed that the ionosphere reflects these variations.

In this paper, studies performed by researchers in Malaysia, particularly in Universiti Kebangsaan Malaysia (UKM) under different conditions of solar activity

S.A. Bahari (✉) · M. Abdullah

Space Science Centre (ANGKASA), Institute of Climate Change, Universiti Kebangsaan Malaysia, 43600 Bangi, Selangor Darul Ehsan, Malaysia
e-mail: sitiaminabahari@ukm.edu.my

S.A. Bahari · M. Abdullah

Department of Electric, Electronic and Systems Engineering, Faculty of Engineering and Built Environment, Universiti Kebangsaan Malaysia, 43600 Bangi, Selangor Darul Ehsan, Malaysia

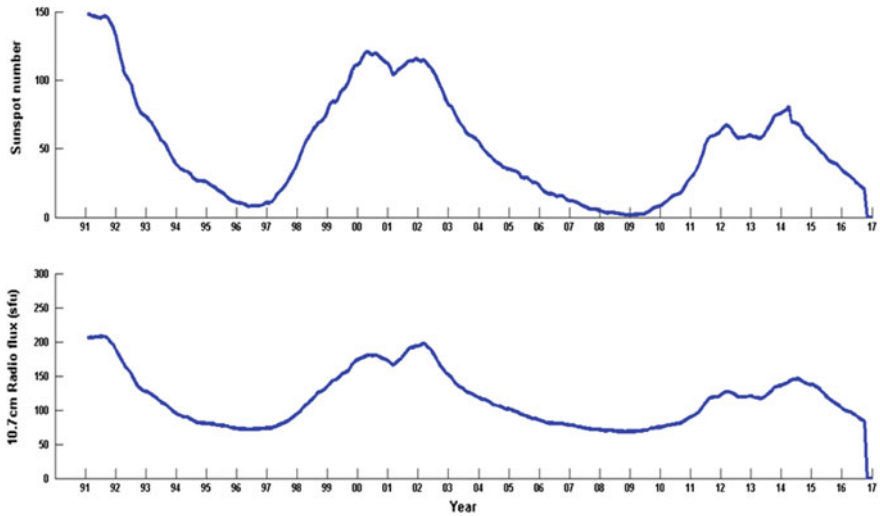


Fig. 1 Sunspot number and F10.7 cm radio flux from 1991 to 2017 which also cover solar cycle 23 and 24 used in this review

are reviewed. This review covers the response of the critical frequency to solar activity, maximum and minimum usable frequencies during low solar activity, and the irregularities of ionospheric in response to solar activity.

Figure 1 presents the solar 10.7 cm radio solar flux index (F10.7) and the sunspot number for solar cycle 23 and solar cycle 24. Studies on ionospheric characteristics under different solar cycles are required to enhance our understanding of the ionospheric structure over the equatorial region. This will also help in determining the ionospheric climatology, and the chemical and physical processes in the ionosphere for ionospheric empirical model development in the future. By studying the response of the ionosphere to solar activity, information relating to space weather prediction and the ionosphere as a solar activity index can be acquired since the ionosphere is known as an open space of the upper atmosphere and any kind of solar activity will have a direct effect on it. This paper highlights reviews of the variability of the ionosphere to solar activity.

2 Characteristics of Ionospheric Response to Solar Activity

2.1 Critical Frequency Profile

The critical frequency is obtained by sending a signal pulse such as an electromagnetic wave launched vertically into the ionosphere. This is reflected back and the highest frequency at which the reflection occurs is obtained. These are not constant but vary diurnally, seasonally and with other solar patterns [3].

Studies on critical frequency were performed by Abullah and Zain [3] and Abdullah [4] during the period of 2005 to 2007, which is considered to be a period of high to low solar activity. These studies were carried out in Batu Pahat, Johor. Only foF1 and foF2 critical frequencies were used in this study. A similar trend of diurnal variations was observed over Batu Pahat from 2005 to 2007 where a high critical frequency was observed at 0930 LT (0000 UT = 0800 LT) to 0000 LT at 8.75 MHz while the lowest critical frequency was observed at 0030 to 0730 LT with a value ranging from 6.8 to 4.2 MHz. The critical frequency in 2005 was higher compared to those in 2006 and 2007. The average value of the critical frequency for 2005 and 2007 was 7.5 MHz, with maximum value of 11.0 MHz and minimum value of 1.8 MHz [4].

The foF1 critical frequency analysis was carried out using the noon observation value. The regression analysis of the critical frequency showed no correlation between the measured number and the sunspot number. The theoretical value showed a high correlation with the sunspot number [4]. In contrast, the foF2 critical frequency was analysed using polynomial analysis. The 3rd, 4th and 5th degree equations had a better plot compared to the 6th degree equation from the measurement value.

The study was then continued by Rhazali [5] where the researcher observed the critical frequency, using hourly data, during the moderate to low solar activity of March, June, September, and December 2006 and 2007. The data were statistically analysed to summarise their main characteristics. The actual height of the F layer was determined from the median values and the coefficient of variability quantified the height deviations.

The median height of peak electron density, h_{\max} during noon time over Parit Raja, Johor, Malaysia was 550 km in all months except June, when it was 420 km. During the nighttime, the average height was around 300 km for all months. In relation to the seasonal variations of the height of electron density, the highest daytime peak was observed during the December solstice and the lowest was observed during the June solstice.

The critical frequency in 2005 at Fraser's Hill, Pahang varied from 4 to 4.2 MHz, which was lower compared to that at Parit Raja, Johor. The virtual height at Parit Raja in 2005 was between 290 to 340 km while for Fraser's Hill it was 230 to 270 km [6]. A study on electron density over Parit Raja and Fraser's Hill showed that the average maximum electron density was $0.75 \times 10^{12} \text{ m}^{-3}$ and $0.25 \times 10^{12} \text{ m}^{-3}$, respectively.

The peak electron density usually occurs in the F-region, which can be subdivided into the F1-layer and F2-layer. Above this layer is considered as a topside layer of ionosphere and known as additional layer or G-layer, which is related to the equatorial plasma fountain [7]. The G-layer is formed during the pre-noon hours at the equator between latitudes of ± 10 and is observed to have a greater maximum plasma concentration than that in the F-layer for a brief period just before noon. This layer is expected to be better observed during solstices and low solar activity. This layer was renamed the F3-layer as studies have shown that the layer arises from the dynamics of the F-layer at low latitudes.

A study conducted by Zain et al. [6] showed that the critical frequency for the F3 layer varied from about 8.2 MHz in January to 8.4 MHz in December 2003 and February 2004, and from 6.4 MHz in January 2005 to 7.1 MHz in February 2005 for the F2 layer. The virtual height of the F3 layer at Parit Raja varied from 480 to 900 km. Malaysia's greatest occurrence of the F3 layer was during winter of 2004 which was a period of high solar activity, with the highest reading being between 1100 to 1300 LT, while the lowest reading was within the period of 2300 to 0200 LT [6].

The study by Zain et al. [7] where data for the year 2005 was analyzed using an ionogram showed that the existence of the F3-layer in January was high, at about 35% as a result of the winter season. It decreased to about 10% in February, to about 15% in October and then increased to 50% in November, with the highest recorded value in December at 80%. The occurrence of the F3-layer in January was 35%, occurring mainly between 1900 to 0100 UT. The lowest median critical frequency for the F3-layer in that month was 7.1 MHz while the highest was 8.6 MHz. For the month of December, the lowest and highest median critical frequencies were 6.6 and 8.6 MHz, respectively. The F2-layer median critical frequencies for the months of November and December were 7.1 and 8 MHz [7].

The study mentioned above was carried out during the decreasing solar activity of cycle 23, so the results of this study can be used as the basis of modelling or identifying the characteristics of the ionosphere over the equatorial region generally, and in Malaysia specifically. As has been mentioned earlier, ionospheric characteristics vary with solar activity and region, therefore, studying other parameters such as the minimum and maximum usable frequency over Malaysia is essential. This will be explained in the next section.

2.2 Ionospheric Minimum Frequency and Maximum Usable Frequency Response to Solar Activity

“Maximum useable frequency (MUF) is used to determine the highest possible frequency for high frequency (HF) communications that can be used to transmit over a particular path under given ionospheric conditions” [8]. Due to the dispersive medium of the ionosphere, the signal that can be transmitted over the particular path fluctuates continuously [8]. MUF can be defined by the relation:

$$MUF(3000)F2 = foF2 \times M(3000)F2 \quad (1)$$

where $M(3000)F2$ is the propagation factor of an F2 layer on which its influence is significantly less than $foF2$, and $MUF(3000)F2$ is a usable frequency that can be received at a distance of 3000 km when reflected by the ionosphere [8].

The study by Abdullah [4] from 2005 to 2007 revealed that the MUF of the critical frequency over Parit Raja showed the highest value in the morning and the lowest in the late evening until midnight. The different take-off angle of the MUF

demonstrated the increase of the critical frequency values [4]. The study by Malik et al. [8] used actual HF transmissions from the Science and Technology Research Institute for Defense (STRIDE), Malaysia. The test was carried out between Kajang (101.8°E, 2.98°N) and Lumut (100.6°E, 4.22°N), Malaysia between April 2009 and September 2011.

Based on Fig. 1, the duration of these studies can be considered as the increasing phase of solar cycle 24. Diurnal variations of MUF showed an increasing pattern of MUF in the afternoon until pre-sunset and started to decrease post-sunset throughout the years of observation. Analysis on seasonal variations showed that the variability of MUF was greater during the December solstice in 2009, while in 2010 the variability of MUF was higher during the March equinox as shown in Fig. 2.

Figure 2 shows the hourly and monthly median for seasonal variation of MUF from the test compared with the MUF from IRI. The figure is taken from Malik et al. [8]. The test covers 2009 to 2011, which can be considered as a period of increasing of solar activity.

Zain et al. [6] also found that variability of MUF was higher during nighttime compared to daytime except for the year 2011. This might be due to the effects of solar activity where a high solar activity caused decreasing variability of MUF. A strong correlation was observed between the variability of MUF and sunspot number, with a value of 0.73. Other than that, the variability of MUF is also due to

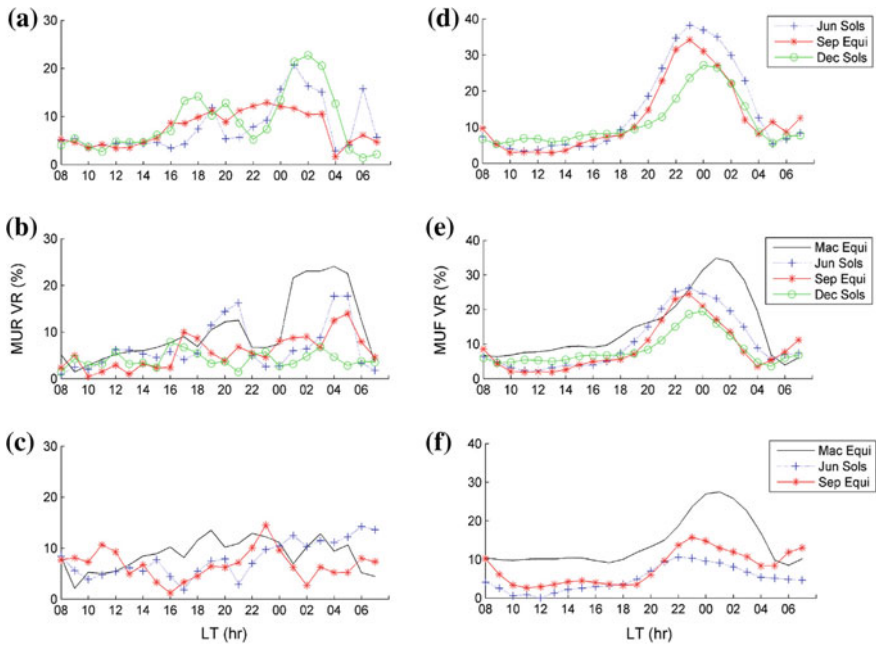


Fig. 2 Hourly monthly median for seasonal variation of MUF VR Test during **a** 2009, **b** 2010, **c** 2011 and MUF IRI during **d** 2009, **e** 2010 **f** 2011 (Figure taken from Malik et al. [8])

variations of energy loss (absorption or attenuation) in the ionospheric D-region. The absorption of a HF signal in the lower portion of the ionosphere can be measured using f_{min} , the minimum frequency for which an echo intensity falls below the minimum recording level.

A study over the African and South American sector during low solar activity (2010) was conducted by Bello et al. [9]. Two DPS-4 digisonde sounder stations at Ilorin in Nigeria, west of Africa (8.50 N, 4.68 E) and Jicamarca (12 S, 76.87 W) were used in the analysis. In this study, f_{min} was observed to be high during daytime and low during nighttime for both stations. The maximum midday f_{min} at Ilorin ranged from 2.3 to 2.7 MHz, while for the Jicamarca station it ranged from 2.3 to 2.9 MHz. During nighttime, the f_{min} range was from 1.9 to 2.2 MHz for both stations.

The highest f_{min} was observed during the equinoctial months for both stations at 1100 to 1300 LT and the lowest f_{min} was during the June solstice which is in agreement with the seasonal variations of TEC [9]. Regarding longitudinal variations, it was found that the relative variability (VR) index for Ilorin station was consistent, having a higher value during the nighttime and lower value during the daytime. However, the VR index for the Jicamarca station was observed to be relatively unstable throughout the day. This proved that f_{min} varies along the magnetic longitude [8].

This study was carried out over the equatorial region at different longitudes. Further study, using data from Malaysia, is needed to determine the f_{min} for the Malaysian region. A study of the correlation between TEC and f_{min} should be performed in the future in order to enhance knowledge of the characteristics of the ionosphere over the equatorial region, and for modelling purposes.

The variability of f_{min} and MUF can be correlated with TEC and the occurrence of other ionospheric perturbations over the equatorial region. It is well known that the ionosphere over Malaysia is not only influenced by solar activity but also by other factors such as neutral winds. Furthermore, in this region, the magnetic field is horizontally oriented from south to north and the field-aligned direction is in the meridional plane ($E \times B$) which becomes the source of equatorial ionospheric anomaly occurrences such as plasma bubbles, fountain effects and others [10]. The response to ionospheric perturbation over the equatorial region as investigated by a researcher in Malaysia is discussed in the next section.

2.3 Response of Scintillation to Solar Activity

A radio signal from a satellite to a receiver on Earth that propagates through the ionosphere experiences rapid fluctuations of amplitude and phase known as ionospheric scintillation [12]. A study on scintillation by Abdullah et al. [11] during high solar activity (30 November to 23 December 2005) at Sipitang and Parit Raja, Johor showed that a quiet scintillation event was observed during most weeks. It

Table 1 Categories of scintillation activity

Scintillation index	Categories
$S4 \leq 0.25$	Quiet
$0.5 \leq S4 \leq 0.25$	Moderate
$1 \leq S4 \leq 0.5$	Severe

should be noted that scintillation activity can be grouped into four categories as shown in Table 1.

A study of gigahertz scintillations during the period of increasing phase of the solar activity cycle 24 (2011) was conducted by [13]. Scintillations over UKM and Langkawi were analysed. Strong scintillations were observed at UKM compared to Langkawi with the S4 indices exceeding 0.5. This is due to the location of Langkawi, which is nearer to the dip equator. Scintillations at the dip equator are expected to be lower than the scintillations over a station located further from the dip equator [13].

The diurnal and seasonal variations of scintillations during this period of the study showed that during equinoxes, scintillations reached their peak in the morning, noon and evening while during summer it was around 1100 LT and reached its maximum in the late afternoon. A maximum of scintillations was observed during equinoxes and a minimum during summer at both stations [12]. Figure 3, which was taken from Seif et al. [12], shows an example of the occurrence of scintillations at UKM in 2010. From the figure, it can be seen that scintillation is high during equinoxes and at a minimum during summer, a similar pattern to that found in the seasonal variation of TEC. The low occurrence of scintillations during summer might be due to the persistence of equatorial spread-F (ESF), reduction of F region height and vertical drift along with low ambient electron density [12].

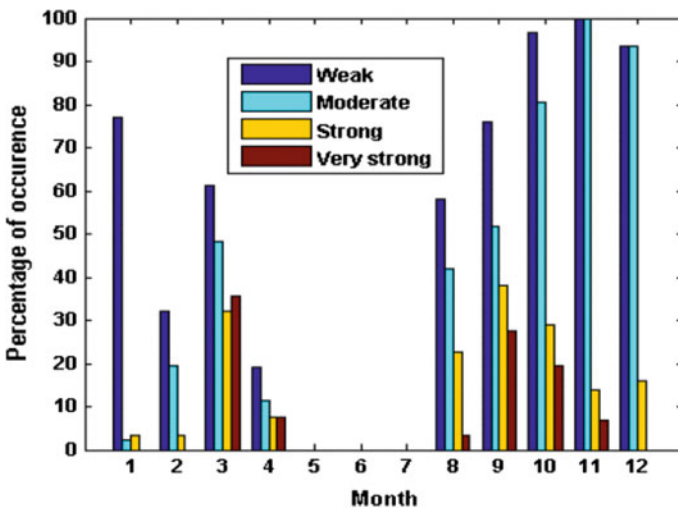


Fig. 3 Monthly variations in the occurrence of scintillations at UKM in 2010 (Figure taken from Seif et al. [12])

2.4 *Response of the Equatorial Plasma Bubble to Solar Activity*

One of the well-known ionospheric irregularities occurring in the equatorial region is the equatorial plasma bubble (EPB). The EPB can be defined as a depletion of plasma density in the equatorial F layer. It is generated at the magnetic equator and elongated along the magnetic field in the North-South field-aligned structure of depleted plasma through the Rayleigh-Taylor instability.

A study conducted by Buhari et al. [14, 15] on 5 April 2011 during an increasing phase of solar activity found that 16 EPBs with lifetimes varying from 50 min to 7 h were generated continuously over Malaysia. The separation distances of these EPBs were from 100 to 550 km and were at 10 min intervals. The EPBs propagated 440 to 3000 km towards the east with velocities of 83 to 162 ms⁻¹ [14, 15].

GPS data from 2003 to 2013 was used to study the equatorial plasma bubble (EPB) over Malaysia. This study covered almost two solar cycles, which were cycle 23 and cycle 24. The evolution of EPB over Malaysia was detected using the 2D map of the Rate of TEC change index (ROTI) [16]. The occurrence of EPBs was at a maximum during the equinoctial months, which were Mar-Apr and Sep-Oct each year. The maximum occurrence in a year increased from 60% in 2008 and 2009 to more than 90% in 2010 to 2013. On the other hand, the minimum occurrence rate of EPB was during the solstice seasons from December-January and June-July [16].

Low solar activity was recorded on 33% of the days with EPBs and 67% of the days without EPBs. During high solar activity, 66% of the days were affected by EPBs and 34% of the days were without EPBs. During the low solar activity period, 319 out of 365 (87%) days were recorded as non-successive EPB days and 46 (13%) days as were recorded as successive EPB days. On the other hand, 306 out of 598 (51%) days were successive EPB days and 292 (49%) days were registered as non-successive EPB days during the high solar activity period. The occurrence rate of EPB days exhibited considerable variation with SSN for the years of 2008–2010. The occurrence rate of EPB days was in agreement with the average of the solar flux index for the period of 2011–2013, which was during the high solar activity [16].

The results implied that most of the EPBs that occurred during the equinoctial months in 2011–2013 tended to occur successively along the observed longitudes. These results revealed for the first time that the successive EPBs are likely to occur during the equinoctial months in high solar activity periods due to the strong growth rate of RTI. The probability of EPBs that occur successively is higher during the high solar activity periods [16]. The occurrence day of EPBs was found to be relatively active only in the equinoctial months during low solar activity. The results suggest that strong perturbation is a prerequisite for the development of EPBs during low solar activity years [16].

2.5 *Response of Ionospheric Delay to Solar Activity*

A study during the decreasing phase of solar activity (2005) of solar cycle 23 showed that the delay could be corrected by more than 90%. On the other hand, a study carried out during the increasing phase of solar activity of cycle 24 (2011) by Elmunim et al. [17] showed that the diurnal trend of the ionospheric delay peaked during the post-noon period, while the minimum was observed during the early morning. The range of the delay during quiet time was from 1.5 to 4.5 m. The seasonal variations of the ionospheric delay showed that the maximum ionospheric delay was in November with 7.7 m while the minimum was in July with 0.3 m.

During the deep solar minimum (2009–2010), it was shown that the mean ionospheric delay throughout the 15-month period varied in the range of 2–6 m. It was observed that the error increased slightly with a significant difference between the curves of actual and forecasted delay during summer, where both models underestimated 1 m of delay in May 2010. In contrast, an overestimation of 3 m was seen in June 2010 throughout the observation period.

A prominent difference of about 3 m of ionospheric delay was also observed for both models in October 2010 during 1500–2100 h LT. The average error between the actual and forecasted delay throughout the observation period was in the range of 0–2 m [17].

3 **Conclusion**

Variability in solar activity is embodied in the ionosphere globally, while chemical and dynamical processes vary on a different spatial scale. Therefore, more attention should be given to not only global characteristics but also to local particularities in ionospheric variations, particularly during high solar activity.

Various instruments have been used to study the ionosphere in Malaysia. Based on studies conducted by researchers in Malaysia, it can be observed that the effects of solar activity on the ionosphere are increasing with the development of detection methods and instruments, the accumulation of a huge quantity of data, and development of solar radiation and ionospheric models.

The studies conducted by researchers in Malaysia proved that solar activity does play an important role in the variations of the ionosphere. Studies that cover two solar cycles can be used as a basis to develop the ionospheric model and the space weather prediction centre in Malaysia, which can ultimately help our government in maintaining and enhancing the performance of space communications in Malaysia.

Acknowledgements This research is supported by Universiti Kebangsaan Malaysia under the GUP-2015-052 grants.

References

1. Liu L, Wan W, Chen Y, Le HJ (2011) Solar activity effects of the ionosphere: a brief review. *Chin Sci Bull* 56:1202–1211
2. Adewale AO, Oyeyemi EO, Olwendo J (2012) Solar activity dependence of total electron content derived from GPS observations over Mbarara. *Adv Space Res* 50:415–426
3. Abdullah S, Zain AFM (2009) A 3-year observation of the ionospheric critical frequency over Malaysia. In: Paper presented at MUCET2009 Malaysian technical universities conference on engineering and technology, 20–22 June 2009
4. Abdullah S (2011) Observations of F-region critical frequency variation over Batu Pahat, Malaysia during low solar activity. PhD Thesis, Universiti Tun Hussein Onn Malaysia (UTHM)
5. Rhazali ZA (2014) Modeling the F region ionospheric peak height variations over Malaysia by antenna pattern synthesis technique. PhD Thesis, Universiti Malaysia Pahang (UMP)
6. Zain AFM, Abdullah M, Ho YH et al (2005) First ionospheric experimental campaign and observations at Fraser's Hill, Malaysia: results of vertical sounding. In: Paper presented at 2005 Asia-pacific conference on applied electromagnetics proceedings, Johor Bahru, Johor, Malaysia, 20–21 Dec 2005, pp 129–132
7. Zain AFM, Abdullah S, Homam MJ et al (2008) Observations of the F3-layer at equatorial region during 2005. *J Atmos Solar Terr Phys* 70:918–925
8. Malik RA, Abdullah M, Abdullah S et al (2016) Comparison of maximum usable frequency (MUF) variability over Peninsular Malaysia with IRI model during the rise of solar cycle 24. *J Atmos Solar Terr Phys* 138–139:87–92
9. Bello SA, Abdullah M, Abdul NSA (2017) Investigation of ionospheric minimum frequency near dip equator. *Adv Sci Lett* 33:1329–1332
10. Bahari SA, Abdullah M, Hasbi AM (2015) A review of ionospheric studies in Malaysia using GPS. In: Proceeding of the 2015 international conference on space science and communication (IconSpace), Langkawi, Malaysia, 10–12 Aug 2015, pp 95–100
11. Abdullah M, Zain AFM, Ho YH et al (2009) TEC and scintillation study of equatorial ionosphere: a month campaign over Sipitang and Parit Raja stations, Malaysia. *Am J Eng Appl Sci* 2(1):44–49
12. Seif A, Abdullah M, Hasbi AM et al (2013) Seasonal variations of amplitude scintillation events using GPS data at Malaysia. In: Proceeding of the 2013 international conference on space science and communication (IconSpace), Melaka, Malaysia, 1– 3 July 2013, pp 416–419
13. Seif A, Tsunoda RT, Abdullah M et al (2015) Daytime gigahertz scintillations near magnetic equator: relationship to blanketing sporadic E and gradient-drift instability. *Earth, Planets and Space* 67:177
14. Buhari SM, Abdullah M, Hasbi AM et al (2014) Two-dimensional structure of equatorial plasma bubble observed using GPS networks in South East Asia region. In: Paper presented at 2014 international conference on electronics, information and communications (ICEIC 2014), Kota Kinabalu, Malaysia, 15–18 Jan 2014, pp 16–17
15. Buhari SM, Abdullah M, Hasbi AM et al (2014) The spatial and temporal evolution of equatorial plasma bubble observed using ground based GPS TEC measurement. In: Paper presented at Japan geoscience union meeting 2014, Pacifico Yokohama, Kanagawa, Japan, 28 April–2 May 2014, pp 1–2
16. Buhari SM, Abdullah M, Yokoyama T et al (2017) Climatology of successive equatorial plasma bubbles observed by GPS ROTI over Malaysia. *J Geophys Res* 122(2):2174–2184
17. Elmunim NA, Abdullah M, Bahari SA (2015) Comparison of statistical holt-winter models for forecasting the ionospheric delay using GPS observations. *Indian J Radio Space Phys* 44:28–34

The Time Derivative of the Horizontal Geomagnetic Field for the Low Latitude MAGDAS Langkawi Station for the Estimation of Geomagnetically Induced Current

Farah Adilah Mohd Kasran, Mohamad Huzaimy Jusoh,
Akimasa Yoshikawa, Zahira Mohd. Radzi and MAGDAS/CPMN
Group

Abstract The time derivative of the horizontal magnetic field component (dH/dt) is directly related to geomagnetically induced current (GIC). From Faraday's law of induction, the changes in geomagnetic field due to space weather perturbations can produce an electrical current to flow on the Earth's surface and this process is the so-called GIC. Historically, many GIC activities have been reported from high latitude regions due to the very frequent and intense geomagnetic activity observed in the area. However, during strong sudden impulse (SI) events, the impact of geomagnetic disturbance may extend to low latitude regions, thus leading to GIC activity. Long-term analysis of ground magnetic changes, with dH/dt exceeding 30 nT/min at MAGDAS Langkawi station during ascending and peak Solar Cycle 24 (SC 24) was conducted in order to select the significant SI event. The analysis of the Solar Wind Speed V_x component, Interplanetary Magnetic Field, IMF B_z component and magnetic indices (AU, AE and DST) was then conducted to reveal the behavior of each of those parameters during the events. We found that during SI events in this study period, the average of the time derivative of the H-component magnetic field, dH/dt was 37.8 nT/min. Three SI events were analyzed and was observed that the characteristics of solar wind speed and interplanetary magnetic

F.A.M. Kasran (✉) · M.H. Jusoh
Applied Electromagnetism Research Group, Universiti Teknologi MARA,
40450 Shah Alam, Malaysia
e-mail: farahadilah87@gmail.com

F.A.M. Kasran · M.H. Jusoh
Faculty of Electrical Engineering, Universiti Teknologi MARA,
40450 Shah Alam, Malaysia

A. Yoshikawa MAGDAS/CPMN Group
International Center for Space Weather Science and Education,
Kyushu University, Fukuoka, Japan

Z.Mohd. Radzi
National Space Agency, 42700 Banting, Malaysia

field during the storm can influence the strength of the local geomagnetic disturbance. Furthermore, the signature of magnetic disturbance process and amplitude of dH/dt at this station also depended strongly on which side of the Earth's was facing the SI event. The findings of the study show that an SI event during noon side with IMF Bz component points southward induce stronger ground magnetic disturbance and a larger amplitude of dH/dt even though a smaller increase of solar wind speed V_x is recorded compared to any SI events that occurred on night side with northward pointing of IMF Bz. In overall, the analysis on dH/dt of this study shows the possibility of GIC occurrence in Malaysia and further investigation and experimentation on GIC activity is strongly recommended.

1 Introduction

Geomagnetically induced current (known afterwards as GIC) is one of the effects of space weather perturbation that has significant potential to be explored and subsequently impact Earth surface technologies and buried equipment such as electrical equipment, railways, pipelines, telecommunication cables and oil and gas technology [1–4]. During space weather perturbation, the solar wind input energy gives rise to large atmospheric current vortices above Sun-lit northern and southern hemispheres. High variations of atmospheric current will be affecting the geoelectric field at the Earth's surface and this in turn drives GIC—also known as telluric currents—along electrically conductive technological networks. Historically, a lot of research on GIC has been conducted in high latitude regions since the effects of space weather perturbation are the most intense and most frequent in this region. Plus, the most famous GIC event was reported in the Quebec Province of Canada during a March 1989 storm, blacking out the region for nine hours [5–7]. Nevertheless, during major space weather storms, large geomagnetic disturbances may also occur at much lower latitudes, indicating the possibility of GIC problems there too [8–13]. Furthermore, the magnitude GIC depends significantly on the network topology, configuration and resistance [3]. So, all this shows that GIC issues have to be taken into account in mid- and low-latitude networks.

Several methods can be employed to estimate and to identify the value of GIC, which are based on calculation of the rate-of-change of the horizontal component of the magnetic field [2, 6, 10, 14, 15] and on on-site measurement whether directly at the cable linking the neutral of the transformer and the earth of the star connection or from magnetometer observations under the transmission lines carrying hundreds of kilovolts [3, 6, 7, 9, 10, 16]. The rate of change of the horizontal component of the magnetic field is the driver of GIC. The changes of geomagnetic field generate electrical current that flows on the Earth's surface. This phenomenon is based on

Faraday's law of induction where the induced electric field at the Earth's surface, E can be calculated from the rate of change in the geomagnetic field, B as in Eq. 1.

$$\nabla \times E = -\partial B/\partial t \quad (1)$$

The disruption of electrical power due to GIC is needs to be considered seriously since our society depends most on the availability and reliability of electricity. However, the progress of this novel impact on the technology is slow due to the lack of understanding and awareness in fundamental and theoretical aspects of the significant effects due to space weather perturbation, especially in the equatorial region (low-latitudes) and specifically in Malaysia. Therefore, this study proposes a fundamental investigation of geomagnetic field changes (dH/dt) as a precursor to GIC occurrence due to SI events in Langkawi station, located in north Malaysia. The investigation covers the impact of space storms on the ground magnetic field during the ascending period of solar cycle SC 24.

2 Methodology

2.1 Data Sets and Data Processing

We analysed the whole period from 2009 to 2016 which included a magnetic quiet period followed by a storm, using a ground-based magnetometer (MAGDAS) in Langkawi, Malaysia to investigate the possibility of geomagnetically induced current (GIC) occurrence in Malaysia. This time period covered the ascending and the peak of Solar Cycle 24. The selection of the MAGDAS station during this period was made regarding the availability of ground magnetic data.

2.1.1 Data Sets

Figure 1 shows the location of Langkawi MAGDAS observatory and Table 1 gives the code, name, geographic and geomagnetic coordinates of the station. The horizontal geomagnetic component (H-comp) was extracted from the raw data of the MAGDAS network.

Several studies have revealed that time derivatives of geomagnetic H component resemble GIC [3–5, 7, 9–12, 16] and investigations by some of the studies [11] revealed that from 1-min time derivative of H component with exceeding of 30 nT/min ($dH/dt > 30$ nT/min), will cause an undesirable effect in power grids. Therefore, in this study, the H component of magnetic field at Langkawi was first extracted to find its derivative value (dH/dt), then the significant value of $dH/dt > 30$ nT/min was filtered out for further analysis.

Satellite data from SOHO was observed to determine the existence of solar flares, coronal hole (CH) and coronal mass ejection (CME). The solar wind

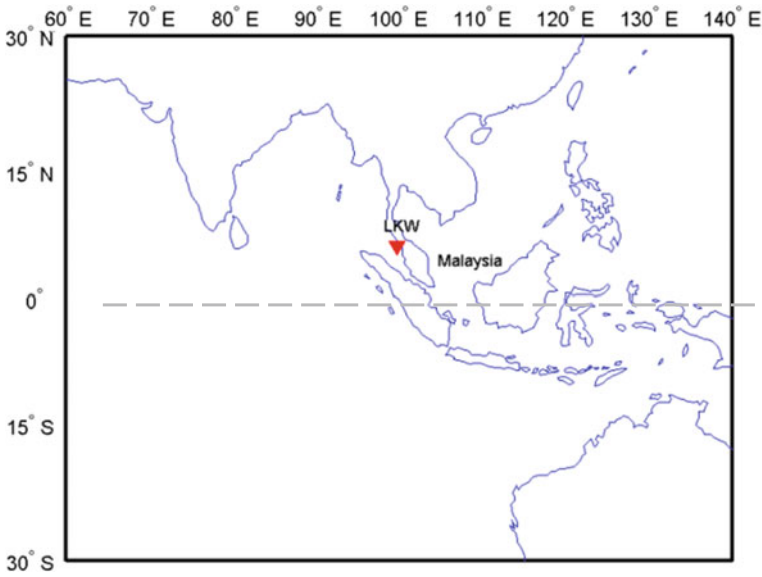


Fig. 1 Location of MAGDAS Langkawi observatories

Table 1 Geographic and geomagnetic coordinates of the magnetic observatory

Code	Name	Geographic		Geomagnetic		Local time
		Latitude	Longitude	Latitude	Longitude	
LKW	Langkawi, Malaysia	6.30	99.78	-2.32	171.29	GMT +8

parameters were then analyzed in order to study the connection between space events and ground surface activity. The solar wind parameters, V_x and interplanetary magnetic field, (IMF) B_z were recorded on board the ACE satellite, the magnetic indices, Dst, AU and AE are from the Data Analysis Center for Geomagnetism and Space Graduate School of Science, Kyoto University database, the A_m magnetic indices are from the International Service of Geomagnetic Indices database and geomagnetic events are from the Erbe Observatory database.

The magnetic indices, Dst, AU and AL give an estimation of the magnetospheric and auroral electric currents while the A_m magnetic indices allow the identification of magnetic quiet days. The criterion of a magnetic quiet day is that the daily average A_m index is smaller than 20 nT. Typically, the geomagnetic occurrence is due to Sudden Commencement (SC) which can be categorized as Sudden Impulse (SI) and Sudden Storm Commencement (SSC). The phenomena studied was SC (sudden commencement), which can be due to SSC (storm sudden commencement) if it is a subsequent magnetic disturbance, or SI (sudden impulse) if there is no further disturbance.

2.1.2 Data Processing

The horizontal component of MAGDAS magnetic field was obtained from Eq. 2. In this study, we use the time derivative of ground horizontal magnetic field and Eq. 3 to estimate GIC activity in Malaysia with a 1-minute time resolution.

$$H = \sqrt{x^2 + y^2} \quad (2)$$

$$\frac{dH}{dt} = \sqrt{dx/dt^2 + dy/dt^2} \quad (3)$$

3 Data Analysis, Results and Discussion

3.1 Data Analysis

In this present study, the main criterion to select the geomagnetic events in this station is based on the derivative of the horizontal component, $dH/dt > 30\text{nT/min}$. The value of derivative, $dH/dt > 30\text{nT/min}$ indicates the possibility of geomagnetic induced current (GIC) occurrence at the ground surface. Figure 2a–n shows 14 significant events in LKW station with $dH/dt > 30\text{nT/min}$ and corresponding date. This figure is superimposed on a grey transparency box which represents the local night time. Table 2 provides the maximum values of dH/dt and local time for each of the 14 significant events. Of these events, ten (Fig. 2a–b, d–h and l–n) occurred during the daytime while the other four events (Fig. 2c and i–k) happened during nighttime. The highest dH/dt was 88.28 nT/min, recorded on 2nd October 2013 at 09:54 in the morning while the lowest was on 8th February 2014 at 12:15 in the afternoon when dH/dt was 30.8 nT/min. The standard deviation, σ has been applied to identify the typical value range of dH/dt throughout 2009–2016 at LKW station and 0.82699 was obtained as the value of σ for this time period. Therefore, during quiet geomagnetic activity, the regular variation of dH/dt is in the range of 0.8271 nT/min and -0.8269 nT/min. Nevertheless, a large spike of dH/dt can be observed if there is any geomagnetic disturbance. The dH/dt variation in Fig. 2c, d, i–k) shows a sudden increase at 15:03, 05:26, 15:54, 11:14 and 18:57 UT respectively before it decreases to the regular pattern which tends to 0 nT/min. While Fig. 2e, f has the same variations as the first pattern but high variation of dH/dt still occurred during certain periods after the sudden increase at 06:00 and 01:54 UT respectively. High variation of dH/dt can be seen before and after the sudden increases at 05:50, 04:10, 07:15, 07:50, 02:07, 03:50 and 02:55 UT respectively as shown in Fig. 2a, b, g–h and l–n) and classified as the third pattern. The detailed explanation of the

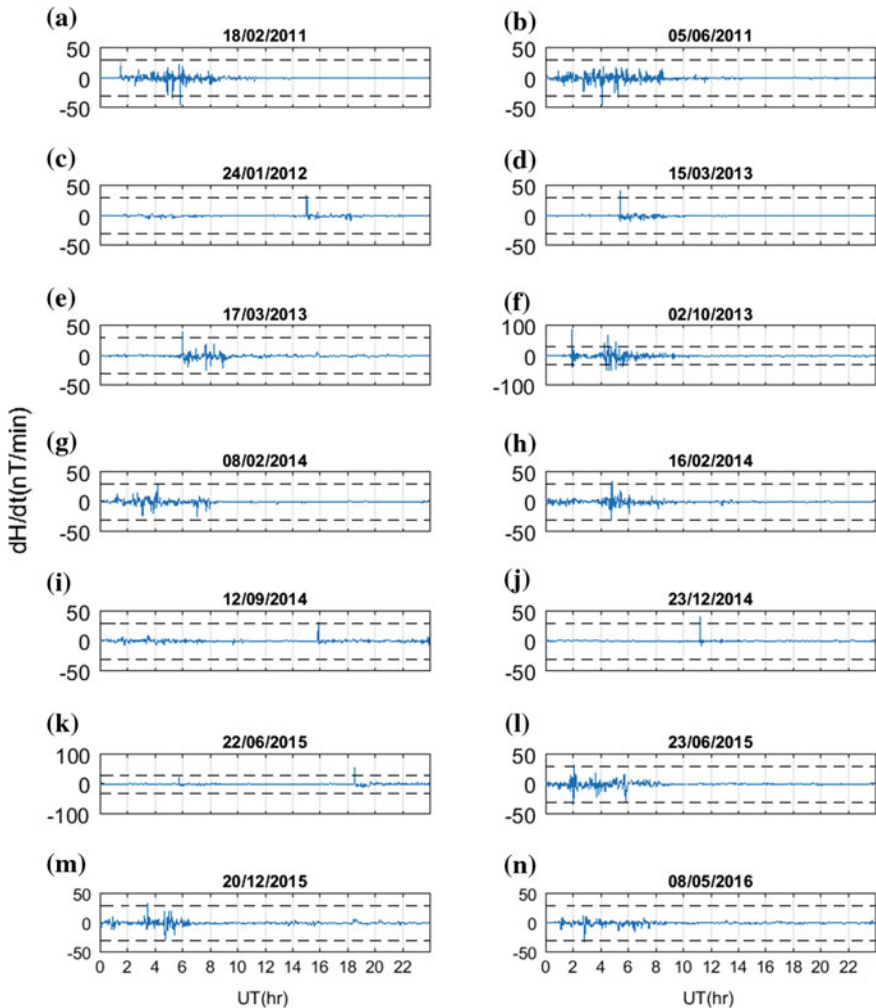


Fig. 2 14 variations of derivative H component (dH/dt) exceeding 30 nT/min with corresponding date at Langkawi station from 2009–2016. Dashed black lines of each plot indicate ± 30 nT/min

factors that influence dH/dt variations remain unexplored but we believe that the behaviour of geomagnetic disturbance is strongly related to those dH/dt patterns. Table 2 gives the values of maximum dH/dt and its occurrence time for each event in both universal and local time (UT and LT).

To discover the significance of the role of geomagnetic events in the rise of high magnetic field changes, dH/dt in this dip equator station (as presented in Fig. 2), we need to identify the geomagnetic event behaviour for each event and the local time of occurrence. The geomagnetic field exhibits variations due to different phenomena. These are regular variations with no geomagnetic storm occurrence and irregular

Table 2 Maximum values of dH/dt for the event from 2009–2016 with corresponding universal and local time of occurrence, at Langkawi station

Year	Day	Max dH/dt (nT/min)	Time (UT)	Time (LT)
2011	18 Feb	-45.07	05:50	13:50
	5 June	-44.87	04:15	12:15
2012	24 Jan	34.83	15:07	23:07
2013	15 Mar	42.2	05:45	13:45
	17 Mar	41.2	06:00	14:00
	2 Oct	88.28	01:54	09:54
2014	8 Feb	30.8	07:15	15:15
	16 Feb	35.11	04:50	12:50
	12 Sept	31.46	15:54	23:54
	23 Dec	40.44	11:25	19:25
2015	22 June	54.31	18:57	02:57
	23 June	31.63	02:07	10:07
	20 Dec	33.44	03:50	11:50
2016	8 May	-32.37	02:55	10:55

Table 3 Detail of sudden impulse (SI) event occurrence time with A_m index

Year	Day	Time (UT)	Time (LT)	Geomagnetic classification	$\langle A_m \rangle$ nT
2013	15 Mar	05:26	13:26	SI	12 quiet
2014	7 Feb	17:05	01:05	SI	40
	23 Dec	11:14	19:14	SI	26

variations due to any geomagnetic activity, considered in this sense as magnetic disturbances. The H component of geomagnetic field from the MAGDAS LKW station was examined to further understand the consequences of different geomagnetic phenomena manifesting a high value of dH/dt . In this study, we examine dH/dt that exceeding 30nT/min only during SI (sudden impulse) events.

Table 3 lists the SI events from the selected SC events with $dH/dt > 30$ nT/min for further analysis. The events were compared with the quietest day to study the different levels of geomagnetic variation with respect to the local time (daytime and nighttime).

Of the events selected, only three events on 15 March 2013, 7 February and 23 December 2014 are classified as sudden impulse (SI) while the other events are classified as storm sudden commencement (SSC). Besides that, only one SI event on 15 March 2013 happened during quiet geomagnetic activity with $\langle A_m \rangle$ index of 12 nT. On 7 February 2014, SI occurrence manifested high magnetic changes with a maximum value of 30.8 nT/min recorded on the following day. Therefore, analysis of two days (7–8 February 2014) geomagnetic activity was performed for this event. To identify the regular variation of H component in LKW station, the

Table 4 Most quiet geomagnetic correspond to each month of SI occurrence based on Am index <20 nT

Quiet days	8 Mar 2013	13 Feb 2014	26 Feb 2014	11 Dec 2014
Daily <Am>	2	2	4	7

selected quietest period was obtained based on Am index with daily Am < 20 nT as listed in Table 4. Four quiet periods were selected, which correspond to the month of each of the SI events.

3.1.1 SI Event of 15 March 2013

Figure 3a shows the Vx component of solar wind, Fig. 3b shows the Bz component of interplanetary magnetic field (IMF), Fig. 3c shows the Dst index, Fig. 3d shows AU and AE indices and Fig. 3e shows the magnetic field H component (solid line) on 15 March 2013 superimposed on the quietest reference level H component (dashed line) on 8 March 2013 of the same station as a function of UT time. The dashed line shows the well-known regular pattern of H component during a quiet day in Langkawi, thus enabling analysis of the different pattern of H component between the shock event occurrence and the quiet day. This figure shows that just before 05:00 UT there was a sudden increase in the solar wind component Vx of about 50 km/s, associated with a southward increase of the IMF Bz component (from 0 nT to -8 nT). Later, the IMF Bz turned northward slightly after 05:00 UT before returning toward the south at around 05:30 UT. When IMF Bz increased southward at 06:30 UT, the Dst index gradually decreased illustrating the intensification of a westward ring current. Figure 1d shows the development of auroral activity (AU and AE) simultaneously with the sudden increase of magnetic field H component of 62 nT at 05:26 UT/13:26 LT (solid line). In this event the H component followed the regular pattern except during the shock impulse and for several hours after the SI event (from 05:26 UT to 08:30 UT), indicating that the magnetic disturbance associated with SI event with certain delay. All these observations are the effects of the shock associated with the eruption that peaked at M1.2 and generated a full-halo coronal mass ejection (CME) which reached the Earth on 15 March 2013 followed by high speed solar wind streams.

3.1.2 SI Event of 23 December 2014

For this event we present the geomagnetic effect of the storm related to shock passage associated with coronal mass ejection of 21 December 2014. Figure 4 shows similar parameters to Fig. 3 but this figure corresponds to the SI event on 23 December 2014. A large sudden increase of the solar wind component Vx of 152 km/s at 10:36 UT lead to IMF Bz point northward until 18:00 UT. During this period, the Dst index remained positive before gradually decreasing starting at

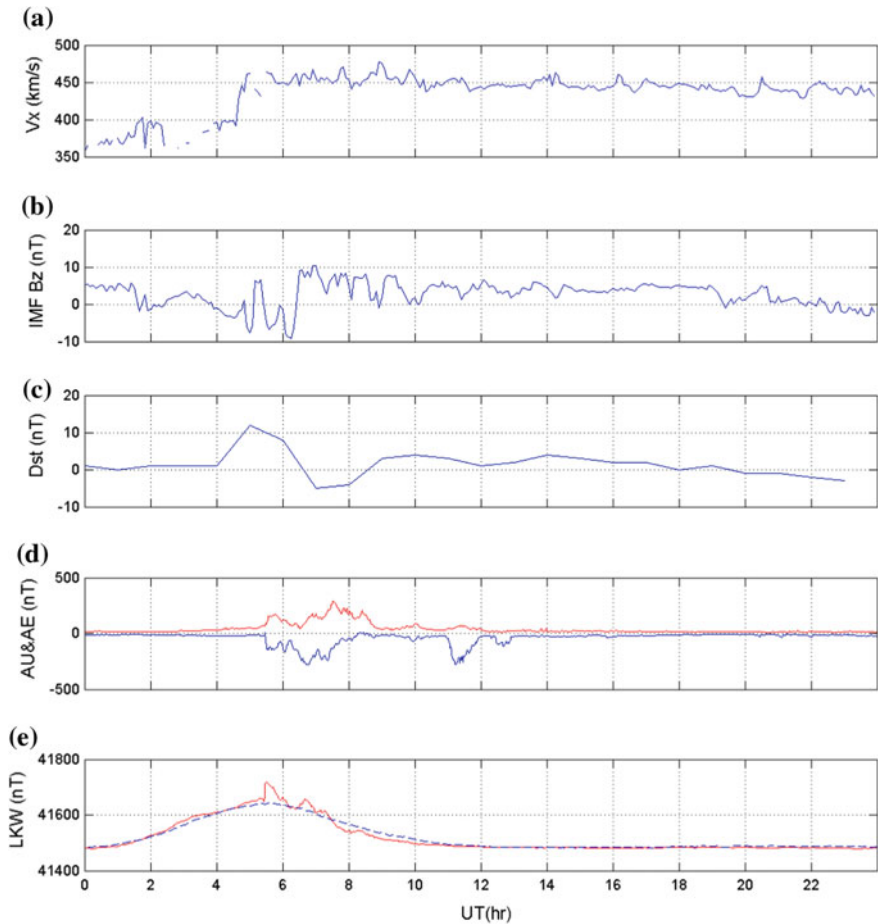


Fig. 3 The solar wind parameters and geomagnetic indices for the SI event on 15 March 2013: **a** component V_x of the solar wind speed, **b** the B_z component of the interplanetary magnetic field, **c** and **d** the Dst index and the AU and AE indices, and **d** Superposition of regular variation (computed for the quiet geomagnetic activity of H component) as a dashed curve and the raw data of H component at LKW station

20:00 UT. The sudden increase of V_x also resulted in the sudden and short enhancement of auroral activity based on the AU and AE indices. H component of magnetic field closely followed the regular pattern (11 Dec 2014) before a sudden increase was recorded at 11:17 UT/19:17 LT which was the response to the shock impact with an almost 1-hour delay. After the SI event, the H component variation decreased to the regular pattern illustrating the recovery phase of the magnetic disturbance but it continued to decrease below the reference variation starting at about 19:30 UT.

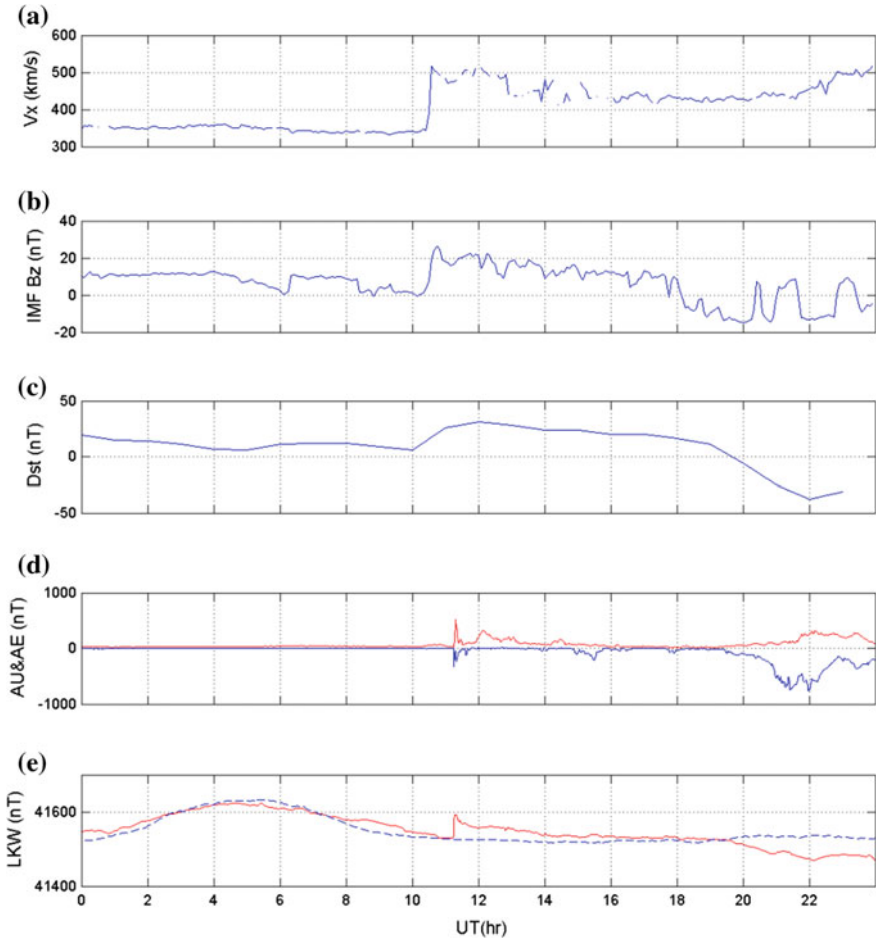


Fig. 4 The solar wind parameters and geomagnetic indices for the SI event on 23 December 2014: **a** component V_x of the solar wind speed, **b** the B_z component of the interplanetary magnetic field, **c** and **d** the Dst index and the AU and AE indices, and **d** Superposition of regular variation (computed for the magnetic quiet day of H component) as a dashed curve and the raw data of H component at LKW station

3.1.3 SI Events of 7 and 8 February 2014

Figure 5 illustrates two days of solar wind speed (V_{sw}), IMF B_z component, ground magnetic indices (Dst, AU and AE index) and local ground magnetic at LKW station. On 7 February 2014, a weak interplanetary shockwave passed the Earth due to an expected weak CME passage and the onset of a coronal holes high speed stream. Just after 16:15 UT, the sudden increased of solar wind speed V_x from 310 km/s to 400 km/s can be observed. This storm exhibits an oscillating IMF

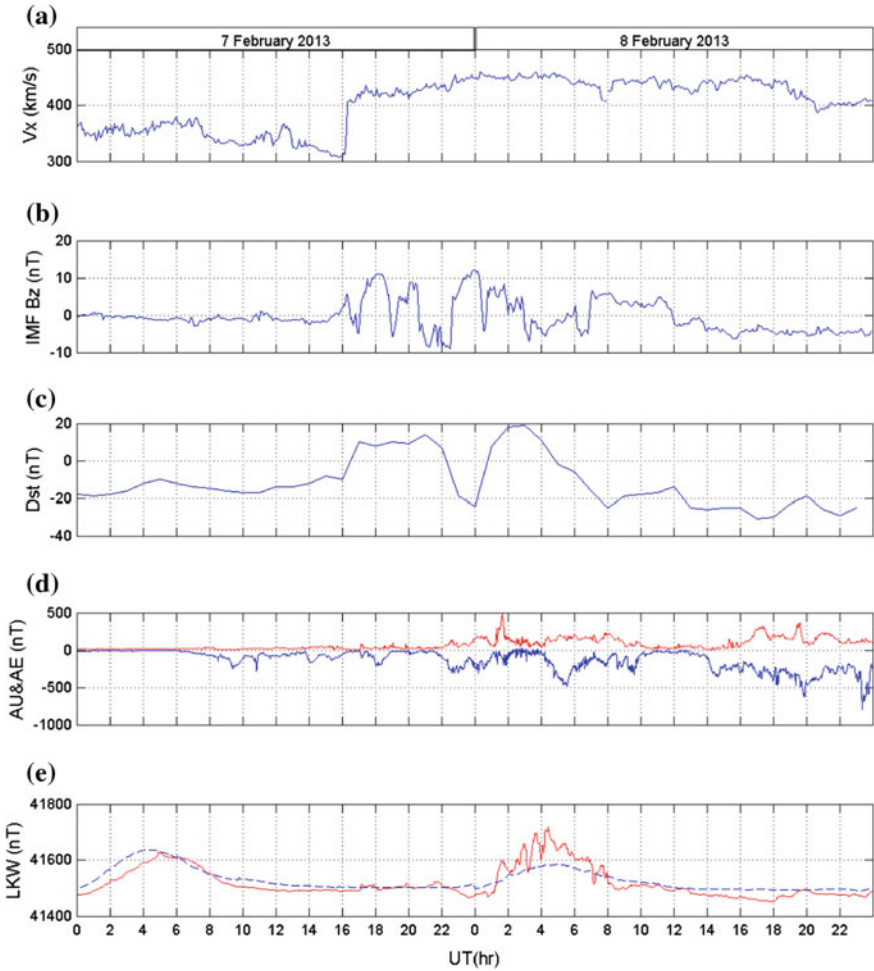


Fig. 5 The solar wind parameters and geomagnetic indices for the SI event on 7 February 2013 and the following day of 8 February 2013: **a** component V_x of the solar wind speed, **b** the B_z component of the interplanetary magnetic field, **c** and **d** the Dst index and the AU and AE indices, and **d** Superposition of regular variation (computed for the magnetic quiet day of H component) as a dashed curve and the raw data of H component at LKW station

B_z component. It began to point southward before turning to a positive value, and this oscillating process continued until noon on the following day (8 February 2014), thus leading to the unstable variation of the ring current based on the Dst index. An increased positive value of Dst was observed just after the shock impulse and it remained until 22:00 UT. It decreased to below 20 nT before it increased again at 00:00 UT back to 20 nT. After the shock event, a small disturbed auroral electrojet was observed based on the AU and AE indices but due to the long period

of high speed solar wind and oscillated IMF Bz, these factors exhibited three main maximum values of the AL index on 8 February 2014 at 05:30 UT (-483 nT), at just before 20:00 UT (-633 nT) and at 23:15 UT (-796 nT). In addition, a high impulse on AU at around 01:40 UT (490 nT) was associated with the sudden increase of magnetic H component at the same time. Overall, the sudden increase of V_x resulted in a small increase of H component of 20 nT recorded at 17:05 UT/01:05 LT but the long period of the high speed solar wind phase led to an oscillated IMF Bz and the observed long magnetic disturbance.

3.2 Results and Discussion

In this paper, we propose criteria of H-component magnetic field changes, dH/dt exceeding 30 nT/min in Langkawi station in order to select sudden impulse (SI) events and then analyse three such cases. All three cases exhibit the same behaviour of solar wind speed V_x (sudden increase of magnitude) but different characteristics of the IMF Bz variation and the Dst variation. In the first case, on 15 March 2013, Sudden increase of V_x during this SI event with southward polarization of IMF Bz caused a geomagnetic disturbance starting with compression, main and recovery phase based on Dst index. In the second case, on 23 December 2014, a sudden increase of V_x led to the IMF Bz turning from southward to northward. Increased variation of Dst index shows a strong magnetopause compression happened during this interplanetary shock. In the third case, on 7 February 2014, a shock impulse associated with a large sudden increase of V_x exhibited an oscillating IMF Bz component. As a consequence, two peaks in the Dst index were observed and they decreased to the recovery phase on the following day. To study the effects of the space storm on geomagnetic H component during the SI events, the detailed characteristics of each storm are provided in Table 5. It comprises the variation of solar wind speed V_x in (km/s), the z-component of the interplanetary magnetic field IMF, Bz (nT), and the characteristics of the Dst index for the three SI events.

From the parameters in Table 6, it is clearly be seen that the increased value of V_x plays important role in influencing the values of IMF Bz and the Dst index. The highest increase of V_x happened on 23 December 2014 with ΔV_x of 152 km/s, and resulted in the highest variation of Bz and the Dst index (27 nT and 25 nT respectively). The lowest solar winds speed variation was recorded on 15 March 2013 and related to the lowest variation of IMF Bz and the Dst index. This finding

Table 5 Solar wind parameter V_x and IMF Bz and magnetic Dst variations during the SI events

Beginning of the storm		Variation of indices		
Day	Time (UT)	ΔV_x	ΔB_z	ΔDst
15 Mar 2013	04:30	49	8.75	11
23 Dec 2014	10:36	152	27	25
7–8 Feb 2013	16:17	90	10.16	20

Table 6 Increased value of H component (ΔH comp) and corresponding maximum dH/dt value on one day at LKW station during SI events

Day	Time (LT)		ΔH comp	Max dH/dt (nT/min)
15 Mar 2013	13:26	Noon	62	42.2
23 Dec 2014	19:14	Dusk	63	40.44

Table 7 Increased value of H component (ΔH comp) and corresponding maximum dH/dt value for the SI event on 7 February 2013

SC event				dH/dt			
Day	Time (LT)		ΔH comp (nT)	Day	Time (LT)		Max dH/dt (nT/min)
7 Feb 2014	01:05	Night	21	8 Feb 2014	07:15	Morning	30.8

shows that a large sudden increase of solar wind speed, V_x influences the variation of IMF B_z (ΔB_z) and also the Dst index value (ΔDst).

One SI event experienced a difference in time between shock impulse and maximum dH/dt as listed in Table 7. In 2014, a SI event happened on 7 February at 17:05 UT/01:05 LT during nighttime and the maximum dH/dt was recorded after 14 h and 10 min of sudden enhancement. This event recorded a small enhancement of H component of magnetic field although it corresponds to a large increase of V_x as the sudden storm happened on the night side. The maximum value of dH/dt of 30 nT/min is small and was clearly influenced by the increased level of geomagnetic H-component.

A sudden increase in the ground magnetic impulse associated with the solar wind speed, V_x , can lead to high magnetic changes, dH/dt , and thus increases the possibility of GIC occurrence at that station. Ground magnetic observations associated with the changes in IMF B_z , AU and AL can be interpreted as the effect of the prompt penetration of the magnetospheric convection electric field. This physical process simultaneously effects high, middle, low and equatorial latitudes [17]. When the shock impulse hit the Earth, LKW station, located in the equatorial region, also experienced the impact based on the H component variation. A negative value of the Dst index indicates a ring current injection which resulted from the transfer of energy, mass and momentum from the solar wind to the Earth’s magnetosphere. The findings in this study proves that local time also plays an important role and influences the space storm effect on the ground magnetic field, thus GIC activity. For instance, a large increase of solar wind speed associated to SI event on 7 February 2014, has caused a smaller impulse of ground magnetic H component compared to SI event on 23 December 2014 that happened during day time. During daytime, solar wind dynamic pressure forces the magnetosphere current at the magnetosphere to compress more closely to the Earth’s surface compared to nighttime, thus cause high risk of GIC activity at this equatorial region even though during insignificant space weather perturbations [4].

4 Conclusions

The findings in this study show the effects of sudden impulse event (SI) that manifest large amplitude of magnetic field changes, dH/dt at Langkawi station. Several parameters during the SI events such as the characteristic of solar wind speed V_x , the B_z component of IMF and the local time (day and night side) play crucial factors in producing the ground magnetic disturbance. From the analyses conducted, it can clearly be seen that even at this station located in dip equator, a large geomagnetic disturbance due to sudden commencement (SC) with dH/dt exceeding 30 nT/min can also occur, illustrating the possibility of GIC occurrence in Malaysia. So far, no severe impacts or problems caused by GIC have been reported. It is, of course, possible that some adverse effects have occurred due to GIC in the past, but because of insufficient awareness they have not been attributed to GIC. A novel development of this research area and exploration of geomagnetically induced current (GIC) could be extended to estimating the GIC levels in Malaysian power systems and to determine the effects of GIC on Malaysia's current and planned power systems. This study has thrown up many questions in need of further investigation. Further work especially on GIC measurement is strongly needed to provide information on GIC activity in this area, moreover, the information on GIC activity can be used as a reference for the planning and designing of power systems, as well for equipment selection in Malaysia.

Acknowledgements This project is financially supported by Fundamental Research Grant Projects, FRGS (Code No. 600-RMI/FRGS 5/3(140/2014)). The authors would like to thank Universiti Teknologi MARA for management support throughout the project. The authors also thank the ACE satellite, World Data Center (WDC), International Service of Geomagnetic Indices (ISGI) and Erbe Observatory for contributions to the data collection and analysis of the research.

References

1. Pirjola R (2002) Review on the calculation of surface electric and magnetic fields and of geomagnetically induced currents in ground-based technological systems. *Surv Geophys* 23:71–90
2. Pirjola R, Viljanen A, Pulkkinen A et al (2004) Ground effects of space weather pipelines in effects of space weather on technology infrastructure. In: Daglis IA (ed). Kluwer Academic Publisher, p 235–256
3. Pirjola R (2012) Geomagnetically induced currents as ground effects of space weather. *InTech*, p 27–44
4. Falayi E, Beloff N (2009) Global study of geomagnetic induced current using time derivatives of geomagnetic fields. *Can J Pure Appl Sci* 3:943–951
5. Viljanen A, Pulkkinen A, Amm O et al (2004) Fast computation of the geoelectric field using the method of elementary current systems and planar Earth models. *Ann Geophys* 22:101–113
6. Radasky WA and Kappenman JG (2010) Impacts of geomagnetic storms on EHV and UHV power grids. Paper presented at 2010 Asia-Pacific international symposium on electromagnetic compatibility, Beijing, China, 12–16 April 2010

7. Falayi EO, Beloff N (2012) Modelling of geomagnetically induced currents during geomagnetic storms using geoelectric fields and auroral electrojet indices. *Indian J Phys* 86:423–429
8. Kappenman JG (2003) Storm sudden commencement events and the associated geomagnetically induced current risks to ground-based systems at low-latitude and midlatitude locations. *J Sp Weather* 1:1–16
9. Trivedi NB, Vitorello I, Kabata W et al (2007) Geomagnetically induced currents in an electric power transmission system at low latitudes in Brazil: a case study. *Sp Weather* 5:1–10
10. Bernhardt EH, Tjimbandi TA, Cilliers PJ et al (2008) Improved calculation of geomagnetically induced currents in power networks in low-latitude regions. In: *PSSC Proceedings 677*
11. Falayi EO, Beloff N (2010) Estimating geomagnetically induced currents at subauroral and low latitudes to assess their effects on power systems. *Can J Pure Appl Sci* 4:1187–1197
12. Ngwira CM, McKinnell L-A, Cilliers PJ (2011) Geomagnetic activity indicators for geomagnetically induced current studies in South Africa. *Adv Sp Res* 48:529–534
13. Zheng K, Liu L, Ge HY, Li WX (2012) Comparative study of the GIC amplitudes and characteristics in different power grids in China. *CIGRE 2012*:1–7
14. Pulkkinen A, Pirjola R, Viljanen A (2007) Determination of ground conductivity and system parameters for optimal modeling of geomagnetically induced current flow in technological systems. *Earth Planets Sp* 59:999–1006
15. Liu C, Liu L, Pirjola R et al (2009) Calculation of geomagnetically induced currents in mid- to low-latitude power grids based on the plane wave method: a preliminary case study. *Sp Weather* 7:1–9
16. Liu CM, Liu LG, Pirjola R (2009) Geomagnetically induced currents in the high-voltage power grid in China. *IEEE Trans Power Deliv* 24:2368–2374
17. Fathy I, Amory-Mazaudier C, Fathy A et al (2014) Ionospheric disturbance dynamo associated to a coronal hole: case study of 5–10 April 2010. *J Geophys Res Sp Phys* 119:4120–4133

Comparison of Measured and Predicted HF Operating Frequencies During Low Solar Activity

Rafidah Abd Malik, Mardina Abdullah, Sabirin Abdullah
and Mariyam Jamilah Homam

Abstract There is a need to find reliable and accurate HF operating frequencies because of the uncertainty and variability of the ionospheric region. Therefore, the aim of this study was to observe and analyze the HF operating frequencies in Peninsular Malaysia. Comparison of HF operating frequency performances was undertaken using ASAPS and ICEPAC prediction software. This study was carried out in Peninsular Malaysia, located in the equatorial region, and at the beginning of solar cycle 24, namely from April to December of 2009. The HF operating frequencies included the maximum usable frequency (MUF) and the operating working frequency (OWF), and were based on hourly monthly median values. Results of the comparison carried out show that MUF and OWF of ASAPS slightly overestimated measurement of MUF and OWF by about 11 and 12% respectively. In contrast, MUF ICEPAC highly underestimated MUF measurement by about 39%. However, OWF ICEPAC slightly overestimated MUF measurement by about 16%. This indicates that the MUF and OWF measurements of HF operating frequencies in the Malaysian region are aligned with the MUF and OWF from the prediction software, particularly the OWF. This study also confirms that HF operating frequencies can be predicted. This study can be used to provide data and assist HF researchers in modeling MUF models for predicting HF operating frequencies in the Malaysian region.

R.A. Malik (✉) · M. Abdullah

Department of Electrical Electronic and Systems Engineering, Universiti Kebangsaan Malaysia, 43600 Bangi, Selangor Darul Ehsan, Malaysia
e-mail: rafidah@siswa.ukm.edu.my

M. Abdullah · S. Abdullah

Space Science Centre (ANGKASA), Institute of Climate Change Universiti Kebangsaan Malaysia, 43600 Bangi, Selangor Darul Ehsan, Malaysia

R.A. Malik

Communication Branch Science & Technology Research Institute for Defence (STRIDE), 43000 Kajang, Selangor Darul Ehsan, Malaysia

M.J. Homam

Universiti Tun Hussein Onn Malaysia, 83000 Batu Pahat, Johor Darul Takzim, Malaysia

1 Introduction

In the 1950s and 1960s, High Frequency (HF) communication was the backbone of long-range radio communication systems. However, in the late 1960s and early 1970s, satellite technology changed the perspective of long-range communication systems [1, 2] because of its reliability and ease of operation. Then, during the Gulf War, HF communication became popular again due to the limitations of Satcom (satellite communication) [2, 3]. Since then, HF communication has continued to play a major role in providing worldwide radio coverage alongside Satcom. HF transmission using skywave propagation is widely used for voice and data communication by both military and civilian users. Therefore, using the right frequencies for conveying information is important.

HF communication is unique because it relies upon the ionospheric medium that acts as a radio reflector. The ionosphere is an uncertain region and highly variable in all time scales, namely within an hour, throughout the day, from season to season and within the 11-year solar cycle. The HF radio frequency that is used for transmission in prevailing ionospheric conditions is called the maximum usable frequency (MUF) [4–6]. Hence, the variations in the ionosphere play a significant role in HF propagation in that a frequency which may provide successful communication now may not do so an hour later as shown in the example in Fig. 1.

Figure 1 shows HF transmission that was carried out for three consecutive days from 28 to 30 Dec 2009 in the morning, afternoon and at night. It was found that frequencies were irregular and constantly changing in the morning, afternoon and in

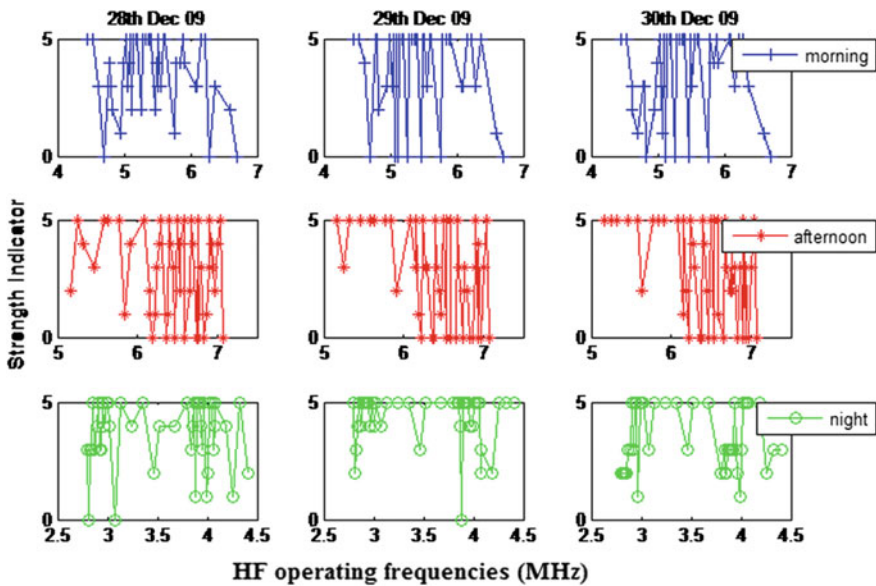


Fig. 1 Three consecutive days of HF transmission from 28 to 30 Dec 2009

the evening. HF radio frequencies fluctuated from high, medium and low signal strength and sometimes no communication occurred at all. The daytime MUFs were in the range of over 4 MHz to almost 7 MHz, and the nighttime MUFs were in the range of over 3 MHz to nearly 4.5 MHz. Therefore, it is vital to predict and select an optimum operating frequency for HF radio at a certain time of day [7]. The accuracy of MUF prediction is important in the planning and operation of HF radio frequencies [8, 9]. Therefore, it is vital to obtain reliable and accurate HF predictions between the paths [10].

The aim of the study was to observe and examine HF operating frequencies obtained from the Science and Technology Research Institute for Defence (STRIDE), Malaysia by comparing them with the prediction software, namely ASAPS and ICEPAC. The purpose of the comparison was to ensure that HF operating frequencies can be predicted using prediction software, and the frequency predictions are reliable and can be used in the Malaysian region. Thus, this study was conducted in Peninsular Malaysia, which is located in the equatorial region of Southeast Asia (SEA) in 2009, at the beginning of an 11-year solar cycle.

2 HF Operating Frequency

As mentioned previously, the HF operating frequency that is used for transmission in the ionospheric medium is the MUF. Generally, the best HF frequency to use for communication between two locations is determined by the MUF [11] and the frequency depends in part on the distance between two locations under specific working conditions such as antennas, power, and emission type. The MUF formulation [12] between two locations is:

$$\text{MUF} = \frac{f_{\text{cr}}}{\sqrt{1 - \left(\frac{R}{R+h}\right)^2}} \quad (1)$$

where

f_{cr} = Critical frequency

$$f_{\text{cr}} = \sqrt{\frac{N_e}{1.24 * 10^{10}}}$$

N_e = Degree of ionization of the ionosphere

R = Radius of the earth

h = Height of the ionosphere

MUF varies from day to day due to the prevailing conditions in the ionosphere. Consequently, it is not possible to predict exact values of MUFs. However, it is

possible to predict frequencies with a 10, 50 or 90% chance of successful propagation within a month [7, 8]. These frequencies are called the upper, median, and lower decile MUFs as illustrated in Fig. 2.

Frequencies greater than the upper decile should provide communications for just three (10%) days of the month, while the median decile MUF should provide communications for up to 15 (50%) days of the month. Additionally, frequencies less than the lower decile should provide successful communications for 27 days of the month, which is 90% of the time. Significantly, the lower decile MUF, which is also known as the Optimum Working Frequency (OWF) and sometimes called FOT (Frequency of Optimum Transmission) is appropriate for HF operating frequency to use for transmission of the HF signals compared to the upper and median deciles.

The OWF is usually chosen below the predicted MUF to ensure a good link of communication between two locations. It is often taken as $0.85 \times \text{MUF}$ [7, 13] or 15% less than the MUF. OWF for a given path is commonly calculated between 80 and 90% of the MUF. In addition, the percentage of usable days may be from 50 to 90% depending on what model is used for determining MUF and OWF. For example, VOACAP which was developed by ITS, USA uses 50% of MUF. The most important element for successful operation of an HF link is the selection of an OWF that will achieve a time availability approaching 100% of days and night, year-round [7]. Finally, OWF will be specified by 50–90% of MUF. The transmitting frequency must remain below the MUF as illustrated in Fig. 3 in order for the transmitting signal to be refracted by the ionosphere [14]. If a transmitting frequency exceeds the MUF, the signal will propagate through the ionosphere without being reflected back to the earth, and the closure of the communication link cannot occur.

Fig. 2 HF operating frequencies illustrating the upper, median, and lower decile MUF (OWF)

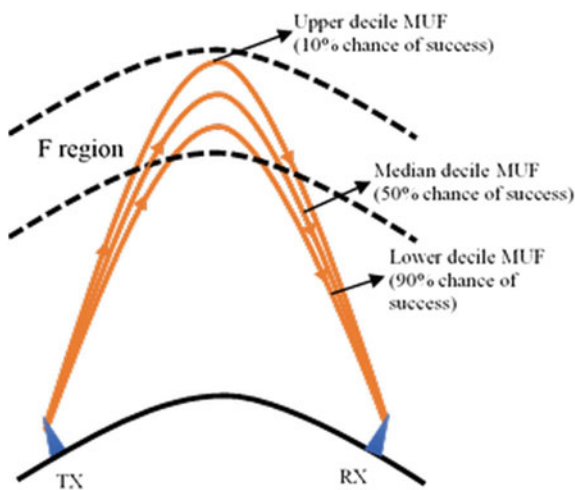
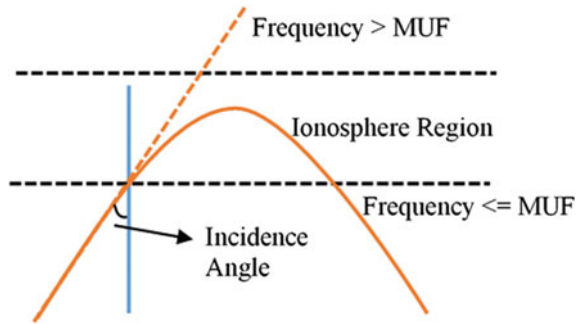


Fig. 3 Ionospheric HF signal propagation



3 HF Prediction Models

There are several methods of frequency management such as computer prediction, experience, ionospheric sounders and others. However, computer prediction is very popular compared to the others, and is a prediction model based on daily variation in accordance to time of the day. According to Hanbaba [8] and Jha [15], a model which is based on daily variation in accordance to time of day is often used to design an HF radio system to predict the frequency. There are numerous HF prediction software packages available and the best-known and most widely applied prediction model is the International Reference Ionosphere (IRI) model which was produced by a joint COSPAR/URSI Working Group [16] and is updated from time to time. It is an empirical standard model that provides the basis for the simulation and prediction of the ionospheric radio wave propagation. The model takes into account daily and seasonal variations, perturbed and quiet conditions as well as the impact of solar activity on the ionospheric plasma. The IRI model is a more acceptable HF propagation model for high latitudes compared to the equatorial region as reported by Wichaipanich [17] and Blagoveshchensky [18]. Moreover, Malik [19] discovered that the IRI model highly overestimated MUF measurement over Peninsular Malaysia which is located in the equatorial region.

The US has a full performance model for HF communication circuits called the Ionospheric Communications Enhanced Profile Analysis and Circuit (ICEPAC). ICEPAC is developed by the Institute for Telecommunication Sciences (ITS), National Telecommunications and Information Administration (NTIA), US, which is an enhancement of the Ionospheric Communications Analysis and Prediction Program (IONCAP). ICEPAC predicts the expected performance of HF broadcast systems and in doing so is useful in the planning and operation of HF transmissions for all four seasons, different sunspot activities, hours of the day, and geographic locations [20, 21]. Many researchers have selected ICEPAC as an ionospheric model [21–27]. Findings by Tanyer [23] stated that ICEPAC shows a good performance in the winter months.

Another piece of prediction software that has been widely adopted in many countries is the Advanced Stand Alone Prediction System (ASAPS) [28]. ASAPS

was developed by Space Weather Services of the Australian Bureau of Meteorology and the ITU-R/CCIR models. This program is based on the ITU-R/CCIR noise model and it allows for the prediction of skywave communication conditions in the HF and low VHF radio spectrum or Short Wave Band (1–45 MHz) [14, 23]. ASAPS is different from other prediction systems because it uses the T index to change solar-geomagnetic conditions rather than the sunspot number. The T index is used to quantify the response of the ionosphere to solar activity. Thus, ASAPS predictions are especially accurate when they are driven by real time T indices for the circuit or region of interest. As revealed by Tanyer [23], ASAPS shows a good performance in the equinox/summer months.

4 Data and Location

The HF operating frequencies data were obtained from real time HF transmissions from the Science and Technology Research Institute for Defense (STRIDE), Malaysia. The HF Telefunken Radio was used as the transceiver system to obtain HF operating frequencies data which complies with the world's strictest standards for radio communications equipment, including MIL-STD-810 and ALE per MIL-STD-188-141B. The HF operating frequencies data are in the hourly monthly median values.

The locations of the transmission tests are between Kajang (2.98°N, 101.8°E) and Lumut (4.22°N, 100.6°E) in Peninsular Malaysia, which is located in the equatorial region [29]. The transmission tests were conducted from April to December 2009, during the solar minimum of Solar Cycle 24. Coincidentally, 2009 was the beginning of solar cycle 24 and the yearly average value of the sunspot number was 6.4. Solar cycle 24 rose much more slowly than any other space age solar cycle, with the solar activity in 2013 being the weakest peak in 100 years [30–32].

For purposes of comparison, MUF predictions from ASAPS and ICEPAC prediction software were used to compare the HF operating frequencies data. ASAPS and ICEPAC were also used by Tanyer [23] to compare the monthly median values of the MUF and the hourly values of the MUF measured in the oblique sounding campaigns over Europe. In this study, analysis of error, namely mean absolute error (MAE) and mean absolute percentage error (MAPE) were used to calculate the error. MAE is used to measure how close predicted data are to measurement or observation data.

5 Results and Discussion

In this study, observation and analysis of HF operating frequencies involved two operating frequencies, namely measurement of the MUF and OWF. OWF was selected because OWF provides successful communication for 90% of the time or

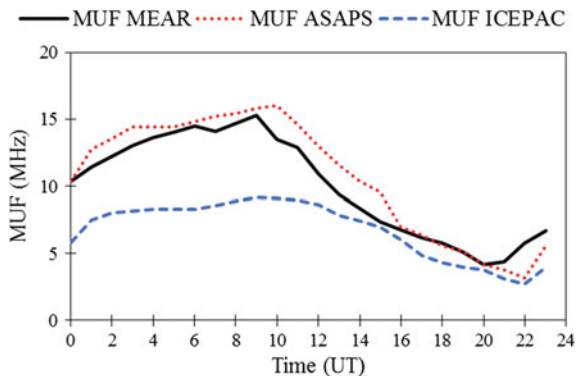
27 days of the month compared to the upper and median decile MUF. The following are the performance results of the measurement of MUF and OWF when compared to ASAPS and ICEPAC.

5.1 Analysis of MUF Measurement

Figure 4 illustrates the diurnal variations of MUF from April to December 2009 for MUF measurement and MUF from ASAPS and ICEPAC. The plots are MUF against universal time (UT), which is local time (LT) in Peninsular Malaysia, namely UT + 8 h. The hourly monthly median plot shows that the MUF magnitudes are all the same size. MUF values are higher during the daytime and lower at nighttime until pre-sunset. Later, the frequencies start to decrease from post-sunset until pre-sunrise. In the meantime, the MUF values are always changing or fluctuating from day to night as illustrated in Fig. 1. MUF fluctuates with different frequencies over a day because solar activity causes electron density levels to be different during the daytime and the nighttime. Therefore, ionization of the ionospheric layers varies, especially in the daytime. In contrast, at night the ionization level is lower making nighttime MUF lower than daytime MUF [11].

Further observation shows that MUF ICEPAC overestimated MUF measurement especially in the daytime until pre-midnight. After that, MUF ICEPAC approached MUF measurement. In contrast, MUF ASAPS slightly overestimated MUF measurement especially in the daytime until pre-midnight. However, MUF ASAPS became quite similar to MUF measurement later. This has been proven by the MAE as illustrated in Fig. 5. MAE in Fig. 5 is divided into four situations, namely morning, evening, night and pre-dawn. Noticeably, the figure shows MAE between MUF measurement and ASAPS is lower than MAE between MUF measurement and ICEPAC, at <2. MAE between MUF measurement and ICEPAC shows that MAE is higher in the daytime, and lower in the nighttime and at pre-dawn, at around 5 and <2 respectively. Overall, MAE for MUF measurement and ASAPS and ICEPAC are around 1 and 3 respectively.

Fig. 4 Hourly monthly median of MUF measurement, ASAPS and ICEPAC for the months of April–December 2009



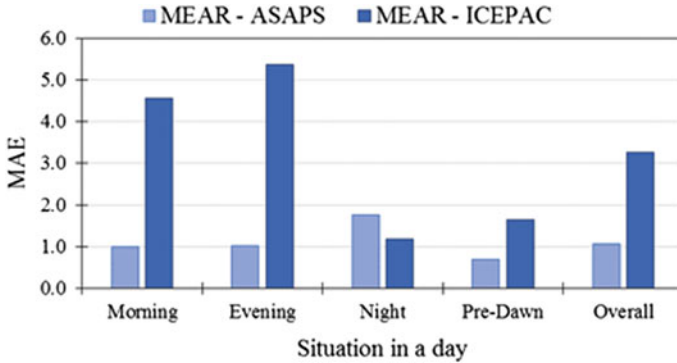


Fig. 5 MAE between MUF measurement and ASAPS, and MUF measurement and ICEPAC in the morning, evening, at night and pre-dawn

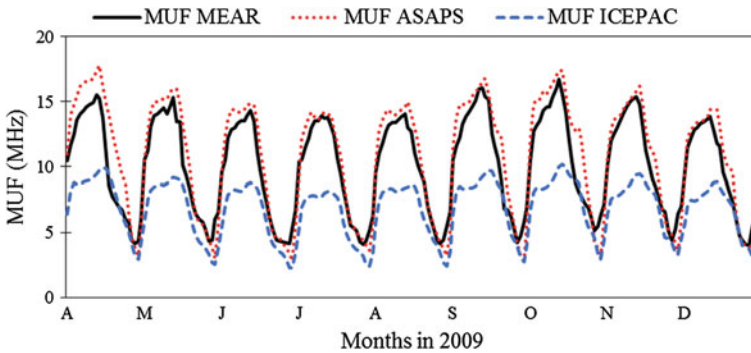


Fig. 6 Hourly monthly median of MUF measurement, ASAPS and ICEPAC from April to December 2009

The following presents the result of the hourly monthly median of MUF measurement, ASAPS and ICEPAC from April to December 2009. The plots reveals that the highest frequencies are in April, September and October, at >14 and <16 MHz around 0600 to 1000 UT. However, for MUF ICEPAC, the highest frequencies are around 10 MHz. The lowest frequencies are in July, August and December for all MUFs. Clearly, the plots from Fig. 6 indicate that ASAPS slightly overestimated MUF measurement and ICEPAC underestimated MUF measurement from April to December 2009. This has been verified by the MAE as illustrated in Fig. 7, in which the MAE is based on the situation over a day, in other words morning, evening, night and pre-dawn from April to December 2009. From the figure, MAE between MUF measurement and ASAPS is higher at night. This signifies that ASAPS greatly overestimates in the nighttime especially in April, September and October. Contrastingly, for ICEPAC, MAE is highest in the evening and morning, at >4 respectively. Hence, ICEPAC greatly underestimated MUF

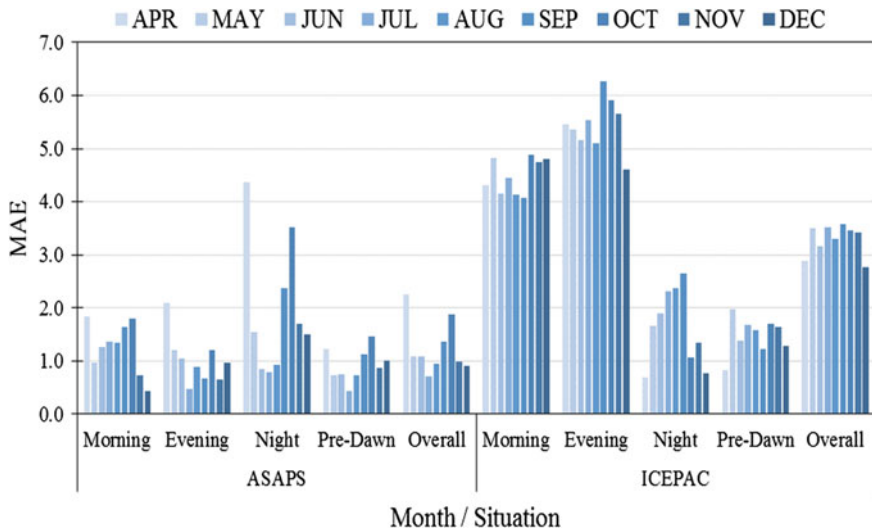
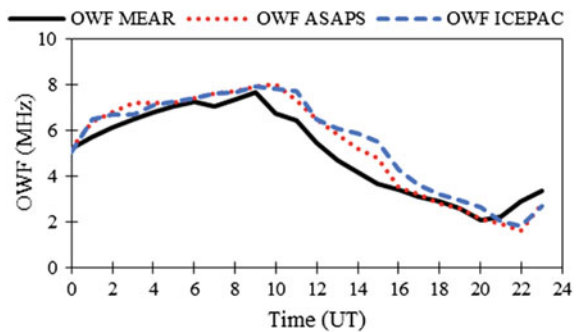


Fig. 7 MAE between MUF measurement and ASAPS and ICEPAC for April–December 2009

Fig. 8 Hourly monthly median of OWF measurement, ASAPS and ICEPAC from April to December 2009



measurement especially in the morning and evening. From MAPE analysis, MUF ASAPS overestimated MUF measurement by about 11% and ICEPAC underestimated MUF measurement by about 39%.

5.2 Analysis of OWF Measurement

The following are the results of the OWF measurement, ASAPS and ICEPAC as revealed in Fig. 8. As mentioned earlier, OWF is earned within a range of 50 and 90% of the MUF. The plots in Fig. 8 show that the OWF magnitudes are all parallel, and both OWF ASAPS and ICEPAC slightly overestimate OWF measurement. Noticeably, OWF for ICEPAC is different from MUF ICEPAC, on other

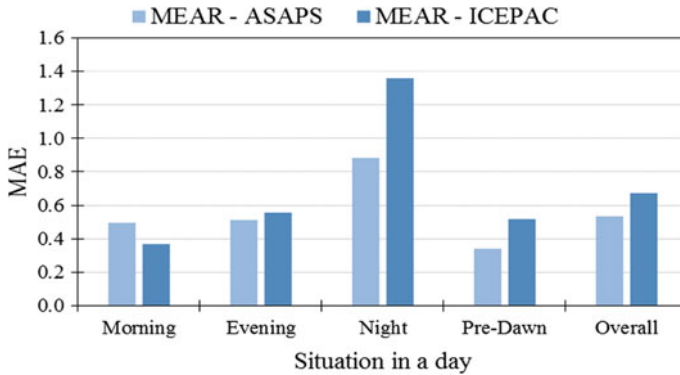


Fig. 9 MAE between OWF measurement and ASAPS and ICEPAC in the morning, evening, at night and pre-dawn

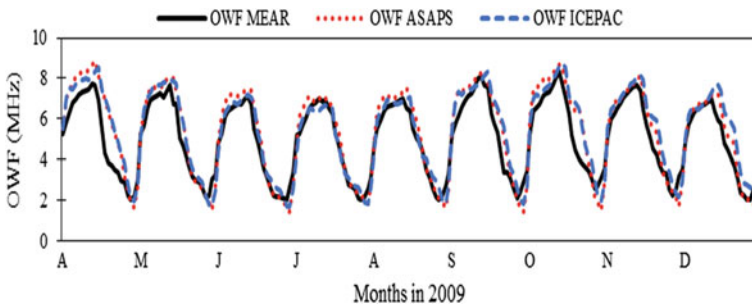


Fig. 10 Hourly monthly median of OWF measurement, and ASAPS and ICEPAC for April–December 2009

words OWF ICEPAC is nearing OWF measurement and slightly overestimates OWF measurement. This has been proven by the MAE as shown in Fig. 9.

Figure 9 shows MAE between OWF measurements and ASAPS and ICEPAC are 0.5 and 0.7 respectively. Both MAE for ASAPS and ICEPAC are higher at night, at nearly 0.9 and 1.4 respectively compared with other situations. The lowest MAE is in the pre-dawn for ASAPS and in the morning for ICEPAC, at nearly 0.4 respectively. Next, Fig. 10 shows the result of the hourly monthly median from April to December 2009 for OWF measurement, OWF ASAPS and OWF ICEPAC. The plots clearly show that ASAPS and ICEPAC slightly overestimated OWF measurement from April to December 2009. As with MUF performance, the highest frequencies are in April, September and October, at >8 MHz and <10 MHz around 0600 UT until 1000 UT including OWF ASAPS. The lowest frequencies are in July, August and December.

Results of MAE in Fig. 11 show that MAE between OWF measurement and OWF ASAPS is higher in the nighttime especially for April, September and October. This indicates that ASAPS overestimates in the nighttime in a similar way

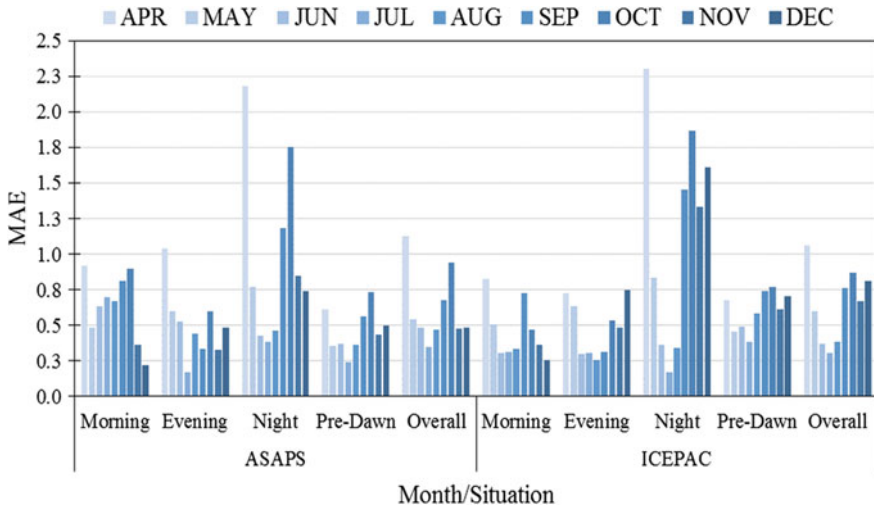


Fig. 11 MAE between OWF measurement and ASAPS and ICEPAC for April–December 2009

to MUF ASAPS. For ICEPAC, MAE is also higher in the nighttime, especially for April, October and December. Hence, ICEPAC also overestimated OWF measurement especially in the nighttime compared to other situations.

From the MAPE assessment, OWF ASAPS and ICEPAC overestimated MUF measurement by about 12 and 16% respectively. This result indicates that OWF ICEPAC is more suitable for predicting HF operating frequency compared to MUF ICEPAC. However for ASAPS, both MUF and OWF are suitable for predicting HF operating frequency. Therefore, lower decile MUF, namely OWF is the more appropriate range for HF operating frequency. The analysis also indicates that prediction software such as ASAPS and ICEPAC can be used to predict HF operating frequencies in Peninsular Malaysia especially in the OWF range.

6 Summary

The present study aimed to observe and analyze the HF operating frequencies in Peninsular Malaysia. The HF operating frequencies were later compared with the prediction software, namely ASAPS and ICEPAC. The selected HF operating frequencies were basic MUF and the lower decile MUF, in other words OWF that ranged between 50 and 90% of MUF compared to the upper and median decile MUF.

The results of the comparison between MUF measurement and ASAPS and ICEPAC show that the ASAPS slightly overestimated MUF by about 11% and it greatly overestimated it in the nighttime. By contrast, ICEPAC underestimated MUF measurement by about 39% and it greatly underestimated in the morning and

evening. Comparison of OWF measurement with OWF ASAPS and OWF ICEPAC shows that OWF ASAPS and ICEPAC slightly overestimated OWF measurement by about 12 and 16% respectively. Both OWF ASAPS and ICEPAC greatly overestimated in the nighttime. Therefore, OWF ICEPAC is more suitable for predicting HF operating frequencies compared to MUF ICEPAC. However for ASAPS, both MUF and OWF are suitable for predicting HF operating frequencies. These findings indicate that lower decile MUF is the most suitable range for HF operating frequencies.

7 Conclusion

On the whole, measurements of MUF and OWF were of a similar magnitude to ASAPS and ICEPAC and did not stray far from the ASAPS and ICEPAC prediction software. Therefore, both pieces of prediction software can be used to predict HF operating frequencies in Peninsular Malaysia.

The present study can be used to assist researchers in developing HF prediction models for predicting HF operating frequencies in the Malaysian region. Continued effort and study are needed to make HF prediction more accurate in the prediction of HF radio frequency, particularly in Malaysia and the equatorial region in general.

Acknowledgements The author would like to thank the Communication Branch, Instrumentation & Electronics Technology Division, Science & Technology Research Institute for Defence (STRIDE), Ministry of Defence, Malaysia for providing the experimental data. Gratitude is also extended to ANGKASA for supporting the research under the FRGS/1/2016/TK04/UKM/02/4 Grant.

References

1. Harris R (2005) Radio communications in the digital age, vol 1. Harris Corporation
2. Canestorp D (2006) Sky satellites: the marine corps' solution to its over-the-horizon communication problem
3. Zain AFM, Abdullah M (2000) Death of HF radio communication: fact or myth?. In: Paper presented in international wireless and telecommunication system, pp 109–112
4. Bradley PA, Dudeney JR (1973) A simple model of the vertical distribution of electron concentration in the ionosphere. *J Atmos Sol-Terr Phys* 35(12):2131–2146
5. Maslin NM (1987) HF communications: a systems approach. Pitman Publishing, London
6. Mudzingwa C, Nechibvute A, Chawanda A et al (2013) Maximum useable frequency prediction using vertical incidence data. *Int J Eng Res Technol* 2(8):2050–2056
7. Freeman RL (2006) Radio system design for telecommunication (3rd Ed 98). Wiley-Interscience publication, New Jersey
8. Hanbaba R (1998) Performance prediction methods of HF radio systems. *Ann Geophys* 41(5–6):715–742

9. Stocker AJ, Warrington E, Siddle DR (2007) A comparison between the measured and predicted parameters of HF radio signals propagating along the midlatitude trough and within the polar cap. *Radio Sci* 42:1–16
10. Lakshmi DR (1994) Tropical ionosphere and radio communications. *Proc Indian Nat Sci Acad Part A* 60:243–262
11. Larson K (2008) Maximum usable angle. Conejo Valley Amateur Radio Club. Available online: <http://www.cvarc.org/tech/maxusableangle.html>. Accessed: 11 Feb 2010
12. Tarplee MC (2008) HF radio wave propagation. ARRL South Carolina Section. Available online: <http://www.arrl-sc.org/>. Accessed: 11 Feb 2010
13. LiPing Z, YongGui L (2010) Modeling and simulation of useable frequencies in the ionosphere on HF sky-wave band. In: Presented in information engineering and electronic commerce (IEEC), 2010 2nd International Symposium 1–4
14. Jha KK (2003) Skip zone free HF propagation study for tactical application. In: Presented in 8th international conference on electromagnetic interference and compatibility, pp 229–231
15. Reilly MH and Daehler M (1986) Sounder updates for statistical model predictions of maximum usable frequencies on HF sky wave paths. *Radio [16]*; D. Bilitza et al. (2014) The international reference ionosphere 2012—a model of international collaboration. *J Sp Weather Sp Clim* 4, A07
16. Wichaipanich N, Supnithi P, Tsugawa T et al (2012) Comparison of ionosphere characteristic parameters obtained by ionosonde with IRI-2007 model over Southeast Asia. *Adv Sp Res* 52 (10):1748–1755
17. Blagoveshchensky DV, Maltseva OA, Anishin MM et al (2016) Modeling of HF propagation at high latitudes on the basis of IRI. *Adv Sp Res* 57(3):821–834
18. Malik RA, Abdullah M, Abdullah S et al (2016) Comparison of maximum usable frequency (MUF) variability over Peninsular Malaysia with IRI model during the rise of solar cycle 24. *J Atmos Solar-Terres Phys* 138–139:87–92
19. Luxorion (1998) Review of HF propagation analysis and prediction programs. Available online: <http://www.astrosurf.com/luxorion/qs1-review-propagation-software-nonvoacap.htm>
20. Athieno R, Jayachandran PT, Themens DR et al (2015) Comparison of observed and predicted MUF(3000)F2 in the polar cap region. *Radio Sci* 50(6):509–517
21. Earle GD, Desourdis Jr RI (1994) Advanced modeling of HF radio propagation. In: Presented in military communications conference, 1994, MILCOM'94. Conference Record, IEEE, pp 895–899
22. Tanyer SG, Erol CB (1998) Broadcast analysis and prediction in the HF band. *IEEE Trans Broadcast* 44(2):226–232
23. Lu JH, An JP (2009) Modeling and simulation of HF band transmission loss over china oceans. In: Presented in image and signal processing, CISP'09. 2nd International Congress, pp 1–4
24. Lu J, Liu H (2009) Modeling and simulations of high frequency propagation over China sea-surface. In: Presented in information science and engineering (ICISE), 2009 1st International Conference, pp 2653–2657
25. Li W, Su D, Wang J et al (2013) Prediction of short-wave communication effects based on ICEPAC model. In: Proceedings of 2013 2nd international conference on intelligent system appl mater, pp 295–298
26. Zolesi B, Fontanaa G, Perronea L et al (2008) A new campaign for oblique-incidence ionospheric sounding over Europe and its data application. *J Atmos Sol Terres Phys* 70 (6):854–865
27. Zolesi B, Cander LR (2014) Ionospheric prediction and forecasting. Springer Geophysics
28. Malik RA, Khamis K, Zakariya AS et al (2010) Determination of maximum usable frequency (MUF) for high frequency (HF) communications. *Def Sci Technol Tech Bull* 3(1):1–13
29. Komitov B, Kaftan V (2013) The sunspot cycle no. 24 in relation to long term solar activity variation. *J Adv Res* 4(3):279–282

30. Hao YQ, Shi H, Xiao Z et al (2014) Weak ionization of the global ionosphere in solar cycle 24. *Ann Geophys* 32(7):809–816
31. Kilpua EKJ, Luhmann JG, Jian LK et al (2014) Why have geomagnetic storms been so weak during the recent solar minimum and the rising phase of cycle 24? *J Atmos Solar-Terres Phys* 107:12–19
32. Willmott CJ, Matsuura K (2005) Advantages of the mean absolute error (MAE) over the root mean square error (RMSE) in assessing average model performance. *Clim Res* 30(1):79–82

Ionospheric TEC Response to the Partial Solar Eclipse Over the Malaysian Region

Rohaida Mat Akir, Mardina Abdullah, Kalaivani Chellappan
and Siti Aminah Bahari

Abstract This paper presents the study of ionospheric behavior during the partial solar eclipse on 9th March 2016 over the Malaysian region. The partial solar eclipse event occurred during quiet solar and magnetic activities with maximum Kp index and geomagnetic Dst indices of 2 and -23 nT respectively. Ionospheric total electron content (TEC) was obtained from three GPS Ionospheric Scintillation and TEC Monitors, installed at the Langkawi National Observatory, Langkawi, LGKW ($06^{\circ}19'N$, $99^{\circ}51'E$), Universiti Kebangsaan Malaysia, UKM ($02^{\circ}55'N$, $101^{\circ}46'E$) and Universiti Malaysia Sarawak, UNIMAS ($01^{\circ}28'N$, $110^{\circ}25'E$) stations. The selected stations have a coverage of between 68 and 87% over Peninsular Malaysia and Sarawak. This study compared the vertical TEC (VTEC) level during the partial solar eclipse period and the VTEC on the day before, the day after and the mean VTEC of quiet days. Results at these three stations show a clear occurrence of VTEC depletion in the range between 6 and 19% during the partial solar eclipse. The findings shows that depletion of VTEC during the partial solar eclipse was due to the reduction of ionization.

R.M. Akir (✉) · M. Abdullah · K. Chellappan · S.A. Bahari
Department of Electric, Electronic and Systems Engineering, Faculty of Engineering
and Built Environment, Universiti Kebangsaan Malaysia, 43600 Bangi,
Selangor Darul Ehsan, Malaysia
e-mail: rohaida@uthm.edu.my

M. Abdullah
e-mail: mardina@ukm.edu.my

M. Abdullah · K. Chellappan · S.A. Bahari
Space Science Centre (ANGKASA), Institute of Climate Change, Universiti Kebangsaan
Malaysia, 43600 Bangi, Selangor Darul Ehsan, Malaysia

R.M. Akir
Faculty of Electrical and Electronic Engineering, Universiti Tun Hussein Onn Malaysia
(UTHM), 86400 Parit Raja, Johor, Malaysia

1 Introduction

The ionosphere is part of the upper atmosphere that can affect radio wave propagation. Total electron content (TEC) is one of the quantities which can describe ionospheric behavior. A solar eclipse is a unique phenomenon that provides the opportunity to study the behavior of the ionosphere. There are two types of eclipse, namely total solar eclipse and partial solar eclipse. Both solar eclipses occur when the moon passes through either directly or partially between the Earth and the Sun, blocking the Sun's rays and causing a shadow on the Earth [1–4]. As shown in Fig. 1, during the solar eclipse, the moon will partially block the Sun disk and create the moon shadow.

The number of electrons and ions in the ionosphere will decrease during the solar eclipse due to the obstruction of solar radiation. When the solar eclipse occurs, the level of solar and geomagnetic disturbances, geographical longitude and latitude and the local time are factors that contribute to the effect of changes in the ionosphere [2, 5]. Researchers have used a variety of methods such as network ionosonde, incoherent scatter radar (ISR), the Global Positioning System (GPS) and satellite measurements to study ionospheric response to solar eclipses [1, 2, 6–8].

This study aimed to investigate the effect on the ionosphere during the partial solar eclipse based on TEC measurement using GPS Ionospheric Scintillation and TEC Monitor (GISTM) data. This research focused on the measurement of the vertical TEC (VTEC) level during the partial solar eclipse. The data were obtained during the solar eclipse, the day before the event, the day after the event and the mean of quiet days VTEC was used as reference days.

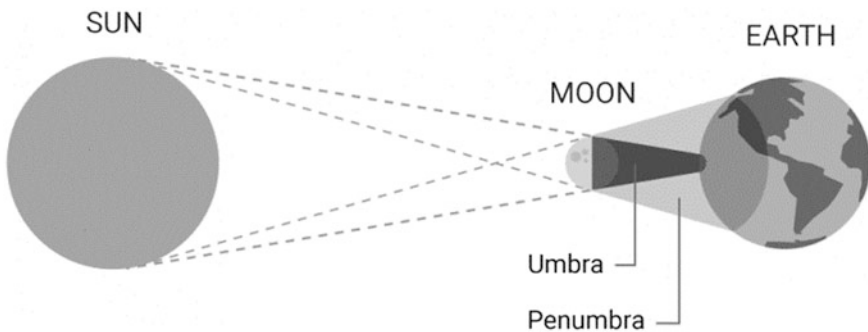


Fig. 1 Solar eclipse

2 Methodology

2.1 Data and Location

The partial solar eclipse of 9th March 2016 was investigated at three different GISTM stations in Malaysia, namely at the Langkawi National Observatory, Langkawi, LGKW (06°19'N, 99°51'E), Universiti Kebangsaan Malaysia, UKM (02°55'N, 101°46'E) and Universiti Malaysia Sarawak, UNIMAS (01°28'N, 110° 25'E) stations which are shown in Fig. 2. Data were obtained for the day before, the day after, the mean of quiet days VTEC and during the partial solar eclipse. The studied VTEC was based on data obtained from the GISTM stations.

2.2 Data Processing

In this study, only 20° and above of elevation angle were used to minimize multipath effects on VTEC measurement [9–11]. The GPS receiver can simultaneously track the information from available satellites and convert the information to slant TEC (STEC). By using a parsing program, ParseIsmr.exe, all the data from the Novatel GPS receiver can be converted from binary data to ASCII data. This program was used to convert the binary-format data records to a comma-delimited format. The STEC is a measure of the total electron content of the ionosphere along the ray path from the satellite to the receiver. As shown in Fig. 3, a single layer model (SLM) mapping function was used to convert the STEC into VTEC based on Eq. (1).

$$VTEC = STEC(\cos x')$$
(1)

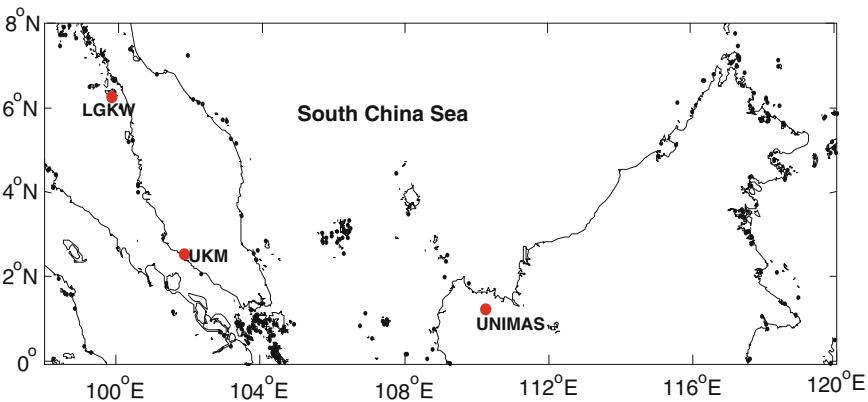
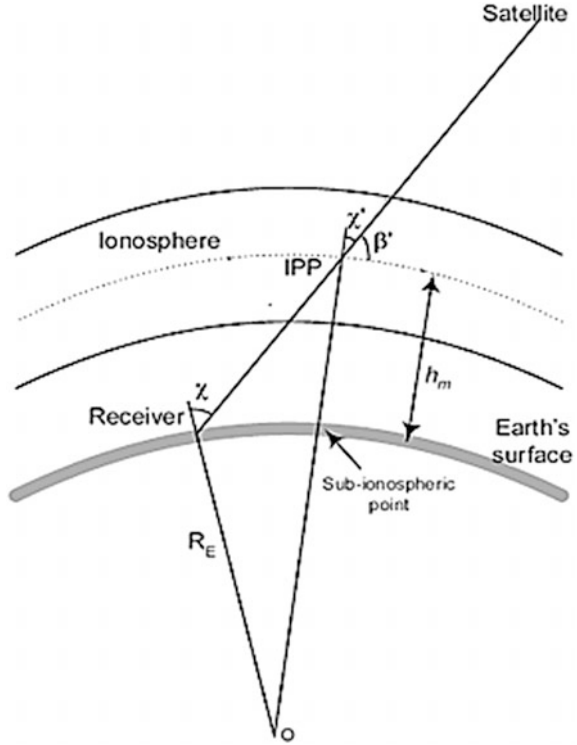


Fig. 2 GISTM stations at LGKW, UKM and UNIMAS

Fig. 3 Ionospheric single layer model [9, 10, 12]



SLM can be written as

$$F(x) = \frac{TEC(x)}{TEC(0)} = \frac{1}{\cos x' \text{ (or } \sin \beta')} = \frac{1}{\sqrt{1 - \sin^2 x'}} \quad (2)$$

$$\sin x' = \frac{R_E}{R_E + h_m} \sin x \quad (3)$$

where, x and x' are the zenith angle of the satellite as seen from the observing station, R_E is the radius of the Earth set to 6371 and h_m is the height of maximum electron density. In order to evaluate the VTEC, we made the assumption that the ionosphere which surrounds the Earth is situated at a height of about 350 or 450 km. In this study, the height was set at an altitude of 450 km because this height is the most ideal and suitable to be applied in the equatorial region, which is known to have the highest electron density as mentioned by Yaacob et al. [6].

The ionospheric response during the partial solar eclipse was determined by analyzing the comparison of VTEC measurements the day before, the day after and on the mean quiet days. VTEC with respect to the partial solar eclipse was also examined. On 9th March 2016, the partial solar eclipse was observed from the GISTM stations in Malaysia. The times at the start, the maximum, and the end of

Table 1 The geographical condition of the partial solar eclipse at 3 stations [13]

Station	Geo. coordinate		Start of eclipse (lt)	Maximum eclipse (LT)	End of eclipse (LT)	Coverage (%)
	Lat (°)	Long (°)				
LGKW	6.19 N	99.51 E	07:30:00	08:25:08	09:30:22	68
UKM	2.55 N	101.46 E	07:24:20	08:23:36	09:30:48	79.4
UNIMAS	1.28 N	110.25 E	07:24:40	08:29:01	09:42:49	86.9

the eclipse over the GISTM stations are illustrated in Table 1. The partial solar eclipse was examined based on local time (LT), where LT is 8 h ahead of universal time (UT).

The geomagnetic and solar data, obtained from World Data Center, (WDC) and the National Oceanic and Atmospheric Administration (NOAA) databases respectively were analyzed. Both data sets can be downloaded freely. Figure 4 depicts the solar radio flux, F10.7 cm and geomagnetic disturbance storm time, (Dst) index for 3rd–13th March 2016. It can be seen from Fig. 4 that the maximum Dst excursion was -59 nT on 7th March 2016, two days before the solar eclipse occurred. During the time of the solar eclipse, the geomagnetic Dst on that day was fairly quiet, at around -23 nT and the readings of solar radio flux, F10.7 cm were 96. Based on Fig. 4, Dst and F10.7 cm for the day before and the day after the solar eclipse showed a quiet day of geomagnetic conditions and solar activity.

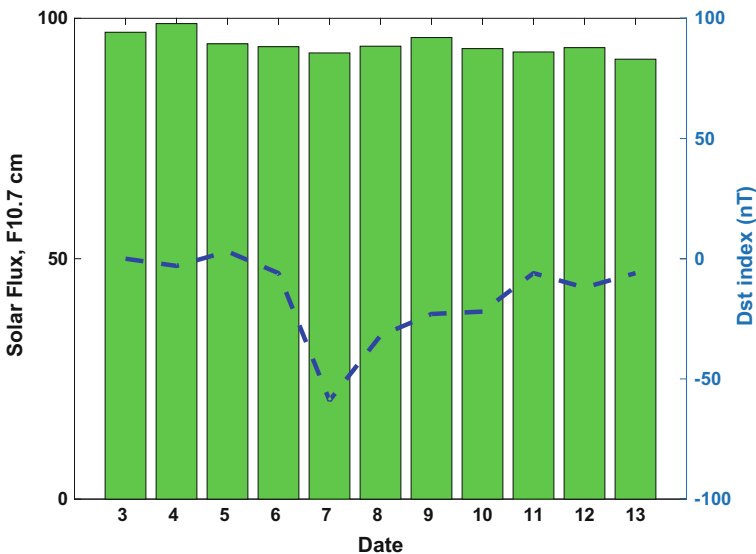


Fig. 4 Solar radio flux, F10.7 cm and geomagnetic Dst index from 3rd to 13th March 2016. The solar eclipse was on 9th March

3 Results and Discussion

Daily VTEC variations during the eclipse period at the GISTM stations were compared with the VTEC variations for the same period on the day before and the day after the partial solar eclipse on 8th and 10th March 2016 respectively and with the mean of quiet days VTEC (QDVTEC). The mean of quiet days was obtained from five quiet days, namely 3rd, 5th, 8th, 10th and 13th March 2016. The quiet day was defined as a day with planetary magnetic Kp index of less than or equal to 2. The analysis was conducted in the early morning when the TEC started recording at three stations from 06:00 to 10:00 LT, as shown in Fig. 5. The maximum TEC in Malaysia is post-noon, between 1300 to 1600 LT while the minimum TEC is during early morning between 0100 to 0600 LT [10, 11]. Figure 5 shows that the observation result for the partial solar eclipse at all GISTM stations was between 07:30 and 09:30 LT. The stations at UKM and LGKW both had some missing data on 8th March 2016.

Figure 5(a) presents the variation of VTEC at LGKW station from 8th to 10th March 2016 and QDVTEC. Observations at this station clearly showed that there was a depletion of VTEC value. This depletion occurred at the beginning of the partial solar eclipse at approximately 07:30 LT. The depletion of VTEC value during the partial solar eclipse was not seen on either the day before or after the solar eclipse event. Comparison of VTEC values during the occurrence of the solar

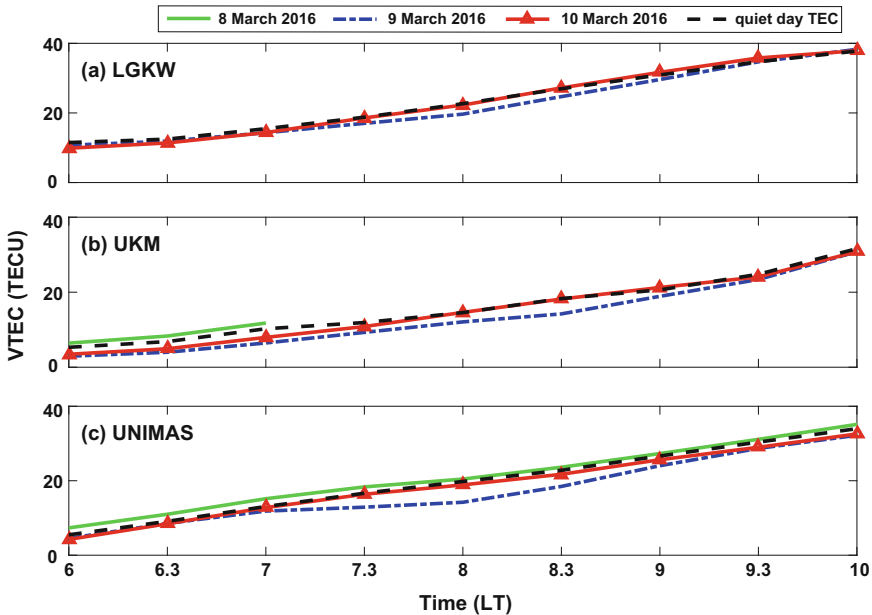


Fig. 5 VTEC response during the 9th March 2016 partial solar eclipse at (a) LGKW, (b) UKM and (c) UNIMAS stations

eclipse shows that the value of VTEC decreased by 7.28% from the day after the eclipse event. Meanwhile, the comparison between the time of the eclipse and QDVTEC shows a decrease of about 6.26%. VTEC gradually increased to the normal level after the partial solar eclipse period ended, at approximately 09:30 LT.

The VTEC variations at UKM station are shown in Fig. 5(b). The comparison of the VTEC variation at this station shows that the VTEC value started to decrease when the partial solar eclipse began and became more noticeable during the period of the occurrence of the partial solar eclipse. From the observations, the maximum depletion of VTEC occurred at 08:23 LT with 6 TECU on QDVTEC and 4 TECU on the day after the eclipse. During the partial solar eclipse, the total VTEC level decreased by about 12.49% compared to the day after the partial solar eclipse. In addition, the differential between the time of the partial solar eclipse on 9th March 2016 and QDVTEC shows a depletion of about 13.65% with 12.31 TECU of total VTEC.

The VTEC variations at the UNIMAS station are shown in Fig. 5(c). At the UNIMAS station in Sarawak, VTEC variation during the partial solar eclipse was observed to have the lowest total VTEC value with 98.39 TECU compared to the VTEC value on the day before and after the event with 120.82 TECU and 111.61 TECU. From the observations, VTEC depletion occurred 30 min before the beginning of the partial solar eclipse at 07:24 LT. At the end of the partial solar eclipse, the VTEC value started to recover to the normal level at approximately 09:30 LT. Table 2 shows the VTEC level and percentage of VTEC depletion during the period of the partial solar eclipse at the three different stations.

From Table 2, the VTEC value at the UNIMAS station during the eclipse, on the day before, and after the eclipse was 18.65% and 11.94% respectively. VTEC level during the partial solar eclipse period with respect to the QDVTEC value is 16.12%. Comparison between the VTEC on the 8th, 10th March 2016, and QDVTEC clearly shows the occurrence of depletion of the VTEC value during the partial solar eclipse compared with the day before, after and QDVTEC. With respect to the day before, after and QDVTEC, the range of the percentage of VTEC depletion is between 6 and 19% for all three stations. It is due to the decline of ionization during the partial solar eclipse.

Table 2 Total VTEC level and percentage of VTEC depletion during the partial solar eclipse period at the three stations

Station	∑VTEC (TECU)					Percentage of VTEC depletion (%)		
	8th March	9th March	10th March	QDVTEC	Std. dev. QDVTEC	With respect to 8th March	With respect to 10th March	With respect to QDVTEC
LGKW	–	125.64	135.51	134.03	6.34	–	7.28	6.26
UKM	–	77.87	88.98	90.18	5.05	–	12.49	13.65
UNIMAS	120.82	98.29	111.61	117.18	5.08	18.65	11.94	16.12

Note—indicates no data

From the results, the UNIMAS station has a higher percentage of VTEC depletion of between 16.12% with respect to QDVTEC and 18.65% with respect to 8th March 2016, compared to the other two stations in Peninsular Malaysia. This happened due to the partial solar eclipse coverage of approximately 86.9% at UNIMAS, which decreased in the Northern region of Peninsular Malaysia with 79.4% coverage at UKM and 68% at LGKW as mentioned in Table 1.

4 Conclusion

This paper has presented the ionospheric response during the partial solar eclipse on 9th March 2016 at three affected GISTM stations in Malaysia. The analysis was performed by comparing the value of VTEC during the partial solar eclipse with the days before and after the partial solar eclipse as well as the mean average of quiet days VTEC (QDVTEC). The QDVTEC was the mean average of the VTEC value during the 3rd, 5th, 8th, 10th and 13th March 2016. It has been shown that during the eclipse event, the percentage deviations of VTEC compared to QDVTEC of March 2016 ranged from 6 to 19%. The VTEC value will decrease during the partial solar eclipse and return to normal after the eclipse ends. Further analysis using more GPS stations should be performed in order to gain a better understanding of the effects of eclipses over the region.

Acknowledgements The author would like to express her gratitude to Universiti Tun Hussein Onn Malaysia (UTHM) for giving her study leave, enabling her to conduct this research. Utmost appreciation is also expressed to Universiti Kebangsaan Malaysia (UKM), Universiti Malaysia Sarawak (UNIMAS) and the National Space Agency of Malaysia (ANGKASA) at Langkawi National Observatory for the installation and maintenance of the GISTM in UKM, UNIMAS and LGKW stations. This research is funded by the Malaysian Government through Universiti Kebangsaan Malaysia under the SA1213001. The authors would like to acknowledge the World Data Center (WDC) and the National Oceanic and Atmospheric Administration (NOAA) for the solar and geomagnetic data.

References

1. Li S, Peng J (2011) Ionospheric TEC change analysis in response to solar eclipse on 22 July 2009. In: Proceedings of 2011 International conference electronics communication control, pp 4359–4362. doi:[10.1109/icecc.2011.6067924](https://doi.org/10.1109/icecc.2011.6067924)
2. Didong RD, Momani MA (2009) The ionospheric response to the annular solar eclipse on 26th Jan 2009. In: Proceedings of international conference on space science communication ionospheric processing, pp 147–152. doi:[10.1109/ICONSPACE.2009.5352652](https://doi.org/10.1109/ICONSPACE.2009.5352652)
3. Panda SK, Gedam SS, Rajaram G, Sripathi S, Bhaskar A (2015) Impact of the 15 Jan 2010 annular solar eclipse on the equatorial and low latitude ionosphere over the Indian region. *J Atmos Solar-Terrestrial Phys* 135:181–191. doi:[10.1016/j.jastp.2015.11.004](https://doi.org/10.1016/j.jastp.2015.11.004)

4. Panda SK, Gedam SS, Rajaram G (2013) GPS derived ionospheric TEC response to annular solar eclipse over Indian region on 15 Jan 2010. In: Proceedings of international conference on space science communication iconsphere, pp 213–218. doi:[10.1109/iconspace.2013.6599467](https://doi.org/10.1109/iconspace.2013.6599467)
5. Momani MA, Sulaiman S (2011) Ionospheric response to the annular solar eclipse on 15th Jan 2010 as observed by ionosonde receivers. *J Adv Sci Eng* 1:238–245
6. Ya'acob N, Yusof AL, Ali MT, Salleh MKM, Pasya I, Sharihuddin SYM (2011) Investigation of the annual solar eclipse by using total electron content (TEC) measurements. ISWTA 2011—2011 IEEE symposium on wireless technology and application, pp 124–128. doi:[10.1109/iswta.2011.6089393](https://doi.org/10.1109/iswta.2011.6089393)
7. Hoque MM, Wenzel D, Jakowski N, Gerzen T, Berdermann J, Wilken V, Kriegel M, Sato H, Borries C, Minkwitz D (2016) Ionospheric response over Europe during the solar eclipse of Mar 20, 2015. *J Sp Weather Sp Clim* 6:A36. doi:[10.1051/swsc/2016032](https://doi.org/10.1051/swsc/2016032)
8. Choudhary RK, St.-Maurice JP, Ambili KM, Sunda S, Pathan BM (2011) The impact of the Jan 15, 2010, annular solar eclipse on the equatorial and low latitude ionospheric densities. *J Geophys Res Sp Phys* 116:1–12. doi:[10.1029/2011ja016504](https://doi.org/10.1029/2011ja016504)
9. Akir RM, Abdullah M, Chellappan K, Hasbi AM (2015) Preliminary vertical TEC prediction using neural network: input data selection and preparation. In: Proceedings of 2015 international conference space science communication, pp 283–287. doi:[10.1109/iconspace.2015.7283767](https://doi.org/10.1109/iconspace.2015.7283767)
10. Radzi ZM, Abdullah M, Hasbi AM, Mandeep JS, Bahari SA (2013) Seasonal variation of total electron content at equatorial station, Langkawi, Malaysia. In: International conference space science communication iconsphere, pp 186–189. doi:[10.1109/iconspace.2013.6599461](https://doi.org/10.1109/iconspace.2013.6599461)
11. Akir RM, Abdullah M, Chellappan K, Bahari SA (2017) Comparative study of TEC for GISTM stations in the Peninsular Malaysia region for the period of January 2011 to December 2012. *Adv Sci Lett* 23:1304–1309
12. Abdullah M (2004) Modelling and determination of ionospheric effects on relative GPS measurements. University of Leeds
13. Agensi Angkasa Negara (2016) Partial solar eclipse in Malaysia 9 March 2016. www.angkasa.gov.my/?q=en/node/1315. Accessed 31 Mar 2016

Effect of Geomagnetic Storms on Fluctuations of Total Electron Content at an Equatorial Station

Siti Zainab Hamzah and Mariyam Jamilah Homam

Abstract This paper aims to investigate the effect of geomagnetic storms (categorized as intense and moderate) on the fluctuations of Total Electron Content (TEC) in the ionosphere. The TEC obtained from ground-based GPS receivers is utilised to observe the effect of geomagnetic storm activity. The TEC data from an equatorial station, namely Libreville (NKLG) station (0.4162° N, 9.4673° E) for the years 2011 and 2013 were processed. The fluctuations of TEC during intense and moderate storm periods are related to the geomagnetic storms. The TEC perturbation during storms indicates the presence of plasma uplift due to eastward penetration of electric fields at the equatorial station.

1 Introduction

The interaction between a solar wind shock wave or magnetic field cloud within the magnetosphere via the southern component of the interplanetary magnetic field (IMF) cause a provisional disturbance in Earth's magnetosphere, specifically a geomagnetic storm. This incident involves a transfer of energy and charged particles into the magnetosphere [1–3]. These charged particles pass through magnetic field lines into the magnetosphere, producing an injection of plasma in the nightside of the magnetosphere, or they become trapped in closed geomagnetic field lines, forming regions called radiation belts within the terrestrial environment [4–6]. A geomagnetic storm will increase the ring current. The D_{st} index is believed to be an indicator of the ring current. With regards to the magnetic equator, the D_{st} index predicts the averaged change of the horizontal component of the Earth's magnetic field [7, 8]. A D_{st} index that passes -100 nT is considered as an intense

S.Z. Hamzah · M.J. Homam (✉)

Wireless and Radio Science Centre, Faculty of Electrical and Electronic Engineering, Universiti Tun Hussein Onn Malaysia, 86400 Batu Pahat, Johor, Parit Raja, Malaysia
e-mail: mariyam@uthm.edu.my

S.Z. Hamzah

e-mail: sitizainabhamzah@gmail.com

geomagnetic storm, while -50 to -100 nT is considered as a moderate geomagnetic storm. The K_p index is a 3-h range index created to measure the irregular variations based upon the geomagnetic activity intensity caused by the electric currents in the ionosphere [9]. The IMF B_z is the north–south direction of the interplanetary magnetic field and is created by waves and other disturbances in the solar wind in which a southward IMF B_z is vital for geomagnetic storms to occur.

In order to investigate the effects of geomagnetic storms on TEC, ionospheric TEC data obtained from the NKLG station (0.4162° N, 9.4673° E) in 2011 and 2013 are used in this study.

2 Methodology

2.1 Ionospheric Total Electron Content

Irregularities in the ionosphere may cause degradation of the radio waves propagation passing through it. Practically, signal degradation cause a propagation time delay. This time delay is proportional to the amount of TEC. GPS measurements based on dual-frequency signals f_1 , (1575.42 MHz) and f_2 (1227.60 MHz) were used to obtain the vertical TEC data in 2011 and 2013 at the NKLG station. The slant TEC, $STEC$ is measured at 30 s interval and is used to calculate vertical TEC, $VTEC$ [10]. The vertical TEC is the total number of electrons in a vertical column with a cross-sectional area of 1 m^2 along the ray path [11]. In practice, $VTEC$ is given by [12]:

$$VTEC = (STEC - b_s - b_r) \cos \left[\left(\sin^{-1} \frac{R_E \cos \alpha}{R_E + h} \right) \right] \quad (1)$$

$STEC$ is the slant path of TEC, b_s and b_r are the satellite and receiver biases, R_E is the Earth's radius of 6378 km, h is the height of the ionospheric layer, and α is the elevation angle of the satellite.

The cut-off elevation angle of 25° is selected to reduce the time delay and to avoid unnecessary errors caused by the multipath and uncertain amount of data. A pseudo-range with low elevation is more likely to be affected by the multipath effect and the decrease in reliability than one with high elevation. If the elevation angle is too high, few satellites will record data to the ground-based GPS receiver, resulting in a decline in the measured data. $STEC$ is calculated from the pseudo-ranges (P_1 and P_2) as shown below.

$$STEC = \frac{(f_1 f_2)}{40.3(f_1^2 - f_2^2)} (P_2 - P_1) \quad (2)$$

GPS has been widely used in navigation and communication systems including in TEC monitoring. The International GNSS Service (IGS) has become one of the important sources of real-time TEC observations. These data are accessible from several servers. One such server is the Crustal Dynamics Data Information System (CDDIS) server (<ftp://cddis.gsfc.nasa.gov/pub/gps/data/daily/>). The data used for this study were obtained from the IGS, at the Libreville (NKLK) station. Libreville station Local Time (LT) is 1 h ahead of Universal Time (UT). The D_{st} and K_p Index data were obtained from the Data Analysis Center for Geomagnetism and Space Magnetism, Graduate School of Science, Kyoto University (<http://wdc.kugi.kyoto-u.ac.jp/index.html>) and the IMF B_z data were obtained from NASA (<ftp://sohoftp.nascom.nasa.gov/>).

Intense geomagnetic storm periods observed on 25 October 2011 and 17 March 2013, and moderate geomagnetic storms observed on 4 February 2011 and 1 May 2013 were used in this study to investigate their effect on TEC variation. Hourly (UT) averages of vertical TEC were used to relate variation in vertical TEC with effects of geomagnetic storms.

3 Results and Discussion

Intense geomagnetic storms on 25 October 2011 and 17 March 2013 at NKLK station are shown in Figs. 1 and 2. Sudden storm commencement (SSC) was observed at 1700 UT on 24 October 2011. The IMF B_z sharply decreased southward at 1900 UT on 24 October 2011 and reached a maximum negative value of -12.9 nT at 2300 UT. The K_p Index reached a maximum value of 7 during the storm. However, in Fig. 2, the SSC was observed at 0600 UT on the day of the intense storm (17 March 2013). The IMF B_z gradually decreased southward at 0100 UT on 17 March 2013, and reached a maximum negative value of -10.7 nT at 0800 UT. The K_p Index reached a maximum value of 7 during the storm.

A sudden decrease in D_{st} value during the SSC to a minimum value of -147 nT at 0200 UT on 25 October 2011 and a gradual decrease in D_{st} value during the SSC on 17 March 2013 to a minimum value of -132 nT at 2100 UT explain a notable enhancement of the ring current [2, 13]. A strong intensity of geomagnetic storms caused by the enhanced ring current leads to the formation of ionosphere irregularities at lower latitudes by the electric field penetration from high latitude to lower latitudes [2].

The positive phase of IMF B_z during the storm period in 2011 just before the SSC, was observed at 1900 UT with 5.2 nT and the positive phase of IMF B_z during the storm period in 2013 just before the SSC, was observed at 0100 UT with 3.2 nT. It implies that the field is compressed and it has a relationship with the southward turning of the IMF [6].

There is a similarity between Figs. 1 and 2 in that before the southward turning of IMF B_z , the K_p Index started rising and it was still high even when the IMF B_z

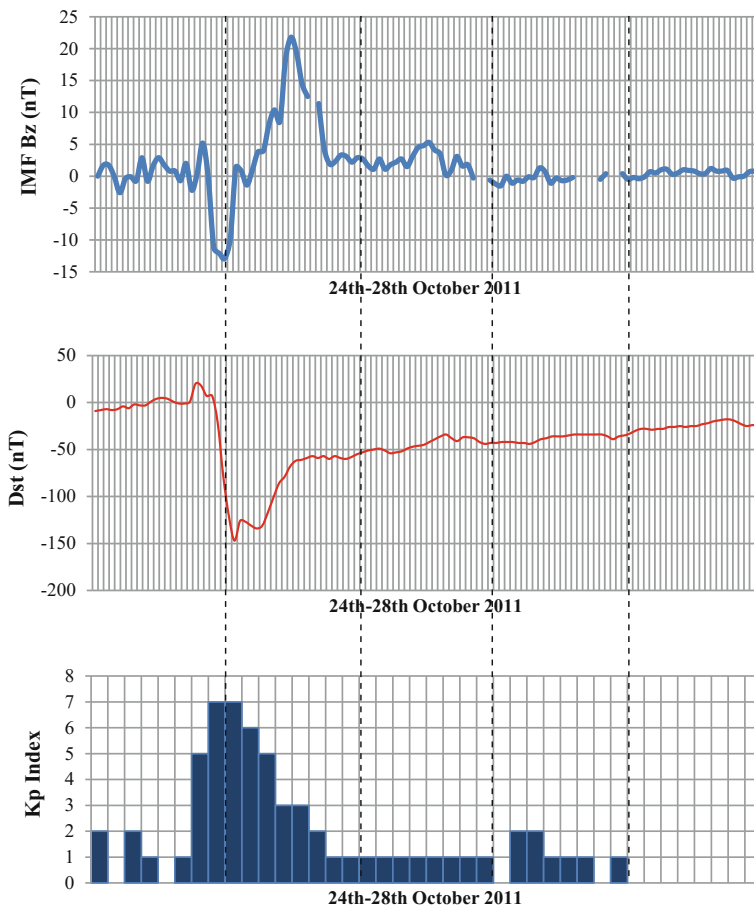


Fig. 1 The intense storm on 25 October 2011

changed direction, and it decreased more slowly than it rose. This observation shows that K_p Index is correlated with the southward turning of the IMF B_z .

The diurnal variation of TEC during the disturbed day (*D day*) was investigated in comparison to the diurnal variation of TEC during the quiet day (*Q day*) as shown in Figs. 3 and 6 for the respective intense and moderate storms. The TEC on the *D day* represents averaged TEC data on 25–26 October and 17–18 March while the *Q day* represents averaged TEC data on 9–10 October and 8–9 March for 2011 and 2013 respectively as shown in Fig. 3. During 2011, the maximum TEC values observed during the *D day* was ~ 110 TECU and during the *Q day* was ~ 102 TECU.

The percentage change in TEC values is obtained by the following equation.

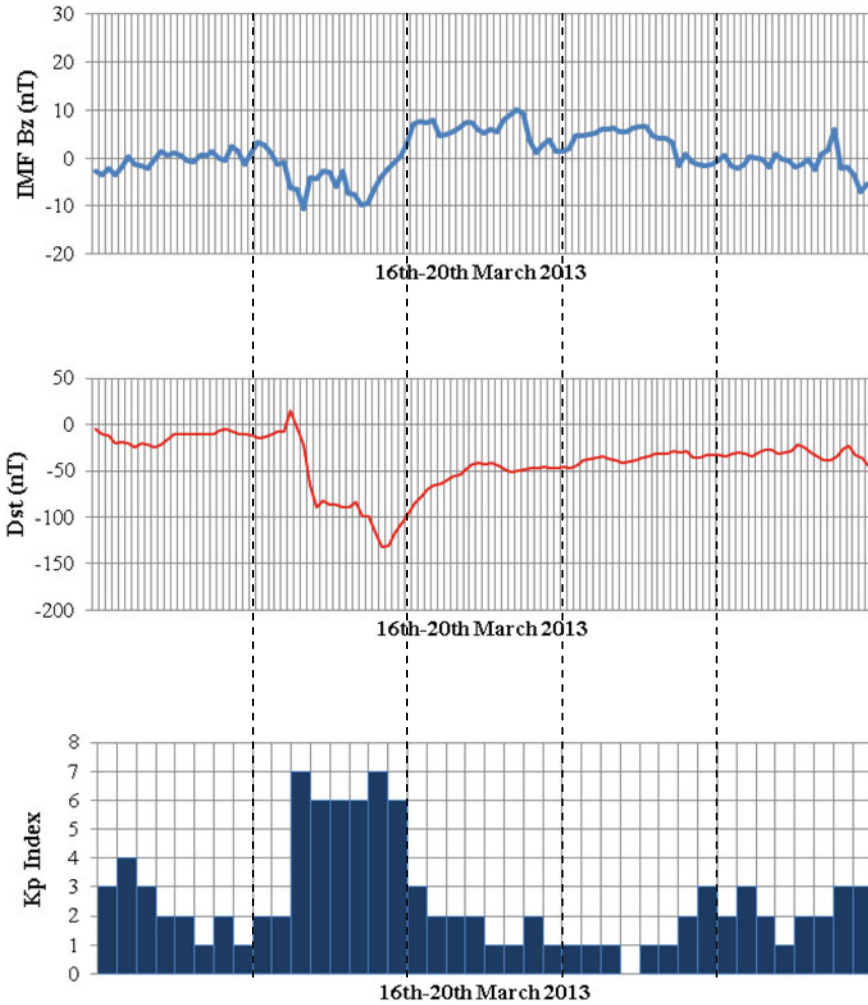


Fig. 2 The intense storm on 17 March 2013

$$\%TECchange = \frac{(D_{TEC} - Q_{TEC})}{Q_{TEC}} \times 100 \tag{3}$$

The TEC values on the *D* day observed are slightly higher than those in the *Q* day except at 1600–1700 UT. It could be due to the D_{st} values reaching its lowest value around this time at -34 nT on 26 October. The storms period began at midnight on 25 October and ended its recovery phase on the following day at 0900 UT. The constant increase of TEC values between 0400 and 1100 UT on the *D* day

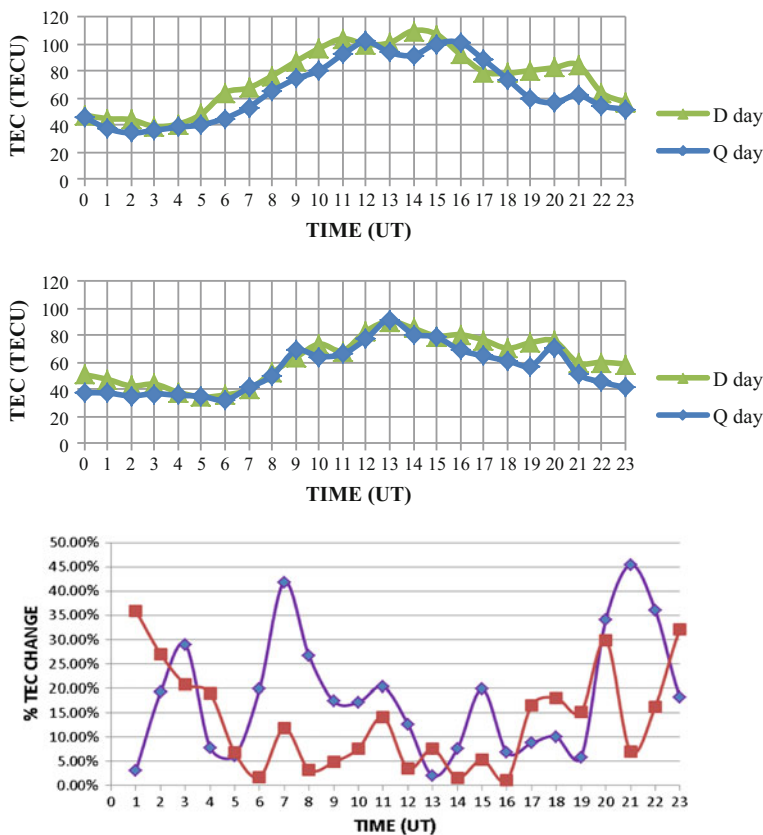


Fig. 3 The diurnal TEC during the intense geomagnetic storms in 2011 (top panel) and 2013 (bottom panel) and the % TEC change

indicates that the effect of intense storms occurred around 0200 UT. The maximum percentage change in TEC observed on the *D day* is 45% as shown in Fig. 3.

However, during 2013, the maximum TEC values observed for both the *D day* and the *Q day* showed no significant difference being ~ 90 TECU and ~ 92 TECU, respectively. The storms period began at 1000 UT on 17 March and ended at 0900 UT on the following day. The maximum percentage change in TEC observed on the *D day* was 41% as shown in Fig. 3.

Moderate geomagnetic storms on 4 February 2011 and 1 May 2013 are shown in Figs. 4 and 5, respectively. The SSC was observed at 1400 UT on 4 February 2011. The IMF B_z steeply decreased southward at 1300 UT on 4 February 2011, and reached a maximum negative value of -16.4 nT at 1900 UT. The K_p Index reached a maximum value of 6 during the storm, as illustrated in Fig. 4. From Fig. 5, the SSC was observed at 1800 UT on 30 April 2013. The IMF B_z gradually decreased southward at 1200 UT on 30 April 2013, and reached a maximum negative value of -9.8 nT at 0500 UT. The K_p Index also reached a maximum

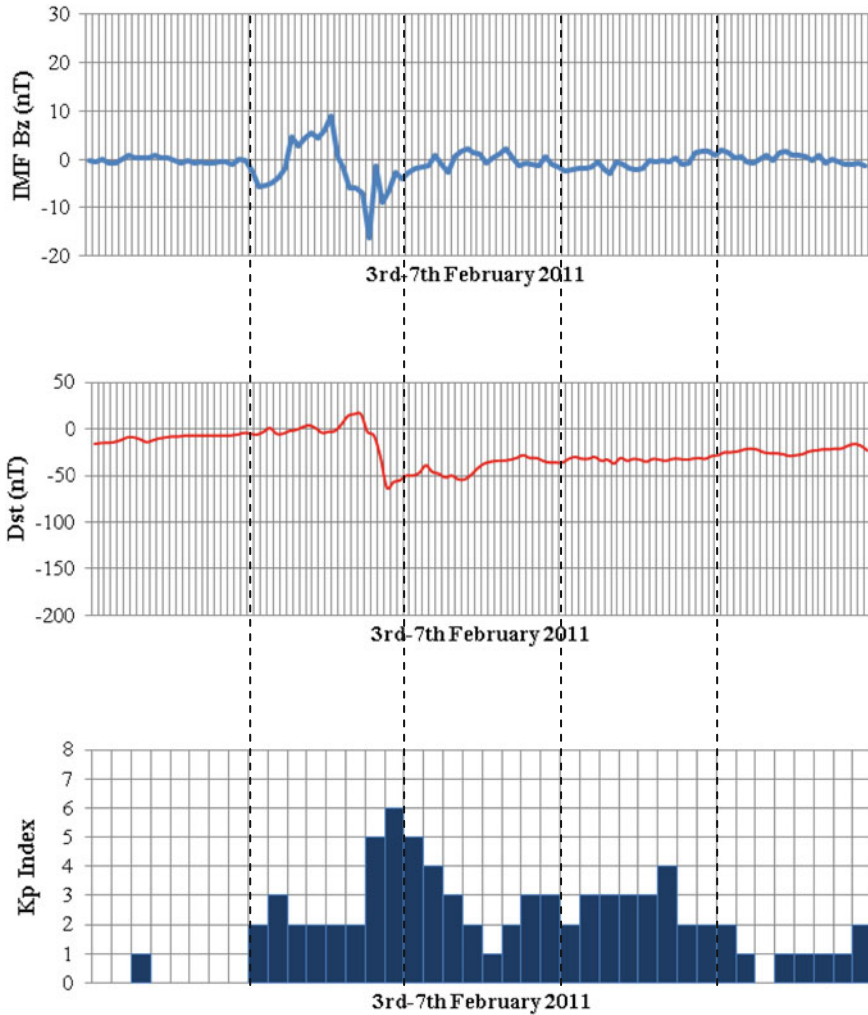


Fig. 4 The moderate storm on 4 February 2011

value of 6. The highest negative D_{st} values observed at 2200 UT on 4 February 2011 and at 1900 UT on 1 May 2013 were -63 nT and -67 nT respectively as depicted in Figs. 5 and 6. The positive phase of IMF B_z during the storm period in 2011 just before the SSC, was observed at 1300 UT with 8.9 nT and the positive phase of IMF B_z during the storm period in 2013 just before the SSC was observed, at 1200 UT with 8.4 nT.

In contrast to the observation of the southward turning of IMF B_z during intense storms mentioned above, before the southward turning of IMF B_z during moderate storms, the K_p Index abruptly rose and started to decrease even when the IMF B_z changed direction, and it decreased more slowly than it rose. However, the K_p

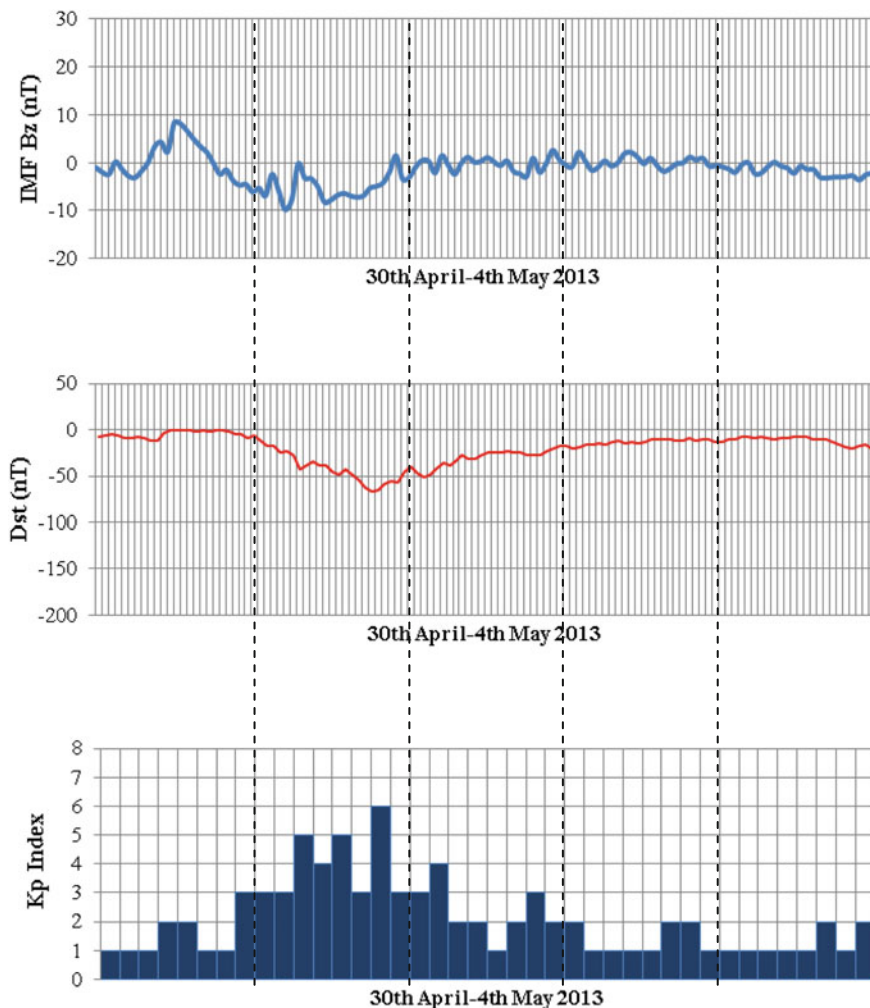


Fig. 5 The moderate storm on 1 May 2013

Index observed in 2013 shows inconsistent rising and falling values. It could be due to the perturbation of IMF B_z changing.

The TEC on the *D day* represents the averaged TEC data of 4–5 February and 1–2 May meanwhile the *Q day* represents the averaged TEC data of 26–27 February and 10–13 May for 2011 and 2013 respectively, as shown in Fig. 6. During 2011, the maximum TEC values observed during the *D day* was ~ 77 TECU and during the *Q day* was ~ 91 TECU.

The TEC values observed on the *D day* were slightly lower than those on the *Q day* [14] except at 0400 UT and 0900–1000 UT. It could be due to the D_{st} values reaching its lowest value at 0400 UT around -39 nT compared to other D_{st} values

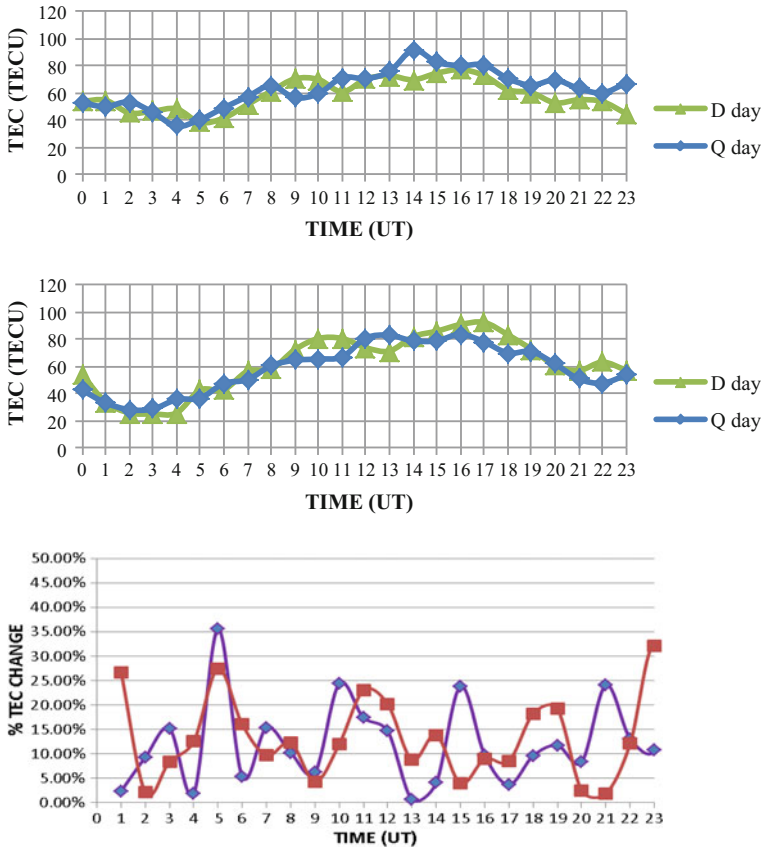


Fig. 6 The diurnal TEC during the moderate geomagnetic storms in 2011 (top panel) and 2013 (bottom panel) and the % TEC change

within the storms period. The storms period began at 2200 UT on 4 February and ended at 0900 UT on the following day. The storms phase ended at 0900 UT and this explains the increase of TEC at 0900–1000 UT to higher than those on the *Q day*. The maximum percentage change in TEC observed on the *D day* is 36% as shown in Fig. 6.

However, during 2013, the maximum TEC values observed for both the *D day* and the *Q day* were not significantly different at ~92 TECU and ~84 TECU respectively. The storms period began at 1700 UT on 1 May and ended at 0300 UT on the following day. The maximum percentage change in TEC observed on the *D day* is 32% as shown in Fig. 6.

The positive ionospheric storms represent the increase in TEC value and the negative ionospheric storms represent the decrease in TEC value. The negative ionospheric storm is prominent during the moderate storm period of 4 February 2011 as a decrease in TEC shown in Fig. 6. The most influential mechanisms used

to describe the occurrence of positive ionospheric storms are electrical field variations and neutral winds [15]. During the main phase of the storm period, the electrical field moves eastward in the daytime and westward during the recovery phase. The westward current restrains the eastward current and thus produces a counter electrojet. The neutral wind moves equatorward and it reduces the downward diffusion of plasma along the geomagnetic field lines, causing the ionosphere to uplift where the chemical loss is reduced [16]. The negative ionospheric storms occurred during nighttime on 4 February 2011 as shown in Fig. 6. The resulting decrease in TEC has been attributed to the disturbance in dynamo-electrical fields as well as the changes in thermospheric chemical composition signified by a reduced $[O/N_2]$ ratio [17].

4 Concluding Remarks

During the intense geomagnetic storms, the highest negative D_{st} value in 2011 was -147 nT while the highest negative D_{st} value in 2013 was -132 nT. The maximum percentage change in TEC in 2011 and 2013 was 45% and 41%, respectively. For the moderate geomagnetic storms, the highest negative D_{st} value in 2011 was -63 nT meanwhile the highest negative D_{st} value in 2013 was -67 nT. The maximum percentage changes in TEC in 2011 and 2013 were 36% and 32%, respectively.

The sudden southward turning of IMF B_z observed during the SSC shows the presence of the prompt penetration electric fields. The perturbations in TEC indicate that there could have been plasma uplift due to eastward penetration electric fields. The intense storms occurred at 0200 UT in 2011 and 2100 UT in 2013 while the moderate storms occurred at 2200 UT in 2011 and 1900 UT in 2013. All the geomagnetic storms periods occurred from post-sunset hours until late midnight.

Acknowledgements The authors would like to express their gratitude to the IGS Data Centers for providing the data.

References

1. Gonzalez WD, Tsurutani BT, De Gonzalez ALC (1999) Interplanetary origin of geomagnetic storms. *Space Sci Rev* 88(3–4):529–562
2. Basu S et al (2007) Response of the equatorial ionosphere at dusk to penetration electric fields during intense magnetic storms. *J Geophys Res Space Phys* 112:A8
3. Oryema B et al (2015) Investigation of TEC variations over the magnetic equatorial and equatorial anomaly regions of the African sector. *Adv Space Res* 56(9):1939–1950
4. Rama Rao PVS et al (2009) Geomagnetic storm effects on GPS based navigation. *Ann Geophys* 27:2101–2110
5. Bartels J, Heck N, Johnston H (1939) The three-hour-range index measuring geomagnetic activity. *Terr Magn Atmos Electr* 44(4):411–454

6. Davis C et al (1997) Ionospheric and geomagnetic responses to changes in IMF B z: a superposed epoch study. *Ann Geophys* 15(2):217–230
7. D'ujanga F et al (2013) Total electron content of the ionosphere at two stations in East Africa during the 24–25 October 2011 geomagnetic storm. *Adv Space Res* 51(5): 712–721
8. Burke W et al (2011) Estimating Dst indices and exospheric temperatures from equatorial magnetic fields measured by DMSP satellites. *J Geophys Res Space Phys* 116:A1
9. Lincoln JV (1967) Geomagnetic indices, in physics of geomagnetic phenomena, 1st ed International Geophysics Series, vol. 1, ed. by S. Matsushita, W.H. Campbell vol. 1 (Academic Press Inc, 111 Fifth Avenue, New York, New York 10003, 1967), pp 67–98
10. Ma G, Maruyama T (2003) Derivation of TEC and estimation of instrumental biases from GEONET in Japan. *Ann Geophys* 21:2083–2093
11. Klobuchar JA (1996) Ionospheric effects on GPS. In: Spilker JJ, Parkinson BW (eds) *Global positioning system: theory and applications*, 1. AIAA: 485–515; Liu G et al (2012) Vertical TEC variations and model during low solar activity at a low latitude station, Xiamen. *Adv Space Res* 49(3): 530–538
12. Förster M, Jakowski N (2000) Geomagnetic storm effects on the topside ionosphere and plasmasphere: a compact tutorial and new results. *Surv Geophys* 21(1):47–87
13. Adeniyi J et al (2014) Magnetic storm effects on the variation of TEC over Ilorin an equatorial station. *Radio Sci* 49(12):1245–1253
14. Balan N et al (2013) Physical mechanisms of the ionospheric storms at equatorial and higher latitudes during the recovery phase of geomagnetic storms. *J Geophys Res Space Phys* 118(5):2660–2669
15. Balan N et al (2010) A physical mechanism of positive ionospheric storms at low latitudes and midlatitudes. *J Geophys Res Space Phys* 115:A2
16. Galav P, Sharma S, Pandey R (2011) Study of simultaneous penetration of electric fields and variation of total electron content in the day and night sectors during the geomagnetic storm of 23 May 2002. *J Geophys Res Space Phys* 116: A12

Analysis of Critical Frequency Measured from Ionosonde System During Low Solar Activity in Malaysia Region

Sabirin Abdullah and Ahmad Faizal Mohd Zain

Abstract This paper studied the variability of critical frequency in the Malaysia region. The critical frequency is obtained from radio wave reflections in the F_1 and F_2 layers of the ionosphere. Data was collected from the ionosonde system at Batu Pahat, Johor and experimental data from 2005 was used in the analysis. Data from two locations were then compared to data from the IRI model. The pattern of critical frequency was observed daily and monthly. Results showed that the Parit Raja location had the highest critical frequency at an average of 8.11, followed by that from the IRI model at 7.01 and Darwin station at 6.87. This could be used to define the pattern of critical frequency in the Malaysia region and further studies are needed to provide a better understanding of the mechanism.

1 Introduction

The ionosphere is a layer of the atmosphere that contains a high electron density and is affected by the sun's activity [1]. Studies show that the ionosphere layer profile varies daily and this affects the high frequency (HF) value. Ionosphere studies in Malaysia started in 1946 by a Japanese researcher [2], and the early research and experiments were conducted on Penang Island. The study found that the island had a higher HF communication. However, no further study was performed in Malaysia until 1990 when ionosphere study began again with research on HF propagation, focusing on total electron content [3], and where the observation values were collected through a GPS (Global Positioning System) receiver located at Jabatan Ukur Pemetaan Malaysia (JUPEM) station [4]. This station used

S. Abdullah (✉)

Space Science Centre (ANGKASA), Institute of Climate Change,
Universiti Kebangsaan Malaysia, 43600 Bangi, Selangor Darul Ehsan, Malaysia
e-mail: dr_sabirin@ukm.edu.my

A.F.M. Zain

Faculty of Science and Technology, Universiti Sains Islam Malaysia (USIM),
Bandar Baru Nilai, 71800 Nilai, Negeri Sembilan, Malaysia

four different locations for data measurement. Ionosphere studies continued in 1995 with research on propagation through the ionosphere layer by observing HF signals transmitted from several parts of the world [5]. Critical frequency studies are useful in HF communication where the frequency can determine the Maximum Usable Frequency (MUF) for a certain location. In the Malaysia region, MUF is determined by using experimental data and a comparison model [6]. Moreover, analysis on the variation of critical frequency based on diurnal and seasonal factors is also capable of providing information on the critical frequency [7].

The recording system of an echo received from the ionosphere uses an electronic time base to modulate the intensity of a spot of light. The distance along the time base represents the time of flight of the radio pulse. In this recorder, the photographic film moves at right angles to the time base as the frequency varies. This traces the virtual height against radio frequency. These recordings are commonly known as ionograms [8]. An ionogram consists of the F-layer frequency and height of the frequency, as shown in Fig. 1. An ionogram recorded using the ionosonde system is shown in Fig. 2. The critical frequency value (MHz) is defined from the ionogram display that capture from the inosonde system. This ionogram records the reflection of the signal that is transmitted to the ionosphere layer before being reflected back to the system. The reflection of the ionosphere from the ionosonde is in the form of critical frequency and the ionosphere layer virtual height values. The ionogram displays the frequency that is reflected from the ionosphere layer in real time. Due to the variation in the electron density in the ionosphere layer as a result of the solar activity, the critical frequency also varies on a 24/7 basis. It is important to study the

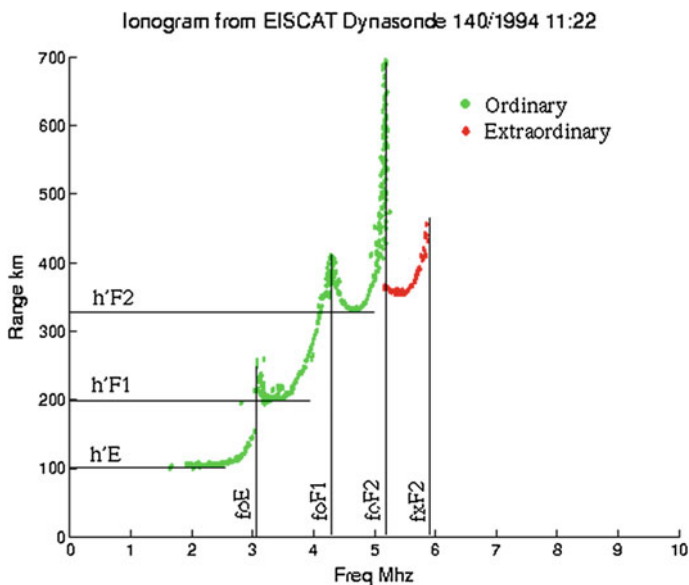


Fig. 1 Ideal Ionogram from the ionosonde system *Source:* EISCAT Dynasonde 140/1994 11:22

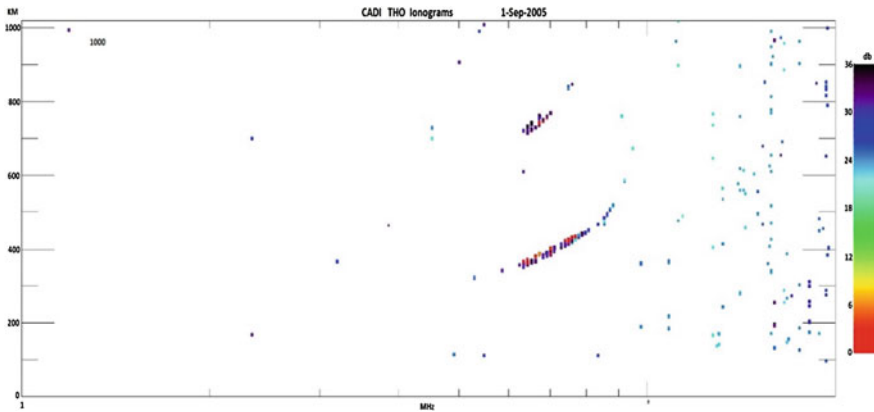


Fig. 2 Ionogram recorded from the ionosonde system at Batu Pahat, Johor, Malaysia on 1 September 2005

profile of the critical frequency – in the Malaysia region especially – as it will provide the basic availability of the frequency for HF communication. Daily critical frequency can be analysed by using measurement of the ionosphere layer via the ionosonde system. The resulting ionogram gives the critical frequency which will determine the MUF. An interesting feature of the equatorial region is that it had several unstable phenomena which are not yet fully understood and for which further investigations are therefore required [9]. The short terms analysis of the critical frequency can give hourly values every day for communication reference.

This study observed the short-term ionosphere critical frequency in 2005 in order to determine the highest frequency that occurred during daytime. Results are compared to a nearby equatorial region with good data availability. Hence, in order to fulfil the objective of this study, data was taken from the ionosonde system located at Batu Pahat, Johor in Malaysia.

2 Critical Frequency

Plasma frequency, also known as the critical frequency, is defined using the equation below:

$$f_{Ni} = f_N(m/M)^{1/2} \tag{1}$$

where f_N = critical frequency, f_{Ni} = Ion plasma frequency, m = rest mass of an electron and M = rest mass of an ion [10]. This equation is derived from the plasma properties of the wave propagation. Vertical reflection occurs when the critical frequency f_N equals the wave frequency f . Hence, when the wave frequency exceeds the maximum critical frequency of the layer, the wave will penetrate the layer. The

critical frequency is in the form of an ordinary wave and an extraordinary wave when reflected from the ionosphere layer. When collision is negligible, the wave with the positive sign is usually called the ordinary wave since it is reflected at the same height as it would be in absence of the magnetic field and this phenomenon is also known as gyro frequency [11] whereas an extraordinary wave is when the refractive index depends on the magnetic field.

MUF is defined as [12]:

$$MUF(3000)F_2 = f_oF_2 \times M(3000)F_2 \quad (2)$$

where $M(3000)F_2$ is the propagation factor, f_oF_2 is the critical frequency and $MUF(3000)F_2$ is the useable frequency at a distance of 3000 km. There is also a simple formula to determine the MUF using critical frequency value [13]:

$$MUF = M(D)f_oF_2 \quad (3)$$

where $M(D)$ is the M-factor for a hop equal to distance, D . The critical frequency value from the experiment was determined from the ionogram interpretation.

3 Ionogram Interpretation

Basically, an ionosonde system can be used to observe the ionosphere layer 24/7. An ionosonde system is special radar that can transmit and receive signals from the ionosphere layer. Nowadays, ionosonde systems mostly use a computer management system and data collection is much easier than it was with the old system. Some of the systems display real time data of the critical frequency and height of the ionosphere. This type of data is presented in a display graph called an ionogram.

An ionogram is a data display of the ionosphere layer produced by an ionosonde. Typically, an ionosonde station records an ionogram every 5 to 15 min, depending on the settings of the system [14]. An ionogram display shows the frequency that reflected from the ionosphere layer in a form of a curve. The ionogram is capable of showing both important and basic data. Figure 2 shows the basic reflection F_2 layer and Fig. 3 shows the reflection of the E, F_1 and F_2 layers.

Figure 4 shows the ordinary and extraordinary curves captured by ionogram. The ionogram shows the range of critical frequency values. Based on Fig. 4, the minimum and maximum values of the critical frequency are approximately 3.4 and 5.1 MHz respectively.

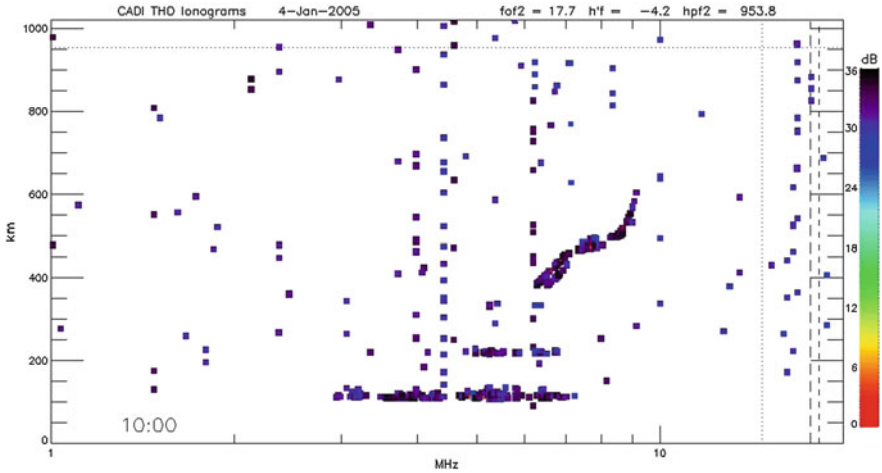


Fig. 3 The reflection of the ionosphere layer consisting of E, F₁ and F₂ layers

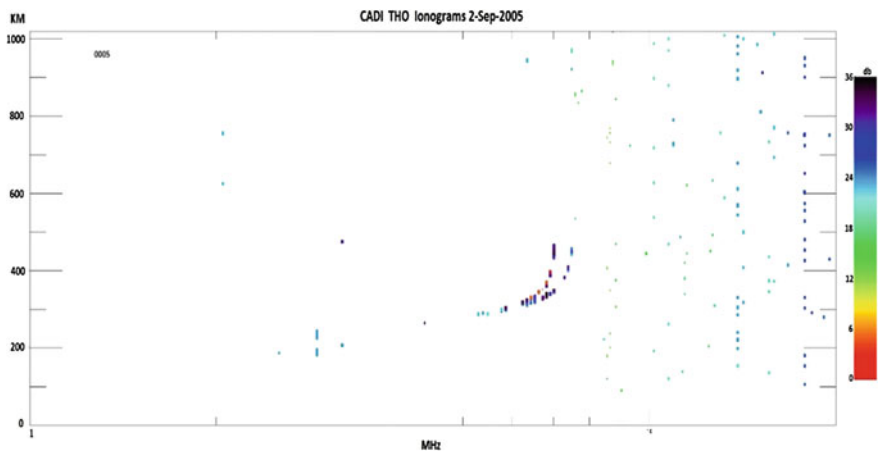


Fig. 4 The reflection of ionosphere layer of ordinary (Left) and extraordinary (Right) curves

4 Data and Location

The data were obtained from the real time ionosonde system at the Wireless and Radio Science Centre (WARAS) (1°52 N, 103°48E), Batu Pahat, Johor, Malaysia. The ionosonde system was fully active on a 24/7 basis in 2005 and it used four receivers with a vertical incident sounding. A transmitting card was connected to the computer from the preamp to boost transmitted signals. The antenna design for transmitter is a delta antenna and the receiving antenna consisted of four dipole

antennas. The swept frequency normally ranged from 3 to 20 MHz with a vertical sounding system [15]. The oblique sounding used more than one ionosonde system [16]. The ionosonde system used four receiver antennas and a single delta antenna for transmission. The global positioning system was used to synchronize the UTC time. Coincidentally, the solar cycle in 2005 was solar cycle 23 and solar activity continued to decrease until 2009 [17].

5 Results and Discussion

The result of this study is an analysis of observed values of the critical frequency based on the median critical frequency in 2005. The analysis consists of f_oF_1 and f_oF_2 critical frequency. The analysis of f_oF_1 critical frequency consists of theoretical and measurement values. The f_oF_2 critical frequency was compared with results from the Darwin station (-12.45°N , 130.95°E) in the Australasian region and for data availability and also IRI model for 2005. This gave the trend and frequency value during low solar activity.

5.1 Analysis of Comparisons of f_oF_1 Critical Frequency

The result of the regression analysis plot for f_oF_1 in 2005 is shown in Figs. 5, 6, 7, 8, 9, 10, 11, 12, 13, 14, 15 and 16. The solid line in the figures shows the measurement values while the dashed line shows the theoretical values. The R^2 is the correlation between the measurement f_oF_1 critical frequency and sunspot number. In this section, the analysis was performed to reveal the correlation between the f_oF_1 critical frequency and sunspot number for the measurement and theoretical values.

For the monthly regression analysis, the results show a low correlation between the critical frequency and the sunspot number. The theoretical value, however, shows a high correlation between sunspot number and the critical frequency.

The median critical frequency for this figure is the regression analysis using the measurement and theoretical values. The equation for 2005 is $y = 0.0003x + 4.685$, $R^2 = 0.0001$. The sunspot number for 2005 is of a high value ranging from 11 to 192. There were 17 days for which the sunspot number is not available.

Fig. 5 Regression analysis for January 2005

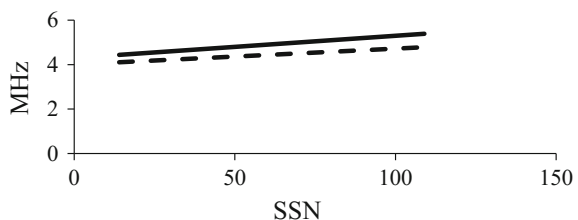


Fig. 6 Regression analysis for February 2005

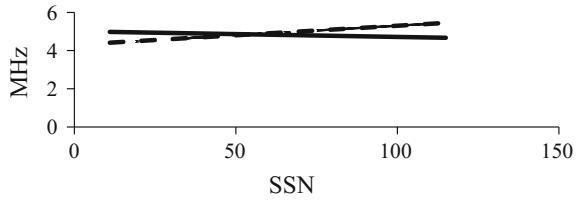


Fig. 7 Regression analysis for March 2005

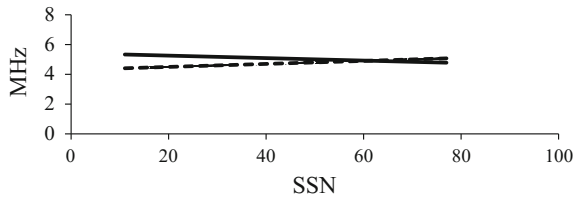


Fig. 8 Regression analysis for April 2005

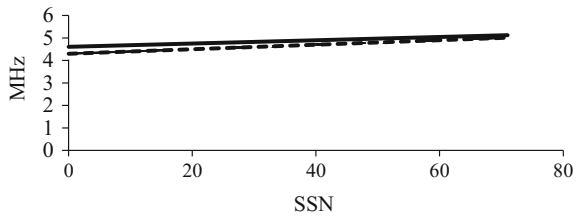


Fig. 9 Regression analysis for May 2005

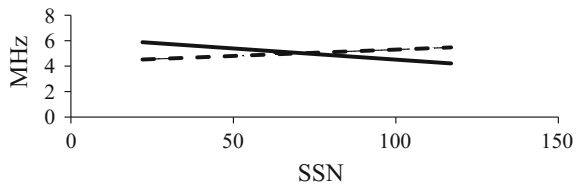


Fig. 10 Regression analysis for June 2005

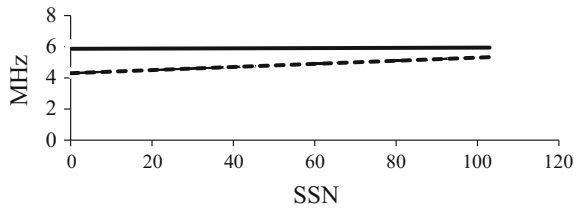


Fig. 11 Regression analysis for July 2005

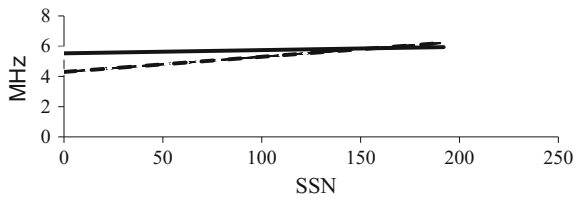


Fig. 12 Regression analysis for August 2005

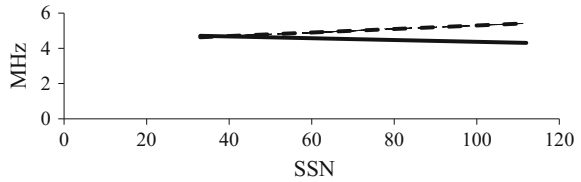


Fig. 13 Regression analysis for September 2005

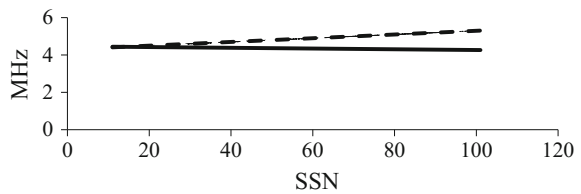


Fig. 14 Regression analysis for October 2005

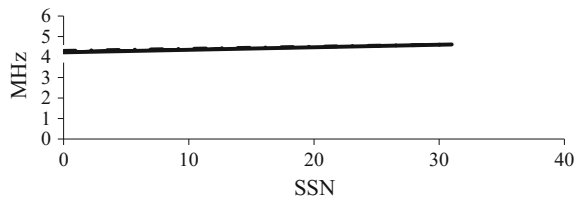


Fig. 15 Regression analysis for November 2005

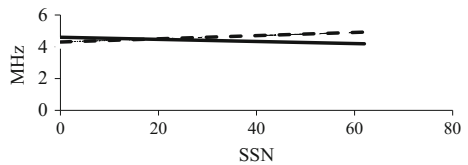
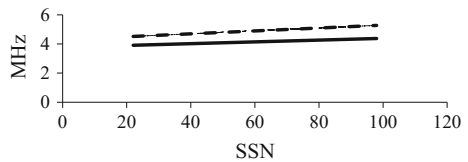


Fig. 16 Regression analysis for December 2005



The correlation between the measurement and sunspot number value is shown in Table 1. The M_x is the value for the x axis and C is the value where the lines intercept with the y axis. R is the correlation between the measurement value and the sunspot number.

In Table 1, the correlation for 2005 is small for each month except July where the correlation is high compared to the other months. The correlation value in July is 0.4325 which does not correlate with the measurement and theoretical values.

Table 1 Correlation results between measurement value of f_oF_1 and sunspot number

Month	Mx	C	R
January	0.0071	4.0046	0.1026
February	-0.0029	5.0072	0.0111
March	-0.0083	5.4201	0.1287
April	-0.0073	4.6052	0.0272
May	-0.0175	6.2662	0.2542
June	0.0008	5.864.3	0.0110
July	0.0021	5.5251	0.4325
August	-0.0051	4.8797	0.0518
September	-0.0020	4.4671	0.0111
October	0.0124	4.2272	0.0911
November	-0.0067	4.5993	0.0832
December	0.0061	3.7794	0.0555
Average	-0.00056	4.887117	0.105

The f_oF_1 critical frequency shows that there is poor correlation between the measurement value and sunspot number. The theoretical value is well correlated with the sunspot number compared to the measurement value. This value is obtained from the estimation of the noon f_oF_1 critical frequency only and is calculated using f_oF_1 formula [10].

$$f_oF_1 = (4.3 + 0.01R_{12})\cos^{0.2}\chi \tag{4}$$

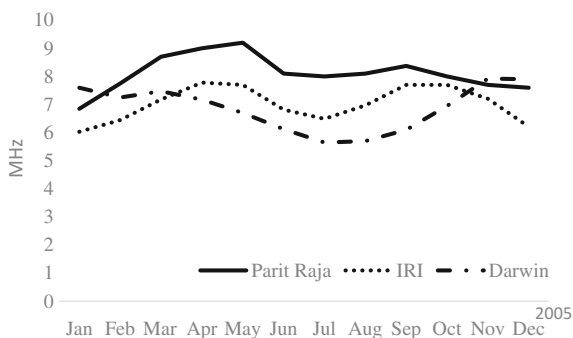
where R is the sunspot number and χ is the solar zenith angle. The theoretical values of the f_oF_1 critical frequency are highly correlated with sunspot numbers but the measured values show no correlation with sunspot numbers.

5.2 Comparison of f_oF_2 Critical Frequency

The critical frequency of the f_oF_2 was determined using the observation values from 2005. The analysis of the critical frequency used the trend line analysis from the daily values. The critical frequency value was taken from the daily median value and each value was determined from the sounding routine from the digisonde. The observation value of the critical frequency of f_oF_2 clearly has a high image of the reflection of the ionosphere during high noon from 8:00 AM until late evening at 5:00 PM local time (LT). The UTC time for this particular time is from 0:00 until 13:00 UTC.

In 2005, as shown in Fig. 17, the median critical frequency for Parit Raja was from 6 to 8.4 MHz in January. The highest critical frequency was on 22 January, but the Darwin station had a higher value of 9.7 MHz on 6 January and IRI model was 6.21 MHz. The lowest critical frequency was on 29 January at 6 MHz but the Darwin station had a higher critical frequency at 7.9 MHz and the IRI model was

Fig. 17 Monthly median critical frequency comparison in 2005



6.17 MHz. In February, the critical frequency ranged from 5.5 to 7.9 MHz for Parit Raja. Half of the days in February showed 7 MHz for the critical frequency value, but on 13 February the critical frequency was low at 5.5 MHz. The value for Darwin station was between 5.5 and 11.6 MHz and IRI model was 6.12 to 6.93 MHz. In March, the lowest critical frequency was 6 MHz but the critical frequency in this month increased to 9.1 MHz. Darwin station had 9.3 MHz as the highest critical frequency and 5.35 MHz. The critical frequency in April was 9.5 MHz which was an increase compared to the other months, while the lowest critical frequency for this month was 8 MHz. Darwin station had 10.9 MHz as the highest and 5.95 MHz as the lowest. The highest critical frequency in 2005 was in May, and was 11 MHz. The lowest critical frequency in May was 8.15 MHz which was higher in comparison to the lowest critical frequency in January to April. However, there were 4 days where the station did not have any observation values due to system maintenance. The highest value at Darwin station was 9 MHz and the lowest was 6.1 MHz. The IRI model ranged from 7.34 to 7.97 MHz.

The highest critical frequency in June was 8.7 MHz and the lowest was 7.5 MHz and Darwin station was 6.8 and 5.05 MHz which was lower than Parit Raja. The IRI model was from 6.55 to 7.35 MHz. The highest critical frequency in July was 10.75 MHz and the lowest was 1.8 MHz, and there were 5 days without recorded critical frequency because the system was shut down to prevent damage from lightning and for system maintenance. Darwin station had a low frequency compare to Parit Raja with 7 and 5 MHz and in August 7.4 and 4.9 MHz. The critical frequency in August was 9.3 MHz which was lower. The lowest critical frequency in August was 6.9 MHz. The lowest critical frequency in September was 7.8 MHz which was much higher than that recorded in August, while the highest critical frequency in September was 8.9 MHz. Darwin station also had a low frequency compare to Parit Raja, at 7.85 and 4.65 MHz in September. In October, the systems were shut down for one day because of a power failure. The highest critical frequency was 9.1 MHz and the lowest was 7.65 MHz in October. The systems were also shut down for a day due to a lightning strike during the bad weather, however, Darwin station was 8.65 and 6.05 MHz. In November, the highest critical frequency was 8.1 MHz and the lowest was 7.1 MHz while Darwin station was 8.65 and 5.3 MHz. The critical frequency was 8.4 MHz in December which was

the highest, while the lowest critical frequency was 6.9 MHz for that month. Darwin station was 9.35 and 6.1 MHz. The average value for Parit Raja was 8.1 and Darwin was 6.87. The IRI model was 7.0.

6 Conclusion

This study has analysed the measurement of the ionosphere observation values obtained from an ionogram. The ionogram was recorded by an ionosonde system that provided f_oF_1 and f_oF_2 critical frequencies. The ionosonde is located at Parit Raja station, Batu Pahat, Johor, Malaysia. The analysis of f_oF_1 showed a correlation between f_oF_1 critical frequency and sunspot number for the measurement and theoretical values. Results show that theoretical values of the f_oF_1 critical frequency are highly correlated with sunspot numbers but the measured values show no correlation with sunspot numbers. Moreover, the highest critical frequency was at Parit Raja with an average of 8.11, followed by that of the IRI model at 7.01 and Darwin station at 6.87.

This can be used as a reference for the critical frequency value for future studies of a similar nature. Finally, this study can also be related to HF communication in Malaysia where further studies are needed in the equatorial region.

Acknowledgements The authors wish to thank Universiti Kebangsaan Malaysia for funding this project, Universiti Tun Hussein Onn Malaysia for providing the experimental data and the Australian Space Weather Services World Data Centre for data download. The authors also express gratitude to University Kebangsaan Malaysia grant GGPM-2012-071 and ANGKASA grant FRGS/1/2016/TK04/UKM/02/4 for supporting this research.

References

1. MacNamara LF (1994) Radio amateurs guide to the Ionosphere. Krieger Publishing Company, Florida, pp 17–20
2. Maeda K (1986) Fifty years of the Ionosphere. *J Radio Res Lab* 33(140):103–167
3. Zain AFM, Abdullah M (1999) Initial results of total electron content measurements over Arau Malaysia. In: 4th IEEE Malaysia international conference on communications and 4th IEEE Asia Pacific international symposium on consumer electronics MICC & ISCE99 Malaysia
4. Zain AFM, Abdullah M (2000) Measurement of total electron content variability at Miri Sarawak: Short Term Analysis. In: The 16th international conference on advanced science and technology (ICAST 2000) Fermi National Accelerator Laboratory Wilson Hall Batavia Illinois 60510 USA, 3 June 2000
5. Hassan SIS, Nazim MM, Yagasena A (1995) Observation of F-layer propagation in Malaysia. *IEEE Catalog*:592–595
6. Malik RA, Abdullah M, Abdullah S et al (2015) Ionospheric empirical model: initial approach to MUF modeling in the Malaysia region. In: 2015 international conference on space science and communication (IconSpace) Langkawi Malaysia, 3–5 July 2015 252–255

7. Abdullah S, Zain AFM (2012) Diurnal and seasonal variation of critical frequency in Malaysia from 2005 to 2007. *Appl Mech Mater* 225:448–452
8. Rishbeth H, Garriott OK (1969) *Introduction to ionospheric physics*. Academic Press Inc, New York
9. Rishbeth H (2000) The equatorial F-layer: progress and puzzles. *Ann Geophys* 18:730–739
10. Davies K (1996) *Ionospheric radio*. Peter Peregrinus Ltd, London
11. Zain AFM, Abdullah S, Rhazali ZA (2013) Determination of gyro frequency from critical frequency measurement over Parit Raja Malaysia. In: 2013 IEEE International conference on space science and communication (IconSpace) Melaka Malaysia, 1–3 July 2013, pp 440–443
12. Malik RA, Abdullah M, Abdullah S et al (2016) Comparison of maximum usable frequency (MUF) variability over Peninsular Malaysia with IRI model during the rise of solar cycle 24. *J Atmos Sol-Terr Phys* 138–139:87–92
13. Jonas RS, Inez SB, Renata GDFC (2013) A simple method to calculate the maximum useable frequency. In: 13th international congress of Brazilian Geophysical Society 1–5
14. MacDougall JW (2002) *CADI Software manual*. University of Western Ontario Edited December 1996 Feb Mar 1997 Feb Dec 2000 May 2002
15. MacDougall JW, Grant IF Shen X (2000) *The Canadian advanced digital ionosonde: design and results*. Department of Electrical Engineering University of West Ontario London Ont Canada
16. Fenwick RB, Barry GH (1966) Sweep-frequency oblique ionospheric sounding at medium frequencies. *IEEE Trans Broadcasting* BC 12(1):25–27
17. Maris G, Popescu MD, Besliu D (2004) Solar Cycle 23 analysis. In: *Proceedings international astronomical union symposium*, p 223

Comparison Between UKMtrapcast and SPENVIS in Forecasting Distribution of High Energy Protons in the SAA Region

Gusrizal, Wayan Suparta and Karel Kudela

Abstract The distribution of high energy particles in the South Atlantic Anomaly (SAA) region was examined. This study attempted to compare the results between UKMtrapcast and the Space Environment Information System (SPENVIS) in forecasting the distribution of high energy protons in the SAA during severe and quiet periods. Results showed that the accuracy of UKMtrapcast was around 80–90%. The maps of UKMtrapcast also indicated that during the quiet period, the flux value tended to increase and vice versa, and this phenomenon was in line with National Oceanic and Atmospheric Administration (NOAA) observations. In other words, the UKMtrapcast could perform dynamic forecasting. On the other hand, the results of SPENVIS showed a similar pattern for all particles in all periods with an inappropriate position of SAA core. These findings indicated a positive contribution opportunity for UKMtrapcast to study the Earth's space radiation particles.

Gusrizal (✉)

Universitas Muhammadiyah Kepulauan Riau, Tanjungpinang Kepulauan Riau, Indonesia
e-mail: gusrizal.almadani@gmail.com

W. Suparta (✉)

Space Science Centre (ANGKASA), Institute of Climate Change, Universiti Kebangsaan Malaysia, 43600 Bangi, Selangor Darul Ehsan, Malaysia
e-mail: drwaynesparta@gmail.com

W. Suparta

Dept of Electrical Engineering, Sanata Dharma University, Yogyakarta 55282, Indonesia

K. Kudela

Institute of Experimental Physics, Slovak Academy of Sciences, Kosice, Slovakia

K. Kudela

Nuclear Physics Institute, Czech Academy of Sciences, Řež, Czech Republic

1 Introduction

The structure and behavior of energetic protons and electrons trapped in the Earth's radiation belts have fascinated and puzzled scientists since their discovery. These belts can be categorized into two regions, the inner and outer belts. The inner belt is dominated by high energy protons and low energy electrons. This belt occupies the Earth's magnetic field line (L) at $L < 2$. The outer belt, on the other hand, is dominated by high energy electrons at $L > 3$. The area between the two belts is called the slot region and serves as a depleting area for electron population [1].

The inner belt is relatively stable with a typical lifetime of 10 years [2]. The inner proton radiation belt is a major cause of anomalies and lifetime reduction in low earth orbit (LEO) satellites because it contains the South Atlantic Anomaly (SAA) [3, 4]. The SAA is located over Brazil where the Earth's inner belt is the closest to the Earth's surface due to the offset between Earth's magnetic and geographic poles [5]. The SAA contains trapped electrons and protons at all altitudes, and these particles have energies of up to 10^2 keV (electrons) and 10^2 MeV (protons). These particles may affect spacecraft and their crews that pass through the region, especially in the LEO regions due to their ability to ionize matter [6]. Although the SAA is a dangerous area for LEO satellites, it became worth the risk due to the benefits that LEO offers to remote sensing satellites, especially near to an Equatorial orbit (NEqO) [7]. To overcome this challenge, the system to address the forecasting of the distribution of trapped particles in LEO—NEqO is needed to improve future satellite developments.

Due to the challenges stated above, the Space Science Centre (ANGKASA) at Universiti Kebangsaan Malaysia (UKM), Malaysia has attempted to produce an alternative method by which to study the distribution of LEO trapped particles, especially for the trapped particles forecasting system at NEqO. The system developed, UKMtrapcast [8], functions as a forecasting system of trapped particles flux distribution at LEO—NEqO orbit. The system employs a hierarchical Bayesian spatio temporal (HBST)—Gaussian Process (GP) [9] model combined with the Universal Kriging [10] interpolation technique that can overcome the limitations of other established models i.e.: (1) It can be applied to both electrons and protons and is not affected by solar variations (2) It uses dynamic rather than static data.

This paper aims to study the results of the UKMtrapcast and the Space Environment Information System (SPENVIS) which was developed to study the space radiation environment [11]. The SPENVIS depends on AP-8 and AE-8 models which are the de facto models in the space industry.

2 Methodologies

2.1 Noaa—Meped Data

Medium-energy proton and electron detector (MEPED) data from National Oceanic and Atmospheric Administration (NOAA) satellites was used in this study because it corresponded to the forecasting target. However, the MEPED data suffers contamination in both electron and proton detection. After a rigorous literature review, the work of Yando et al. [12] was chosen to be used as a reference for our work. Yando et al. [12] stated that the channels that were free from contamination issues were P4–P5 and P6 Omni—P9 Omni.

It was crucial for this study to treat >16 meV proton observations in the SAA from the MEPED omnidirectional detectors rather than the lower energy proton fluxes (P4–P5). Therefore, four omnidirectional proton detector channels (P6–P9 Omni), i.e. >16 , >36 , >70 and >140 meV were selected to be employed in this study. This selection was made in order to give a significant contribution to the field of space weather and space climate, since >30 meV proton fluxes were commonly used to indicate the likelihood of single event upsets [13]. Thus, these four channels nicely bracket the energy range relevant to space weather effects in the SAA. The NOAA data used were adjusted to correspond with the pre-determined area and period limitation. In terms of area, the data was restricted to the inside of the SAA region (0° to -40° of latitude and -90° to 40° of longitude).

In terms of period, the SAA region was examined during two severe events, namely 28 October 2003 and 17 January 2005 and one quiet event, namely 21 August 2008. The date of 28 October 2003 was commonly known as the Halloween solar flare which was a massive solar flare event, while 17 January 2005 was a moderate event. These two severe events occurred in solar cycle 23. In regards to quiet events, there was no significant event occurring from 2007 to 2009 due to the period being the declining phase of solar cycle 23 and the starting phase of solar cycle 24. Hence, 21 August 2008 was selected to represent the quiet event. All three events were evaluated on three consecutive days, in other words before, during and after the event. A number of NOAA satellites' data were used in these evaluations, namely NOAA 15–17 for the Halloween solar event and NOAA 15–18 for the remaining two events. All the severe events mentioned above were described in the NOAA solar proton event catalog (<ftp://ftp.swpc.noaa.gov/pub/indices/SPE.txt>).

2.2 UKMtrapcast System

The UKMtrapcast was developed by combining the HBST—GP method applied in the *spTimer* [14] package with the Universal Kriging technique employed in the *field* [15] package. Both packages are R packages. These R packages are embedded in a Matlab platform and employ the NOAA data as an input. Detail regarding the

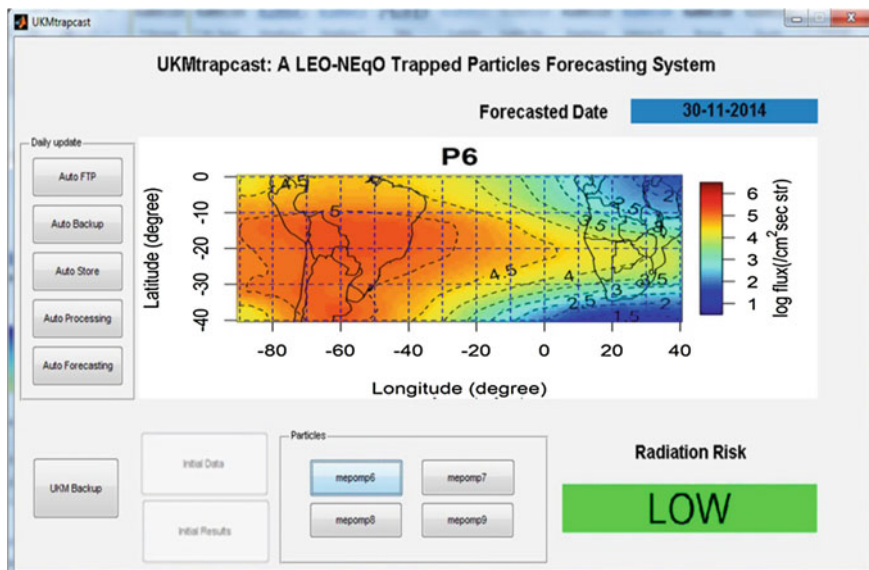


Fig. 1 Overview of UKMtrapcast system

HBST—GP and Kriging technique applied in this work can be found in Suparta and Gusrizal [16], and Suparta et al. [17]. The overview of UKMtrapcast system is given in Fig. 1 and it is explained in detail in Gusrizal [8].

The NOAA data employed in UKMtrapcast was set as mentioned in Sect. 2.1. In order to find the accuracy of UKMtrapcast results, three validation parameters were used in the HBST-GP validation, namely the root mean square error (RMSE), mean absolute percentage error (MAPE), and bias (BIAS) [18]. Meanwhile, the error prediction in the Kriging method was constructed by using the mean squared prediction error. In geostatistics terminology, this value is often called the estimation variance or the Kriging variance ($\hat{\sigma}_0^2$) [10].

2.3 SPENVIS System

The UKMtrapcast results in the SAA region were compared with two output types generated from SPENVIS, namely the invariant-based coordinate and the geographical map. The invariant-based coordinate was based on high energy protons in order to evaluate the distribution of trapped particles in the magnetic coordinate.

Once the user had logged into the SPENVIS system, the miscellaneous menu was selected and a list of options were made available. In order to generate the trapped particles map in the invariant coordinate, the L range was set as $L = 1$ to $L = 4$. We also chose the AP-8 model to generate trapped protons fluxes. The models have two variants, namely MAX and MIN for the solar maximum and minimum respectively.

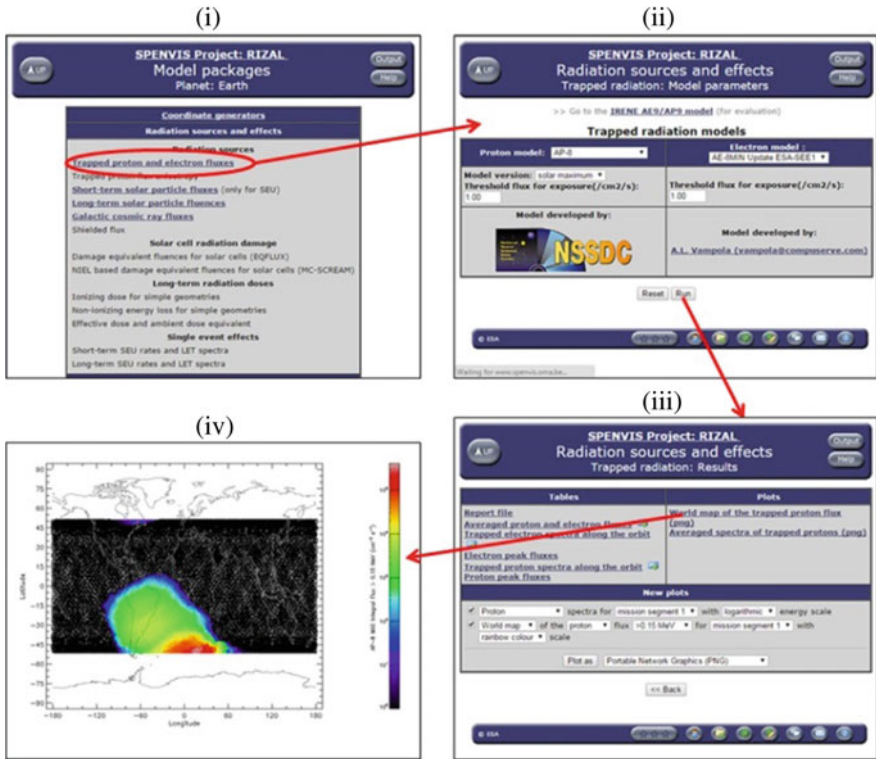


Fig. 2 SPENVIS features used in this work

Four sets of energy thresholds were selected from the output to cover trapped particles' energy level in accordance with that of the NOAA data employed in this study. The energy thresholds were >20 meV and >40 meV for electrons and >70 meV and >150 meV for protons in order to represent P6 Omni-P9 Omni, respectively. The date was also set as mentioned in Sect. 2.1. Figure 2 shows the SPENVIS features used in this work.

3 Results and Discussion

3.1 Results

3.1.1 Result of UKMtrapcast System

The results for HBST—Kriging over the SAA region are presented in Fig. 3(I)–(IV) which represent the results of mepomp6, mepomp7, mepomp8, and mepomp9,

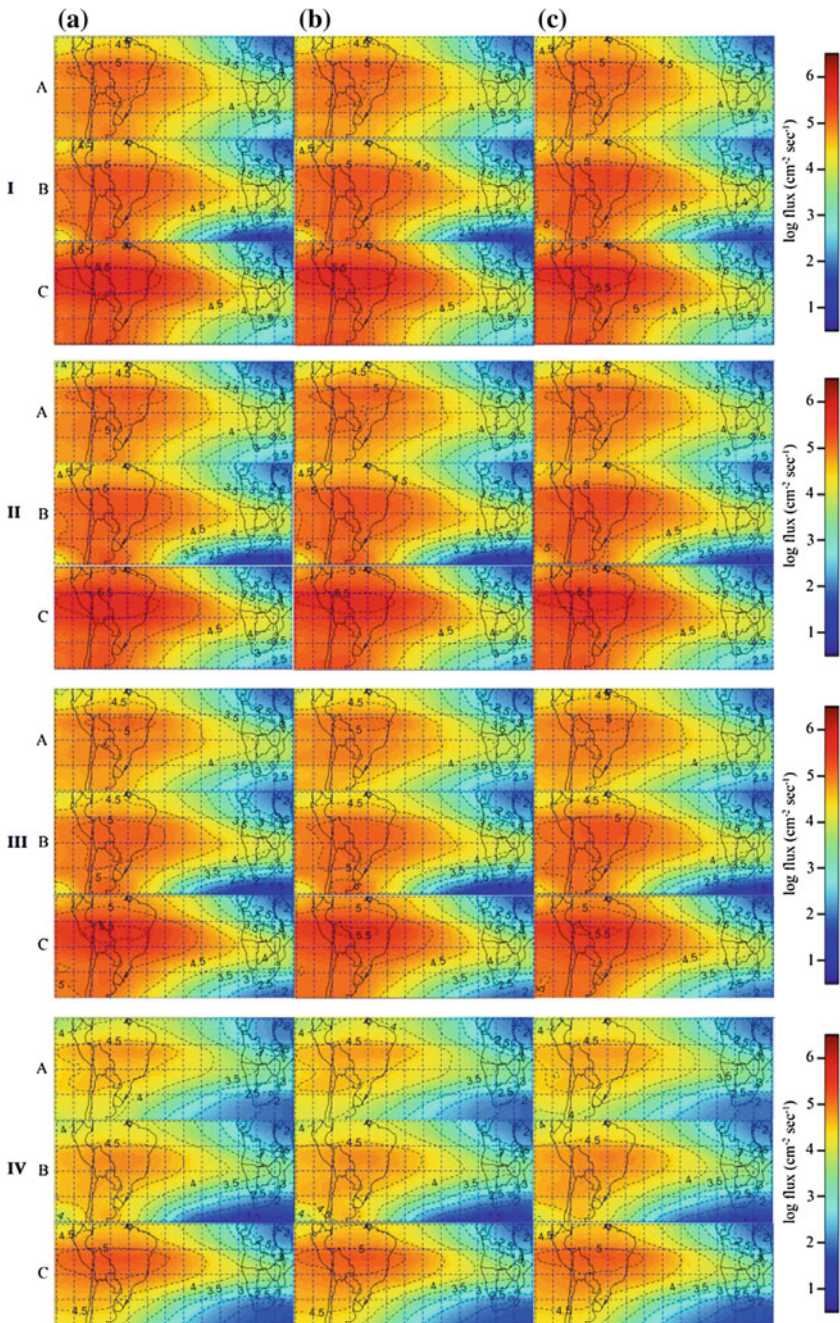


Fig. 3 HBST—Kriging generated maps of mepomp6 (I), mepomp7 (II), mepomp8 (III), and mepomp9 (IV) over the SAA region for (A) 27–29 October 2003, (B) 16–18 January 2005, and (C) 21–23 August 2008. The letters a, b, and c indicate the three days for each respective period

Table 1 MAPE average values of proton particles over SAA region

Parameters	Date	Average value			
		P6	P7	P8	P9
MAPE	27-10-03	14.18	14.18	14.76	18.93
	28-10-03	16.38	15.49	17.54	19.78
	29-10-03	17.10	15.72	17.45	18.90
MAPE	16-01-05	13.23	13.52	13.86	14.09
	17-01-05	9.05	9.96	9.45	10.92
	18-01-05	14.25	13.90	14.41	14.31
MAPE	21-08-08	8.81	8.81	9.27	9.17
	22-08-08	9.88	10.37	10.33	10.63
	23-08-08	12.62	12.63	12.20	12.46

respectively. These periods were 27–29 October 2003, 16–18 January 2005, and 21–23 August 2008 which were represented as indexes A, B, and C, respectively. The letters of a, b, and c represent the sequence of the three days for each period. The unit in each figure is in log flux ($\text{cm}^{-2} \text{s}^{-1}$). A contour line of flux value is added to each figure in order to ease the examination of them.

Based on Fig. 3(I)–(IV), it can be seen that the maximum value of fluxes is around 5–5.5 for all particles, except for mepomp9 (>140 meV) that has a value of 4.5–5 (Fig. 3(IV)). The mepomp6 (>16 meV) and mepomp7 (>36 meV) have a bigger high-flux area where their maximum flux value contour areas are wider than those of other particles. Furthermore, all three periods show higher fluxes during lower solar activity. Figure 3(I(A)–IV(A)) which represent the period of 27–28 October 2003 (a major solar event) have a lower maximum flux compared to Fig. 3(I(B)–IV(B)) representing 16–18 January 2005 (a moderate solar event). However, Fig. 3(I(C)–IV(C)) representing 21–23 August 2008 have the highest maximum flux values. The distribution pattern for each particle also slightly changes in a period and has significant variance between each period, especially between severe and quiet periods.

The average values of the HBST—GP MAPE validation parameter of all particles for the days in the three periods are shown in Table 1. The MAPE values determine the accuracy of the HBST—GP model during a severe period. Based on the table, the average values of MAPE for all events are around 10–20%. This confirms that the accuracy of the HBST—GP method employed for the SAA region is around 80–90% for all periods.

The validation of Kriging is indicated by the value of its variance. We found that the variance values of all particles are below 0.10 except for the period 16–18 January 2015 where it was around 0.15. The results also show that both events have similar patterns, which means that the Kriging technique is able to perform consistently during these events. These results demonstrate that the HBST—GP results are quite adequate to be employed in the Kriging technique.

3.1.2 Results of SPENVIS

Figure 4 shows the distribution of high energy protons in the invariant coordinate during (i) quiet and (ii) severe periods. Here, it is found that higher energy levels have a lower area. For example, the >20 meV energy level occupy more area of L as compared to >40 meV energy. It is also found that the protons' distributions are quite stable for both periods (Fig. 4(i)–(ii)). Figure 4 also gives a general overview of the habitual population area for the proton particles. It seems that the higher flux area for all high energy protons occurred at $1 < L < 2$, which is the area of the inner radiation belt. All SPENVIS generated maps were made with the assumption that there was no significant solar event during both periods. In order to investigate the ability of the SPENVIS AP-8 model on different solar activities in the SAA area, generating maps of high energy protons in defined quiet and severe periods was attempted.

Figure 5(I–IV) represent the results of SPENVIS simulation of >20 meV, >40 meV, >70 meV and >150 meV respectively, during quiet and severe periods. The indexes of A, B, C in Fig. 5(I–IV) represent 27–29 October 2003, 16–18 January 2005 and 21–23 August 2008, respectively. The letters of a, b, and c respectively represent the first, second, and third day of each period. The unit in each figure is in flux ($\text{cm}^{-2} \text{s}^{-1}$). The dashed blue circle is encircled in each figure to signify the area that has the specified values listed in the colour legend. The white area is the area that has a high flux value and is suggested to represent the core of the SAA. The suggested core area of the SAA is found to be lower than the actual position of the SAA core for the three periods. The black area in each figure shows that the area has very little value of flux.

For all particles, the maximum values of fluxes are around 1000, or 3 in logarithmic value. Based on Fig. 5(I–IV), proton energy >20 meV has the highest maximum flux while proton energy >150 meV has the lowest maximum flux. This agrees with the maximum values results obtained at the invariant coordinate (Fig. 4). It can also be seen that the population area of energy >20 meV is higher compared to other particles, while energy >150 meV occupies the smallest area. From this, it can be concluded that the habitual area for proton particles in LEO orbit is in the SAA region.

The distribution pattern for each particle is similar in each event even though these events actually differ significantly from each other; the period of 27–29 October 2003 was a major solar storm event that occurred in solar cycle 23 while period of 16–18 January 2005 was a moderate storm event and the period of 21–23 August 2008 was a quiet period with no major storms.

3.2 Discussion

Results from these methods show that the particles fluxes values vary according to the solar activity condition. The proton fluxes decrease during high solar activity

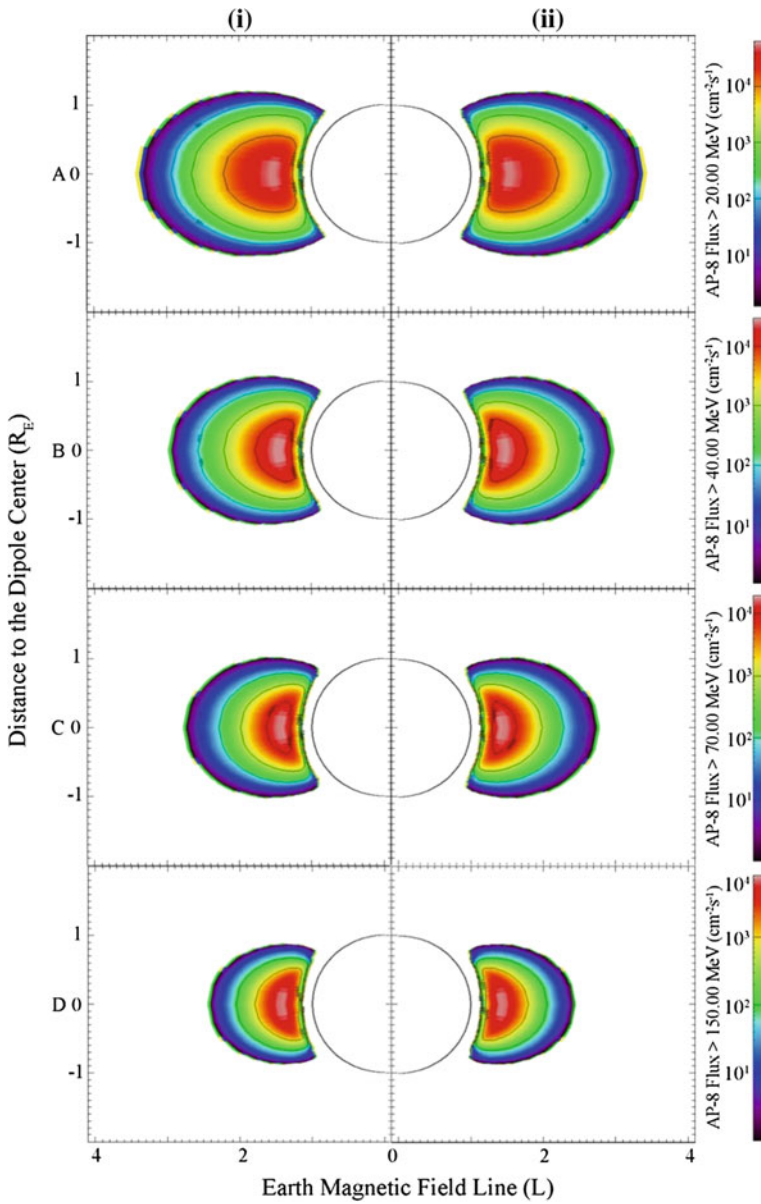


Fig. 4 The SPENVIS generated maps of particles on invariant coordinates for (A) proton > 20 meV, (B) proton > 40 meV, (C) proton > 70 meV, and (D) proton > 150 meV. The letters (i) and (ii) indicate Min and Max of solar activity respectively. The unit of log flux is in particles $\text{cm}^{-2} \text{sec}^{-1}$

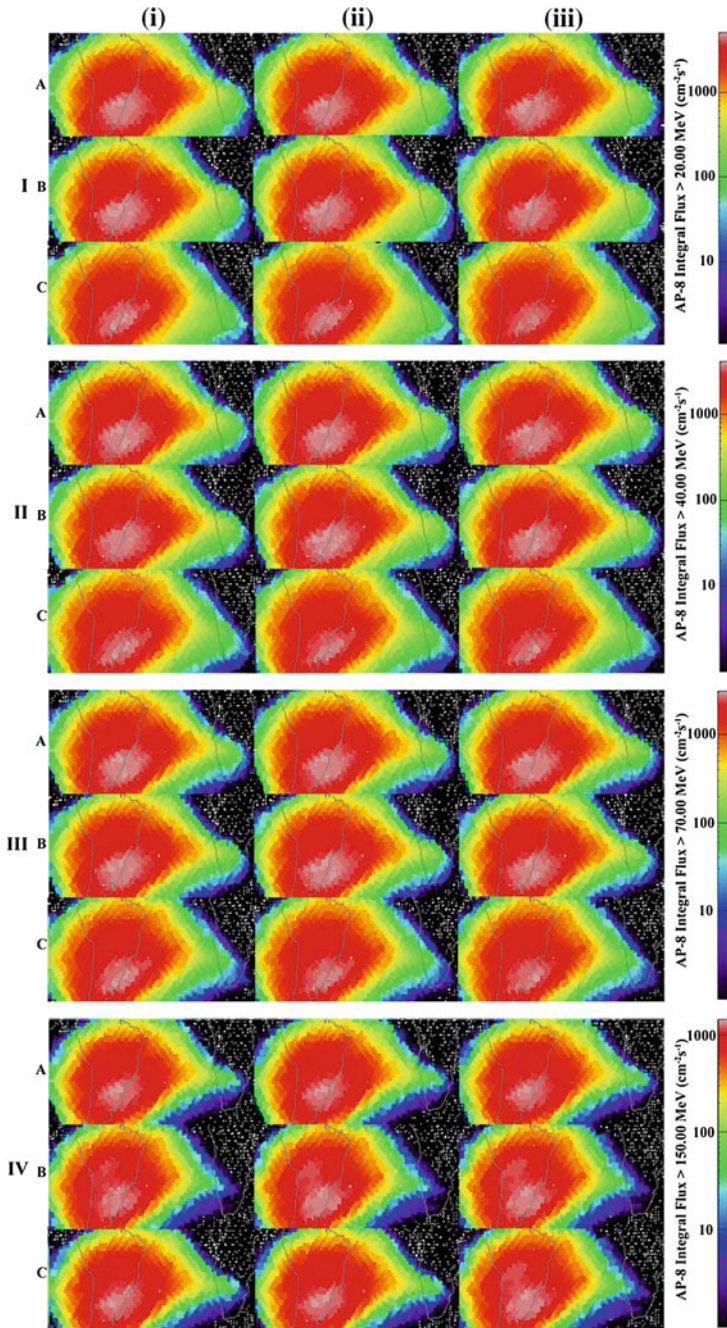


Fig. 5 SPENVIS generated maps of proton >20 meV (I), >40 meV (II), >70 meV (III), >150 meV over the SAA region for (A) 27–29 October 2003, (B) 16–18 January 2005, and (C) 21–23 August 2008. The letters a, b, and c indicate the first, second and third day respectively of the period

and increase during low solar activity. This is in line with the study dedicated to trapped proton fluxes in the inner belt [19, 20]. Qin et al. [20] stated that the enhancement of solar activity can trigger an increasing upper atmosphere density and lead to the decrease of proton flux. The HBST—GP results also indicate that a high solar storm would reduce the proton flux as shown in the 27–29 October 2003 period. This agrees with the results conducted by Zou et al. [21] who stated that the losses of protons in the inner radiation belt are found during large solar storms. Zou et al. [21] also added that the 35–70 meV proton channel shows a flux reduction during large storms with a minimum Dst < -200 nT, whereas the storm with minimum Dst < -350 nT can decrease the fluxes of 70–140 meV and give a small effect on the fluxes of 140–500 meV.

This is in agreement with results obtained in this study where the 27–29 October 2003 event with a Dst index near to -400 has more impact compared to the 16–18 January 2015 event which has a minimum Dst index around -100. The HBST—Kriging results also present a dynamic pattern throughout the days in the defined period. This confirms the suitability of the Kriging technique employed in this study.

We also attempted to compare the result of the UKMtrapcast system to the results based on an established model and system. This task was done by generating the maps of trapped particles in invariant and geographic coordinate by employing a NASA AP-8 model implemented in the SPENVIS system. These maps were also built during high and low solar activity. From the results, it can be seen that the distribution pattern of particles is similar in all periods of solar activity. This shows that the distribution of proton particles in the inner belt is static. This finding is in contrast to the nature of the proton population in the inner belt. The inner belt proton population is highly dynamic and is influenced by several factors [20], namely (1) solar proton events, (2) the collision effects between the upper atmosphere and the proton itself, (3) cosmic ray albedo decay, and (4) the long-term variation of the geomagnetic field. It is assumed that the static condition of AP-8 maps is due to the use of magnetic field models corresponding to the epoch at which the data were taken [22].

The second limitation of the NASA model is the value of proton flux. Results in Sect. 3.2 stated that the maximum flux values for all particles are in order of 3 in the logarithmic scale. However, this is a difference of around two logarithmic scales from the maximum flux values recorded by NOAA which are in order of 5. Furthermore, the NASA model in the SPENVIS system only provides coordinate data for peak values but does not provide detailed coordinates for proton fluxes throughout the orbit. This makes it difficult to validate the SPENVIS results with real data.

The following describes the limitations of this study. The first limitation is related to the HBST model used. Generally, the model has a good ability to forecast particles fluxes but it does not use any solar parameter such as $F_{10.7}$ indices or any geomagnetic indices such as Kp or Dst to integrate into the model's computation. Such parameters are important for solar event applications. Moreover, the model also has limitation in terms of forecasting period. While the distribution of trapped

particles in the inner belt is relatively stable, the use of HBST—Kriging is more valuable if it is utilized to predict the distribution of trapped particles in a given time at a given location rather than predicting the $T + 1$ distribution. The ability to predict fluxes at a given time and location would enable the calculation of radiation dose during a mission. Apart from that, the model lacks in terms of coordinate framework. The model would perform better if it could also be applied at the (B, L) coordinate because this type of coordinate type can include the nature of trapped particles as compared to a geographical coordinate type.

4 Conclusion

The development of a LEO-NEqO trapped particles forecasting system has been delivered. The employment of HBST-Kriging technique showed that the accuracy of the HBST-Kriging technique was around 80–90%. In addition, the Kriging variance was close to zero. This method was also able to produce a dynamic map that followed the trend of the distribution of trapped particles in accordance to solar activity. The study of the distribution of trapped particles generated by the AP-8 model implemented in SPENVIS showed that its generated maps were in static condition and its maximum flux values differed by the order of 2 in the logarithmic scale. It was difficult to validate this model due to the unavailability of flux values and their coordinates.

In order to improve studies relating to the UKMtrapcast system, and for this study to be of practical interest to the space weather and space climate community, the HBST-Kriging technique should present the capability of estimating fluxes at any time (rather than a 1-day forecast) in a given area. It also needs to incorporate some solar and geomagnetic indices in order to enhance the usefulness of this method. Apart from that, the usefulness of the method will increase if it can also be applied to the (L, B) coordinate.

Acknowledgements The work was supported by the Ministry of Science, Technology and Innovation (MOSTI), Malaysia with grant code 06-01-02-SF0808 and from the Ministry of Education (MoE), Malaysia with grant code FRGS/2/2013/SG02/UKM/02/3. Our gratitude is also addressed to the National Oceanic and Atmospheric Administration (NOAA), United States (US) for providing data to be used in the UKMtrapcast system, and European Space Agency (ESA) for their development of the online tool, the Space Environment Information System (SPENVIS). K. Kudela wishes to acknowledge support of APVV agency project APVV-15-0194, and support from OP RDE, MEYS, Czech Republic under the project CRREAT, CZ.02.1.01/0.0/0.0/15_003/0000481.

References

1. Baker DN, Blake JB (2013) SAMPEX: a long-serving radiation belt sentinel. Dynamics of the Earth's radiation belts and inner magnetosphere. *Geophys Monogr Ser*:21–40. doi:[10.1029/2012gm001368](https://doi.org/10.1029/2012gm001368)
2. Shao X, Papadopoulos K, Sharma AS (2009) Control of the energetic proton flux in the inner radiation belt by artificial means. *J Geophys Res-Space*. doi:[10.1029/2009ja014066](https://doi.org/10.1029/2009ja014066)
3. Štěpánek P, Douša J, Filler V (2013) SPOT-5 DORIS oscillator instability due to South Atlantic Anomaly: mapping the effect and application of data corrective model. *Adv Space Res* 52:1355–1365. doi:[10.1016/j.asr.2013.07.010](https://doi.org/10.1016/j.asr.2013.07.010)
4. Koshiishi H (2014) Space radiation environment in low earth orbit during influences from solar and geomagnetic events in December 2006. *Adv Space Res* 53:233–236. doi:[10.1016/j.asr.2013.11.014](https://doi.org/10.1016/j.asr.2013.11.014)
5. Casadio S, Arino O (2011) Monitoring the South Atlantic Anomaly using ATSR instrument series. *Adv Space Res* 48:1056–1066. doi:[10.1016/j.asr.2011.05.014](https://doi.org/10.1016/j.asr.2011.05.014)
6. Vainio R, Desorgher L, Heynderickx D et al (2009) Dynamics of the Earth's particle radiation environment. *Space Sci Rev* 147:187–231. doi:[10.1007/s11214-009-9496-7](https://doi.org/10.1007/s11214-009-9496-7)
7. Johnson-Freese J (2007) Space as a strategic asset. Columbia University Press, New York
8. Gusrizal (2015) The Development of LEO—NEqO trapped particles forecasting system. Universiti Kebangsaan Malaysia, Thesis
9. Banerjee S, Carlin BP, Gelfand AE (2015) Hierarchical modeling and analysis for spatial data. CRC Press, Taylor & Francis Group, Boca Raton
10. Cressie N (2015) Statistics for spatial data, revised edition. Wiley, Hoboken
11. Heynderickx D, Quaghebeur B, Wera J, et al (2004) New radiation environment and effects models in the European Space Agency's Space Environment Information System (SPENVIS). *Space Weather*. doi:[10.1029/2004sw000073](https://doi.org/10.1029/2004sw000073)
12. Yando K, Millan RM, Green JC, Evans DS (2011) A Monte Carlo simulation of the NOAA POES medium energy proton and electron detector instrument. *J Geophys Res-Space*. doi:[10.1029/2011ja016671](https://doi.org/10.1029/2011ja016671)
13. O'brien TP (2009) SEAES-GEO: a spacecraft environmental anomalies expert system for geosynchronous orbit. *Space Weather*. doi:[10.1029/2009sw000473](https://doi.org/10.1029/2009sw000473)
14. Bakar KS, Sahu SK (2015) spTimer: spatio-temporal Bayesian modeling using R. *J Stat Softw*. doi:[10.18637/jss.v063.i15](https://doi.org/10.18637/jss.v063.i15)
15. Nychka D, Furrer R, Paige J, Sain S (2015) Fields: tools for spatial data. doi:[10.5065/D6W957CT](https://doi.org/10.5065/D6W957CT)
16. Suparta W, Gusrizal (2014) The application of a hierarchical Bayesian spatiotemporal model for forecasting the SAA trapped particle flux distribution. *J Earth Syst Sci* 123:1287–1294. doi:[10.1007/s12040-014-0459-3](https://doi.org/10.1007/s12040-014-0459-3)
17. Suparta W, Gusrizal, Kudela K, Isa Z (2016) A hierarchical Bayesian spatio-temporal model to forecast trapped particle fluxes over the SAA region. *Terr Atmos Ocean Sci*. doi:[10.3319/TAO.2016.02.25.01\(AA\)](https://doi.org/10.3319/TAO.2016.02.25.01(AA))
18. Bakar KS (2012) Bayesian analysis of daily maximum ozone levels. Dissertation, University of Southampton
19. Kuznetsov NV, Nikolaeva NI, Panasyuk MI (2010) Variation of the trapped proton flux in the inner radiation belt of the earth as a function of solar activity. *Cosm Res* 48:80–85. doi:[10.1134/s0010952510010065](https://doi.org/10.1134/s0010952510010065)
20. Qin M, Zhang X, Ni B et al (2014) Solar cycle variations of trapped proton flux in the inner radiation belt. *J Geophys Res-Space* 119:9658–9669. doi:[10.1002/2014ja020300](https://doi.org/10.1002/2014ja020300)
21. Zou H, Zong QG, Parks GK et al (2011) Response of high-energy protons of the inner radiation belt to large magnetic storms. *J Geophys Res-Space*. doi:[10.1029/2011ja016733](https://doi.org/10.1029/2011ja016733)
22. Evans D, Garrett H, Jun I et al (2008) Long-term observations of the trapped high-energy proton population ($L < 4$) by the NOAA Polar Orbiting Environmental Satellites (POES). *Adv Space Res* 41:1261–1268. doi:[10.1016/j.asr.2007.11.028](https://doi.org/10.1016/j.asr.2007.11.028)

Space Weather Monitoring System Competition for Secondary School Students in Malaysia

Mardina Abdullah, Rosadah Abd Majid, Badariah Bais,
Nor Syaidah Bahri and Mohd Hezri Mokhtar

Abstract Competition is one of the best and most popular tools in the educational process. Through competition, new talent emerges in specific areas. This research focuses on secondary school students' interest in space weather monitoring systems during and after their involvement in this competition. The objective of the research was to highlight the competition process. The competition was held in Malaysia and was open to all form 4 and form 5 secondary school students between the ages of 16 and 17. Each school was represented by one team and each team was comprised of four students guided by science teachers acting as mentors in a competition based on a module developed by researchers from Universiti Kebangsaan Malaysia (UKM). Each team was required to build and design a VLF antenna, assemble the electronic components on the PCB to build the preamplifier and then analyze the data that they received. They had to create graphs and identify peaks indicating solar flares. Their findings were compared to GOES satellite data for verification. They were also required to prepare and upload their progress and final technical

M. Abdullah · N.S. Bahri (✉)
Space Science Centre, Institute of Climate Change,
Universiti Kebangsaan Malaysia (UKM), 43600 Bangi, Selangor, Malaysia
e-mail: syaidah12@yahoo.com

M. Abdullah
e-mail: mardina@ukm.edu.my

R. Abd Majid
Department of Education and Community Wellbeing, Faculty of Education,
Universiti Kebangsaan Malaysia (UKM), 43600 Bangi, Selangor, Malaysia
e-mail: rosadah@ukm.edu.my

M. Abdullah · B. Bais
Department of Electrical, Electronic and Systems Engineering,
Faculty of Engineering and Built Environment,
Universiti Kebangsaan Malaysia (UKM),
43600 Bangi, Selangor, Malaysia
e-mail: badariah@ukm.edu.my

M.H. Mokhtar
Faculty of Engineering Technology, Universiti Tun Hussein Onn Malaysia,
86400 Parit Raja, Batu Pahat, Johor, Malaysia

reports to be evaluated by a panel of judges. As stated in Vision 2020, this competition will hopefully cultivate interest amongst future scientists in the country especially the younger generation. This project revealed that the students were able to conduct research with minimal guidance and that they enjoyed participating in the competition.

1 Introduction

Space weather is a multidisciplinary field that includes fundamental science activities such as forecasting, observation, application and monitoring activities. Space weather has a daily impact to human life on Earth and large variety of domains of human's activities. The incident of energetic particles can poses threat to aircraft crew and passengers [1]. In the twenty-first century, most of the world's developed countries depend on space weather operations for navigation, communications, scientific observation, treaty monitoring, weather forecasting, and other activities [2]. The magnetic storms and the bursts of radiation in severe space weather events caused by the Sun's coronal mass ejections (CMEs) may impact the safety of astronauts, affect satellite operations and result in power outages on Earth [3]. The World Meteorological Organisation (WMO) defined space weather as "the interaction of Earth with the physical and phenomenological state of the natural space environment including the Sun, the solar wind, the magnetosphere, the ionosphere and the thermosphere". Through observation, monitoring, understanding the driving processes, analysis and modelling and prediction of the state of the Sun, the associated discipline aims to forecast the potential impacts of these disturbances on ground-based and space-based infrastructure, human life and health [4].

A solar flare is a rapid and sudden intense variation in brightness that occurs when the magnetic energy that has been built up is suddenly released in the solar atmosphere. Sudden Ionospheric Disturbances (SIDs) "occur in association with solar flares and have very strong and relatively long-lasting effects on the ionosphere to knock out satellites and network communications. Earth's dayside ionosphere responds quickly and dramatically (2.5 min $1/e$ rise time) to the X-ray and EUV input by an abrupt increase in total electron content" [5]. In Malaysia, awareness of space weather was realized with the establishment of the Planetarium Division, Department of the Prime Minister in 1989 and continued with the establishment of the National Space Agency in 2002. Space weather has become an increasingly important research area in space science in recent years, with studies on the effects of the sun on the environment of the earth, satellites, and communication systems, etc. Space science research has been conducted at the Faculty of Engineering, Universiti Kebangsaan Malaysia (UKM) since 1999 [6].

The Sudden Ionospheric Disturbance (SID) Space Weather Monitoring program is an educational project aimed at building and distributing inexpensive ionospheric monitoring to students around the world. The program was introduced by the Stanford SOLAR Centre of Stanford University. A low-cost sensitive space weather

monitor named as SuperSID for SID detection via VLF remote sensing was developed by Stanford University Solar Center [6]. This project takes place in conjunction with International Space Weather Initiatives (ISWI) and developing countries worldwide. Signal processing is done via soundcard instead of datalogger as in conventional SID-VLF [6]. However, there is no record of deployment of SuperSID in Malaysia and its effectiveness still needs to be determined. The purpose of the experiment was to build a VLF receiver system, known as UKM-SuperSID, in UKM for SID detection and develop and determine the effectiveness of a teaching kit for a SuperSID Introductory Project to secondary school students in Malaysia. UKM-SuperSID was installed at UKM, Malaysia (3.13°N, 101.7°E). The receiver was tuned to receive the 19.8 kHz VLF signal from a transmitter station at North West Cape (NWC), Australia (21.8°S, 114.2°E).

UKM researchers started the SID Introductory project in 2012 to generate publicity and early space weather education to high school students. In 2013, the National Space Agency took the opportunity to raise awareness among the public by organizing the space weather competition among secondary school students together with the Space Science Centre, Institute of Climate Change, UKM with support from the Ministry of Education. The competition was initiated due to the participation of Malaysia in the International Space Weather Initiative (ISWI) in 2010 where the country's National Space Agency was one of the committee members. The initiative was a program of international cooperation to advance space weather science and communicate results to the public and students through a combination of instrument deployment, and analysis and interpretation of space weather data from the deployed instruments in conjunction with space data [7].

In Malaysia, awareness of space science among school students is relatively low. Through this project, students could expect to gain knowledge about space science, particularly space weather monitoring by conducting experiments related to solar activities such as solar flares. The purpose of this project was to raise awareness of and enhance science education through the study of space weather and to increase the number of schools involved in using the SID receiver. The study was carried out by observing VLF data to detect the presence of solar flares. A teaching module and observation equipment were constructed and provided to students. In the project, UKM researchers were able to share research findings with the community, especially students, and encourage their involvement in the field of space science and support the government's efforts in promoting space science education.

2 School Community Project

The main goals of education are to improve students' ability and thinking skills for a better life in the future. Science education represents the gateway to a world of creativity, innovations and discoveries. In Malaysia, the "Ministry of education (MOE) is striving to emphasize the learning of science because the future of the world rests upon new breakthroughs and cutting-edge technologies" [8]. The MOE

is enhancing the teaching of science to entice more youths into these areas especially as schools are considered as the first phase in preparing future scientists [8]. Science education teaches meaningful concepts and allow students to realize the concepts that can be applied in their life.

Learning scientific concepts during primary and secondary school is important for students in order to help them to construct new knowledge. In science especially, it is critical that students get the opportunity to engage in innovation and creativity. By its very nature, science is a discipline of questioning, experimenting and thinking outside the box. Being able to engage in inquiry, innovation and creativity within the science classroom in particular is important for students' learning. Students learn best by doing practical activities. Students will be able to remember better if they have done related activities. Educating more students about space science and technology through experience and entertaining students outside of ordinary schools is a good method to secure the workforce for future space development and to get public support for sustainable national space programs [9].

In 2012, UKM researchers succeeded in building the VLF receiver system known as UKM-SID. The UKM-SID system, which includes a teaching module, was developed for the SID Introductory Project aimed at promoting awareness and a better understanding of space weather among high school students in Malaysia, in addition to cultivating students' interest in research through hands-on activities and usage of the UKM-SID ionospheric monitor. The UKM-SID teaching kit was introduced as a pilot project to four schools in Selangor and Cyberjaya. Several meetings and workshops were conducted in order to brief the students and teachers about the UKM-SID system. Students were required to build the UKM-SID system according to the specified schedule. They were aided by UKM postgraduate and undergraduate students actively involved in space science research [9].

Through the antenna development, students' critical thinking, ability to work in a team and other skills were enhanced. They were also required to record their activities in a log book, complete their assignments and present their work. These activities will strengthen their communication skills. As for data analysis, students utilized various software programs which will keep them abreast of current developments in information technology. In addition, the students were also required to search for information in order to complete the task given. These activities will harness the students' self-learning skills and enhance their knowledge of space science.

3 Space Weather Competition

Competition is one of the best ways to provide motivation for students to learn new knowledge, information or strengthen previous learned material. Through competition, students can compete with their peers from the same school or other schools. Usually, this type of motivation is difficult to provide in a normal classroom. Competition can also provide a starting point for students' enjoyment of learning

science [10]. This is extrinsic motivation and intrinsic discovery for students. Competition can teach students how to succeed and how to accept failure. Students learn how to face failure and behave like mature people and how to continue improving their skills, knowledge and performance in the future. This is one of the most important aspects for students in learning how to cope with their emotions and to develop their self-esteem—things that cannot easily be provided in normal classrooms [11].

Competitive activities can be a powerful tool for boosting confidence, developing high-level technical competence and encouraging self-reliance. Competitions can also inspire younger learners to emulate the learning they see at higher levels. They watch and practise in order to try to reach the same standard. Students learn how to set goals, learn the rules of the game, develop skills, develop their problem-solving abilities, develop competence in an area, handle loss, enhance their popularity, learn about their strengths and weaknesses and how to work in a group [12]. Thus, in this space weather competition, practical work or hands-on activities are included, not only to spark the students' interest in science but also to engage them in the learning process through active participation.

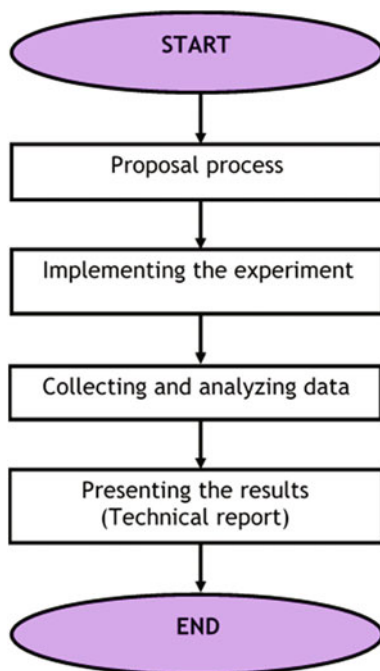
The space weather competition is also known as a Science Research Based Competition (SRBC). The competition involved both non-academic and out-of-classroom activities. The competition aimed to identify remarkable young talent and foster school students' willingness challenge themselves through science research. These competitions promote knowledge of new and improved products, innovation, ideas, investigations or experiments and their findings. Research shows that participation in science competitions helps students to become aware of their potential and contributes to their self-confidence [12]. The process of space weather competitions is described in Fig. 1.

The competition was open to all Malaysian students between the ages of 16 (in form four) and 17 (in form five). Further information about the competition can be found on the National Space Science Centre website, www.angkasa.gov.my. A total number of 152 students from 38 schools in urban and rural areas participated in the competition. The objective of the competition was to enhance innovative thinking, creativity, and investigative ability amongst the school students towards space science research. Students were involved in a four-month-long research project following scientific methodology. Students conducted this project in groups of four students under the supervision of a teacher. In addition, students could directly ask and discuss with their mentor from UKM. In these small groups, students were encouraged to take responsibility for their own learning and the development of the project that they were going to compete with.

3.1 Antenna Development

VLF signals are transmitted around the world and accessed through a wire loop antenna after being reflected by the ionosphere. The antenna consists of a wire loop

Fig. 1 The process of the space weather monitoring system competition



of various shapes and sizes. The shape can be rectangular, square, circle, and hexagonal, etc. The VLF reception is better when the antenna is larger [6, 13]. The loop antenna needs to be designed and built according to the specification provided to the student. In the competition, students were required to construct a wire loop antenna for the VLF system. However, students were allowed to shape the loop antenna without necessarily constructing or assembling it as shown in the module provided to them. Figure 2 shows students making the VLF loop antenna to pick-up the VLF signal from various VLF transmitter stations. Figure 3 shows another type of loop antenna. This antenna is 1m x 1m square shape with 29 turns.

3.2 *Preamplifier Assembly*

The students were required to assemble the electronic components on the PCB and build the preamplifier. The preamplifier is used to amplify the VLF signal as the signal received from the antenna is typically very low in amplitude (0.1 mV). The preamplifier amplifies the signal a thousand times so that it can be detected by the sound card. A simplified PCB on a single layout was designed to suit manual assembly [6, 13]. The single layout PCB was preferred for this competition because



Fig. 2 Students making the VLF loop antenna

Fig. 3 Loop antenna



it is easier for the students to assemble than the double layer PCB developed by Stanford University. A program running on a personal computer (PC) tracked the VLF transmission signal strength and processed the data. Students knew there was a



Fig. 4 Student soldering the preamplifier

solar flare on the Sun when the reflected radio signals were strongly influenced by the Sun's radiation and from plots of the signal strengths over time [7]. Figure 4 shows a student soldering the preamplifier.

3.3 Software Installation, System Testing and Data Collection

After the antenna and preamplifier construction, the students needed to install software and test the VLF system. The participating students would have already learned basic electronics during their third year in secondary school. This will have served as an advantage when building the VLF system. The software and instrument testing were fully explained in the module provided to the students. The third segment is the datalogger, which consists of a computer with a sound card and configured software. The sound card recommended was a High Definition audio card with a minimum sampling rate of 96 kHz. The installed software processed the VLF signal and plotted the output signal [6, 13]. Students needed to run this process carefully to ensure that the SID system was fully functioning. Students were instructed to collect continuous data in order to monitor the occurrence of solar flares.

3.4 *Collecting and Analyzing Data*

Upon completion of the construction of the VLF system, the students analyzed the data. Students had to detect diurnal variation by plotting the data in local time. They were also required to make a comparison between Geostationary Operational Environmental Satellite (GOES) data—which were available online—with the data they had obtained [7]. This process is important in validating the system and its capability to detect solar flares and SID events. Figure 5 shows students testing the VLF system and observing their results on the monitor.

3.5 *Presenting the Results*

One of the most important aspects of research is sharing what has been learnt. When students share their research findings they are contributing to the scientific process by adding information to a larger body of knowledge about a given topic. The competition gave students the opportunity to learn how to write and format a good research report. The students were also required to share their findings with others through oral presentations. Figure 6 shows students presenting their project.



Fig. 5 Students testing the VLF system and observing their results on the monitor

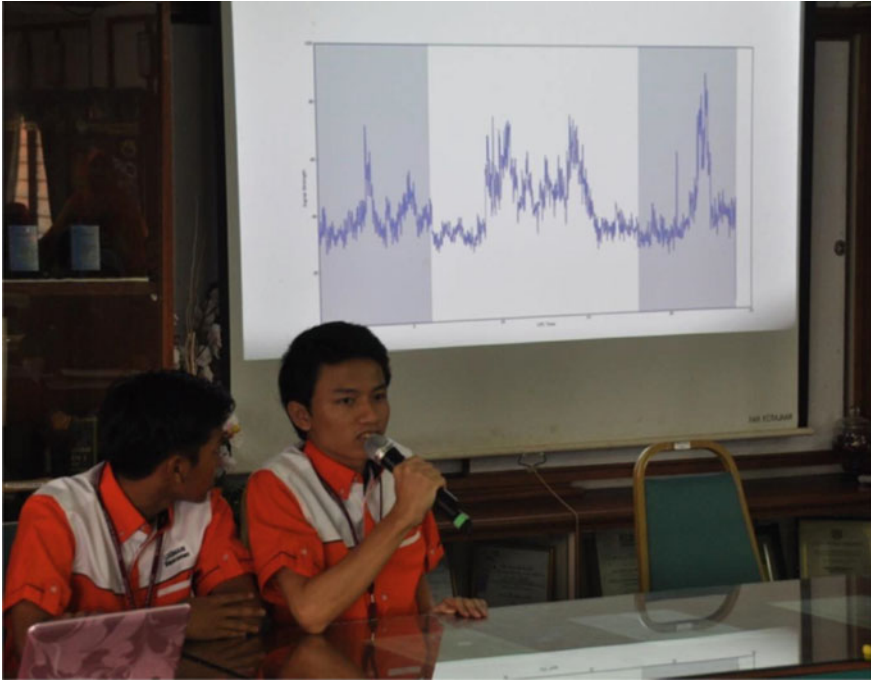


Fig. 6 Students presenting their project

4 Discussion

Informal education plays an important role in the education system especially in science-related subjects. Through informal education, students are given the opportunity to learn science through hands-on activities. Through the antenna development, preamplifier assembly and data processing, students' technical skills, critical thinking and ability to work in team are enhanced. This competition shows that students were very interested to learn science, and especially keen to learn about space weather. Students actively and confidently voiced their opinions, arguments and reasoning on space weather issues. As for the data analysis, students utilized various software programs which will keep them abreast of the future developments in information technology. In addition, the students were also required to search for information in order to complete the given task. These activities harness the students' self-learning skills and enhance their knowledge of space science [6, 9].

In addition, working as a team in this competition increased students' confidence and improved their communication skills. Students were able to exchange ideas and discuss their science ventures openly and confidently. The cooperation they showed was regarded as helpful in lessening the pressure they faced and in building their

confidence to proceed further, and this was regarded as pleasing. Students cannot understand scientific practices, nor fully appreciate the nature of scientific knowledge itself, without directly experiencing those practices for themselves.

5 Conclusions

This competition gave an opportunity to students to enhance their knowledge and skills in space science education and especially in space weather research. The competition also helped to raise students' awareness of research culture and develop their basic research skills and provided them with opportunity to gain experience in problem-solving projects. Through this competition, students were able to work independently, develop their scientific enquiry skills in order to understand and start applying research methods and consider the idea of research in the space science field as a future career. Students were also able to communicate with other school pupils beyond the classroom on a nationwide basis. The hands-on experience which they have had gone through via this competition will enhance their confidence level and reinforce positive feelings about their science ability. Overall, this competition stimulated students' interests and should positively influence their academic achievement, as well as expand their sense of future science career options.

Acknowledgements The authors would like to express an appreciation to the teachers and students of Malaysia for their participation in this project. We also would like to thank the Ministry of Education Malaysia, National Space Agency Malaysia, Stanford Solar Center and Society of Amateur Radio Astronomers of Stanford University for their support. Special thanks to Prof. Deborah Scherrer for her kind support. The project was funded by UKM's internal grant (Komuniti-2012-016) and the Ministry of Science, Technology and Innovation (MOSTI) grant (KK 2013-008).

References

1. Suparta W, Abdul Rashid ZA, Mohd Ali MA, Yatim B, Fraser GJ (2008) Observation of Antarctic precipitable water vapor and its response to the solar activity based on GPS sensing. *J Atmos Sol-Terr Phys* 70:1419–1447
2. Vanlommel P, Messerotti M, Liliensten J, Calders S, Bonte K, D'Huys E, Z'igman V (2014) Exploitation, dissemination, education and outreach in the frame of the COST action ES0803 developing space weather products and services in Europe. *J Space Weather Space Clim* 4 (A05). doi:[10.1051/swsc/2014002](https://doi.org/10.1051/swsc/2014002)
3. Dusenbery PB, Harold JB, McLain B, Curtis L (2008) Space weather outreach: an informal education perspective. *Adv Space Res* 42:1837–1843
4. Carlowicz M, Lopez R (2002) Storms from the sun: the emerging science of space weather. Joseph Henry Press, Washington DC
5. Plainaki C, Liliensten J, Radioti A, Andriopoulou M, Anna Milillo A, Nordheim TA, Dandouras I, Coustenis A, Grassi D, Mangano V, Massetti S, Orsini S, Lucchetti A (2016)

- Planetary space weather: scientific aspects and future perspectives. *J. Space Weather Space Clim* 6:A31
6. Abdullah M, Bais B, Hasbi AM, Abd Majid R, Yatim B, Mohd Ali MA, Bahari SA, Mat Daud N, Mokhtar MH, Mohd Zain AF, Asillam MF (2012) Development of UKM-SID teaching module for space science education. In: *Proceedings of international forum on engineering education 2012*, pp 1–5
 7. Scherrer D, Mitchell R, Huynh T, Lord W, Lord M (2009) *SuperSID users manual*; Stanford Solar Center, Stanford University
 8. Curriculum Development Centre (2005) *Integrated curriculum for secondary schools: curriculum specifications biology form 4*. Ministry of Education, Putrajaya
 9. Abdullah M, Hasbi AM, Bais B (2014) Space weather innovation competition. *ISWI Newsletter* 6:035
 10. Kuech R, Sanford R (2014) Academic competitions: perceptions of learning benefits from a science bowl competition. *Eur Sci J* 1:388–394
 11. Ozturk AM, Debelak C (2008) Affective benefits from academic competitions for middle school gifted students. *Gift Child Today* 31:48–53
 12. Blankenburg JS, Hoffler TN, Peters H, Parchman I (2016) The effectiveness of a project day to introduce sixth grade students to science competitions. *Res Sci Technol Edu* 34:342–358
 13. Wong PW, Abdullah M, Hasbi AM, Bahari SA (2012) Development of a VLF receiver system for sudden ionospheric disturbances (SID) detection. In: *Proceeding of IEEE Asia-Pacific conference on applied electromagnetics*, pp 98–103

Current Status of Radio Astronomy in University of Malaya

Zamri Zainal Abidin and Zainol Abidin Ibrahim

Abstract Radio Astronomy is an important branch of multi-wavelength astronomy and is essential in any investigations of celestial objects including our own Sun. In University of Malaya, this research field has been taken to the forefront of astronomical research by the Radio Cosmology Research Lab, which was established in 2005 by the two authors of this review paper. Scientific research topics include dark matter, evolution of galaxy clusters and galaxies, star formation law, pulsars and molecular clouds. The technical side of the research involves radio frequency interference, receiver testing and international interferometer network testing investigations. Other research areas include space weather especially the study of solar radio bursts, as well as its relationship to seismic activity. An important landmark in this research is the completion of the construction of the UPSI-UM Radio Telescope for observation of galaxy clusters and also the Half-Wave Dipole Antenna for the monitoring of solar radio bursts, both in 2016. A brief report on future plans will also be included in this review.

1 Introduction

In 1928, a Physics graduate, Karl Jansky, was employed as an engineer at the telecommunication company Bell Laboratories in the United States of America. While undertaking a direct communication testing across the Atlantic Ocean, the testing that he was involved in experienced a low level interference at an unknown frequency. Although they eventually discarded it as insignificant to their project, Jansky went further and requested to build a radio telescope to investigate it further. His request was swiftly rejected. Eight years later, a part-time amateur radio astronomer, Grote Reber, finally built such a telescope. He looked deeper into what Jansky discovered and, more significantly, he managed to prove that the low level

Z.Z. Abidin (✉) · Z.A. Ibrahim
Radio Cosmology Research Lab, Physics Department, University of Malaya,
50603 Kuala Lumpur, Malaysia
e-mail: zzaa@um.edu.my

signal actually originated from the centre of the Milky Way. This is a very important milestone in the history of radio astronomy research as it proved that there is another branch of astronomy besides the more conventional optical astronomy. Although there are other wavelengths of astronomy such as infrared and ultraviolet, radio astronomy is the only alternative to optical astronomy in terms of its capability of making observations from the ground level.

Due to the fact that radio astronomy is able to observe celestial objects at unique frequencies and is also able to collect signals from the furthest objects in the universe, it has been used in much scientific research ever since. Another huge advantage of radio astronomy is its direct application in telecommunication technology due to the direct similarities of their instruments, as was demonstrated by Jansky's early discovery. Radio astronomy has also been used in space weather study particularly as antennas can be constructed at radio wavelengths in order to study solar radio activity.

The application of the interferometer technique in radio astronomy has also introduced a mechanism in extending borders between countries in terms of research and scientific collaborations. Such networks of interferometers have already been involved in astrophysics discoveries as proven by the success of the Very Long Baseline Interferometer (VLBI). This technique is also useful for the study of geodesy and astrometry.

Radio astronomy is a fast-emerging research field in Malaysia, especially following the establishment of the Radio Cosmology Laboratory at the University of Malaya in 2005 by both authors of this review work. This coincided with the graduation of the author ZZA's doctorate from the Jodrell Bank Centre of Astrophysics in the UK in his the field of radio astronomy, specializing in cosmic microwave background polarization.

2 Radio Astronomy in the University

2.1 Focus on Teaching

In general, radio astronomy in Malaysia involves education, research and promotional activities. Formal radio astronomy education is only offered at postgraduate level at universities with the University of Malaya heading the number of current and graduate students. However, a few other universities in Malaysia have also included basic radio astronomy topics in their teaching syllabus.

In the University of Malaya, this research field is introduced to the undergraduate students within the Bachelor of Science (physics) course under the two elective courses namely "Astrophysics" and "Cosmology and Relativity". But more significantly, undergraduate students can select this research topic as their field of study for their final year project. Up until the time of writing, forty-six students have made this choice.

Among the topics that these students have chosen from are radio waves from Jupiter, instrumentation for Jupiter radio observation (calibrator), meteor study using radio frequency, basic interferometer technique study, radio frequency interference (RFI) analysis using the Kurtosis method, space weather study at radio wavelengths, solar radio bursts detection using CALLISTO spectrometer, basic VLBI network testing between Malaysia and Australia, Neutral Hydrogen and dark matter study in galaxy cluster A426 and radio quiet zone (RQZ) candidate identification using Geographical Information System (GIS) mapping.

The other half of the education focus of this research topic lies in the post-graduate study, namely masters and doctorates in science (physics). At the time of writing, there are eight masters and four doctorate graduates from this research field. The current postgraduate student count is seven for masters and six for doctorate.

Among the topics that these postgraduate students have chosen for their theses are RFI survey for choosing the best site for construction of a radio telescope in Malaysia, radio astronomical observations using University Malaya's Small Radio Telescope (SRT), the study of the relationship between solar bursts Type II and III and coral mass ejection (CME), the study of dark matter in galaxies and galaxy clusters, spectrum management in radio astronomy, study of neutralino and Kaluza-Klein particles as candidates for dark matter, the relationship between solar wind and the geomagnetic induced current (GIC) and the possibility of the effect of solar activity on seismicity.

2.2 Focus on Research

In terms of instrumentation there are many antennas being constructed to study the RFI in selected sites in Malaysia, including discones, log-periodic and feedhorn antennas. At the same time, low noise amplifiers (LNA) are also being built and studied.

As mentioned before, the most significant instrumentation landmark of the radio astronomy research in the University of Malaya is the construction of the UPSI-UM Radio Telescope, which is located at one of the selected sites for RQZ, namely at the Universiti Pendidikan Sultan Idris (UPSI) in Tanjung Malim, Perak. It is geographically located about 80 km to the north of Kuala Lumpur. The authors would like to thank academicians and staff from UPSI, especially Wan Zul Adli Wan Mokhtar, Dr Razak Abd Samad Yahya and Associate Professor Dr Zulkifley Mohamed for their support in this project from the beginning. Figure 1 shows a schematic diagram of the 7.3 m UPSI-UM Radio Telescope.

The telescope is a parabolic dish with dual-shaped technology (main reflector and sub reflector). According to the technological requirements of the design, the antenna provides high gain, high efficiency, low noise, low side lobe and exceptional pattern characteristics, which fully meet the mandatory requirements of the International Telecommunication Union on the wide-angle side-lobe electrical level

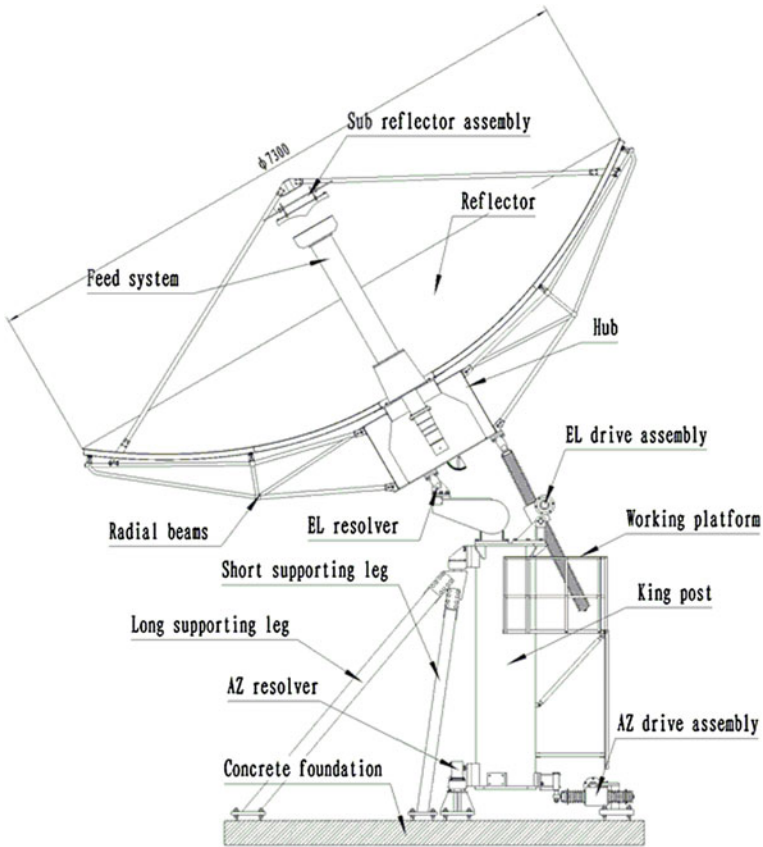


Fig. 1 Schematic diagram of the UPSI-UM Radio Telescope

and cross polarization isolation for this kind of parabolic dish antenna. Specifically, it operates at radio frequencies between 1.1 to 1.5 GHz, with a typical gain of 38.08 dBi at 1.3 GHz and VSWR of 1.3:1. Its beamwidth at -3 dB is 2.05° . The antenna noise temperature at 20° elevation is 43 K. It can resist wind speeds of between 97 and 105 km/h at its operational mode and 200 km/h when parked upwards (heavenwards).

As for the receiver, a series of technical tests done together with our collaborators from the Korean Astronomy and Space Science Institute (KASI) showed that it has a passband gain and noise temperature of approximately 81 dB and 50 K respectively. More specifically, the passband noise temperature is between 43 and 53 K at 1–2 GHz. The test summarizes that gain stability, input/output matching, noise temperature and flatness characteristics are all good. The authors would like to thank Professor Dr Young-Chol Minh, Dr Do-Heung Je and Dr Bong Won-Sohn for making the tests a big success.



Fig. 2 Photo of the UPSI-UM Radio Telescope in Tanjung Malim

Figure 2 shows a photo of the actual telescope on-site. The telescope operates at L-Band and aims to study the core of galaxy clusters in order to investigate the evolution of these objects. Future upgrades for the telescope to other frequencies in order to study other astrophysical properties of galaxy clusters and also galaxies are planned, pending successful research grant applications.

As a feasibility study for the scientific targets of the UPSI-UM Radio Telescope, observations were made with a similar sized and designed radio telescope at Jodrell Bank Observatory and results have shown that the science is indeed doable with this new telescope. As mentioned in introduction section, radio astronomy has an advantage of increasing observation sensitivity by applying the VLBI technique. The UPSI-UM Radio Telescope will use this technique and a future network linking Malaysia with China and Australia is in the planning. A journal article that explores the connectivity and method of data correlation via the internet was written and accepted for publication (at the time of writing of this review paper) in the Indian Journal of Physics under the title “Radio Astronomy Interferometer Network Testing for a Malaysia-China Real-Time e-VLBI”. The paper, among others, concluded that the internet connection between Malaysia and China needs improvement in terms of transfer speed and by solving the bottleneck of data flow problem.

Another radio observatory site has also been identified by the same RQZ identification study that selected the UPSI-UM Radio Telescope. This observatory is located at the University of Malaya’s Glemi Lemi Research Centre in Jelevu, Negeri Sembilan, which is about 70 km south of Kuala Lumpur. It is named the Jelevu Observatory (JbO). The site belongs to the University of Malaya’s Institute of Biological Sciences (ISB). The ISB has been heavily supporting this project including providing assistance for on-site monitoring for RFI and soil testing.

The authors would like to thank them for such great support from the moment they proposed this project. The principal individuals from the ISB that helped this project from the beginning are Professor Dr Rosli Hashim and Dato' Professor Dr Mohd Sofian Azirun. Figure 3 shows a photo of this site, which is located in a fairly remote rural area and hence it has a relatively low average radio frequency interference (RFI) level. Using a spectrum analyzer, the average noise from man-made interferences was detected as very low. The JbO site is also a naturally good site for building a radio telescope since it has the lowest annual rainfall measurement in Peninsular Malaysia and the majority of the site is protected by nearby mountains.

At the moment, JbO is used for solar radio bursts array observations. Figure 4 shows a schematic diagram and Fig. 5 shows a photo of this array. This antenna array operates at 55–65 MHz frequencies and the main aim of it is to study the frequency splitting of Type II solar bursts.

The data obtained from this array will also complement the work that the space weather team within the Radio Cosmology Lab has been doing with the spectrometers from the CALLISTO (i.e. the Compound Astronomical Low-cost Low-frequency Instrument for Spectroscopy and Transportable Spectrometers)



Fig. 3 Photo of the Jelebu Observatory (JbO) in Negeri Sembilan. Bottom left indicates the cabin site while the slightly cleared area near the top right of the picture indicates the site for a potential large radio telescope construction

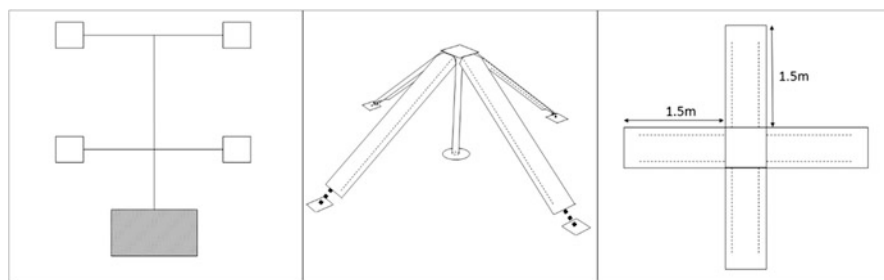


Fig. 4 Schematic diagrams of the solar bursts array. (Left) Top view of the array configuration. (Middle) side view, and (Right) top view of a single pair of antenna in the array



Fig. 5 Photo of the solar bursts array

project. Pending success of research grant proposals, a large 25 to 30 m radio telescope is planned to be built at JbO.

Having said that, it should be reiterated here that solar radio astronomy research is also one of the main aims of the Radio Cosmology Research Lab at the University of Malaya. The study of solar radio bursts will also be applied to the study of solar activity in general, especially in its relation to the solar cycles, solar wind (such as its speed and input energy), the ionosphere and magnetosphere and also seismic activity.

Both authors of this review have been actively involved in international refereed journals that publish the results of radio astronomical research. Most of the publications have already been cited in this review. A few titles of significant articles that have been published are “Investigation of radio astronomical windows between 1 MHz and 2060 MHz in Universiti Malaya” [1], “RFI profiles of prime candidate sites for the first radio astronomical telescope in Malaysia” [2], “An RFI investigation for setting up a VLBI station below 2.8 GHz in Malaysia” [3], “Optimization of an antenna array using genetic algorithms” [4], “The Nonlinear Least Square Fitting for Rotation Curve of Orion Dwarf Spiral” [5], “Redshifts Distribution in A262” [6], “Kennicutt-Schmidt Law in the Central Region of NGC 4321 as Seen by ALMA” [7] and “Study of seismic activity during the ascending and descending phases of solar activity” [8].

From a scientific research point of view, the Radio Cosmology Research Lab has been involved in studies in astrophysics and cosmology not just at radio wavelengths, but also at other frequencies for completeness. Research of radio waves coming from the sun is also a priority of radio astronomy study in the University of Malaya as proven by our work in establishing the solar radio burst array, as mentioned earlier. Another branch of radio astronomy that has been pursued is the radio spectrum protection through spectrum management study. It should be noted here that there is still not enough focus being given to protecting the radio astronomical frequency windows in Malaysia. Radio astronomers have not been heavily represented whenever radio spectrum allocation has been discussed, with radio telecommunication dominating a huge majority of the spectrum. The authors have been working closely with the Malaysian Communication and Multimedia

Commission (MCMC) and also the Malaysian Research and Education Network (MyREN) in order make sure that radio astronomers' presence is felt nationally.

As radio astronomy research is relatively new in Malaysia, the main strategy for its development includes knowledge transfer from better established researchers from abroad. Among the collaborators of the Radio Cosmology Research Lab are the Jodrell Bank Centre of Astrophysics (JBCA) in the United Kingdom, National Astronomical Research Institute of Thailand (NARIT) in Thailand, International School for Advanced Studies (SISSA) in Italy, International Centre for Radio Astronomy Research (ICRAR) and Commonwealth Scientific and Industrial Research Organisation (CSIRO), both in Australia, National Central University (NCU) in Taiwan, Auckland University of Technology (AUT) in New Zealand, National Astronomical Observatories of China (NAOC), Chinese Academy of Sciences (CAS), Yunnan Astronomical Observatory (YNAO), both in China, Korea Astronomy and Space Science Institute (KASI) in South Korea, and most recently the University of Durham in the United Kingdom.

In Malaysia, the Radio Cosmology Research Lab has formed working collaborations with Universiti Kebangsaan Malaysia (UKM), Universiti Putra Malaysia (UPM), Universiti Teknologi Malaysia (UTM), Universiti Pendidikan Sultan Idris (UPSI), Universiti Sultan Zainal Abidin (UniSZA) and Universiti Teknologi Mara (UiTM). Significantly, the University of Malaya has signed a memorandum of Agreement (MOA) with UPSI regarding radio astronomy research using the UPSI-UM Radio Telescope, which is built on their campus site in Tanjung Malim. It is also worth noting that these universities also have a few researchers in radio astronomy especially in the instrumentation side of things. Universiti Sains Malaysia (USM) has the first ever Malaysian radio astronomy doctorate graduate. The main author of this review is the second graduate in this research field. Both graduated from the University of Manchester's School of Physics and Astronomy, which is based at the Jodrell Bank Centre of Astrophysics in Cheshire, United Kingdom.

2.3 Focus on Promotion

Promotional efforts in radio astronomy have been made by the authors and also other local universities. A huge contributor to our promotional work is the effort put in by the National Space Agency or the Agensi Angkasa Negara (ANGKASA). ANGKASA has been making tremendous efforts in hosting workshops and hosting radio astronomical experts from all around the world. A few examples of the special talks that they hosted are seminars by Professor Tim O'Brien from JBCA, UK in September 2008, Professor Steven Tingay from ICRAR, Australia in March 2012, and workshop by Professor Hwang Chorng-Yuan from NCU, Taiwan in April 2013. The University Malaya has also been an accommodating host to a number of radio astronomers such as Professors Jun Lin and Min Wang from Yunnan Observatory, China in April 2014, Professor Ping Jinsong from CAS, China in

January 2014, John Morgan and Cormac Reynolds from ICRAR, Australia in April 2014 and Nur Adlyka Ainul Anuar in September 2016.

UKM has also been playing a great part in promoting not just radio astronomy, but astronomy in general by organizing the International Conference on Space Science and Communication (IconSpace) and making radio astronomy an important topic for presenters. ANGKASA and UM have also contributed in assisting radio astronomers from the Radio Cosmology Lab in obtaining previous grants such as the grants from the Ministry of Science, Technology and Innovation (MOSTI), Ministry of Higher Education, University Malaya Research Grant (UMRG) and also the High Impact Research (HIR) grant, which contributed the majority of the previous funding. It is worth highlighting the fact that the success of the HIR grant has been the catalyst of the recent great progress in research by radio astronomers in the University of Malaya.

3 Summary

Radio astronomy in Malaysia has progressed quite well since 2005 especially after the establishment of the Radio Cosmology Research Lab at the University of Malaya. It is still a long way from reaching a level comparable to that of research institutes abroad such as the radio astronomy research at Jodrell Bank Centre of Astrophysics in the United Kingdom, but the general opinion in Malaysia is that it is on the right track. A successful establishment of a VLBI network with other countries is one of the biggest future aims of the Radio Cosmology Research Laboratory at the University of Malaya. It is hoped that many cutting edge sciences can be studied through this radio astronomical technique. It is also hoped that the Radio Cosmology Research Laboratory can work together with other branches of astronomy and sciences in order to further extend its influence on knowledge gathering to benefit humankind, present and future.

Acknowledgements The authors would like to again thank all the grant providers and research collaborators mentioned in the main article. Previous and current grant providers include University of Malaya (High Impact Research Grant, University Malaya Research Grant, University Malaya Research Grant Program), the Ministry of Science Technology and Innovation of Malaysia, the Ministry of Higher Education of Malaysia. Current scientific and technical collaborators include Universiti Pendidikan Sultan Idris (UPSII), Universiti Teknologi Mara (UiTM), Universiti Kebangsaan Malaysia (UKM), Universiti Putra Malaysia (UPM), Universiti Teknologi Malaysia (UTM), Universiti Sultan Zainal Abidin (UniSZA), Universiti Sains Malaya (USM), Agensi Angkasa Negara (ANGKASA), National Astronomical Observatories of China (NAOC) of the Chinese Academy of Sciences, Yunnan Astronomical Observatories of China (YNAO), Xinjiang Astronomical Observatories of China (XAO), National Central University of Taiwan (NCU), Jodrell Bank Centre of Astrophysics of the UK (JBCA), Korean Astronomical and Space Science Institute (KASI), Auckland University of Technology of New Zealand (AUT) and Suranaree University of Technology of Thailand (SUT).

References

1. Abidin ZZ, Ibrahim ZA, Syed Adnan SBR, Anuar NK (2009) Investigation of radio astronomical windows between 1 mhz and 2060 mhz in Universiti Malaya, Malaysia. *New Astron* 14:579–583
2. Abidin ZZ, Bahari SBRS, Ibrahim ZA (2009) RFI profiles of prime candidate sites for the first radio astronomical telescope in Malaysia. *New Astron* 15:307–312
3. Abidin ZZ, Ibrahim ZA, Rosli Z, Malim FF, Anim NM, Noorazlan N (2012) An RFI investigation for setting up a VLBI station below 2.8 GHz in Malaysia. *New Astron* 17(2):61–64
4. Kiehadrouinezhad S, Noordin NK, Sali A, Abidin ZZ (2014) Optimization of an antenna array using genetic algorithms. *Astro J* 147(6):147–156
5. Hashim N, Abidin ZZ, Ibrahim UFSU, Hassan MSR, Hamidi ZS, Umar R, Ibrahim ZA (2015) The nonlinear least square fitting for rotation curve of orion dwarf spiral. *Sains Malays* 44 (3):1–16
6. Hassan MSR, Abidin ZZ, Ibrahim UFSU, Hashim N, Lee DAA (2016) Redshifts distribution in A262. *MNRAS* 458(1):264–269
7. Azeez JH, Hwang C-Y, Abidin ZZ, Ibrahim ZA (2016) Kennicutt-Schmidt law in the central region of NGC 4321 as Seen by ALMA. *Sci Rep* 6:26896
8. Sukma I, Abidin ZZ (2017) Study of seismic activity during the ascending and descending phases of solar activity. *Ind J Phys* 7:1–12

GPS PWV and Its Response to ENSO Activities in the Western Pacific Region During 2009–2011

Wayan Suparta, Ahmad Iskandar and Ford Lumban Gaol

Abstract This paper investigates the influence of El Niño Southern Oscillation (ENSO) activity through precipitable water vapor (PWV) variability to understand ENSO dynamics. PWV data over the western Pacific Ocean taken from Global Positioning System (GPS) and Radiosonde has been analyzed. An ENSO event represented by a sea surface temperature anomaly (SSTa) in the Niño 3.4 and 4 regions for the period of 2009–2011 was chosen. During this period, the PWV time series during increasing El Niño intensity were dominated by the seasonal cycle and a strong correlation found with SSTa for PIMO ($R^2 = 0.81$) and a modest correlation for TOW2 ($R^2 = 0.66$). An anticorrelation between SSTa and PWV was found at PIMO and TOW2 stations due to the fact that they are in opposite hemispheres, and a positive correlation was shown for the station near the equatorial line. This suggests that the strengthening and weakening of the trade winds moving from the central to the western Pacific Ocean during a La Niña event will bring to the surface warm water from the central to the western Pacific and cause PWV increases, and vice versa for an El Niño event.

Keywords GPS PWV · ENSO influence · Western Pacific Ocean · Physical mechanism

1 Introduction

Interaction between ocean and atmosphere in the central Pacific Ocean is correlated with the El Niño Southern Oscillation (ENSO) in the western Pacific Ocean. Bjerknes [1] highlighted the large-scale atmospheric circulation along the equatorial

W. Suparta (✉) · A. Iskandar
Space Science Centre (ANGKASA), Institute of Climate Change, Universiti Kebangsaan Malaysia, 43600 Bangi, Selangor Darul Ehsan, Malaysia
e-mail: wayan@ukm.edu.my; drwaynesparta@gmail.com

W. Suparta · F.L. Gaol
Doctor of Computer Science, Bina Nusantara University, 11530 Jakarta Barat, Indonesia

Pacific Ocean, known as the Walker Circulation. In this circulation, the wind in the upper troposphere is blown from the east to the west Pacific Ocean and returned from the west to the east. The Walker Circulation is influenced by the ENSO event, in which the wind movement will be faster from the east to the west during a La Niña phase and an opposite will occur in the El Niño phase. This causes the ENSO activity to influence the western Pacific Ocean, where one of the atmospheric components is water vapor. Water vapor plays a crucial role in developing the interactions between the atmosphere and the ocean. Water vapor derived from a Global Positioning System (GPS) in terms of precipitable water vapor (PWV) is more sensitive in detecting this interaction.

Advances in understanding of the interactions between the atmosphere and the ocean will help to mitigate the effects of ENSO activity. One of the responses of GPS water vapor variability on the La Niña event over the year 2011 was reported by Suparta et al. [2]. In their study they found that the variability of GPS PWV on the SSTa during a La Niña event shows a strong response in ASO and OND cases. For that purpose, they interpolate the meteorological data, which are not collocated with the GPS position to compute PWV data more precisely. In this interpolation, a weighted mean temperature (T_m) proposed by Bevis et al. [3] was employed to estimate PWV. The results obtained during the 2011 between GPS PWV and PWV taken from Radiosonde were then compared. In line with the above findings, this paper aims to investigate the dynamic features of GPS PWV associated with ENSO activity, including El Niño and La Niña events. To obtain the GPS PWV in the western Pacific region to the ENSO response more accurately, the T_m model of more than 15 selected radiosonde stations has been developed [4].

2 Methodology

2.1 Data and Location

In this study of PWV variability in the western Pacific region over the latitude range of 20°N to 20°S and longitude 95°E to 156°E, PWV data were retrieved from GPS and surface meteorological data. The GPS data was collected from Universiti Malaysia Sabah Kota Kinabalu (UMSK) in Malaysia, Nanyang Technological University of Singapore (NTUS) in Singapore, Philippines Islands Manila Observatory (PIMO) in Philippines, Bakosurtanal (BAKO) in Indonesia and Townsville (TOW2) in Australia. Due to limited data access, three years of data (2009–2011) were processed for the case study.

The main base of data used in this study was from UMSK station. The GPS receiving system at UMSK consisted of a Trimble NetR8, dual-frequency with a Zephyr Geodetic 2 antenna and a PC for data logging. The GPS data is recorded in the Receiver Independent Exchange (RINEX) format with a resolution of 30-seconds. The surface meteorological system used was the MET4A sensors

produced by Paroscientific, Inc. (USA). The sensor has to precisely measure the surface pressure (in bars), air temperature (in degrees Celsius) and relative humidity (in percent). The resolution of surface meteorological data is set at 4 s. The measurement system is located in the School of Science and Technology Universiti Malaysia Sabah building, Kota Kinabalu (6.03°N, 116.12°E and 63.49 m altitude). The location of the GPS and RS stations is shown in Fig. 1a together with diagram of GPS PWV measurements at UMSK in Fig. 1b.

GPS data for another station was obtained from the Scripps Orbit Permanent Array Center (SOPAC) website (<http://sopac.ucsd.edu/>). For the surface meteorological data, three stations (BAKO, PIMO and TOW2) were obtained from the Weather Underground website (<http://www.wunderground.com>). PWV data from Radiosonde measurement (RS PWV) to compare with the PWV from GPS was also collected. The RS PWV data were taken from WBKK (Malaysia), WSSS

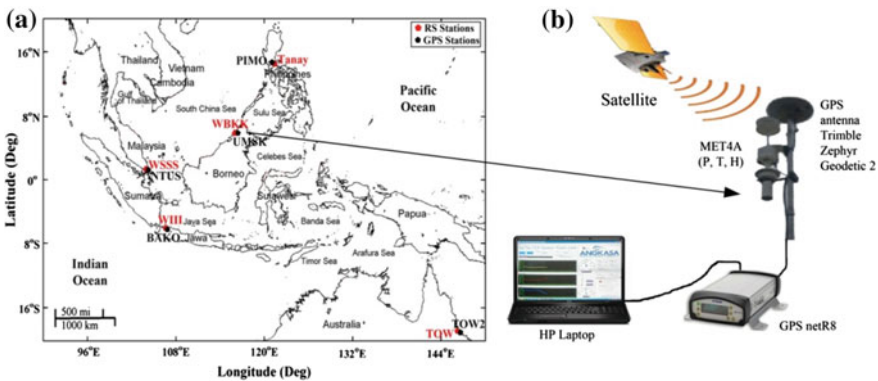


Fig. 1 (a) Location of the GPS and radiosonde stations and (b) GPS PWV measurement system at UMSK station

Table 1 Geographical coordinates of the surface meteorological and radiosonde stations

Station (Country)	Latitude (Degree)	Longitude (Degree)	Height (m)	Resolution
UMSK (M)/WBKK (R) (Malaysia)	6.03 N/5.93 N	116.12E/116.05E	63/3	1-min
NTUS (M)/WSSS (R) (Singapore)	1.35 N/1.36 N	103.68E/103.98E	75/16	1-min
Manila (M)/TANAY (R) (Philippines)	14.50 N/14.56 N	121.00E/121.36E	21/614	1-h
Soekarno-Hatta (M)/WIII (R) (Indonesia)	6.10S/6.11S	106.70E/106.65E	8/8	30-min
Townsville (M)/TOW(R) (Australia)	19.20S/19.25S	146.80E/146.76E	6/9	30-min

^aM and R stand for meteorology and radiosonde stations respectively

(Singapore), TANAY (Philippines), WIII (Indonesia) and TOW (Australia). The RS PWV data were taken from the University of Wyoming (<http://weather.uwyo.edu>), which recorded twice a day or every 12 h (00:00 UT and 12:00 UT). Table 1 shows the geographical coordinates of the surface meteorological and Radiosonde stations used in this study together with the surface meteorological data resolution. In the analysis, SSTa indices from Niño 3.4 and Niño 4 regions to correlate the ENSO activities with GPS PWV were employed. The Niño 3.4 region is located in the latitude range of 5°N to 5°S and longitude range of 170°W to 120°W, while the Niño 4 region is in the range 5°N to 5°S, and 160°E to 150°W. SSTa data from the Oceanic Niño Index (ONI) were obtained from the Climate Prediction Center National Oceanic and Atmospheric Administration (CPC NOAA) (<http://www.cpc.ncep.noaa.gov/data/indices/>) with a weekly temporal resolution.

2.2 Data Processing

The GPS data consists of observation and navigation data. The observation data is information that can be used to reconstruct the GPS observations. Navigation data consists of a satellite's orbit information. Both data were stored in the GPS receiver in a Receiver Independent Exchange Format (RINEX) format. The quality of the GPS data is checked by Translation/Editing/Quality Checking (TEQC) software that was developed by UNAVCO, Inc. (<http://www.unavco.org/>). Then, the GPS data are converted from RINEX to ASCII or MAT files using a MATLAB code for easier processing.

To obtain accurate values of PWV, the position between the GPS receiver and the meteorological sensors should be collocated. This is due to the altitude of surface meteorology having an impact on the quantity of the atmospheric parameters, such as the surface temperature gradual decreasing with increasing of altitude [5]. Since the meteorological station is not collocated with the GPS stations (BAKO, PIMO and TOW2), the interpolation method proposed by Klein Balting et al. [6] to obtain accurate surface meteorological data (pressure— P , temperature— T , and relative humidity— H) at the GPS position was employed.

The next step is the computation of PWV, including GPS and meteorological data. The Zenith Tropospheric Delay (ZTD) based on the Modified Hopfield model [7, 8] was computed first. The second step is to compute the Zenith Hydrostatic Delay (ZHD) which is done using the Saastamoinen model [9]. The third step is to compute the Zenith Wet Delay (ZWD) by separating the ZTD from the ZHD. Then, the ZWD is converted into PWV using the Eq. (1) as proposed by Bevis et al. [3].

$$PWV = \pi(T_m)ZWD \quad (1)$$

where $\pi(T_m)$ is a dimensionless parameter and conversion factor that varies with local climate (e.g. geography, season and weather) and depends on the T_m and is given by

$$\pi(T_m) = \left[\rho_{lw} R_v \left(\frac{k_3}{T_m} + k_2' \right) \right]^{-1} 10^6 \quad (2)$$

where ρ_{lw} is the liquid water density in kg m^{-3} , R_v is the universal dry gas constant in $\text{J Kg}^{-1}\text{K}^{-1}$, k_2' and k_3 are the refraction constants that were computed by Bevis et al. [3]. The T_m equation for the western Pacific region has been obtained by Suparta and Iskandar [4] as in Eq. (3).

$$T_m = 0.83663T_s + 48.103 \quad (3)$$

where T_s is the surface temperature in Kelvin.

Correlation analysis through a coefficient of determination (R^2) is employed to study the response between SSTa and PWV. For that purpose, all of these parameters were processed and analyzed on a weekly basis. A set of Matlab code, the so-called tropospheric water vapor program (*TroWav*) as developed by Suparta [10] was employed.

3 Results and Discussion

3.1 PWV Results

Figure 2 shows the weekly variability of PWV from 2009 to 2011 at five selected GPS and RS stations in the West Pacific. The PWV variations at each station showed a different pattern. The stations located in the south (BAKO and TOW2) has the opposite PWV pattern compared to those in the north (NTUS, UMSK and PIMO). The PWV at NTUS and PIMO shows a similar pattern, where the maximum was from June to August and the minimum was from December to April. This is in contrast to BAKO and TOW2 stations, where the maximum PWV occurred from December to March and the minimum from June to August. Compared to the pattern of GPS PWV, RS PWV shows a similar variation, but the average value is 8 mm higher than the GPS PWV, except for PIMO and TANAY stations.

The PWV for TOW2 station has a greater variation, with a difference between the maximum and minimum of about 29.70 mm with a standard deviation (STD) of 7.65 mm. In contrast, the NTUS station has the lowest variation with a difference between the maximum and the minimum PWV is 10.18 mm with a STD of 1.89 mm. The minimum value for TOW2 is 16.51 mm and the maximum of 53.12 mm was for PIMO. The RS PWV at TOW shows a higher variation compared to other stations, where TOW2 and TOW (Australia) are the stations located nearest the sea, which is the main source of evaporation. In addition to the different values obtained of GPS and RS, altitude is one of the important factors that affected the amount of PWV in the atmosphere.

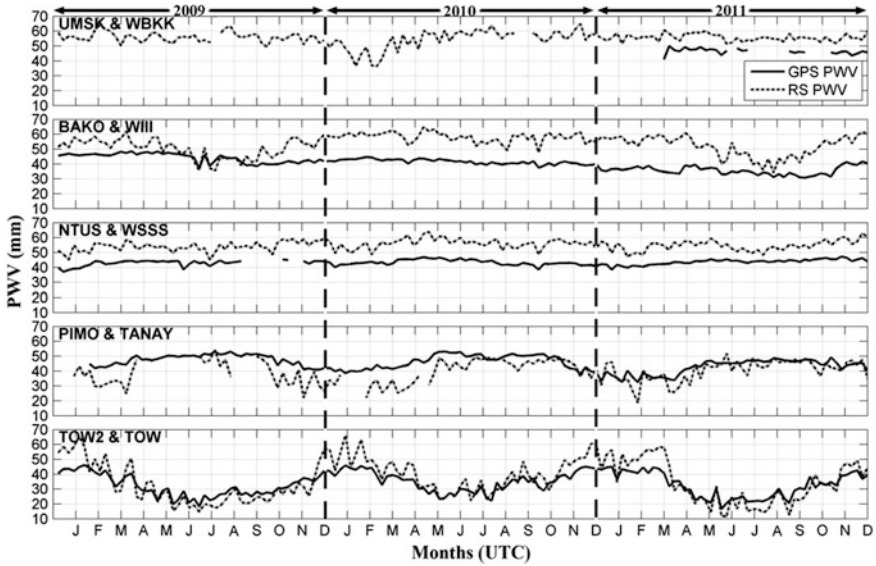


Fig. 2 Variability of PWV from GPS and radiosonde measurements for the period of 2009–2011 at five selected stations in the western Pacific on a weekly basis

From Fig. 2, the comparison of results between GPS PWV and RS PWV showed good agreement with a strong correlation (R^2 varies from 0.88 (WIII and BAKO, Indonesia) to 0.98 (WBKK and UMSK, Malaysia)). Although the RMS average obtained on a weekly basis is about 7.35 mm, these comparison results are also consistent with the studies conducted by Yang et al. [11] and Deblonde et al. [12]. The comparative analysis indicates that the PWV from GPS is promising for ENSO studies. For climate studies, the RS PWV is also advantageous when GPS data are not accessible.

3.2 A Relationship Between GPS PWV and SSTa ENSO

To study the response of PWV during ENSO activity for both the El Niño and La Niña phases, SSTa for Niño 3.4 and Niño 4 regions during the period of 2009–2011 are plotted in Fig. 3. In the analysis, the ENSO intensity was separated based on the increase and decrease in intensities.

3.2.1 Variability of SSTa

As depicted in Fig. 3, one case of the El Niño phase (Niño 3.4 and Niño 4 regions) colored red, and three cases (Niño 3.4 region) and four cases (Niño 4 region) of the

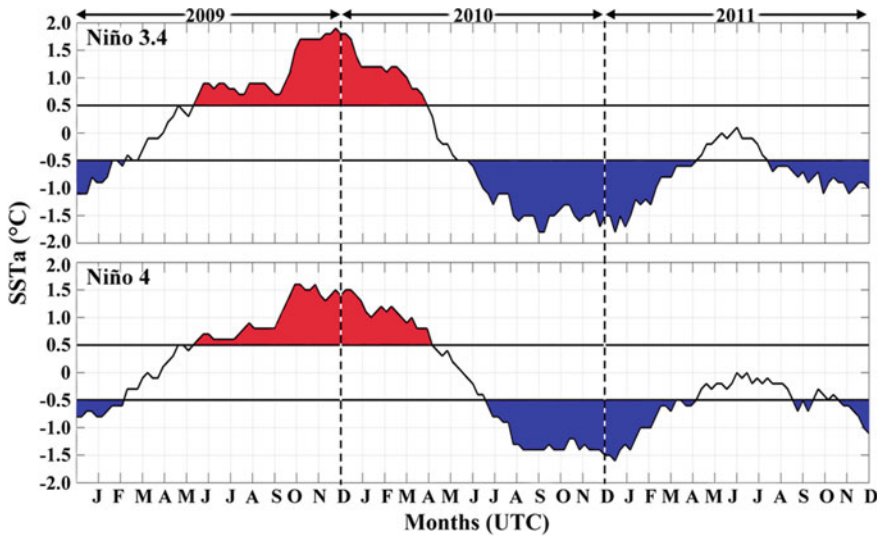


Fig. 3 Weekly variation of SSTa from Niño 3.4 and Niño 4 regions for the period of 2009–2011

La Niña phase, colored blue, are identified. The El Niño occurred from mid-June 2009 to April 2010. The maximum of the El Niño was in December 2009 (Niño 3.4) with SSTa of 1.9°C and in January 2010 (Niño 4) with SSTa of 1.6°C. For La Niña phase of Niño 3.4 region, the first case occurred from January to February 2009, the second case was from mid-June 2009 to April 2010, and the third case was from August to December 2011. Referring to SSTa for Niño 4 region, four La Niña cases were recorded.

The first case is from January to February 2009, the second case is from mid-July 2010 to April 2011, the third case is from mid-September to mid-October 2011, and the last case is from mid-November to December 2009. The maximum of La Niña occurred in October 2010 (Niño 3.4) with SSTa of -1.8°C and in January 2011 (Niño 4) with SSTa of -1.6°C .

3.2.2 El Niño Phase

In this case, the El Niño event was analyzed using data from June 2009 to April 2010. The relationship between PWV and SSTa at five selected stations for Niño 3.4 and 4 regions is depicted in Fig. 4. For the Niño 3.4 region, their relationship was strong during increasing El Niño intensity (see Fig. 4a) with R^2 of -0.81 and 0.66 for TOW2 and PIMO stations respectively. There was no correlation at any stations for decreasing intensity (see Fig. 4b), which possibly all the El Niño energies are stored during the increased his intensity.

For the Niño 4 region, the relationship between PWV and SSTa during *increasing* intensity of El Niño (Fig. 5a) at BAKO and NTUS stations is weak, except

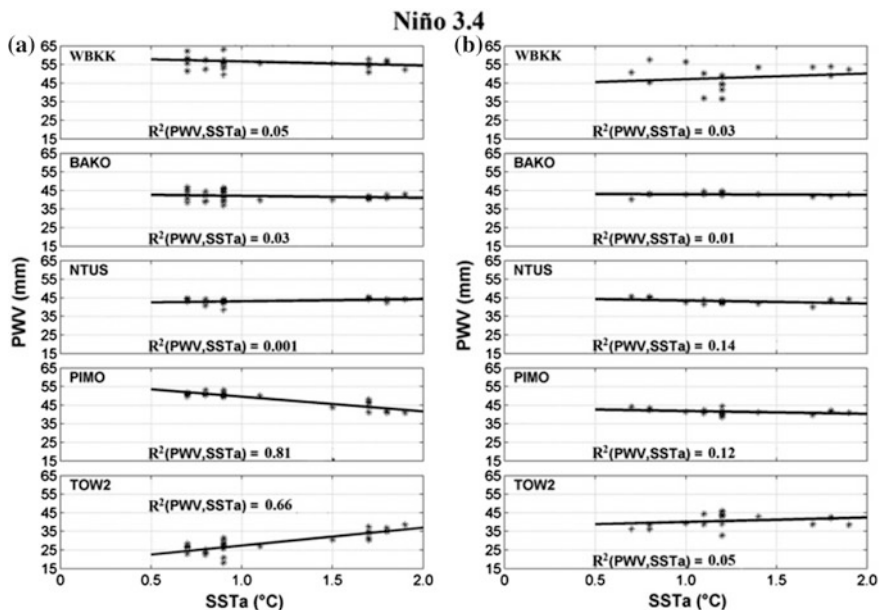


Fig. 4 The relationship between PWV and SSTa at five selected stations in the case of an El Niño event for the Niño 3.4 region during (a) *increased* intensity and (b) *decreased* intensity

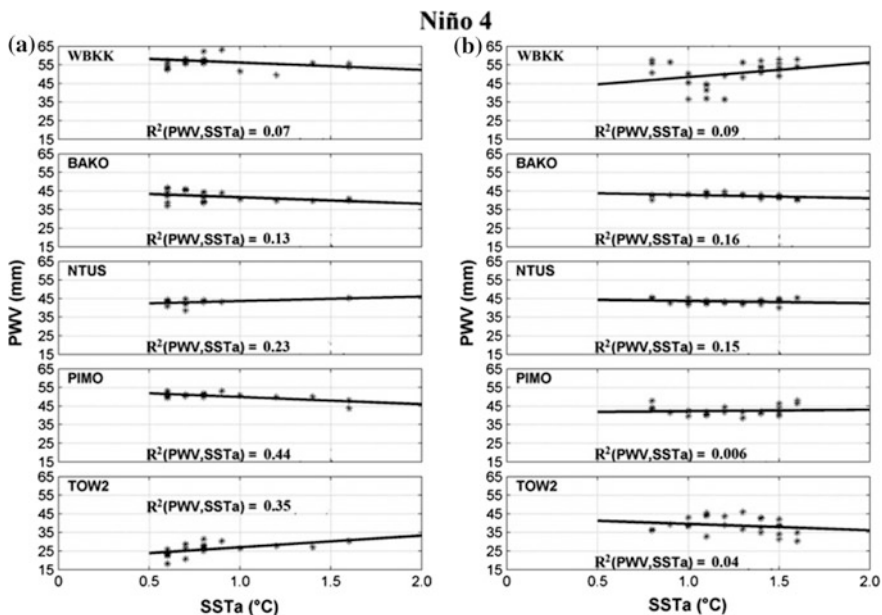


Fig. 5 The relationship between PWV and SSTa at five selected stations in the case of an El Niño event for the Niño 4 region during (a) *increased* intensity and (b) *decreased* intensity

for a modest correlation for the PIMO and TOW2 stations. During *decreasing* El Niño intensity (see Fig. 5b), the NTUS station showed a weak correlation and the rest of the stations showed no correlation. The modest (Niño 4) and the strong (Niño 3.4) relationships during El Niño intensity were increased for TOW2 and PIMO stations. The gradients of the regression line between the two stations have opposite values due to being in different hemispheres indicating that PWV at PIMO is decreasing, and increasing at the TOW2 station. In other words, the impact of the El Niño phase on the western Pacific during decreasing El Niño intensity is weak.

3.3 La Niña Phase

In this analysis, the phase of SSTa variability in the Niño 3.4 and Niño 4 regions is divided into three cases. The *first case* is from January to February 2009 with only an increased phase, the *second case* is from July 2010 to April 2011 with decreased and increased phases, and the third case is from August to December 2011 with only a decreased phase. Figure 6 shows the relationship between PWV and SSTa for the *first case* of La Niña. The intensity of La Niña in the Niño 3.4 region (see Fig. 6a) was lower, however, it shows a strong correlation at all stations except for PIMO due to their being no GPS data during this period. For the Niño 4 region (Fig. 6b), only BAKO and NTUS showed a modest relationship.

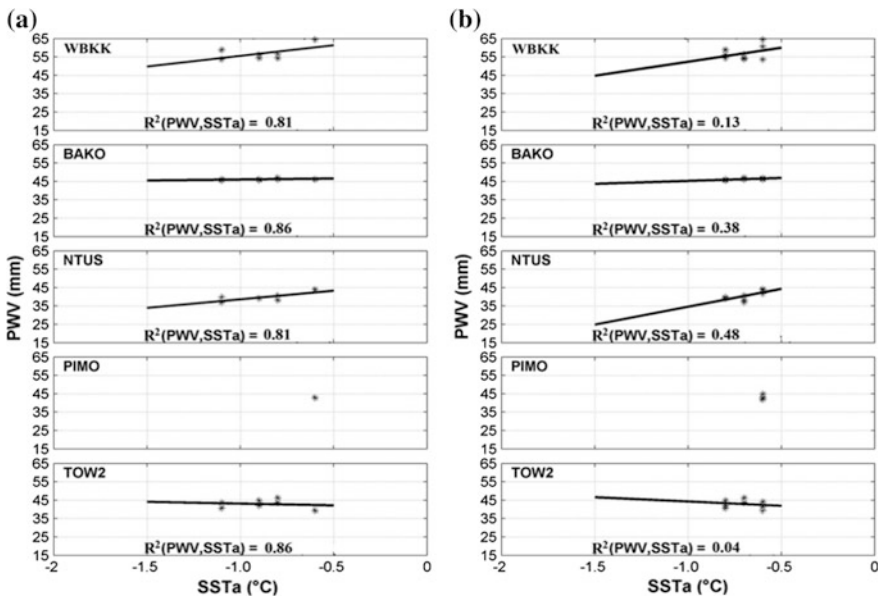


Fig. 6 The relationship between PWV and SSTa for (a) the first case of La Niña at (a) Niño 3.4 region and (b) Niño 4 region

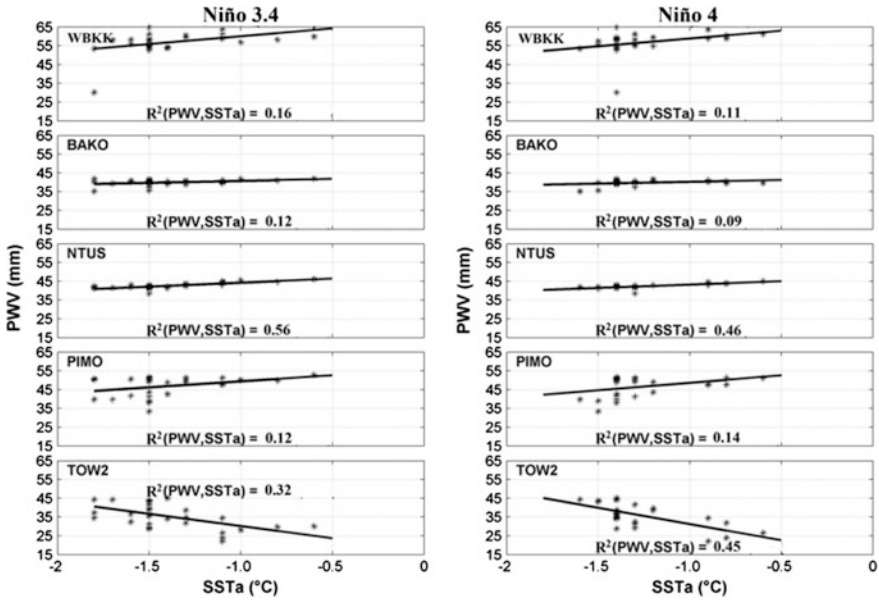


Fig. 7 The relationship between PWV and SSTa for the *second case of La Niña* at Niño 3.4 region and Niño 4 region during *increased* intensity

For the *second case* during increased La Niña intensity (Fig. 7), a modest relationship was obtained only at NTUS ($R^2 = 0.56$) for the Niño 3.4 region and a weak relationship at NTUS and TOW2 for the Niño 4 region. During decreased intensity (Fig. 8), a weak relationship for Niño 3.4 at NTUS and a modest relationship at all stations for the Niño 4 region were obtained. For the *third case* as depicted in Fig. 9, the intensity of La Niña is increased and no correlation was found for Niño 3.4 except a weak correlation ($R^2 = 0.32$) at TOW2. A modest relationship with R^2 from 0.46 to 0.59 was obtained at all stations for the Niño 4 region. From the figure, only the TOW2 station showed an opposite pattern to the relationship trend and is consistent during phase of La Niña event.

3.4 Physical Mechanism Proposed of GPS PWV During ENSO Activity

From the correlation analysis, a significant impact of ENSO occurred at the PIMO and TOW2 stations during increased El Niño intensity. For the other three stations, the phase during decreased El Niño intensity was weak. The effect of El Niño in the northern part (PIMO) on PWV is decreased during increased El Niño intensity and its effect is contrasted with the south (TOW2). Based on the characteristic of water

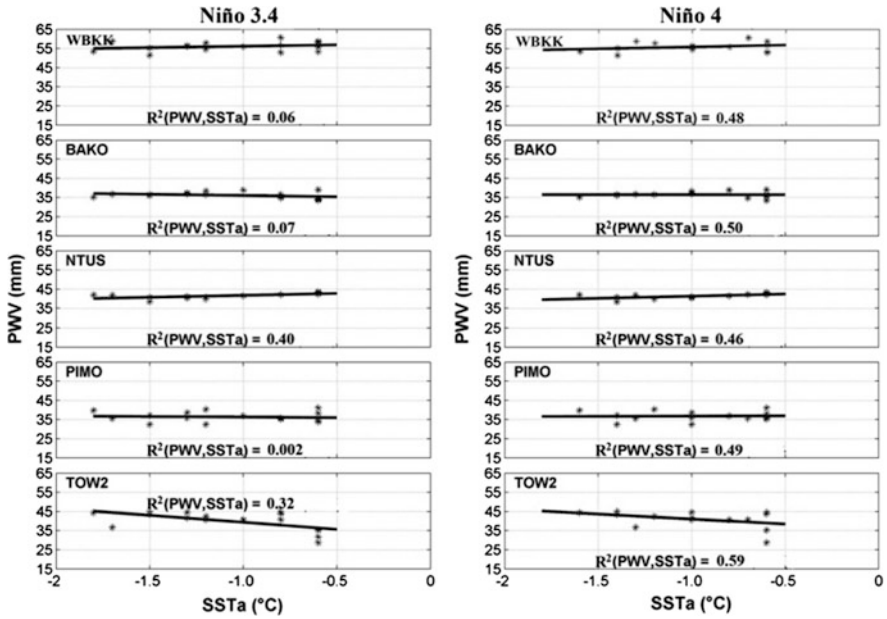


Fig. 8 The relationship between PWV and SSTa for the *second case of La Niña* at Niño 3.4 region and Niño 4 region during *decreased* intensity

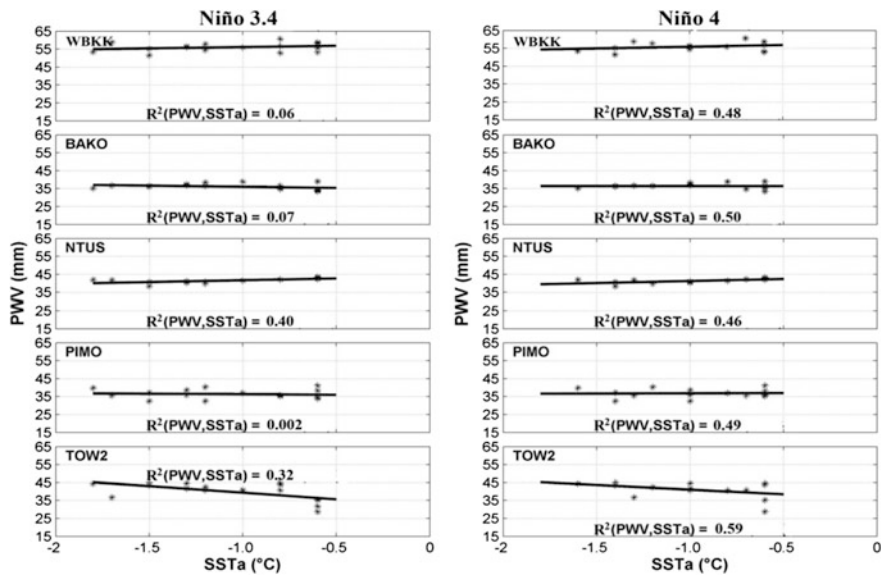


Fig. 9 The relationship between PWV and SSTa during the *third case of La Niña* for *decreased* intensity

vapor distribution over the western Pacific region, the response of El Niño and La Niña phases is explained as below.

During an El Niño event, SSTa in the central Pacific is increased and surface pressure is decreased [13]. The increased PWV in the central Pacific is because of the increases of the evaporation of sea water, and the increases of SSTa (decreased pressure) in the central Pacific can cause the change of wind direction from the west to the east Pacific [14]. This process causes the atmospheric water vapor in the western Pacific to move to the central Pacific, and drought and heavy rainfall will happen in the western Pacific and in the central Pacific respectively. On the other hand, clouds and rainfall are closely connected to the distribution of water vapor [15].

Figure 10 shows the illustration of an ENSO event affecting water vapor circulation during the El Niño phase. As shown in the figure, a dynamic distribution of PWV between PIMO and TOW2, probably associated with the movement of wind and seasons occurred in both areas. During increasing El Niño intensity (June to December), in the south it will be winter in the north it will be summer. Consequently, the monsoon wind moved from the south to the north Pacific where it was deflected to the right (Philippines) by the Coriolis Effect [16] after passing the equator. This event will decrease the PWV in PIMO. In contrast, during decreases of El Niño intensity (December to April), the monsoon wind moved from the north to the south Pacific, and the wind was deflected to the left, and PWV in Australia decreased. Table 2 summarizes the PWV different (Δ) between occurred of El Niño

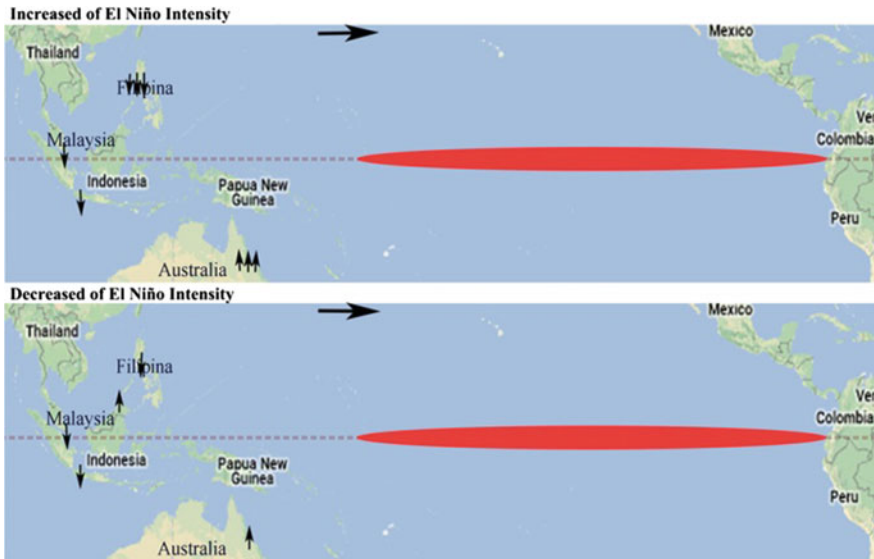


Fig. 10 The proposed mechanism of ENSO event influence on water vapor, where (↑) indicates increased PWV, (↓) is indicates decreased PWV and (→) is the wind direction of the El Niño phase

Table 2 The PWV difference between occurred El Niño phase and normal phase (ENSO does not occur) for the period from 2009 to 2011

Station	Niño 3.4			Niño 4		
	Normal (mm)	El Niño (mm)	Δ (mm)	Normal (mm)	El Niño (mm)	Δ (mm)
WBKK	55.92	53.07	-2.85	56.00	53.14	-2.86
BAKO	41.56	42.32	0.76	40.54	42.32	1.78
NTUS	44.39	43.19	-1.20	44.41	43.25	-1.16
PIMO	47.20	45.92	-1.28	47.47	45.96	-1.51
TOW2	27.56	33.16	5.60	27.17	33.23	6.06

Normal PWV is calculated by removing the seasonal variability

phase and normal phase for the above process. The significant impact of the El Niño event was at the TOW2 station, where PWV increased by 5.60 mm (Niño 3.4) and 6.06 mm (Niño 4) compared to the normal phase.

From Figs. 6, 7, 8 and 9, the biggest ENSO effect on PWV during the La Niña event occurred at in the first and third cases. *The second case* only shows a moderate effect but had a significant impact on several areas such as Malaysia and Australia. In the *first case*, the PWV decreased at three stations: WBKK, BAKO, and NTUS. In the *third case*, PWV at NTUS and PIMO (only) decreased, and at the rest increased. This characteristic during a La Niña event is associated with wet weather and increased rainfall, especially in the western Pacific Ocean. One of the factors that led to the high rainfall in the region is increases of PWV. PWV was produced from the evaporation process in the region and came from the central and eastern Pacific. This phenomenon causes the pressure in the central and eastern Pacific to be higher than in the West Pacific. Therefore, the trade winds became stronger moving from the central Pacific toward the West and bring warm surface water. Consequently, evaporation in the western Pacific is increased. This incident could potentially increase the rainfall above normal and lead to flooding. The monsoon also has a role in the increase of rainfall during a La Niña event. This will result in cold ocean temperatures due to the increased upwelling from the strong Walker Circulation.

Figure 11 illustrates the possible mechanism of ENSO event impacts on water vapor during the La Niña phase in the West Pacific. The upper panel represents Case I with decreased La Niña intensity, and is followed by Case II in the second and third panels with decreased and increased La Niña intensity, while the last panel shows Case III with increased La Niña intensity. On the figure, monsoon winds are indicated by a down arrow (\downarrow) and move from the north to the south leading to more rainfall in Australia during increases of La Niña intensity and less rainfall in the Philippines (see Case II and Case III during increased La Niña intensity). This process is consistent with the results obtained by Li and Ma [17] over the Southeast China region.

In contrast, during the monsoon from the south to the north (decreased La Niña intensity, see Case I and Case II), more rainfall occurred in the Philippines. This

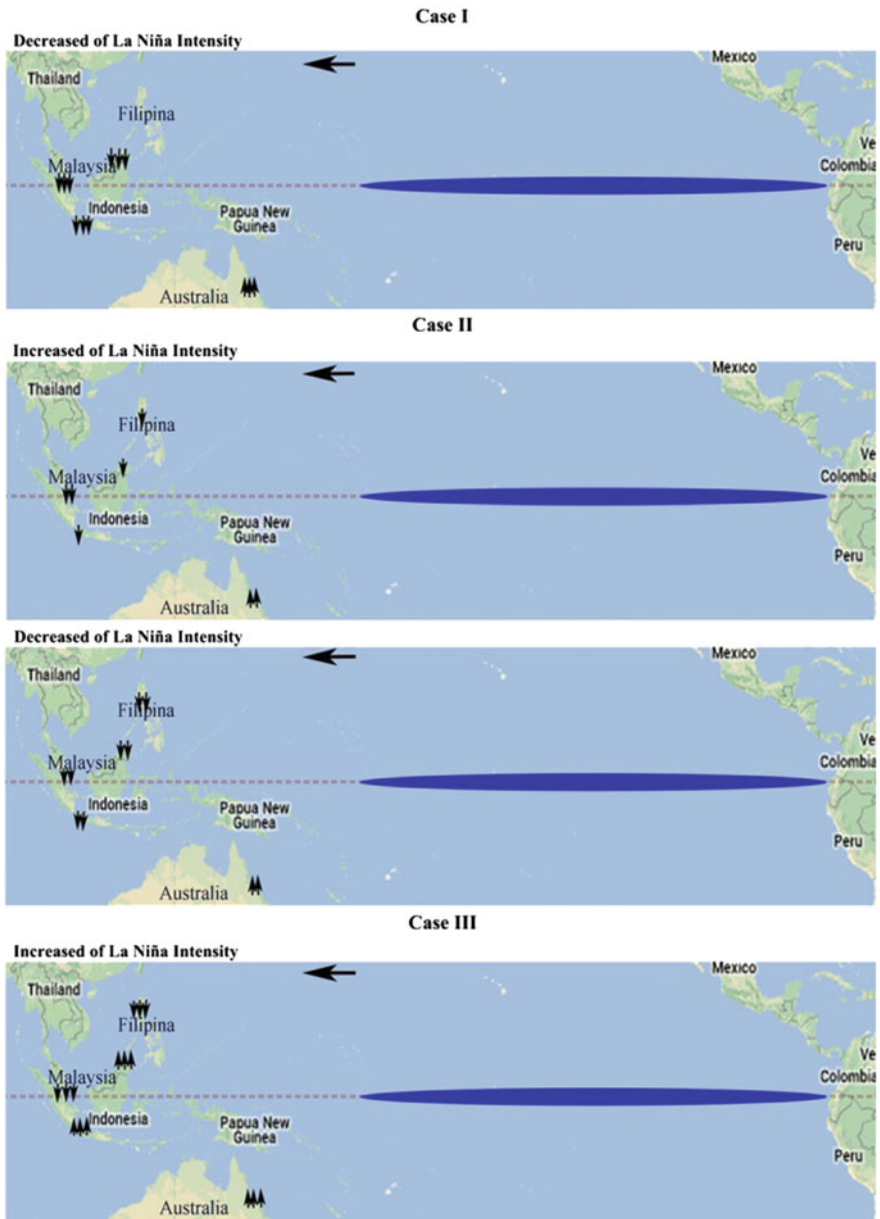


Fig. 11 The relationship between PWV and SSTa for the third case of La Niña from January to February 2011 for (a) Niño 3.4 region and (b) Niño 4 region

effect can be identified by average PWV difference (Δ) during the La Niña phase and the normal phase from 2009 to 2011 (see Table 2). The biggest difference was observed at the PIMO and TOW2 stations, where PIMO decreased by 3.14 mm

(Niño 3.4) and 4.04 mm (Niño 4), and TOW2 increased by 8.85 mm (Niño 3.4) and 10.46 mm (Niño 4). These two opposite regions in the ENSO response to PWV variability are still in need of further investigation.

4 Conclusion

The distribution of atmospheric water vapor in the western Pacific region was observed using ground-based GPS receivers to utilize the applicability of GPS technique for ENSO studies. The case study was conducted for 3-year data from January 2009 to December 2011. Correlation analysis was performed to discover the PWV response to ENSO events for both the El Niño and La Niña phases. The outcome of the study is summarized below.

During the occurrence of an El Niño episode, a good relationship between PWV and SSTa was observed at PIMO ($R^2 = 0.81$) and TOW2 ($R^2 = 0.66$) for the Niño 3.4 region, especially when the intensity is increased. The weakening of a trade wind causes PWV to move from the western to the central Pacific and the pressure in the central Pacific is lower than in the western Pacific, and finally, both stations are affected significantly. For the La Niña episode, a strong relationship was observed in the first case (January to February 2009) for the Niño 3.4 region and in the third case (August to December 2011) with a modest relationship for the Niño 4 region. A modest relationship was also observed in the second case of the La Niña episode. Overall, in the La Niña events from 2009 to 2011, PWV at PIMO for Niño 3.4 decreased by about 1 mm compared to Niño 4, and conversely increased by 2 mm for TOW2. The decreasing or increasing of PWV has a significant effect from the La Niña event due to a stronger trade wind occurring at both stations. This is accompanied by higher pressure in the central Pacific than in the western Pacific, and thereby the winds bring warm water from the central to the western Pacific and cause increases of advection by anomalous vertical motion, which are much larger than evaporation.

Monsoons also influence the PWV distribution, and during increases of El Niño and La Niña (July-December), winter season in the south and summer in the north has happened. This causes the wind to move from the south to the north and conveys the PWV. On the other hand, during a decreasing ENSO event (December-April), the monsoon wind is expected to move from the north to the south. Thus, the motion of the wind direction plays a critical role in PWV distribution, especially during ENSO events, and brings significant changes to the transportation of water vapor.

Acknowledgements This study was partially supported by the Ministry of Education Malaysia (MoE) under FRGS/2/2013/SG02/UKM/02/3 and FRGS/2/2013/TK03/UKM/02/3 grants. The authors sincerely thank the School of Science and Technology, University Malaysia Sabah (UMS) for maintenance of the GPS receiver and meteorological system. We would like to thank the National Oceanic and Atmospheric Administration (NOAA) for archiving the SSTa data and Wyoming University for the PWV Radiosonde.

References

1. Bjerknæs J (1969) Atmospheric teleconnections from the equatorial Pacific. *Mon Wea Rev* 97:163–172
2. Suparta W, Iskandar A, Jit Singh MS, Mohd Ali MA, Yatim B, Mohd Yatim AN (2013) Analysis of GPS water vapor variability during the 2011 La Niña event over the western Pacific Ocean. *Ann Geophys* 563:R0330. doi:[10.4401/ag-6261](https://doi.org/10.4401/ag-6261)
3. Bevis M, Businger S, Chiswel S, Herring TA, Anthes RA, Rocken C, Ware RH (1994) GPS meteorology: mapping zenith wet delay onto precipitable water. *J Appl Meteorol* 33:379–386
4. Suparta W, Iskandar A (2013) Modeling of weighted mean temperature over the western Pacific region to estimate GPS PWV. In: *Proceeding of the 2013 IEEE International Conference on Space and Communications (IconSpace)*. IEEE pp 190–193
5. Wang K, Sun J, Cheng G, Jiang H (2011) Effect of altitude and latitude on surface air temperature across the Qinghai-Tibet plateau. *J Mount Sci* 86:808–816
6. Klein Baltink DH, van Lammeren A, Ambrosius B, van der Hoeven A, van der Marel H, Kleijer F, Kosters A (1999) GPS water vapor meteorology. *Beleids Comm Remote Sens (BCRS)* 3–11
7. Hofmann-Wellenhof B, Lichtenegger H, Collins J (2001) *Atmospheric effect on the Global Positioning System: Theory and Practice*. Springer, Berlin
8. Suparta W, Abdul Rashid ZA, Mohd Ali MA, Yatim B, Fraser GJ (2008) Observation of Antarctic precipitable water vapor and its response to the solar activity based on GPS sensing. *J Atmos Sol-Terr Phys* 70:1419–1447
9. Saastamoinen J (1972) Introduction to practical computation astronomical refraction. *Bull Geod* 106:383–397
10. Suparta W (2014) The development of GPS TroWav tool for atmospheric—terrestrial studies. *J Phys Conf Ser* 495:012037. doi:[10.1088/1742-6596/495/1/012037](https://doi.org/10.1088/1742-6596/495/1/012037)
11. Yang X, Sass BH, Elgered G, Johansson JM, Emardson TR (1999) A comparison of precipitable water vapor estimates by and NWP simulation and GPS observations. *J Appl Meteorol* 38:941–956
12. Deblonde G, Machperson S, Mireault Y, Heroux P (2005) Evaluation of GPS precipitable water over Canada and the IGS network. *J Appl Meteorol* 44:153–166
13. Ma K (1996) A study on flow field and heat exchange anomalies on tropical Pacific surface in the El Niño and La Niña events. *Meteorol Atmos Phys* 611:65–73
14. Zebiak S (1999) El Niño and the science of climate prediction. *Consequences* 5:3–15
15. Bevis M, Businger S, Herring TA, Anthes RA, Rocken C, Ware RH (1992) GPS meteorology: remote sensing of atmospheric water vapor using the global positioning system. *J Geophys Res* 97:15787–15801
16. Persson AO (2005) The Coriolis effect: four centuries of conflict between common sense and mathematics, part I: a history to 1885. *Hist Meteorol* 2:1–24
17. Li C, Ma H (2012) Relationship between ENSO and winter rainfall over southeast China and its decadal variability. *Atmos Sci* 296:1129–1141

Impact of Sea Level Rise on the Coastal Ecosystem

**Khairul Nizam Abdul Maulud, Fazly Amri Mohd,
Wan Hanna Melini Wan Mohtar, Othman Jaafar
and Yannie Anak Benson**

Abstract Rising sea level is a phenomenon that is beginning to impact ecosystems and coastal features and the increasing annual rate of sea level rise will continue to impact on the coastal activities. The shoreline is very vulnerable and is sensitive to a variety of threats, especially erosion and flooding that can have a negative impact on human welfare, the environment and the ecosystem. The coastal area in Batu Pahat is very vulnerable to flooding due to high tides and critical coastal erosion. By using geospatial technology, the impact of sea level rise on coastal communities in Batu Pahat, Johor was identified. The shoreline changes along coastal communities of Batu Pahat can be determined using information from satellite remote sensing imagery. The findings show that sub reaches in Batu Pahat will be changed due to sea level rise by 87.50 ha (43.80%) compared to other sub reach between 2010 and 2040. The effects of sea level rise to the coastal areas near Batu Pahat found actively erosion and flooding events. The research makes recommendations to enhance the policies and related government guidelines for sustainable development in the region.

Keywords Coastal erosion · Sea level rise · Geospatial · Community · Shoreline

K.N. Abdul Maulud (✉) · F.A. Mohd · W.H.M. Wan Mohtar · O. Jaafar
Faculty of Engineering and Built Environment, Department of Civil and Structural
Engineering, Universiti Kebangsaan Malaysia, 43600 Bangi, Selangor, Malaysia
e-mail: knam@ukm.edu.my

K.N. Abdul Maulud
Earth Observation Centre, Institute of Climate Change, Universiti Kebangsaan Malaysia,
43600 Bangi, Selangor, Malaysia

Y.A. Benson
National Hydraulic Research Institute of Malaysia (NAHRIM),
Ministry of Natural Resources and Environment (NRE),
Lot 5377, Jalan Putra Permai, 43300 Seri Kembangan, Selangor, Malaysia

1 Introduction

The phenomenon of sea level rise (SLR) and the movement of sea water are caused by major parameters such as climate change, weather conditions and the reduction in size of the ozone layers. The coastal area is vulnerable and increasing exposure to sea level rise poses significant adverse effects. Sea level rise was recognized as one of the factors contributing to the acceleration of coastal erosion. This phenomenon is one of the most important signs of the impact of climate change and is a global threat particularly for coastal communities. As one of the main factors in sea level rise, coastal erosion problems are of great significance in the case of sea level rise. Therefore, predictions for the rate of future coastal sea level rise can be obtained from observation of trends in the shoreline changes in the recent past. The Intergovernmental Panel on Climate Change (IPCC) has shown that the natural environment and habitat in coastal areas is being seriously affected by global climate change and sea level rise. Furthermore, the changes in sea level indicate the contributions from the dynamic interaction processes between land and ocean at the local and global scale. Thus, Malaysia is one of the countries that are most highly vulnerable to the effects of climatic changes.

According to [1], the flooding, shoreline erosion and destruction of ecosystems such as wetlands and mangroves as a result of global warming will severely affect the coastal areas of many countries of the world. In addition, the socioeconomic and environmental characteristics, for example destruction of assets, loss of human life, emotional health effects, loss of plants, animals and ecosystems are given significant impact due to climate change and SLR. Future sea level rise is expected to have a number of impacts, particularly on the Malaysian coastal systems, such as inundation and flooding, and coastal erosion.

Beach profiling is significant to an understanding and identifying of coastal zone processes. A beach profile as shown in Fig. 1 shows the relationship between land and water. The beach profile in the surrounding area of the mean sea level shows the slope is flattened [2]. The dynamic process effects such as waves, tides, currents and winds are changing rapidly. In other cases, most of the erosion at this coastal area occurs due to interference by human activity. The shoreline can be defined as the intersection between land and water surfaces at a designated tidal height level. Basically, the shoreline area limits of Malaysia are formed at 1 km from the land and 3 km from the sea.

In this century, the sea level is expected to increase at a higher rate. The IPCC prediction estimated that the global sea level will increase by a maximum of 59 cm by 2100 as shown as in Fig. 2 [3]. Note that for the period prior to 1870, the global measurement of sea level is not presented. The grey colour in Fig. 2 displays the uncertainty in the projected long term rate of sea level change. The second column (center) representing by a red line is a reconstruction of global mean sea level from tide gauges with the red shading indicating the range of variation from a smooth curve. The projection for the future (third column) was identified by using the satellite altimetry. Therefore, climate change, exacerbated by the greenhouse effect

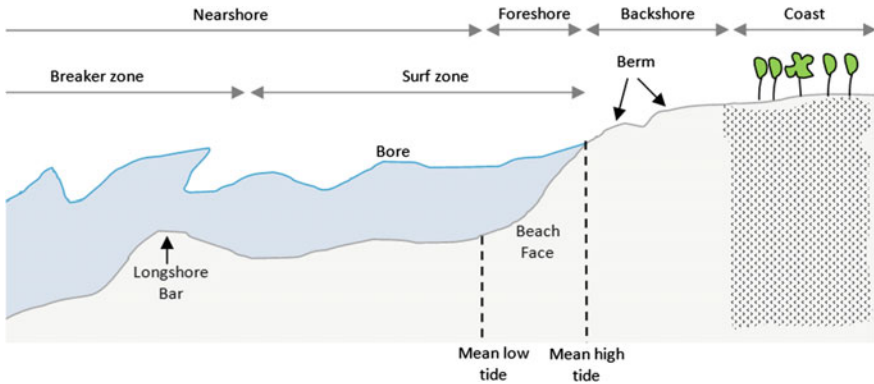
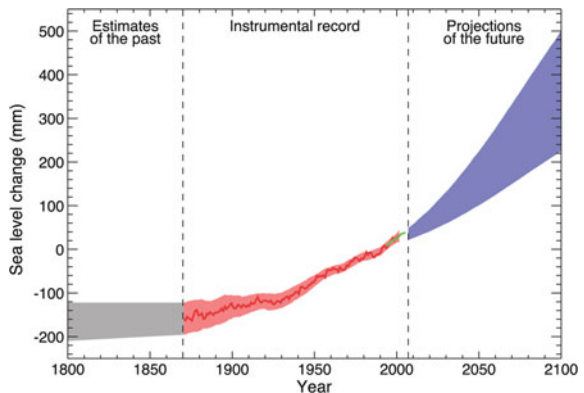


Fig. 1 Beach profile and terminology

is possibly accelerating the rate of sea level rise. In the present day, most of the human residents living in coastal regions and islands are potentially more affected by changes in sea level.

The area is suffering directly from the impact of sea level rise at the coastal zones which consists, rich in resources, heavily populated and a lot of development, and the low-lying background area depends on the strength of wave near the coast. Many countries including Malaysia are taking the sea level rise phenomenon as a serious issue and as one of the effects of global warming. In the 21st century, sea level is expected to rise from 18 to 66 cm [5]. The National Hydraulic Research Institute of Malaysia (NAHRIM) conducted a study and found that Malaysia will be facing a sea level rise in the range of 0.253–0.517 m by the year 2100 using 2010 as baseline study [6]. The most affected areas in Malaysia are identified as regions within Sabah, Sarawak, Kelantan and Kedah. One of the notable areas facing serious threats from erosion and SLR is the shoreline of Batu Pahat, Johor. The sea

Fig. 2 The timeline of global mean sea level prediction [3, 4]



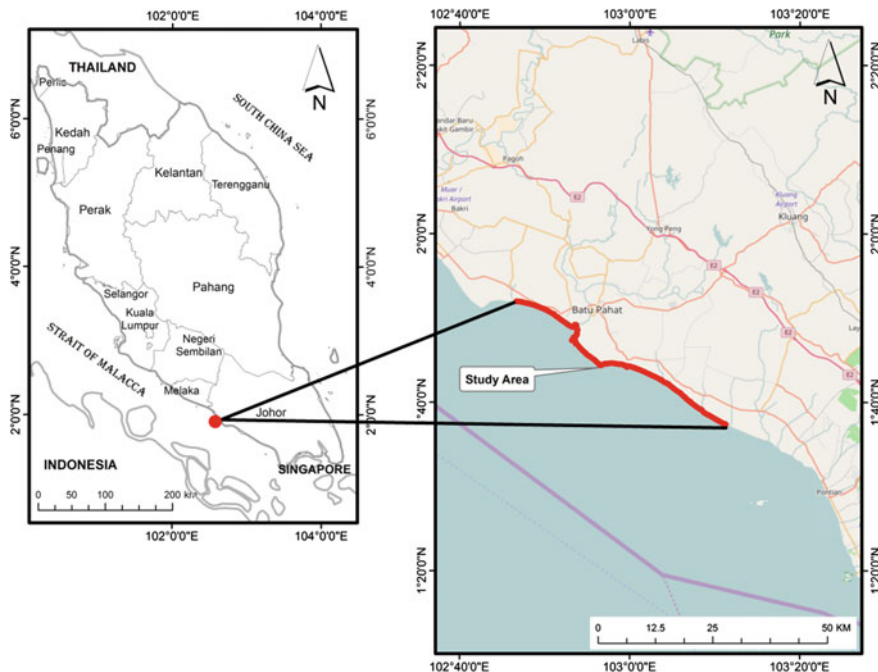


Fig. 3 The study area of Batu Pahat, Johor

level in this region on the West Coast of Peninsular Malaysia, as shown in Fig. 3, is expected to increase between 0.432 to 1.064 m.

Ong [7] stated that erosion is the important and natural replenishment of sand through coastal sedimentation rates but with the minimal rate per year. In addition, the main sources of shoreline erosion are not driven by a single agent but are a result of both natural processes and human activities [8]. The climate impacts such as storms, sea level rise, and temperature, etc. are made worse by the density of the human population. The issue of SLR has received a lot of attention from the Malaysian Government where adaptive and precautionary measures have been given priority.

2 Shoreline Changes

The National Coastal Erosion Study conducted by the Department of Irrigation and Drainage states that a length of 1,300 km out of the 4,809 km Malaysian coastline was identified in 1986 as an area vulnerable to coastal erosion. This length, however, had increased to 2,327 km by the year 2000, which subsequently increased the number of sensitive sites to 74 from the previously determined 47 [9].

Shoreline changes can now be measured by geospatial analysis. This kind of analysis permits continuous shoreline monitoring and assessment based on historical shoreline maps. Considering the outcome of the 1985 NCES study, the Department of Survey and Mapping Malaysia (JUPEM) have attempted to undertake consistent measurements and have produced updated shoreline maps since then. Conventionally, shoreline observation was conducted using aerial photogrammetry and ground survey methods which are rather costly, need expert staff and are time consuming. The preparation of these maps usually requires a time period from one month to several years [10]. As such, the lengthy process might miss significant coastline changes and the map produced may be considered as outdated.

The effects of SLR on the changes to the shoreline through the processes of accretion and erosion can be analyzed using Geographical Information Systems (GIS) to determine changes in shoreline area [5]. The results of temporal period series data were combined and compared to each other in order to identify shoreline changes. The identified geomorphological changes may provide information on the local erosion and accretion processes. Higher erosion rates indicate a more vulnerable coastline and the location is assigned as a high risk area.

Figure 4 shows the shoreline changes in one part of the Batu Pahat coastline, namely Sungai Lurus. The data indicate that the shoreline has visibly changed from

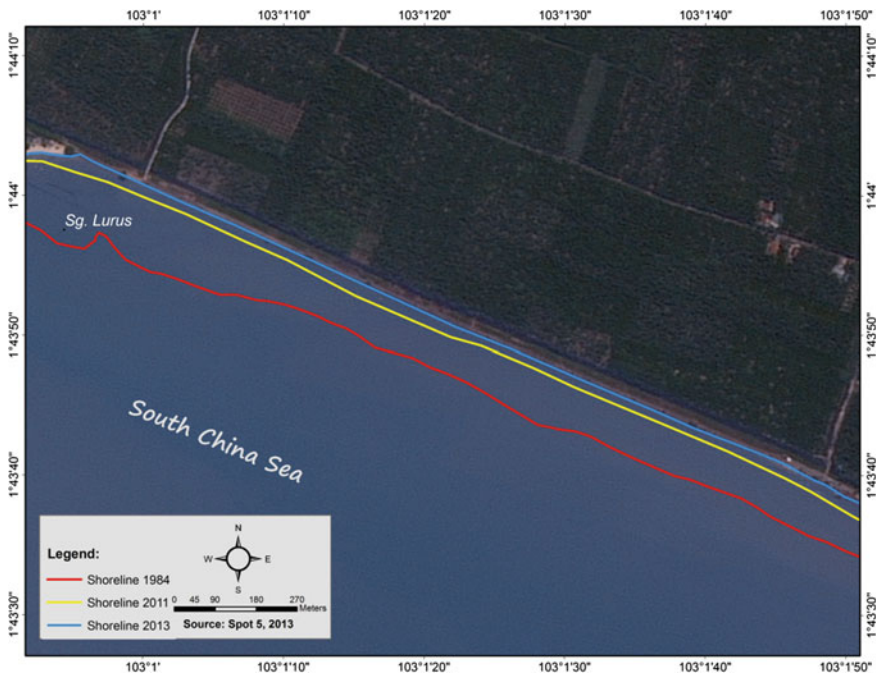


Fig. 4 Shoreline changes at Sungai Lurus, Johor from 1984, 2011 and 2013

the year 1984 to 2013, with the coastline having reduced from 50 to 200 m. The average annual change was calculated at between 1.5 to 7 m.

3 The Impact of Sea Level Rise

Sea level rise has occurred in the past and is rising entering the twenty-first century. The variation in sea level can be locally or globally determined and can be caused by changes in the form of sea basins, total water mass and density.

3.1 Impact on Land Ownership

Shoreline erosion is a natural process that occurs through the continuous actions of currents and waves resulting in the loss of sediment. The effect of SLR has resulted in, for example, a loss of agricultural production, eroded land, loss of profit of fish production, and damage to mangrove areas, etc. For the small islands with the less coastal area, the loss of the agriculture will give significant impact to the economy. Vice versa, many of the world's major cities are located near to the coastal areas resulting in an effect on their local economy due to the impacts of sea level rise.

Globally, a lot of productive agricultural areas are situated in river deltas and on coastal plains. In Egypt and Bangladesh, for example, the fertile alluvial soils at river deltas play a major role in agricultural production. Agriculture may also provide raw materials to the industrial sector and may have a substantial economic impact. Additionally, the relationship between agriculture and tourism also offers potential to both sectors in the supply and demand of food and beverages, and in the employment sector.

One effect of sea level rise is the loss of land. Figure 5 shows the land retreat from the year 1984 to 2013, and it can be clearly seen that several areas of land are now under the sea. As a result the owners automatically lose the title deeds to the land and are left hopeless. Millions of ringgits are at stake should this continue and incorrectly planned countermeasures are implemented. A properly designed shore protection plan, as well as better forecasting of sea level rise would enable property owners to avoid such losses.

Climate change leaked the structure of the coastal aquatic ecosystems. The production of wild fish relies on the condition of estuaries, coral reefs, mangroves and sea grass beds. In riverine areas, the condition and productivity of an ecosystem are related to the water quality, flow and health of wetlands. The parameters of water temperatures and primary production at the lowest water area will have a negative impact on fisheries. In addition, many communities dependent on fisheries are now living in risky and vulnerable conditions due to the lack of essential infrastructure to support their livelihood.

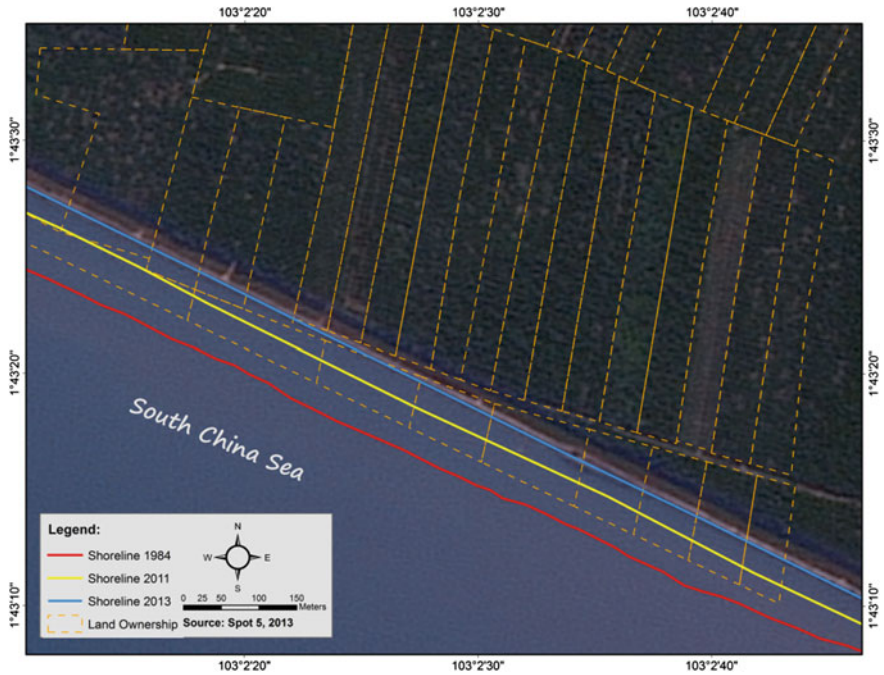


Fig. 5 The shoreline changes due to sea level rise were determined through the shoreline variation between the baseline year of 1984 and 2013

3.2 Future Impact of Increasing Water Levels

The tides and waves is the agents for changing the sea level. The Mean Sea Level (MSL) at a given height position is estimated by averaging tidal observations over a long period. Based on the IPCC study [4], since the twentieth century, sea level has constantly risen at an average rate of 1.7 ± 0.5 mm per year and is predicted to rise by up to 56 cm by the year 2100.

This century, the heights are estimated to increase at a greater rate due to the melting of ice and the thermal heat of the ocean due to warming. The amount of sea level rise is due to increase in the long term. From 1993–2003, the differences were spatially non-uniform and most of the areas had an increase in sea level of more than a few times greater than the global rise.

Based on the study of the Impact of Climate Change on SLR in the Malaysian coast by the year 2100 [11], the projected SLR is between 0.25–0.5 m with the maximum value occurring along the Kelantan and Kedah areas of coastal peninsular Malaysia. The changes in sea level and spatial variations are important for future planning. Regional and local factors are both important and useful for future SLR prediction, particularly in neighboring areas.

The relative sea level rise depends, for example, on vertical land elevation changes, which could be either sinking or rising. Managing existing resources involves knowledge of the effects of the variations in ocean circulation and nutrients on the aquatic and coastal environment. In coastal systems such as Malaysia, the future sea level increase would be expected to have a number of impacts such as inundation, coastal erosion and saltwater disturbance. In Malaysia, one study concerning the Batu Pahat near shore for the period between 2020 and 2040 indicates a rise in water level in several rivers namely at Sungai Ayam, Sungai Suloh Besar, Sungai Koris, Sungai Lurus, Sungai Senggarang, Sungai Parit Botak, Sungai Tongkang and Sungai Rengit as shown in Figs. 6 and 7. The total affected area in 2020 is 1,676.16 ha and 1,875.93 ha in 2040 as shown in Table 1.

Sea level rise will occur for centuries and possibly even thousands of years. The extreme effects of high tides and storm surges will impact further on the sea level rise. The hazards from SLR are not limited to the coast itself. In various cases, flooding may affect areas at greater distances from the sea particularly nearby estuaries, rivers, lakes and lagoons.

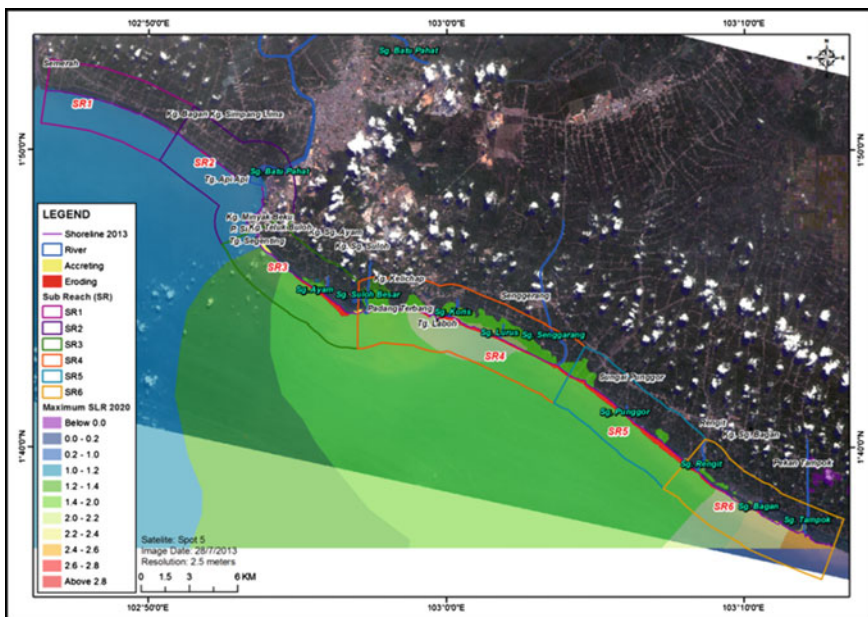


Fig. 6 Prediction of sea level rise by 2020

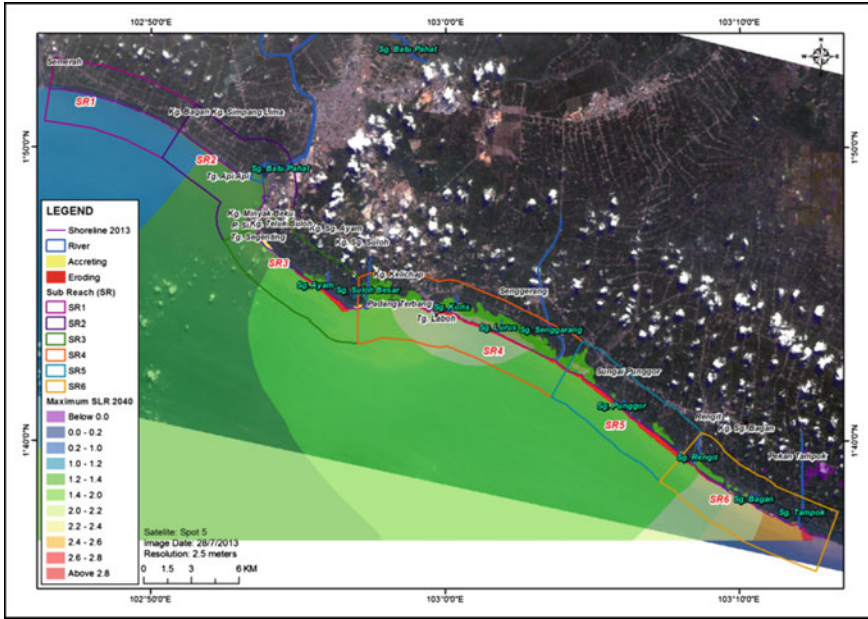


Fig. 7 Prediction of the sea level rise by 2040

Table 1 The changes in affected area due to sea level rise between 2010 and 2040

Sub Reach (SR)	Area (hectare)		Changes	
	2020	2040	Area (hectare)	Percentage (%)
SR1	23.29	30.01	6.72	28.85
SR2	62.77	61.83	-0.93	-1.48
SR3	73.56	83.09	9.53	4.77
SR4	1,162.39	1,249.89	87.50	43.80
SR5	203.40	253.28	49.87	24.97
Total	1,676.16	1,875.93	199.77	100

4 Impact on the Community

Climate change is one of the main threats to human life and livelihoods in the coastal region. Most developing countries have rapid rates of population growth with large portions of their populations living in low-lying coastal areas. The great concentration of people near to coastal areas has resulted in many economic benefits such as tourism, aquaculture, industry, development and recreation. The combination of the effects of increasing population growth, economic and technological development are threatening the ecosystems in these areas.

Bangladesh, Egypt and Vietnam having unprotected river deltas where almost eight to ten million people live. Even more people in these countries would be exposed to the increased strength and frequency of storms. Based on the distribution of the population in relation to the distance from the nearest coastline in 2004, 20.6% of the world's population lives within 30 km of the coast, and 37% within 100 km. As a consequence of migration to coastal areas, and specifically to coastal cities, the coastal population is increasing at a faster rate than the global population [12].

IPCC assessment has confirmed that coastal populations and environments are regularly stressed due to the impacts of climate change. The factors of population growth and associated demands for housing and infrastructure along the coast increases this vulnerability. People who live within the coastal regions may suffer the problem of environmental stresses from upstream activities and inland development. This development can result in pollution, huge deforestation, and inadequate management of soil, water, and fertilizers. These problems pose larger threats to human health when the coastal zones are small and overcrowded. Furthermore, SLR causes the salt water polluting the freshwater sources on which many settlements rely for drinking and farming.

Sea level rise also leads to a loss of property and homes and as such people are seeking safer places to live [13]. The disturbance of hydrological cycle was influencing sea level rise and repeated flooding events to the coastal communities. For example, floods and tidal waves in North Korea between 1995 and 2000 led to 300,000–400,000 people migrating to China's urban centers. As another example, due to storms, land erosion and salt interference into the water system, a massive migration of 12 to 17 million people since the 1950's from Bangladesh to India and West Bengal has occurred.

4.1 Impact on Property

Sea Level Rise poses a major threat to people, property, and infrastructure. SLR has serious impacts such as destruction of assets. SLR in coastal areas is associated with many hazards to property and public safety such as airports, roads, and capital cities, which are often located in coastal areas, especially in densely populated areas as previously discussed. Roads often run along the coast so they have a high possibility of incurring severe damage.

The higher water level in the lower area of rivers and coastal waters may reduce natural drainage of adjoining land areas, impacting roads, buildings and agricultural land. The Paka Power Station in Terengganu, for instance, has had to suffer the effects of coastal plain erosion and has to be protected by costly structural works such as concrete sea walls. This phenomenon is a major concern to electrical power

producers because most of the thermal power stations are located near the sea [14]. SLR and normal tropical storms could also eventually increase the cost of offshore oil exploration and production.

5 Conclusion

Sea level rise has previously focused on a major rising and extremes at many locations, and it is very likely that the phenomena will remain for centuries. Most of the detailed studies will have to be started in Malaysia especially on climate change and sea level rise related issues, vulnerability index for sensitive regions, evaluation of potential impacts of climate change on other vulnerable sectors such as agriculture, water resources, coastal and marine resources. The results from the study indicate that SR 4 in Batu Pahat will be changed due to a sea level rise by 87.50 ha (43.80%) compared other Sub Reach between 2010 and 2040. The Drainage and Irrigation Department has allocated millions of ringgits for mitigation and restoration of the beaches affected by coastal erosion. Findings from the research need to be integrated with existing guidelines or develop new guidelines and each of the new development and activities must remain the sustainability of disaster risks towards the human communities with less risk.

References

1. Sarkar MSK, Begum RA, Pereira JJ et al (2014) Impacts of and adaptations to sea level rise in Malaysia. *Impacts Adapt Sea Level Rise Malays* 11(2):29–36
2. Sorensen RM (2006) *Basic coastal engineering*, 3rd edn. Springer, USA
3. IPCC (2007) *Climate change 2007: the physical science basis*. In: Solomon S, Qin D, Manning M, Chen Z, Marquis M, Averyt KB, Tignor M, Miller HL (eds) *Contribution of working group I to the fourth assessment report of the intergovernmental panel on climate change*. Abbreviated to IPCC, 2007: climate change. I. Cambridge University Press, Cambridge, UK, p 996
4. Bindoff NL, Willebrand J, Artale V et al (2007) *Observations: oceanic climate change and sea level*. In: Solomon S, Qin D, Manning M, Chen Z (eds) *Climate change 2007: the physical science basis. Contribution of working group I to the fourth assessment report of the intergovernmental panel on climate change*
5. Maulud KNA, Rafar RM (2015) *Determination the impact of sea level rise to shoreline changes using GIS*. In: *Determination the impact of sea level rise to shoreline changes using GIS*, pp 352–357
6. Awang A, Hamid MRA (2013) *Sea level rise in Malaysia*. *Hydro link* 2:47–49
7. Ong JE (2014) *Vulnerability of Malaysia to sea level change*. In: *Vulnerability of Malaysia to sea level change*, pp 1–5
8. Mohamad MF, Lee LH, Samion MKH (2014) *Coastal vulnerability assessment towards sustainable management of Peninsular Malaysia coastline*. *Int J Environ Sci Dev* 5(6):533–538

9. Economic Planning Unit, Malaysia(1985) National coastal erosion study—final report Kuala Lumpur, Malaysia. Stanley Consultants, Inc., Moffat & Nichol and Jurutera Konsultant (SEA)
10. R.Zakariya, YR (2006) Shoreline detection and changes for Terengganu River mouth from satellite imagery (Landsat 5 and Landsat 7). *Sustain Sci Manag* 1(1):47–57
11. NAHRIM (2012) Study to assess the impacts of sea level rise at Sandakan, Sabah
12. Jasem MA (2007) Integrated management of the coastal zone for the Gulf region. *World Rev Sci Technol Sustain Dev (WRSTSD)* 4(4)
13. Patz, JA, David, E, John, Last (2000) The effects of changing weather on public health. *Ann Rev Public Health* 21:271–307 (Annual Reviews)
14. Rahman HA (2009) Global climate change and its effects on human habitat and environment in Malaysia. *Malays J Environ Manag* 10(2):17–32

Manifestation of SVM-Based Rectified Linear Unit (ReLU) Kernel Function in Landslide Modelling

Biswajeet Pradhan and Maher Ibrahim Sameen

Abstract Support vector machines (SVM) are the most popular machine learning methods currently used to model landslides. To model the complex nature of landslides, the SVM model parameters (kernel function, penalty parameter) should be fine-tuned to achieve the best possible accuracy. The main objective of this paper is to evaluate the commonly used rectified linear unit (ReLU) activation function in deep learning for the SVM model as a kernel function. A case study of the Cameron Highlands, located in the Peninsular Malaysia, was selected and a dataset was acquired through the airborne LiDAR system, topographical databases, and SPOT satellite images. The SVM modelling with ReLU kernel was implemented in a Matlab environment. Overall, 11 landslide factors and 81 landslide locations (inventory map) were used. Experimental results showed that the ReLU kernel function could achieve a higher accuracy (0.81) than other kernels when using a lower number of landslide factors. It was found that the ReLU kernel function is more accurate (0.73) than RBF kernel (0.71) when using very limited factors (such as altitude, slope, and curvature). The kernel ReLU could improve the performance of landslide susceptibility modelling with SVM while reducing the need to use large datasets.

1 Introduction

Natural disasters such as landslides are a global concern and they pose significant threats to human life, economic developments, and environments. The basic definition of a landslide is the movement of earth, rock, or debris down a slope [1].

B. Pradhan (✉) · M.I. Sameen
Department of Civil Engineering, Faculty of Engineering,
Universiti Putra Malaysia, 43400 Serdang, Selangor, Malaysia
e-mail: biswajeet24@gmail.com; biswajeet@lycos.com

B. Pradhan
School of Systems, Management and Leadership, Faculty of Engineering
and Information Technology, University of Technology Sydney,
Building 11, Level 06, 81 Broadway, PO Box 123, 2007 Ultimo, NSW, Australia

Landslides are triggered by several factors such as heavy and prolonged periods of precipitation, earthquakes, melting ice, and volcanic eruptions. On the other hand, there are many controlling factors identified through extensive studies of landslides. The most commonly studied factors include altitude, slope, aspect, curvature, geology, land use, vegetation density, terrain roughness index (TRI), stream power index (SPI), sediment transport index (STI), topographic wetness index (TWI), and distance to streams, roads, and fault lines.

Landslide phenomena are modelled by establishing relationships between landslide conditioning factors and landslide occurrence in a given area and time period. There are a wide range of statistical, machine learning, and expert-based models used for establishing such relationships. In each category, several algorithms have been proposed and their performance across different datasets and geographic locations has been well reported in recent decades. Among the recommended algorithms, the support vector machine (SVM) has shown excellent accuracy and general performance. However, optimization of SVM parameters and selection of the appropriate kernel function of SVM model remain a hot topic in the field of landslide modeling research.

Several studies have reported satisfactory results of landslide susceptibility assessment using the SVM model. [2] Compared the predictive ability of the model with decision tree and neuro-fuzzy methods. The radial basis function (RBF) was used as a kernel function for the SVM algorithm. The result of the study showed that the SVM model can achieve satisfactory results (prediction rate = 0.82) and is comparable to the other two models. Three data mining approaches (SVM, decision tree, Naïve Bayes) for landslide susceptibility assessment were compared in [3] and the results indicated that the SVM model has the highest prediction accuracy. In addition, [4] studied the SVM model for earthquake-triggered landslide susceptibility in the Jianjiang River watershed, China. The results of the paper showed that the RBF and polynomial are the two most suitable kernel functions to use for predicting landslides in the study area. A success rate of 79.20% and a predictive accuracy of 79.13% with the RBF kernel function were obtained. Evaluation of the SVM model for spatial prediction of landslides in Golestan Province, Iran was reported by [5]. Results indicated that the SVM model with RBF (85%) and a polynomial degree of three (83%) performed better than other types of kernel (polynomial degree of 2 = 78%, sigmoid = 78%, polynomial degree of 4 = 78%, and linear = 77%) model. Furthermore, in a case study in Italy, [6] showed that the SVM model outperforms other techniques (Naïve Bayes and logistic regression) in terms of accuracy and general capacity.

More recently, [7] compared four kernel functions of the SVM model for spatial prediction of landslides. Their results showed that the RBF function (81%) outperforms other kernel types (polynomial = 71.0%, sigmoid = 40%, and linear = 63%). Several other researchers such as [8–11] investigated the SVM model for landslide susceptibility assessment and reported satisfactory results. However, the variations in SVM prediction capability remain only partially understood and more studies on its parameters and kernel functions could provide useful information for advancing landslide modelling techniques.

This paper presents a comprehensive evaluation of the rectified linear unit (ReLU) kernel function for SVM-based landslide modelling. The kernel function, ReLU is widely used in deep learning due to its advantages over other kernel types. The rest of the paper presents the dataset used in this study, modelling methods and procedures, and experimental results obtained.

2 Methodology

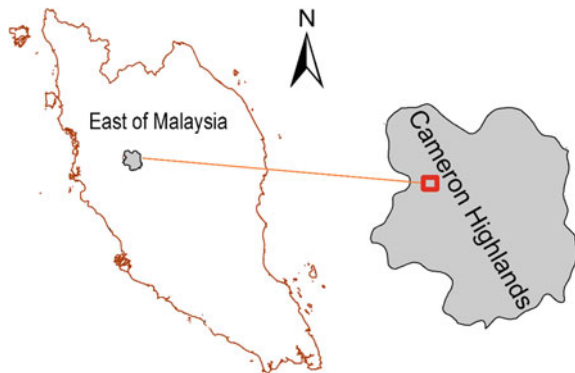
2.1 Study Area and Dataset Modelling

The study area selected was located in the Cameron Highlands in the northern central part of Peninsular Malaysia. It is a tropical rainforest region, geographically located at between $101^{\circ} 24' 00''$ E and $101^{\circ} 25' 10''$ E latitudes and $4^{\circ} 30' 00''$ N and $4^{\circ} 30' 55''$ N longitudes (Fig. 1). The topography of the area is described as hilly and mountainous with land slope ranges of from 0 to 78 degrees. In addition, the lithology in the Cameron Highlands mainly consists of Quaternary and Devonian granite and schist. The granite is classified as megacrystic biotite granite.

The LiDAR data were acquired from an average flight height of 1510 m on January 15, 2015. The data were acquired over the study area and resulted in nearly 8 points per square meter with a 25,000 Hz pulse rate frequency. The absolute accuracy of the LiDAR data should meet the root-mean-square errors of 0.15 m in the vertical axis and 0.3 m in the horizontal axis. The LiDAR data were used to construct a very high-resolution (0.5 m) digital elevation model (DEM) of the area. The DEM model was used to derive the main landslide conditioning factors such as altitude, slope, aspect, curvature, and topographic roughness index (TRI). The topographic map of the study area is presented by a hillshade map shown in Fig. 2.

In addition, the land use map was prepared by classifying a SPOT 5 image (10 m spatial resolution) using a supervised classification method. The method also included refinements and field verification and the final land use map consisted of 11 classes. Additionally, topographical databases were used to derive the road,

Fig. 1 Map of Cameron Highlands located in the Peninsular Malaysia



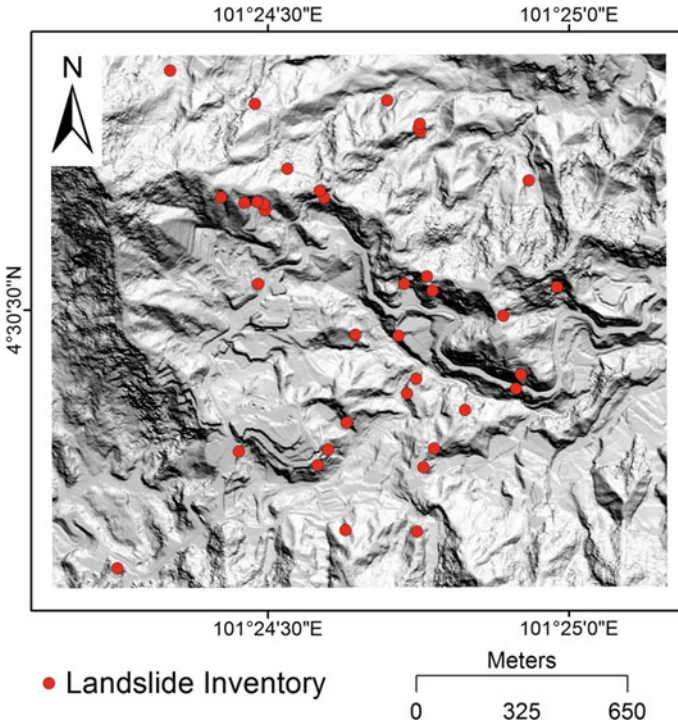


Fig. 2 Topographic map of the study area, a subset from Cameron Highlands

stream, and lineament layers used to prepare the three factors related to these datasets. Finally, vegetation density and normalized difference vegetation index (NDVI) were derived from SPOT image and used as conditioning factors. Overall, 11 factors were prepared and used in the modelling framework (Fig. 3). These factors were reclassified by the quantile classification method in an ArcGIS 10.4 environment.

2.2 Kernel Tricks of SVM

Given a landslide training dataset, the SVM [12, 13] model requires the solution of the following equations:

$$\begin{aligned}
 & \min_{w, b, \xi} \frac{1}{2} w^T w + C \sum_{i=1}^l \xi_i \\
 & \text{subject to } y_i (w^T \phi(x_i) + b) \geq 1 - \xi_i, \\
 & \quad \quad \quad \xi_i \geq 0
 \end{aligned} \tag{1}$$

To solve non-linear problems, SVM maps training vectors x_i into higher dimensional space using the function \emptyset called the SVM kernel trick. A SVM algorithm searches for the optimum hyperspace that can separate the training classes in the higher dimensional space. To allow some errors and to improve the generalization capability of SVM, the penalty parameter $C > 0$ is used. In addition, $K(x_i, x_j) = \emptyset(x_i)^T \emptyset(x_j)$ is called the kernel function. Several kernels (Table 1) have been proposed for the SVM algorithm. In addition to standard kernels, researchers also introduced several new kernels in an attempt to improve the SVM performance for specific applications. This study tries to assess the commonly used ReLU activation function in deep learning for SVM-based landslide modelling. The details of this kernel are described in the following section.

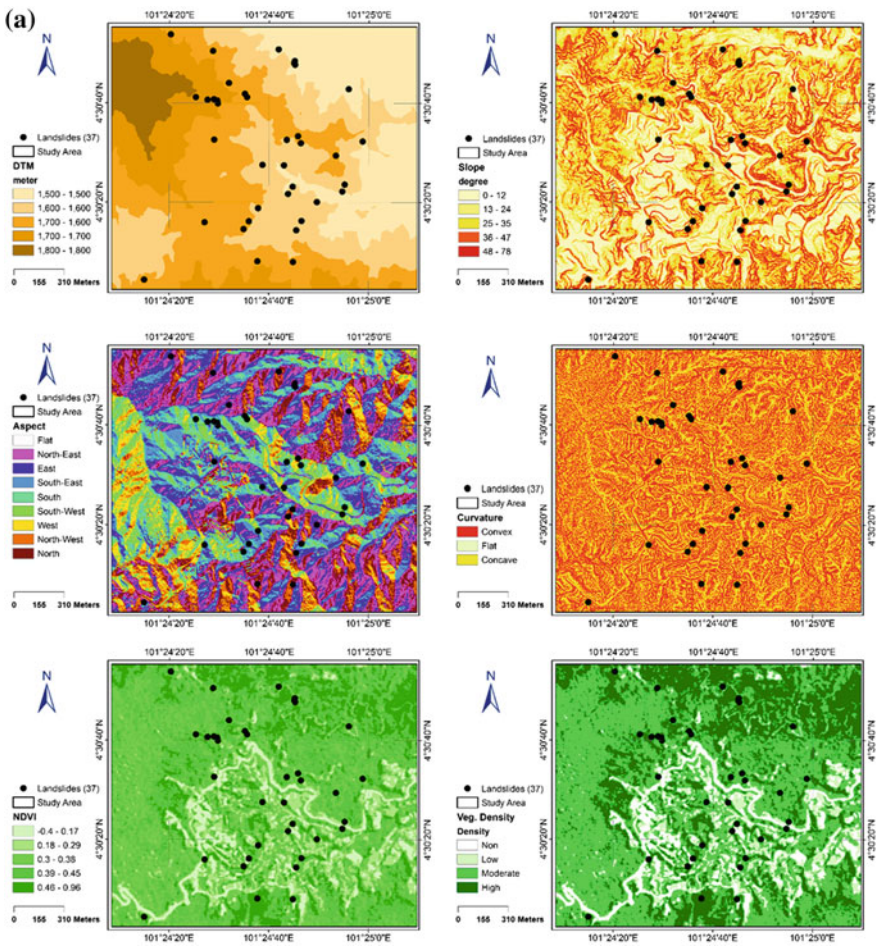


Fig. 3 a Landslide conditioning factors, b Landslide conditioning factors

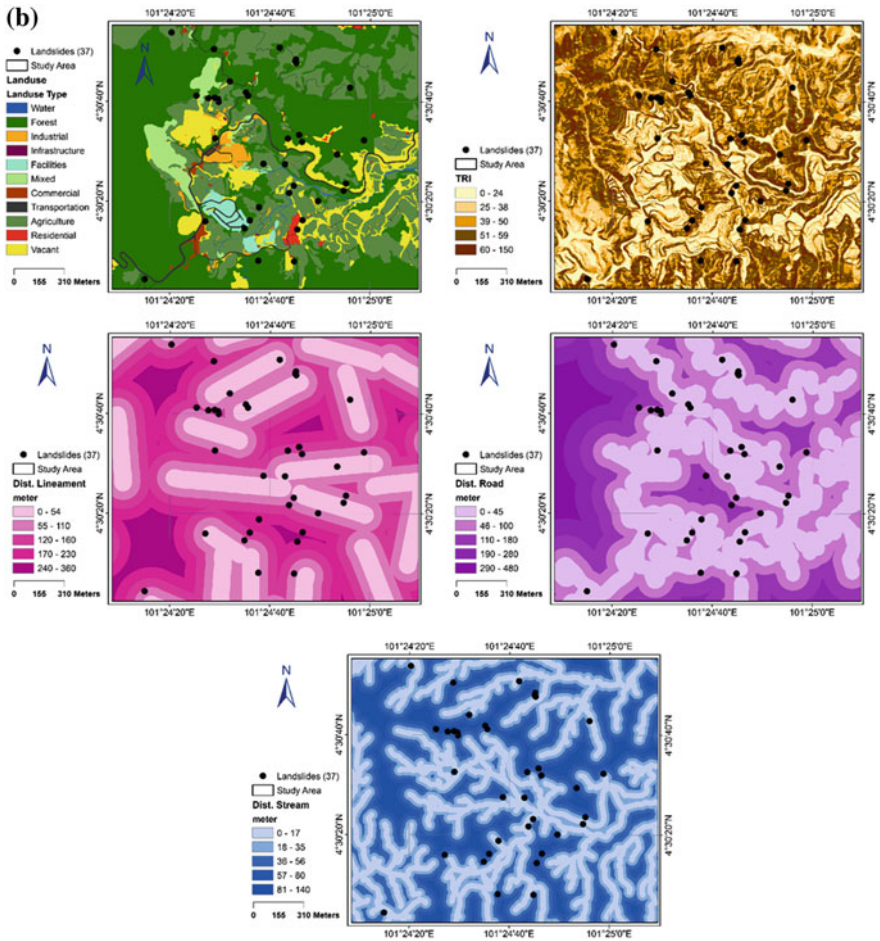


Fig. 3 (continued)

Table 1 Details of standard SVM kernel functions used for landslide susceptibility assessment

Kernel function	Formula	Parameters
ReLU	$f(x) = \max(0, x)$	Penalty parameter (C)
Linear	$K(x_i, x_j) = x_i^T x_j$	Penalty parameter (C)
Polynomial	$K(x_i, x_j) = (\gamma x_i^T x_j + r)^d$	Penalty parameter (C) Kernel width (γ) Polynomial degree (d)
RBF	$K(x_i, x_j) = e^{-\gamma(x_i - x_j)^2}$	Penalty parameter (C) Kernel width (γ)
Quadratic	$K(x_i, x_j) = (\gamma x_i^T x_j + r)^2$	Penalty parameter (C) Kernel width (γ)

2.3 ReLU Kernel Function

The standard method is to model a neuron's output (f) in deep learning as a function of its input x is $f(x) = \tanh(x)$. As part of improving the training time complexity of deep learning while keeping the non-linearity nature of neural networks, the ReLU activation function $f(x) = \max(0, x)$ was introduced [14]. According to Nair and Hinton (2010), deep convolutional neural networks with ReLU train several times faster than their equivalents with tanh units. A smooth approximation to the ReLU is the analytic function as shown in the following expression (called the softplus function):

$$f(x) = \ln(1 + e^x) \quad (2)$$

Advantages of the ReLU function include fast and efficient computation, scale-invariant, and sparsity. For further details of the ReLU function, the reader can refer to the work of [15].

3 Results and Discussion

This study was aimed at evaluating the commonly used activation function (ReLU) in deep learning as a kernel function for SVM-based landslide modelling. The modelling procedure was implemented in a Matlab R2016b programming environment using the built-in statistical and machine learning functions. A personal computer with the following specification was used: Core i7 CPU @2.00 GHz, 16.0 GB installed memory (RAM), and a 64-bit Windows operating system.

The ReLU kernel function was compared with four other kernel functions (linear, polynomial, RBF, and quadratic) in our experiments. To avoid an over-fitting problem while evaluating the accuracy of each kernel function, different subsets and cross-validation accuracy assessment were used. Overall, four subsets with different factor subset percentages (100, 81, 54, and 27%) and fivefold cross validation were used (Table 2).

When 100% (Subset 1) of the factors were used, results indicate that the linear kernel function is the best in terms of accuracy Fig. 4, Table 3. The minimum, maximum, and average accuracy achieved by this kernel function were 0.72, 0.87, and 0.81 respectively. In addition, the standard deviation of the accuracies obtained from 100 runs evaluated for the linear kernel function was 0.028. This indicates that with all factors included in the SVM model, the linear kernel function could achieve relatively stable accuracy. On the other hand, RBF and polynomial kernel functions achieved higher average accuracy (0.79, 0.78) than ReLU and quadratic functions (0.74, 0.72). The standard deviation statistics show that the RBF (0.030) is more stable than ReLU and quadratic kernels. In the second subset, vegetation density and NDVI factors were removed from the analysis and the accuracy of the SVM

Table 2 Subsets of landslide conditioning factors used to evaluate the kernel functions of the SVM model for landslide modelling.6

Subset 1 (100%)	Subset 2 (81%)	Subset 3 (54%)	Subset 4 (27%)
Altitude	Altitude	Altitude	Altitude
Slope	Slope	Slope	Slope
Aspect	Aspect	Aspect	Curvature
Curvature	Curvature	Curvature	
Land use	Land use	Land use	
TRI	TRI	TRI	
Distance to stream	Distance to stream		
Distance to road	Distance to road		
Distance to lineament	Distance to lineament		
NDVI			
Vegetation density			

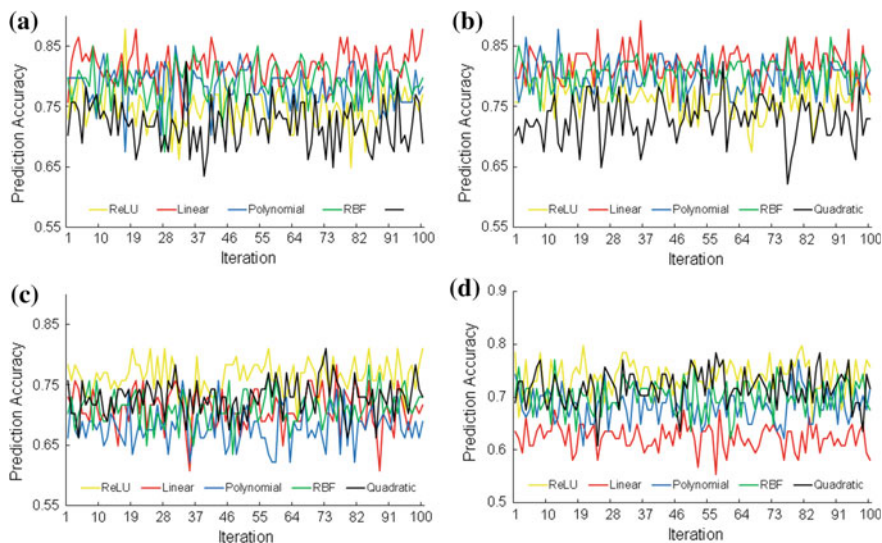


Fig. 4 Prediction accuracy of the SVM model with various kernel functions assessed with different factor subsets, **a** subset 1(100%), **b** subset 2 (81%), **c** subset 3 (54%), and **d** subset 4 (27%)

model with the five kernels was calculated. Similarly, results show that the RBF and polynomial kernels outperform other kernels in terms of average accuracy.

The RBF function was found to be more stable with a standard deviation of 0.026 than other kernels. Using the third and fourth subsets of factors, results indicate that the ReLU kernel outperforms other kernel functions. The average accuracy of the SVM model with an ReLU kernel for the third and fourth subsets

Table 3 Summary statistics of SVM prediction accuracy assessment with various kernel functions and four factor subsets

Factor subset	Summary statistics of accuracy	ReLU	Linear	Polynomial	RBF	Quadratic
100%	Minimum	0.64	0.72	0.67	0.67	0.63
	Maximum	0.87	0.87	0.85	0.85	0.82
	Average	0.74	0.81	0.78	0.79	0.72
	Standard deviation	0.034	0.028	0.031	0.030	0.036
81%	Minimum	0.67	0.74	0.74	0.74	0.62
	Maximum	0.82	0.89	0.87	0.86	0.82
	Average	0.76	0.81	0.79	0.80	0.72
	Standard deviation	0.029	0.026	0.026	0.024	0.035
54%	Minimum	0.68	0.60	0.62	0.63	0.66
	Maximum	0.81	0.78	0.75	0.78	0.81
	Average	0.76	0.70	0.68	0.71	0.72
	Standard deviation	0.027	0.031	0.031	0.027	0.028
27%	Minimum	0.64	0.55	0.60	0.62	0.60
	Maximum	0.79	0.67	0.77	0.77	0.78
	Average	0.73	0.62	0.68	0.70	0.71
	Standard deviation	0.030	0.023	0.029	0.030	0.032

was 0.76 and 0.73 respectively. In addition, the standard deviation statistics show that the ReLU and RBF kernels are more stable than other kernels when third subset of the factors was used. In contrast, when the fourth subset was used, the linear kernel (0.023) was found to be more stable than other types of kernel functions.

The results presented in Fig. 2 and Table 3 show that the accuracy of the SVM model was affected by the kernel function used and the factor subset used as predictors. Experiments showed that the linear and polynomial kernels could achieve better accuracies with a greater number of factors. Instead, with a lesser number of factors, the ReLU and RBF kernel functions were found to be more accurate and stable. A study by [16] showed that there is no need to map data to higher dimensional space if the number of predictors is large and using the linear kernel function can achieve satisfactory results. In other words, the non-linear kernels do not improve the accuracy of the SVM model. Another advantage of using the linear kernel is that one needs to search only for the optimum parameter C. However, in modelling landslide phenomena, a large number of factors requires costly data and further technical issues can arise. By using a large number of factors, multicollinearity and noisy data problems can reduce the efficiency of modelling performance [17, 18]. Therefore, using non-linear kernels in SVM-based landslide modelling is important. The ReLU kernel function has a number of advantages over the RBF kernel such as faster training, sparsity and a reduced likelihood of a vanishing gradient.

4 Conclusion

This study presented an assessment of the ReLU kernel function for SVM-based landslide spatial prediction in a tropical region. To conduct the experiments, a very high resolution DEM was constructed from LiDAR point clouds acquired over the Cameron Highlands in Malaysia. Overall, 11 landslide conditioning factors were used and to avoid an over-fitting problem, four subsets with differing numbers of factors were used. Using overall accuracy calculated by fivefold cross validation, the ReLU kernel was compared with linear, polynomial, RBF, and quadratic kernels. Results showed that there is no need to map data into higher dimensional space when using a large number of landslide factors (>8 factors). In contrast, with a smaller number of factors (<6 factors), the ReLU achieved the best results and the RBF kernel was found to be better than other types of kernel functions. These results indicate that more attention paid to the development of new kernels for the SVM algorithm should improve landslide susceptibility assessment techniques with small datasets. This may also be useful for landslide modelling in data-scarce environments. Although the results of this study are useful to the landslide research community, further detailed assessments with various datasets from different geographic locations of ReLU kernel should be made.

References

1. Crozier MJ (1999) Landslides. Environmental geology. Springer, Netherlands, pp 371–375
2. Pradhan B (2013) A comparative study on the predictive ability of the decision tree, support vector machine and neuro-fuzzy models in landslide susceptibility mapping using GIS. *Comput Geosci* 51:350–365
3. Tien Bui D, Pradhan B, Lofman O, Revhaug I (2012) Landslide susceptibility assessment in Vietnam using support vector machines, decision tree, and Naive Bayes Models. *Math Probl Eng* 974638. doi:[10.1155/2012/974638](https://doi.org/10.1155/2012/974638)
4. Xu C, Dai F, Xu X et al (2012) GIS-based support vector machine modeling of earthquake-triggered landslide susceptibility in the Jianjiang River watershed, China. *Geomorphology* 145:70–78
5. Pourghasemi HR, Jirandeh AG, Pradhan B et al (2013) Landslide susceptibility mapping using support vector machine and GIS at the Golestan Province, Iran. *JESSE* 122(2):349–369
6. Ballabio C, Sterlacchini S (2012) Support vector machines for landslide susceptibility mapping: the Staffora River Basin case study, Italy. *Math Geosci* 44(1):47–70
7. Hong H, Pradhan B, Jebur MN et al (2016) Spatial prediction of landslide hazard at the Luxi area (China) using support vector machines. *EES* 75(1):40
8. Lee S, Hong SM, Jung HS (2017) A Support vector machine for landslide susceptibility mapping in Gangwon province, Korea. *SUSTAIN* 9(1):48
9. Du W, Wu Y, Liu J et al (2016) Landslide susceptibility mapping using support vector machine model. *EJG*:7069–7084
10. Peng L, Niu R, Huang B et al (2014) Landslide susceptibility mapping based on rough set theory and support vector machines: A case of the Three Gorges area, China. *Geomorphology* 204:287–301

11. Marjanović M, Kovačević M, Bajat B et al (2011) Landslide susceptibility assessment using SVM machine learning algorithm. *Eng Geol* 123(3):225–234
12. Boser BE, Guyon IM, Vapnik VN (1992, July) A training algorithm for optimal margin classifiers. Paper presented at Proceedings of the Fifth annual workshop on computational learning theory, pp 144–152
13. Cortes C, Vapnik V (1995) Support-vector networks. *Mach Learn* 20(3):273–297
14. Nair V, Hinton GE (2010) Rectified linear units improve restricted boltzmann machines. Paper presented at Proceedings of the 27th International conference on machine learning (ICML-10), pp 807–814
15. Krizhevsky A, Sutskever I, Hinton GE (2012) Imagenet classification with deep convolutional neural networks. *Adv Neural Inf Process Syst*:1097–1105
16. Hsu CW, Chang CC, Lin CJ (2003) A practical guide to support vector classification. Technical report, Department of Computer Science, National Taiwan University, July 2003. <https://www.csie.ntu.edu.tw/~cjlin/papers/guide/guide.pdf>
17. Pradhan B, Seeeni MI, Kalantar B (2017) Performance evaluation and sensitivity analysis of expert-based, statistical, machine learning, and hybrid models for producing landslide susceptibility maps. In: *Laser scanning applications in landslide assessment*. Springer International Publishing, pp 193–232
18. Pradhan B, Sameen MI (2017) Landslide susceptibility modeling: optimization and factor effect analysis. In: *Laser scanning applications in landslide assessment*. Springer International Publishing, pp 115–132

Subsurface Structural Pattern Distributions of the Magnetic Anomalies in Part of the Nigerian South-Western Precambrian Basement Complex for Sustainability

John Stephen Kayode, Mohd Nawawi Mohd Nordin
and Khiruddin Abdullah

Abstract A study using the subsurface structural patterns technique was carried out to locate, classify and outline the magnetic anomaly source rocks underlying the Omu-Aran Schist belt zone together with determination of the depth of these various source rocks within the study area for sustainability. The processes were carried out through a series of E-W and N-S geomagnetic cross-sections of 58.70 by 56.8 km spread across the study area in part of the Nigerian South-western Precambrian Basement Complex. The primary objective of this study was to use an uncomplicated technique to locate these magnetic anomalies and identify the mineralization potential in the area. The subsurface geological structural patterns in this area were adequately mapped using the Oasis Montaj 2014 source parameter imaging function integrated with Surfer 10 and euldph-x algorithms that automatically compute the depths of the various magnetic anomaly sources using aeromagnetic data acquired from the Nigerian Geological Survey Agency. These anomaly sources as delineated, consist of arrays of north-north-east and south-south-west influencing the underground structures that control the surface geologic characteristics which determine the mineral potential in parts of the north-east, the north-west and the south-western zones of the study area with very low and high values of total magnetic intensity. The large dome-shaped structure that overlies a buried block of inferred meta-sedimentary rocks in this area suggests that subsurface mineral distributions in this area may perhaps be influenced by its location in the highly mineralized Nigerian South-western Basement Complex together with the rich mafic and ultramafic granitic-migmatite Basement Terrain that also underlies the area.

J.S. Kayode (✉) · M.N. Mohd Nordin · K. Abdullah
Geophysics Unit, School of Physics, Universiti Sains Malaysia, 11800 Gelugor, Penang,
Malaysia
e-mail: jskayode@gmail.com

1 Introduction

Many scholars have defined and applied the subsurface structural patterns technique in diverse ways. For example, [1, 2] used the approach on geophysical inversion with the application of the neural nets to study the subsurface. Bois [3] applied the technique to prospect for oil and gas and for the characterization of reservoirs. [4] compared the advantages of wavelet transformation over the Fourier transformation. In furtherance to its application in geophysical methods, Keskes [5], used the technique in his studies. The method is applicable in many fields of study [6].

The application of the subsurface structural patterns technique to establish, classify and define the source rocks of magnetic anomalies in the study Omu-Aran area got its impetus from the fact that the technique makes it possible for computers to mathematically perform intelligent tasks from the aeromagnetic datasets and thereby produce a representation of the integrated geologic structures and shapes of the anomalies.

The magnetic anomalies within the area are the basis by which magnetic minerals are enclosed. These magnetic anomalies are frequently associated with core subsurface basement rocks as the parent rocks. Interpretation of the data was aimed at outlining the regional structural framework of the existing structural patterns of the bedrocks, and at discovering systematic trends for shallow and near subsurface geological features favouring mineralogy in the area [7].

The diversity in the distribution of the magnetization of the Earth crust's is responsible for the formation of the magnetic anomalies sources deep down in the subsurface [8]. A particular magnetic mineral lies within the near surface and produces the local effect of the anomalies [9] while those at a depth of several kilometers—down to the Curie point—produce the regional magnetic effect [10, 11]. In potential fields mapping, lots of challenges confronted the map interpreters and complicate issues such as the source geometries and the direction of magnetization [12].

A large quantity of high quality literature discussing various methods designed for the estimation of the magnetic anomalies shaped by diverse sources has been published with some remarkable achievements in the interpretations [13]. Many studies applied the amplitude and energy spectra of the anomalous fields to efficiently estimate depths to the source of magnetic anomalies, the horizontal and vertical extents, and the magnetization contrasts of the causative bodies [11]. Application of the frequency-domain approach was established as a valuable tool in the delineation of most of the geological features such as a two-dimensional slab and so forth [11, 14]. The success achieved by the use of the techniques for computation of the subsurface magnetic anomalies arises from a variety of models, for instance a line of dipoles was made possible [13, 15].

Some of the literature has analytical assertions for a range of magnetic source parameters such as the depth and so forth. The difficulties arising from the inverse approach have also been resolved and made available via many journals, dividing the techniques into two categories of classification: (i) frequency or spectral

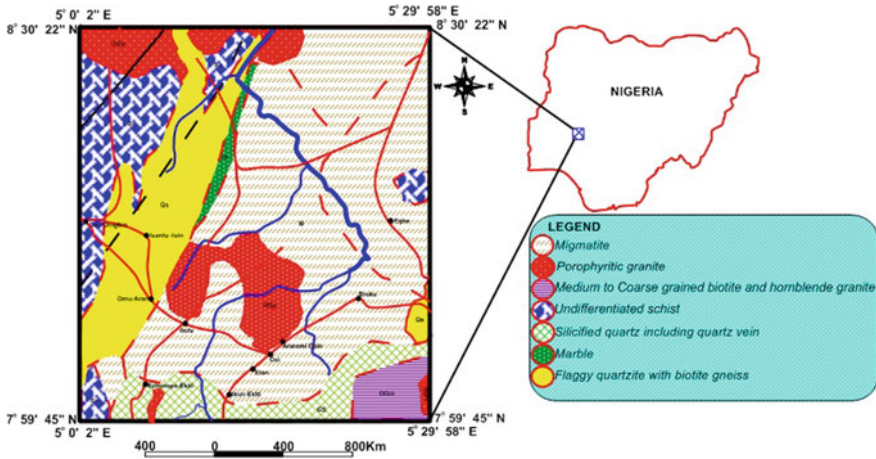


Fig. 1 Detailed geological map of the study area

techniques and (ii) space domain methods [16]. On the other hand, existing modern day space domain techniques are commonly establish on the developmental philosophy. Spectral analysis techniques, though more recent, have made a significant impact on the interpretations of potential field data [11, 17].

In this paper, geophysical and geological datasets were used to study the patterns of the magnetic anomalies within the subsurface structures in the study area, and proposed major mineralized controlling factors by gridding the data in the Omu-Aran Schist belt. The magnetic data acquired was processed and interpreted with the primary aim of defining the subsurface geological and magnetic anomaly structural patterns across longitudes $4^{\circ} 59' 47.26''\text{E}$ and $5^{\circ} 29' 57.95''\text{E}$, and latitudes $7^{\circ} 59' 45.6''\text{N}$ and $8^{\circ} 30' 22.21''\text{N}$ bounded by a land area of about $3,334.16 \text{ km}^2$ (Fig. 1). Data enhancement processes with the application of various filtering techniques to improve the data signals were carried out on the aeromagnetic data.

2 Methodology

2.1 Data Acquisition

The magnetic data was obtained at right angles to the prime local geological strike alongside a sequence of NW-SE flight lines with a spacing of 0.5 km and an average flight elevation of about 80 m, while the tie lines were recorded at average intervals of about 2.0 km [7]. The data were recorded at average intervals of 0.1 s using a Caesium Vapor magnetometer of 3_Sintrex CS3 specifications, with a FASDAS magnetic counter and radar specifications of **KING KR405/KING KR405B** altimeters. Fugro Airborne Survey Services and Patterson Grant and

Watson (PGW) from Canada carried out the data collection from 2007 to the end of 2009. *Enviro Baro/Digiquartz* barometric altimeter specifications were used to cover the entire country. The aeromagnetic data was acquired with narrow line spacing and subtle recording intervals that give the resolution of the magnetic anomalies produced a better quality than that from general high-altitude surveys. The data were made available for research purposes by the Nigerian Geological Survey Agency. The huge technical hitches within the subsurface geology of the Basement environments make subsurface structural delineation awkward for most parts, especially the Nigerian Basement Complex [7].

Necessary data corrections were performed on the magnetic data using the International Geomagnetic Reference Field (IGRS) of January 2005 to remove the geomagnetic gradient from the data. The aeromagnetic data was georeferenced using World Geodetic System 1984 ellipsoid zone 32 N and the Universal Transverse Mercator (UTM) coordinate system for comparative study with the geological map of the area.

2.2 Magnetic Method of Data Processing

In magnetic processing, application of the Fast Fourier Transformation to the data is the first step to success. The method helps in the faster computation of the continuous and discrete potential field data and is less stressful than the Taylor Series Method. Through this approach, the aeromagnetic data was transformed from the space domain to the frequency domain [18].

Using the Fourier transform theory, any functions in the space domain are represented in the frequency domain given by

$$f(x) = a_0 + \sum_{n=1}^N \left[a_n \cos\left(\frac{n\pi}{L}x\right) + b_n \sin\left(\frac{n\pi}{L}x\right) \right] \quad (1)$$

$$\Rightarrow a_0 = \frac{1}{2L} \int_{-L}^L f(x) dx \quad (2)$$

where, $2L = \text{period}$.

Also;

$$a_n = \frac{1}{L} \int_{-L}^L f(x) \cos\left(\frac{n\pi}{L}x\right) dx \quad (3)$$

and,

$$b_n = \frac{1}{L} \int_{-L}^L f(x) \sin\left(\frac{n\pi}{L}x\right) dx \quad (4)$$

But $n = 1, 2, 3, 4, 5, \dots, f_{n-1}$

$$\therefore f(x) = \iint_{-\infty}^{\infty} \left[\begin{matrix} R_c(\omega)(\cos \omega x \cos \omega y + \sin \omega x \sin \omega y) + \\ I_c(\omega)(\sin x \cos \omega y + \cos \omega x \sin \omega y) \end{matrix} \right] dx \quad (5)$$

where R_c = Real Component; I_c = Imaginary Component; x = Coordinates along the x -axis (Longitude), and y = Coordinate along the y -axis (Latitude).

$$\therefore f(x)_{ij} = \sum_{i=1}^{\infty} \sum_{j=1}^{\infty} (\alpha_{m,n} C_n C_m^* + \beta_{m,n} C_n S_m^* + \gamma_{m,n} S_n C_m^* + \delta_{m,n} S_n S_m^*) \quad (6)$$

$$\Rightarrow C_m^* = \cos\left(\frac{2m\pi yj}{\tau_2}\right) \quad (7.1)$$

$$\Rightarrow S_n = \sin\left(\frac{2n\pi xi}{\tau_1}\right) \quad (7.2)$$

$$\Rightarrow S_m^* = \sin\left(\frac{2m\pi yj}{\tau_2}\right) \quad (7.3)$$

Equation 6 is a series of simultaneous equations in a matrix. For gridded data, the cross-product terms in the matrix are equal to zero. Hence, the diagonal terms become the inverted matrix, (in other words an n -by- n matrix) [12]. The fundamental wavelength, τ , is the length of the dataset along the x and y directions; that is, $\tau_1 = N$, along the x -direction, while $\tau_2 = M$, along the y -direction. Then

$$\alpha_{m,n} = \frac{K}{M, N} \sum_{i=1}^N \sum_{j=1}^M f(x)_{ij} \cos\left(\frac{2\pi nxi}{N}\right) \cos\left(\frac{2\pi myj}{M}\right) \quad (8.1)$$

$$\beta_{m,n} = \frac{K}{M, N} \sum_{i=1}^N \sum_{j=1}^M f(x)_{ij} \cos\left(\frac{2\pi nxi}{N}\right) \sin\left(\frac{2\pi myj}{M}\right) \quad (8.2)$$

$$\gamma_{m,n} = \frac{K}{M, N} \sum_{i=1}^N \sum_{j=1}^M f(x)_{ij} \sin\left(\frac{2\pi nxi}{N}\right) \cos\left(\frac{2\pi myj}{M}\right) \quad (8.3)$$

$$\delta_{m,n} = \frac{K}{M, N} \sum_{i=1}^N \sum_{j=1}^M f(x)_{ij} \sin\left(\frac{2\pi nxi}{N}\right) \sin\left(\frac{2\pi myj}{M}\right) \quad (8.4)$$

where $K = 1$, if $n = 0$ and $m = 0$, $K = 2$, if $n = 0$ or $m = 0$, but not both.

$K = 4$, if $n > 0$ and $m > 0$, n = harmonic number along x -direction

m = harmonic number along the y -axis. M = number of data points along y -axis, and N = number of points along the x -axis. But $n = N/2$, and $m = M/2$.

From Euler's Equation

$$dB \frac{(x - x_0)}{dx} + dB \frac{(y - y_0)}{dy} + dB \frac{(z - z_0)}{dz} = S(L - B) \quad (9)$$

where B = the observed magnetic field at orthogonal points [19], in other words statistically free points. In addition, (x_0, y_0, z_0) = source of the anomaly location, namely depth. L = base level of the observed magnetic field and S = structural index.

The depth of the magnetic anomaly is given by Eq. 10.

$$z_b = 2z_0 - z_t \quad (10)$$

where z_b = depth to the bottom of the anomaly, z_0 = depth to the deeper anomaly bodies, and z_t = depth to the shallow near-surface anomaly bodies. To avoid the loss of many useful data points, a 3×3 window that gives a higher and better resolution of the near-surface anomalies was selected and used for the data analysis in this paper.

2.3 Method of Structural Index (SI) Determination

In the identification of the SI values using Eq. 9, the point source of the magnetic anomaly burial is considered as a magnetic dipole located at the subsurface position of x_0, y_0 and z_0 , with the change in total magnetic intensity, ΔB , as given in Eq. 11.

$$\Delta B(x, y) = f[(x - x_0), (y - y_0), z_0] \quad (11)$$

Standard potential theory Eq. 9 was used to determine the gradients in the three orthogonal directions, although the data that were processed in this paper are in gridded form, but lines of parallel profiles, (i.e., Fig. 2) were created along the horizontal East-West (six profiles), and the vertical North-South (six profiles) directions as shown in Figs. 3 and 4 respectively before the application of the equation to better map the subsurface of the area.

The x-coordinate in UTM corresponds to the distance along the x-axis. During the analysis, the northings, i.e., the y-coordinate was set to zero to allow plotting of the magnetic values recorded against the x-axis. If this process is applied to Euler's Equation in 9 above, it means the quantity

$$dB \frac{(y - y_0)}{dy} = 0 \quad (12)$$

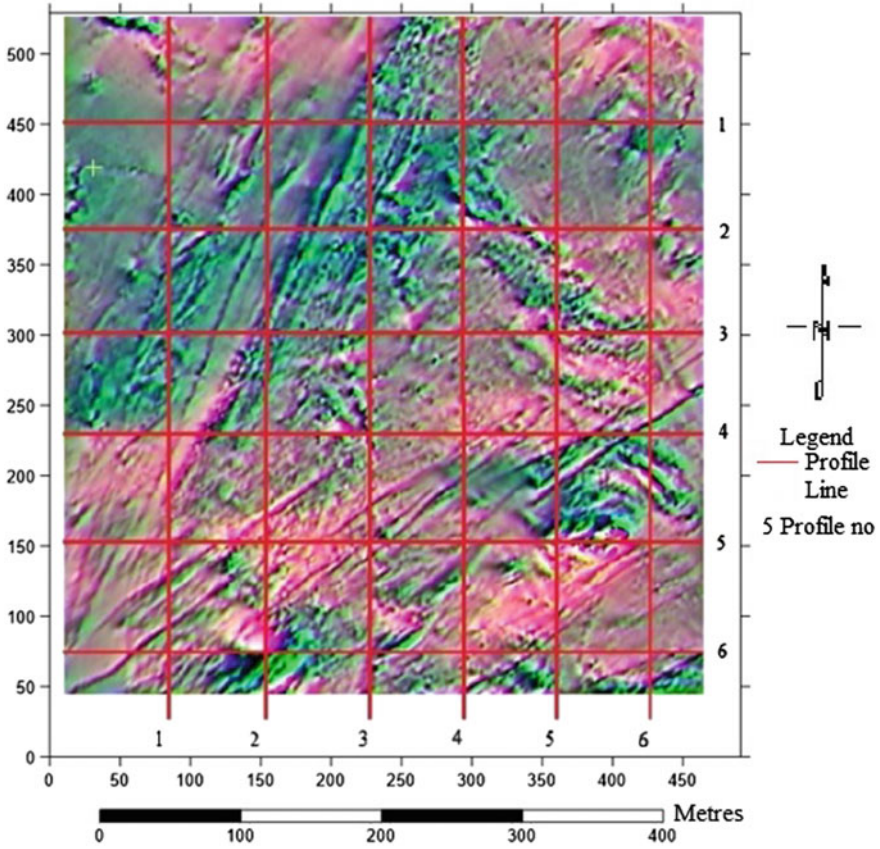


Fig. 2 E-W and N-S profiles of total aeromagnetic intensity of the study area

Fig. 3 A typical E-W profile of the total aeromagnetic intensity of the study area

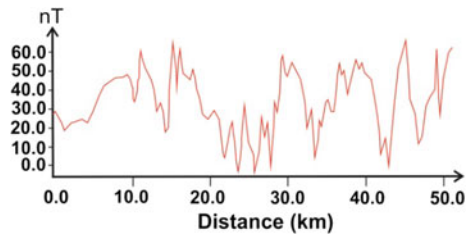
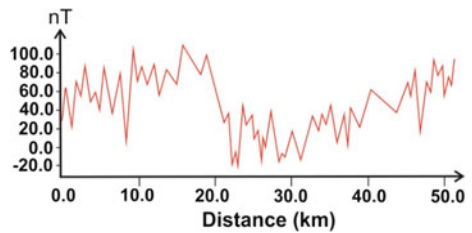


Fig. 4 A typical N-S profile of the total aeromagnetic intensity of the study area



This assumption is broadly accepted and implemented in potential field data analysis and interpretations [19]. Putting Eq. 12 into Eq. 11 yields the following expression

$$dB \frac{(x - x_0)}{dx} - dB \frac{(z_0)}{dz} = -SB(x) \quad (13)$$

Rearranging Eq. 13 helps in the determination of the derivatives from the magnetic data. Therefore, Eq. 14 presents the required Equation given by Thompson [20].

$$z_0 \frac{dB}{dz} + x_0 \frac{dB}{dx} = x \frac{dB}{dx} + SB(x) \quad (14)$$

where (x_0, z_0) = depth and source of the anomaly subsurface location, dB = the magnetic field data recorded, and S = structural index of the magnetic anomaly which invariably defined the type of the magnetic anomaly source rock.

The analytical signal allows the resolution of the dip angle, depths to the causative subsurface geological structures, and the magnetic susceptibility contrast between the causative rock bodies. For a homogeneous function of the Nth degree and also for the $N + 1$ degree of homogeneities, Euler's Equation turns out to be

$$-AS = (x - x_0) \frac{dA}{dx} + (y - y_0) \frac{dA}{dy} + (z - z_0) \frac{dA}{dz} \quad (15)$$

where A = the analytical signal of the total magnetic intensity field and S = the structural index. Therefore, to determine the source parameters, the analytical signal over a magnetic contact is

$$A(x, z) = \alpha \frac{1}{[(x - x_0)^2 + (z - z_0)^2]^{\frac{1}{2}}} \quad (16)$$

where x_0 and z_0 are the position and depth of the magnetic contact and

$$\alpha = 2kFc \sin d \quad (17)$$

where k = susceptibility of the magnetic structure, F = Earth's magnetic field, d = the angle declination, and c = constant for horizontal, total and vertical magnetic fields respectively.

Equation 16, therefore, is the expression for the determination of structural indices for various subsurface models in the study area.

2.3.1 Process of Structural Index (SI) Determination

The magnetic field data were processed through the applications of reduction to the pole and digital convolution filtering processes for the removal of noisy signals, thereby enhancing the quality of the data utilizing folding (Nyquist) frequency and Kriging methods using the euldph-x algorithm developed to automatically calculate depths to the various magnetic anomaly sources from the gridded aeromagnetic data.

Euler Deconvolution was used to calculate the various depths of the magnetized rock bodies. On the other hand, a potential theory more often than not does not give a single inverse explanation—especially with magnetic methods. The subsurface distributions of the magnetic models are relatively distinctive. The shape and nature of the source rocks of magnetic anomalies in this area is a function of the SI values obtained. The depth solutions for all of the 12 traverses are presented in Figs. 5 and 6 with the various calculated SI values together with their corresponding depths.

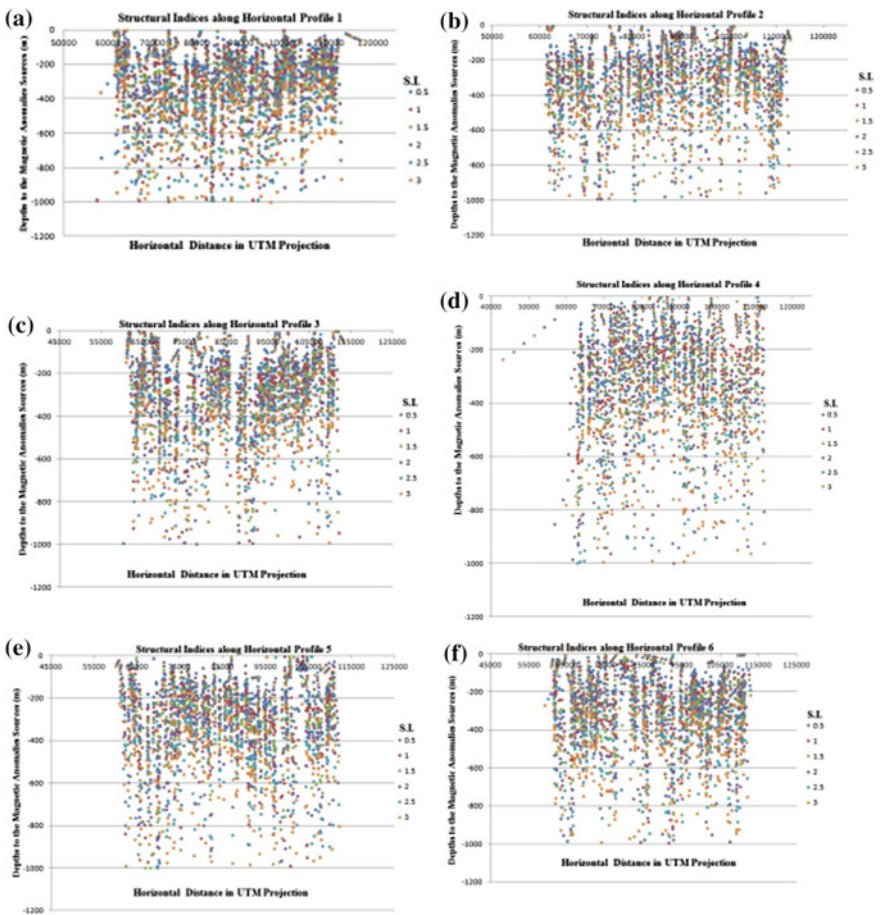


Fig. 5 E-W profiles of plots 1-6 of the study area showing the structural indices with depths

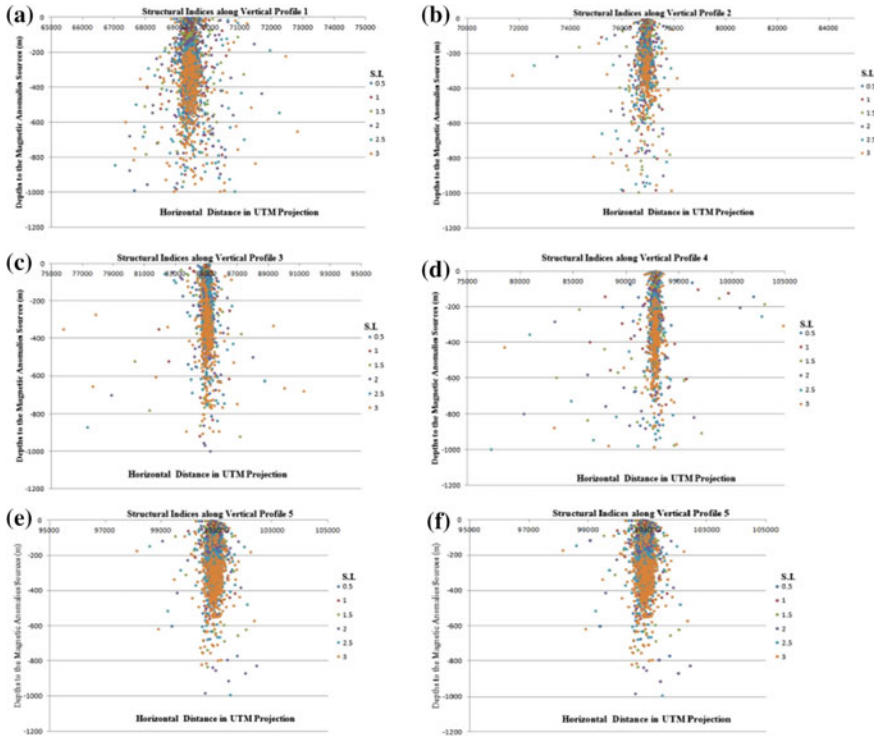








Fig. 6 N-S profiles of plots 1-6 of the study area showing the structural indices with depths

2.4 Subsurface Structural Pattern Analysis

For the purpose of this work the major steps adopted are: (i) Observation of the magnetic anomaly patterns in the study area, (ii) Examination of the interactions among the various subsurface magnetic anomaly structural patterns, (iii) Location of the positions of the magnetic anomaly source rocks, i.e., depth determination of the different structures in the area, (iv) Identification of the various structural shapes and ascribing of colors (Table 1) to differentiate them, (v) Prediction of the subsurface structural patterns in the study area.

To make realistic solutions available for all potential inputs of the magnetic data, and also to execute possibly similar output data to the inputs through the application of statistical computations, the technique of subsurface structural patterns was adopted and executed in this study. The processes enabled quick and accurate identification of magnetic anomaly features; identification of structures to the deepest point possible; correctly distinguished magnetic anomaly shapes at several angles of observation; and correctly classified the various structural shapes. The method helps in the generation of sets of solutions in order to identify the structural

Table 1 Structural Indices, SI, of magnetic anomalies obtained from the depth solutions

SI	Magnetic anomaly type	Colour symbol
0.5	Rock contact	
1.0	Dyke	
1.5	Sill	
2.0	Cylinder	
2.5	Pipe	
3.0	Sphere	

patterns and shapes. The interpreted SI are presented in Table 1. The approach is very relevant to many general purpose uses, particularly for image classifications analysis and structural analysis of various geological shapes, and it has been proved to be better regarding the accuracy and speed of object classification [6].

3 Results and Discussion

3.1 Magnetic Data Interpretation

The magnetic method of geophysical prospecting is known to be the best method capable of defining subsurface structural patterns in detail, irrespective of the area of coverage [7]. The Total Magnetic Intensity Contour map shown in Fig. 7 illustrates the major subsurface structural units in the study area. The map delineates an elongated ridge-like subsurface anomaly that trends predominantly in the NNE-SSW direction. The other major anomalies trending in the most parts of the NE, NW, NE-SW directions in the Omu-Aran area are recognised to be the granitic boulder intrusions into the Basement Complex. The bulk of these anomalies showed various linear structural patterns along the NNE-SSW directions.

The Analytical Signal map presented in Fig. 8 delineates a significant dislodgment in the central part of the study area. The major offset as observed in the map was delineated as the most fundamental subsurface geological structural features controlling mineralization in the area [7]. The map clearly defined the displacements of these structures and it represents the true features together with the rock contacts as emplaced in the area. Through the analytical signal map the exact subsurface geological structural patterns of the study area are exposed and it could be used as the proper subsurface structural configurations of the area. The map clearly distinguished the boundaries of the magnetic anomalies with the granitic rocks terrain easily identify by the higher magnetic intensity values as indicated by the red to magenta colors with white circles on the map.

The different subsurface geological terrains in the Omu-Aran Schist belt are as presented in the E-W and N-S profile plots shown in Figs. 5 and 6. The results from the depths against the x-axis in UTM show some beautiful patterns in the distributions of various structures underlying the area. The range of SI obtained in the

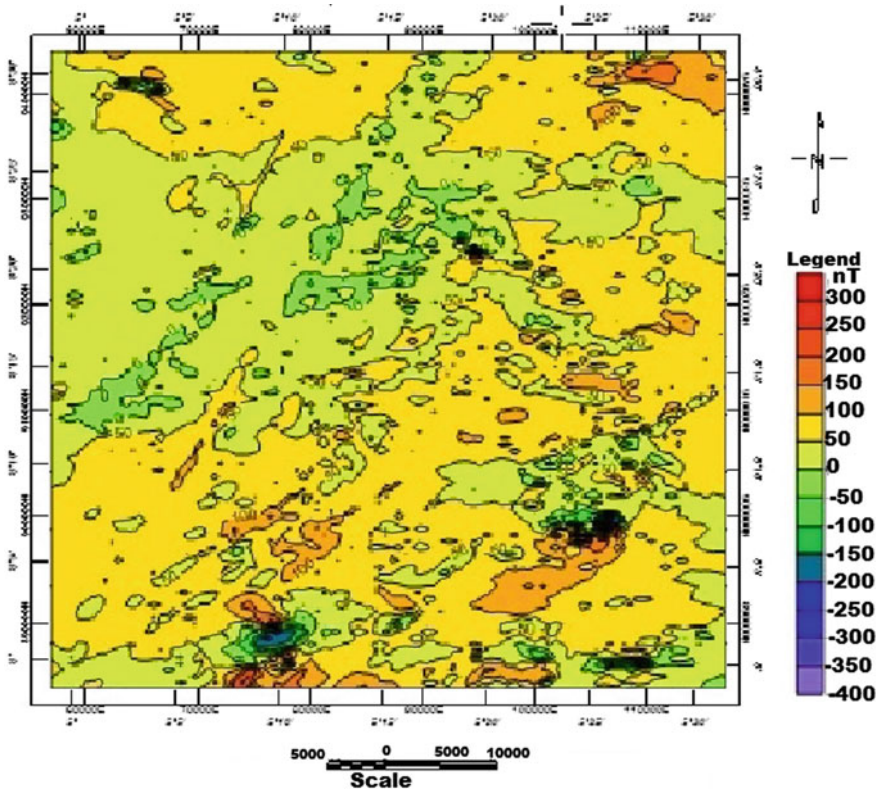


Fig. 7 Aeromagnetic contour map of the study area, created using Surfer 10

area through the applications of the solutions to Eq. 14, as implemented in the *culdph-x* algorithm as presented in Table 1. However, thorough examinations of the clustering as indicated in the indices plotted in Figs. 5 and 6 enabled allotment of SI value to a particular magnetic anomaly source. Although Euler's Deconvolution method involved difficult depths estimator, [7], it is the best of all magnetic methods for depth determination. This study delineates six structural patterns in the Omu-Aran Schist belt. Various geological source models such as rock contacts, dykes, sills, cylinders, pipes and spheres were delineated in the study area.

The complexity of the structures gives rise to the clumsy nature of the Euler's solutions obtained. This research work was able to show the reality of the sub-surface basement faults block patterns that control the mineralogy and lithology of the area under investigation. These trends, in essence, are a function of the magnetic susceptibility variations within the source rocks of the anomalies in the area. The algorithm assigned the SI estimates to the different colours with the six E-W profiles showing quite similar patterns. Figures 5 and 6 showed series of the structures underlying the area with a maximum constrained depth of about 1.2 km. The maximum depth constraint is necessary as the structures densely populate the near

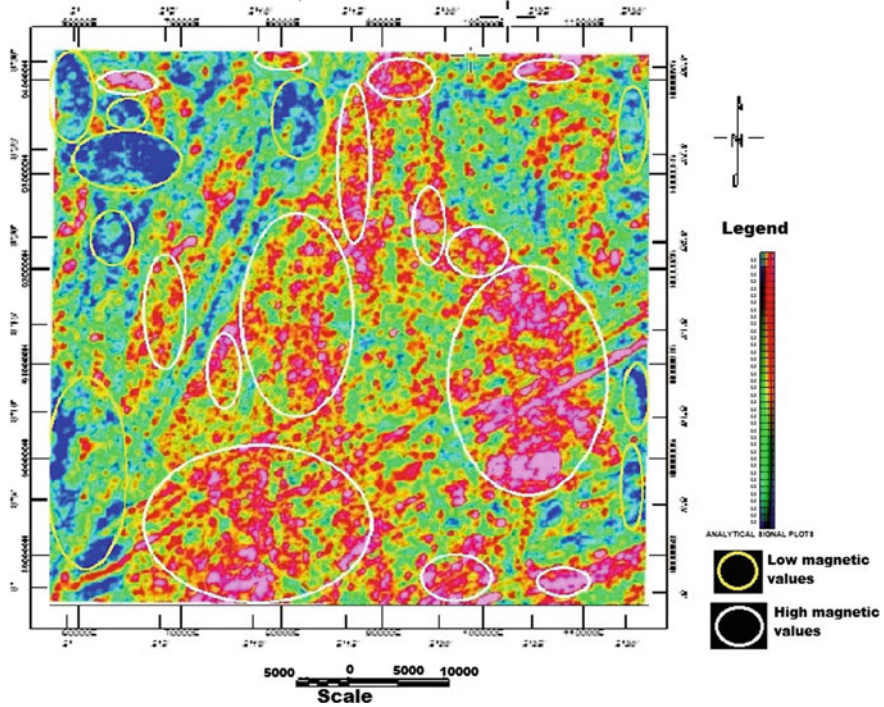


Fig. 8 Analytical signal map of the study area created using Oasis Montaj 2014

surface up to a depth of about 0.5 km, after that the structures become sparsely distributed in a downward direction as shown in Fig. 5 with a north-south series of continental crust magnetic anomalies. The induced magnetic and remnant magnetization in each of these structural blocks contribute to the magnetic inclination of the source parameters across this area.

However, the results of the responses along the six N-S profiles presented in Fig. 6 differed widely from the E-W profiles that showed the structural patterns of the subsurface anomalies blocks distinctly. The grouping of the SI along these north-south profiles could be seen as series of clusters of spherical-like shapes that were vertically positioned with sparsely scattered pieces of anomalies around the central part of each profile. The algorithm delineated magnetic anomalies up to about 1.2 km identical with the E-W profiles. The information on the subsurface structural patterns of Omu-Aran area as revealed in this work is precious to solid minerals investors and mining engineering firms in their search for these precious subsurface materials.

The subsurface activities of the ridge-shaped basement faults and the super firm granitic rocks formed during the metasedimentary deposition of these rocks control to a large extent most of the geological structural shapes and a huge amount of the stratigraphic sequence in the Omu-Aran Schist belt segment of the Nigerian

South-western Precambrian Basement Complex. These basement structural patterns as presented in Fig. 9 correlate well with the patterns obtained in the Analytical Signal method shown in Fig. 8, and also control to a great extent the topography and lithology of the area as visibly observed at the ground surface. It is these magnetic anomalies that on the whole further control the subsurface anomaly patterns and surface stratigraphy at the time of the consolidated gravitational system in this area.

The results of this work confirmed the emplacement of mineral occurrence in the Omu-Aran Schist belt as extremely shallow and structurally controlled. In most places of mining activities visited during the geological fieldwork, it was observed that these precious materials were very close to the ground surface. The study of this phenomena proved the usefulness of aeromagnetic methods of geophysical prospection as the best tool for mapping the structural patterns of subsurface anomalies that correlate well with the geological stratigraphic features in the area of study that are critical to the exploration of solid minerals in the area.

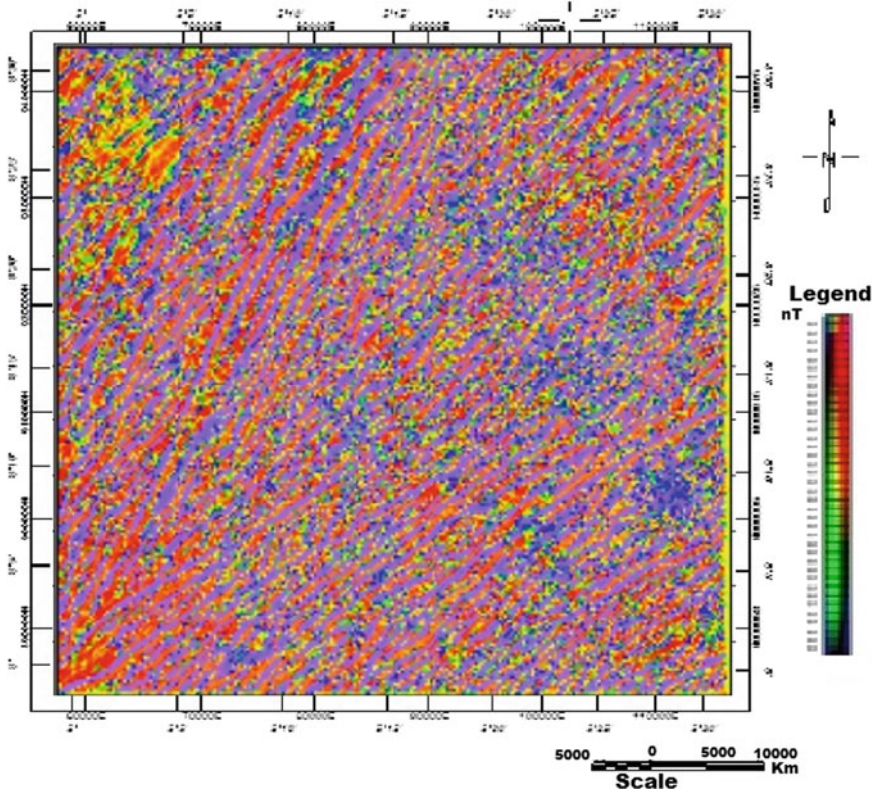


Fig. 9 Map of the Omu-Aran Schist belt zone showing the structural patterns of the subsurface magnetic anomalies

4 Conclusion

The aeromagnetic data was used to define and delineate subsurface structural patterns of the study area for sustainable development of this part of the Nigerian South-western Precambrian Basement Complex. For ease of interpretation, the area was divided into 6×6 E-W and N-S profiles respectively. Various filtering techniques were applied to enhance the data to obtain the best results together with sampling at a Nyquist frequency and the application of an ordinary Kriging method of statistical analysis on the gridded data. The maps of magnetic anomalies generated for the area clearly delineate the subsurface structural patterns controlling the stratigraphic, lithological and topography of the Omu-Aran Schist belt zone. The granitic and metasedimentary terrains of the area are mostly characterized by the high frequency and high amplitude magnetic anomalies. The large dome-shaped structure overlying a buried block of inferred meta-sedimentary rocks in this area suggests that subsurface mineralized distributions may perhaps be influenced by the location of the area in the highly mineralized Nigerian South-western Precambrian Basement Complex together with the rich shallow mafic and ultramafic granitic-migmatite Basement Terrain underlying the area.

The discovery from the present results of the six structural indices is a departure from previous studies that limited structural indices of magnetic anomalies to five. The best estimator of the various values obtained gives the minimum root-mean-square errors selected and grouped into SI values shown in Table 1. The methods for the interpretation of magnetic anomalies adopted for this work helped to better map the hidden subsurface structural anomaly patterns in the Omu-Aran area for sustainability purposes. Though magnetic data are prone to noise, the choice of a small window size together with the application of data enhancement techniques gave high accuracy to the SI determination and the analytical signal plots of the source parameters. Excellent results were achieved through the statistical analysis as the aeromagnetic statistical properties greatly differ from the noise signals properties, and separation of the two by the application of various filters becomes a straightforward task. This research work has been able to shed great light on the patterns of the anomalies emplaced in the Omu-Aran area. This research was carried out to assist in the prevention of the depletion of subsurface natural resources in order to preserve the ecological equilibrium of the area.

Acknowledgements This research was partially supported by the Universiti Sains Malaysia IPS Postgraduate Fellowship awards.

References

1. Raiche A (1991) A pattern recognition approach to geophysical inversion using neural nets. *Geophys J Int* 105:629–648
2. Al-Garni MA (2016) Artificial neural network inversion of magnetic anomalies caused by 2D fault structures. *Arab J Geosci* 9:156. doi:[10.1007/s12517-015-2256-y](https://doi.org/10.1007/s12517-015-2256-y)

3. Bois P (1980) Autoregressive pattern recognition applied to the delimitation of oil and gas reservoirs. *Geophys Prospect* 28:572–591. doi:[10.1111/j.1365-2478.1980.tb01243.x](https://doi.org/10.1111/j.1365-2478.1980.tb01243.x)
4. Sifuzzaman M, Islam M, Ali M (2009) Application of wavelet transform and its advantages compared to Fourier Transform. *J Phy Sci* 13:121–134
5. Keskes N (1999) Automatic seismic pattern recognition method. Google Patent
6. Fukunaga K (2013) Introduction to statistical pattern recognition. Academic Press
7. Kayode JS, Nawawi MNM, Khiruddin BA (2016) Structural analysis of part of the Nigerian South-western basement complex using aeromagnetic data. In: *Proceeding of 7th international conference on applied geophysics*, pp 145–158
8. Tlas M, Asfahani J (2011) A new best-estimate methodology for determining magnetic parameters related to field anomalies produced by buried thin dikes and horizontal cylinder-like structures. *J Pure Appl Geophys* 168:861–870. doi:[10.1007/s00024-010-0104-2](https://doi.org/10.1007/s00024-010-0104-2)
9. Rozimant K, BÜYÜKsaraÇ A, Bektaş Ö (2009) Interpretation of magnetic anomalies and estimation of depth of magnetic Crust in Slovakia. *J Pure Appl Geophys* 166:471–484. doi:[10.1007/s00024-009-0447-8](https://doi.org/10.1007/s00024-009-0447-8)
10. Hussein M, Mickus K, Serpa L (2013) Curie point depth estimates from aeromagnetic data from death valley and surrounding regions, California. *J Pure Appl Geophys* 170:617–632. doi:[10.1007/s00024-012-0557-6](https://doi.org/10.1007/s00024-012-0557-6)
11. Saleh S, Salk M, Pamukçu O (2013) Estimating curie point depth and heat flow Map for Northern Red Sea Rift of Egypt and its surroundings, from aeromagnetic data. *J Pure Appl Geophys* 170:863–885. doi:[10.1007/s00024-012-0461-0](https://doi.org/10.1007/s00024-012-0461-0)
12. Beiki M, Pedersen LB (2012) Estimating magnetic dike parameters using a non-linear constrained inversion technique: an example from the Särna area, west central Sweden. *Geo Pros* 60:526–538. doi:[10.1111/j.1365-2478.2011.01010.x](https://doi.org/10.1111/j.1365-2478.2011.01010.x)
13. Kayode JS, Nawawi MNM, Baioumy HM, Khalil AE, Khiruddin BA (2014) Delineation of the subsurface geological structures of Omu-Aran area, south-western Nigeria, using aeromagnetic data. In: *AIP conference proceeding*, vol 1657, p 040012. doi:[10.1063/1.4915173](https://doi.org/10.1063/1.4915173)
14. Ates A, Bilim F, Buyuksarac A, Aydemir A, Bektas O, Aslan Y (2012) Crustal structure of Turkey from aeromagnetic, gravity and deep seismic reflection data. *Surv Geophys* 33:869–885. doi:[10.1007/s10712-012-9195-x](https://doi.org/10.1007/s10712-012-9195-x)
15. Megwara JU, Udensi EE (2014) Structural analysis using aeromagnetic data: case study of parts of Southern Bida Basin, Nigeria and the surrounding basement rocks. *Earth Sci Res* 3:27. doi:[10.5539/esr.v3n2p27](https://doi.org/10.5539/esr.v3n2p27)
16. Guo L, Meng X, Shi L (2012) Gridding aeromagnetic data using inverse interpolation. *Geophys J Int* 189:1353–1360. doi:[10.1111/j.1365-246X.2012.05448.x](https://doi.org/10.1111/j.1365-246X.2012.05448.x)
17. Kasidi S, Nur (2013) A spectral analysis of magnetic data over Jalingo and Environs North–Eastern Nigeria. *Int J Sci Res* 2:447–454
18. Abdel Kader A, Kordik P, Khalil A, Mekkawi M, El-Bohoty M, Rabeh T, Refai M, El-Mahdy A (2013) Interpretation of geophysical data at EL Fayoum-Dahshour Area, Egypt using three dimensional models. *Arab J Sci Eng* 38:1769–1784. doi:[10.1007/s13369-012-0385-0](https://doi.org/10.1007/s13369-012-0385-0)
19. Ghidella ME, Zambrano OM, Ferraccioli F, Lirio JM, Zakrajsek AF, Ferris J, Jordan TA (2013) Analysis of James Ross Island volcanic complex and sedimentary basin based on high-resolution aeromagnetic data. *Tectonophysics* 585:90–101. doi:[10.1016/j.tecto.2012.06.039](https://doi.org/10.1016/j.tecto.2012.06.039)
20. Thompson D (1982) EULDPH: a new technique for making computer-assisted depth estimates from magnetic data. *Geophysics* 47:31–37. doi:[10.1190/1.1441278](https://doi.org/10.1190/1.1441278)

The Measurement of Solar Ultraviolet Ambient Dose Using EBT3 Film

Intan Nadia Mohammad Saleh, Umami Shuhada Osman
and Ahmad Fairuz Omar

Abstract Gafchromic EBT3 films were analyzed for their response towards ultraviolet UV-A and UV-B doses of solar radiation. This work was done to investigate the ambient daytime UV dose through the color changes of external beam therapy films, in other words EBT3 that was quantified using a visible absorbance spectroscopy technique. The experiment was conducted by exposing the EBT3 films to ambient solar radiation at several randomly selected places around Universiti Sains Malaysia. The experiment was conducted at three different times of the day (namely morning, noon and afternoon) and on two consecutive days, named as Day 1 and Day 2. The results from Day 1 were later combined to form a calibration dataset generating UV dose (mJ/cm^2) measurement algorithms while data from Day 2 were combined to form a prediction dataset. From the experiment, the most important single wavelength in generating a highly accurate calibration algorithm was 650 nm. The calibration algorithm was developed using wavelengths of 536, 547, 550, 650 and 693 nm, and the coefficient of determination R^2 was recorded at 94.12% with a Root Mean Square Error of Prediction (RMSEP) of $685.85 \text{ mJ}/\text{cm}^2$. All the empirical results presented in this paper show that EBT3 film is capable of giving a good response in quantifying UV dose.

1 Introduction

Ultraviolet (UV) radiation consists of wavelengths between 100 and 400 nm and can be further divided into Vacuum UV ($\lambda = 100\text{--}200 \text{ nm}$), UV-C ($\lambda = 200\text{--}280 \text{ nm}$), UV-B ($\lambda = 280\text{--}315 \text{ nm}$) and UV-A (wavelength of 315–400 nm). The sun is the earth's main natural source of UV radiation [1, 2]. Though small amounts of UV are beneficial in the production of vitamin D and can be used to treat diseases including rickets, psoriasis, eczema and jaundice, continuous or overexposure to solar UV radiation can cause various damaging effects to human such as

I.N. Mohammad Saleh · U.S. Osman · A.F. Omar (✉)
School of Physics, Universiti Sains Malaysia, 11800 Gelugor, Penang, Malaysia
e-mail: thinker_academy@yahoo.com

degenerative effects to the eyes, sunburn and even skin cancer [3–5]. As the solar UV radiation that reaches the earth contains mostly UVA and only a small portion of UVB with no UVC [6], the study of solar UV radiation only focuses on UVA and UVB. The measurement of solar UV radiation is essential in continuously monitoring the level of UV dose in order to minimize human risk against the hazard of UV overdose.

External Beam Therapy 3 (EBT3) film, despite mainly being used for X-ray dose measurements during diagnostic radiology, including computed tomography (CT), interventional radiology (IVR), and quality control (QC) and quality assurance (QA) [7], has been independently tested by several researchers as to its efficiency in measuring UV radiation dose. For example, Aydarous et al. [8] have applied EBT3 film in the measurement of UVA (365 nm), UVB (302 nm) and UVC (254 nm) radiation doses. Their findings indicate that the color changes of the films were dependent on UV intensity as well as wavelength. They also discovered that EBT3 films were approximately 10 times more sensitive towards UVA and UVB compared to UVC. EBT3 films have also been used for the measurement of solar UVA and UVB radiance dose. For example, Tajuddin and Omar [9] applied EBT3 films to the measurement of solar UV (A + B). Through a visible absorbance spectroscopy technique, they discovered that the five best wavelengths that can be used to develop a calibration algorithm for quantifying solar UV dose are 506.77, 604.68, 658.17, 692.99 and 699.83 nm and they managed to obtain the predicted result with $R^2 = 98.3\%$ and $RMSEP = 381.92 \text{ mJ/cm}^2$.

In another application of EBT3 films for the measurement of UV dose, Yusuf et al. [10] applied EBT3 films in the measurement of radiation dose from UV LEDs with peak emission wavelengths of 365 and 375 nm. Through the application of multiple linear regression to the visible absorbance spectra of EBT3 films, they managed to obtain high calibration accuracies with $R^2 = 98.3\%$, $RMSEC = 687.116 \text{ mJ/cm}^2$ and $R^2 = 98.8\%$, $RMSEC = 470.721 \text{ mJ/cm}^2$ for UV LED with peak emission wavelengths of 365 and 375 nm respectively.

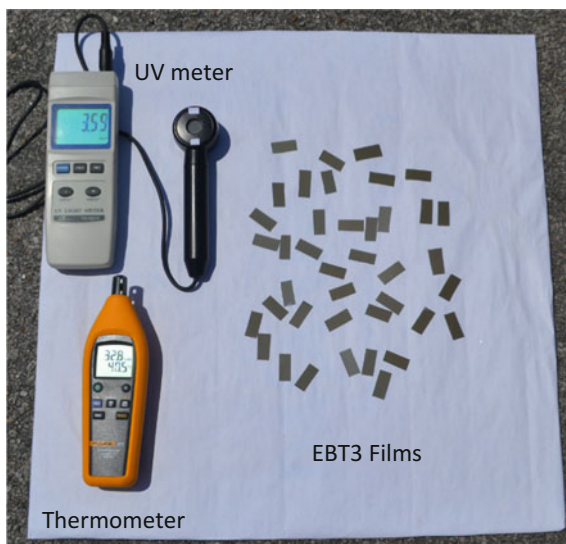
Osman and Omar [11] on the other hand have written a brief review of several different techniques that can be used for the measurement of UV irradiance and listed EBT films as one of the promising techniques in measuring UV radiation dose. Hence, the objective of this research is to test the ability of EBT3 films to retain their accuracy when used to measure the ambient solar UV dose at several randomly selected open places around Universiti Sains Malaysia campus and at three different time (namely morning, noon and afternoon).

2 Materials and Methods

2.1 EBT3 Films Exposure to Solar UV Radiation

The experiments for this research were conducted on two consecutive sunny days namely Day 1 and Day 2. The experiments for both Day 1 and Day 2 were conducted in three sessions; in the morning (from 8.30 am until 9.17 am), noon

Fig. 1 Experimental setup for solar UV exposures on EBT3 films



(from 11.50 am until 12.37 pm) and afternoon (from 4.00 pm until 4.48 pm) at different randomly selected open places around Universiti Sains Malaysia. Data from Day 1 were used for the development of a calibration algorithm while data from Day 2 for the prediction accuracy of the developed algorithm.

A total of 46 pieces of EBT3 film was used for each session of the experiment. The EBT3 film was cut into $3\text{ cm} \times 2\text{ cm}$ pieces. All the films were placed on mahjong (white) paper to ensure they did not have direct contact with the surface of the measurement area. The UV meter (YK-35UV) was placed exactly next to the EBT3 films during measurement. The UV meter has two ranges, namely 2 mW/cm^2 ($1.999\text{ mW/cm}^2 \times 0.001\text{ mW/cm}^2$) and 20 mW/cm^2 ($19.99\text{ mW/cm}^2 \times 0.01\text{ mW/cm}^2$) and has an effective detector spectrum between 290 and 390 nm thus making it suitable for the measurement of UVA and UVB irradiance.

During the experiment, one film was taken from the paper every minute along with the reading from the UV meter. After the exposed film was taken away, it was immediately placed in a black envelope to avoid further exposure to UV radiation. After 46 min, all the 46 EBT3 films were collected. A similar experimental setup was used for Day 2 in order to obtain the prediction dataset. Figure 1 shows the experimental setup during the exposure process of EBT3 films to the solar UV radiation.

2.2 Visible Absorbance Measurement

As the accumulated dose is closely related to the color changes of the EBT3 films, a visible absorbance spectroscopy technique was employed to represent the color of

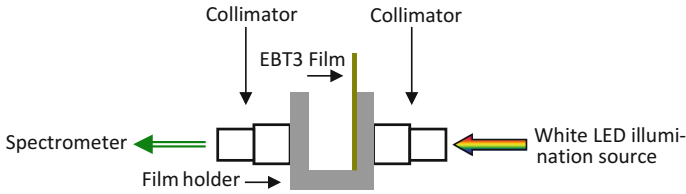


Fig. 2 Visible absorbance spectroscopy measurement of EBT3 film

the films and was subsequently used to determine the measured UV dose. The visible spectroscopy measurement was made using a Jaz spectrometer (Ocean Optics Inc.) with an effective range of wavelength located within the visible spectrum ($\sim 400\text{--}700\text{ nm}$). A white LED was used as the illumination light source.

The Jaz spectrometer was connected to a LS-450 LED Light Source and a CUV 1 cm Cuvette Holder via optical fiber cables. The spectrometer was connected to a computer that was equipped with SpectraSuite software. SpectraSuite is spectroscopy software which is used to capture and analyze spectral data from a spectrometer. An unexposed EBT3 film was used as a reference instead of air to ensure that the range of absorbance measured was smaller and acceptable for the entire films used in the experiment. All the EBT3 films were placed in a CUV 1 cm Cuvette Holder. The absorbance spectroscopy experimental setup is illustrated in Fig. 2.

2.3 The Selection of Wavelengths

Based on the collected spectra and the nature of the films' color transition, only wavelengths between 500.13 and 700.16 contribute to useful information on the color changes of the EBT3 films. One to five values of wavelengths were selected from this region based on their ability to produce a measurement with the highest accuracy (high R^2 (Eq. 1) and low RMSE (Eq. 2) with a P-value preferably below 0.05). The purpose of selecting a different number of wavelengths is to justify the rate of accuracy improvement when a higher number of wavelengths were selected in the development of calibration algorithm. The absorbance for the selected wavelengths was regressed with the measured UV dose (mJ/cm^2) using Minitab (Version 17) software to obtain a calibration algorithm. A coefficient of determination (R^2) greater than 0.8 is generally described as strong, while a value of R^2 lower than 0.5 is generally described as weak. This description however can differ based on the nature of the data being examined.

$$R^2 = \frac{[n \sum xy - (\sum x)(\sum y)]^2}{[n \sum x^2 - (\sum x)^2][n \sum y^2 - (\sum y)^2]} \quad (1)$$

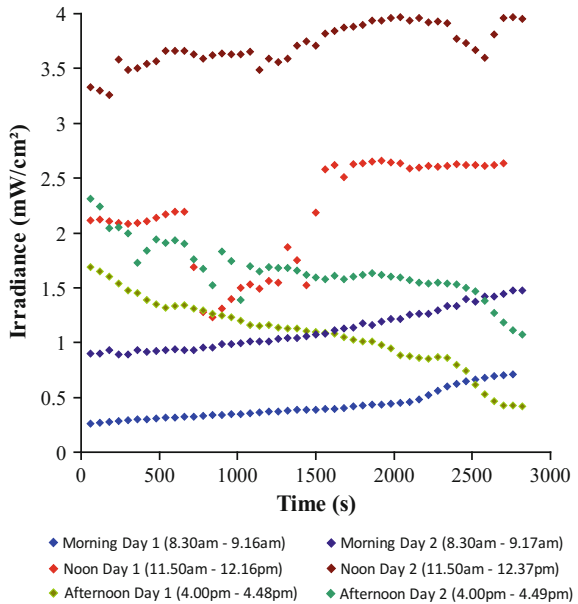
$$RSME = \sqrt{\frac{\sum (y - Y)^2}{n - 1}} \tag{2}$$

3 Results and Discussion

Throughout the experiment the weather was generally sunny in the morning and afternoon. However, at times the sun was covered by rapidly moving clouds during the noon sessions of the experiment. As a result, some drastic falls of UV irradiance value were observed. Figure 3 shows the distribution of UV irradiance throughout the six experimental sessions.

The highest recorded irradiance was 2.658 mW/cm² at 12.22 pm. The lowest recorded irradiance was 0.261 mW/cm² at 8.30 am. The cumulative dose for Day 1 morning, noon and afternoon experimental sessions was recorded at 1162.32 mJ/cm², 5854.80 mJ/cm² and 3032.82 mJ/cm² respectively. On Day 2, the ambient temperature was relatively higher than Day 1 with an average temperature throughout the experiment of 34.7 °C in the morning, 42.6 °C at noon and 39.9 °C in the afternoon. The highest irradiance value obtained was 3.970 mW/cm² at 12.24 pm and 12.36 pm. The lowest irradiance value obtained was 0.891 mW/cm² at 8.35 am. The cumulative doses for Day 2 morning, noon and afternoon experiments were 3138.72 mJ/cm², 10474.80 mJ/cm² and 4733.4 mJ/cm².

Fig. 3 Solar UV irradiance measurements on Day 1 and Day 2



The visible absorbance spectroscopy analysis was first conducted in finding the single wavelength that responds the best with the measured UV dose. Figure 4 shows the graph of R^2 versus wavelength of the morning, noon and afternoon sessions for Day 1 and Day 2.

The best R^2 from the morning session were recorded at wavelengths of 580.25 nm and 640.24 nm for Day 1. For Day 2, the best R^2 was recorded at a wavelength of 640.24 nm. The best R^2 values for the noon session were recorded at wavelengths of 500.13 nm and 620.17 nm on Day 1. For Day 2, the best R^2 were recorded at wavelengths of 500.13 nm and 660.15 nm. The best R^2 was recorded at a wavelength of 640.24 nm on Day 1 for the afternoon session. For Day 2, the best R^2 was recorded at a wavelength of 600.28 nm. Generally, the difference in spectral responsivity is directly related to the total measured dose for each session of the experiment, which in turn is related to the final change in the color of the EBT3 films. It is also influenced by the linearity index or linear relationship between absorbance and UV dose.

In order to obtain a high calibration accuracy, a multiple linear regression technique is frequently employed. Similarly in this experiment, the entire data for Day 1 were combined to form calibration algorithms using a different number and combination of wavelengths. All the data from Day 2 were combined to form the

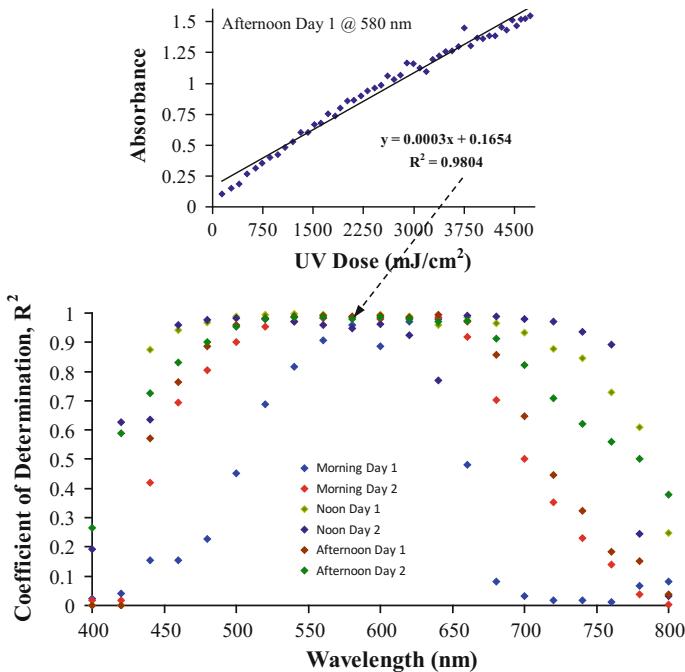


Fig. 4 R^2 versus wavelength for all six experimental sessions and the regression sample result for the Afternoon Day 1 dataset generated at $\lambda = 580$ nm

prediction dataset. Equations 3–7 show the calibration algorithms obtained through the multiple linear regression technique with the respective selected wavelengths.

$$\text{UV Dose (mJ/cm}^2\text{)} = - 98.2 + 6391 A_{650} \tag{3}$$

$$\text{UV Dose (mJ/cm}^2\text{)} = 20.0 + 22656 A_{650} - 23732 A_{536} \tag{4}$$

$$\begin{aligned} \text{UV Dose (mJ/cm}^2\text{)} = & - 108.4 + 20096 A_{650} \\ & + 25050 A_{536} - 38822 A_{547} \end{aligned} \tag{5}$$

$$\begin{aligned} \text{UV Dose (mJ/cm}^2\text{)} = & - 150.6 + 19191 A_{650} + 66495 A_{536} \\ & - 71520 A_{547} - 12274 A_{693} \end{aligned} \tag{6}$$

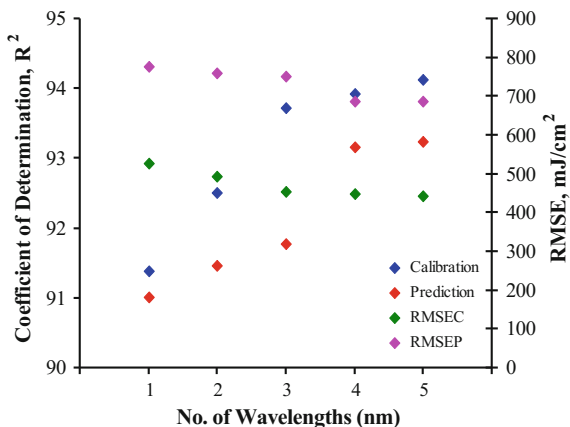
$$\begin{aligned} \text{UV Dose (mJ/cm}^2\text{)} = & - 53.3 + 14679 A_{650} + 61177 A_{536} \\ & + 10085 A_{547} - 17744 A_{693} - 67293 A_{550} \end{aligned} \tag{7}$$

Figure 5 illustrates the increment of calibration and prediction accuracy (in other words a higher value of R^2) in relation to the higher number of selected wavelengths. For single wavelength calibration, which was calculated using absorbance at a wavelength of 650 nm, the R^2 obtained was recorded at 91.39% with RMSEC of 526.78 mJ/cm^2 . The associated prediction result recorded R^2 at 91.01% with RMSEP of 777.92 mJ/cm^2 . The five wavelengths calibration algorithm, which was calculated using wavelengths of 536, 547, 550, 650 and 693 nm, raised R^2 to 94.12% with RMSEC of 442.45 mJ/cm^2 . The prediction result for the five wavelength algorithm recorded R^2 at 93.24% with RMSEP of 685.85 mJ/cm^2 .

From the results it can be observed that the higher number of wavelengths used in the development of a calibration algorithm improves the accuracy of the measurements.

Table 1 lists the other possible random combinations of closely related wavelengths and their respective results developed using the calibration (Day 1) dataset.

Fig. 5 Calibration and prediction results for different numbers of selected wavelengths



All in all, the combination of random but closely related wavelengths (to the best selected wavelengths as written in Eq. 7) may result in up to 1.7% deviation of calibration R^2 and approximately 60 mJ/cm^2 of RMSEC for calibration (RMSEC).

In addition, Fig. 6 shows results from other randomly selected wavelengths in the development of the calibration algorithm. The graphs shows R^2 and RMSEC for the algorithm developed using two, three and four wavelengths which were randomly selected between 500.13 and 700.16 nm.

From the graphs it can be seen that although the variation of R^2 is within 3.33%, there is still the possibility that incorrectly combined wavelengths may significantly reduce the accuracy of the calibration algorithm. For instance, the lowest R^2 in the

Table 1 Calibration results for different combinations of wavelengths

Wavelengths	R^2 (Calibration) %	RMSEC (mJ/cm^2)
485, 547, 580, 606, 693	92.39	503.49
536, 547, 550, 580, 605	92.80	489.81
485, 536, 547, 550, 580	93.07	480.55
485, 536, 606, 650, 693	93.76	455.93
485, 536, 547, 550, 650	93.78	455.06
536, 547, 606, 650, 693	93.96	448.42
536, 547, 605, 650, 693	94.00	447.25
580, 605, 606, 650, 693	94.09	443.59

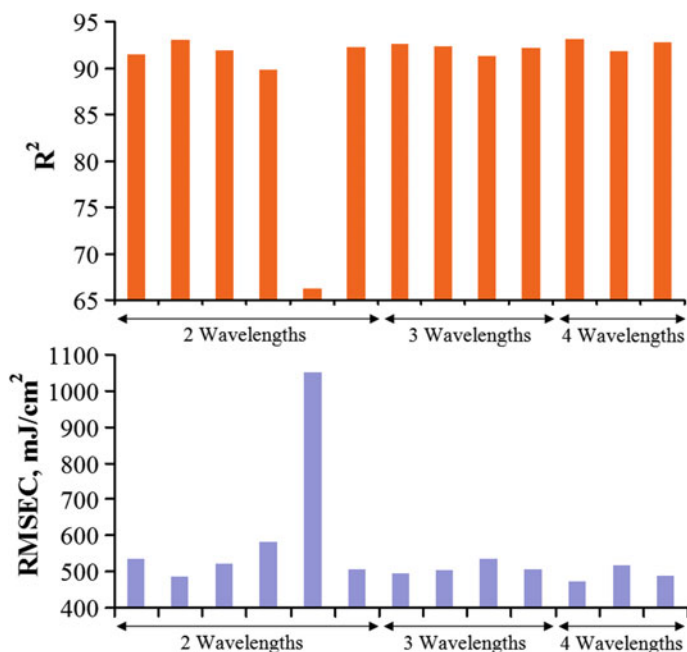


Fig. 6 Calibration results for other randomly selected wavelengths

graphs was recorded at 66.21% with RMSEC recorded at 1054.13 mJ/cm² for calibration algorithms developed using wavelengths of 632 and 641 nm. Also there is no evidence from the graphs that a higher number of wavelengths used in regression leads to better results. Carefully selected wavelengths in the development of a calibration algorithm are the key to obtaining higher values R² and lower values of RMSE.

4 Conclusion

In this research, the measurement of ambient daytime UV dose through the color changes of EBT3 films was successfully determined using the application of visible absorbance spectroscopy. The accuracy of the developed spectroscopic-based algorithm was tested with a prediction dataset obtained from a different day of solar UV measurement. It was determined through experiment that the final cumulative dose on the films, which is highly correlated to the darkest color of the films at the end of the solar UV exposure time, can influence the spectroscopic analysis, specifically the measurement responsivity within the visible region of wavelengths. It was also identified that a higher number of selected wavelengths may improve the accuracy of the developed calibration algorithms. However, this may not always be economical if it is to be translated into product development, especially if the additional number of variables (wavelengths) in the developed algorithm are only capable of slightly increasing the accuracy of measurement. Hence, through the experiment, EBT3 films have shown their consistency in retaining a high accuracy in the measurement of solar UV dose even under ambient solar exposure.

Acknowledgements This study was financially supported by the Ministry of Higher Education—Fundamental Research Grant Scheme (Grant No. 203/PFIZIK/6711491). Thanks are also extended to Universiti Sains Malaysia (USM) for support and encouragement.

References

1. Butson ET, Yu PKN, Butson MJ (2013) Solar ultraviolet radiation response of EBT2 Gafchromic, radiochromic film. *Phys Med Biol* 58(21):N287–N294
2. Belkin M, Césarini JP, Diffey B et al (1994) Protection against exposure to ultraviolet radiation world health organization. World Health Organization, Geneva
3. Diffey BL (1982) Ultraviolet radiation in medicine. CRC Press, Boca Raton
4. Albritton DL, Watson R, Aucamp P (1995) Scientific assessment of ozone depletion: 1994
5. Prinn R et al (1998) Long-lived ozone-related compounds. Scientific Assessment of Ozone Depletion: World Meteorological Organization Global Ozone Research and Monitoring Project Report No 44, 1999, pp 229–241
6. Katsuda T, Gotanda R, Gotanda T, Akagawa T, Tanki N, Kuwano T, Yabunaka K (2015) Comparing three UV wavelengths for pre-exposing Gafchromic EBT2 and EBT3 films. *J Appl Clin Med Phys* 16(6)

7. Yu KN, Chun SL, Chan PM (2015) Long-term passive monitoring of solar UV radiation using radiochromic films. In: 3rd Southern African solar energy conference, South Africa, 11–13 May 2015
8. Aydarous A, Al-Omary EA, El Ghazaly M (2014) Characterization of Gafchromic EBT3 films for ultraviolet radiation dosimetry. *Radiat Eff Defects Solids* 169(3):249–255
9. Tajuddin MA, Omar AF (2017) Measuring solar ultraviolet exposure dose on EBT3 film through the application of visible absorbance spectroscopy. In: 9th international conference on robotic, vision. Signal processing and power applications, pp 639–646
10. Yusof NA, Osman US, Omar AF (2016) Measuring UV LEDs radiation dose using EBT3 film. In: IEEE international conference on advances in electrical, electronic and systems engineering (ICAEES), 14 Nov 2016, pp 5–10
11. Osman US, Omar AF (2016) Solar ultraviolet measurement: a mini review. In: IEEE international conference on advances in electrical, electronic and systems engineering (ICAEES), 14 Nov 2016, pp 252–257

Open Platform Orbit Determination Systems Using a Mixture of Orbit Estimator and Orbit Propagator

Hilmi Sanusi and Wayan Suparta

Abstract This paper describes a flexible orbit determination method that uses a mixture of orbit estimator and orbit propagator with the ability to perform corrections if the ephemeris from GPS, ground track or other method is obtainable. The satellite uses various sensors including Global Positioning Systems (GPS) or trusted orbit propagator in order to obtain the orbital information with the minimum delay and error at the lowest cost. Orbit propagator uses an orbital dynamic model where the analytic form needs to be constantly updated in order to maintain its accuracy and the integrator needs heavy computation but both constitute the error propagation in which the accuracy depends on the complexity and selection of orbital elements. Orbit estimator uses set of sensors data to produce an estimate where the accuracy depends on measurement noise characteristic and the model used. To avoid divergence, a sensible process and measurement noise model are selected. The orbit estimate is derived from an Extended Kalman Filter (EKF) while the Variation of Parameters (VOP) is used to propagate from one state to the other. Any obtainable ephemeris will be used as an initial state. The EKF uses the Position and Velocity elements as they possess dynamics that are beneficial to the estimator. The propagator uses the Keplerian elements as it consists of slow varying elements [a , e , i] and fast varying elements [ω , Ω , v]. The EKF will be more difficult to diverge towards any abrupt disturbance if the slow varying elements from the orbit propagator are blended with the orbital elements produced by the orbit estimator and prevent the estimator from diverging.

H. Sanusi (✉)

Department of Electric, Electronics and Systems Engineering,
Universiti Kebangsaan Malaysia, 43600 Bangi, Malaysia
e-mail: hilmisanusi@ukm.edu.my

W. Suparta

Department of Electrical Engineering, Sanata Dharma University,
Yogyakarta 55282, Indonesia
e-mail: drwaynesparta@gmail.com

1 Introduction

Emerging new technologies have allowed micro-satellites to carry out an increasing range of functions. The compact size, lower power consumption and high computation ability of microprocessor technology mean that it has been one of the major breakthroughs that have allowed micro-satellites to perform more complicated tasks in real time. As is the current trend, the sensor module itself has computational capability whereby the data can be shared among the sensors. Distributing the sensor data enables the satellite attitude sensors to generate the orbit information without additional hardware by adding a new algorithm for that purpose. Although Global Positioning Systems (GPS) have been used extensively in micro-satellites for navigation purposes, the availability of a GPS signal cannot be guaranteed. The method suggested in this paper is based on an open platform concept whereby the estimator uses any available sensors even with only magnetometer data. The estimation is more effective if the GPS information is used to initialize the estimator. In order to keep the accuracy as high as possible an orbit propagator is also used in parallel with the orbit estimator and the ephemerides from both are mixed. With further study, it seems possible that better orbital information can be obtained using an augmentation of a geomagnetic model corrector for better attitude information. As the satellite attitude and its orbit are interrelated, better orbit information will allow greater pointing accuracy.

Previously, most microsatellites have had an orbit propagator for sensor orientation and an orbit estimator for orbit determination. The orbital information is used for orbit maintenance and for attitude determination. The propagator will provide the rough information about the orbit while the orbit estimator will provide better information through the updated measurements. The orbit propagator needs updates as its accuracy degrades with respect to time. Initially, most micro-satellites used SGP4 or Simplified General Perturbation onboard with sufficient accuracy for most applications. Some used an analytical propagator for long-term accuracy such as the Surrey Satellite Technology Ltd (SSTL) epicycle model [6]. Some satellites also implement a High Precision Orbit Propagator, based on Cowell's Method, which requires rigorous computations and a long computation time in order to be propagated—a risky option in a harsh environment [2, 16]. Concurrently, a magnetometer-based orbit estimator was extensively studied using various orbital elements [15]. Some researchers also combined it with other sensors for a better estimate. The accuracy of the orbit estimator depends mainly on the measurement and the model used [8]. Well-modelled sensor noise, along with a more accurate system model and a high sampling rate of data (which need more computation time), will give a good estimate [2]. The main concern is when the sensor noise behaves beyond its modeled noise or the process noise does not include unmodeled perturbation. This event is very likely to occur during high solar activity and might cause divergence in the filter [3].

Countries in the Equatorial region would like to have their satellite in a near-equatorial plane as it will increase the revisit frequency [14]. For example, a

satellite at about 1000 km with 10° inclination will make about 8 passes a day. For microsattelites with limited sensors, relying on magnetometer data for attitude determination can create a problem during high solar activity, causing the earth magnetic field vector to be offset by up to 15° , as observed by Oersted's satellite [7, 9]. The introduction of the IGRF correction term is among the steps taken to overcome this problem as few sensors are usable most of the time. Having a more accurate attitude estimate means it will take less time for the filter to settle when high accuracy sensors such as a star sensor are used as the filter innovation.

Well-judged selected orbital elements will reduce the amount of computation needed and will optimize its performance. Keplerian Elements were selected and divided into two parts based on common characteristics, namely Slow Varying Elements (SVE), $[a, e, i]$ and Fast Varying Elements (FVE), $[\omega, \Omega, v]$. SVE, which is less dynamic, varies slowly with time and is affected by certain perturbations which are well documented in orbit propagator literature. In order to track this SVE in an estimator, a very tight model must be used. Not only does it cause the problem mentioned earlier, but it also restricts the number of a data sample used to update the estimator due to the limited computation time in real time application. On the other hand, the more dynamic FVE varies rapidly in time and can be tracked nicely by a state estimator but is difficult to propagate by an orbit propagator for the same reasons.

The magnetometer data, with a combination of other sensors will feed the Extended Kalman Filter (EKF) to estimate the state of the satellite. Concurrently, the orbital parameter is also generated by employing a Variation of Parameter (VOP) as orbit propagator. The VOP needs current position, velocity and perturbs accelerations at current position to generate the orbital parameter. An orbit propagator based on VOP can yield moderate accuracy for a small time step. The result from the orbit estimator and propagator is mixed with a weighting factor using a multiplying vector K_1 and K_2 . The new weighted value is used as a new estimated value for both the estimator and propagator. By doing so, it enables the propagator to use the measurement to update its orbit propagation. Complementing the advantage offered by the orbit propagator and estimator, a new method of orbit determination is presented in this paper as the initial step towards open platform orbit determination systems.

2 Orbit Propagator and Estimator Model

Keplerian Elements $[a, e, i, \omega, \Omega, v]$ follow the standard notation; a is semi-major axis, e is an eccentricity, i is an inclination, ω is an argument of perigee, Ω is the right ascension of ascending node (RAAN) and v is a true anomaly. The satellite can also be represented in the I - J - K coordinate system where \mathbf{r} is the position vector, \mathbf{v} is the velocity vector and \mathbf{f} is the resultant of acceleration or perturbing forces exerted on it. Since it easier to compute all perturbing forces in the I - J - K coordinate system, Keplerian elements need to be transformed to Position and

Fig. 1 Definitions of Keplerian elements and position and velocity vectors [1]

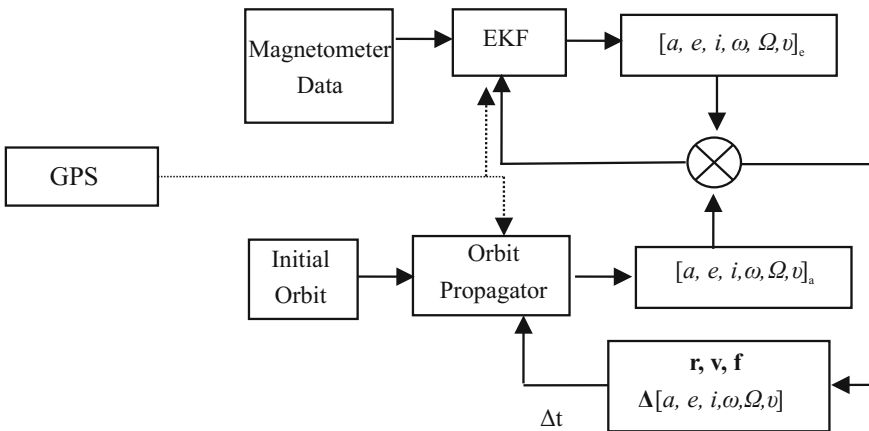
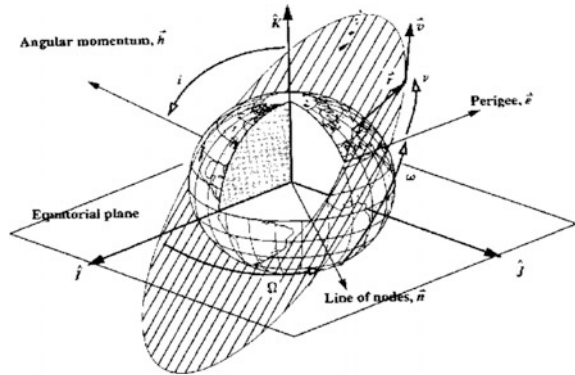


Fig. 2 Hybrid Orbit Propagator/Estimator block diagram [14]

Velocity elements and all Variation of Parameters of Keplerian elements are computed using \mathbf{r} , \mathbf{v} , and \mathbf{f} vectors [1, 17] (Fig. 1).

The EKF is used as the state estimator to estimate the Keplerian Elements. Both the estimator and propagator run in parallel and mix at the later stage as in Fig. 2.

The block diagram above can be described by defining both the orbit propagator and state estimator that were used. Variation of Parameter is not the best alternative for the orbit propagator but it serves its purpose well and with sufficient accuracy but should be more accurate than the state estimator, which is a standard EKF-based one [11]. The acceleration model will not be discussed in detail as it has been well established in the literature, but the interested reader can refer to [16].

2.1 Variation of Parameters

The method of Variation of Parameter used in this study is adopted from [4]. For this, it is assumed that the incremental of Keplerian elements is

$$\Delta[a, e, i, \omega, \Omega, v] \cong \frac{d[a, e, i, \omega, \Omega, v]}{dt} \Delta t \quad (1)$$

The $\frac{d[a, e, i, \omega, \Omega, v]}{dt}$ is calculated from \mathbf{r} , \mathbf{v} , and \mathbf{f} . The conversion from Keplerian Elements to Position and Velocity is done using a transformation from Keplerian to P - Q - W elements to I - J - K elements as below:

The transformation matrix:

$$\Gamma_{313} = \begin{bmatrix} C_\omega C_\Omega - S_\omega C_i S_\omega & -S_\omega C_\Omega - C_\omega C_i S_\omega & S_i S_\Omega \\ C_\omega C_\Omega + S_\omega C_i S_\omega & -S_\omega C_\Omega + C_\omega C_i S_\omega & -S_i C_\Omega \\ S_\omega S_i & C_\omega S_i & C_i \end{bmatrix} \quad (2)$$

where

$$C_{(\circ)} = \cos(\circ)$$

$$S_{(\circ)} = \sin(\circ)$$

The position and velocity in I - J - K are given by:

$$\mathbf{r} = \Gamma_{313} \begin{bmatrix} \frac{p \cos(v)}{1 + e \cos(v)} \\ \frac{p \sin(v)}{1 + e \cos(v)} \\ 0 \end{bmatrix} \quad (3)$$

$$\mathbf{v} = \Gamma_{313} \begin{bmatrix} \sqrt{\mu/p} \sin(v) \\ \sqrt{\mu/p}(e + \cos(v)) \\ 0 \end{bmatrix} \quad (4)$$

The acceleration or perturbation force exerted on the satellite is a well-understood subject. The acceleration model used should be selected based on the satellite altitude, inclination and year of operation as the accuracy of models might vary. The selected models are set to be optimized in terms of the computation time and the accuracy needed.

Tai and Noerdlinger [16] give a good guide to the acceleration models that need to be accounted for. The significance of the acceleration models was judged by switching off the function or altering the models and comparing them with the reference satellite ephemerides that were simulated using Cowell's method from SUNSAT SLR raw data [3]. The acceleration models selected should include

perturbation due to drag, geopotential, third body due to sun-moon, solar radiation pressure and earth radiation pressure. The most significant factor in the accuracy of the model is the acceleration due to drag, and is very much dependent on the atmospheric model used. The atmospheric model should at least have the accuracy of the Harris-Priester model. If the computation power is large, the Jaccia-Robert atmospheric model will serve this purpose very well. Acceleration due to earth's gravitational force was set to the order and degree of 18×18 . However, for any analytical evaluation, the minimum order and degree should be at least 6×6 . Low precision sun and moon orbit propagators are sufficient for this purpose as there is no propagated error. Perturbation forces due to solar radiation pressure and earth radiation pressure are only significant in high elliptical orbit.

The perturbation forces are

$$\mathbf{f} = \mathbf{f}_d + \mathbf{f}_g + \mathbf{f}_{tb} + \mathbf{f}_{srp} + \mathbf{f}_{erp} \tag{5}$$

where

- \mathbf{f}_d is perturbation due to drag
- \mathbf{f}_g is perturbation due to geopotential
- \mathbf{f}_{tb} is perturbation due to the third body
- \mathbf{f}_{srp} is perturbation due to Solar Radiation Pressure
- \mathbf{f}_{erp} is perturbation due to Earth Radiation Pressure

The Variation of Parameter is then defined by first evaluating the $\frac{d[a,e,i,\omega,\Omega,v]}{dt}$ and they are given by Eqs. (1)–(5) below by first defining the specific angular momentum \mathbf{h} and its magnitude as

$$\mathbf{h} = \mathbf{r} \times \mathbf{v} \tag{6}$$

where $h^2 = \mu a (1 - e^2)$

Then, the $\frac{d[a,e,i,\omega,\Omega,v]}{dt}$ are given by:

$$\frac{da}{dt} = \frac{2a^2}{\mu} \tag{7}$$

$$\frac{de}{dt} = \frac{1}{\mu ae} [(pa - r^2)(\mathbf{v} \cdot \mathbf{f}) + (\mathbf{r} \cdot \mathbf{v})(\mathbf{r} \cdot \mathbf{f})] \tag{8}$$

$$\begin{bmatrix} h \sin i \frac{d\Omega}{dt} \\ -h \frac{di}{dt} \\ \frac{dh}{dt} \end{bmatrix} = \begin{bmatrix} C_\Omega & -S_\Omega C_i & S_\Omega S_i \\ S_\Omega & C_\Omega C_i & -C_\Omega S_i \\ 0 & S_i & C_i \end{bmatrix}^T (\mathbf{r} \times \mathbf{f}) \tag{9}$$

$$\frac{dv}{dt} = \frac{1}{reh} \left[p \cos v (\mathbf{r} \cdot \mathbf{f}) - (p + r) \sin v \frac{dh}{dt} \right] \tag{10}$$

$$\frac{d\omega}{dt} = -\cos i \frac{d\Omega}{dt} - \frac{dv}{dt} \tag{11}$$

2.2 State Estimator

This study uses the available literature [5, 13, 15] to select the main parameter that will determine the performance of the filter. It also described the criteria for the selection of $[x_{k-1/k-1}, P_{k-1/k-1}, W, V]$ and the behavior of the selected parameters. Several issues were taken into account during consideration of the selected state vector. The state is the Keplerian Elements themselves and s defined as

$$X^T = [a, e, i, \omega, \Omega, v] \tag{12}$$

Even though another state can be selected and transformed into Keplerian Elements, it will not serve the purpose well because of the loss of dynamic in the true anomaly. The main reason is the separation of the Keplerian Elements into two distinct parts. The materials used in the filtering of magnetometer data for navigation can be referred to in [10, 11, 19]. For the purpose of the flow of this paper, some materials from [15] will be presented here.

2.3 System Model

The system of the model is presented as

$$\dot{X}(k) = F(X(k), k) + w(t) \tag{13}$$

The perturbation is considered as part of the process noise, $w(t)$. The Jacobian matrix $F_k(X)$ is described by an orbit generated by a central force only, based on the following state equation [19]

$$\dot{X} = \begin{bmatrix} 0 \\ 0 \\ 0 \\ 0 \\ 0 \\ \frac{\sqrt{\mu_e}(1 + e \cos v)^2}{\sqrt{[a(1 - e^2)]^3}} \end{bmatrix} \tag{14}$$

where μ_e is the earth gravitational constant.

The Jacobian matrix is given by

$$F_k(X) = \frac{\partial(\dot{X})}{\partial X} = \begin{bmatrix} 0_{5 \times 6} \\ F_{6,1} & F_{6,2} & 0 & 0 & 0 & F_{6,6} \end{bmatrix} \quad (15)$$

where

$$F_{6,1} = \frac{1.5}{a} [\dot{X}_6]$$

$$F_{6,2} = \left[\frac{3e}{1-e^2} - \frac{2 \cos v}{1+e \cos v} \right] [\dot{X}_6]$$

$$F_{4,4} = \frac{2e \sin v}{1+e \cos v} [\dot{X}_6]$$

The measurement model used is given by

$$y_k = N(\mathbf{B}(t_k)) + v_k \quad (16)$$

where $\mathbf{B}(t_k)$ = magnetic field vector propagated at time k from IGRF 2000 model, and $N(\mathbf{B}) = \sqrt{B_r^2 + B_\theta^2 + B_\phi^2}$, where v_k = measurement noise, zero mean Gaussian white noise.

The measurement matrix H_k :

$$H_k = \left. \frac{\partial N(\mathbf{B}(\mathbf{R}_g(X)))}{\partial X} \right|_{X=\hat{X}_{k/k-1}} \quad (17)$$

and can be computed by using a chain rule as

$$H_k = \left. \frac{\partial N(\mathbf{B})}{\partial \mathbf{B}} \cdot \frac{\partial \mathbf{B}}{\partial \mathbf{R}_g} \cdot \frac{\partial \mathbf{R}_g}{\partial \mathbf{R}_i} \cdot \frac{\partial \mathbf{R}_i}{\partial X} \right|_{X=\hat{X}_{k/k-1}} \quad (18)$$

where

$\mathbf{R}_g = [r \ \theta \ \phi]$ or geographical coordinate.

$\mathbf{R}_i = [r \ \alpha \ \delta]$ or inertial spherical coordinate

The selection of the initial parameter will determine the characteristic of the estimator. The selection of initial position $X_{0/0}$ and covariance matrix $P_{0/0}$ will mainly affect the convergence speed. However, the actual behavior of the estimator depends on the process noise and measurement noise. As a guideline in this study, perturbation forces were first calculated and summed. The standard deviation of the process noise was chosen at slightly greater than the highest summed perturbation force and integrated once for the velocity error and twice for the position as no perturbations were included in the model.

The filter was initialized and tuned with the following:

$$X_{0/0} = \Gamma_{\frac{KE}{IK}} \left\langle \begin{bmatrix} \mathbf{r}_{0/0} \\ \mathbf{v}_{0/0} \end{bmatrix} \right\rangle \quad (19a)$$

$$P_{0/0} = \Gamma_{\frac{KE}{IK}} \left\langle \begin{bmatrix} \sigma_{\mathbf{r}_{0/0}} \\ \sigma_{\mathbf{v}_{0/0}} \end{bmatrix} \right\rangle \quad (19b)$$

$$V = \Gamma_{\frac{KE}{IK}} \langle \sigma_v \cdot \mathbf{I}_{6 \times 6} \rangle \quad (19c)$$

$$W = \Gamma_{\frac{KE}{IK}} \left\langle \begin{bmatrix} \sigma_{wT} \mathbf{I}_{3 \times 3} & \mathbf{0}_{3 \times 3} \\ \mathbf{0}_{3 \times 3} & \sigma_{wV} \mathbf{I}_{3 \times 3} \end{bmatrix} \right\rangle \quad (19d)$$

where $\Gamma_{\frac{KE}{IK}}$ is the operation of converting the position and velocity to Keplerian Elements.

For the sake of convenience, the significance of the number selected is easier to evaluate by initializing the filter using position and velocity before conversion into Keplerian Elements. In the case of SUNSAT, Jordaan [7] recommended that the covariance matrix suitable for the accuracy of magnetometer sensor should be 180 km^2 and $2500\text{-km}^2/\text{h}^2$ for position and velocity error. The selection of V and W will determine the position error, steady state, and stability and therefore should be tuned carefully. W was selected from the step mentioned earlier and the measurement noise, V , is selected to be about ten times greater than W , as a baseline assumption in a normal practice.

2.4 Mixed Orbit Propagator/Estimator

The idea of mixing both orbit propagator and estimator arises from the need for a more accurate simple orbit propagator with no update requirement and a more reliable orbit estimator free from divergence. The method proposed is intended for the usage of micro-satellites that require precise information on satellite orbit.

An orbit propagator provides the orbit information analytically from a given position and an orbit estimator supplies the orbit recursively from the collection of input if mixed, and will incorporate the measurement into the orbit propagator. The mixing was done by a weighting factor K_1 and K_2 . K_1 and K_2 can be a weighting vector that gives weight to the individual elements. The weight given in the mixing vector, K , depends on which orbital elements are more reliable. If $K_1 = 0$, $K_2 = 1$ the system only trusts the orbit propagator. If $K_1 = 1$, $K_2 = 0$ the system only trust orbit estimator. If $K_1 = 0.5$, $K_2 = 0.5$ the system trusts both equally. If the system has equal trust, the propagator will incorporate the measurement for a closed-loop system (Fig 3).

The concept of Split Keplerian Elements is also introduced in this paper. For the reason mention earlier an orbit propagator can better depict the SVE and can simplify the estimator model. At the same time, an orbit estimator can provide more

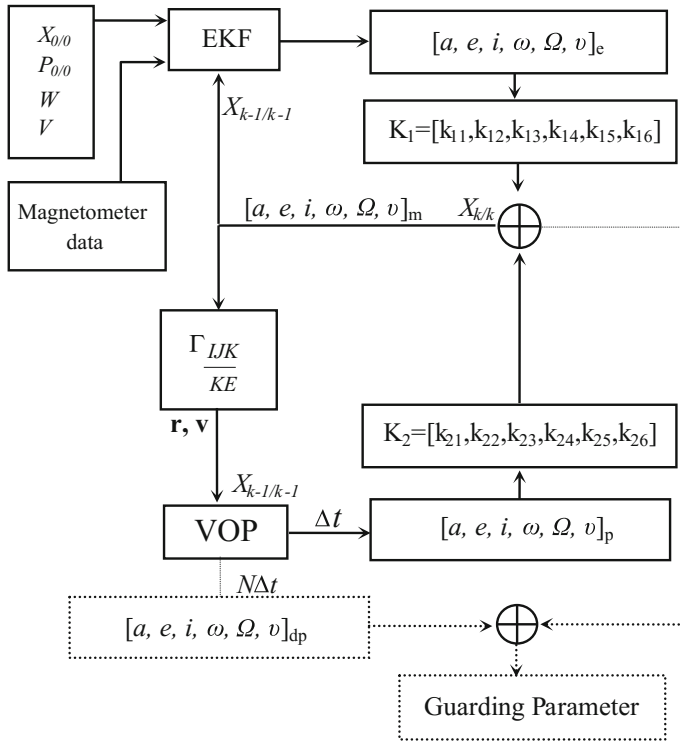


Fig. 3 Block diagram of Mixed Orbit Propagator/Estimator (MOPE)

information on the FVE through measurement update. This can eliminate the need for a drag coefficient estimator as it can be calculated analytically and can be corrected through the measurement. For that reason, the weighting multiplier K_1 and K_2 consist of a vector where

$$K_1 = [k_{1,1} \quad k_{1,2} \quad k_{1,3} \quad k_{1,4} \quad k_{1,5} \quad k_{1,6}] \tag{20}$$

$$K_2 = [k_{2,1} \quad k_{2,2} \quad k_{2,3} \quad k_{2,4} \quad k_{2,5} \quad k_{2,6}] \tag{21}$$

It is interesting to see that one can rely more on the propagator for SVE and rely more on the estimator for FVE. Putting greater weight on the first three elements and less weight on the last three elements of K_2 make it able to perform the task.

2.5 Open Platform Orbit Determination Systems

The Guarding Parameter, which compares the propagated orbit for a delayed time, N , with a mixed orbit which will be used later in the innovation of the filter.

The other investigated method which is very useful for NEO satellites is the event monitor that detects the entrance and exit points to the shadow zone during satellite eclipse. The epoch time is used to give more information on eclipse anomalistic time and satellite-sun angle to give better information on drag, satellite height and earth's horizon form factor. A differential correction method can be used to make a better estimate of the epoch at entrance and exit of the eclipse.

3 Results

The simulation was done using MATLAB®, but an external program is used to generate the satellite position and velocity vectors and set as a reference orbital parameters. During the simulation, MATLAB utilized the stored orbital parameters. The satellite ephemeris for a given epoch was used as an initial position for the orbit generators. SGP4 was used to find the sensor error due to the inaccuracy of the orbit propagator. The reference orbit generator was based on Cowell's Method. The results from SLR data were used to tune the reference orbit propagator. Both Jacchia-Robert71 and (Mass Spectrometer Incoherent Scatter)-MSIS90 were used as the atmospheric model but MSIS90 produced slightly better results when compared to the SLR data and was therefore used as the reference orbit. The MSIS90 atmospheric model used solar flux published by JPL. The generated data was only used to test the filter and its performance in tracking the artificial measurement noise.

The Extended Kalman Filter used is a standard EKF based on Eqs. (6)–(12). Two state models are used in the EKF, one of the state models is a standard two-body motion and the other one includes the J_2 perturbation in the state model. The generated magnetometer data is used to tune the filter so that suitable $P_{0/0}$, V , and W can be selected. The artificial data used 10 s or less of sampled data for this purpose. The filter was able to converge and P was set to give the fastest settling time because the available raw data were mostly less than ten orbits with a sampling rate of 30 s and 60 s.

Various perturb acceleration models were used. The simplest, which is an analytic acceleration model, was used first. It consists of geopotential perturbation up J_6 , linear drag model and sun-moon perturbation. Other perturb acceleration models used spherical harmonics with the order and degree of 18×18 for the geopotential model. A Harris-Priester atmospheric model was used for the drag, and Solar Radiation Pressure was also tried.

The EKF has a difficulty in estimating the satellite ephemeris without J_2 (earth oblateness perturbation) in the model and other investigators have confirmed this situation. However, mixing the result with a good perturbation model can overcome the problem. Even without using a Split Keplerian Elements approach the convergence time is much better. Accommodating the J_2 term in the model has less significance to the system, but implementing a Split Keplerian Elements approach, together with a good perturbation model is able to settle faster in under 3 orbits with 30 s of sampled data (Fig. 4).

Figure 5 below shows the ability of the EKF to track the orbital element in about 12 orbits. The filter has difficulty tracking slow varying elements such as

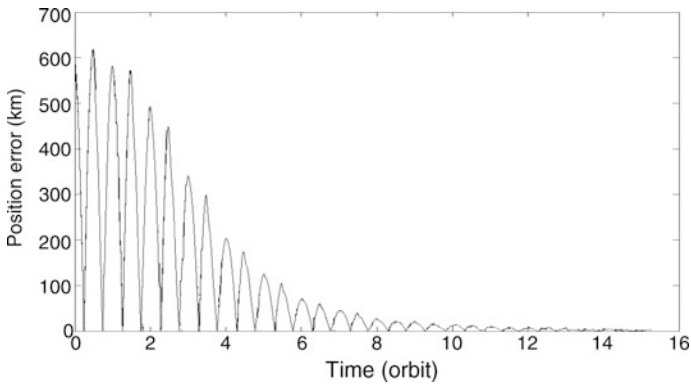


Fig. 4 The position error of EKF with J_2 with respect to a reference generated orbit. EKF with process noise, Q , $[0.4 \text{ km } 1.7 \times 10^{-6} \text{ km/s}]$, measurement noise, R , 500nT and covariance matrix, P , $[180 \text{ km } 1.8 \times 10^{-3} \text{ km/s}]$

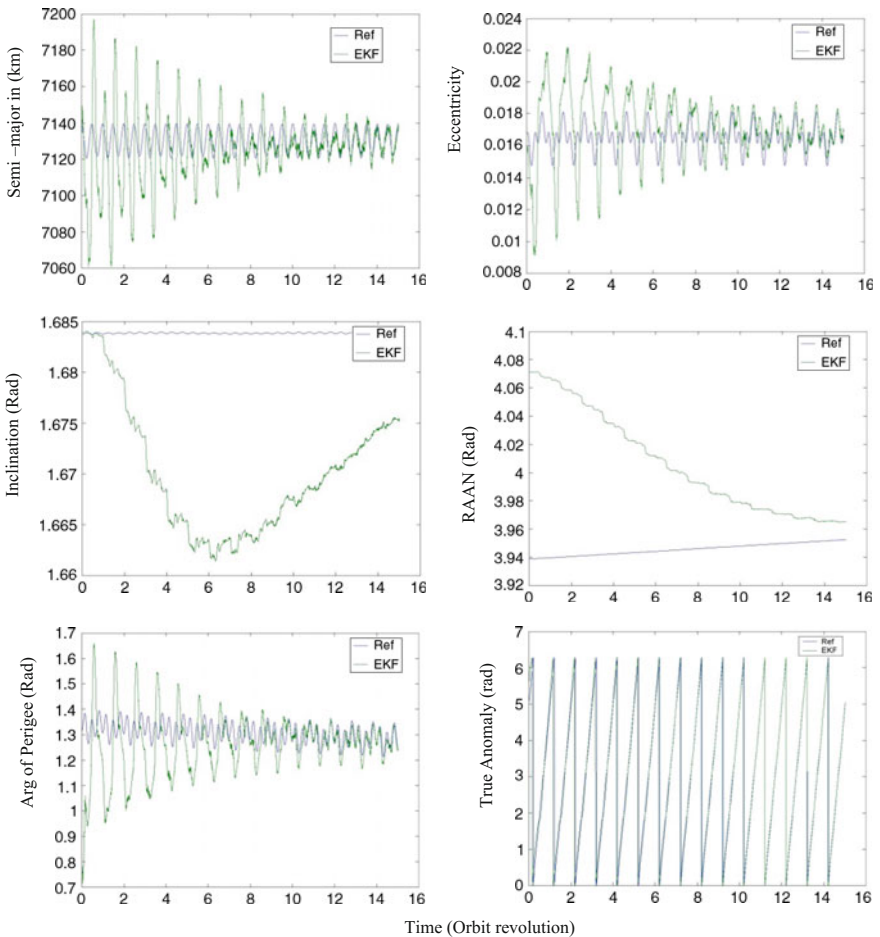


Fig. 5 Keplerian Elements as estimated by the EKF with $Q = [0.4 \text{ km } 1.7 \times 10^{-6} \text{ km/s}]$, $R = 500\text{nT}$ and $P = [180 \text{ km } 1.8 \times 10^{-3} \text{ km/s}]$

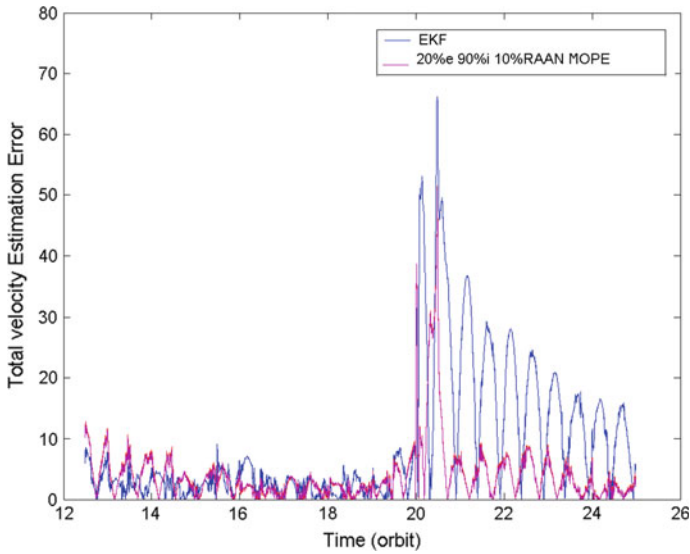


Fig. 6 The position error of MOPE without initial value and with the mixture of $K_1 = [1 \ 0.8 \ 0.1 \ 0.9 \ 1 \ 1]$ and $K_2 = [0 \ 0.2 \ 0.9 \ 0.1 \ 0 \ 0]$ compared with EKF when a disturbance occurs after the filter reaches steady state

semi-major axis, eccentricity, and inclination. In the RAAN, the estimate requires a good initialization for quicker convergence. This is because the simulated orbit is near equatorial so the magnetic variation is smaller and tracking the RAAN depends mainly on the South Atlantic Anomaly. Since the orbital dynamic as in Eq. 8 depends only on the true anomaly, the RAAN and the argument of perigee will take a longer time to converge (Fig. 6).

It is also interesting to see that the estimator convergence time can be accelerated if a known position was used to initialize the orbit propagator. The gain vectors can also give a different performance to the convergence of the estimator. If K_2 is much larger than K_1 , then a known initial position is a must.

The stability of the proposed method was also investigated. Injecting spikes in the magnetometer raw data imitates the spurious noise that can cause divergence in the estimator. The comparison was made between the EKF system and hybrid system only. The divergence of the filter was based on the density of the spikes and as the simulation can only be done for 8 orbits because of the availability of the data, actual divergence problems can't be addressed. In the hybrid system, however, depending on the perturbation model used, the estimator shows no significant effect from the disturbance. If the density of spikes is high, it means the spike is no longer an intermittent noise but can be considered as measurement noise and therefore not applicable.

4 Conclusion

The mixture of Orbit Propagator and Estimator proposed in this study was able to force the orbit estimator to be more robust and more stable with better accuracy. The advantage posed in the proposed method can be used as a backup to the current system. The mixed orbit generator also can easily replace widely used onboard orbit propagator, such as SGP4 as it can act as an orbit propagator with infrequent updates. Limited data duration hinders the investigation regarding the true capability and limitations of the suggested method. The raw data has bias in its measurement and other unexpected noise that is difficult to imitate. However, the behavior of the system very much depends on the selected weighting factor. A conservative approach with an equal multiplier shows significant improvement. Indeed, the advantages gained in the mixed orbit generator only requires minimal computational load from the current onboard orbit propagator, unlike other methods such as batch filter.

However, the Split Keplerian Elements approach poses a possible complication when too much trust is put on the propagator. Even though it is more stable and can be more accurate, the estimator acts to slow the reaching of a steady state. Optimum coefficients are essentials to gain benefit from it. One can also use gain scheduling so that this method can be fully utilized.

The global objective of this whole study is to come up with an IGRF correction model that can be derived from the measurement vector innovation. This can be achieved by the means of another sensor in order to give the attitude information of the satellite.

Appendix

$$\mathbf{f}_d = \frac{1}{2} \frac{C_D A}{m} \rho v_{rel}^2 \frac{\vec{v}_{rel}}{v_{rel}}$$

where

C_D is the coefficient of drag. A dimensionless coefficient that can be adjusted to suit the result of the orbit, which depends on the shape of the satellite and materials used. A crude approximation, $C_D = 2$ for initial orbit determination. Usually $2 \leq C_D \leq 2.3$

A is the effective area of the satellite normal to velocity vector

m is the mass of the satellite

ρ is atmospheric density

\vec{v}_{rel} is the relative velocity vector of the satellite to the atmosphere

v_{rel} is the magnitude of the velocity vector

The perturbation due to geopotential is given by:

$$f_g = \Delta \frac{GM}{r} \sum_{n=0}^{\infty} \sum_{m=0}^n \frac{R^n}{r^n} \bar{P}_{nm} \sin(\phi) (\bar{C}_{nm} \cos m\lambda + \bar{S}_{nm} \sin m\lambda)$$

where

P_{nm} is the Legendre polynomial
 C_{nm} and S_{nm} are the geopotential coefficient with degree n and order m , and the detail can be represented as

$$f_{tb} = \mu_M \cdot \left(\frac{\vec{s} - \vec{r}}{|\vec{s} - \vec{r}|^3} \right) - \mu_{earth} \frac{\vec{r}}{|\vec{r}|^3}$$

where the mass of the satellite is negligible compared to earth and third body and

μ_M is the gravitational constant due to body M
 s is the geocentric coordinate of body M
 r is the geocentric coordinate of the satellite

$$f_{SRP} = - \frac{P_{SR} C_R A_{\oplus}}{m} \frac{\vec{r}}{|\vec{r}|}$$

where

r is the radius of the satellite from the Earth
 m is the mass of the satellite
 $C_R I + \epsilon$ is the reflective coefficient (dependent on materials). $1.2 \leq C_R \leq 1.8$
 A_{\oplus} is the area perpendicular to the sun or the acceleration can be expressed as

$$f_{ERP} = \sum C_R \left(v_j a_j \cos \theta_j^E + \frac{1}{4} \epsilon_j \right) P_{SR} \frac{A}{m} \cos \theta_j^S \frac{dA_j}{\pi r_j^2} e_j$$

References

1. Bate RR, Mueller DD, White JE (1971) Fundamentals of astrodynamics. Dover Publications Inc, New York
2. Chory M, Hoffman, DP, LeMay JL (1986) Satellite autonomous navigation—status and history. In: Proceeding of IEEE position, location and navigation symposium (Las Vegas, NV). Institute of Electric and Electronic Engineer, New York, pp 110–121
3. du Plessis JAF (1999) Low earth orbit satellite propagators. Master’s thesis, University of Stellenbosch
4. Escobal PR (1965) Methods of orbit determinations. John Wiley & Sons Inc, New York

5. Fox SM, Pal PK, Psiaki M (1990) Magnetometer-based autonomous satellite navigation (MAGNAV). *Am Astronaut Soc AAS Pap* 90-051:369-382
6. Hosken R, Wertz JR (1995) Microcosm autonomous navigation system on-orbit operation. *Am Astronaut Soc AAS Pap* 95-074:491-506
7. Jordaan JJ (1996) An extended Kalman filter observer for autonomous orbit determination. Master's thesis, University of Stellenbosch
8. Nagarajan N, Bhat MS, Kasturirangan (1991) A novel autonomous orbit determination system using earth sensor (scanner). *Acta Astronaut* 25(2):77-84
9. Primdahl FG, Merayo JM, Brauer P et al (2003) Design, calibration, and testing of precise magnetometers. In: *Proceedings of IEEE sensors 2003 (IEEE Cat. No.03CH37498)*, vol 1, pp 466-467
10. Psiaki M, Martel F (1989) Autonomous magnetic navigation for earth orbiting spacecraft. In: *Presented at third annual AIAA/USU conference on small satellites*, Logan, Utah, USA
11. Psiaki M, Martel R, Pal PK (1990) Three-axis attitude determination via Kalman filtering of magnetometer data. *J Guid Control Dyn* 13(3):506-514
12. Psiaki M, Huang L, Fox SM (1993) Ground tests of magnetometer-based autonomous navigation (MAGNAV) for low earth orbiting spacecraft. *J Guid Control Dyn* 16(1):206-214
13. Psiaki M (1995) Autonomous orbit and magnetic field determination using magnetometer and star sensor data. *J Guid Control Dyn* 8(3):584-592
14. Sanusi H, du Plessis JJ (2000) Investigations of using epoch time in correction of geomagnetic models in estimating orbit for low earth equatorial orbit satellites. In: *Presented at 2nd international conference on advances in strategic technologies*, Malaysia
15. Shorshi G, Bar-Itzhack IY (1995) Satellite autonomous navigation based on magnetic field measurements. *J Guid Control Dyn* 18(4):843-850
16. Tai F, Noerdlinger PD (1989) A low-cost autonomous navigation system. *Am Astronaut Soc AAS Pap* 89-001:3-23
17. Vallado DA (1997) *Fundamentals of astrodynamics and applications*. McGraw-Hill, New York
18. Wertz JR, Cloots JL, Collins JT et al (2000) Autonomous orbit control: initial flight results from UoSAT-12. In: *Presented at 23rd annual aas guidance and control conference*, Colorado
19. Wiegand M (1996) Autonomous satellite navigation via Kalman filtering of magnetometer data. *Acta Astronaut* 38(4-8):395-403

Deployment Challenges and Co-tier Interference Management Techniques for Ultra-dense Femtocell Networks

Ibrahim Shgluof, Mahamod Ismail, Rosdiadee Nordin,
Nor Fadzilah Abdullah and Azizul Azizan

Abstract Network densification is one of the imperative mechanisms expected to enable next generation 5G networks to meet the highly foreseen 1000-fold increase in capacity. In this regard, densification of femtocells is a promising concept to meet growing mobile service requirements and for sustainability of users' Quality of Service (QoS), especially for hotspots. In this context, this paper first investigates the inter-cell interference scenarios within a typical small femtocell cluster and then discusses the challenges facing femtocell densification in terms of co-tier interference. Moreover, the concept of femtocell classification into different classes is demonstrated. Finally, the article presents a case study where an interference and resource management approach for ultra-dense femtocell networks (UDFNs) is introduced. This proposal organizes the users in each femtocell into two categories, where the first category is for critical users only and the second is for non-critical users. A disjoint cluster is then formed for the first category within each femtocell and its aggressor/s. Moreover, the approach implements a dynamic resource allocation mechanism, based on the status of each user within each femtocell. This mechanism allows ranging from the shared resources for the first category and its aggressor/s, to the frequency reuse one for the second category. The simulation results show that the proposal outperformed one of the prominent related techniques

I. Shgluof (✉) · M. Ismail · R. Nordin · N.F. Abdullah
Department of Electric, Electronics and Systems Engineering, Universiti Kebangsaan
Malaysia, 43600 Bangi, Malaysia
e-mail: i.shellmani@uob.edu.ly

M. Ismail
e-mail: mahamod@eng.ukm.my

R. Nordin
e-mail: adee@eng.ukm.my

N.F. Abdullah
e-mail: fadzilah.abdullah@ukm.edu.my

A. Azizan
Advanced Informatics School, Universiti Teknologi Malaysia, Jalan Semarak,
Kuala Lumpur, Malaysia
e-mail: azizulazizan@utm.my

in the literature, namely the X2 with UE support (X2-UEs) for all deployment density scenarios from sparse to ultra-dense. The evaluations were made in regard to the users' average throughput and the mean capacity of femtocells. The simulation results show that the SCC technique outperformed its counterpart by an average gain of 32.58% for the aforesaid first metric, and an average enhancement of 16.79 Mbps for the later metric compared to only 6.26 Mbps achieved by the X2-UEs.

1 Introduction

Due to the advances in computing and communication technologies that enable the processing of vast volumes of multimedia streams, Mobile Network Operators (MNO) are able not only to increase their network capacity but also to deliver multimedia streaming services in a sustainable manner. The spread of Heterogeneous Networks (HetNets) has to some extent provided the required QoS standards [1]. However, due to the immense growth in data usage, the conventional methods to enhance system capacity will be lacking this massive growth in data rate demands by 2020 [2]. The latest studies and research envision an increase of 10 times the number of users and 100 times for the demand of data traffic per user per day [3, 4]. As a result and with the users' anticipations of higher QoS, MNOs have been motivated to enhance the coverage and capacity of their existing infrastructure. Consequently, their attention has recently shifted to network densification.

Network densification simply means the deployment of more small cells to gain more spatial reuse of the spectrum. Explicitly, the small cells can be equal to or greater than the active users. Another definition is given merely in terms of the cell density, regardless of the active users' density [5, 6]. Nonetheless, efficient spectrum management is one of the key aspects for the sustainability of future wireless networks. Network densification is emerging as one of the most efficient solutions to deal with the exponentially increasing traffic demands and has the most potential to provide user satisfaction with regard to QoS demands. Furthermore, it is a fundamental mechanism expected to enable next generation 5G networks and beyond. The deployment of low-cost and low-power small cells is seen as the ultimate cost-effective match for network densification, especially in hotspot zones where traffic demand is high. Therefore, to meet users' QoS, it is expected that densely deployed femtocell networks, which can be referred to as ultra-dense femtocell networks (UDFNs) will dominate the next generation of wireless networks.

2 Evolution Towards 5G Networks

Owing to the customary use of smart wireless devices like tablets and smartphones in recent years, the demanding QoS applications and mobile traffic has substantially increased over the last decade. This tendency is projected to continue, especially

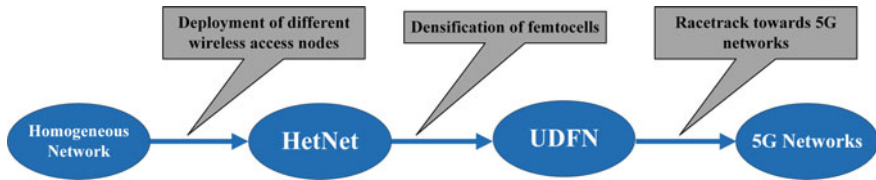


Fig. 1 The road to 5G networks: from homogeneous to UDFNs and beyond

with the deployment of 5G and beyond networks. The evolution towards 5G network deployments is expected to be heterogeneous and ultra-dense, chiefly through the deployment of small cells such as femtocells. The deployment of a small number of femtocells with regular macro-cells is designated in the literature and standards as HetNet. However, HetNets in general represent an evolution from homogeneous networks [7]. On the other hand, as illustrated in Fig. 1, UDFNs are regarded as another evolution from HetNets in the race towards 5G networks.

2.1 Femtocell Densification

The growth of smart devices and applications in recent years have resulted in a different approach to future wireless networks, one where the concept of Ultra-Dense Network (UDN) represents a new paradigm shift [8–10]. Thus, UDFNs are endorsed as one of the main technologies that can achieve the requirements of a 1000-fold increase in mobile data throughput in contrast to LTE [11].

As mentioned earlier, the deployment of femtocells is seen as the most effectual and realistic option for network densification, particularly in indoor and outdoor hotspots where traffic is expected to be intensive. Network densification comes in two different approaches, either horizontal or vertical. In horizontal densification, the femtocells are densified in the horizontal plane, e.g. in the streets, on the roofs of buildings or houses, on lamp-posts, and so on. In this approach, the femtocells are deployed in a semi-planned manner by mobile operators and usually operate in Open Subscriber Group (OSG) mode. However, in the vertical densification, the femtocells are deployed by the owners or subscribers in apartments or small offices within tower-type buildings. Contrary to horizontal densification, femtocells are expected to be operated in either Closed Subscriber Group (CSG) mode or Hybrid Subscriber Group (HSG) mode.

3GPP have considered the concept of femtocell deployment prior to Release 12. The co-channel heterogeneous deployments of femtocells under the coverage of macro-cells was considered by 3GPP in LTE Releases 10 and 11. Even so, these deployments were limited to small clusters of femtocells only, to support “bursty” traffic. However, the focus of Release 12 is now on denser deployment scenarios and the requirement of several improvements at the physical layer such as co-tier interference coordination amongst femtocells in order to envision throughput gains.

Furthermore, in Release 12, 3GPP considered three main possible femtocell deployment scenarios for evaluation: Scenario 1: Femtocells deployed outdoors in small clusters and operated in the same carrier frequency as the macro-cell. Scenario 2: Femtocells deployed in indoor clusters and in a carrier different from the macro-cell. Scenario 3: Standalone deployment of femtocell clusters without macro-cell coverage. In this Scenario, the femtocell clusters can either be indoors or outdoors. These studies and other technical requirements are detailed in a technical report [12].

2.2 Challenges of Femtocell Densification

To achieve the evolutionary QoS requirements and capture the full benefits of femtocell densification, there are a number of challenging issues that have to be tackled. We briefly highlight some of these challenges as follows:

- As femtocells get denser, a plurality of non-serving femtocells are in the vicinity of a given active user. In contrast to macro-cells, the inter-site distance would be in the range of meters or tens of meters. Hence, this introduces a different and challenging (especially in CSG and HSG modes) wireless coverage environment, where several non-serving femtocells would be in close proximity to other users.
- The femtocells in close vicinity to each other in UDFNs generates severe interference between neighbouring cells which is a limiting factor for capacity. Therefore, the necessity of efficient interference management techniques is unavoidable in order to mitigate the inter-femtocell interference [13–17].
- The coverage of femtocells in ultra-dense cellular networks is obviously less than the macro-cell coverage of traditional cellular networks. Thus, for a high-speed mobile user, the frequent handovers of this particular user not only increase redundant overheads but also can decrease the user QoS.
- Backhauling in dense femtocell environments is another challenging issue. It might be difficult for mobile operators to guarantee an ideal high-speed low-delay backhaul for each femtocell. Besides, the backhaul of a femtocell can be the bottleneck of its capacity, as the backhaul capacity would limit the air-interface capacity, [6, 18–20].

2.3 Inter-femtocell Interference Scenarios

To meet growing requirements for higher capacities in LTE-A networks, researchers have switched their studies towards dedicated deployments of small cells with higher frequency bands [21]. Accordingly their focus has turned to confront the co-tier interference between the same classes of nodes. Most of the

research and studies on intra-layer interference between small cells in the literature has considered femtocells as they can signify a high risk for co-tier interference [22]. Therefore, inter-cell interference is one of the issues that arise as a result of network densification through deployment of standalone femtocells in hot zones or through their addition to current macro-cell infrastructure, particularly when they operate in CSG mode [23]. As a result, downlink interference can become complex with an ambiguous definition of victim, victim-aggressor and aggressor femtocells, and some of the traditional interference mitigation technologies cannot be easily exploited due to the large number of the deployed femtocells with unstructured topology [16].

To design an efficient interference management technique, a thorough study of the interference distribution between neighboring femtocells and users is needed. Aggressors for a user equipment (UE) can be defined as the group of interferers sorted in a descending manner. An active UE receives a number of power signals from nearby non-serving femtocells in the form of interferers. The principal or dominant interferer (*DI*) is the strongest amongst all the interferers to that particular user. The dominant interference ratio (*DIR*), is quantified as the ratio between the main interferer and the rest of the perceived interference and can be formulated as:

$$DIR = \frac{I_1}{\sum_n I_n - I_1 + N}, \quad I_1 \geq I_2 \geq \dots \geq I_n \quad (1)$$

where I_1 , is the signal power received from the *DI*, $\sum_n I_n$ designates the total amount of received interference and N is the thermal noise power. Equation (1) indicates that the gain in signal to interference and noise ratio (*SINR*) from ideal elimination of *DI* is proportional to the *DIR*. Furthermore, this can give a sensible approximation of whether any interference management approach can focus solely on the *DI*, or if it is necessary to exclude other weaker interferers as well. However, any mitigation method must be dynamic in order to capture the variations in the interference, which can be very evident in UDFNs where each femtocell serves a low number of users.

3 Classification of Femtocells

In UDFNs, where more privately owned CSG femtocells are deployed and cells get closer to each other, a different coverage environment is presented, which is challenging in several ways. In UDFNs, even within the same femtocell, users can capture different neighboring femtocells as their leading aggressors. Thus, one victim femtocell can have a plurality of aggressors. Accordingly, the definition of victim and aggressor femtocells is not apparent. Therefore, the key aspect of any interference mitigation method is to organize femtocells into their different classes of being either, victim, victim-aggressor, aggressor or neutral. The class of a

femtocell depends on the status of each of its active users being either critical or non-critical. However, it can also be influenced by its behavior towards other users within its one-hop neighbor femtocells.

Figure 2 represents a typical small femtocell cluster, consisting of four femtocells with identities F1 to F4, from left to right. Each femtocell is serving a number of users. Each user or UE has a two digit identity, with the second digit specifying the identity of its respective serving femtocell. Assuming all users within each femtocell in this cluster are in active mode, we can classify femtocells in terms of interference into four Classes: Class 1: Victim femtocell, where at least one or more of its users are above a predefined threshold value (UE 31) and regarded as critical user(s) (F1). Class 2: Victim-aggressor femtocell, where one or all of its active users are considered as critical (UE 32), and at the same time causes the metric to rise above the threshold value for at least one or more of the users serviced by its neighboring femtocells (F2). Class 3: aggressor femtocell, where all of its active users are regarded as non-critical, but causing one or more of the users served by one of its neighbor femtocells to be in the critical status (F3). Class 4: Neutral femtocell where all of its active users are considered non-critical, while having no effect on any of the users served by its one-hop neighbor femtocells and it is considered neither victim nor aggressor (F4). The status of any user is time variant and can switch from one status to the other (namely critical to non-critical) or vice versa. Subsequently, the Class of any femtocell can switch from one Class to another.

The weight or severity of interference depends on a number of aspects such as the cell density, used bandwidth, transmitted power, and mechanism used for channel access. However, there are a few mitigation techniques in the literature for interference management such as beamforming, precoding techniques and adaptive power. However, for the next generation of dense femtocell networks, cell clustering has been proposed in several studies. Clustering techniques are based on cooperation between one-hop neighboring femtocells for interference and resource management. However, the cooperation between the entire members of the cluster is not possible in large clusters, since this would require a lot of pilots and feedback signaling. Thus cell clustering has been recommended to integrate the cooperation between limited numbers of femtocells within specific areas.

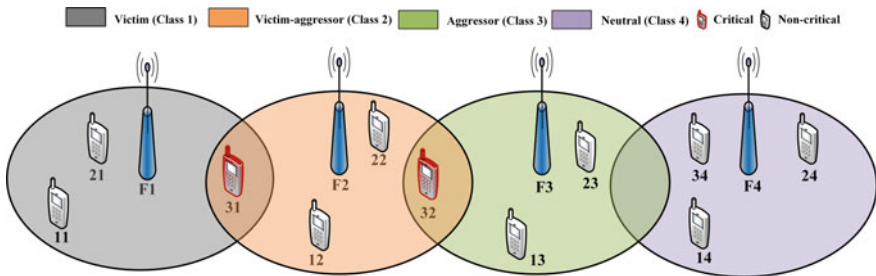


Fig. 2 Interference scenario in a typical cluster of femtocells

4 Case Study

In this case study, we introduce a new interference and resource management method based on semi-clustering, namely the Semi-clustering of Cells for Interference and Resource Management in Ultra-dense Femtocell Networks (SCC) scheme. The main aim of the proposed SCC algorithm is to manage interference among femtocells without the use of any initial fixed frequency planning procedure. The SCC algorithm comprises five steps which can be detailed as follows:

- Step 1: Once a femtocell is switched on, it immediately starts receiving the measurement reports from its active users to identify aggressor femtocells within its one-hop neighbors. The measurements list is then shared with its corresponding one-hop neighbors and also with the FGW via the S1 interface. In our simulation, the user is considered critical if the value of *DIR* is greater than 3 dB, and the ratio of the desired signal power to the dominant interferer *SDIR* is less than 10 dB, otherwise the user is regarded as non-critical.
- Step 2: Once critical and non-critical users in all femtocells are distinguished, the classification of femtocells takes place. In this procedure, a femtocell can be a victim, victim-aggressor, aggressor or neutral, in other words Class 1, Class 2, Class 3 or Class 4 respectively.
- Step 3: Based on the Class of each femtocell, the SCC approach divides each victim, victim-aggressor femtocell (Class 1 and Class 2) into two virtual cells, otherwise it remains intact. The first virtual cell serves critical users only, while the second serves non-critical users.

Figure 3 illustrates the concept of Step 3. Taking Fig. 1 as an example of a typical cluster of femtocells (Fig. 3a), and as mentioned earlier, F1 and F2 are members of Class 1 and Class 2 (victim and victim-aggressor respectively). F1 serves users (UE11, UE21 and UE31), while F2 serves users (UE12, UE22 and UE32). Thus F1 is partitioned into F1A (Fig. 3b) where it serves critical user (UE31), and F1B (Fig. 3d) serves non-critical users (UE11 and UE21). In addition, F2 is split into F2A (Fig. 3c), with critical user (UE32), and F2B (Fig. 3d) with non-critical users (UE12 and UE22). However, F3 and F4 remain intact and no splitting takes place with them as they are both non-victims.

- Step 4: Once all victim and victim-aggressor femtocells are split into pairs of virtual cells, the FGW embarks on the clustering phase. The clustering information is then sent to each victim and aggressor femtocell, again through the S1 interface. The SCC scheme forms one cluster for each virtual cell that serves critical users only and its aggressor/s, as was shown in Fig. 3. Also from Fig. 3, it can be seen that no interference can occur between any two neighboring femtocells in all clusters (b, c and d). In other words, the SCC scheme can make all Class 1 and Class 2 femtocells switch to Class 4, in other words all femtocells become neutral.

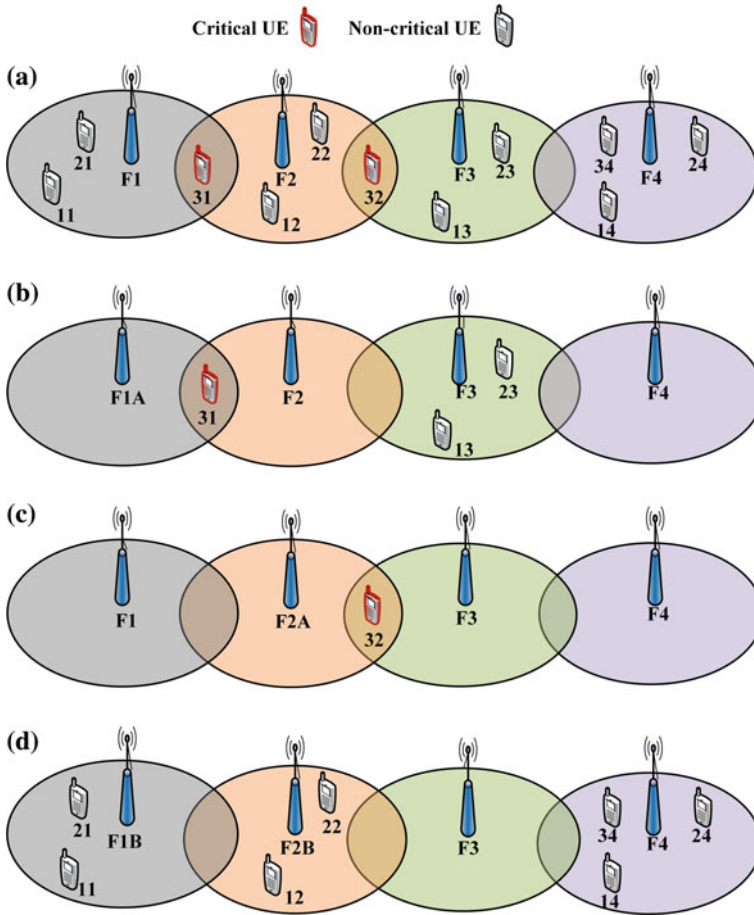


Fig. 3 The concept of femtocell splitting

Step 5: Once the clustering information is received from the FGW, resource allocation is performed by each cluster based on the status of each active user. The coordination between victim and aggressor femtocells within each cluster regarding resource distribution can be reached through the X2 interface. In this mechanism, all non-critical users within Class 1, Class 2 and Class 4 can fully exploit the available radio resources. However, critical users have to share the available resources with their aggressors in frequency reuse 2 manner. Nonetheless, non-critical users within Class 3 femtocells (aggressor) have to share the resources with their victims since they still maintain their aggressiveness property towards their victims.

Figure 4 depicts the notion of Step 5. Figure 4a, b, c and d represent the resource management for the different clusters shown in Fig. 3a, b, c and d respectively. In

Fig. 4 SCC resource management

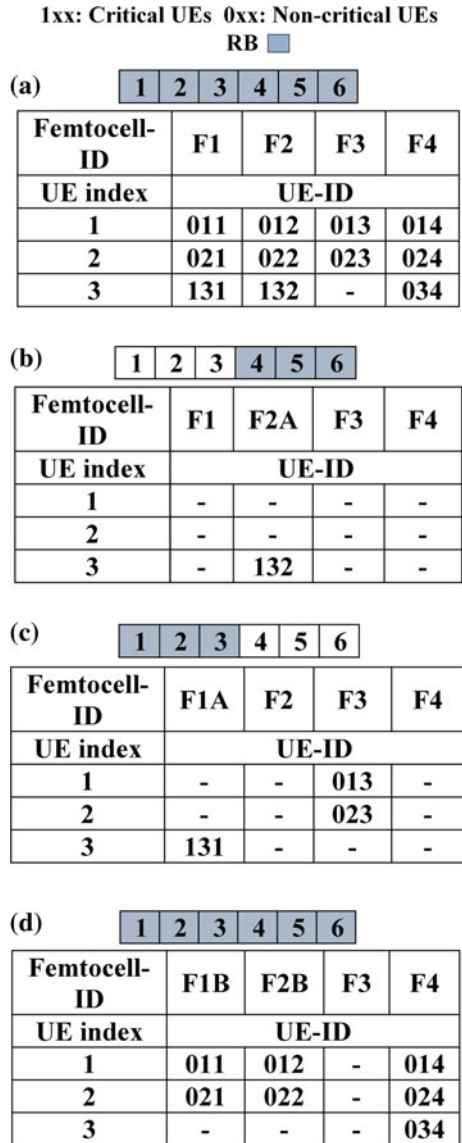


Fig. 4a, the scheduler allows sharing of the same resources to all femtocells regardless of co-tier interference between femtocells. In this case, severe interference occurs between F1 and F2, and also between F2 and F3 as was discussed earlier in Sect. 3. However, the scheduler makes sure that the critical users in F1A cannot obtain the same resources as the critical users in F2A. Moreover, the critical users in F2A cannot obtain the same resources as users in F3 as they interfere with each other as was shown in Fig. 3a. Nevertheless, non-critical users within these

two cells (F1B and F2B) along with users in F4 (neutral) can obtain all the resources, and at the same time, regardless of any aggressors as shown in Fig. 4d.

It must be mentioned here that for simplicity reasons, virtual cells that are serving critical users and their aggressors in this example share resources equally. However, the SCC scheme adopts a dynamic mechanism for resource sharing between the victim cells and their respective aggressor/s. For optimal utilization of the available resources, the SCC takes into consideration two factors that are inconstant and time variant.

The first factor is the ratio of the number of critical users within victim and aggressor femtocells in the case of Class 2 (namely victim-aggressor). The second is the total number of users within victim and aggressor/s. This factor will ensure fairness for non-critical users within Class 3 femtocells (namely aggressor). Thus, the resource sharing between victim and aggressor femtocells can be formulated as follow:

$$F_{RB}(i) = \left[\left(\frac{N_{u_c, F_i}}{T_{u_c, C_i}} + \frac{N_{u_s, F_i}}{T_{u_s, C_i}} \right) / 2 \right] \times RB_{Total}, \quad (2)$$

where N_{u_c} is the number of critical users within femtocell F_i , and T_{u_c} is the total number of critical users within cluster C_i . N_{u_s} is the number of users (critical and non-critical) within F_i and T_{u_s} is the total number of users (critical and non-critical) within cluster C_i . RB_{Total} is the number of the available resource blocks.

Simulation models follow 3GPP specification [24], more specifically focusing on the test case with an indoor cluster of femtocells, referred to as Scenario 3 by 3GPP. As a difference from [24], we consider a denser femtocell deployment scenario with a quad-strip model. Femtocells and users are randomly dropped according to a Poisson point process (PPP) in the restricted apartment area, with a minimum distance to the inner walls of 25 cm and 10 cm respectively. The traffic model assumed is full buffer, since it characterizes the worst case interference environment and cannot be easily solved by straightforward scheduling techniques. The available number of resource blocks is 25 RBs. Other important parameters in the simulation can be found in [24].

5 Results Analysis

In this section, we analyze the performance of the proposal to investigate its efficiency for different femtocell density and crowding scenarios. The first comparator for the SCC scheme is one of the existing state of the art X2-based algorithms. Explicitly, the comparison will be with the X2-UEs scheme. More details of this technique can be found in [25]. Both SCC and X2-UEs are evaluated with respect to frequency reuse 1, where no clustering takes place and all femtocells share all available radio resources. This scheme will be referred to as the Non Inter-cell Interference Coordination (Non-ICIC) method in the following discussion. All schemes are evaluated in terms of two key system metrics; the average throughput of users and the mean capacity of femtocells.

Figures 5 and 6 show the percentages of different classes of femtocells with regard to femtocell density. As femtocells get denser, the percentage of Class 2 (victim-aggressor) increases from 0% to more than 60%. On the other hand, a minor decrease of only about 10% for Class 1 femtocells (victim) is depicted in Fig. 5. Moreover, Class 4 has decreased from 50% to approximately 13% as shown in Fig. 6. Finally, there is only a small change of 13% for Class 3. To sum up, in sparse deployments, victims and aggressors are more or less equal, and each victim femtocell has only one aggressor. Nevertheless, as femtocells get denser, they tend to have the property of being victims and aggressors at the same time. Thus, one femtocell would have more than one aggressor. Therefore, identifying dominant interferers in dense femtocell networks is not a straightforward task and starts to become a complex matter.

Fig. 5 Percentages of Class 3 and 4

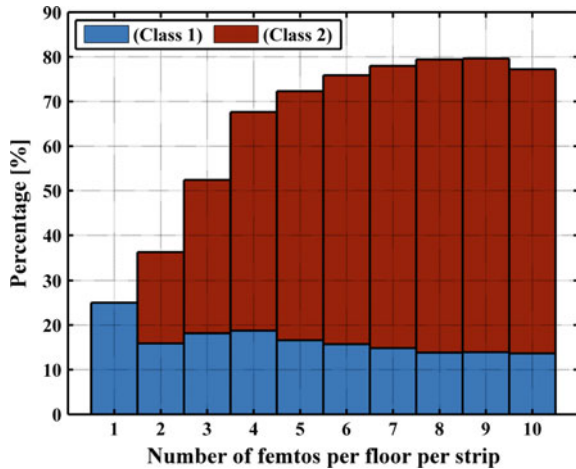


Fig. 6 Percentages of Class 1 and 2

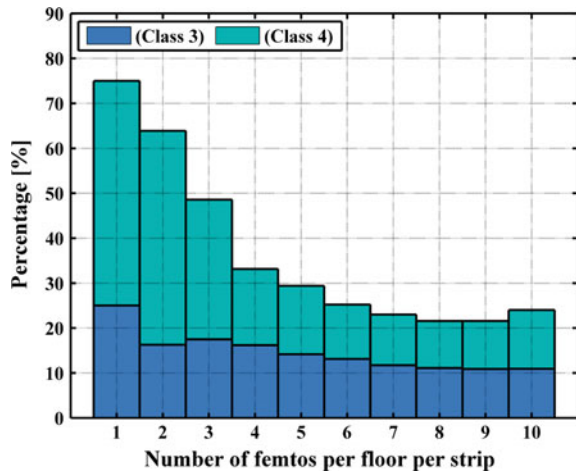


Figure 7 illustrates the average throughput of users achieved by the SCC scheme with different femtocell densities. It can be seen that the benefit of the SCC scheme in terms of throughput begins with a single femtocells per floor and remains even when the number of femtocells per floor increases to a density of 10 femtocells. The average gain in the mean users' throughput is approximately 1.79 Mbps or 32.58% compared to the X2-UEs technique, with respect to a Non-ICIC scenario.

In Fig. 8, the average throughput of users with different crowding densities is shown. The crowding density ranges from one user per femtocell to the maximum of 10 users. The outperformance of the proposed scheme over its counterpart is apparent in all crowding scenarios. This outperformance ranges from 8.10 Mbps for a low crowding density to 0.81 Mbps when the crowding density is at its uppermost of 10 users per femtocell.

Finally, Fig. 9 shows the overall achievement of both the SCC and X2-UEs with respect to the average capacity of femtocells as a function of different deployment

Fig. 7 Mean throughput of users with respect to femtocell density

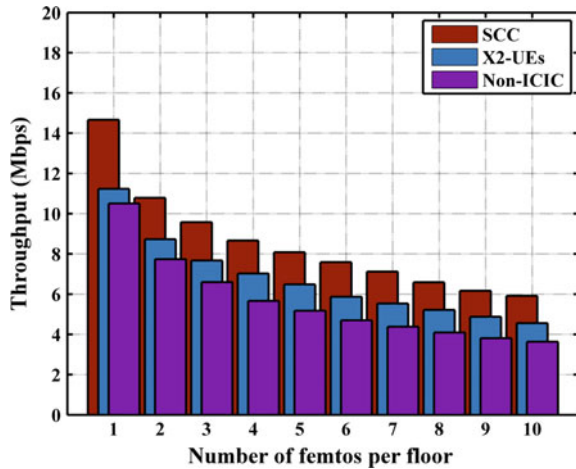


Fig. 8 Mean throughput of users with respect to crowding density

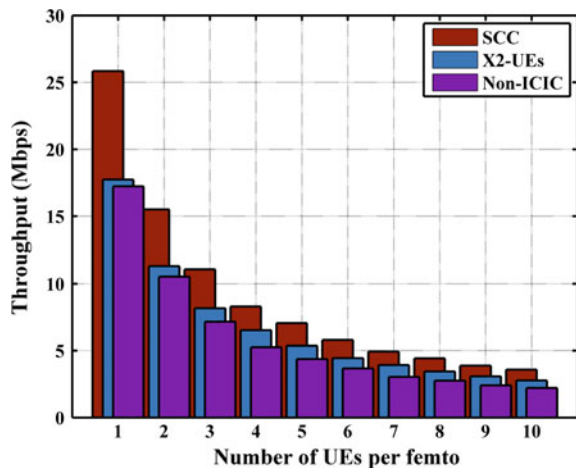
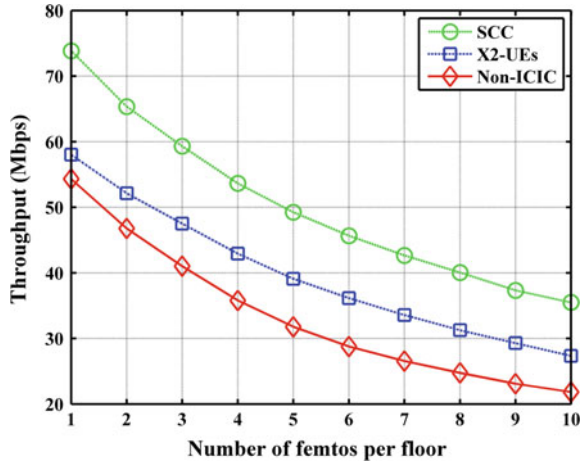


Fig. 9 Average capacity of femtocells with respect to femtocell density



densities. From Fig. 8, it can be seen that the SCC managed to enhance the overall capacity by an average of 16.79 Mbps, while the X2-UEs could only improve the capacity by an average value of 6.26 Mbps.

6 Conclusion

Femtocell densification has been considered as an encouraging method to meet ever-increasing mobile service requirements, particularly for hotspots. However, some issues have to be addressed before the benefits of femtocell densification can be realized. Of these issues, co-tier interference emerges with a new significance and opens new opportunities for research and study. In this article, we have discussed the migration of homogenous networks to ultra-dense small cell networks. We also addressed some of the challenges facing the deployment of ultra-dense femtocell networks. Moreover, we presented a new concept of radio resource and co-tier interference management based on the semi-clustering of cells (SCC). This proposal was rehearsed in different femtocell density environments, ranging from sparse to ultra-dense femtocell deployment. Simulation results show that the SCC approach outperformed one of the state of art techniques, namely the X2-UEs, for all deployment density scenarios. Both techniques were evaluated in term of the average users’ throughput and the mean capacity of femtocells.

References

1. Kim SH, Yoo KJ, Won Y (2017) Transmission algorithm with QoS considerations for a sustainable MPEG streaming service. Sustainability 9:367
2. Andreev S (2014) Delivering uniform connectivity and service experience to converged 5G wireless networks in Internet of Things (WF-IoT), presented at 2014 IEEE World Forum on, 2014: 323–324

3. Raaf B, Zirwas W, Friederichs KJ et al (2011) Vision for beyond 4G broadband radio systems. In: Presented at 2011 IEEE 22nd international symposium on personal, indoor and mobile radio communications, pp 2369–2373
4. Nokia Siemens Networks (2011) 2020 Beyond 4G radio evolution for the gigabit experience, 2011 White paper
5. Bhushan N, Li J, Malladi D et al (2014) Network densification: the dominant theme for wireless evolution into 5G. *IEEE Commun Mag* 52:82–89
6. López-Pérez D, Ding M, Claussen H et al (2015) Towards 1 Gbps/UE in cellular systems: understanding ultra-dense small cell deployments. *IEEE Commun Surv Tutor* 17:2078–2101
7. Andrews JG (2013) Seven ways that HetNets are a cellular paradigm shift. *IEEE Commun Mag* 51:136–144
8. Bhushan N, Li J, Malladi D et al (2014) Network densification: the dominant theme for wireless evolution into 5G. *IEEE Commun Mag* 52:82–89
9. Hwang I, Song B, Soliman SS (2013) A holistic view on hyper-dense heterogeneous and small cell networks. *IEEE Commun Mag* 51:20–27
10. Zander J, Mähönen P (2013) Riding the data tsunami in the cloud: myths and challenges in future wireless access. *IEEE Commun Mag* 51:145–151
11. Nguyen VM, Kountouris M (2017) Performance limits of network densification. *IEEE J Sel Areas Commun* 99:1
12. GPP TR 36.872 (2013) Small cell enhancements for E-UTRA and E-UTRAN-physical layer aspects (Release 12)
13. Li C, Zhang J, Letaief KB (2014) User-centric intercell interference coordination in small cell networks. In: 2014 IEEE international conference on communications (ICC), pp 5747–5752
14. Li C, Zhang J, Haenggi M et al (2015) User-centric intercell interference nulling for downlink small cell networks. *IEEE Trans Commun* 63:1419–1431
15. Polignano M, Mogensen P, Fotiadis P et al (2014) The inter-cell interference dilemma in dense outdoor small cell deployment. In: 2014 IEEE 79th vehicular technology conference (VTC Spring), pp 1–5
16. Soret B, Pedersen KI, Jørgensen NT et al (2015) Interference coordination for dense wireless networks. *IEEE Commun Mag* 53:102–109
17. Wang X, Visotsky E, Ghosh A (2015) Dynamic cell muting for ultra dense indoor small cell deployment scenario. *IEEE Int Conf Commun Workshop (ICCW) 2015*:148–153
18. Chen DC, Quek TQ, Kountouris M (2015) Backhauling in heterogeneous cellular networks: modeling and tradeoffs. *IEEE Trans Wirel Commun* 14:3194–3206
19. Li YNR, Xiao H, Li J et al (2014) Wireless backhaul of dense small cell networks with high dimension MIMO. In: *Globecom Workshops (GC Wkshps)*, pp 1254–1259
20. Li B, Zhu D, Liang P (2015) Small cell in-band wireless backhaul in massive MIMO systems: a cooperation of next-generation techniques. *IEEE Trans Wirel Commun* 14:7057–7069
21. Nakamura T, Nagata S, Benjebbour A et al (2013) Trends in small cell enhancements in LTE advanced. *IEEE Commun Mag* 51:98–105
22. Garcia LG, Pedersen KI, Mogensen PE (2009) Autonomous component carrier selection: interference management in local area environments for LTE-advanced. *IEEE Commun Mag* 47:110–116
23. Zhang H, Chu X, Guo W et al (2015) Coexistence of Wi-Fi and heterogeneous small cell networks sharing unlicensed spectrum. *IEEE Commun Mag* 53:158–164
24. 3GPP E U T R Access (2010) Further advancements for E-UTRA physical layer aspects. TR 36.814 Tech. Rep
25. Colas SG, Del Rio JFM, Gómez P (2013) Realistic implementation of X2-based interface management for LTE femtocells Interference coordination for dense wireless networks. *Waves* 5(1):89–97

Design and Analysis of an Optimized S-shaped Resonator Based Triple Band Microstrip Antenna for Satellite Applications

Md. Naimur Rahman, Gan Kok Beng, Md. Samsuzzaman,
Touhidul Alam and Mohammad Tariqul Islam

Abstract This article presents the architecture and exploration of a compact S-shaped resonator based triple band microstrip antenna for satellite applications. The proposed antenna is modeled for use in C (4–8 GHz) band, X (8–12 GHz) band, and Ku (12–18 GHz) band satellite applications. The antenna is composed of a circular ring-shaped patch with an S-shaped resonator. The antenna size is 24 mm × 18 mm and the prototype is imprinted on Rogers RT/duroid 5880 materials with a depth of 1.57 mm. The substrate has a relative permittivity of 2.2 and a dielectric constant of 0.0009. The excitation is supplied through a 50 Ω microstrip line. The performance of the presented antenna has been simulated and verified using High-Frequency Structural Simulator (HFSS) and Computer Simulation Technology (CST). The prototype has been measured after fabrication. The results show that the antenna covers the frequency spectrum of 5.4–7.1 GHz (C-band), 8.6–11.7 GHz (X-band), and 14.5–18 GHz (Ku band) with a 10 dB return loss. The face-to-face and side-by-side fidelity factor of the proposed antenna are 0.8195 and 0.7740 respectively. The antenna has a 6.60 dBi maximum gain with stable radiation patterns throughout the operating bands which make the proposed antenna compatible with satellite application in the C-band, X-band, and Ku-band.

Keywords Compact · Microstrip antenna · Satellite applications · Triple band

Md.N. Rahman · G.K. Beng · T. Alam · M.T. Islam (✉)
Department of Electrical, Electronic and Systems Engineering, Universiti Kebangsaan
Malaysia, 43600 Bangi, Malaysia
e-mail: tariqul@ukm.edu.my

Md.N. Rahman
e-mail: p86256@siswa.ukm.edu.my

Md.N. Rahman · Md.Samsuzzaman
Patuakhali Science and Technology University, Patuakhali 8602, Bangladesh

M.T. Islam
Kyushu Institute of Technology, Kitakyushu, Japan

1 Introduction

In recent times, the development of communication systems has seen gradually increasing bandwidth and higher data rates. With the development of the technology, the demand for short range and long range frequency spectrum coverage using lightweight, compact wireless devices has also grown rapidly. With attractive characteristics such as an uncomplicated design, low cost, low complexity, high data rate, and larger bandwidth, microstrip technology is increasingly used in today's radar and satellite communication systems. The wider bandwidth provides more channels for communications. Moreover, it also transmits data, sound, and video at higher speeds. Despite having lots of positive features, this technology also has some disadvantages such as its low efficiency and counterfeit feed radiations. It is still a challenge to design an electronically small and efficient antenna to perform multiple band communications. A lot of patch antenna has been proposed for use in multiple service wireless communications such as radar and satellite communications, radio frequency identification (RFID), telemedicine, global positioning system (GPS), mobile, and Wi-Max etc. Quite a few antennas which can be used for multiple band satellite communications are reported and studied in [1–20]. A multiband patch antenna was reported in [1] which covers the C and X band frequencies having a relatively larger size of $35.5 \text{ mm} \times 55 \text{ mm}$. In [2], a conventional patch antenna having a rectangular shape and a larger size of $27.31 \text{ mm} \times 31.48 \text{ mm}$ was presented which covers the S and X-bands. A dual band microstrip patch antenna was presented in [3], which covers the C and X-bands. In [4], a dual ultra-wideband antenna for C and X-band was presented with a relatively large size of $30 \text{ mm} \times 21 \text{ mm}$. As reported in [5], a new model concept has been adapted for dual band communication covering the Ku-band and K-band, but this antenna has a large size of $40 \text{ mm} \times 40 \text{ mm}$. An inverted-A shape multiband antenna was reported in [6] which can be used in WiMAX and C-band applications. A dual band X shape patch antenna was presented in [7] which covers the Ku-band and K band. A planar UWB antenna with multi-slotted ground was reported in [8] which has a relatively large size of $30 \text{ mm} \times 22 \text{ mm}$ and covers the bandwidth from 2.57 to 16.72 GHz.

In [9], a multiband antenna for wireless handheld devices with a larger size of $41 \text{ mm} \times 14 \text{ mm}$ was presented. A circularly polarized microstrip antenna was presented in [10] for satellite applications. In [11], an X-band antenna aimed at radar and satellite communications was rendered with a larger size of $30 \text{ mm} \times 25 \text{ mm}$. A single layer, dual band patch antenna was reported in [12], which can be used in Ku-band satellite applications. In [13], a split P-shaped antenna was presented for present-day communications. A genetic algorithm inspired tri-band patch antenna was presented in [14] which can be used in WiFi, WiMAX, and HiperLAN. The antenna reported in [15] has a larger size of $32.85 \text{ mm} \times 26.5 \text{ mm}$ and covers the channel for Ku-band satellite applications. An E-shaped microstrip patch antenna was reported in [16] which covers the Ku-band frequencies having a relatively larger size of $34 \text{ mm} \times 27 \text{ mm}$. In [17], a circular patch microstrip array

antenna with a larger size of $72 \text{ mm} \times 72 \text{ mm}$ was presented which covers the Ku-band. A tri-band antenna which was presented in [18], covers the C, X, and Ku-bands. In [19], a slotted antenna for X-band application was reported. As reported in [20], a dual band patch antenna was adapted for serving the Ku-band and K-band satellite communications. Modern communication systems demand an electronically small antenna instead of a traditional larger dish antenna for satellite communications. A number of techniques have been adapted in the papers discussed in order to obtain multiband performances in a single wireless device. These techniques include multi slot-loaded antennas, a multilayer stacked patch, and the inclusion of resonators, etc.

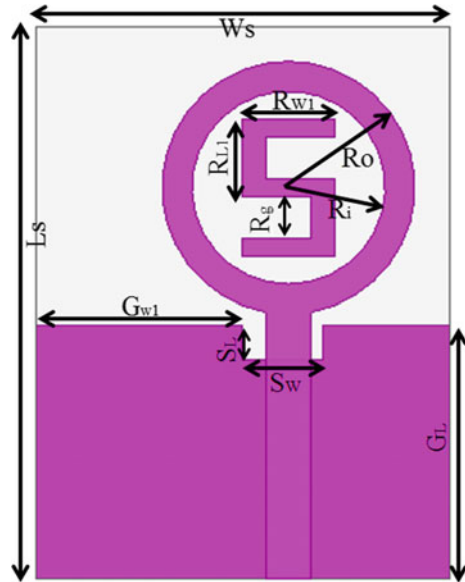
In this article, an S-shaped resonator-based antenna with slotted partial ground having a compact size of only $24 \text{ mm} \times 18 \text{ mm}$ only is proposed. The results reveal that the presented antenna covers the bandwidths 5.4–7.1 GHz (C-band), 8.6–11.7 GHz (X-band), and 14.5–18 GHz (Ku band) with a 10 dB return loss. The antenna can be used for full-time satellite television networks as the C-band is used for the open satellite communications. The antenna is suitable for military use as the X-band has been employed in missiles, marine radar, tracking, and mapping, etc. Due to it covering the Ku band, this antenna can be useful in satellite communications as well as military applications because the Ku-band becomes the I band in military countermeasure band designation. The proposed antenna has a maximum gain of 6.60 dBi, considerable efficiency, and a stable radiation pattern throughout the operating bandwidth.

2 Antenna Design and Parametric Study

It is a challenge to plan a compact and simple antenna which reveals little distortion having a large frequency range as it is the basic component in wideband systems. Figure 1 displays the proposed S-shaped resonator based microstrip patch antenna with slotted partial ground. The antenna is made up of a circular patch within which an S-shaped resonator exists, and a slotted partial ground plane.

The microstrip patch and the resonator of the proposed antenna are printed one portion of Rogers RT/duroid 5880 substrate material. The material has a compact size of $24 \text{ mm} \times 18 \text{ mm}$ and a depth of 1.57 mm. The substrate has a relative permittivity of 2.2 with a 0.0009 dielectric loss tangent. A feedline is impersonated on the same portion of the material acting as the radiating component. The slotted partial ground with length G_L is impersonated on the opposite part of the material. The length and width of the slot on the partial ground plane are S_L and S_W respectively. The radiating patch of the antenna consists of a circular disc of radius R_O mm from which a circle of radius R_i mm is carved out. The parameters of the antenna are: $L_S = 24 \text{ mm}$, $W_S = 18 \text{ mm}$, $G_L = 11 \text{ mm}$, $G_{WI} = 9 \text{ mm}$, $S_L = 1.5 \text{ mm}$, $S_W = 3.5 \text{ mm}$, $R_{WI} = 4 \text{ mm}$, $R_{LI} = 3.4 \text{ mm}$, $R_g = 1.8 \text{ mm}$, $R_O = 5.5 \text{ mm}$, $R_i = 4.2 \text{ mm}$.

Fig. 1 Layout of the presented antenna structure



To observe the specific design properties of the proposed antenna, a parametric study was carried out. The electrical and geometrical parameters affect the antenna performances. The parameters chosen were: ground plane length, the presence of the slot on the ground, and the presence of the S-shaped resonator in the radiating patch. The S-shaped resonator of the patch with slotted partial ground can produce multiple resonances providing multiple bands. The effects of changing the ground plane length, the presence of the slot on the ground, and the circular shape patch with the S-shaped resonator were observed, and this has a significant role in impedance matching. In the simulations, during the observation of one parameter, the other parameters were kept constant.

The ground length is a very important parameter in wideband antenna design. Figure 2 displays the reflection coefficient for the different ground plane lengths during simulation. From the figure, it can be seen that the impedance bandwidth depends on the ground length. The ground length is more significant at lower frequencies where the current is concentrated more for impedance matching. By varying the length of the ground from a certain value causes a reduction in bandwidth. From the figure, it can be seen that the proposed ground plane with a length of 11 mm with a slot has a better impedance bandwidth covering the C-band, X-band, and Ku-band. Figure 3 shows the role of the slot on the ground plane in impedance matching. The presence of the slot in the ground has a vital role in increasing bandwidth. This is because of the mutual coupling among the slotted ground and the radiating patch. Figure 4 displays the effects of the presence of the S-shaped resonator within the circular radiating patch on impedance bandwidth. From the illustration, it can be seen that the resonator within the patch has a

Fig. 2 Return loss characteristics for different lengths of the ground plane

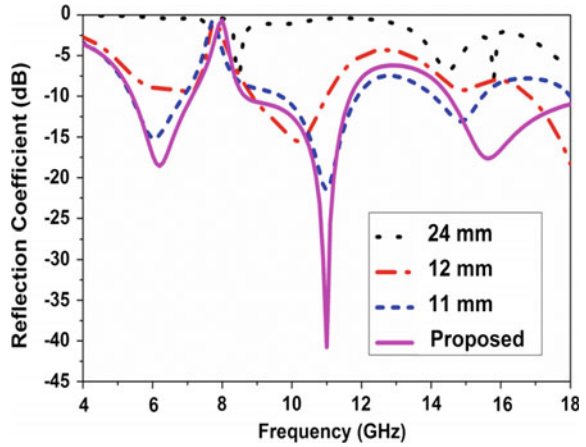


Fig. 3 Return loss characteristics for the presence of the slot on the ground

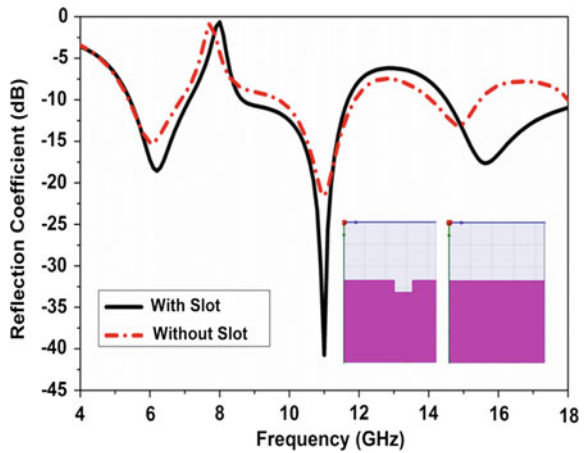
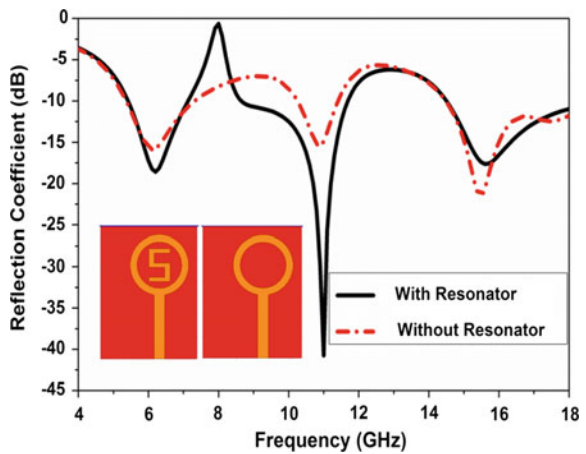


Fig. 4 Return loss characteristics for the presence of the S-shaped resonator within the patch



negligible effect at lower frequencies, but at higher frequencies above 8 GHz, the effects are more significant. By inserting the resonator in the patch, the impedance bandwidth can be increased as well as the resonance point.

3 Antenna Performance Analyses

The antenna performances were inspected and validated using High-Frequency Structural Simulator (HFSS). The time domain characteristics were analyzed using Computer Simulation Technology (CST). The prototype was fabricated on the printed circuit board for the practical experiment. The measurement was performed in the microwave laboratory at the department of Electrical, Electronic and Systems Engineering (JKEES), UKM, Malaysia. For the measurement of the proposed antenna, a N5227A PNA Microwave Network Analyzer (10 MHz–67 GHz) and a Satimo Near Field Measurement Laboratory (measurement range 1.0–18.0 GHz) were used.

Figure 5 shows the reflection coefficient in opposition to the frequency. The antenna covers bandwidths from 5.4 to 7.1 GHz (1.7 GHz), 8.6 to 11.7 GHz (3.1 GHz), and 14.5 to 18 GHz (3.5 GHz) with a 10 dB return loss corresponding to the C-band, X-band, and Ku-band respectively. The gain of the proposed S-shaped resonator based antenna is displayed in Fig. 6. The figure shows the gain from 4 GHz to 18 GHz. It can be clearly seen from the figure that the antenna has 4.34 dBi average gain with a maximum gain of 6.60 dBi. Figure 7 shows the efficiency of the proposed S-shaped resonator based microstrip patch antenna. The presented antenna has an average efficiency of 83.67%. This higher radiation efficiency means that more power is radiated in comparison with power that is retained in the antenna. That means that the antenna will be cooler, and as a result will be able to be used for longer periods without performance degradation.

Fig. 5 Reflection coefficient of the presented antenna

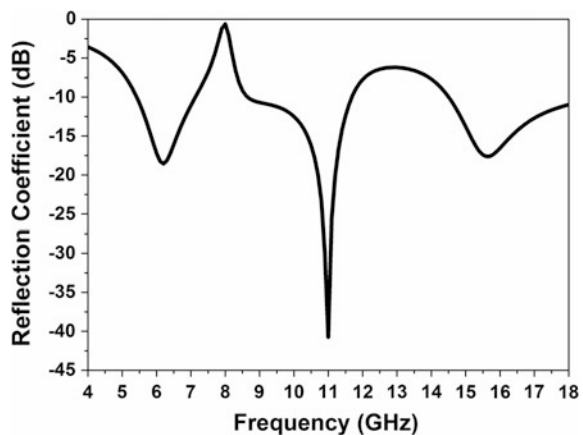


Fig. 6 Peak gain of the presented antenna

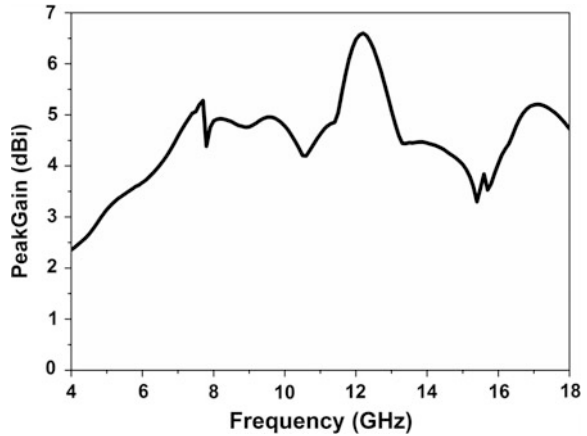
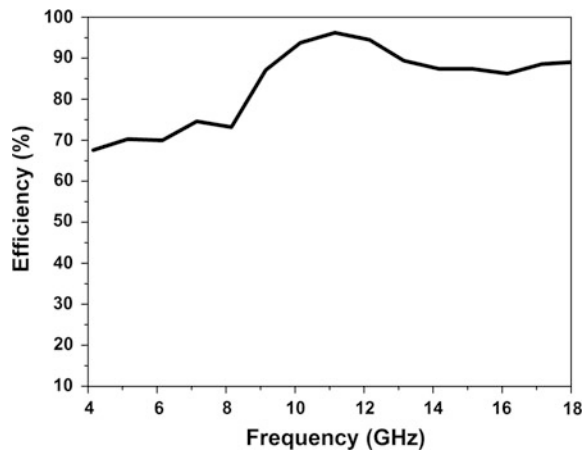


Fig. 7 Efficiency of the presented antenna



The current distributions on the surface of the resonator based antenna at three resonance frequencies, namely 6.2, 11, and 15.6 GHz are illustrated in Fig. 8a–c, respectively. To realize a multiband antenna design, it is necessary to overlap adjacent modes with each other. The overlap of the resonance modes causes the current distribution of several modes. The proposed antenna achieves the multiple bands because of the current flow keeping up a harmonic order in both the radiating patch and slotted partial ground. Figure 8a displays the distribution of current at the first resonance at 6.2 GHz. The current distribution at 11 GHz is illustrated in Fig. 8b, indicating a second order harmonic. The complicated current distribution at 15.6 GHz, corresponding to the third harmonic, is illustrated in Fig. 8c. According to the figure, the current is mainly distributed along the microstrip feed-line, the circular patch, and the resonator. The ground close to the feed-line and patch acts as the radiating plane. From the figure, it can be seen that at lower frequencies the

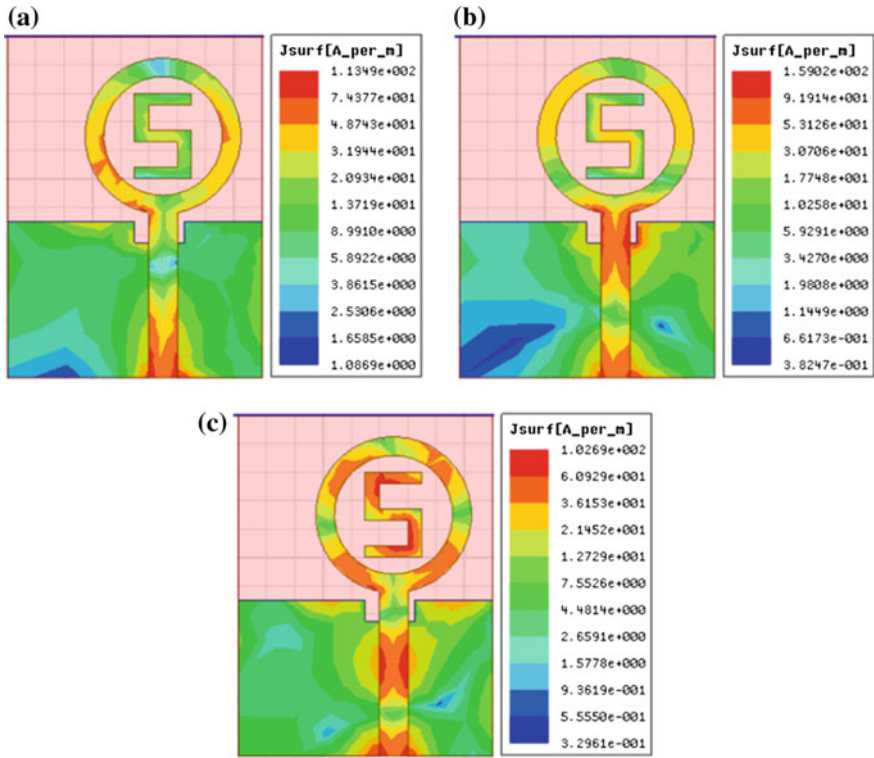


Fig. 8 Distribution of current of the at **a** 6.2 GHz **b** 11 GHz **c** 15.6 GHz

current maintains a symmetrical distribution on the radiator, but at higher frequencies the current distribution is asymmetrical on the radiator.

The radiation pattern with co-polarization and cross-polarization of the proposed S-shaped resonator based slotted partial ground microstrip patch antenna for the same frequencies in xz -plane or E-plane ($\varphi = 0$) and yz -plane or H-plane ($\varphi = 90$) are displayed in Fig. 9a–c. It was found that at 6.2 GHz, the radiation pattern of the proposed prototype is omnidirectional both in the xz -plane and the yz -plane. At frequency 11 GHz, the radiation pattern remains persistent enough to be omnidirectional. The radiation pattern of the antenna turns directive at the higher frequency of 15.6 GHz for the higher order current excitation. The omnidirectional pattern becomes directive at higher frequencies due to several factors. Firstly, the order of slot resonance becomes higher as the frequency increases. Secondly, at higher frequencies, the patch and the resonator resonated by themselves. Thirdly, the microstrip feedline resonates at the higher frequencies. The results of Fig. 9a–c illustrate that the patterns are durable within the entire operating bands.

At the receiving antenna, the output pulse is the convolution of the transfer function and the input pulse. By using the inverse Fourier transform, the transfer function changes to the time domain. Figure 10 shows the input pulses and output

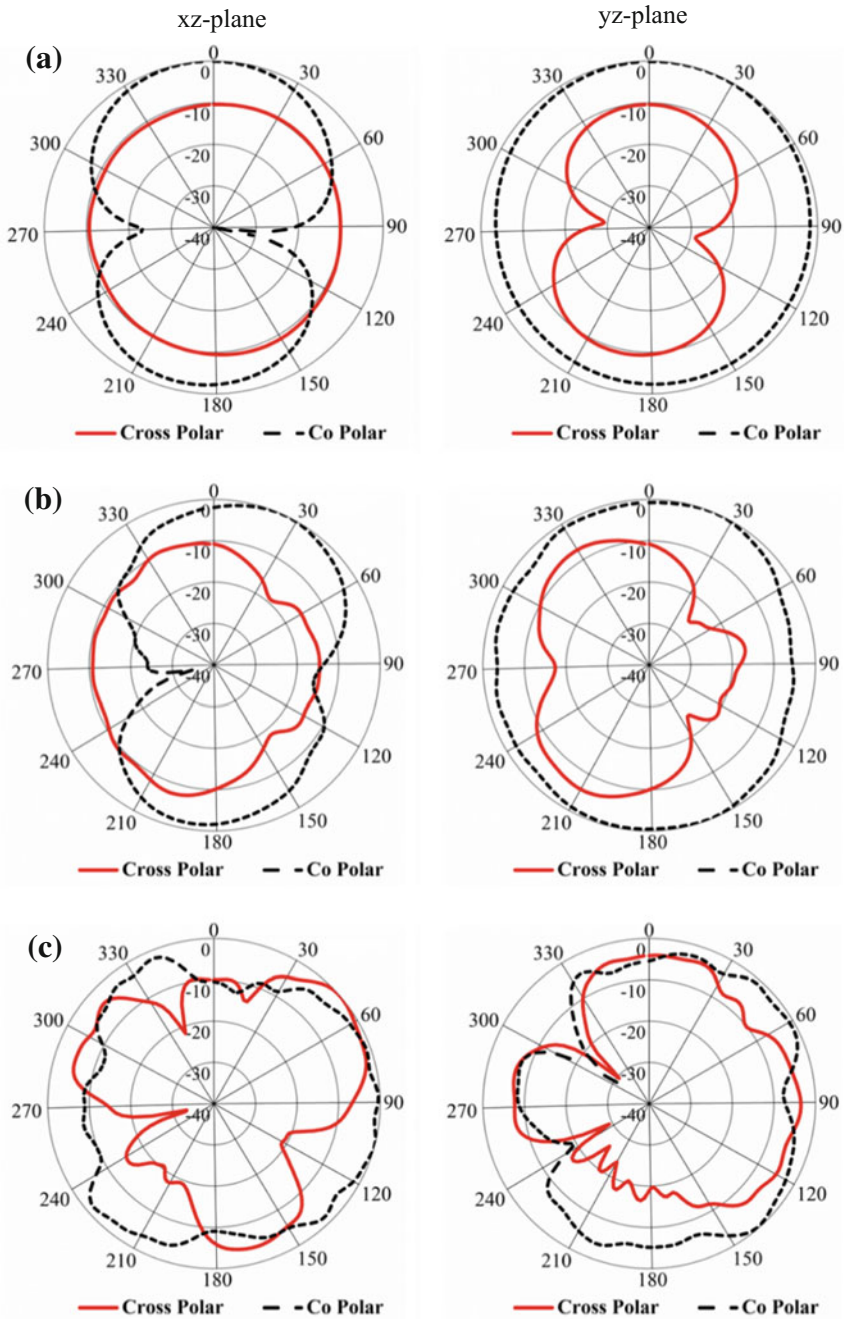


Fig. 9 Radiation Pattern at **a** 6.2 GHz **b** 11 GHz **c** 15.6 GHz

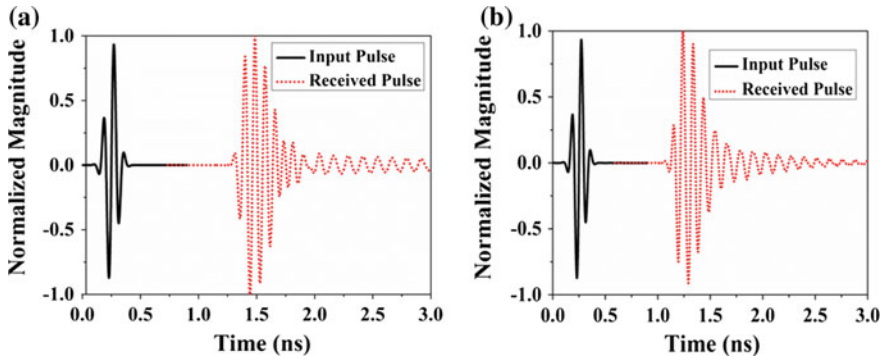


Fig. 10 Input and received pulses **a** Face-to-face orientation **b** Side-by-side orientation

pulses when the antennas are in face-to-face and side-by-side orientation. It is clearly observed that in face-to-face and side-by-side orientation, the input pulse and the received pulse are similar. As a result, the antenna can radiate short pulses with negligible distortion. To estimate the signal distortion, the fidelity parameter was used. Fidelity is the peak amplitude of the cross-correlation among the input signal and the received signal. Equation 1 is used to find the fidelity factor.

$$F = \max \frac{\int_{-\infty}^{+\infty} x(t)y(t+\tau)dt}{\sqrt{\int_{-\infty}^{+\infty} |x(t)|^2 dt \int_{-\infty}^{+\infty} |y(t)|^2 dt}} \quad (1)$$

where $x(t)$ and $y(t)$ correspond to the input pulse and received pulse respectively.

The face-to-face and side-by-side fidelity factor of the proposed antenna were 0.8195 and 0.7740 respectively, found by using Eq. 1. The higher the fidelity factor value, the lower the distortion of the pulse in the antenna.

4 Conclusion

In this article, a compact S-shaped resonator based slotted partial ground microstrip antenna has been presented for satellite communications. High-Frequency Structural Simulator (HFSS) and Computer Simulation Technology (CST) were used to simulate and validate the antenna's performance. The reflection coefficient covers the C, X and Ku bands. The proposed antenna covers the frequency spectrum 5.4–7.1 GHz (C-band), 8.6–11.7 GHz (X-band), and 14.5–18 GHz (Ku band) with a 10 dB return loss. The antenna has a maximum gain of 6.60 dBi and considerable efficiency, providing durable radiation patterns. The face-to-face and side-by-side fidelity factor are 0.8195 and 0.7740 respectively. Thus, these characteristics make the proposed antenna suitable for C, X, and Ku triple band satellite applications.

Acknowledgment This work is supported by the Ministry of Education Malaysia (MOE) under grant no FRGS/1/2014/TK03/UKM/01/1.

References

1. Prema N (2016) Design of multiband microstrip patch antenna for C and X band. *Optik Int J Light Electron Opt* 127:8812–8818
2. Sidhu AK, Sivia JS (2016) Microstrip rectangular patch antenna for S and X band applications. In: International conference on wireless communications, signal processing and networking (WiSPNET), pp 248–251
3. Gupta S, Dhillon SS, Khera P, Marwaha A (2013) Dual band U-slotted microstrip patch antenna for C band and X band radar applications. In: 2013 5th international conference on computational intelligence and communication networks (CICN), pp 41–45
4. Meloui M, Essaaidi M (2014) A dual ultra wide band slotted antenna for C and X bands application. *Prog Electromagn Res Lett* 47:91–96
5. Ahsan M, Islam M, Habib Ullah M, Aldhaheer R, Sheikh M (2015) A new design approach for dual-band patch antenna serving Ku/K band satellite communications. *Int J Satell Commun Netw*
6. Ahsan MR, Islam MT, Ullah MH (2014) A compact multiband inverted a-shaped patch antenna for WiMAX and C-band. *Microw Opt Technol Lett* 56:1540–1543
7. Samsuzzaman M, Islam M, Misran N, Ali MM (2013) Dual band X shape microstrip patch antenna for satellite applications. *Procedia Technol* 11:1223–1228
8. Azim R, Islam MT, Misran N, Cheung S, Yamada Y (2011) Planar UWB antenna with multi-slotted ground plane. *Microw Opt Technol Lett* 53:966–968
9. Rao Q, Geyi W (2009) Compact multiband antenna for handheld devices. *IEEE Trans Antennas Propag* 57:3337–3339
10. Ferrero F, Luxey C, Jacquemod G, Staraj R (2005) Dual-band circularly polarized microstrip antenna for satellite applications. *IEEE Antennas Wirel Propag Lett* 4:13–15
11. Tripathi AK, Singh B (2013) A cpw fed x-band antenna for satellite & radar applications. In: 2013 international conference on microwave and photonics (ICMAP), pp 1–3
12. Islam M, Misran N, Mobashsher A (2010) Compact dual band microstrip antenna for Ku-band application. *Inf Technol J* 9:354–358
13. Alam MJ, Faruque MRI, Islam MM (2016) Design of a split P-shaped multiband microstrip patch antenna for modern communication system. In: 2016 19th international conference on computer and information technology (ICCIT), pp 68–71
14. Fertas K, Kimouche H, Challal M, Aksas H, Aksas R, Azrar A (2015) Design and optimization of a CPW-fed tri-band patch antenna using genetic algorithms. In *ACES*, 2015, p 754
15. Malisuwan S, Sivaraks J, Madan N, Suriyakrai N (2014) Design of microstrip patch antenna for Ku-Band satellite communication applications. *Int J Comput Commun Eng* 3:413
16. Ahmed R, Islam MF (2013) E-shaped microstrip patch antenna for Ku Band. *Int J Comput Appl* 80
17. Lai T, Mahadi WNL, Soin N (2008) Circular patch microstrip array antenna for ku-band. *World Acad Sci Eng Technol* 48:298–302
18. Hamza H, Hussien K (2014) Tri-band dual-polarized multilayer SAR microstrip antenna. In: *PIERS Proceedings*
19. Shahu BL (2015) A compact slotted microstrip antenna for X-band application in satellite communication. *Int Res J Eng Technol (IRJET)* 2:498–501
20. Islam M, Islam MT, Faruque MRI (2013) Dual-band operation of a microstrip patch antenna on a Duroid 5870 substrate for Ku-and K-bands. *Sci World J* 2013

Negative- μ Metamaterial-Based Stacked Antenna for 1U CubeSat Communication

Farhad Bin Ashraf, Touhidul Alam, Mengu Cho, Norbahiah Misran and Mohammad Tariqul Islam

Abstract The 1U CubeSat is a well-known modern nanosatellite and has a typical volume of $10 \times 10 \times 10 \text{ cm}^3$ and weighs as little as 1.33 kg. Compact high-performance antennas are used in CubeSats. This paper presents a low-profile high-gain metamaterial-based stacked antenna for CubeSats. The antenna achieves a fractional bandwidth of 11.48% with overall antenna dimensions of $0.84\lambda \times 0.82\lambda \times 0.099\lambda$ at the lower end frequency of 8.29 GHz. The realized gain was increased to 37.32% (increased from 8.01 dB to 11 dB) by using a negative- μ metamaterial ground plane. The antenna performance was also investigated using a 1U CubeSat body.

1 Introduction

Scientists are currently planning to send CubeSats to other planets for deep space environment analysis. MarCo, a CubeSat is planned for launch in next year (2018) to observe the Mars environment [1]. CubeSats require high gain antennas and in previous years, many studies have been investigated the feasibility of their use in satellites [2–7]. However, deployment of high gain antennas has experienced some difficulty in space. To circumvent these limitations researchers have turned their attention to patch antennas. Big challenges still have to be faced due to some patch antenna characteristics such as low efficiency and the large size need to achievement high gain. In [5], Islam et al. proposed an S-band circular polarized antenna for nanosatellite application.

F.B. Ashraf (✉) · T. Alam · N. Misran · M.T. Islam
Department of Electrical, Electronic and Systems Engineering,
Universiti Kebangsaan Malaysia, 43600 Bangi, Selangor D.E., Malaysia
e-mail: farhadbinashraf@siswa.ukm.edu.my

M.T. Islam
e-mail: tariqul@ukm.edu.my

M. Cho · M.T. Islam
Kyushu Institute of Technology, Kitakyushu, Japan

Metamaterials are artificially formed structures which have shown great potential to exploit the unconventional properties of the materials. The unit cell forms a two-layer metamaterial structure used as a substrate for gain enhancement of a stacked antenna at 8.55 GHz [8]. In [9], a microstrip patch antenna acts as the source and a metamaterial unit cell acts as a ground plane. The peak gain of the antenna is 18.4 dBi at 10 GHz. A simple yet unconventional wideband resonant cavity antenna with a high gain was presented in [10], and showed a bandwidth of 25% with a peak gain of 17.7 dBi.

In this paper, a high gain metamaterial-based stack antenna is proposed for 1U CubeSat application. The antenna performance was investigated using a 1U CubeSat structure. The operating range is from 8.29 GHz to 9.30 GHz in the X-band microwave spectrum.

2 Design Methodology

The geometry of the proposed stacked antenna is presented in Fig. 1. The 1st layer and 2nd layer of the proposed stacked antenna were designed using a Rogers RT5880 substrate material having a relative permittivity of 2.2, and heights of 0.58 mm and 1.575 mm. Four spacers are used to separate the two layers. The conventional ground plane of the 2nd layer is replaced by the metamaterial unit-cells. The overall antenna dimensions are $29.80 \times 30.30 \times 2.66 \text{ mm}^3$. A 1U CubeSat was designed to analyze the antenna performance and was integrated with the satellite body as shown in Fig. 2.

3 Metamaterial Characteristics

The proposed unit cell is shown in Fig. 1e. It uses Rogers 5880 as a substrate with a thickness d of 1.575 mm. Perfect electric conductor (PEC) and perfect magnetic conductor (PMC) boundary conditions are applied in the x and y planes respectively. Two electromagnetic waveguide ports are placed between the unit cell, and the propagating direction k is along the z -plane. To get the effective parameters, reflection (S_{11}) and transmission (S_{21}) coefficients were calculated using CST Microwave Studio 2017. Then effective parameters of the proposed unit-cell were retrieved by using the following equation [11], and attained relative impedance z , refractive index η and relative permeability μ .

$$z = \pm \sqrt{\frac{(1 + S_{11})^2 + S_{21}^2}{(1 - S_{11})^2 + S_{21}^2}} \quad (1)$$

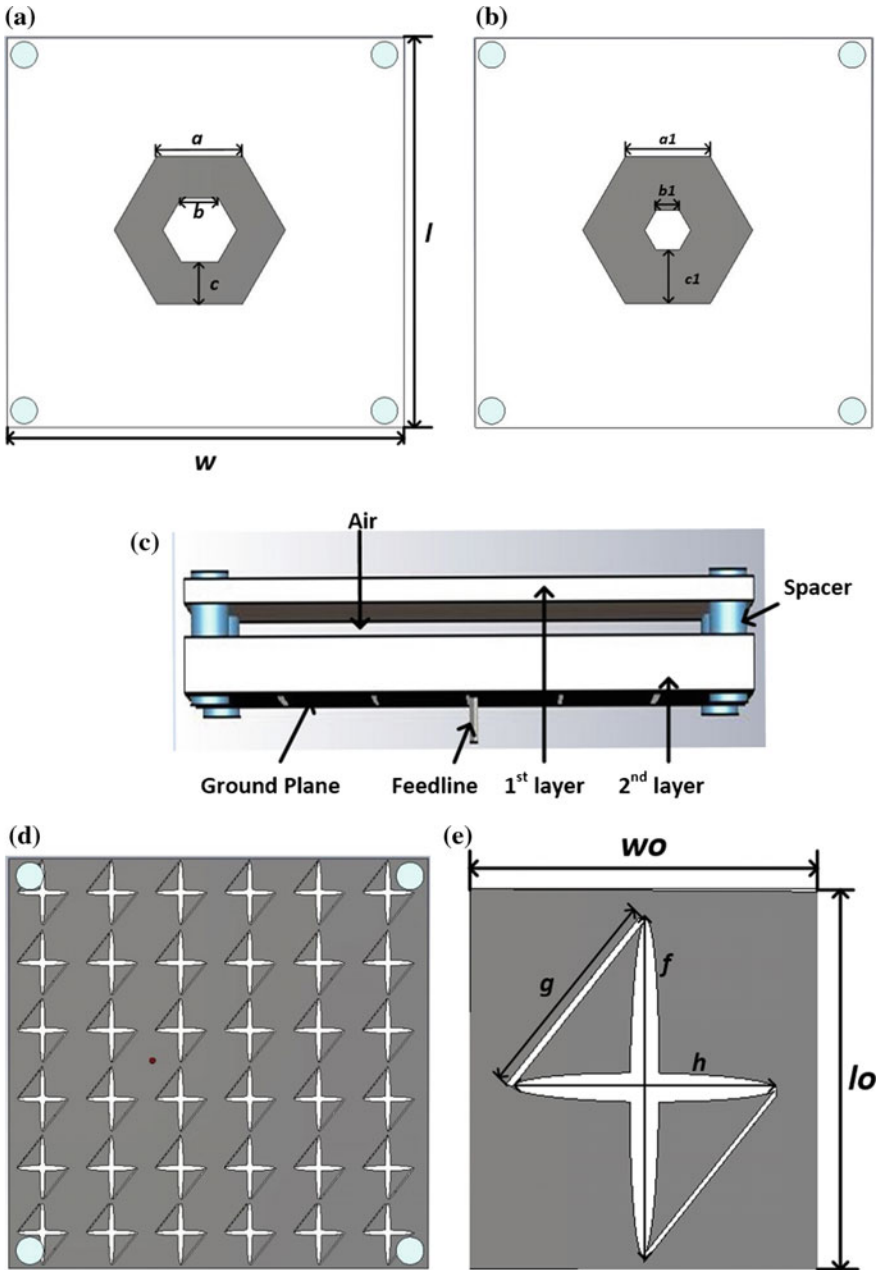


Fig. 1 Schematic layout of the proposed antenna **a** Top view **b** Bottom view **c** Side view **d** Ground plane and **e** unit cell

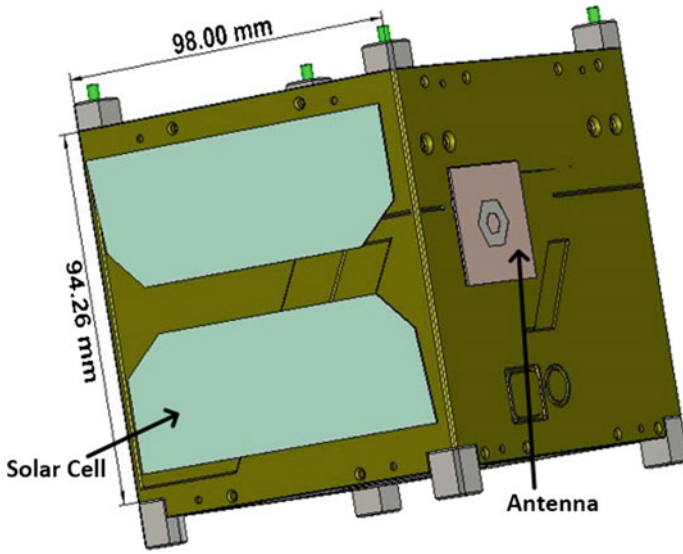
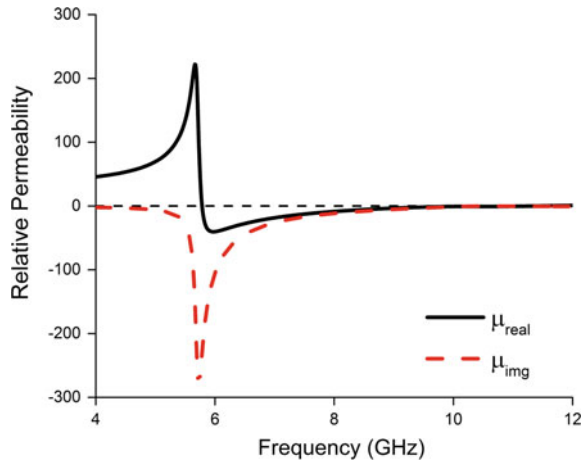


Fig. 2 1U satellite body with antenna attached

Fig. 3 Analytically calculated relative permeability of the unit cell



$$\eta = \frac{1}{kd} \cos^{-1} \left[\frac{1}{2S_{21}} (1 - S_{11}^2 + S_{21}^2) \right] \tag{2}$$

$$\mu = \eta z \tag{3}$$

Based on the Eqs. (1, 2 and 3), the proposed stacked antenna exhibits relative permeability (μ) from 5.78 to 11.4 GHz as shown in Fig. 3. The feeding potential

difference between patch and ground was considered to be caused by an electric field instead of a magnetic field.

4 Results and Discussion

The return loss of the proposed metamaterial antenna was analyzed and is shown in Fig. 4. It can also be seen from Fig. 4 that the antenna achieves about 1 GHz of -10 dB bandwidth. The operating range is 8.29 to 9.30 GHz. The antenna performance was increased by using a metamaterial antenna. The main feature of the proposed antenna is the increased gain through use of the metamaterial surface as shown in Table 1.

The polar and 3D radiation patterns with and without the metamaterial are shown in Figs. 5 and 6 respectively. From Figs. 5 and 6 it can be seen that by using the metamaterial gain was increased by 37.32% at 8.55 GHz.

Fig. 4 Return loss of the proposed stacked antenna

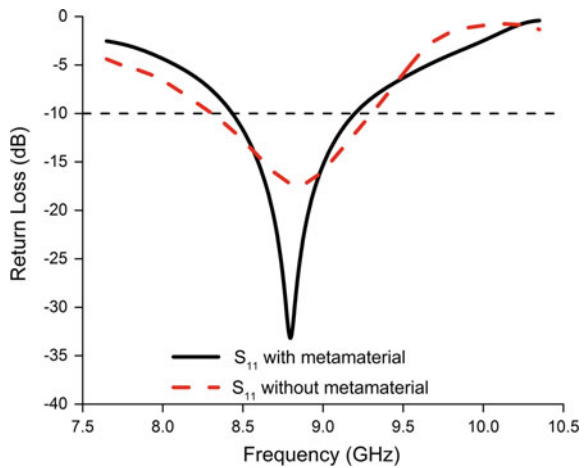


Table 1 Optimised antenna design parameters

Parameters	Value (mm)	Parameters	Value (mm)
l	29.8	c_1	4.1
w	30.3	l_0	4.8
a	6.5	w_0	3.8
b	2.8	f	4.7
c	3.2	g	2.3
a_1	6.5	h	3.6
b_1	1.8		

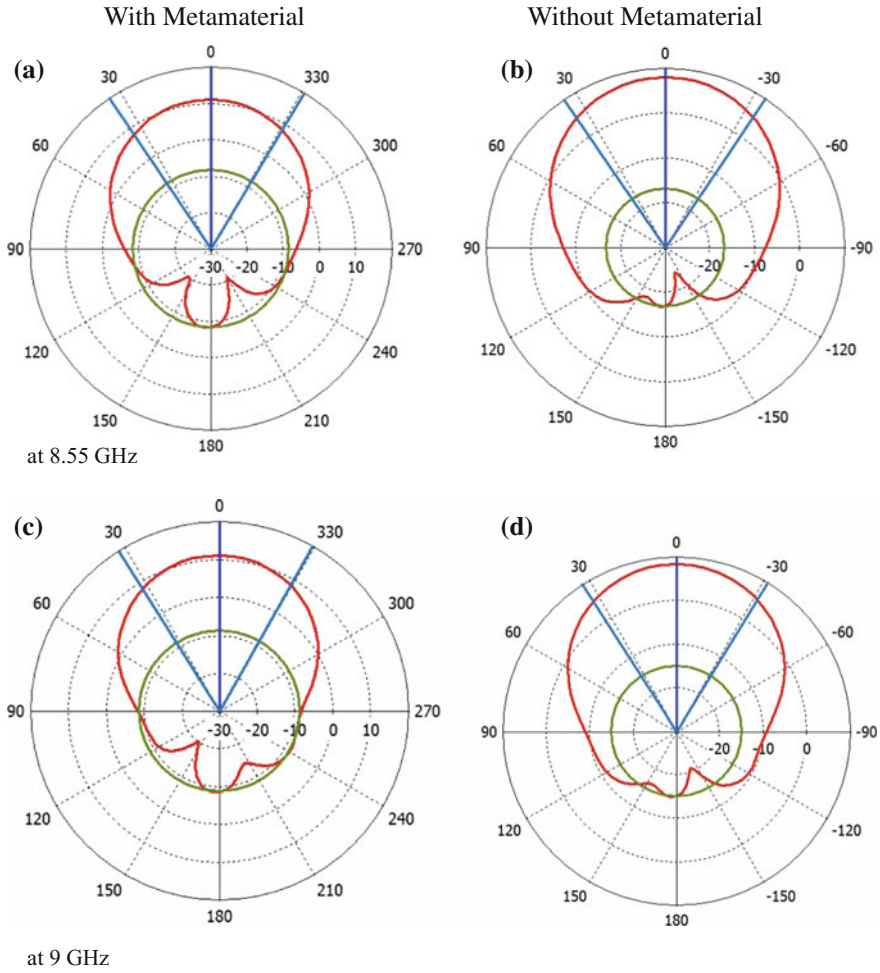


Fig. 5 Farfield radiation patterns of the proposed stacked antenna (a), (b) at 8.55 GHz and (c), (d) at 9 GHz

The realized gain over frequency is shown in Fig. 7. From Fig. 7, it can be seen that the antenna gain increased significantly over the operating range. In Fig. 8, the total efficiency of the metamaterial antenna can be seen. The efficiency lies between 70 to 80%, which is quite efficient for nanosatellite application.

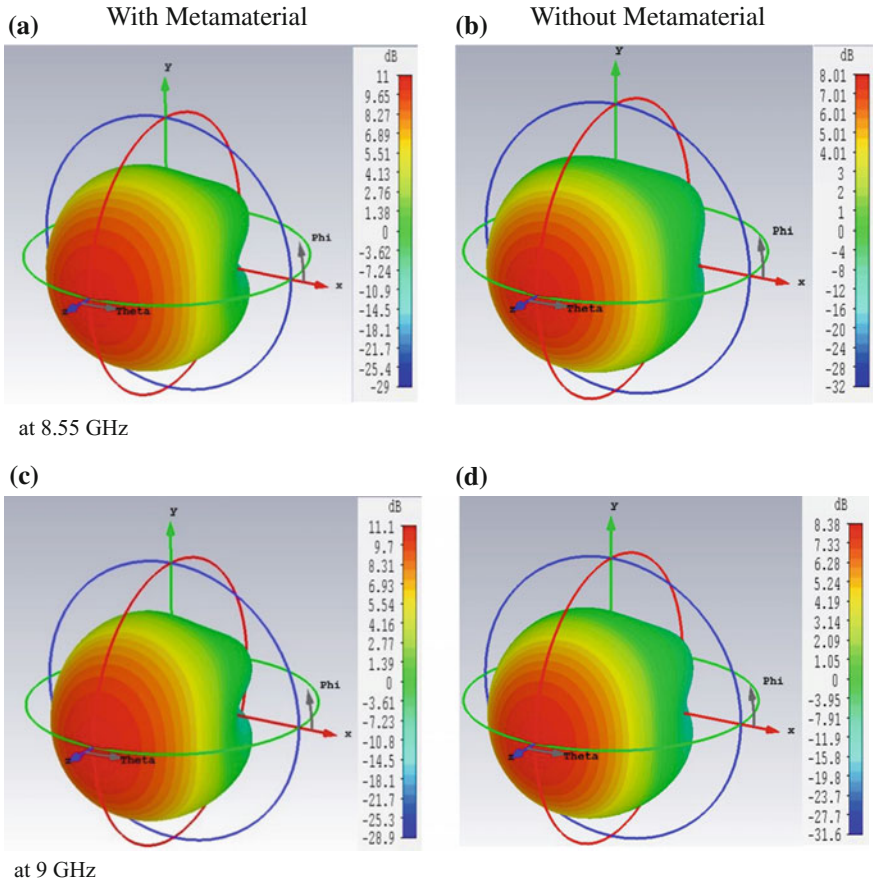


Fig. 6 3D directivity patterns of the proposed stacked antenna (a), (b) at 8.55 GHz and (c), (d) at 9 GHz

Fig. 7 Realized gain of the proposed antenna

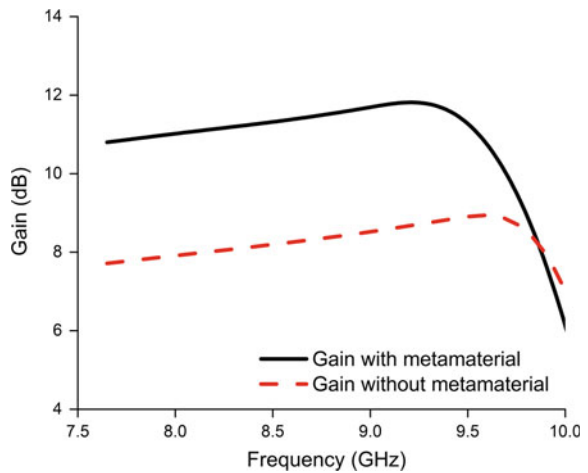
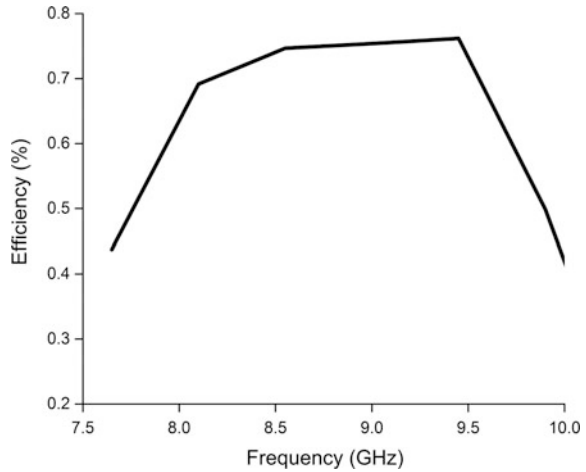


Fig. 8 Total efficiency of the proposed metamaterial antenna



5 Conclusion

A negative- μ metamaterial-inspired high-gain stacked antenna is presented for 1U CubeSat application. The realized gain of the proposed antenna was significantly increased from 8.01 to 11.1 dB by using a metamaterial ground plane without degrading other aspects of performance. The antenna occupies a small volume of $29.8 \times 30.30 \times 2.66 \text{ mm}^3$ in the 1U satellite body. From above investigation, the proposed antenna shows a satisfactory performance for x-band nanosatellite application.

References

1. Chahat N, Sauder J, Hodges RE, Thomson M, Rahmat-Samii Y (2017) Telecommunication cubesat antenna. *IEEE Antennas Propag Mag* 1045
2. Compact, M.-B. F.-S. P (2017) For satellites, think small, dream big. *IEEE Antennas Propag Mag* 59(2):22–30
3. Rahmat-Samii Y (2017) Special issue on antenna innovations for cubesats and smallsats [Guest Editorial]. *IEEE Antennas Propag Mag* 59:16–127
4. Silva JS, García-Vigueras M, Debgović T, Costa JR, Fernandes CA, Mosig JR (2017) Stereolithography-Based Antennas For Satellite Communications In Ka-Band. *Proc IEEE* 105:655–667
5. Alam T, Faruque MR, Islam M (2015) Octagonal shaped circular polarized C-band antenna for small satellite communication. In: *Proceeding of the 2015 IEEE International Conference on Space & Communications (IconSpace)*. pp 379–382
6. Islam MT, Samsuzzaman M, Kibria S, Cho M. (2014) Development of S band antenna for nanosatellite. In: *2014 IEEE Asia-Pacific Conference On Applied Electromagnetics (APACE)*. pp 379–382
7. Islam MT, Cho M, Samsuzzaman M, Kibria S (2015) Compact antenna for small satellite applications [Antenna Applications Corner]. *IEEE Antennas Propag Mag* 57:30–36

8. Li D, Szabo Z, Qing X, Li E-P, Chen ZN (2012) A high gain antenna with an optimized metamaterial inspired superstrate. *IEEE Trans Antennas Propag* 60:6018–6023
9. Jiang H, Xue Z, Li W, Ren W, Cao M (2016) Low-RCS high-gain partially reflecting surface antenna with metamaterial ground plane. *IEEE Trans Antennas Propag* 64:4127–4132
10. Wu F, Luk KM (2017) Wideband high-gain open resonator antenna using a spherically-modified, second-order cavity. *IEEE Trans Antennas Propag*. doi:[10.1109/TAP.2016.2647700](https://doi.org/10.1109/TAP.2016.2647700)
11. Hasar UC, Muratoglu A, Bute M, Barroso JJ, Ertugrul M (2017) Effective constitutive parameters retrieval method for bianisotropic metamaterials using waveguide measurements. *IEEE Trans Microw Theory Tech* 65(5):1488–1497

Performance Analysis of an X-Band Circular Polarized Antenna for Nanosatellite Communication

Touhidul Alam, Mandeep Singh Jit Singh, Mengu Cho and Mohammad Tariqul Islam

Abstract Nanosatellite are revolutionizing the modern satellite industry due to their size, cost and shorter development time. CubeSats have limited communication ability due to their limited volume and power. As a result, their components need to be very small. In this paper, a small circular polarized x-band patch antenna is proposed for 1U nanosatellite applications. The antenna was designed and characterized using CST microwave studio simulation software. This real-time project used a truncated-shaped hexagonal slot rectangular patch antenna operating in the 9.82 GHz to 11.68 GHz frequency bands, and integrated with a 1U satellite body. The antenna shows 3 dB axial ratio at 10.15 GHz and achieved a maximum realized gain of 8.11 dB at 11 GHz. The antenna has the potential to be used in small satellites.

1 Introduction

CubeSats are a new type of small satellite, and are usually a fraction of the size of a typical satellite [1, 2]. With the development of the modern satellite industry, CubeSats are widely used for telecommunication systems, earth observation, imaging and so on, as a substitute for a typical satellite. The antenna is a fundamental element of the satellite. For CubeSat application, the typical antenna system must be able to fit within the limited volume and antenna researchers are working on these challenges. Several types of antenna are being studied for satellite application. A deployable antenna is one of the most widely-used antennas in

T. Alam · M.S.J. Singh · M.T. Islam (✉)
Department of Electrical, Electronic and Systems Engineering,
Universiti Kebangsaan Malaysia, 43600 Bangi, Malaysia
e-mail: tariqul@ukm.edu.my

T. Alam
e-mail: touhid13@siswa.ukm.edu.my

M. Cho · M.T. Islam
Kyushu Institute of Technology, Kitakyushu, Japan

nanosatellites [3–5], but the complexity of the deployment system is a big concern. To avoid the problem of complex deployment, patch antennas were used on many satellite missions [6]. Islam et al. proposed a circular polarized (CP) antenna for the HORYU-IV nanosatellite, which operates at 2.4 GHz [6]. A right and left circularly polarized antenna was proposed for small satellites by [7], which can operate in the X-band. A monofilar spiral antenna was developed by Luo et al. for Ku-band nanosatellite communication [8] with a size of $18 \times 18 \times 14 \text{ mm}^3$. Moreover, several circularly polarized antennas have been proposed for satellite applications [9, 10]. Hodges et al. developed a folded-panel reflectarray antenna for the first CubeSat mission to Mars [11]. The antenna was designed for Earth to Mars communication at 8.425 GHz with dimensions of $10 \times 20 \times 34 \text{ cm}^3$.

This paper addresses a circular polarized directional patch antenna for nanosatellite application. The proposed antenna is customized from the established CP antenna method for nanosatellites. The performance features of the antenna were verified with it integrated with the satellite body

2 Antenna Design Methodology

The schematic layout of the proposed antenna is presented in Fig. 1. The proposed antenna was designed on a Rogers RT5880 (lossy) substrate material having a dielectric constant of 2.2 and a height of 1.575 mm. The overall antenna dimensions are $25.955 \times 25.95 \text{ mm}^2$. The circular polarization of the proposed antenna is achieved by using the established truncating opposite corners method. The hexagonal slot is introduced to create capacitance in the radiating patch. The wide operating frequency band is achieved by using a thick substrate material. The antenna is fed using a 50Ω probe feeding technique. The optimized design

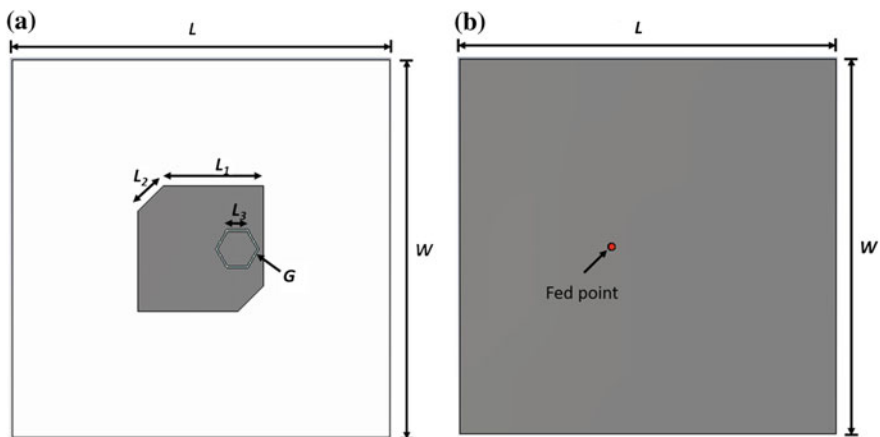


Fig. 1 Schematic layout of the proposed antenna **a** Top view **b** Bottom view

Fig. 2 Antenna integrated with the 1U satellite body

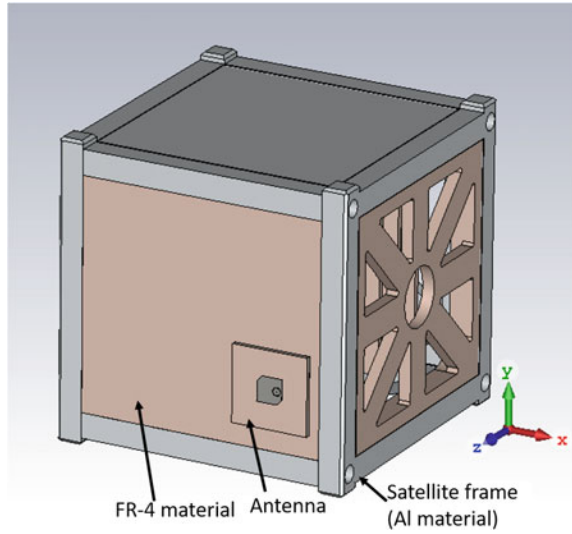


Table 1 Optimised antenna design parameters

Parameters	Value (mm)
L	25.95
W	25.95
L_1	6.86
L_2	2.53
L_3	1.49
G	0.13
H	1.575

parameters of the proposed antenna are listed in Table 1. A 1U CubeSat was designed in order to analyze the performance of the antenna integrated with the satellite body as shown in Fig. 2. The antenna is mounted in the +Z axis.

3 Results and Discussion

The performance of the CP antenna was analyzed using the commercial software CST microwave studio. The reflection coefficient of the antenna is illustrated in Fig. 3. It can also be seen from Fig. 3 that the antenna achieves a -10 dB reflection coefficient from 9.82 GHz to 11.168 GHz, covering the x-bands. The antenna was integrated with the satellite structure and its performance was analysed. Figure 3 shows that the antenna’s performance did not degrade when it was integrated with the satellite structure.

The axial ratio of the proposed antenna is shown in Fig. 4. The axial ratio vs frequency was plotted and the antenna shows a 0.8 normalized polarization level,

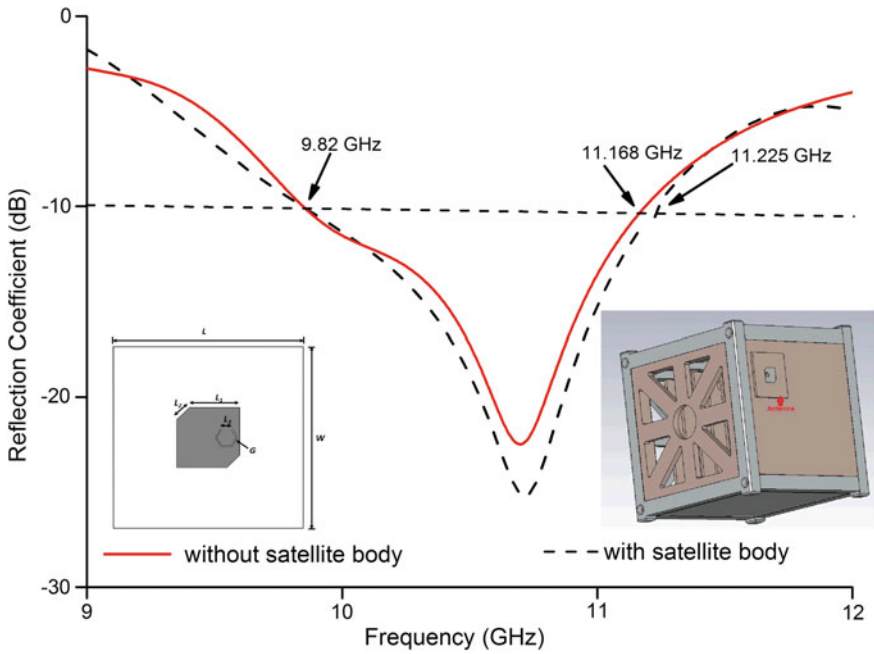


Fig. 3 Reflection coefficient of the proposed CP antenna

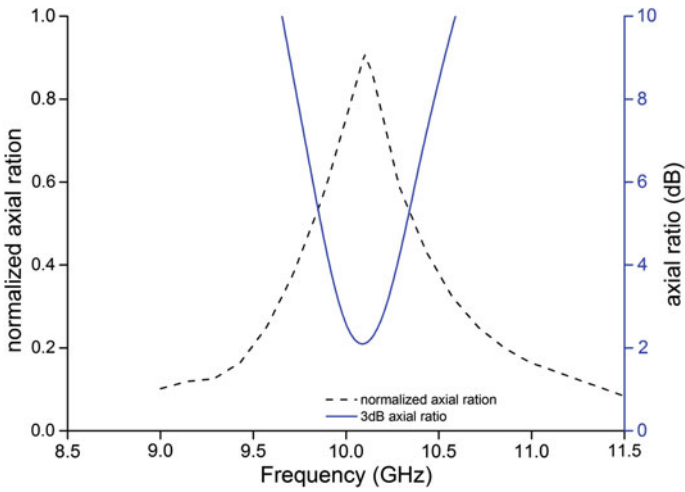


Fig. 4 Axial ratio of the proposed CP antenna

where the 1 value referred to the perfectly circular polarized antenna. In addition, the 3 dB axial ratio was also investigated and was found to be 10.2 GHz.

The surface current distribution at 10.2 GHz is shown in Fig. 5. It can be seen that the majority current direction at 0° is upward, at 90° is left, at 180° is downward and at 270° is rightward, in other words the current rotates in an anti-clockwise direction. So, the antenna shows RHCP (Right Hand Circular Polarization) at 10.2 GHz. The polar radiation patterns were also analyzed at four different frequencies as shown in Fig. 6. From Fig. 6, it can be seen that at

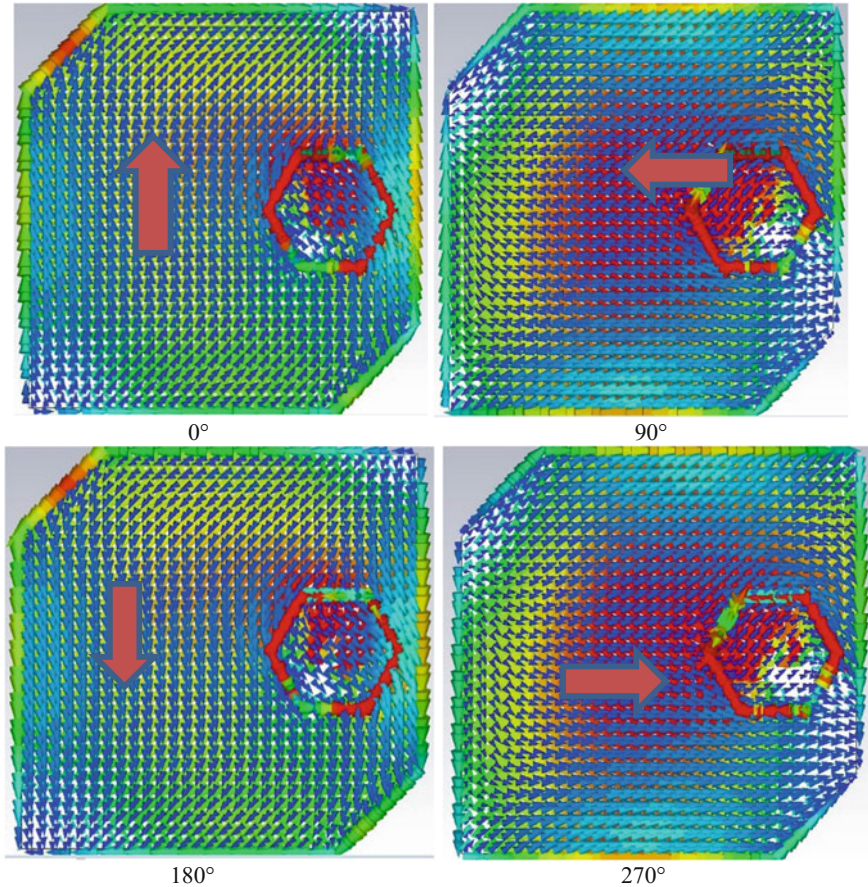


Fig. 5 Surface current distribution of the proposed CP antenna at 10.2 GHz

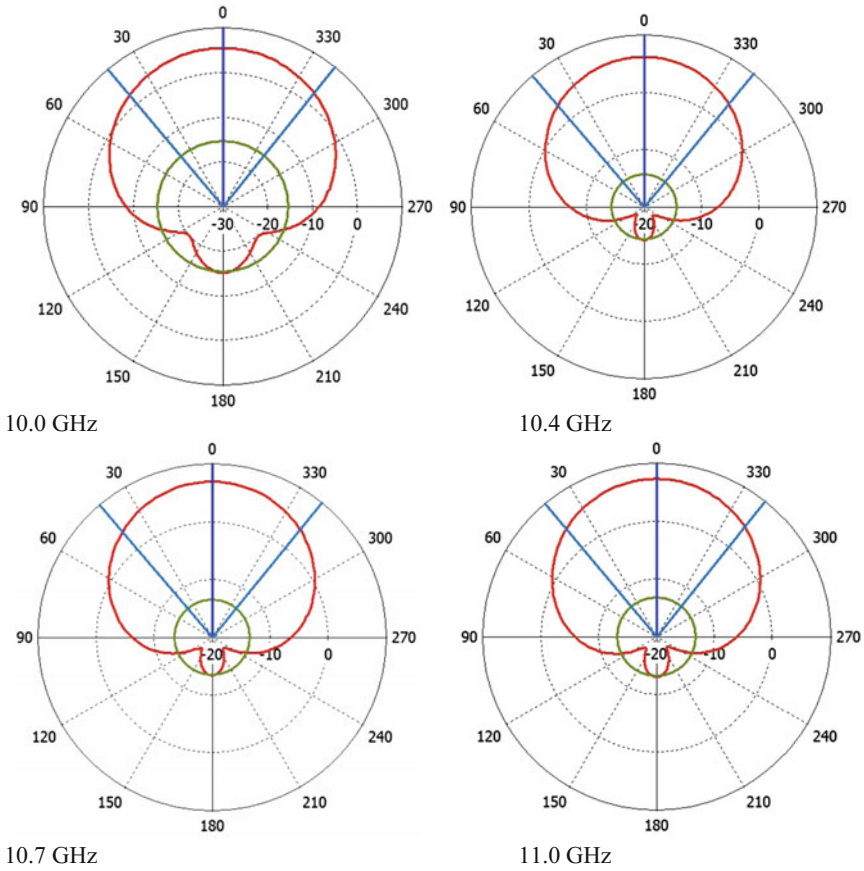


Fig. 6 Polar radiation pattern of the proposed antenna

10.0 GHz the realized gain main lobe magnitude is 7.2 dB and at 10.7 GHz the main lode realized gain is 7.8 dB. The 3D radiation pattern is also shown in Fig. 7. The farfield radiation pattern of the satellite antenna was investigated with the satellite body as shown in Fig. 8. It can be seen from Figs. 7 and 8 that the antenna shows a realized gain of 8.01 and 8.35 dB at 10.7 GHz with and without mounting of the satellite body respectively. So, it can be said that the antenna radiates in the +z direction without and degradation of its performance.

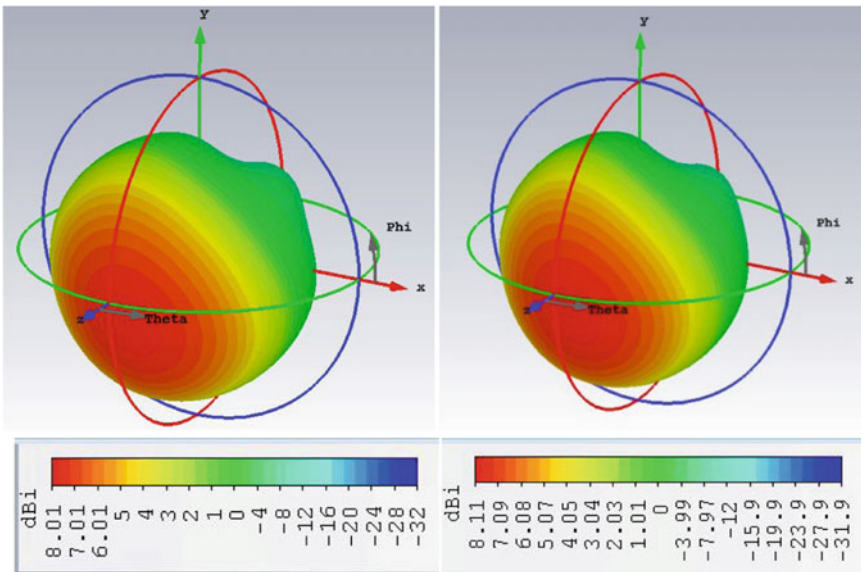
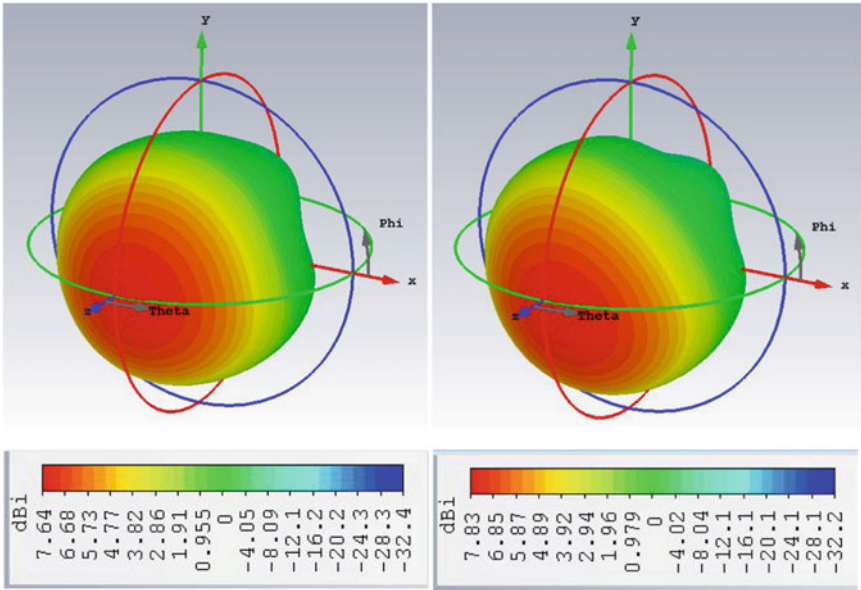


Fig. 7 3D directivity pattern of the proposed antenna

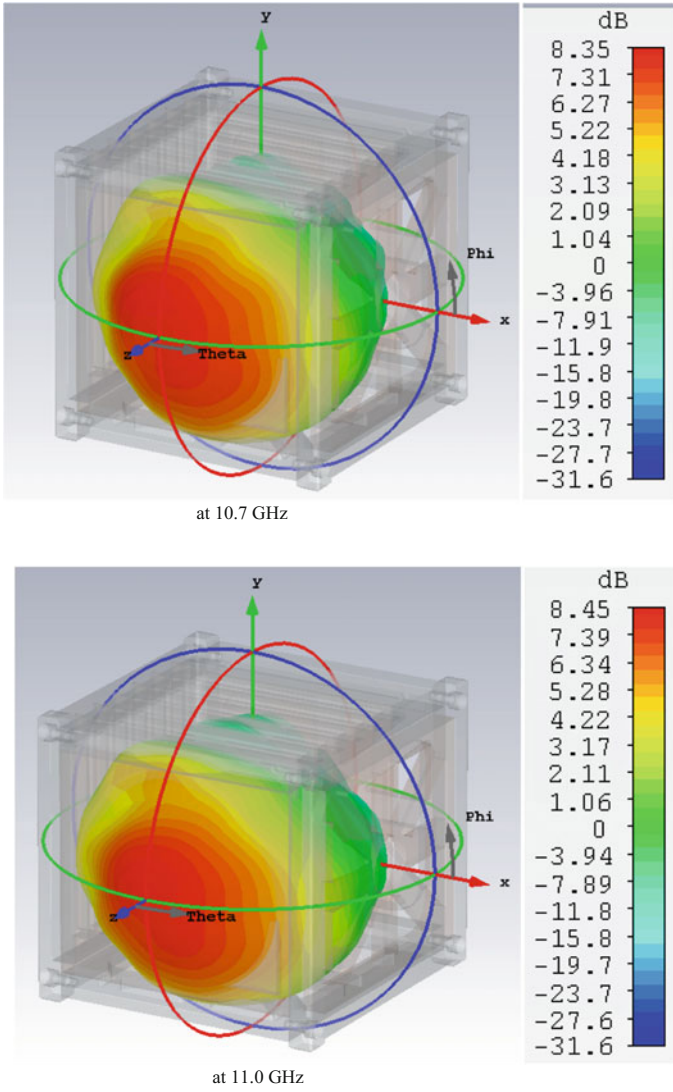


Fig. 8 3D directivity pattern of the proposed antenna integrated with the satellite body

4 Conclusion

In this paper, a high gain circular polarized antenna is proposed for the 1U nanosatellite space communication system. The proposed antenna achieved a fractional bandwidth of 12.83% with an electrical size of $0.85 \times 0.85 \times 0.05$ at a lower frequency of 9.82 GHz. The antenna was mounted on a 1U satellite body in order to investigate its performance. As a result, based on the antenna's performance, the proposed antenna could be used for future satellite application.

Acknowledgement This work is supported by the Kyushu Institute of Technology research grant (KK-2016-007).

References

1. Rahmat-Samii Y (2017) Special issue on antenna innovations for cubesats and smallsats [Guest Editorial]. *IEEE Antennas Propag Mag* 59:16–127
2. Rahmat-Samii Y, Manohar V, Kovitz JM (2017) For satellites, think small, dream big. *IEEE Antennas Propag Mag* 1045
3. Ashida H, Fujihashi K, Inagawa S, Miura Y, Omagari K, Miyashita N et al (2010) Design of tokyo tech nano-satellite Cute-1.7 + APD II and its operation. *Acta Astronaut* 66:1412–1424
4. Costantine J, Tawk Y, Christodoulou CG, Banik J, Lane S (2012) CubeSat deployable antenna using bistable composite tape-springs. *IEEE Antennas Wirel Propag Lett* 11:285–288
5. Sakovsky M, Pellegrino S, Costantine J (2017) Rapid Design of Deployable Antennas for CubeSats: A tool to help designers compare and select antenna topologies. *IEEE Antennas Propag Mag* 59(2):50–58
6. Islam MT, Cho M, Samsuzzaman M, Kibria S (2015) Compact antenna for small satellite applications [Antenna Applications Corner]. *IEEE Antennas Propag Mag* 57:30–36
7. Kaneko T, Shigeki M, Hirobumi S (2017) Right and left circular polarized wave antenna for small satellite. In: *Topical Workshop on. Internet of Space (TWIOS)*. IEEE
8. Luo Q, Gao S, Sobhy M, Li J, Wei G, Xu J (2017) A broadband printed monofilar square spiral antenna. *IEEE Antennas Propag Mag* 1045
9. Azim R, Samsuzzaman M, Alam T, Islam MT, Faruque MRI, Zaman M et al (2015) Circularly polarized patch antenna for S-band satellite applications. In: *Proceeding of the 2015 IEEE International Confer-ence on Space and Communications (IconSpace)*. pp 402–405
10. Alam T, Faruque MR, Islam M (2015) Octagonal shaped circular polarized C-band antenna for small satellite communication. In: *Proceeding of the 2015 IEEE International Confer-ence on Space and Communications (IconSpace)*. pp 379–382
11. Hodges RE, Chahat N, Hoppe DJ, Vacchione JD (2017) A deployable high-gain antenna bound for mars. *IEEE Antennas Propag Mag* 1045

A Reflector Type 3D Triband Directional Antenna for CubeSat Applications

Md. Amanath Ullah, Farhad Bin Ashraf, Touhidul Alam,
Mohd Tarmizi Ali and Mohammad Tariqul Islam

Abstract In this paper, a three-dimensional antenna for CubeSat applications is proposed. The proposed antenna achieved unidirectional radiation characteristics at its operating bands. Different optimization techniques such as a folded radiating structure, shorting wall and ground reflector are used to achieve a standard performance from the antenna. The proposed antenna successfully achieved three operating bands: 1.55–1.67 GHz, 1.99–2.27 GHz and 2.53–3.58 GHz. A front-to-back ratio of 15 authenticates its directive radiation pattern. The proposed antenna achieved a peak gain of 4 dB. The antenna has been designed in such a way that it can be fabricated for mass production easily from a single copper sheet using folding technique. Computer Simulation Technology (CST) Microwave Studio software has been used to design and perform the simulation work. A lower operating band, unidirectional radiation characteristics, and a satisfactory amount of gain over the operating frequency make the antenna a candidate to be used in CubeSats for space communication purposes.

1 Introduction

Currently, Cube satellites (CubeSats) are becoming a popular option for space research in universities due to their low cost, ease of construction and reduced development time. Antennas are one of the most important components in CubeSat development, and are used to provide uplink and downlink communication [1, 2].

Md.A. Ullah · F.B. Ashraf · T. Alam · M.T. Islam (✉)
Dept of Electrical, Electronic and Systems Engineering,
Universiti Kebangsaan Malaysia, 43600 Bangi, Malaysia
e-mail: tariqul@ukm.edu.my

Md.A. Ullah
e-mail: amanath@siswa.ukm.edu.my

M.T. Ali
Centre for Communication Eng. Studies, Universiti Teknologi Mara, Skudai, Malaysia

In recent years, three-dimensional antennas have attracted the attention of researchers due to a lack of deployable antennas and low efficient patch antennas. Moreover, 3D structures have some advantages over 2D structures, such as the use of the whole volume of the structure for impedance matching and obtaining good radiation characteristics [3, 4]. Several antennas have been used in different types of modern nanosatellite [5, 6]. In [7–10], a printed circularly polarized patch antenna was proposed for satellite application. Samsuzzaman et al. proposed an S-band antenna for satellite applications, but the efficiency of the antenna is lower with the satellite [8]. A circularly polarized S-band antenna has been developed; which worked in nanosatellite HORYU-IV [9].

In this paper, a three-dimensional antenna with a unidirectional radiation pattern is proposed. The antenna achieved three operating bands: 1.55–1.67 GHz (bandwidth about 120 MHz), 1.99–2.27 GHz (bandwidth about 280 MHz) and 2.53–3.58 GHz (bandwidth about 1.05 GHz). The antenna achieved a peak realized gain of 4 dBi. Larger operating bandwidths can use the achieved gain effectively. A unidirectional radiation pattern along the y axis, an operating bandwidth of less than 4 GHz and a satisfactory gain make the proposed antenna suitable for us in the field of CubeSat space communication.

2 Methodology

The design and simulation process was performed using commercially available CST Microwave Studio software. The coaxial feeding method was used to reduce the effect of spurious radiation. Figure 1a illustrates the 3D view of the proposed antenna. Folding technique was employed to achieve a low frequency operating band and to make the overall structure compact [1].

The folded radiating structure reduces the overall size of the antenna. The reflector is used to get a unidirectional radiation pattern. The reflector wall also helps to achieve a satisfactory gain. The inner folded radiating structures are extremely helpful in attaining a better reflection coefficient at lower frequency. The shorting wall technique is also effective in getting resonance at lower frequency and a better reflection coefficient. The proposed radiating structure was kept as simple as possible.

The design parameters of the proposed antenna are presented in Table 1. The position of the shorting wall is crucial to the design as it aids the achieving of a good reflection coefficient and resonance. The main radiating element is bent through 90 degrees in order to achieve a better directive property which is perpendicular and parallel to the reflector depending on viewing angle.

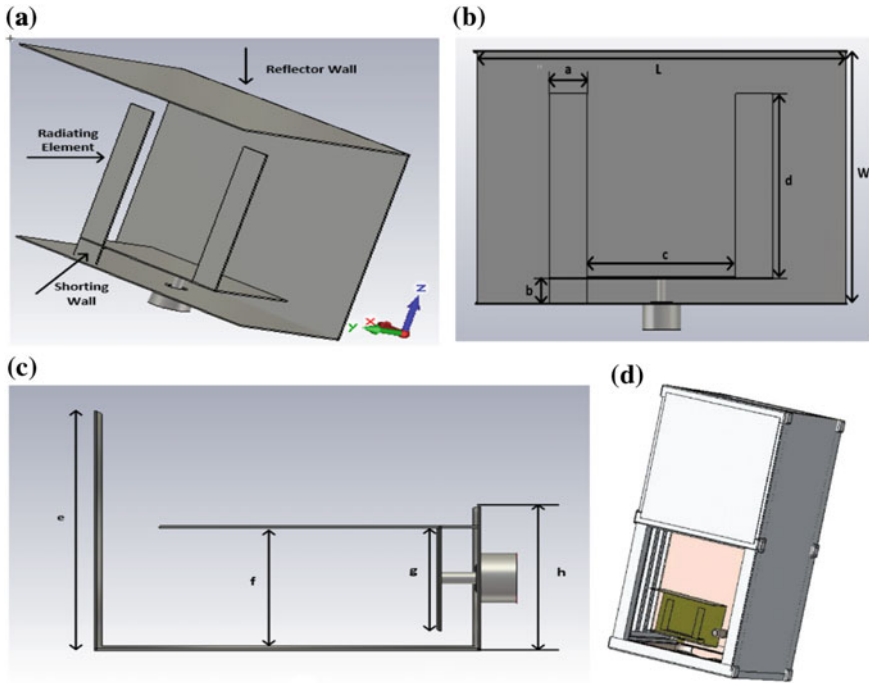


Fig. 1 Geometric configuration of the proposed antenna **a** 3D view, **b** front view, **c** side view, **d** placement of the proposed antenna with a typical 2U Cubesat body

Table 1 Parameters of the proposed antenna

Parameters	Value (mm)	Parameters	Value (mm)
<i>L</i>	50	<i>d</i>	22
<i>W</i>	29.8	<i>e</i>	24.8
<i>a</i>	5	<i>f</i>	13
<i>b</i>	3	<i>g</i>	11.9
<i>c</i>	30	<i>h</i>	15

3 Results and Discussion

The simulated result of the reflection coefficient is illustrated in Fig. 2. The proposed antenna obtained an operating bandwidth at three places, namely, 1.55–1.67 GHz (bandwidth about 120 MHz), 1.99–2.27 GHz (bandwidth about 280 MHz) and 2.53–3.58 GHz (bandwidth about 1.05 GHz). However, it was most resonant at 2.19 GHz. Figure 3 represents the peak gain of the proposed structure. The antenna showed a maximum peak gain of 4 dB. The front-to-back ratio of the proposed antenna is presented in Fig. 4. The antenna has a peak front-to-back ratio of 15 dB (direction), which validates the directional radiation pattern. (Table 2)

Fig. 2 Reflection coefficient of the proposed antenna

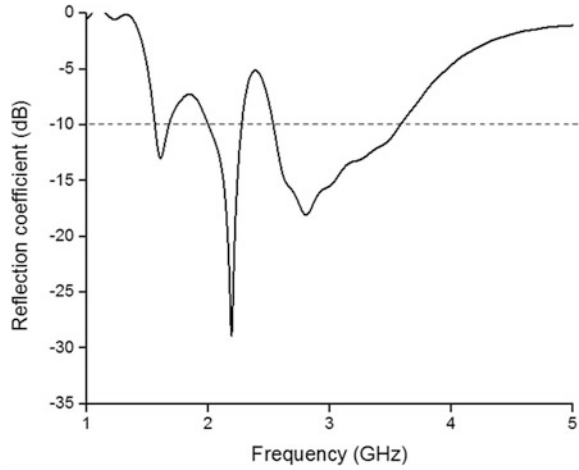
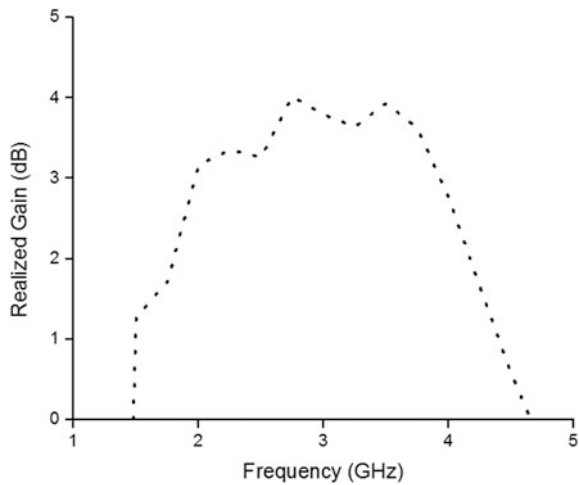


Fig. 3 Peak gain of the proposed antenna



The antenna achieved a maximum radiation efficiency of about 95% in a simulation environment, as shown in Fig. 5.

The surface current distribution of the proposed antenna is shown in Fig. 6. It can be seen that the folded radiating element exhibits a strong current and this is responsible for the directive radiation characteristics.

Radiation characteristics of the proposed antenna are presented in Figs. 7, 8 and 9. The radiation patterns at the three resonant frequencies seem to be consistent. The front-to-back ratio of Fig. 4 and the radiation patterns validate each other and prove the directive property.

Fig. 4 Front-to-back ratio of the proposed antenna

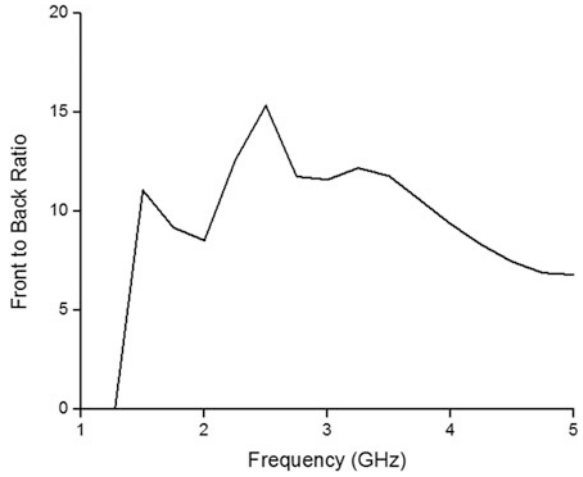
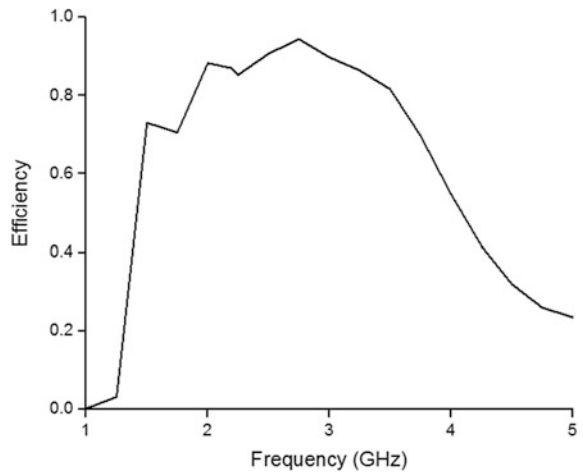


Table 2 Specifications of the proposed antenna

Specification	Value (mm)
Operating band	1.55-1.67 GHz, 1.99-2.27 GHz and 2.53-3.58 GHz
Peak realized gain	4 dB
Directivity	Unidirectional
Front-to-back ratio	15
Efficiency	95%

Fig. 5 Efficiency of the proposed antenna



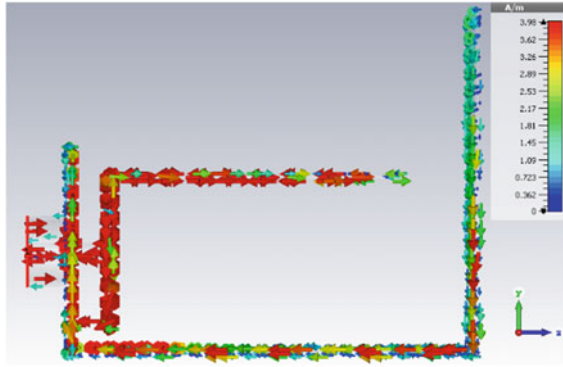


Fig. 6 Surface current distribution of the proposed antenna

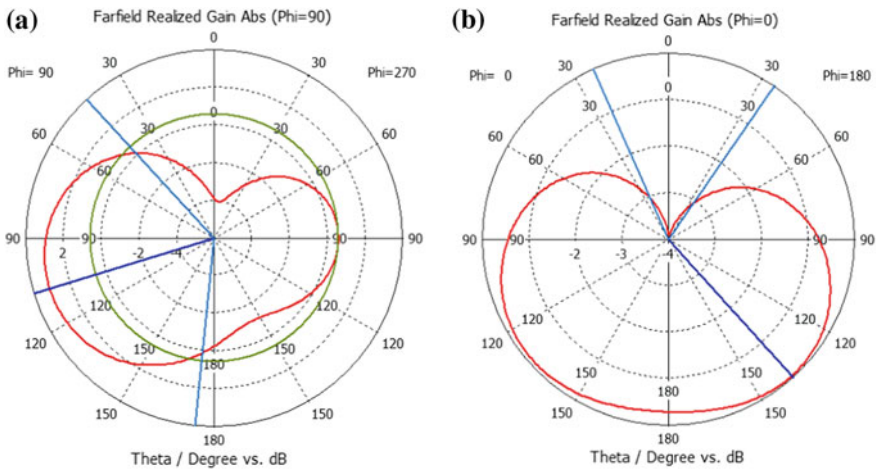


Fig. 7 Radiation pattern of the proposed antenna at 1.67 GHz a Phi 90 degrees b Phi 0 degrees

At 1.6 GHz, the 3 dB angular width is 133 degrees and the main lobe magnitude is 2.48 dB. At 2.19 GHz, the angular width decreases to 119 degrees and the main lobe direction is 114 degrees. Finally at 2.8 GHz, the main lobe magnitude is 3.96 dB and the angular beam-width increases to 133 degree.

As mentioned earlier the presence of the shorting wall for the proposed antenna is crucial. Figure 10 validates the statement and shows the reflection coefficients of the proposed antenna with and without the shorting wall. It can surely be seen that, the shorting wall made the reflection coefficient much better.

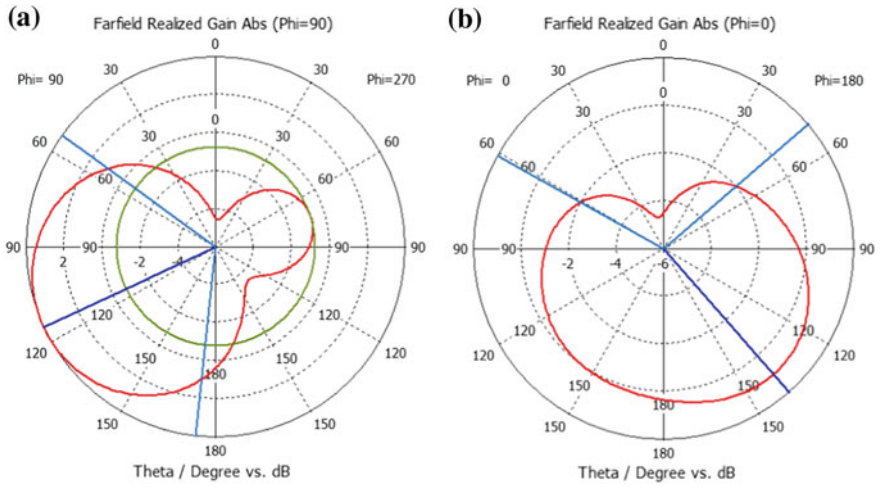


Fig. 8 Radiation pattern of the proposed antenna at 2.19 GHz a Phi 90 degrees b Phi 0 degrees

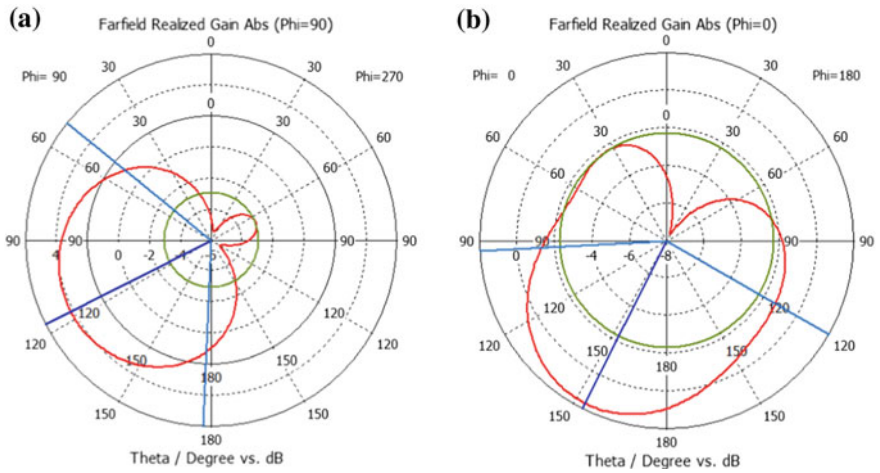
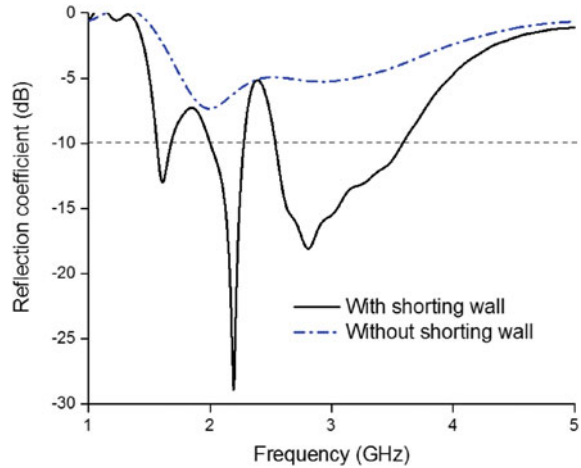


Fig. 9 Radiation pattern of the proposed antenna at 2.79 GHz a Phi 90 degrees b Phi 0 degrees

Fig. 10 Reflection coefficient with and without the shorting wall



4 Conclusion

The proposed three-dimensional structure has successfully achieved the basic requirements to be applied in CubeSat applications. The larger bandwidths will reduce the risk of frequency shifting in harsh environments. The antenna has a realized gain of 4 dB and a front-to-back ratio of 15dBi. Radiation patterns remained stable as the frequency changed.

Acknowledgements This work is supported by the Ministry of Education Malaysia (MOE) under grant no. FRGS/1/2014/TK03/UKM/01/1, and the University research grant code no. DIP-2014-029.

References

1. Bouwmeester J, Guo J (2010) Survey of worldwide pico-and nanosatellite missions, distributions and subsystem technology. *Acta Astronaut* 67(7):854–862
2. Rodriguez-Osorio RM, Ramirez EF (2012) A hands-on education project: antenna design for inter-cubesat communications [education column]. *IEEE Antennas Propag Mag* 54:211–224
3. Wu J, Zhao Z, Nie Z, Liu QH (2013) A broadband unidirectional antenna based on closely spaced loading method. *IEEE Trans Antennas Propag* 61(1):99–116
4. Zhang GM, Hong JS, Wang BZ, Song G, Zhang P (2011) Compact wideband unidirectional antenna with a reflector connected to the ground using a stub. *IEEE Antennas Wirel Propag Lett* 10:1186–1189
5. Gao S, Clark K, Unwin M, Zackrisson J, Shiroma, WA, Akagi JM, Maynard K, Garner P, Boccia L, Amendola G Massa G (2009) Antennas for modern small satellites. *IEEE Antennas Propag Mag* 51(4)
6. Pointer M, Sweeting N (2009) Antennas for modern small satellites. *IEEE Antenna Propag Mag* 51:21–30

7. Azim R, Samsuzzaman M, Alam T, Islam MT, Faruque MRI, Zaman MR, Islam MM (2015) Circularly polarized patch antenna for S-band satellite applications. In: Presented at the 2015 International Conference on Space Science and Communication (IconSpace). pp 402–405
8. Samsuzzaman M, Islam MT, Nahar MK, Mandeep JS, Mansor F, Islam MM (2015) Circularly polarized high gain S band antenna for nanosatellite. *Int J Appl Electromagn Mech* 47(4):1039–1049
9. Islam MT, Cho M, Samsuzzaman M, Kibria S (2015) Compact antenna for small satellite applications [antenna applications corner]. *IEEE Antennas Propag Mag* 57(2):30–36
10. Nascetti A, Pittella E, Teofilatto P, Pisa S (2015) High-gain S-band patch antenna system for earth-observation CubeSat satellites. *IEEE Antennas Wirel Propag Lett* 14:434–437

An Effective Medium Ratio Obeying Wideband Left-Handed Meta-Atom for Multiband Applications

Mohammad Jakir Hossain, Mohammad Rashed Iqbal Faruque and Mohammad Tariqul Islam

Abstract A new wideband left-handed (LH) meta-atom based on planar modified multiple hexagonal split ring resonators is described in this paper. The LH meta-atom was simulated to maintain left-handed properties at 9.40 GHz. Performance and comparison of different structures were analyzed that follow better effective medium ratio (EMR) and wideband (5.54 GHz) for multi-band operations in the microwave spectra. The finite-difference time-domain (FDTD) method-based CST electromagnetic simulator was implemented in order to observe the design of the meta-atom. The meta-atom showed a multiband response in conjunction with wideband and LH properties above the definite frequency band in the microwave spectra and EMR was considerably improved compared to previously reported metamaterials.

1 Introduction

Left-handed meta-atoms (LHMs) are engineered metamaterials with simultaneous relative negative permittivity (ϵ less than 0) and permeability (μ less than 0), and have exotic properties in terms of well-known phenomena like Cherenkov radiation, Snell's law, and the Doppler effect, etc. [1, 2]. Due to these exotic properties, the scientific community has turned its attention to the meta-atoms for unusual characteristics and diverse applications in energy harvesting, invisibility cloaking [3, 4], filtering, electromagnetic absorbers [5] perfect lenses [6], and SAR reduction [7]. Left-handed meta-atoms are typically periodically arranged at scales that

M.J. Hossain (✉) · M.R.I. Faruque
Space Science Centre (ANGKASA), Institute of Climate Change, Universiti
Kebangsaan Malaysia, 43600 Bangi, Selangor, Malaysia
e-mail: jakir@siswa.ukm.edu.my

M.R.I. Faruque
e-mail: rashed@ukm.edu.my

M.T. Islam
Dept of Electrical, Electronics and Systems Engineering, Universiti
Kebangsaan Malaysia, 43600 Bangi, Malaysia

maintain the subwavelength of the phenomena. Because of not having the LH characteristics in natural materials, this aspect was given less important until 2003. Negative permittivity properties of the materials could be found, but making an engineered material with negative permeability was challenging work. US physicists D.R. Smith et al. achieved success in developing a new man-made meta-atom with peculiar characteristics, namely negative permeability and permittivity in 2000 [8]. The ratio between the wavelengths to unit-cell dimension is termed as the effective medium ratio which is important to design compact meta-atom. Having seen the LH characteristics in artificial structures, the Researcher showed more attention at multi-band meta-atoms and arrays of the meta-atoms with high effective medium ratio and wide negative index bandwidth. On the other hand, the inadequate design has been focused on constructing such metamaterials. Islam et al. reported a $10 \times 10 \text{ mm}^2$ “II-shaped” meta-atom which was suitable for the operation of electromagnetic invisibility cloaking in the X-band, whereas the effective medium ratio was very small at 3.58 and the near-zero refractive index was around 2 GHz [9]. A $25 \times 25 \text{ mm}^2$ rectangular “U-shaped” metamaterials was shown to have double negative properties at different frequencies such as 5, 6, and 11 GHz for different array structures by Mallik et al. in [10]. Zhou et al. suggested a “double Z-shaped” double negative metamaterial design constructed using coplanar magnetic and electric resonators in which the EMR was 4.80 and the dimensions were $8.5 \times 8.5 \text{ mm}^2$ [11]. Islam et al. recommended a metamaterial unit-cell structure with $30 \times 30 \text{ mm}^2$ dimensions and an “H-shape” that was applicable to the microwave regime. The negative refractive indices of the structure were 0.5 GHz and 0.3 GHz, and the EMR was 3.65 [12]. A left-handed “F-shaped” metamaterial was designed by Rizwan et al. with a 2.3 GHz bandwidth of the negative refractive index for the K- and Ka-bands [13]. Zhou et al. reported a $15 \times 15 \text{ mm}^2$ “S-shaped” chiral metamaterial for the X- and Ku- bands. On the contrary the EMR of the metamaterial was very small at less than 4 [14]. A $5 \times 5 \text{ mm}^2$ “ring-shaped” meta-atom was designed by Yang et al. for cloaking effects in the frequency range 8–13 GHz. Moreover, the EMR of the meta-atom was 6 [15]. Hossain et al. recommended a design structure of $12 \times 12 \text{ mm}^2$ “double C-shaped” metamaterial for multiband operations and the reported EMR was 7.44 with a negative refractive index from 11.304 to 13.796 GHz [16]. The refractive index bandwidths of an $8 \times 8 \text{ mm}^2$ “Hexagonal-shape” left-handed materials were 1.75 GHz and 0.96 GHz respectively that design was recommended by Alam et al. [17].

In this paper, the modified multiple hexagonal-based meta-atom displays multi-resonance at L-, S-, C-, X-, and Ku-bands with a bandwidth of 1.88–2.07 GHz (0.19 GHz), 3.53–4.03 GHz (0.50 GHz), 7.22–7.66 GHz (0.44 GHz), 9.16–11.91 GHz (2.76 GHz), and 13.96–14.67 GHz (0.71 GHz) respectively. The negative refractive indices of the proposed meta-atom are 5.64–7.36 GHz (1.72 GHz bandwidth), 7.9–13.44 GHz (5.54 GHz bandwidth), and 14.09–15.65 GHz (1.56 GHz bandwidth), that are greater in bandwidth than [16, 17]. In addition, the size of the suggested meta-atom is $10 \times 11 \text{ mm}^2$, making it smaller than the reported metamaterials unit-cell in [9, 11, 14–16] with the terms of EMR.

Meta-atoms can operate in the subwavelength spectra if the EMR of the meta-atom is greater than 4. In addition, the characteristics of left-handed metamaterials appear at 9.40 GHz for the meta-atom and the array of the meta-atoms. To compute the scattering parameters such as the transmission coefficient (S_{21}) and reflection coefficient (S_{11}), the commercially available CST electromagnetic simulator 2015 was used. The effective medium parameters, namely effective permeability, permittivity, and refractive index were also retrieved using the well-established Nicolson-Ross-Weir method.

2 Methodology

2.1 Design of Left-Handed Meta-Atom

A combination of multiple hexagonal split ring resonators with a meander line was utilized to observe unconventional characteristics of metamaterials that were usually not found in nature. The proposed meta-atom unit-cell structural parameters and simulation setup are shown in Fig. 1. The dimensions of the substrate are $10 \times 11 \times 1.6 \text{ mm}^3$, and the FR4 lossy material is used as the substrate material. All elements of the resonators are made of copper with a conductivity of $5.8 \times 10^7 \text{ S/m}$ and the thickness of copper resonators is 0.035 mm and is printed on the substrate with standard relative permittivity $\epsilon = 4.3$ as well as loss tangent $\delta = 0.025$.

In Table 1, the design specifications of the meta-atom are listed.

In this paper, the FDTD method-based CST simulator is adopted to examine this design structure. The electric field and magnetic field polarized along the x-axis and the y-axis respectively, whereas z-axis is utilized propagating the electromagnetic wave. PEC- and PMC-type boundary conditions are applied along the x-axis and y-axis respectively, and two waveguide ports are placed on the (+) ve and (-) ve

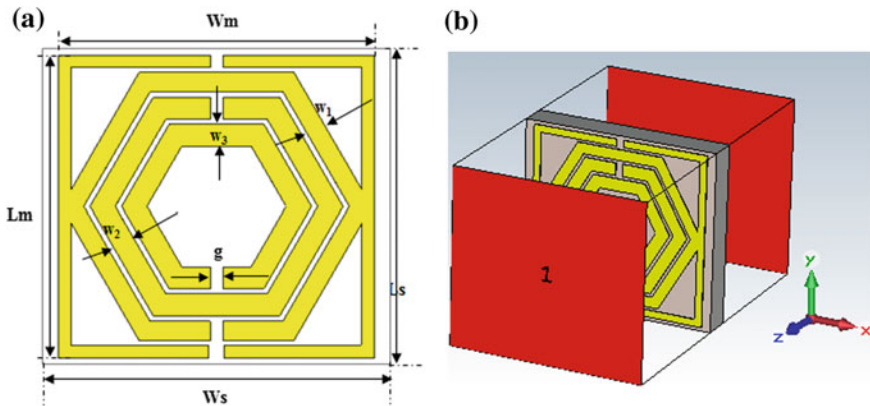


Fig. 1 a The proposed meta-atom structure; b Simulation setup of the proposed design

Table 1 Parameters of the modified hexagonal meta-atom

Parameters	Dimensions (mm)
Lm	10
Wm	9.6
W ₁	0.7
W ₂	0.8
W ₃	0.8
G	0.4

z-axis. The simulation setup of the fabricated design is shown in Fig. 1b. A frequency domain solver is utilized to find the transmission coefficient (S₂₁) and the reflection coefficient (S₁₁) during simulation. Impedance matching was set at 50 ohms. To simulate the design of meta-atom, 1–18 GHz frequency ranges were utilized.

2.2 Calculation of Effective Scattering and Medium Parameters

The Nicolson-Rose-Weir (NRW) method [19] was utilized to determine the medium parameters like effective permeability (μ_{eff}) and permittivity (ϵ_{eff}) from simulated scattering parameters such as the transmission coefficient (S₂₁) and reflection coefficient (S₁₁). The direct refractive index method [20] was applied to calculate the effective refractive index (n_{eff}) from the complex scattering parameters. The following equations are used to find out the effective medium parameters.

Effective permittivity,

$$\epsilon_{\text{eff}} = \frac{2c}{j\omega d} \times \frac{(1 - v_2)}{(1 + v_2)} \quad (1)$$

Effective permeability,

$$\mu_{\text{eff}} = \frac{2c}{j\omega d} \times \frac{(1 - v_1)}{(1 + v_1)} \quad (2)$$

Effective refractive index,

$$n_{\text{eff}} = \frac{2c}{j\omega d} \times \left\{ \frac{(S_{21} - 1)^2 - S_{11}^2}{(S_{21} + 1)^2 - S_{11}^2} \right\}^{1/2} \quad (3)$$

The S-parameters were represented as the addition and subtraction terms as given in Eqs. 4 and 5.

$$v_1 = S_{21} + S_{11}, \tag{4}$$

$$v_2 = S_{21} - S_{11}, \tag{5}$$

Where S_{21} and S_{11} are the transmission coefficient and reflection coefficient of the meta-atom. d is the thickness, c is the velocity of light of the slab and ω is the angular frequency.

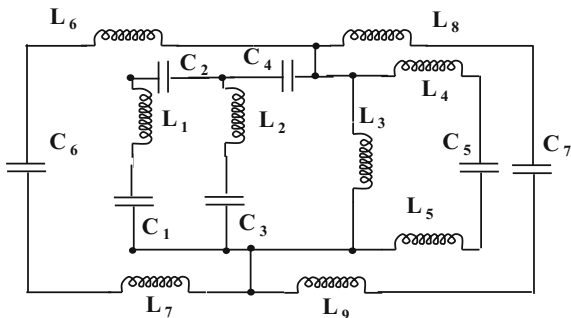
2.3 Equivalent Circuit of the Proposed Meta-Atom

The proposed metamaterial structure comprises with inductance and capacitance. The non-magnetic strip is considered as the inductive parameter, where the split or gap is for the capacitive one. These structures manipulate incident electromagnetic waves, thereby changing the effective medium parameters. The effective medium parameters also depend on the passive capacitor and inductor. The hexagonal split ring resonator displays electromagnetic resonance when electric and magnetic energy are stored in the capacitor and inductors respectively. The changes in capacitance and inductance due to electric dipole moment and magnetic dipole moments form biomolecule that has the capability to handle the shifting of the resonance frequency. The resonance frequency (f_r) of the designed resonator is

$$f_r = (2\pi\sqrt{LC})^{-1} \tag{6}$$

The capacitance and inductance are formed by slit and metal strip of meta-atom for obtaining wideband. The split and gap between the hexagonal rings lead the capacitive effects that are symbolized as $C_1, C_2, C_3, C_4, C_5, C_6,$ and C_7 . On the other hand, inductive effects are denoted by $L_1, L_2, L_3, L_4, L_5, L_6, L_7, L_8,$ and L_9 . Moreover, total capacitance and phase delay of the meta-atom depend on the summation of more splits. The proposed metaatom structure's equivalent circuit is presented in Fig. 2.

Fig. 2 The equivalent LC circuit of the proposed meta-atom



3 Results and Discussion

There are many methods that are used to extract effective parameters, namely the Nicolson–Rose–Weir (NRW) method, the Direct-Retrieval method, the Transmission–Reflection (TR) method, and Direct Refractive Index, etc. Both the real and imaginary data of the permeability, permittivity, and refractive index are suitable to characterize the proposed meta-atom. In this paper, a unit-cell with elevation angle was analyzed.

The simulation results of the modified hexagonal compact meta-atom are presented below. The simulated reflection coefficient (S_{11}), and transmission coefficient (S_{21}) of the unit-cell are demonstrated in Fig. 3. Figure 3a demonstrates the mathematical values of the five frequency ranges of resonance frequencies to be 1.88–2.07 GHz, 3.53–4.03 GHz, 7.22–7.66 GHz, 9.16–11.91 GHz, and 13.96–14.67 GHz designating L-, S-, C-, X-, and Ku-band applications. Figure 3a shows the simulation results. Figure 3b demonstrates the instantaneous surface current distributions at 9.40 GHz where the double negative properties are exposed. The instantaneous surface currents move in the opposite direction in the copper strip of the meta-atom structure because of the design structure of the meta-atom unit-cell. The opposite direction of current flow makes the alternate rotating magnetic fields that nullify each other. This is why the stop band is generated at this frequency. On the contrary, the scattering parameters of simulation results for 0° have been marginally shifted to the lower frequency and little bit shortened comparing with 90° results.

Figure 4a shows the values of the relative negative permittivity to be 1.901–2.088 GHz, 3.159–4.179 GHz, 5.097–9.823 GHz, 10.384–10.520 GHz, and 12.441–13.087 GHz for the 00 elevation angle and 2.734–5.046 GHz, 5.743–7.460 GHz, 7.936–9.466 GHz, 10.333–11.761 GHz, 17.507–18.000 GHz for the 900 elevation angle of the design structure of the meta-atom. The electric and magnetic dipole moment also follow the applied electromagnetic field at lower

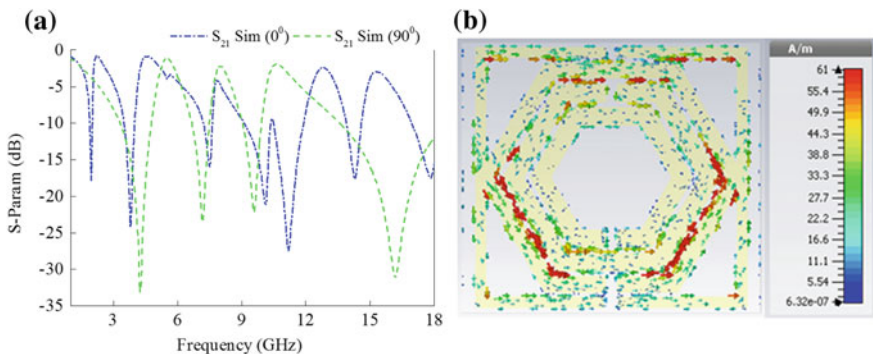


Fig. 3 **a** Simulated and measured S-parameters curve of meta-atom structure; **b** Instantaneous surface current at 9.40 GHz

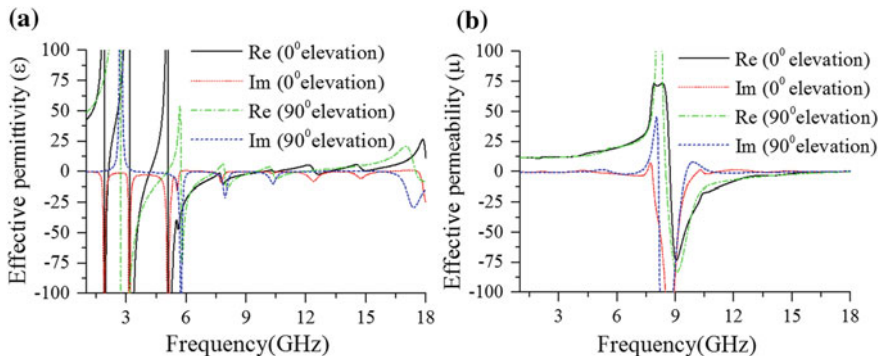
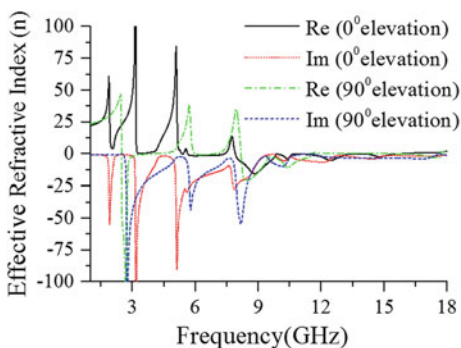


Fig. 4 **a** Permittivity and **b** permeability data of real and imaginary curves for the elevation angle of 0° and 90° of the meta-atom unit-cell

Fig. 5 Refractive index data of real and imaginary curves for the elevation angles of 0° and 90° of the meta-atom unit-cell



frequencies. On the contrary, the dipole moment cannot contend with the applied field. For that reason, the fluctuation of scattering parameters occurred at higher frequencies. Figure 4b displays the values of the relative negative permeability at 8.718–17.677(8.959 GHz) and 8.497–17.762 (9.265 GHz) for the 00 elevation angle and 900 elevation angle of the design structure of the meta-atom respectively. The negative attributes of the permittivity and permeability have changed slightly due to the polarization effect on the interior structure of the meta-atom. Anisotropic materials contain an unequal lattice structure that manipulates the applied electromagnetic field due to the polarization of the dipole moment inside the materials. Hence, a change of design structure also changes the properties of the effective permeability and permittivity of the metamaterials

Figure 5 depicts the relative negative refractive index of 5.641–7.358 (1.717 GHz bandwidth), 7.902–13.444 (5.542 GHz bandwidth), 14.09–15.654 (1.564 GHz bandwidth) and 2.479–3.924 (1.445 GHz bandwidth), 6.032–6.899 (0.867 GHz bandwidth), 8.174–11.506 (3.332 GHz bandwidth), 16.028–17.66 (1.632 GHz bandwidth) for the 00 elevation angle and for the 900 elevation angle of the design structure of the meta-atom. The curves of the effective refractive index become negative when the curves of the permeability and permittivity are

Table 2 Verification of previous array configurations and proposed array configurations

Properties	Ref. 10	Ref. 12	Ref. 18	Ref. 16	Proposed Meta-atom
Applicable band	(5–7) GHz	(2–15) GHz	(0.5–6) GHz	(1–15) GHz	(1–18) GHz
Unit-cell Shape	U	H	G	Double C	Modified hexagonal
Meta-atom type	LHM	LHM	NIM	NIM	LHM
EMR	1.99	3.65	11.90	7.44	13.84

simultaneously negative. The design structure of the meta-atom showed left-handed properties at 9.40 GHz because the permittivity, permeability, and refractive index were simultaneously negative at that point, and this is presented in Table 2.

The comparison between the proposed meta-atom and other reported metamaterials is shown in Table 2. The comparison parameters of the metamaterial considered here include the dimension of the applicable band, unit-cell shape, characteristics of suggested metamaterials and effective medium ratio. From Table 2, in Ref. [10], the author presented a U-shaped design and obtained 1.99 EMR. Another author in Ref. [12], analyzed an H-shaped configuration for DNG metamaterials but he achieved lower EMR of 3.65. Hossain et al. [18] displayed a modified hexagonal shape with NIM and a small EMR. On the other hand, the author obtained a very small EMR with the single negative metamaterial property at the resonance frequency. Finally, in this paper, a modified hexagonal shape was analyzed and achieved a higher EMR (13.84) with a wideband refractive index (5.542 GHz). In conclusion, The proposed meta-atom has a simple design with wideband refractive index comparing to all mentioned references which are suitable for microwave regime.

4 Conclusion

A new design of a modified hexagonal compact left-handed meta-atom and array of the meta-atom structure were proposed for multiband applications in this paper. These designs exhibited higher EMR (13.84), wider negative refractive index bandwidth (5.542 GHz) and LHM characteristics. The CST electromagnetic simulator was utilized to determine the metamaterial's properties. The proposed meta-atoms are applicable for military telemetry, GPS, GSM, radar and satellite communications, microwave communications, wireless LAN, long-distance radio telecommunications, space communication and radar terrestrial broadband. A comparative analysis was also carried out on unit-cell Shape, metamaterials characteristics and effective medium ratio for multi-band applications. Hence, the meta-atom structure has wide bandwidth with better EMR which is more suitable in the microwave regime.

Acknowledgements This work was supported by the Ministry of Education (MOE) under Fundamental Research Grant Scheme Top Down, Code: FRGS TOP DOWN/2014/TK03/UKM/01/1 and Research Universiti Grant, Dana Impak Perdana Code: DIP-2015-014.

References

1. Veselago VG (1968) The electrodynamics of substances with simultaneously negative values of ϵ and μ . *Sov Phys* 10:509–514
2. Shelby RA, Smith DR, Schultz S (2001) Experimental verification of a negative index of refraction. *Science* 292:77–79
3. Schurig D, Mock J, Justice B, Cummer SA, Pendry JB, Starr A et al (2006) Metamaterial electromagnetic cloak at microwave frequencies. *Science* 314:977–980
4. Cai W, Chettiar UK, Kildishev AV, Shalaev VM (2007) Optical cloaking with metamaterials. *Nat Photonics* 1:224–227
5. Bowen PT, Baron A, Smith DR (2016) Theory of patch-antenna metamaterial perfect absorbers. *Phys Rev A* 93:063849
6. Pendry JB (2003) Perfect cylindrical lenses. *Opt Express* 11:755–760
7. Sil Kwak, Sim D-U, Kwon JH, Yoon YJ (2017) Design of PIFA with metamaterials for body-SAR reduction in wearable applications. *IEEE Trans Electromagn Compat* 59:297–300
8. Smith DR, Padilla WJ, Vier DC, Nemat-Nasser SC, Schultz S (2000) Composite medium with simultaneously negative permeability and permittivity. *Phys Rev Lett* 84:4184–4187
9. Islam SS, Iqbal Faruque MR, Islam MT (2015) A near zero refractive index metamaterial for electromagnetic invisibility cloaking operation. *Materials* 8:4790–4804
10. Mallik A, Kundu AS, Goni MO (2013) The design of a novel two-rectangular U-shaped double negative metamaterial. In: Paper presented at the 2013 IEEE International Conference on Informatics, Electronics and Vision, Dhaka, Bangladesh, 17–18 May 2013
11. Zhou H, Wang C, Peng H (2016) A novel double-incidence and multi-band left-handed metamaterials composed of double Z-shaped structure. *J Mater Sci Mater Electron* 27:2534–2544
12. Islam SS, Iqbal Faruque MR, Islam MT (2014) The design and analysis of a novel split-h-shaped metamaterial for multi-band microwave applications. *Materials* 7:4994–5011
13. Rizwan M, Jin H-B, Rehman F, Hou Z-L, Li J-B, Butt FK, Ali Z (2014) Dual-Band tunable negative refractive index metamaterial with F-Shape structure. *Cent Eur J Phys* 12:578–581
14. Zhou Z, Yang H (2015) Triple-Band asymmetric transmission of linear polarized with deformed S-shape bilayer chiral metamaterial. *Appl Phys A* 119:115–119
15. Yang S, Liu P, Yang M, Wang Q, Song J, Dong L (2016) From flexible and stretchable meta-atom to metamaterial: a wearable microwave meta-skin with tunable frequency selective and cloaking effects. *Sci Rep* 6:21921
16. Hossain MJ, Iqbal Faruque MR, Islam SS, Islam MT (2016) Subwavelength operating metamaterial for multiband applications. *Microw Opt Tech Lett* 58:3004–3008
17. Alam T, Iqbal Faruque MR, Islam MT (2015) A double-negative metamaterial-inspired mobile wireless antenna for electromagnetic absorption reduction. *Materials* 8:4817–4828
18. Hossain MI, Iqbal Faruque MR, Islam MT, Ullah MH (2015) A new wide-band double-negative metamaterial for C- and S-B and applications. *Materials* 8:57–71
19. Nicolson AM, Ross GF (1970) Measurement of the intrinsic properties of materials by time-domain techniques. *IEEE Trans Instrum Meas* 19:377–382
20. Islam SS, Iqbal Faruque MR, Islam MT (2015) a new direct retrieval method of refractive index for the metamaterial. *Curr Sci* 109:337–342

A Terahertz Meta-Surface with Left-Handed Characteristics for Absorbing Applications

Md. Mehedi Hasan, Mohammad Rashed Iqbal Faruque and Mohammad Tariqul Islam

Abstract A meta-surface that absorbs waves from all directions of incidence can be realized if the surface impedance is made to vary as a function of incidence in a specific manner. In this paper, a terahertz meta-surface with left-handed characteristics for high absorbing applications is discussed. The designed small absorber unit was developed by cross-metallic connection of two metal strips printed on epoxy resin fibre material. Finite integration technique-based electromagnetic simulator Computer Simulation Technology Microwave Studio was utilized to simulate and investigate the proposed design. The proposed meta-surface shows resonance at 39.19 THz, 58.47 THz and 77.80 THz and left-handed characteristics at 15.3 THz and 87.7 THz respectively. In addition, the structure of the absorber shows the highest absorption peaks of 99.6% and 89.5% at 16.4 THz and 75.8 THz respectively.

Keywords Absorption · Left-handed · Meta-surface · Terahertz

1 Introduction

In recent years, there has been a renewed interest from the scientific community in the property of near-perfect absorption, originally used in stealth technology to reduce the radar cross-section of objects at specific radar frequencies. The advent of a meta-surface with unique properties played a key role in the development of high quality absorbers ranging from microwaves to optical wavelengths and their integration in numerous functional applications such as imaging, solar energy collection, medical applications,

Md. Mehedi Hasan (✉) · M.R.I. Faruque
Space Science Centre (ANGKASA), Institute of Climate Change,
Universiti Kebangsaan Malaysia, 43600 Bangi, Selangor Darul Ehsan, Malaysia
e-mail: mehedi20.kuet@gmail.com

M.T. Islam
Department of Electrical, Electronics and Systems Engineering,
Universiti Kebangsaan Malaysia, 43600 Bangi, Malaysia

and optical applications, etc. In the past two decades, the field of terahertz technology has experienced remarkable development due to advances in laser and semiconductor technology. This has given rise to various potential applications including sub-diffraction imaging, cloaking, and polarization conversion systems. Meta-surface absorbers can be divided into two broad categories based on their principle of operation. The first category consists of devices impedance-matched to free space, while simultaneously exhibiting large imaginary parts in their effective permittivity and permeability. If the material is impedance-matched with large and lossy values of permittivity and permeability, then the surface will reflection less at normal incidence and the incident field will decay rapidly once inside. The second category of absorbers is based on electrically responsive metamaterial elements closely coupled to a ground plane in such a way that they resemble patch antennas. Such absorbers have been experimentally demonstrated throughout the electromagnetic spectrum from radio to visible frequencies. These absorbers typically involve a resonant structure and therefore have a narrow frequency response. However, the remarkable property of these absorbers is their ability to absorb TM polarization nearly perfectly over all angles of incidence. For many applications, like thermophotovoltaic and microbolometer arrays, the narrow frequency response is a benefit rather than a nuisance, since a deeply sub-wavelength structure that provides a narrowband emission can be used in combination with other narrowband structures to engineer an arbitrary absorption spectrum. In these cases, the broad angular response becomes the limiting factor in the performance of the device.

In 2003, Ziolkowski et al. [1] developed a metamaterial with capacitor loaded strips and split-ring resonators, which exhibited negative permittivity and negative permeability both at the X-band frequencies. In particular, meta-atom absorbers have been studied since Landy et al. [2] introduced them in 2008. They generated electric and magnetic resonances that were independently manipulated for effective permittivity and effective permeability respectively. In 2016, Hasan et al. [3] proposed a compact z-shaped double negative metamaterial for wideband applications. The $10 \times 10 \text{ mm}^2$ structure of the metamaterial unit cell was applicable for C- and X-band operations and the effective medium ratio was 4. In 2017, Hasan et al. [4] projected a negative index meta-atom, resonances at C-, X- and Ku-band with a wide negative refractive index bandwidth from 7.0 to 12.81 GHz. Negative index characteristics, bandwidth, and compactness of the proposed structure are analysed at the z-axis by propagating the electromagnetic waves. In addition, the meta-atom presented negative index characteristics at X- and Ku-bands. In 2017, Karaaslan et al. [5] introduced a multiband absorber based on a multi-layered square split-ring structure. The multi-layered metamaterial structure was designed to be used in frequency bands such as WIMAX, WLAN and satellite communication. The absorption levels of the proposed structure were higher than 90% for all resonance frequencies. A terahertz (THz) meta-surface, with the unit cells consisting of double metal loops and a metallic back film on both sides of the dielectric layer was investigated to find the connection between reflectivity and pattern geometry. The absorber reached 0.102-THz bandwidth and the reflect array antenna gain reached

22 dBi at 0.875 THz in 2017 [6]. Yao et al. [7] suggested a dynamically lambda-tunable graphene-based terahertz metamaterial absorber, which consists of a single layer periodically patterned graphene electric resonant structure and a metal ground plane spaced by SiO₂ dielectric layer. Numerical results revealed that the absorption spectrum of the graphene-based structure displays two perfect absorption values of 99% at 35 μm and 97% at 59 μm respectively. A microstrip patch antenna was designed with an artificial magnetic conductor for telemedicine applications by Sneka et al. [8] and it was observed that the antenna gain was about 6.21 dBi, directivity was around 6.37Bi, return loss almost -29 dB and the radiation efficiency was 96.21%. Wang et al. [9] developed a dual-band terahertz absorber formed by a U-shaped metallic ring and a metallic ground plane separated by a dielectric layer, in 2016. The proposed absorber showed two separated absorption bands and the peaks averaged over 98%. Yahiaoui et al. [10] in 2015 presented a multichannel metamaterial absorber with the aim of using it as a label-free sensing platform in the terahertz regime. The results of the designed metamaterial absorber showed at absorption frequencies of 0.22 THz, 0.48 THz, 0.72 THz and 0.76 THz, and the percentages of absorption were 79%, 80%, 76% and 74% respectively. However, the sensitivity was highest at 139.2 (GHz/RIU). In 2016, Liu et al. [11] demonstrated a dual band metamaterial perfect absorber composed of artificial dielectric molecules with high symmetry. The artificial dielectric molecules consist of four atoms of two different sizes corresponding to two absorption bands with near unity absorptivity. The experimental results showed two reflection minimums with $R = 3\%$ at 9.4 GHz and $R = 2.5\%$ at 11.7 GHz, and therefore two absorption peaks with $A = 97\%$ at 9.4 GHz and $A = 97.5\%$ at 11.7 GHz. Islam et al. [12] projected a new multiband split S-shaped metamaterial for absorption analyses that shown resonance at the S-, X- and Ku-bands in microwave spectra in 2015. The absorption spectra for the proposed metamaterial was 45% achieved at S-band. Moreover, after reducing the coupling capacitance in the z-axis, absorption reached 55% but in the y-axis absorption only reached 47%. Despite the absorption, the proposed metamaterial could be used for various applications like near-zero refractive index, epsilon negative, mu-negative, and double negative metamaterials. Lee et al. [13] recommended a metamaterial absorber for X-band applications. The proposed absorber had a square patch at the center and four circular sectors were rotated around the square patch. The results showed that when the inner angle of the circular sector was 90°, the absorptivity was higher than 90% and the frequency variation was less than 0.96% for incident angles up to 70°. The absorptivity at 10.44 GHz was close to 100% for all the polarization angles under normal incidence. Hasan et al. [14] presented a microwave metamaterial absorber with resonance at C-, X- and Ku-bands with double negative characteristics as well as absorption peaks that were 82%, 67%, and 93% at 6.22 GHz, 8.76 GHz, and 13.05 GHz respectively.

A new 3D meta-surface absorber at terahertz frequency has been designed in this study, with a working frequency range from 0 THz to 100 THz. The proposed meta-surface shows resonance at 39.19, 58.47 and 77.80 THz. The met-surface exhibits left-handed characteristics at 15.3 and 87.7 THz, whereas the permittivity,

permeability and refractive index are -25.21 , -177.5 , -68.28 and -42.38 , -0.78 , -8.12 respectively. The absorber structure showed absorption and the resonance peaks are 99.6% and 89.5% at 16.4 THz and 75.8 THz respectively. The paper is laid out in the following order: The design of the proposed meta-surface absorber with schematic and 3d views is in Sect. 2 and the methodology is explained in detail with a simulated diagram, retrieval methods of effective medium parameters and an equivalent circuit model of the proposed meta-surface absorber in Sect. 3. Analysis of the results is in Sects. 4 and 5 completes the paper.

2 Design of the Proposed Meta-Surface Absorber

The schematic view, top view and 3D view of the proposed meta-surface absorber are shown in Fig. 1a–c. The designed absorber small unit was developed by cross-metallic connection of two metal strips printed on the dielectric substrate material. Epoxy resin fibre is used as substrate material, in which the dielectric constant and loss tangent are 4.5 and 0.002 respectively. The thickness of the substrate material is considered to be 0.1 μm . The total dimensions of the designed meta-surface absorber are $5.1 \times 5.15 \mu\text{m}^2$, whereas the small single unit cell is $1 \times 1.1 \mu\text{m}^2$ (Table 1).

3 Methodology

Finite integration technique-based commercially available CST Microwave Studio was adopted for all the numerical investigations. Boundary conditions were usually used in most of the computer simulations to speed up the computation process. In the simulation from 0 to 100 THz, the electromagnetic waves are propagating along the z-axis, whereas the x- and y-axis are considered as a perfect electric conductor (PEC) and perfect magnetic conductor (PMC) boundaries respectively. The retrieving procedure of the effective parameters is given as follows [15, 16],

$$\text{Impedance, } Z \approx \pm \left[\frac{(1 + S_{11})^2 + S_{21}^2}{(1 - S_{11})^2 + S_{21}^2} \right]^{1/2} \quad (1)$$

$$\text{Permittivity, } \varepsilon_r \approx (n_{\text{eff}}/Z) \quad (2)$$

$$\text{Permeability, } \mu_r \approx (n_{\text{eff}} \times Z) \quad (3)$$

$$S_{11} \approx \left\{ \frac{R_1(1 - e^{-j2\theta})}{1 - R_1^2 e^{-j2\theta}} \right\} \quad (4)$$

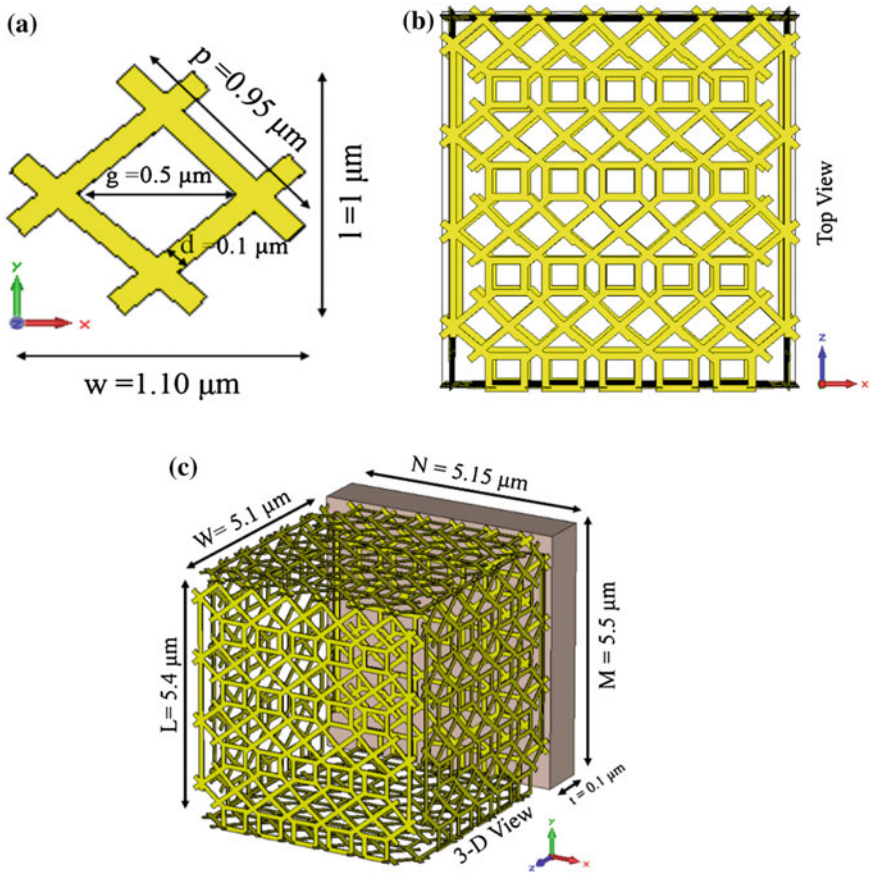


Fig. 1 Schematic view of: **a** unit cell, **b** top view of the designed structure, and **c** proposed meta-surface structure

Table 1 Design parameters of the proposed meta-surface absorber unit cell

Parameters	L	W	p	M	N
Dimensions (μm)	5.4	5.1	0.95	5.5	5.15
Parameters	l	w	d	T	h
Dimensions (μm)	1	1.1	0.1	0.1	0.017

Similarly,

$$S_{21} \approx \left\{ \frac{(1 - R_1^2) e^{-j2\theta}}{1 - R_1^2 e^{-j2\theta}} \right\} \quad (5)$$

where, $\theta = \zeta d$ and ζ is the propagating constant. Moreover, T is defined as exponential transmission.

$$\text{Similarly, } T = e^{-j2\theta} = \left\{ \frac{S_{21} + S_{11} - R_1}{1 - R_1(S_{21} + S_{11})} \right\} \quad (6)$$

$$R_1 = \left\{ \frac{T - S_{21} + S_{11}}{1 - T(S_{21} + S_{11})} \right\} \quad (7)$$

$$k \approx \frac{1}{jd} \times \left\{ \frac{(1 - S_{21} - S_{11})(1 + R_1)}{1 - R_1(S_{21} + S_{11})} \right\} \quad (8)$$

$$k \approx \left(\frac{2\pi f}{c} \right) (\epsilon_r \mu_r)^{1/2} \approx k_0 (\epsilon_r \mu_r)^{1/2} \quad (9)$$

$$\eta_{\text{eff}} \approx \left(\frac{k}{k_0} \right) \quad (10)$$

From Eq. (4–10), it can be written that

$$\text{Refractive Index, } \eta_{\text{eff}} \approx \frac{2}{jkd} \left\{ \frac{(S_{21} - 1)^2 - S_{11}^2}{(S_{21} + 1)^2 - S_{11}^2} \right\}^{1/2} \quad (11)$$

The equivalent circuit of Fig. 2a is a pie-shaped circuit, where the shunt branches of the proposed meta-surface absorber circuit model are purely inductive. The inductive effect raises for the metal part shifted resonance to the lower frequency, whereas the gaps are accountable for capacitive effect. The inductive and capacitive effect are minimized together and set up resonance at a fixed point. In addition, there is a parasitic coupling effect for the mutual inductance and capacitance of the

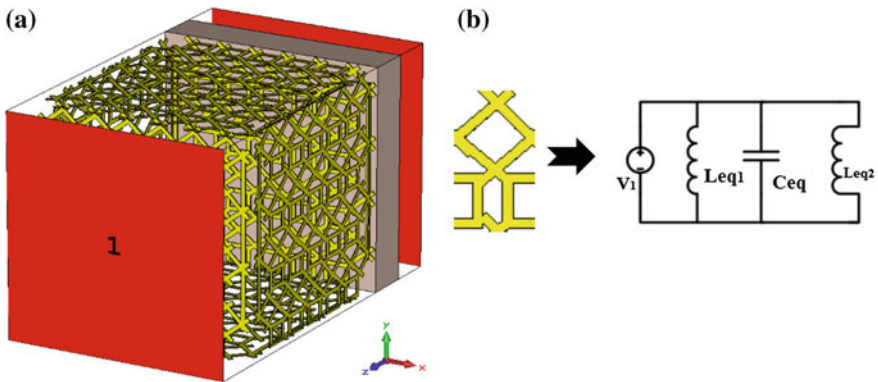


Fig. 2 **a** Boundary condition and simulated structure in the CST Microwave Studio, **b** equivalent circuit of the proposed meta-surface structure

designed structure. However, C_{eq} , L_{eq} , V_1 are represented as capacitance, inductance and external source of the lumped LC-circuit model respectively [17].

4 Results Analysis

The excited surface current distribution on the absorber at 77.8 THz is shown in Fig. 3a. The arrows show the direction of the currents and colour expresses the intensity. As expected, two dominating current paths were found, which primarily cause three resonant modes in the z-axis. The current path is clearly seen by the intensity of the currents. In Fig. 3a the currents are flowing in opposite directions and nullify each other at a certain frequency, creating stop bands. However, the electric field density at 77.8 THz is shown in Fig. 3b.

Figure 4a depicts the magnitudes of the reflection (S_{11}) and transmission (S_{21}) coefficients. The figure shows the resonance at 39.19 THz (magnitude of -41.90), 58.47 THz (magnitude of -48.18) and 77.80 THz (magnitude of -51.93). Figure 4b shows the real magnitude of the effective permittivity curves, while the negative peaks are from 4.4 THz to 46.9 THz and from 87.6 THz to 100 THz. From Fig. 4c the negative permeability curve is from 14.7 THz to 18.8 THz and from 45.7 THz to 89.6 THz. In Fig. 4d, the negative refractive index is from 6.4 THz to 9.2 THz, 13.1 THz to 18.7 THz, 44.2 THz to 46.8 THz and 85.5 THz to 90 THz. If the permittivity and permeability are simultaneously negative, then the refractive index is also negative. Here at 15.3 and 87.7 THz, the designed meta-surface absorber exhibits permittivity, permeability and refractive index parameters of -25.21 , -177.5 , -68.28 and -42.38 , -0.78 , -8.12 respectively. As a result, the meta-surface structure can be characterized as a left-handed meta-surface at 15.3 and 87.7 THz (Table 2).

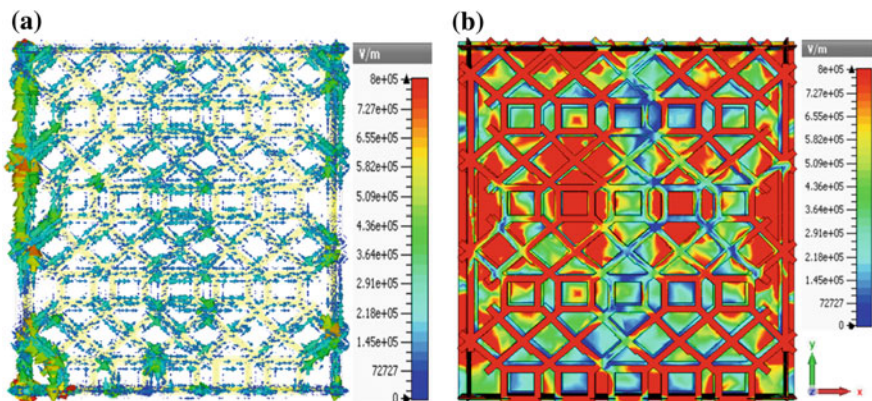


Fig. 3 a Surface current distribution and b Electric field at 77.8 THz of the designed meta-surface absorber

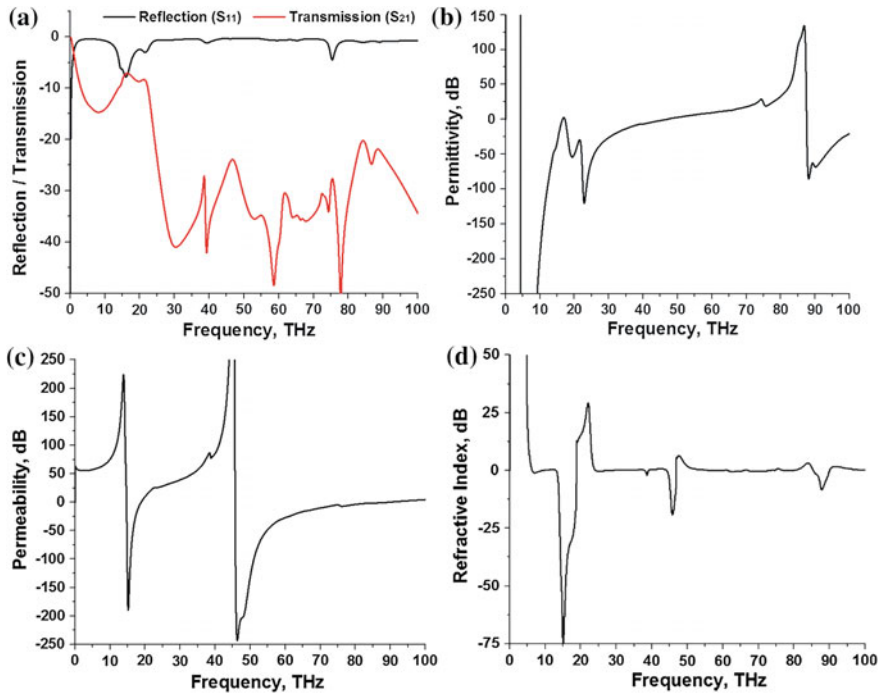


Fig. 4 a Reflection and transmission coefficients, Effective: b permittivity, c permeability, and d refractive index, of the suggested meta-surface

Table 2 Value of effective medium parameters of the meta-surface for the left-handed characteristics

Resonance frequency (THz)	Permeability (μ)	Permittivity (ϵ)	Refractive index (η)
15.3	-25.21	-177.5	-68.28
87.7	-42.38	-0.78	-8.12

Figure 5 shows the reactance impedance curve and at the resonance point the values of the reactance impedance are 5.26–10.13i and 60.5–67.95i.

The electromagnetic wave incident on the absorber and the absorption can be calculated from the reflection and the transmission coefficients,

$$\text{Absorption, } A \approx \left[1 - |S_{11}|^2 - |S_{21}|^2 \right] \quad (12)$$

In Fig. 6, the result of the absorption is shown. Absorption at the resonance peaks is 99.6% and 89.5% at 16.4 THz and 75.8 THz respectively. However, the nature of the absorption can be easily understood by observing the current density in the absorber structure from the surface current distribution curves (Table 3).

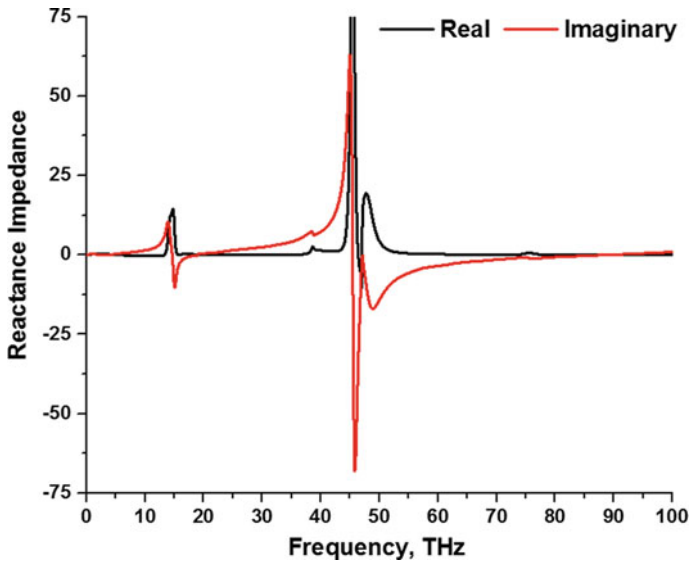


Fig. 5 Reactance impedance of the meta-surface absorber

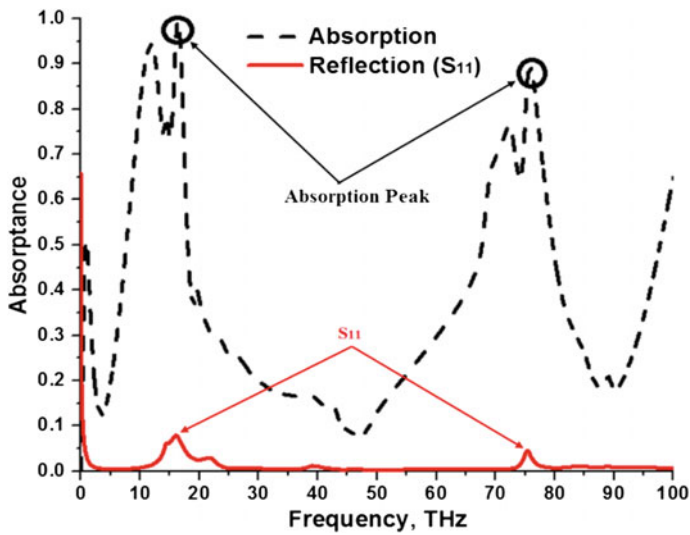


Fig. 6 Calculated absorption of the recommended meta-surface absorber

Table 3 Percentage of absorption of the proposed meta-surface absorber

Resonance of the reflection (S_{11}) (THz)	Absorption rate (%)
16.4	99.6
75.8	89.5

5 Conclusion

This paper focused on a new left-handed meta-surface absorber for absorption applications. The dielectric material of epoxy resin with woven glass fabric composite was used as substrate material to construct the meta-surface absorber structure. The designed structure exhibited left-handed properties at 15.3 and 87.7 THz. The absorber structure also showed the highest absorption peaks of 99.6% and 89.5% at 16.4 THz and 75.8 THz respectively. In addition, the finite integration technique used to analyse the proposed design was explained in detail with the numerical retrieval method of the effective medium parameters. The equivalent lumped inductance-capacitance circuit model was also illustrated in this paper. The proposed design is an ideal candidate for terahertz and energy-harvesting applications.

Acknowledgements This work was supported by the Research Universiti Grant, Geran Universiti Penyelidikan (GUP), code: 2016-028.

References

1. Ziolkowski RW (2003) Design, fabrication, and testing of double negative metamaterials. *IEEE Trans Antennas Propag* 51:1516–1529
2. Landy NI, Sajuyigbe S, Mock JJ, Smith DR, Padilla WJ (2008) A perfect metamaterial absorber. *Phys Rev Lett* 100:1–4
3. Hasan MM, Faruque MRI, Islam SS, Islam MT (2016) A new compact double-negative miniaturized metamaterial for wideband operation. *Materials* 9(10):830
4. Hasan MM, Faruque MRI, Islam MT (2017) A single layer negative index meta atom at microwave frequencies. *Microw Opt Technol Lett* 59:1450–1454
5. Karaaslana M, Bagmancia M, Unala E, Akgola O, Sabahb C (2017) Microwave energy harvesting based on metamaterial absorbers with multi-layered square split rings for wireless communications. *Opt Commun* 392:31–38
6. Chen L, Qu SW, Chen BJ, Bai X, Ng KB, Chan CH (2017) Terahertz meta surfaces for absorber or reflectarray applications. *IEEE Trans Antennas Propag* 65:234–241
7. Yao MHG, Ling F, Yue J, Luo C, Ji J, Yao J (2016) Dual-band tunable perfect metamaterial absorber in the THz range. *Opt Express* 24:1518–1527
8. Sneka N, Kashwan KR (2016) Design and implementation of a metasurface patch antenna array for medical applications. In: *International Conference on Research Advances in Integrated Navigation Systems, India*. pp 1–4
9. Wang BX, Wang GZ, Wang LL (2016) Design of a novel dual-band terahertz metamaterial absorber. *Plasmonics* 11:523–530
10. Yahiaoui R, Tan S, Cong L, Singh R, Yan F, Zhang W (2015) Multispectral terahertz sensing with highly flexible ultrathin metamaterial absorber. *J Phys* 118:083103–083106
11. Liu X, Lan C, Li B, Zhao Q, Zhou J (2016) Dual band metamaterial perfect absorber based on artificial dielectric molecules. *Sci Rep* 6:28906
12. Islam SS, Faruque MRI, Islam MT (2015) Design and absorption analysis of a new multiband split s shaped metamaterial. *Sci Eng Compos Mater*. doi:[10.1515/secm-2014-0376](https://doi.org/10.1515/secm-2014-0376)
13. Lee D, Hwang JG, Lim D, Hara T, Lim S (2016) Incident angle and polarization insensitive metamaterial absorber using circular sectors. *Sci Rep* 6:27155

14. Hasan MM, Faruque MRI, Islam MT (2017) A tri-band microwave perfect metamaterial absorber. *Microw Opt Technol Lett*. doi:[10.1002/mop.30726](https://doi.org/10.1002/mop.30726)
15. Hasan MM, Faruque MRI, Islam MT (2017) Multiband left handed biaxial meta atom at microwave frequency. *Mater Res Express* 4:035015
16. Islam SS, Hasan MM, Faruque MRI, Islam MT (2017) Two components NRI metamaterial for dual band applications. *Microw Opt Technol Lett* 59:1092–1096
17. Hasan MM, Faruque MRI, Islam MT (2017) Left-handed metamaterial using Z-shaped SRR for multiband application by azimuthal angular rotations. *Mater Res Express* 4(4):1–11

Microstrip Feed Slotted Ground Antenna with Parasitic Element for UWB Applications

Girish Awadhwal and Ali Bostani

Abstract A novel method to develop an Ultra-Wide Band (UWB) antenna is proposed in which a defected ground structure technique is employed. The proposed design is excited via a microstrip feed line which is optimized for the best impedance matching performance. The slotted ground is to enhance the UWB performance. The design parameters of the antenna have been optimized using high frequency finite element-based simulation software for the best gain, bandwidth and efficiency performance. The final design successfully meets the requirements of the UWB and even exceeds them, having a bandwidth of 2.55 to 10.85 GHz. The design parameters and the simulation results are reported in this paper and include the radiation pattern at different frequencies within the operating band.

1 Introduction

Higher data transmission rates and expanding high speed communication involving a lot of multimedia data transfer require the trajectory of technological advancement to take a detour along the path of bandwidth enhancement. The large amount of attention that has been devoted to the design and expansion of ultra-wide band (UWB) antennas was a response from scientists in the fields of RF and microwave studies to this demand from the market. These days, UWB antennas have several applications in radar communication such as RF identification devices, high-tech sensor networks, positioning and tracking systems, and in many other wireless communication fields.

G. Awadhwal

Department of Electronics and Communication Engineering Department,
University Institute of Technology RGPV, Bhopal, India
e-mail: Girish.awadhwal.ece10@itbhu.ac.in

A. Bostani (✉)

Electrical Engineering Department, American University of the Middle East,
Egaila, Kuwait
e-mail: ali.bostani@aum.edu.kw

To meet the needs of modern compact portable devices, the best choice for the design of UWB antennas would be a low profile and lightweight option such as printed antennas. This is the reason that we see all kinds of microstrip designs of UWB antenna reported in publications [1–3]. In 2002, the federal communication commission (FCC) allocated a frequency band from 3.1 to 10.6 GHz for commercial applications of UWB [1]. Since then, several designs for UWB antennas [4–6] have been proposed using several different shapes such as square [1], circular [7], pentagonal [2], hexagonal [4], elliptical [5], ring [6] and trapezoidal [8]. There are also various configurations and design techniques, which includes monopoles [1, 2, 5], dipoles and slot antennas [4] and various feeding techniques such as micro-strip [1, 5–7], co-planar-waveguide (CPW) [7]. Lin and Wong [4] and Morioka et al. [8] also used coaxial [9] all those mentioned were successfully employed in UWB applications.

Amongst all the mentioned designs and techniques, printed monopole antennas have received much more attention due to their wideband characteristic, Omni-directional radiation patterns, high radiation efficiency, and compact size [8, 10]. Recent technological advances in the size reduction of electronic circuits have changed wireless communications and sensor network design specifications. In particular, they have exposed the need for electrically small antennas that are efficient and have significant bandwidths. The standard electrically small antenna designs are known to be inefficient due to their large reactance and low resistance, which leads to the poor match to a given source. However, to compensate the impedance mismatch and additional bandwidth, researchers have already introduced the concept of defected ground structure (DGS), defected micro-strip structure (DMS) and other types of defect either in the feed line or in the body of the antenna itself.

On the other hand, the finite element method has been successfully employed to analyze and optimize the design of UWB antennas because of its accuracy and ability to handle the unconventional geometries [11, 12].

In this paper, a defected ground antenna is proposed which is designed based on the DGS concept and optimized for the best performance in terms of impedance matching within the UWB band and the radiation pattern and the gain using high frequency full wave finite element simulation software.

Details of the design concept of the antenna and simulation results are described in Sects. 2 and 3 respectively, as discussed in this section, and the conclusions are described in Sect. 4.

2 Antenna Design

Figure 1 shows the configuration of the proposed wideband antenna which consists of a slotted ground feed by micro-strip line. The proposed antenna, which has compact dimensions of $28 \times 32 \text{ mm}^2$ is constructed on an FR4 substrate with a thickness of 1.6 mm and relative dielectric constant of 4.4. The width of the

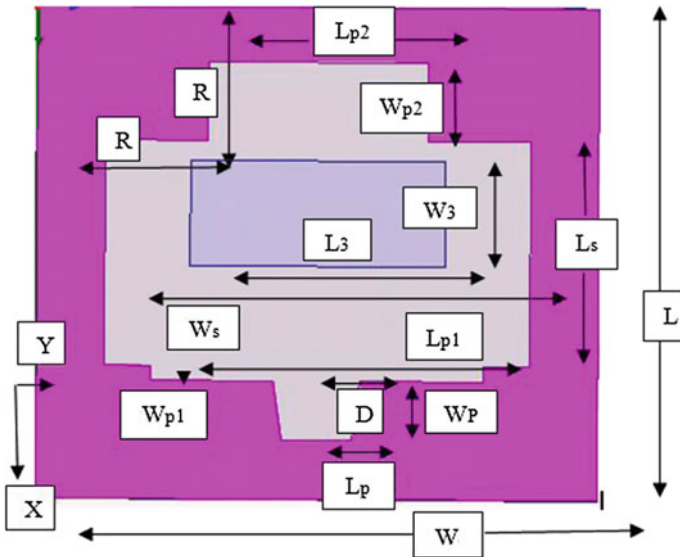


Fig. 1 Top view of the proposed microstrip feed slotted ground antenna

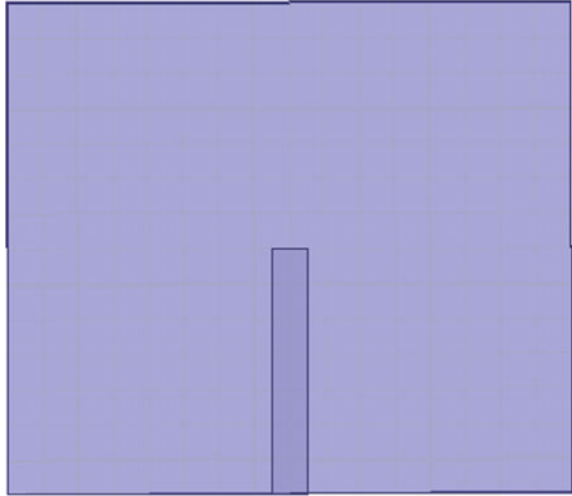
micro-strip feed line is fixed at 2 mm and has a length of 14 mm. The downside of ground slot has an upper side length $D = 5$ mm and a lower side length of $L_p = 4$ mm. The direction of the Z axis is out of the plane. To achieve the maximum impedance bandwidth all the proposed antenna design parameters are optimized by HFSS software. The optimal dimensions of the designed antenna are as follows: $W = 32$ mm, $L = 28$ mm, $L_p = 4$ mm, $W_p = 3.5$ mm, $R = 8.75$ mm, $D = 5$ mm, $W_f = 2$ mm, $L_f = 14$ mm, $W_s = 24.25$ mm, $L_s = 12.8$ mm, $W_{p1} = .875$ mm, $L_{p1} = 19$ mm, $W_{p2} = 4.5$ mm, $L_{p2} = 12.5$ mm, $W_3 = 6$ mm, $L_3 = 14.5$ mm.

The antenna was modeled on a 3D cad and was simulated using high frequency full wave finite element based simulation software. The tetrahedral elements were chosen to make sure that there are no singularities within the entire geometry and the mesh is fine enough to ensure the accuracy of the obtained results. Several passes of the finite element solver confirmed that the designed antenna satisfies all the requirements in the UWB frequency band and show that the impedance matching bandwidth of the antenna can cover a range of 2.58 to 10.74 GHz.

3 Results and Discussions

A parametric study of the proposed antenna was carried out in order to achieve UWB operation. The slots on the ground plane are optimized to make sure that the antenna meets the UWB requirement. To reduce the complexity of the design, some antenna

Fig. 2 Bottom view of the proposed microstrip feed slotted ground antenna



parameters were selected to be fixed as shown in Fig. 1. In this section the effects of the parameters W_f , L_f , W_s , $Wp1$, $Lp1$, $Wp2$, $Lp2$, $W3$, $L3$ on the antenna's performance are reported in detail (Fig. 2).

3.1 Parametric Study of the Effects of Variation of the Feed Line Width (W_f)

Figure 3 illustrates the return loss (S_{11}) plot of the UWB antenna for different values of W_f . It can be seen that the resonant frequencies and operating bandwidth depend on this parameter. The optimized value of W_f was found to be 2.2 mm.

3.2 Parametric Study of the Effects of Variation of the Feed Line Length (L_f)

Figure 4 illustrates the return loss (S_{11}) plot of the UWB antenna for different values of feed line length L_f . It can be seen that the upper cutoff frequency and operating bandwidth depend on this parameter. The optimized value of W_f was found to be 14 mm.

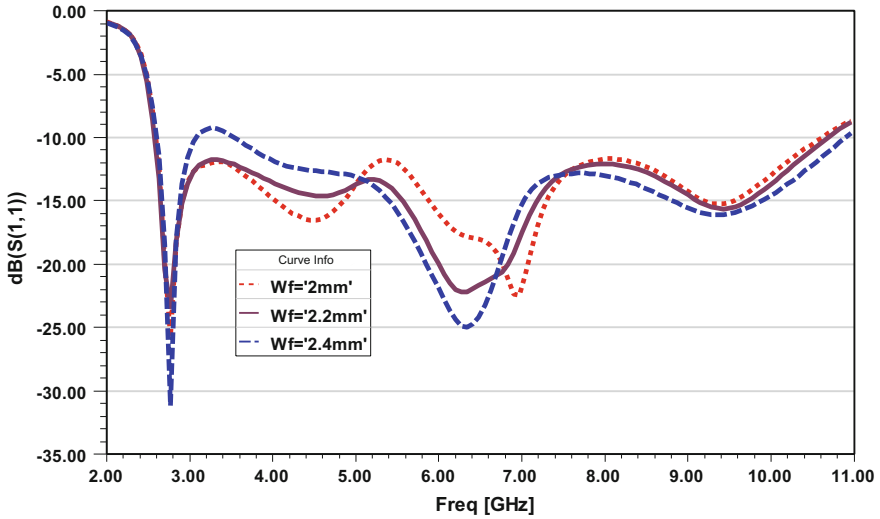


Fig. 3 Simulated return loss against frequency for the proposed antenna with varying feed line width W_f ; other parameters are same as in Fig. 2

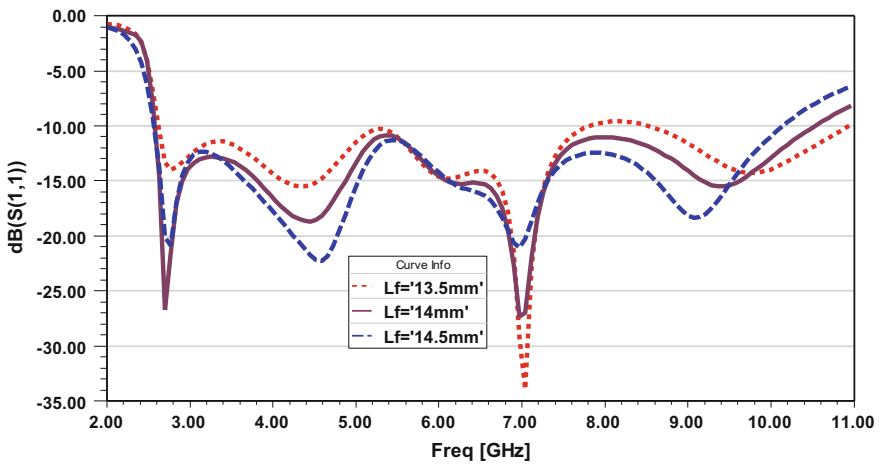


Fig. 4 Simulated return loss against frequency for the proposed antenna with varying feed line length L_f ; other parameters are same as in Fig. 2

3.3 Parametric Study of the Effects of Variation of the Ground Slot Parameter W_s

Figure 5 illustrates the return loss (S_{11}) plot of the UWB antenna for different values of slot parameter W_s . It can be seen that the upper cutoff frequency,

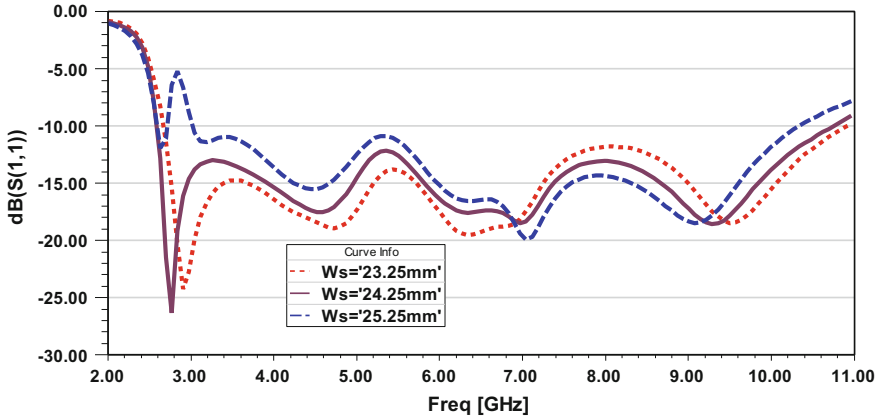


Fig. 5 Simulated return loss against frequency for the proposed antenna with varying ground slot parameter W_s ; other parameters are same as in Fig. 1

resonance frequency and operating bandwidth depend on this parameter. The optimized value of W_s was found to be 24.25 mm.

3.4 Parametric Study of the Effects of Variation of the Ground Slot Parameter W_{p1}

Figure 6 illustrates the return loss (S_{11}) plot of the UWB antenna for different values of parameter W_{p1} . It can be seen that the resonance frequency, upper cutoff

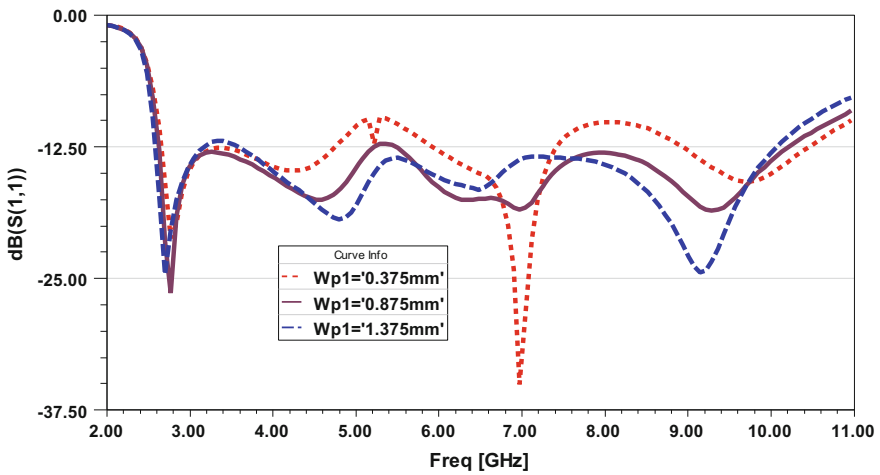


Fig. 6 Simulated return loss against frequency for the proposed antenna with varying ground slot parameter W_{p1} ; other parameters are same as in Fig. 1

Frequency and operating bandwidth depend on this parameter. The optimized value of $Wp1$ was found to be 0.875 mm.

3.5 Parametric Study of the Effects of Variation of the Ground Slot Parameter $Lp1$

Figure 7 illustrates the return loss (S_{11}) plot of the UWB antenna for different values of parameter $Lp1$. It can be seen that the upper cutoff frequency depends on this parameter. The optimized value of parameter $Lp1$ was found to be 19 mm.

3.6 Parametric Study of the Effects of Variation of the Ground Slot Parameter $Wp2$

Figure 8 illustrates the return loss (S_{11}) plot of the UWB antenna for different values of parameter $Wp2$. It can be seen that the resonance frequency depends on this parameter. The optimized value of parameter $Wp2$ was found to be 4.5 mm.

3.7 Parametric Study of the Effects of Variation of the Ground Slot Parameter $Lp2$

Figure 9 illustrates the return loss (S_{11}) plot of the UWB antenna for different values of parameter $Lp2$. It can be seen that the resonant frequency depends on this parameter. The optimized value of parameter $Lp2$ was found to be 6.25 mm.

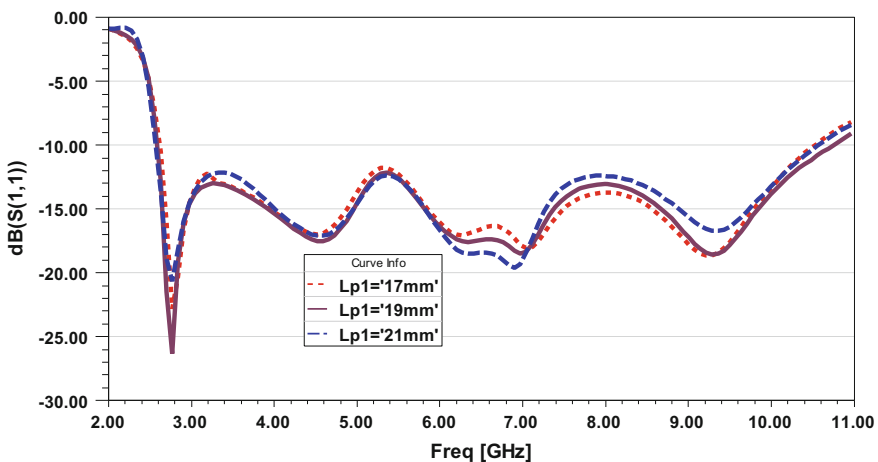


Fig. 7 Simulated return loss against frequency for the proposed antenna with varying slot parameter $Lp1$; other parameters are same as in Fig. 1

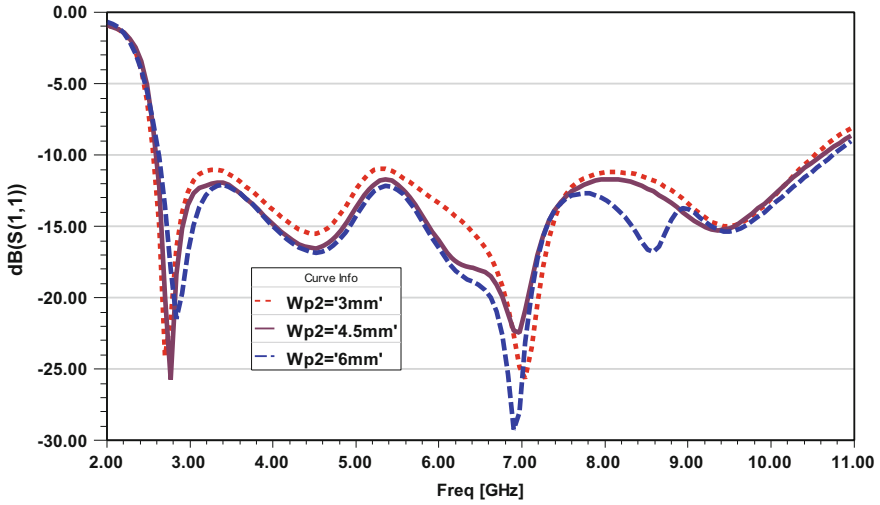


Fig. 8 Simulated return loss against frequency for the proposed antenna with varying ground slot parameter $Wp2$; other parameters are same as in Fig. 1

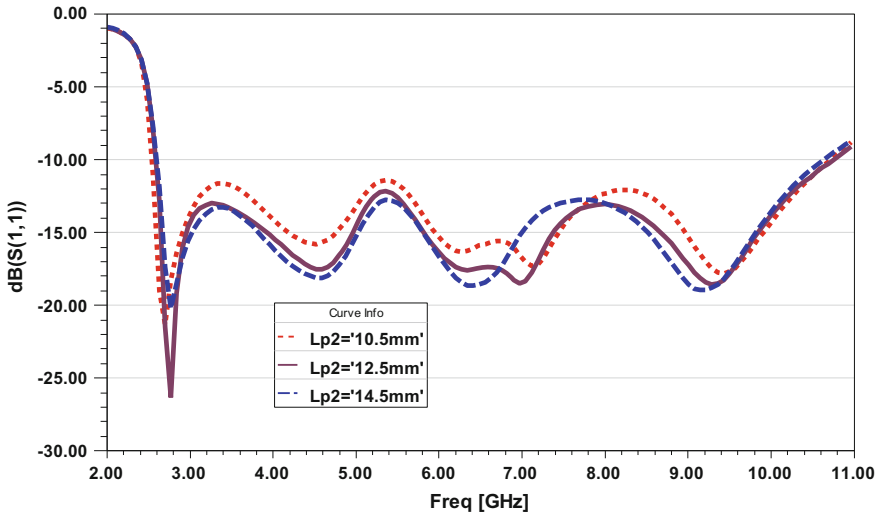


Fig. 9 Simulated return loss against frequency for the proposed antenna with varying slot parameter $Lp2$; other parameters are same as in Fig. 1

3.8 Parametric Study of the Effects of Variation of the Parasitic Element Parameter W_3

Figure 10 illustrates the return loss (S_{11}) plot of the UWB antenna for different values of parameter W_3 . It can be observed that the lower cutoff frequency, upper cutoff frequency and resonant frequency depend on this parameter. The optimized value of parameter W_3 was found to be 6 mm.

3.9 Parametric Study of the Effects of Variation of the Parasitic Element Parameter L_3

Figure 11 illustrates the return loss (S_{11}) plot of the UWB antenna for different values of parameter L_3 . It can be seen that the resonance frequency depends on this parameter. The optimized value of parameter W_3 was found to be 14.5 mm.

3.10 The Optimized Structure

Figure 12 illustrates the return loss plot of the simulated optimized structure of the micro-strip feed slotted ground antenna which covers the UWB. Figure 13 illustrates the VSWR (1) plot of the simulated optimized structure of the micro-strip feed slotted ground antenna, which is less than 2 above the UWB.

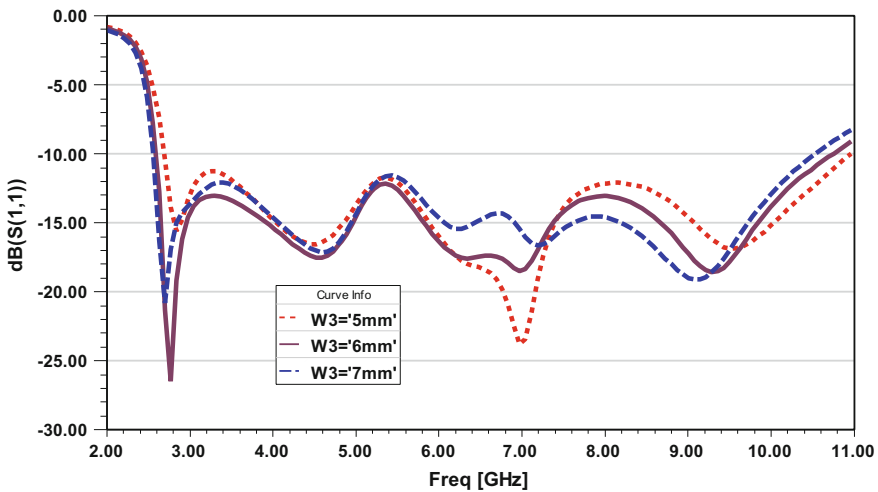


Fig. 10 Simulated return loss against frequency for the proposed antenna with varying parameter W_3 ; other parameters are same as in Fig. 1

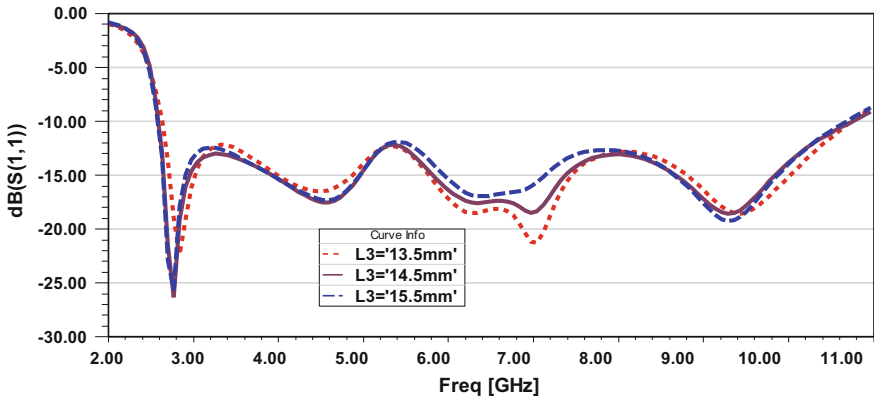


Fig. 11 Simulated return loss against frequency for the proposed antenna with varying parameter W_3 ; other parameters are same as in Fig. 1

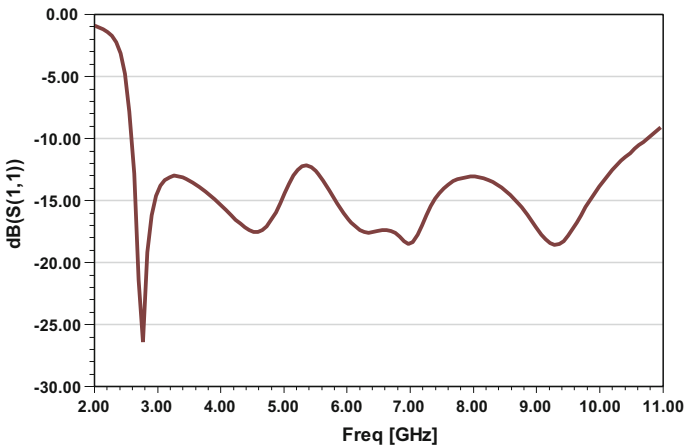


Fig. 12 Simulated return loss against frequency for the proposed optimized micro-strip feed slotted ground antenna

The radiation characteristics were also investigated. Figures 13, 14, 15, 16, 17, 18, 19 present the far field 10 dB normalized radiation patterns of the E plane and the H plane for the designed antenna at 2.7, 3.5, 4.31, 5.57, 6.55, 7.25, 9.7 and 10.54 GHz. The radiation pattern is directive for both E_plane and H_plane withing the whole frequency band. (Figs 20, 21, 22, 23).

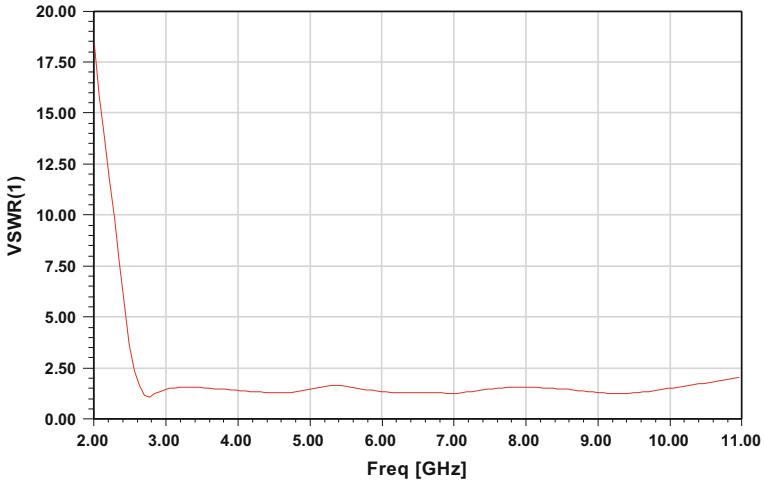


Fig. 13 Simulated VSWR against frequency for the proposed optimized micro-strip feed slotted ground antenna

Fig. 14 Radiation pattern for 2.7 GHz. Solid line shows E Plane ($\phi = 0^\circ$), Long dash shows H Plane ($\phi = 90^\circ$)

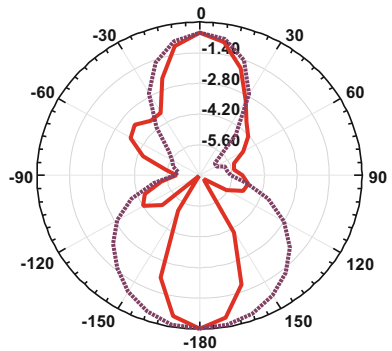


Fig. 15 Radiation pattern for 3.4 GHz. Solid line shows E Plane ($\phi = 0^\circ$), Long dash shows H Plane ($\phi = 90^\circ$)

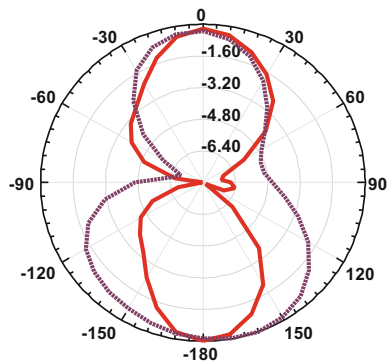


Fig. 16 Radiation pattern for 4.31 GHz. Solid line shows E Plane ($\phi = 0^\circ$), Long dash show H Plane ($\phi = 90^\circ$)

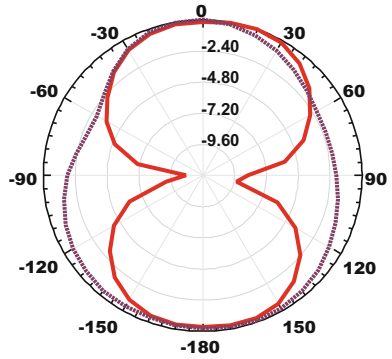


Fig. 17 Radiation pattern for 5.57 GHz. Solid line show E Plane ($\phi = 0^\circ$), Long dash shows H Plane ($\phi = 90^\circ$)

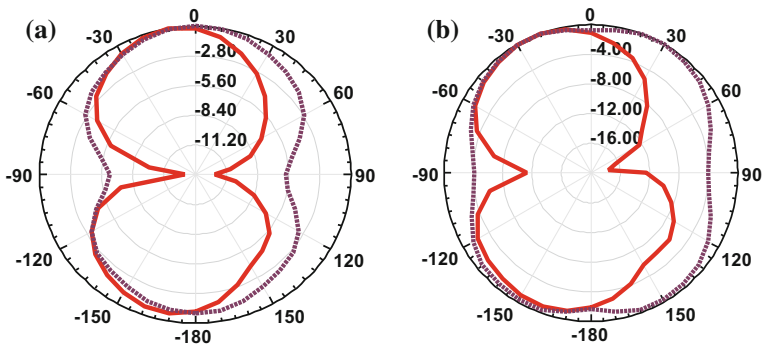
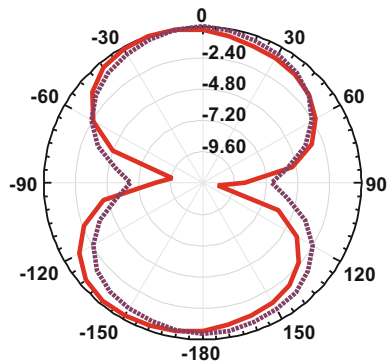


Fig. 18 **a** Radiation pattern for 6.55 GHz. Solid line shows E Plane ($\phi = 0^\circ$), Long dash shows H Plane ($\phi = 90^\circ$). **b** Radiation pattern for 7.25 GHz. Solid line shows E Plane ($\phi = 0^\circ$), Long dash shows H Plane ($\phi = 90^\circ$)

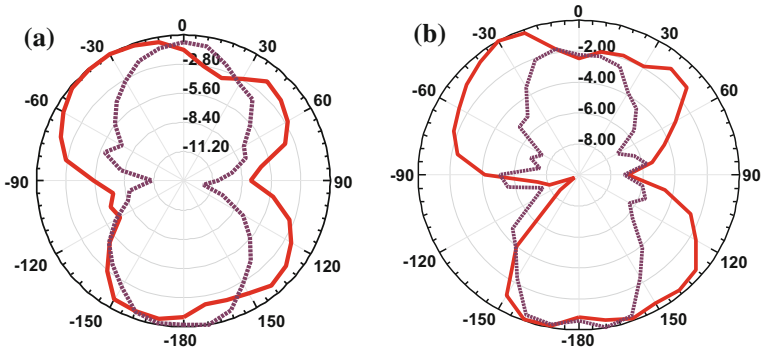


Fig. 19 **a** Radiation pattern for 9.7 GHz. Solid line shows E Plane ($\phi = 0^\circ$), Long dash shows H Plane ($\phi = 90^\circ$). **b** Radiation pattern for 10.54 GHz. Solid line shows E Plane ($\phi = 0^\circ$), Long dash shows H Plane ($\phi = 90^\circ$)

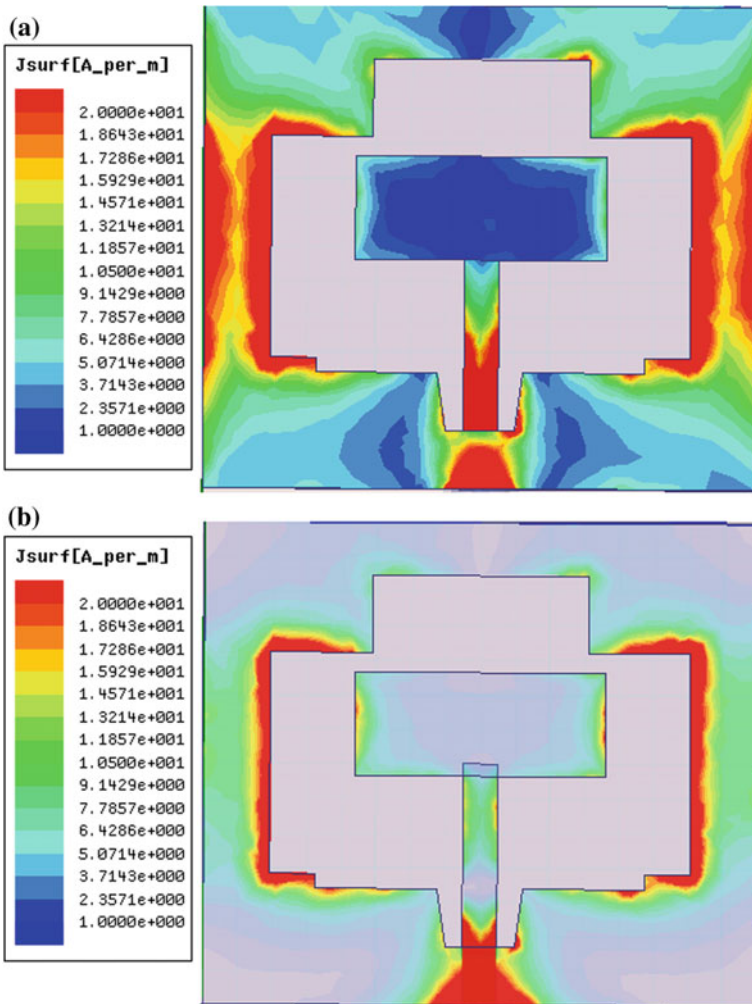


Fig. 20 **a** 3.3 GHz. **b** 4.3 GHz

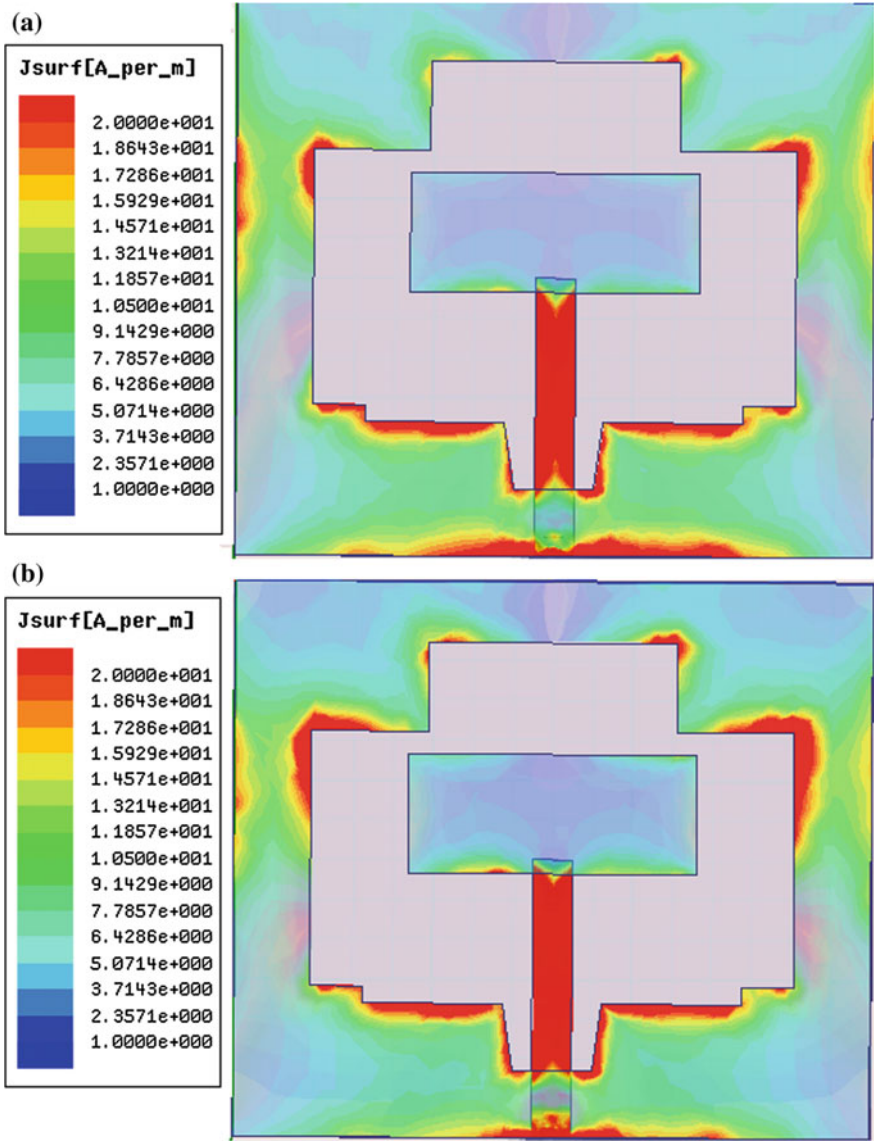


Fig. 21 a 5.1 GHz. b 6.06 GHz

Figure 30 shows the current density at different frequencies on the micro-strip feed line, parasitic element and slotted ground. At 3.3 GHz and 10.4 GHz the current density is concentrated on the slotted ground, parasitic element and feed line but for the remaining frequency current density is high on the feed-line and slotted ground compared to the parasitic element (Figs. 24, 25, 26, 27, 28, 29, 30).

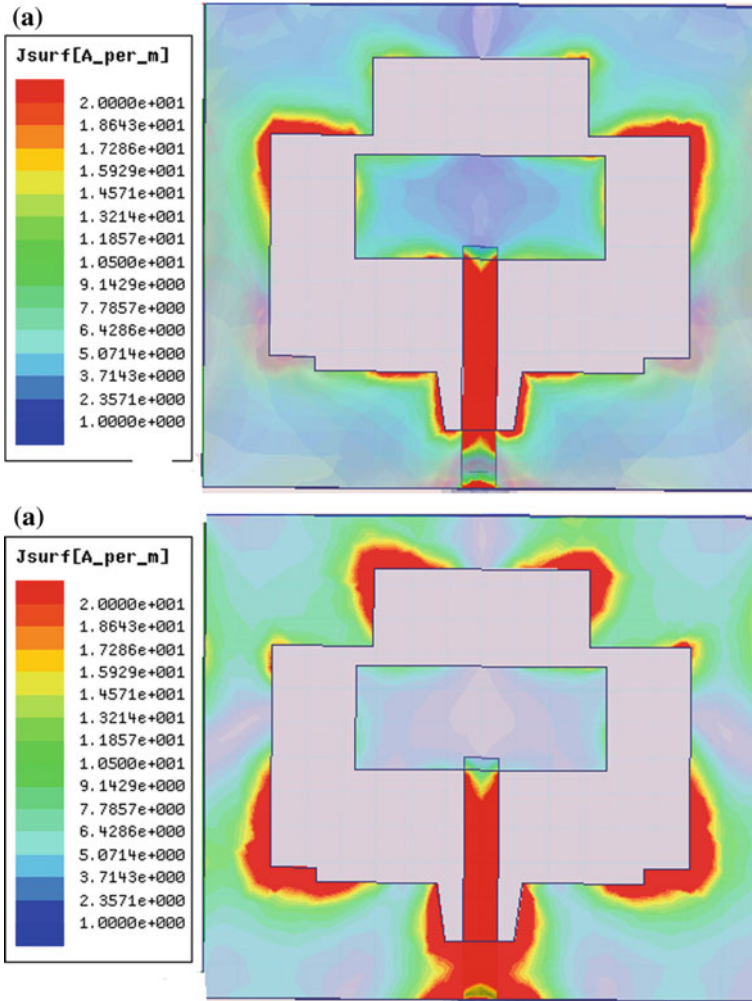


Fig. 22 a 7 GHz. b 8 GHz

Figures 24, 25, 26, 27, 28, 29, 30 show the total gain for different frequencies. At frequency 3.05 GHz, the total gain is maximum for $\theta = 180^\circ$. At frequency 7, 4.1 and 10.4 GHz the total gain is maximum for $\theta = 0^\circ$ and $\theta = 180^\circ$. At frequency 5.5 GHz total gain is maximum for all values of θ .

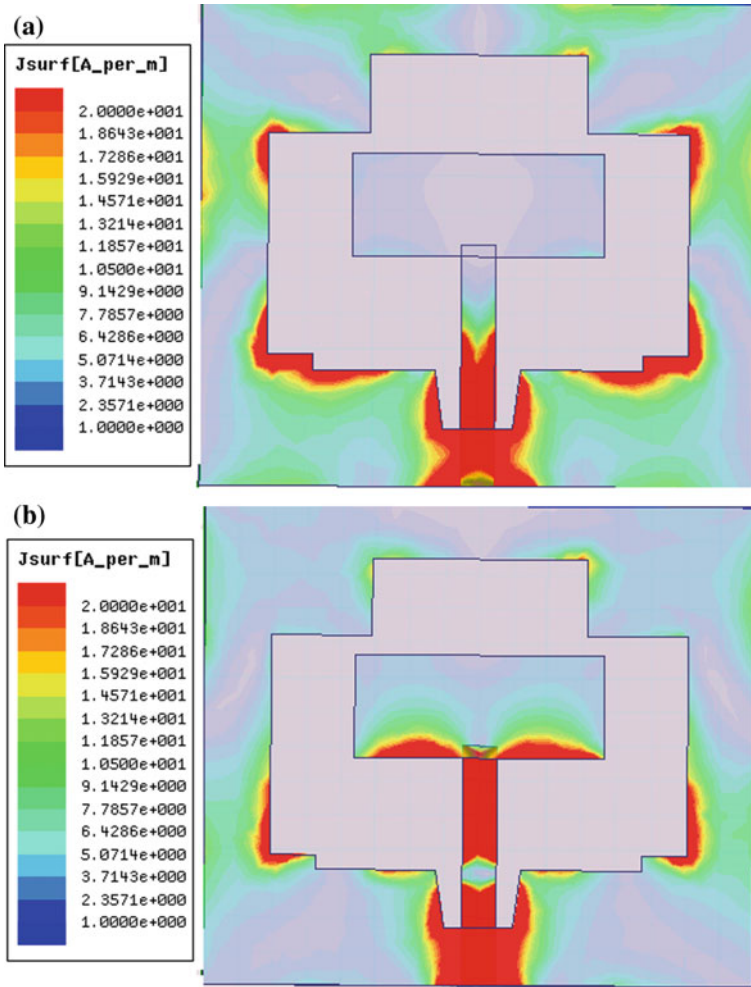


Fig. 23 a 9 GHz. b 10.4 GHz

Fig. 24 Gain Total in dB at 3.05 GHz

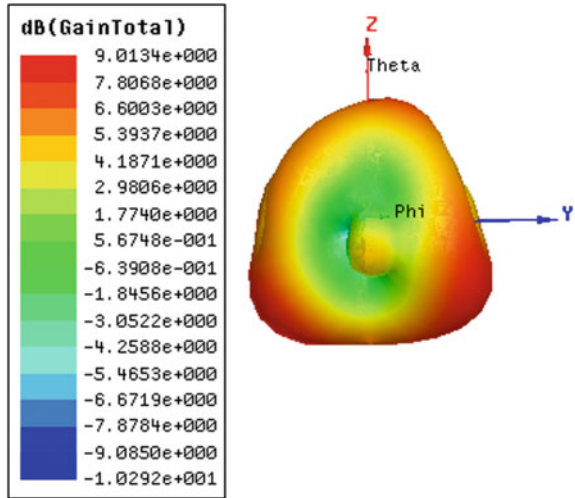


Fig. 25 Gain Total in dB at 4.1 GHz

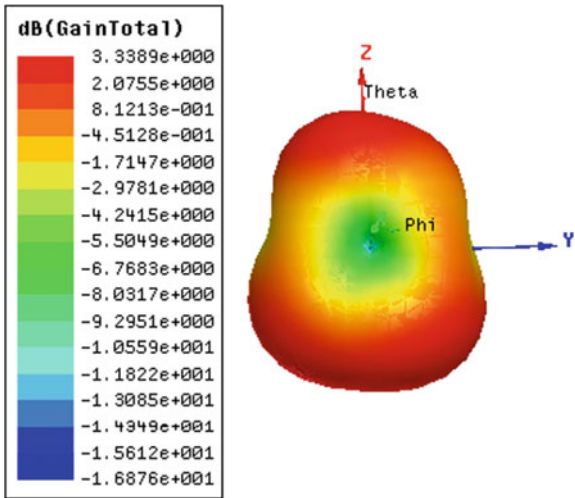


Fig. 26 Gain Total in dB for at 5.5 GHz

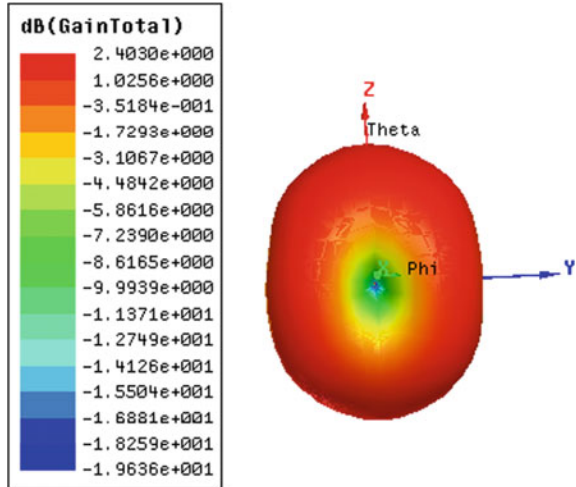


Fig. 27 Gain Total in dB at 7 GHz

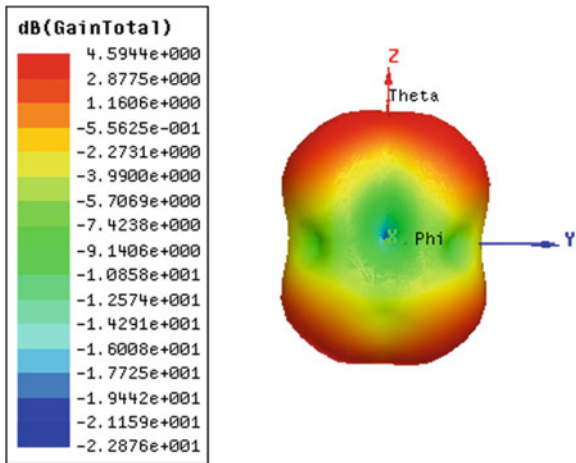


Fig. 28 Gain Total in dB at 8.3 GHz

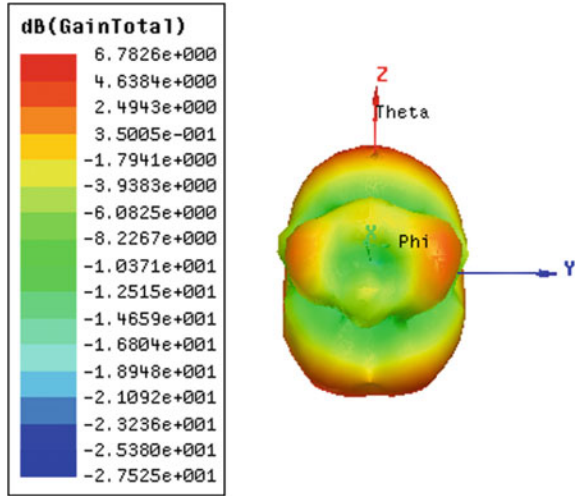


Fig. 29 Gain Total in dB at 9.28 GHz

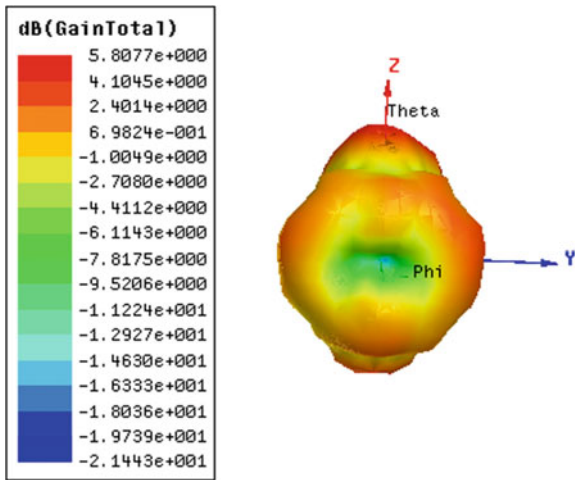
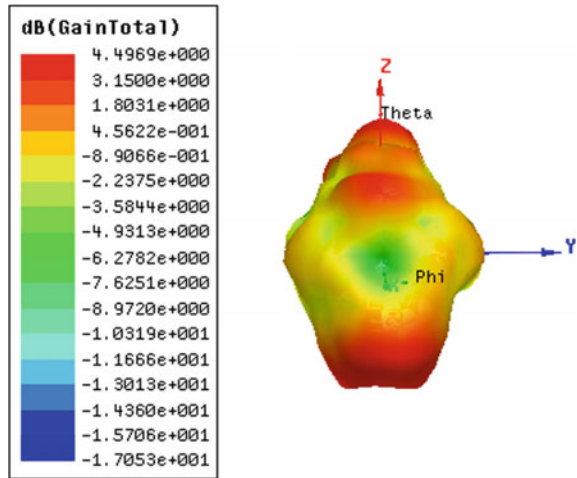


Fig. 30 Gain Total in dB at 10.4 GHz



4 Conclusion

A micro-strip feed slotted ground antenna was proposed and demonstrated in this study. According to the simulation results, the UWB band can be obtained by properly selecting the variable parameters of the antenna and optimizing the values. The return loss is below -10 dB for the whole band and the radiation pattern was monitored within the band and showed an acceptable omnidirectional pattern.

References

1. Ranga Y, Esselle KP, Weily AR (2010) Compact ultra-wideband CPW-fed printed semicircular slot antenna. *Microw Opt Technol Lett* 52(10):2367–2372
2. Liu WC (2005) Broadband dual-frequency cross-shaped slot CPW fed monopole antenna for WLAN operation. *Microw Opt Technol Lett* 46(4):353–355
3. Shagar AC, Wahidabanu RSD (2010) New design of CPW fed rectangular slot antenna for ultra wideband applications. *Int J Electron Eng* 2(1):69–73
4. Lin SY, Wong KL (2001) A dual-frequency micro-strip line fed printed slot antenna. *Microw Opt Technol Lett* 28:373–375
5. Morioka T, Araki S, Hirasawa K (1977) Slot antenna with parasitic element for dual band operation. *Electron Lett* 33:2093–2094
6. Li P, Liang J, Chen X (2006) Study of printed elliptical/circular slot antennas for ultra wide band applications. *Trans Antennas Propag* 54(6):1670–1675
7. Gand Ma T, Tseng CH (2006) An ultra wide band coplanar waveguide-fed tapered ring slot antenna. *IEEE Trans Antennas Propag* 54(4):1105–1110
8. Bostani A, Denidni TA (2008) Design of a new ultra wideband antenna with band rejection in WLAN frequencies. In: 2008 IEEE antennas and propagation society international symposium

9. Lee KF, Luk KM, Tong KF et al (1977) Experimental and simulation studies of the coaxially fed U-slot rectangular patch. *IEEE Proc Microw Antenna Propag* 144(5):354–358
10. Habib MA et al (2010) Ultra wideband CPW-fed aperture antenna with WLAN band rejection. *Progress Electromagn Res* 106:17–31
11. Bostani A, Webb JP (2011) A sparse finite-element method for modeling evanescent modes in the stopband of periodic structures. *IEEE Trans Magn* 47(5):1186–1189
12. Bostani A, Webb JP (2011) A model-order reduction method for the passband and stopband characteristics of periodic structures. In: 2011 41st European microwave conference, Manchester, pp 167–170

Bee-Comb-Shape Left-Handed Metamaterial for Terahertz Application

Md. Mehedi Hasan, Mohammad Rashed Iqbal Faruque,
Mohammad Tariqul Islam and Sikder Sunbeam Islam

Abstract A bee-comb-shaped left-handed metamaterial for terahertz frequency applications is presented in this paper. The proposed metamaterial is designed on an epoxy resin composite with woven glass fiber in a complex structure and is driven by the average connectivity of the metallic strips formed in a honeycomb shape. The finite integration technique-based electromagnetic simulator Computer Simulation Technology Microwave Studio was used to design simulation purpose of the proposed design. The structure exhibits resonance at 36.82, 57.71 and 74.23 THz and left-handed characteristics at 81.79 THz, whereas the electromagnetic waves are propagated along the z-direction. The structure was also analyzed by propagating the electromagnetic waves in the x- and y-directions through the metamaterial structure to observe the rotation effects of the direction of wave propagation on the reflection and transmission coefficients.

1 Introduction

Metamaterials are artificially structured sub-wavelength elements that manipulate light differently to other natural materials. These materials achieve their electromagnetic properties from their geometry rather than their chemistry or band structures. Moreover, metamaterials have attracted increasing attention due to their exotic electromagnetic properties that do not occur in nature such as negative refractive index, invisibility, perfect lensing, and perfect absorbing. In addition, metamaterials have been used to facilitate a wide range of applications including in satellites, microwave filter applications, optics lenses, electromagnetic cloaks,

Md. Mehedi Hasan (✉) · M.R.I. Faruque · S.S. Islam
Space Science Centre (ANGKASA), Institute of Climate ChangeUniversiti
Kebangsaan Malaysia, 43600 Bangi, Selangor Darul Ehsan, Malaysia
e-mail: mehedi20.kuet@gmail.com

M.T. Islam
Department of Electrical, Electronics and Systems Engineering, Universiti
Kebangsaan Malaysia, 43600 Bangi, Malaysia

electromagnetic absorption, hyper-spectral imaging, medical imaging, SAR reductions, energy harvesting, and high power applications, etc. In 2000, Smith et al. [1] presented a material that showed negative permittivity and permeability at the same time with some unique properties. In 2003, Ziolkowski et al. [2] developed a metamaterial with capacitor loaded strips and split ring resonators, which exhibited negative both permittivity and permeability at X-band frequencies. In 2015, Galinski et al. [3] suggested a new complex structures were driven by the average connectivity of the metallic network to focus on the use of metallic nano-scale networks, sustaining plasmonic resonances. At variance with classical meta-surfaces, which are mostly lattice-based structures, the key element of the network architecture was the local connectivity between different elements. In 2016, Hasan et al. [4] proposed a compact z-shaped double negative metamaterial for wideband applications. The $10 \times 10 \text{ mm}^2$ structure of the metamaterial unit cell was suitable for C- and X-band operations and the effective medium ratio was 4. In 2016, Faruque et al. [5] presented a compact square split z-shaped meta-atom with left-handed features, and wide bandwidth for S-, C-, X- and Ku-band applications. The presented meta-atom was investigated at 0° , 15° , 30° , 45° , 60° , 75° and 90° (xy-axis) rotation angles. The designed structure showed resonances at the S-, C-, X-, and Ku-bands with 5.67 GHz wide bandwidth. The compact meta-atom had an effective medium ratio of 9.1 and exhibited left-handed characteristics at 8.50 GHz. In 2017, Hasan et al. presented a metamaterial structure that was a combination of split-ring and square-shaped split-ring resonators and had an effective medium ratio of 8.90. The proposed structure showed resonance at 3.36, 5.98, 9.83, and 13.10 GHz with negative index characteristics at 8.25 GHz [6]. In 2016 Mulla et al. [7] presented a design composed of three layers in which the interaction among them gave rise to plasmonic resonances for the harvesting of solar energy in the visible frequency regime. It was found that the proposed metamaterial absorber had 98.2% absorption capability at 445.85 THz and 99.4% absorption capability between 624 and 658.3 THz. In 2017, a negative index metamaterial with two component analysis for the C- and X-bands was presented by Islam et al. [8]. The structure had two arrows and a metal arm that connected the two arrows and looked like a double-arrow shape printed on the epoxy resin fiber. The epoxy resin formation processes were also explained step by step. In 2017, a broadband terahertz metamaterial absorber was developed, in which the unit cell was made up of two circular split rings, a dielectric substrate and a metallic ground was presented by Pan et al. [9]. The simulation results showed that the absorber achieved a broadband absorption from 0.85 to 1.926 THz with an absorptivity beyond 90% at normal incidence, and the bandwidth was 1.076 THz. Sreekanth et al. [10] suggested a coupled hyperbolic perfect absorber for high flexibility in electromagnetic absorption and applicable for polarization independence, wide angle range, and both broadband and narrowband modes, etc. The absorption spectra of Pd-GC HMM for different angles of incidence (30 to 60 degrees) showed above 98% absorption. Zhong et al. [11] in 2017, proposed a simple multiple-metal metamaterial perfect absorber. The size of the proposed design was only 221 nm for the visible wavelength range from 400 to 700 nm. A titanium (Ti), nickel (Ni), and

aluminum (Al) triple-metal configuration was used to demonstrate the concept experimentally. Hu et al. [12] in 2016, presented a six-band terahertz perfect metamaterial absorber composed of a metal U-shaped closed-ring resonator, a dielectric spacer, and a metal back plate. The results demonstrated that it can be performed absorption peaks at six resonant frequencies with average peaks of 97.3%.

In this paper, a honeycomb-shaped metamaterial at terahertz frequency is proposed, which exhibits resonance at 36.82, 57.71 and 74.23 THz. The metamaterial shows left-handed characteristics at 81.79 THz, whereas the permittivity, permeability and refractive index are -0.37 , -43.64 and -5.16 respectively, when the electromagnetic waves are propagated in the z-direction through the metamaterial structure. The designed structure was also investigated by incident the electromagnetic waves along the x- and y-direction pass through the metamaterial in order to observe the direction of wave propagation effects on the result of the reflection and transmission coefficients. The paper is arranged as follows: In Sect. 2, the methodology is explained in detail with a schematic view, simulation process, retrieval methods of the effective medium parameters and an equivalent circuit model of the proposed metamaterial. The results are analyzed in Sect. 3 and the effects of wave propagation along the x-, y- and z-axes on the scattering parameters are also explained. Finally, Sect. 4 concludes the paper.

2 Methodology

The proposed honeycomb-shaped metamaterial is developed by a complex structure, which is driven by the average connectivity of the metallic strips formed a honeycomb-like shape. Epoxy resin fibre is used as substrate material, in which the dielectric constant and loss tangent are 4.5 and 0.002 respectively. The thickness of the substrate material is considering as $0.1 \mu\text{m}$. The total dimensions of the designed metamaterial structure are $5.1 \times 5 \mu\text{m}^2$, whereas the small single unit cell is $1.0 \times 0.85 \mu\text{m}^2$. The schematic view, top view and the 3D view of the proposed metamaterial structures are shown in Fig. 1a-c (Table 1).

Finite integration technique was applied in the simulation of the mentioned metamaterial, which helped to compute the scattering constitutive parameters. This is a spatial discretization method used to solve electromagnetic field problems numerically in both frequency and time domains. The commercially available CST Microwave Studio was adopted for all the numerical investigations. Boundary conditions were used in most computer simulations to speed up the computation process. The electromagnetic waves were propagated along the z-axis, whereas the x-axis and the y-axis were considered as a perfect electric and magnetic boundary respectively. A frequency domain solver with a standardized impedance of 50Ω was set for simulation from 0 to 100 THz as shown in Fig. 2a. Moreover, the retrieving procedure of the effective parameters is given as follows [13, 14],

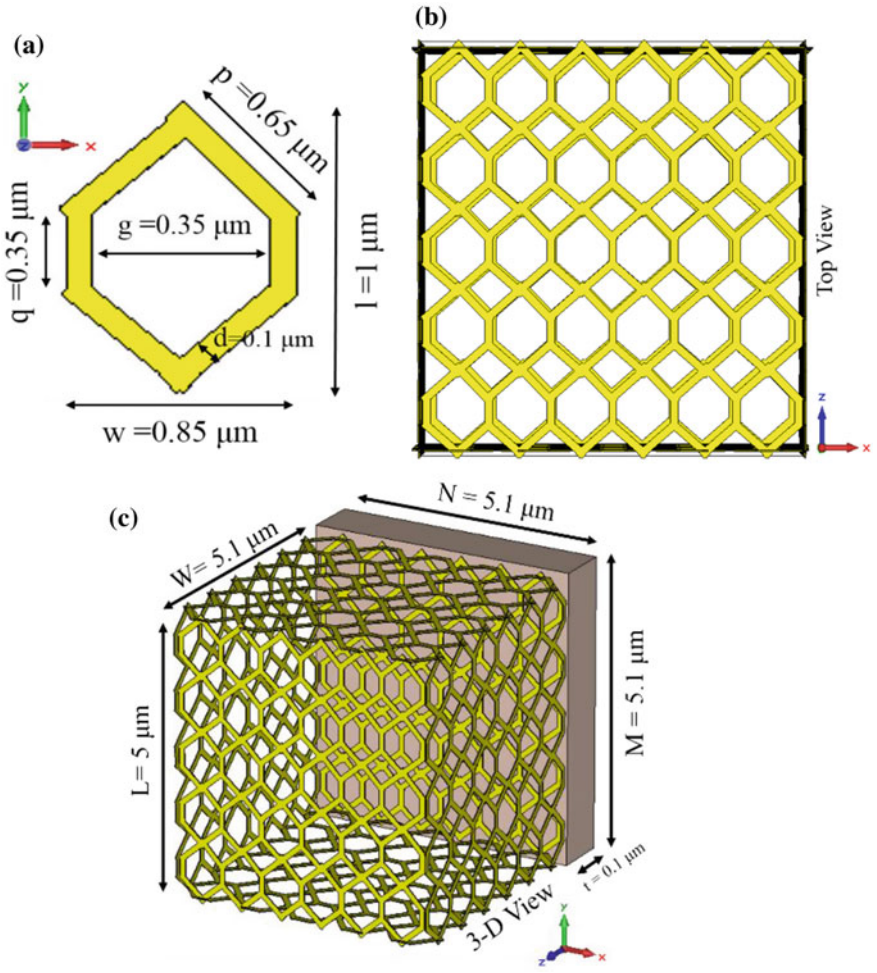


Fig. 1 Schematic view of: **a** single unit cell, **b** top view of the designed structure, and **c** 3D view of the proposed honeycomb-shaped metamaterial structure

Table 1 Design specification of the proposed network structure

Parameters	L	W	p	q	M	N
Dimensions (μm)	5.0	5.1	0.65	0.35	5.1	5.1
Parameters	L	w	d	g	t	h
Dimensions (μm)	1.0	0.85	0.1	0.35	0.1	0.017

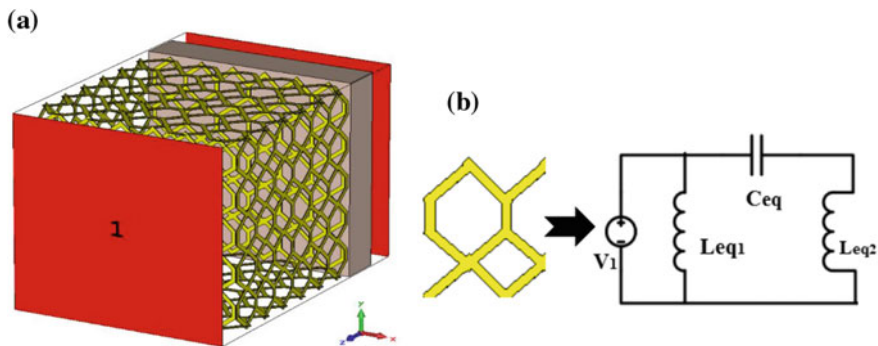


Fig. 2 **a** Simulated view with boundary condition in the CST-MWS in the z -direction of wave propagation, **b** equivalent lumped circuit model of the honeycomb-shaped metamaterial structure

$$\text{Impedance, } Z_{\text{eff}} = \pm \left(\frac{(1 + S_{11})^2 - S_{21}^2}{(1 - S_{11})^2 - S_{21}^2} \right)^{1/2} \quad (1)$$

$$\text{Refractive Index, } n_{\text{eff}}(\omega) \approx n'_{\text{eff}}(\omega) + ik_{\text{eff}}(\omega) \quad (2)$$

$$n_{\text{eff}} \approx \frac{1}{k_0 d} \{ \text{Im}[\text{In}(e^{iN_{\text{eff}}k_0 d})] + 2m\pi - i\text{Re}[\text{In}(e^{iN_{\text{eff}}k_0 d})] \} \quad (3)$$

$$n'_{\text{eff}}(\omega) \approx \frac{1}{k_0 d} \{ \text{Im}[\text{In}(e^{iN_{\text{eff}}k_0 d})] + 2m\pi \} \quad (4)$$

$$k_{\text{eff}}(\omega) \approx -\frac{1}{k_0 d} \{ \text{Re}[\text{In}(e^{iN_{\text{eff}}k_0 d})] \} \quad (5)$$

$$\text{Permittivity, } \varepsilon_{\text{eff}} \approx \frac{n_{\text{eff}}}{Z_{\text{eff}}} \quad (6)$$

$$\text{Permeability, } \mu_{\text{eff}} \approx n_{\text{eff}} \times Z_{\text{eff}} \quad (7)$$

The equivalent circuit of the proposed metamaterial structure unit cell is shown in Fig. 2b, where C_{eq} , L_{eq} , V_1 represent capacitance, inductance and external source of the lumped circuit model respectively. Moreover, metal strips are formed inductive effects, whereas the gaps are accountable for the capacitive effect [15, 16].

3 Analysis of Results

Surface current distribution is shown in Fig. 3a, where the opposite current is flowing in the two opposite side arrow of the honeycomb structure. The arrows show the directions of the current and the colour express the intensity. However, the

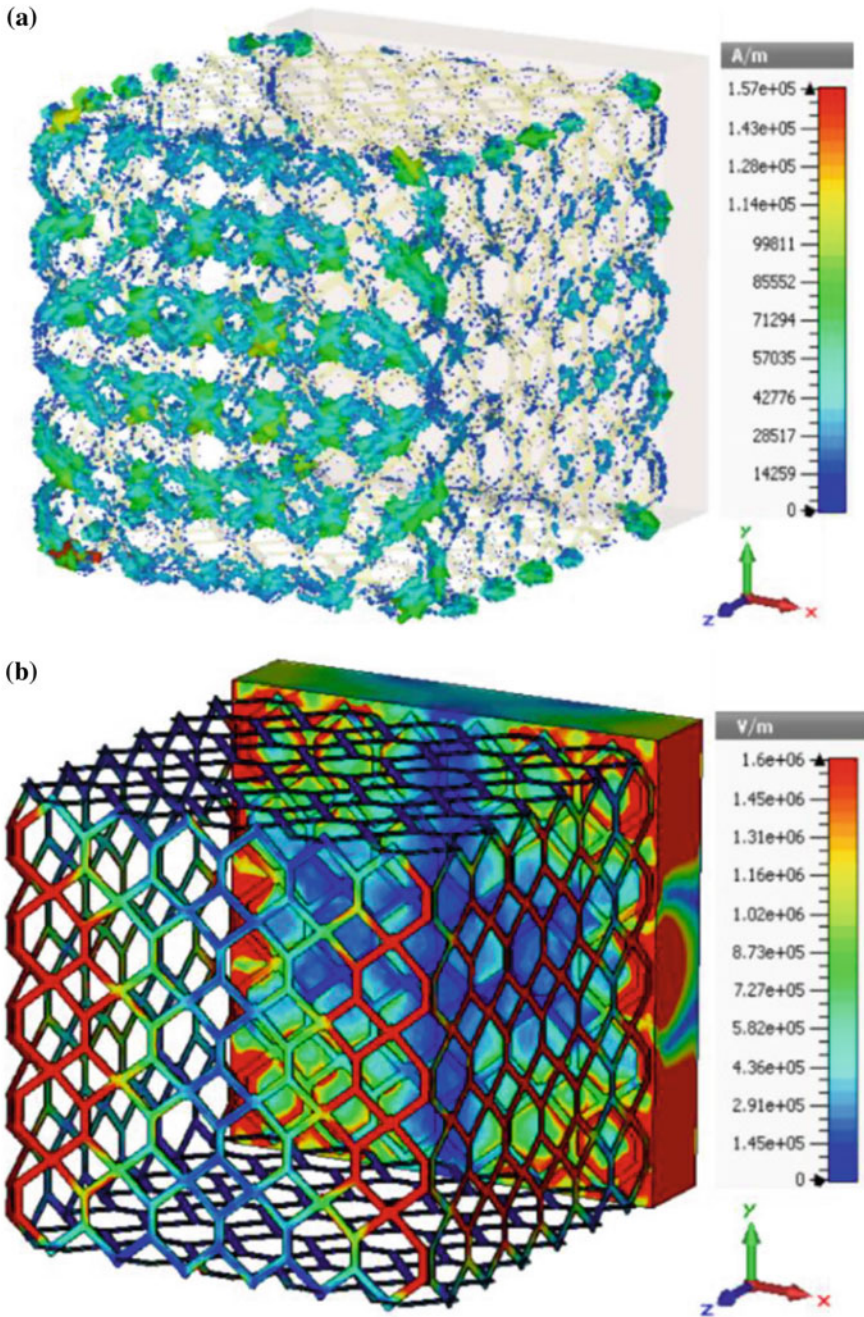


Fig. 3 a Surface current distribution, b Electric field distribution at 36.82 THz

current is flowing in opposite directions nullify each other at a certain frequency and establish the stop band. The electric field density at 36.82 THz is shown in Fig. 3b.

In Fig. 4a, the transmission (S_{21}) and reflection (S_{11}) coefficients for the proposed metamaterial are shown. It demonstrates that the extent of transmission coefficient display resonance frequencies at 36.82, 57.71 and 74.23 THz. The obtained permittivity (ϵ) and permeability (μ) against frequency are depicted in Fig. 4b and c separately. In the Fig. 4b, the real magnitude of the permittivity displays a negative value from 1.0 to 22.29 THz, and 26.47 to 82.78 THz and the permeability curves show a negative region from 22.69 to 26.10 THz and 81.6 to 92.54 THz in Fig. 4c. Figure 4d depicts the refractive index of the material, and the curve displays a negative peak from 26.47 to 31.84 THz, 49.6 to 61.29 THz and 67.66 to 85.77 THz. Moreover, at 81.79 THz frequency zones of the refractive index curve, permeability curve and permittivity curve also display a negative peak. This is why the material can be characterized as a left-handed metamaterial in this region (Table 2).

Further analysis was done on the honeycomb-shaped metamaterial by placing it at the x- and y-axes and propagating the electromagnetic waves through the metamaterial in those directions. The electromagnetic waves were propagating through the metamaterial along the x-axis as in Fig. 5a. The resonances of the transmission (S_{21}) coefficient are 16.82 THz (magnitude of -40.38 dB) and

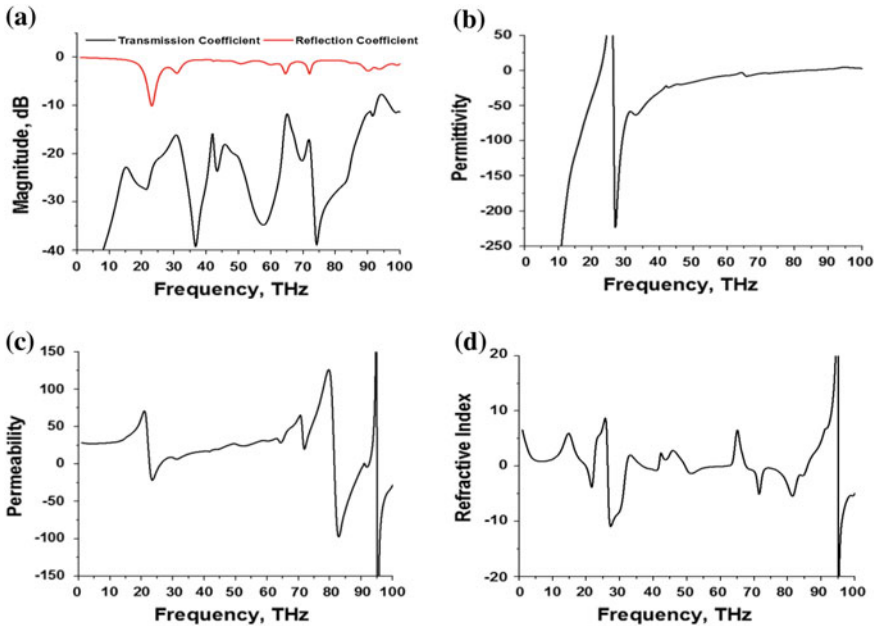


Fig. 4 Results of: **a** Reflection and transmission coefficients, **b** Effective permittivity, **c** Effective permeability, and **d** Effective refractive index, of the proposed metamaterial with wave propagation in the z-direction

Table 2 Value of effective medium parameters for the left-handed characteristics

Resonance frequency	Permeability (μ)	Permittivity (ϵ)	Refractive index (η)
81.79 THz	-0.37	-43.64	-5.16

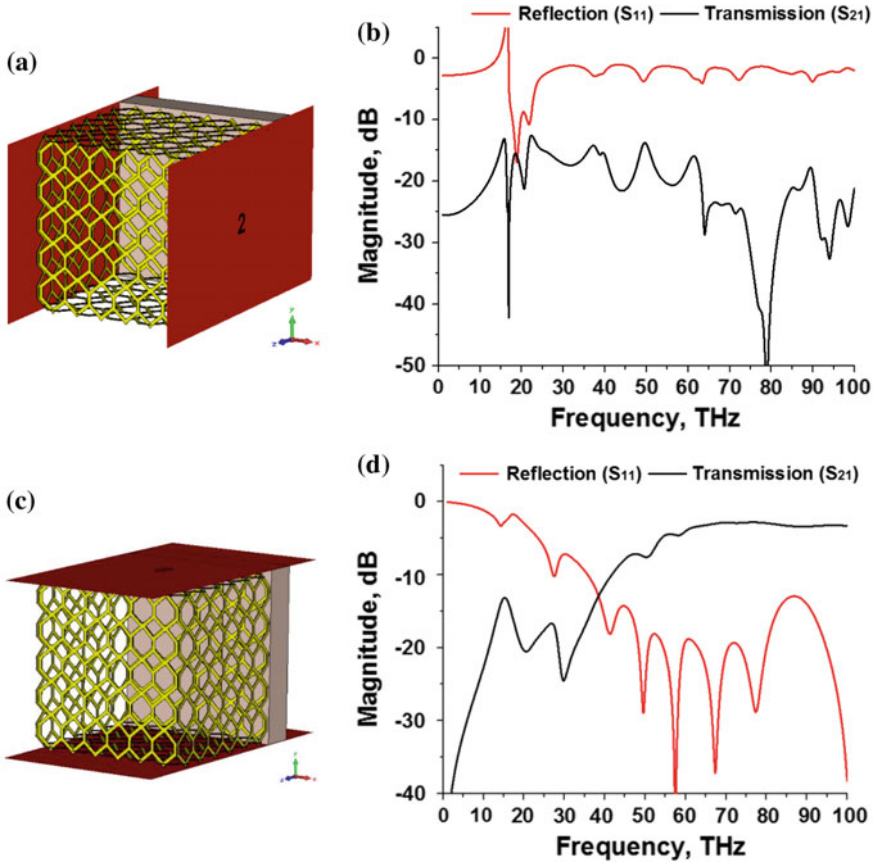


Fig. 5 **a** Simulated view with boundary condition at the x-axis, **b** Reflection and transmission coefficient amplitude with wave propagation in the x-direction, **c** Simulated view with boundary condition at the y-axis, **d** Reflection and transmission coefficient amplitude of the proposed metamaterial with wave propagation in the y-direction

78.89 THz (magnitude of -65.66 dB) as shown in Fig. 5b. In addition, from Fig. 5c, the electromagnetic waves were propagated through the proposed structure in the y-direction and the results are displayed in Fig. 5d, where the resonances of the transmission (S_{21}) coefficient are 20.26 (magnitude of -20.49 dB) and 30.24 THz (magnitude of -24.11 dB).

4 Conclusion

A new honeycomb-shaped left-handed metamaterial is presented for terahertz frequency applications. The metamaterial exhibits left-handed characteristics for z-axis wave propagation at 81.79 THz. The designed structure was also investigated by propagating the electromagnetic waves along the x- and y-axes to observe the effects of the direction of wave propagation on the result of the reflection (S_{11}) and transmission (S_{21}) coefficients. The proposed structure is developed from the lumped model of inductance-capacitance resonators and could find a wide range of applications in terahertz absorption, terahertz cloaking, terahertz filter and optical applications, etc.

Acknowledgements This work was supported by the Research Universiti Grant, Geran Universiti Penyelidikan (GUP) with code: 2016-028.

References

1. Smith DR, Padilla WJ, Vier DC et al (2000) Composite medium with simultaneously negative permeability and permittivity. *Phys Rev Lett* 84:4184–4187
2. Ziolkowski RW (2003) Design fabrication and testing of double negative metamaterials. *IEEE Trans Antennas Propag* 51:1516–1529
3. Galinski H, Fratolocchi A, Capasso F (2016) Network metamaterials an alternative platform for optical materials. In: *Meta Conference Spain*, July 2016
4. Hasan MM, Faruque MRI, Islam SS et al (2016) A new compact double-negative miniaturized metamaterial for wideband operation. *Materials* 9(10):830
5. Faruque MRI, Hasan MM, Islam MT (2016) Wideband 90° azimuthal miniaturized meta atom with left-handed characteristics. *IEEE Antennas Wirel Propag Lett*. doi:[10.1109/LAWP.2016.2624757](https://doi.org/10.1109/LAWP.2016.2624757)
6. Hasan MM, Faruque MRI, Islam MM et al (2017) Multi band negative index metamaterial based on split square shape resonators. Paper presented at 19th International Conference on Computer and Information Technology ICCIT Bangladesh, pp 99–102
7. Mulla B, Sabah C (2016) Multiband metamaterial absorber design based on plasmonic resonances for solar energy harvesting. *Plasmonics*. doi:[10.1007/s11468-015-0177-y](https://doi.org/10.1007/s11468-015-0177-y)
8. Islam SS, Hasan MM, Faruque MRI et al (2017) Two components NRI metamaterial for dual band applications. *Microw Opt Technol Lett* 59:1092–1096
9. Pan W, Yu X, Zhang J, Zeng W (2017) A broadband terahertz metamaterial absorber based on two circular split rings. *IEEE J Quantum Electron* 53:8500206
10. Sreekanth KV, Alapan Y, Rashed AR et al (2016) A multiband perfect absorber based on hyperbolic metamaterials. *Sci Rep* 6:26272
11. Zhong YK, Fu SM, Tu MH, Chen BR, Lin A (2016) A multimetal broadband metamaterial perfect absorber with compact dimension. *IEEE Photonics J* 8:6801810
12. Hu D, Wang HY, Zhu QF (2016) Design of six-band terahertz perfect absorber using a simple u-shaped closed-ring resonator. *IEEE Photonics J* 8:5500608
13. Szabo Z, Park GH, Hedge R et al (2010) A unique extraction of metamaterial parameters based on kramers–krönig relationship. *IEEE Trans Microw Theory Tech* 58(10):2646–2653
14. Hasan MM, Faruque MRI, Islam MT (2017) Multiband left handed biaxial meta atom at microwave frequency. *Mater Res Express* 4:035015

15. Hasan MM, Faruque MRI, Islam MT (2017) A single layer negative index meta atom at microwave frequencies. *Microw Opt Technol Lett* 59:1450–1454
16. Hasan MM, Faruque MRI, Islam MT (2017) A mirror shape chiral meta atom for c-band communication. *IEEE Access*. doi:[10.1109/ACCESS.2017.2677463](https://doi.org/10.1109/ACCESS.2017.2677463)